This thesis has been accepted for the award of the degree in the Faculty of Engineering

To my most beloved dad and mom

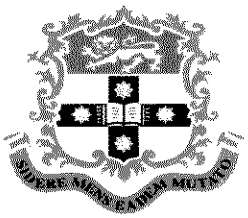

ELASTIC WAVE-BASED QUANTITATIVE DAMAGE IDENTIFICATION TECHNIQUE USING ACTIVE SENSOR NETWORK

Zhongqing SU

B.S. (*1997*, Beijing University of Aeronautics & Astronautics, P.R. China)
M.E. (*2000*, Beijing University of Aeronautics & Astronautics, P.R. China)

A thesis submitted in fulfillment
of the requirements for the degree of
Doctor of Philosophy

Laboratory of Smart Materials & Structures (LSMS)
Centre for Advanced Materials Technology (CAMT)
School of Aerospace, Mechanical & Mechatronic Engineering (AMME)
The University of Sydney

February 2004

Acknowledgments

No work is done in isolation and the preparation of this thesis is no exception. I would like to sincerely thank all the people who have given their invaluable assistances during my pursuit of the degree of Doctor of Philosophy at the *School of Aerospace, Mechanical and Mechatronic Engineering, University of Sydney*. First of all, my most pure-hearted appreciation goes to my supervisor, Professor Lin YE, for his meticulous supervision and measureless encouragement throughout my study. He has always believed in my abilities and has provided every opportunity to benefit my future professional career. It is guidance from such an eminent scholar with encyclopaedic knowledge that has made my study so enjoyable.

I wish to express my gratitude to all members at the *Centre for Advanced Materials Technology* (CAMT) for offering me such an outstanding academic environment. Special thanks should be addressed to my associate supervisor, Professor Yiu-Wing MAI. I am indebted to Dr. Xiongzhu Bu and Mr. Nao Huang for their indispensable contribution to hardware establishment and software development. My study has also greatly benefited from discussion with Dr. Xiaoming Wang and Dr. Meng Lu.

Dr. Meng Hou and Mr. Stephen Francesconi in CRC-ACS helped me greatly in specimen preparation. Important assistance also came from Dr. Zuorong Chen, Dr. Wenyi Yan, Dr. Xinping Zhang, Dr. Chen Yan and Mr. Hasso Nibbe. Without them, this thesis would have not been possible. Heartfelt appreciation also goes to all my office-mates, Ki-young Kim, Ye Lu, Kan Ding, Liling Yan and Choupani Naghdali, for so many unforgettable memories.

I am proud to have been the recipient of an *International Postgraduate Research Scholarship* (IPRS) from the *Department of Education Science and Training* (DEST),

Australia, an *International Postgraduate Award* (IPA) from the *University of Sydney*, and a supplementary scholarship from the *School of Aerospace, Mechanical and Mechatronic Engineering, University of Sydney*.

Finally, my utmost acknowledgement is reserved for my most beloved dad and mom, as well as my sister's family. It is their self-giving love that encourages me eternally.

Declaration of Originality

I hereby declare that no part of this work has previously been accepted for the award of any other degree in any university or institute. This thesis was completed during my enrolment for the degree of Doctor of Philosophy at the University of Sydney, and to the best of my knowledge the material presented is original except where due reference is made in the text of the thesis.

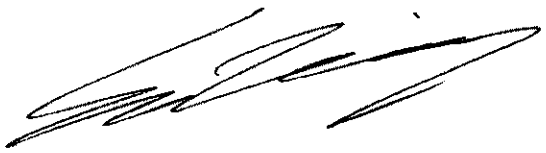

Zhongqing SU

Abstract

Though serving as competitive candidates to meet current and future challenges imposed on aeronautical vehicles, carbon fibre/epoxy (CF/EP) composite structures still run a considerable risk of losing efficiency as a result of structural damage, which can potentially lead to catastrophic failure of the whole system without timely detection. Cost-effective and reliable damage detection techniques are therefore critical for the confident acceptance of composite materials. This thesis presents an elastic wave-based quantitative damage identification technique and an active online structural health monitoring (SHM) system for in-service engineering structures made from metal alloys and CF/EP composite laminates.

Rigorous investigation into propagation characteristics of guided elastic waves in beams and plates, in particular Lamb waves in quasi-isotropic CF/EP laminates, and their interaction with common structural defects (crack, through-hole or delamination) was undertaken, via theoretical analyses, finite element method (FEM) simulation and experimental verification. A parameterised modelling technique (PMT) was developed to assist model creation for complicated structures. Results were analysed in the time–frequency domain, and it was seen that spectrographic characteristics of elastic waves in the time–frequency space are quantitatively sensitive to structural damage, offering the capability to detect damage exactly at its onset. Based on this observation, an elastic wave-based damage detection technique was developed.

During the study, it has been noticed that elastic wave signals are notoriously complicated in composite materials due to their unique dispersive features in viscoelastic substances. Under such a circumstance, traditional signal processing approaches cannot offer efficient identification for these wave signals. For this, an *Intelligent Signal Processing and Pattern Recognition* (ISPPR) technique, taking

advantages of wavelet transform and artificial neural algorithms, was developed. In this signal processing package, a concept of *Digital Damage Fingerprints* (DDF) was established, capable of extracting and digitising characteristics from wave signals to describe diverse forms of damage. Hosting DDF, Damage Parameters Databases (DPDs) for several typical damages were constructed, which were then used to train a feedforward artificial neural network (ANN), under supervision of an error-backpropagation (BP) neural algorithm, to achieve quantitative damage identification.

Supported by ISPPR, an *Active Online Structural Health Diagnosis* (AO-SHD) system, with active actuating/sensing networks involving distributed piezoelectric transducers, was configured on a *VXI* instrument platform following general industry standards. A *Standard Sensor Unit* (SSU) technique was introduced, by which transducer networks could be flexibly and expeditiously customised to accommodate diverse practical applications.

The proposed technique and AO-SHD system were then validated by identifying representative types of damage in metal alloy and CF/EP composite structures with increasing complexity, including transverse crack, through-hole and delamination. Diagnostic results showed excellent performance of the technique and system in selected case studies. Quantitative identification (presence, location, shape, size and orientation) for structural damage was achieved.

Recognised as an artificial intelligence (AI)-based *inverse* pattern recognition, the accuracy and feasibility of the damage detection technique can be subjected to a wide range of factors, such as ANN configuration, modelling precision, excitation condition, etc. The influence of these factors was also discussed. Finally, problematic issues to be dealt with in further study were considered.

Nomenclature

a	*Scale* variable in time-scale domain
b	*Time* variable in time-scale domain
$\vec{b}$	Bias vector of ANN
c_{ij}	Piezoelectric compliance constant
c_L	Wave velocity for longitudinal mode
c_T	Wave velocity for transverse mode
d	Thickness of laminate
d_{ij}	Piezoelectric strain constants
d_r	Equivalent radial elastic deformation of PZT sensor
f	Frequency
h_{PZT}	Thickness of PZT
$h(x)$	Hanning function
k	Wavenumber
l	Width of beam cross-section
$\vec{o}$	Output vector of ANN
p_i	Piezoelectric dielectric permittivity
p_0	Piezoelectric dielectric permittivity of free PZT sensor
$\vec{p}$	Input vector of ANN
u	Displacement field
u_θ	Tangential displacement
v_{wave}	Wave propagation velocity
w	Lateral displacement field
$\vec{w}$	Weight vector of ANN
$w(t)$	Filter function
x	x-coordinate of damage centre
y	y-coordinate of damage centre
A	Cross-section area

A_0	Fundamental anti-symmetric Lamb mode
C	Capacitance
C_{mn}	DWT coefficient
E	Elastic modulus
E_i	Electric field (voltage/length)
E_{PZT}	Elastic modulus of PZT
E_{LMT}	Elastic modulus of laminate
G	Shear modulus
H	Depth of beam cross-section
H_d	Depth of transverse crack
I	Moment of inertia
K	Iteration number of ANN training
K_3	Piezoelectric relative dielectric constant of free PZT transducer
P	Signal energy intensity
Q	Electric displacement (charge/area)
R	Radius
Ref	Reflection coefficient
S_0	Fundamental symmetric Lamb mode
S_{0ref}	Fundamental symmetric Lamb mode induced by boundary
S_0'	Fundamental shear mode
S'_{0Delam}	Fundamental shear mode induced by delamination
S_{ss}	Spectral densities of scatter signal
S_{bs}	Spectral densities of baseline signal
T	Transfer function of ANN
V	Voltage
V_{otp}	Output voltage of PZT
V_{S_0}	Velocity of fundamental symmetric Lamb mode
$V_{S'_{0Delam}}$	Velocity of damage-induced fundamental shear mode
W	Continuous wavelet transform coefficient

α	Length of semi-major axis of damage
α_K	Learning rate of ANN
β	Length of semi-minor axis of damage
ε	Strain
ε^i	Interface strain
ε_x	Axial strain of beam
ε_r	Radial strain
ε_θ	Tangential stress
ϕ	Angle between damage major axis and 0° fibre direction
κ	Shear correction coefficient
λ	Lamé constant
λ_{wave}	Wavelength of Lamb wave
μ	Lamé constant
ν	Poisson ratio
θ	Percentage of delaminated area in laminate
ρ	Mass density
ρ_{STFT}	Energy density for Short Time Fourier Transform
σ	Stress
σ^i	Interface stress
σ_r	Radial stress
σ_θ	Tangential stress
σ_x	Normal stress of beam
ω	Circular frequency
ξ	Vertical distance to laminate left edge from damage centre
ζ	Vertical distance to laminate bottom edge from damage centre
Θ	Electric charges
Ω	Volume percentage
$\Psi(t)$	Orthogonal wavelet transform function

Acronyms

AE:	Acoustic Emission
AI:	Artificial Intelligence
ANN:	Artificial Neural Network
AO-SHD:	Active Online Structural Health Diagnosis
AR:	Auto-regressive
BGD:	Basic Gradient Descent
BP:	Back-propagation
CAIB:	Columbia Accident Investigation Board
CCAS:	Central Control/Analysis Subsystem
CWT:	Continuous Wavelet Transform
DAS:	Data Acquisition Subsystem
DDF:	Digital Damage Fingerprints
DF:	Digital Filter
DoF:	Degrees of Freedom
DPD:	Damage Parameters Database
DWT:	Discrete Wavelet Transform
EC:	Eddy-current
EMAT:	Electro-magnetic Acoustic Transducers
FFT:	Fast Fourier Transform
FoM:	Figure of Merit
FRF:	Frequency Response Function
FT:	Fourier Transform
GDA:	Gradient Descent with Adaptive Learning Rate
GDM:	Gradient Descent with Momentum
GDMA:	Gradient Descent with Momentum and Adaptive Learning Rate
IM:	Input Element
ISPPR:	Intelligent Signal Processing and Pattern Recognition
LBU:	Laser-based Ultrasonic
LI:	Laser Interferometer

LM:	Levenberg-Marquardt
MEV:	Maximum Energy Variation
MPC:	Multi-point Constraints
MSE:	Mean Square Error
NDE:	Nondestructive Evaluation
ODS:	Operational Deflection Shapes
ONERA:	French Aeronautics and Space Research Centre
OV:	Output Variable
PCA:	Principal Component Analysis
PCL:	Patran Command Language,
PMT:	Parameterised Modelling Technique
PVDF:	Polyvinylidene Fluoride
PZT:	Piezoelectric Lead Zirconate Titanate
RBP:	Resilient Back-propagation
SGS:	Signal Generation Subsystem
SH:	Shear Horizontal
SHM:	Structural Health Monitoring
SICL:	Standard Instrument Control Library
SMIS:	Shuttle Modal Inspection System
SNR:	Signal-to-Noise Ratio
SP:	Sampling Point
SPP:	Signal Processing Package
SSU:	Standard Sensor Unit
STFT:	Short Time Fourier Transform
SVG:	Scaled Conjugate Gradient
ToF:	Time of Flight
TP:	Time Point
UD:	Unidirectional Prepreg
VISA:	Virtual Instrument Software Architecture
WF:	Woven Fabric Prepreg
WT:	Wavelet Transform
WVD:	Winger-Ville Distribution

Table of Contents

CHAPTER 3

CHAPTER 4

List of Figures

List of Tables

Chapter 1

Introduction

1.1 Lessons from *Columbia* Tragedy

Smiles on seven joyous faces are forever frozen in the air. The snapshot in Figure 1.1(a), taken on 31st January 2003, becomes our lasting memory of the brave *Columbia* crew. A short time later, debris was seen falling from the sky above Texas, Figure 1.1(b), during *Columbia*'s re-entry from orbit after a *16*-day mission. A day of shining triumph turned into one of sorrow. The crew is lost, lost for all mankind. The whole world mourns.

When *Columbia* disintegrated into pieces, it claimed not only seven persons but a piece of the world's space science capability. With grief, an unavoidable but challenging issue for NASA, as well as for the entire scientific community, arises: what happened to *Columbia*? And where can we go from here?

NASA report [NASA-CAIB, 2003], released by the *Columbia Accident Investigation Board* (CAIB), attributes this technical tragedy to an impact puncture occurring in the leading edge of *Columbia*'s left wing (made from reinforced carbon-carbon composites), which eventually led to ineffectivity of the heat isolation materials and consequently a steep rise of temperature in the cockpit. Real-time video-recording confirmed that the shuttle suffered from an unexpected strong airflow at the *62nd* second during launching on *16th* January, and the leading edge was subsequently

struck by a piece of foam block desquamated from the fuel tank at a speed of over *700* feet per second. The impact incurred a through-puncture at the 87^{th} second, as seen in Figure 1.2(a).

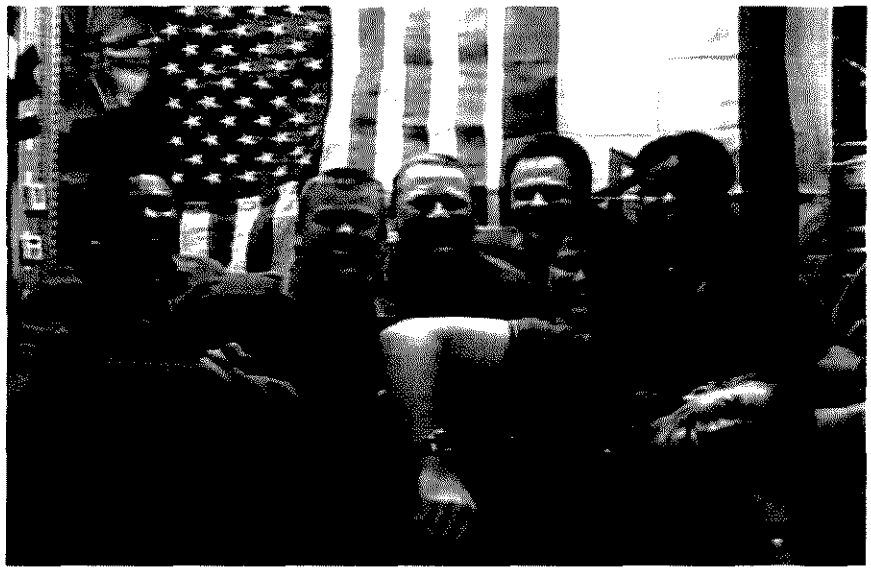

(a)

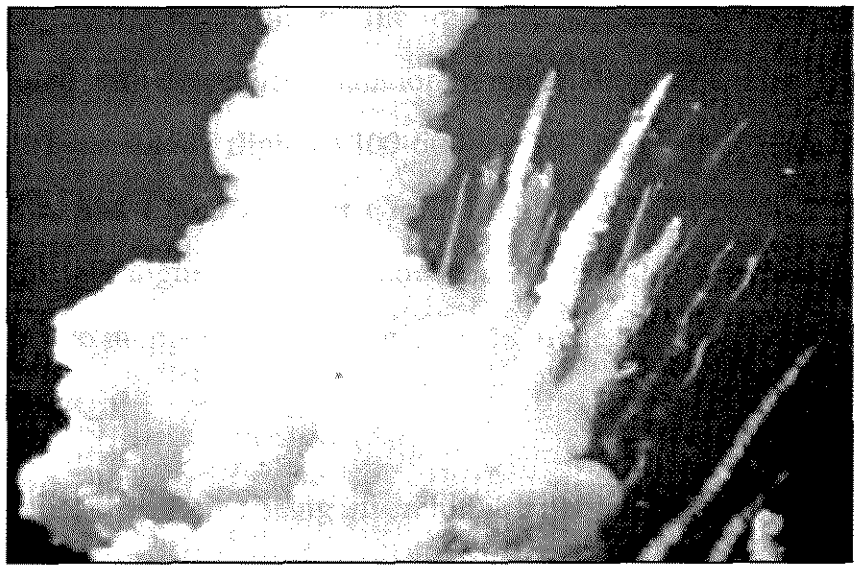

(b)

Figure 1.1 Memorial of *Columbia* space shuttle [*Discovery® Channel*]: (a) on 31st January 2003 in the cockpit; (b) at 7:50 AM CST on 1st February 2003 over Texas

Columbia's *16*-day travel in outer space implies that such a puncture was not lethal when it occurred. However, growth of the *nonfatal* deterioration unfortunately continued under fatigue loading, and ultimately became the main culprit of this disastrous disassembly after *16* days. A subsequent test conducted by CAIB confirmed this presumption. In this test, a composite panel, with structure identical to *Columbia*'s wing structure, was examined, subjected to a flying foam block (*21.375* × *11.5625* × *5.625* inches in volume, *1.69* pounds in weight, similar to the desquamated foam in the accident). A hole measuring *2* feet on the panel and numerous cracks were thereafter observed, as indicated in Figures 1.2(b) and (c) [NASA-CAIB, 2003]. Now, doubt has arisen as to whether the catastrophe could have been avoided and the crew could have been saved, if such non-fatal damage had been correctly assessed during service of the shuttle in orbit.

1.2 Background of the Study

It is actually easy to cite numerous similar tragedies happening worldwide every year, directly associated with defect accumulation in materials or structures. Disintegration of *American Airlines AA587* flight (A300-600) on 12th November 2001 due to failure of composite fin, and *China Airlines CI611* flight (B747-200B) on 25th May 2002 incurred from metal fatigue damage, announced *260* and *225* lives lost, respectively. However, these two numbers just claim only *15%* of the total civil aviation casualties in 2001 and 2002.

Today serious consideration is being given to the safety of transportation vehicles, in particular aerospace and aeronautical craft, whose failure usually brings on non-rescuable calamities. Similar concern also exists for civil constructions (e.g. bridges, highways, power plants, tunnels, offshore platform, etc.), and the maritime, automobile, machinery and medical industries. Nowadays, reliability, performance and life cycle have become the most essential issues for all in-service systems.

(a)

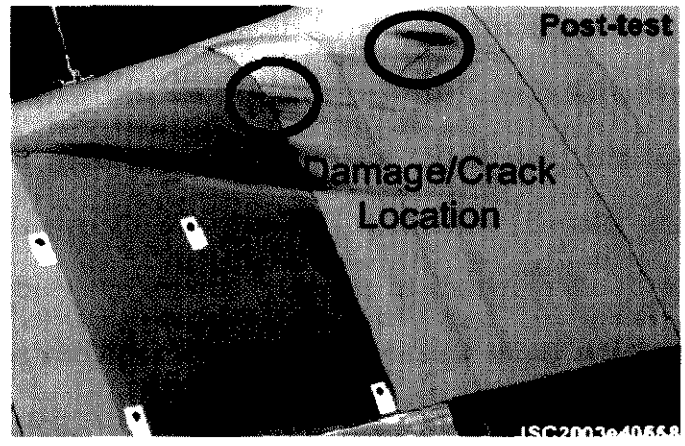

(b)

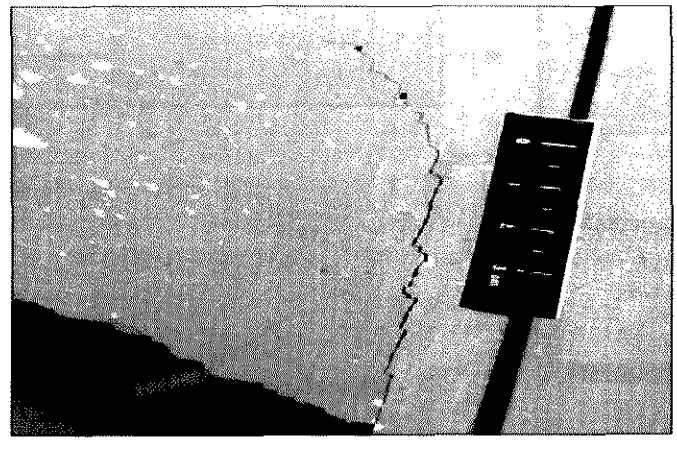

(c)

Figure 1.2 (a) Synthesised image for wing of *Columbia* after foam impact; (b) NASA test results; (c) crack observed from NASA test

Aircraft fleets are increasing worldwide, as is their age. *Columbia* was lost at *21*, and the aircraft of Flight *CI611* was *25* years old. Statistics [Boller, 2001] show that the numbers of civil aircraft older than *15* and *25* years, built by major American and European manufacturers, were *4600* and *1900* respectively in 1997, and these numbers increased to *4730* and *2130* respectively in 1999. For military aircraft, in-service fighters aged over *40* (e.g. F4, T-38, MiG21) are not exceptional.

The older an aircraft becomes, the more its reliability deteriorates. With safety regarded as the paramount factor for transportation, airworthiness criteria must be strictly met. For example, the Federal Aviation Administration (FAA) of America requires a '*walk-around*' inspection for visual damage before every flight; detailed visual inspection for most components every *150* flights; and tear-down of critical metallic components every *6,000-12,000* flight hours [Kessler and Spearing, 2002]. Periodic inspection between service intervals, as shown in the flowchart in Figure 1.3 [Chang, 2002b], was perhaps the only way to ensure safety before 1990.

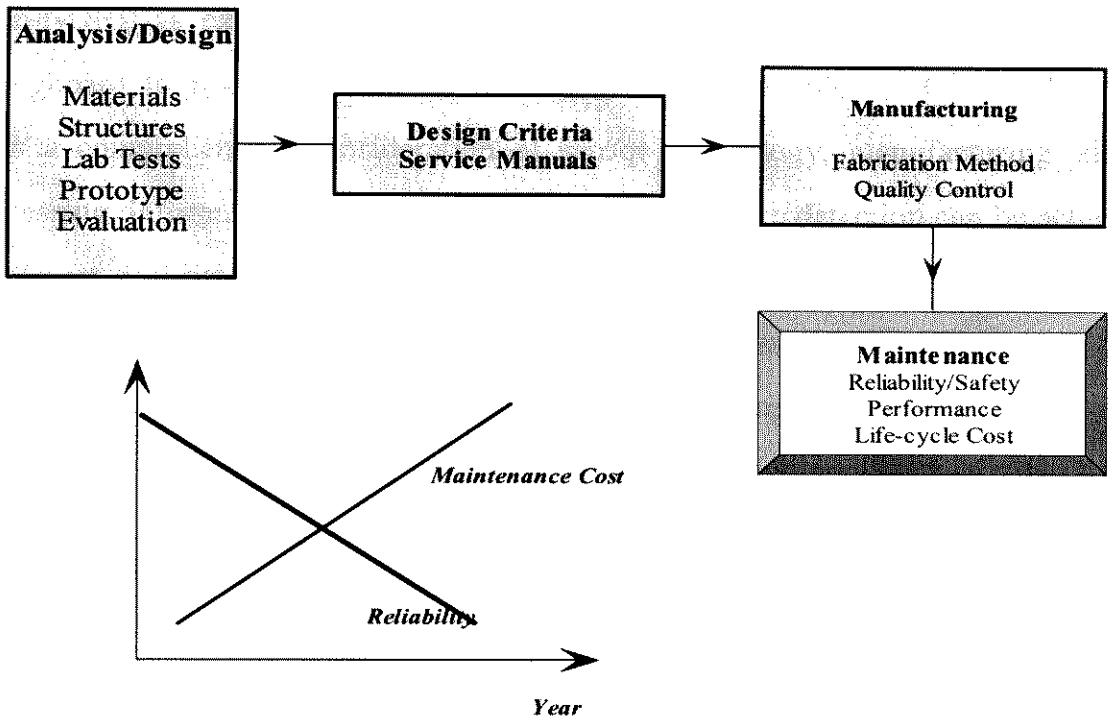

Figure 1.3 Traditional design-service-maintenance for aircrafts [Chang, 2002b]

Under such a traditional design-service-maintenance philosophy, *25%* of aircraft life cycle cost is spent by commercial airlines on safety-related inspections (more than US$*1.3* trillion has been consumed for this purpose in the past 5 years in the US, and more than US$*100* billion per year in Japan), accompanied by indirect expenditure such as management for aged fleet [Chang, 2002a].

However, the frequency of accidents has been challenging the effectiveness of this traditional maintenance, besides the huge cost. Conducted following a specific schedule, maintenance is time-consuming, labour-intensive and cost-expensive. Independent of actual working conditions that aircraft may experience, inspection criteria based on laboratory tests or empirical knowledge can never be appropriately updated without taking into account the continuous structural deterioration. Shortening maintenance intervals may help, but it is at the cost of substantial monetary increase.

Since last decade, the introduction of condition-based nondestructive evaluation (Con-NDE), as explained in Figure 1.4, seems to have offered an encouraging springboard to revamp traditional damage detection techniques. Con-NDE stems from a comprehensive consideration of sensor technology, manufacturing, signal processing, informatics and diagnostics, by which damage detection can be achieved in almost real-time considering the actual operational conditions and structural ageing. In such a way, maintenance criteria and schedules can be updated from time to time. It has been demonstrated that Con- NDE is capable of lowering the total maintenance cost by over *30%*, sustaining reliability and keeping catastrophes to the minimum [Chang, 2002a].

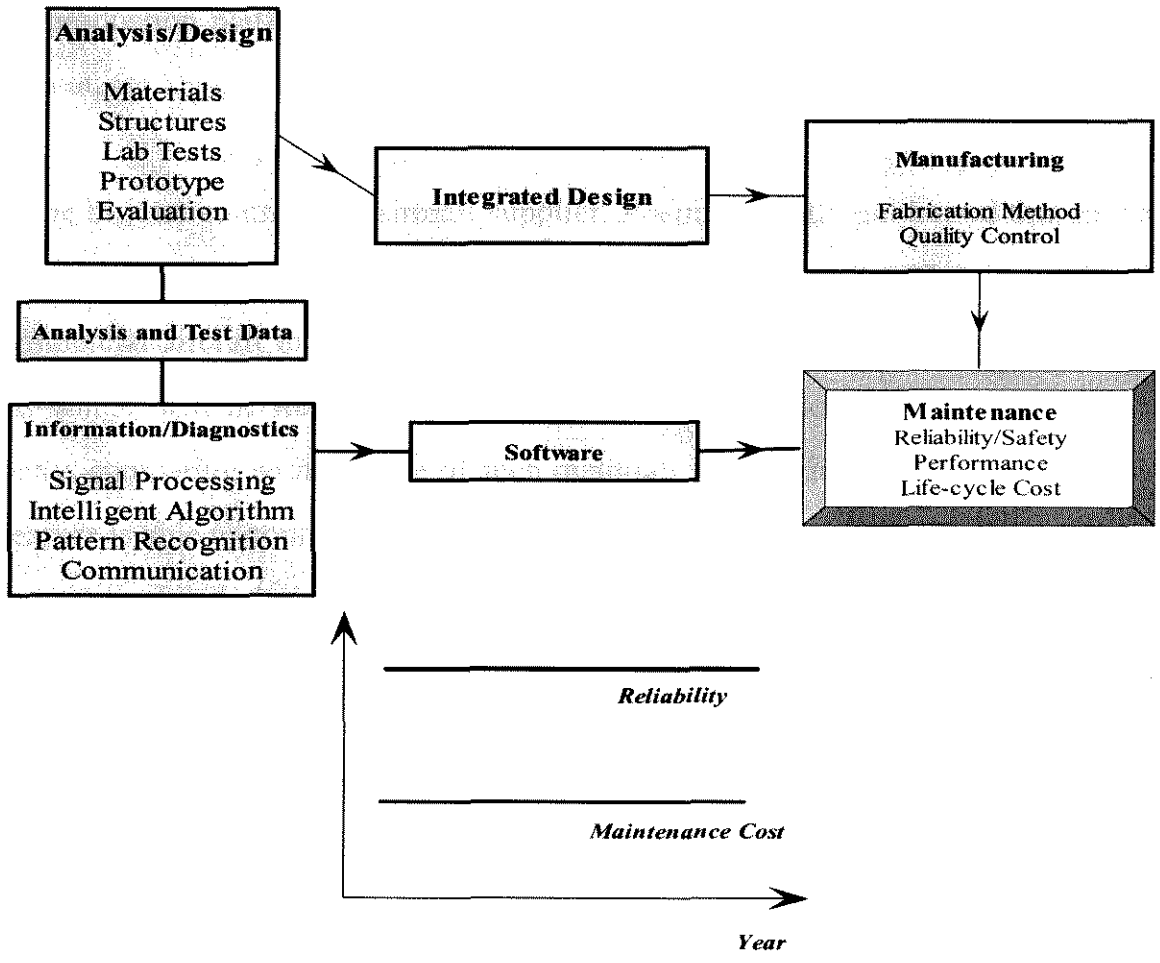

Figure 1.4 Condition-based design-service-maintenance for aircrafts [Chang, 2002b]

On the other hand, composite materials, patented by the *DeHavilland* Aircraft Company in the 1930s [Chimenti, 1997] and probably firstly introduced into commercial use as fuselage skin for the *Vultee BT-15* trainer plane in 1944 [Hoskin and Baker, 1986], have exponentially pervaded into various commercial applications, serving as attractive candidates to satisfy highly demanding requirements from current and new generation aero-structures. Due to their superb strength-to-weight and stiffness-to-weight ratios, substantial weight saving and performance improvement for the entire system can be achieved, compared with conventional counterparts such as aero-aluminium alloy. They appear more frequently in transportation vehicles (aircraft, space shuttle, cars, vessels, etc.), civil infrastructure

(oil production platforms, bridge, building, etc.), and sporting items (F1, golf club, sailboat, etc.).

As the biggest commercial aircraft supplier, *Boeing* recently publicised that its new-generation super-efficient commercial aircraft, *Dreamliner B-7E7*, will be the first commercial aircraft in which the majority of its main structures, including fuselage and wings, will be made of lightweight, super-strong blends of carbon fibres and epoxy, comparing with a usage of such materials of *11%* in its latest jet *B-777*. This measure is able to contribute to at least *3%* fuel saving [Talbot, 2003; Boeing, 2003]. Competitively, *Airbus* also launched its ambitious program, the *A380* project, with claims that *22%* of components will be fabricated using advanced composite materials [Airbus, 2003].

Regardless of their numerous merits, sad lessons still remind us that composite structures still run a high risk of suffering damage due to abrupt impact or to the accumulation of material defects, potentially leading to catastrophic failure of the whole system. Under such circumstances, integrity and ongoing performance become key concerns for the confident acceptance of these composite structures.

Motivated by this, Con-NDE techniques have been particularly tailored for composite structures in recent years. Distinct from metallic or plastic materials, composite materials are of high-order inhomogeneity or anisotropy. Their properties are direction-, fibre-, matrix- and manufacture process-dependent. In most cases, damage in composite structures occurs beneath the surface and is invisible. These factors considerably complicate the inspection process. There is no shortage of research activity in this field and numerous approaches have been developed, playing an indispensable role in preventing system failure and improving structural reliability. The majority of approaches, however, can accommodate specific applications only, and are characterised as time/money/labour-consuming or having

poor precision. A balance is yet to be achieved between the degree of practicability and accuracy that they can offer.

1.3 Scope of the Thesis

Ultimately aimed at a structural health monitoring (SHM) technique/system to offer online and exact deterioration assessment for in-service engineering structures, particularly carbon fibre reinforced composites, a quantitative damage detection technique based on elastic wave propagation is developed in the thesis.

The chapters are hierarchically organised. A brief literature review of state-of-the-art NDE approaches for composite structures is conducted in Chapter 2; where various detection methodologies are categorised as non-model-based and model-based approaches in terms of their mechanisms. Sensor technology for damage detection is also introduced. Chapter 3 concerns the study of fundamentals of elastic waves in solid media, by analytical derivation, FEM simulation and experiment, particularly Lamb wave in multi-layered composite laminates, as the basis for the wave propagation-based damage detection technique in this study.

A signal processing and interpretation technique is developed in Chapter 4, to serve as a basic tool in the study. With the assistance of such a technique, interaction between elastic waves and structural damage is rigorously evaluated using both FEM and experimental verification, detailed in Chapter 5. From the characteristics observed, a guided elastic wave-based damage detection strategy is then established.

Chapter 6 describes the development of an inverse pattern recognition algorithm, taking advantage of the artificial neural network technique, which is essential to quantitative identification of structural damage. Based on the above-mentioned methods, in Chapter 7 an active online structural health diagnosis (AO-SHD) system

is configured on a *VXI* instrument platform. The system is then calibrated and tested by selectively generating pure Lamb wave modes.

In Chapters 8 to 10, three actual case studies in a hierarchical order of difficulty, ranging from crack growth detection in an alloy structural beam to through-hole type damage and delamination in CF/EP composite plates, are conducted to validate the proposed methodology and the AO-SHD system. Finally, concluding remarks and recommendations for future research are presented in the last chapter.

Note that, in addition to a general survey regarding NDE techniques for composite structures at beginning of the thesis, reviews of each related topic occur throughout the entire thesis wherever first introduced.

Chapter 2

Nondestructive Evaluation (NDE) for Composite Structures

2.1 Introduction

Exponential acceptance of composite structures in industry has significantly stimulated the development of particular nondestructive evaluation (NDE) techniques, and efforts have therefore been strengthened in a variety of fashions over the years. Damage in a composite structure can be manifested as fibre breakage, matrix cracking, local delamination, or combination of these [Islam and Craig, 1994], which determine the uniqueness of methodology adopted in NDE. In this chapter, state-of-the-art NDE techniques actively serving composite structures are surveyed in light of their respective merits and weaknesses. Roughly speaking, existing NDE methods for composite structures can be categorised depending on whether they rely on *in prior* models or not.

2.2 Non-Model-Based Methodologies

Non-model-based NDE, ranging from tapping to ultrasonic detection and radioscopy, has played an indispensable role in practice since their debut, because of the wish to avoid of developing complex theoretical models.

Visual Inspection and Tapping

Perhaps the oldest damage detection means, methods by visual inspection, coin tapping or mechanical impedance-based tapping [Cawley, 1984; Wegman, 1989] are normally operated by skilled workers with rich experience, to roughly localise damage. Performed subjectively and relying on the naked eye, such a primary approach cannot provide quantitative assessment for composite structures.

Ultrasonics

Introduced in 19^{th} century as a sonar technique [Bindal, 1999] for blemish detection, ultrasonics serves as one of the most powerful tools for omnifarious industries [Scarponi and Briotti, 2000]. Modern ultrasonics is often implemented with a pair of ultrasonic probes, coupled with angle-adjustable perspex wedges, which are moved in tandem to send and collect ultrasonic waves. Damage identification is based on understanding of flaw-reflected ultrasonic waves. *A*-, *B*- and *C*-scans are major styles of ultrasonics [Bindal, 1999].

Ultrasonics-based NDE features high precision, applicable even for the detection of small size defects. It can provide intuitive and exact true-to-scale images for invisible damage. Emitted waves in the ultrasonic frequency range are able to penetrate a large thickness (up to depths of several meters) [Bindal, 1999]. However, a temporary downtime of structures to be surveilled is usually required to ensure appropriate operation of probes. None of the three scan types provides access to both sides of a structure, so parts may need disassembling for inspection. Ultrasonic probes are often of non-negligible size and weight, working with a couplant (though some non-contact techniques have been developed, referring to Section 3.3.3), and must be moved back and forth on the structure surfaces [Rose, 2000]. For signal calibration, benchmark may be required. All these features considerably impede their applications to *online* or rapid assessment, or to structures with complicated geometry and non-flat or rough surfaces.

Acoustic Emission (AE)

Acoustic emission (AE) is a phenomenon that rapid release of strain energy generates transient elastic waves [Tandon and Choudhury, 1999]. It can be caused by alteration in a structure under mechanical or thermal stresses such as the occurrence/propagation of cracks or growth of delamination. AE-based NDE approaches can be used to triangulate the damages by calculating the propagation duration of damage-emitted acoustic waves.

Representative work in this field [Benmedakhene *et al*, 1999; Blanas *et al*, 1999; Shih and Mal, 1999; Green and Green, 2000; Hurlesbaus *et al*, 2001; Grondel *et al*, 2002] has demonstrated good performance of AE approaches for locating damage and predicting growth of cracks, especially for rolling bearings components. However, such a technique can be compromised by diverse noises, particularly in the low frequency ranges. And the AE signal collected from composite structures is very complex to interpret. Known as passive detection, AE-based methods could normally not be expected to perform quantitative damage assessment easily. Moreover, the high damping ratio of AE signal limits its application to relatively small structures only [Grondel *et al*, 2002].

Eddy-Current (EC)

Taking advantage of the fact that much better conductivity exists along a carbon fibre than in matrix, evaluation methods using eddy-current (EC) have emerged as a novel means, which can detect changes in electromagnetic impedance of a composite structure and consequently identify discontinuity along fibre. It is actually the second most frequently adopted inspection approach in the aerospace industry after ultrasonics [Kessler, 2002], because of its simplicity. Though successful applications to carbon-fibre composite materials has been widely reported [Mamishev *et al*, 1998; Zahn, 1998; Goldfine *et al*, 1999, 2000], the effectiveness of EC-based NDE can be

diminished by factors such as the insulating properties of epoxy matrices. A large amount of power is usually required to excite an eddy current, which is not always feasible in practice. Moreover, EC signals are among the most complicated to interpret.

Radioscopy

Sharing a large NDE market, radioscopy (X-ray) works in virtue of the observation that different transects of a structure have different X-ray absorption rates and different X-ray topography. Any damage singularity with an abnormal transect can accordingly be characterised by its unique ray absorption. Radioscopy offers a clear, intuitive and exact image for explanation, particularly suitable for inspecting both superficial and internal damage [Gray and Tillack, 2001].

Recent improvements in radioscopy excitation sources, data analysis and image reconstruction has strengthened the capability of radioscopy-based NDE. But the requirement for large and costly ray-excitation equipment has hindered further application to cost-effective *online* damage detection. Another challenge relates to the fact that the technique usually needs access to both sides of structural sections in order to emit and collect ray radiation, and, in some cases, inaccessible components must be removed or disassembled for individual inspection.

Infrared Thermography and Miscellaneous Methods

It is known that discontinuity in materials causes heat dissipation and leads to an infrared thermal field different from that of perfect counterparts. Based on this observation, thermography-based NDE has found increasing application. Luong [1998] successfully applied such a technique to detect fatigue damage in metal. Though promising, this technique can accommodate certain applications only, and it is considered still as a laboratory tool.

Some other more exotic non-model-based techniques include approaches using dye penetration [Shen and Sharpe, 1998], electro-magnetic field [Lemistre and Balageas, 2002a, 2002b], triboluminescent materials, optical surface reflection and resistance of thermoplastic films [Tamiatto *et al*, 1998; Banaszak *et al*, 1999; Sage *et al*, 1999; Kessler, 2002], electronic shearing interferometry [Hou, 2003], imaging methods [Wang and Chang, 2003] etc. Most of these approaches are in the explorative stage and applications are quite tentative.

2.3 Model-Based (Vibration-Based) Methodologies

Aimed at avoiding the disadvantages of non-model-based methods, NDE techniques in terms of theoretical models have been motivated in parallel [Doebling *et al*, 1996; Farrar *et al*, 2001a]. Their basic mechanisms rely on the fact that the occurrence of structural damage can alter material (or structural) stiffness, mass, damping ratio or energy dissipation properties, in turn altering structural dynamic responses. Thus the difference between data collected from objects under inspection and those pre-obtained from theoretical models (or benchmarks) can act as an indicator of damage location or degree. Although the philosophy appears intuitive, its actual implementation poses many significant technical challenges.

Modal Data Analysis

Dominating model-based NDE, detection techniques using modal data are valued for their simple implementation, money- and labour-saving potential. Eigen-frequencies, mode shapes, dynamic flexibility, damping ratios or a combination of these are often employed. The most successful applications are in blemish detection for rotating machinery or joints [Lichtenwalner *et al*, 1997; Vecchio and Auweraer, 2001; Tandon and Choudhury, 1999], aircraft components [Mickens *et al*, 2003], and civil infrastructure [Wahab *et al*, 1999; Fritzen and Bohle, 2001, Gorl and Link, 2001],

especially for bridges [Farrar and Jauregui, 1998a, 1998b; Thyagarajan *et al*, 1998; Wang *et al*, 1998].

The aerospace engineering community has employed similar approaches for composite components in space shuttles since the 1970s. The *Shuttle Modal Inspection System* (SMIS), developed by NASA in 1987 [NASA, 2003], is able to identify fatigue damage in reusable aero-components such as composite fuel tanks, control surfaces or fuselage panels. Under regulations, all orbiter reusable vehicles in NASA have been periodically subjected to SMIS evaluation since the 1980s.

A. Frequency

The number of detection approaches relying on shifts in eigen-frequencies, Frequency Response Function (FRF) and their variants is quite large [Valdes and Soutis, 1999; Yam *et al*, 2002; Mickens *et al*, 2003; Worden *et al*, 2003a, 2003b]. As a typical example, Tracy and Pardoen [1989] established the relationship between the first four eigen-frequencies of a composite beam and delamination location/length, as shown in Figure 2.1, where the lowest eigen-frequency is observed to be most insensitive to both delamination location and length, while the 4^{th} eigen-frequency is conversely the most sensitive, though all are unaffected by very short delaminations.

However, frequency-based approaches have increasingly been challenged by evidence from practice. Tests on bridges [Doebling *et al*, 1996] have demonstrated that no significant reduction in frequencies could be measured when the cross-sectional stiffness at the centre of a main plate girder was reduced by *96.4%*, which already reduced the bending stiffness of the overall bridge cross-section by *21%*. Actually, it is now well acknowledged that only when the damage covers over *10%* of the whole structural area can detection precision be guaranteed [Yan and Yam,

2002]. Higher frequencies may be more sensitive to defect; however, this is at a high cost for excitation.

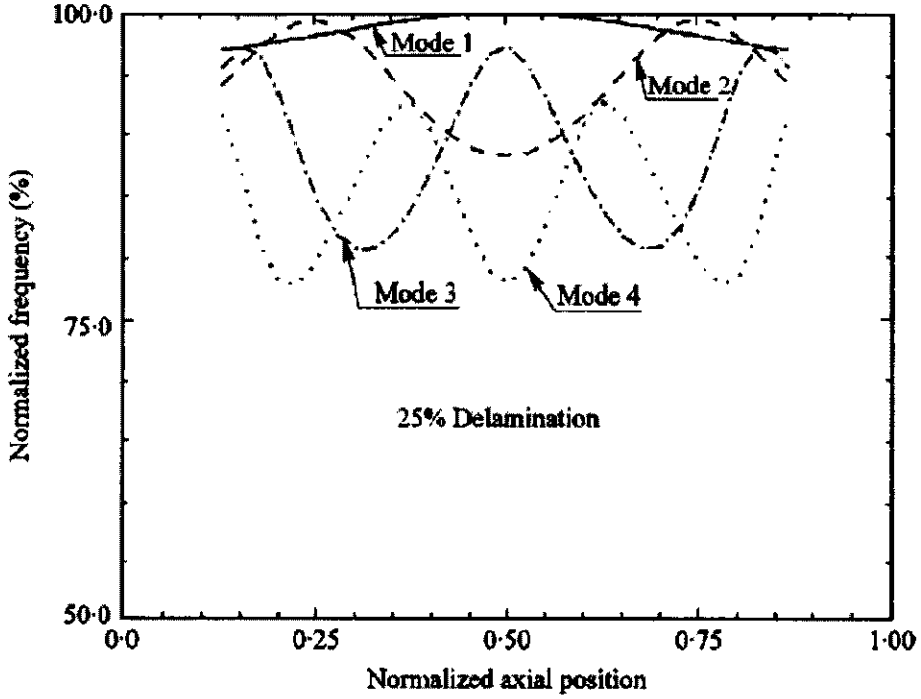

(a)

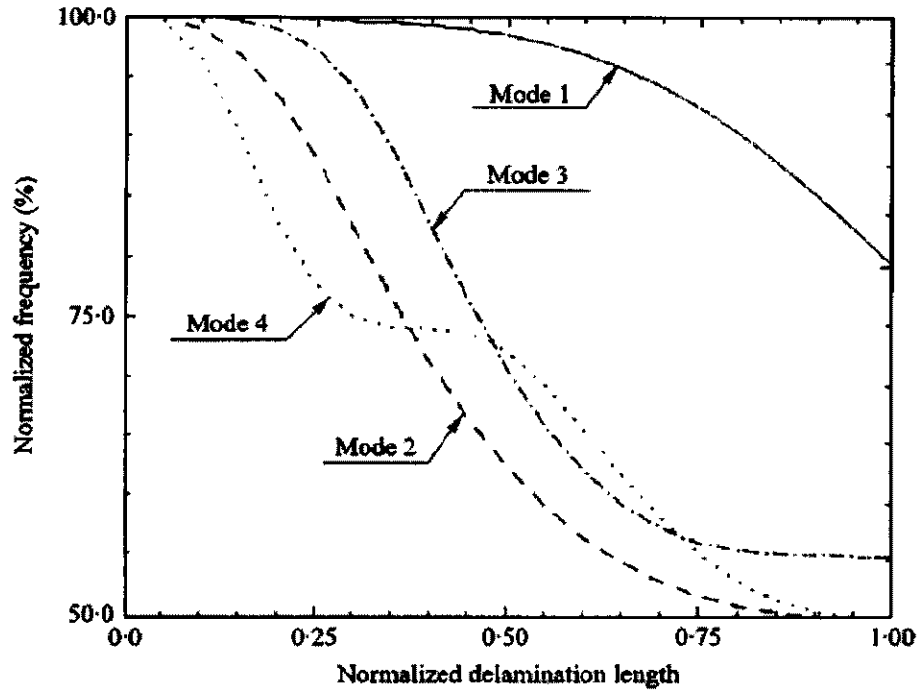

(b)

Figure 2.1 Relation between structural eigen-frequencies and (a) delamination location; (b) delamination length [Tracy and Pardoen, 1989]

B. Mode Shape

With similar mechanisms, reduction in stiffness/mass and shift in original mode shapes can also be associated with defects [Stubbs and Kim 1996; Lu and Hsu, 1999; Waldron *et al*, 2002]. Studies [Pandey *et al*, 1991; Shen and Grady, 1992] have shown that delamination in a composite beam caused irregularity in mode shape curves, the extent of which depended on the delamination size and location: the larger the delamination, the more irregular the mode shape; and the closer to the structural surface the delamination, the more irregular the mode shape.

As a variant of mode shape-based NDE with spatially distributed features, mode shape curvatures, obtained by mathematically differentiating the identified mode shape vectors twice, exhibit much high sensitivity than the mode shape itself and eigen-frequencies [Pandey *et al*, 1991; Doebling *et al*, 1996]. Alternatively, Stubbs *et al* [1992] and Shi *et al* [1998] proposed another effective approach using the damage-induced decrease in modal strain energy. The good performance of this approach was confirmed by Chen and Swamidas [1994] with crack identification in a cantilever plate. It is worth emphasising that Chance *et al* [1994] observed that numerically calculated mode shape curvatures might result in unacceptable errors for small damage, but the result could be dramatically improved when strains were used to describe the curvatures directly.

Suffering from the same problem, modal shape-based NDE is unwieldy for small defects, which contribute little to modal data shift. Indeed, local delaminations have no noticeable effect on the modal shape [Shen and Grady 1992]. Though an improved signal processing technique using the Laplacian operator has been developed to address this issue [Ratcliffe, 1997], the majority of relevant work is still limited to relatively severe damage cases (greater than *10%*). In addition, a large number of measurement locations is often required to ensure sufficient resolution.

In addition to those specified above, modal data-dependent NDE techniques are also represented by methods using flexibility shift [Pandey and Biswas, 1994; Zhang and Aktan, 1995; Park *et al*, 1998], residual flexibility [Doebling, 1995], stiffness matrix methods [Peterson *et al*, 1995], model improvement and model updating [Cunha and Perreux, 1998; Wahab *et al*, 1999], optimal matrix modification [Smith and Beattie, 1991; Kim and Bartkowicz, 1993], sensitivity-based updating [Hemez, 1993; Yam *et al*, 2002], eigenstructure assignment [Lim, 1995; Schulz *et al*, 1996], and combined modal data approaches [Lan *et al*, 1998] etc.

Electrical/Mechanical Impedance Analysis

Novel options relying on modifications in electro-mechanical impedance have recently proven promising for *in-situ* NDE of carbon fibre reinforced polymers, civil infrastructure, and cracks in graphite/epoxy composites [Ayres *et al*, 1998; Giurgiutiu and Rogers, 1998; Lopes *et al*, 2001; Todoroki *et al*, 2000; Pohl *et al*, 2001; Salvia and Abry, 2002], particularly for defects in planar structures [Cawley, 1984; Wong *et al*, 1993]. The principles originate from the fact that each component in a mechanical system contributes a certain amount to the total electrical and mechanical impedance. Any shift caused by a defect can thus be qualified/quantitated by comparison with a perfect benchmark. Chiu *et al* [2000] used a piece of boron/epoxy patch surface-bonded on an aluminum plate to measure the local impedance, and detected the debonding between the patch and plate. But it was also pointed out in their study that impedance-based techniques were unable to find debonding in fields far from the sensors, and that damage had to be sufficiently large to affect measurable impedance.

Static Parameters Analysis

Difficulties in obtaining structural dynamic data have driven efforts with methods using static parameters. Recent studies have substantiated the possibility of static

data for damage detection, such as displacement [Sanayei and Onidepe, 1991; Wang and Deng, 1999; Chou and Ghaboussi, 2001], strain or strain energy [Soeiro and Hajela, 1993; Hwu and Liang, 2001], a combination of displacement and strain [Soeiro and Hajela, 1993], and static fracture toughness [Jih and Sun, 1993], etc. In addition to simplicity in measurement, static parameters can be more locally sensitive to defects than natural frequencies and mode shapes, especially for identifying changes in material properties or geometric entity, e.g. Young's modulus, cross-section or internal discontinuities. But many concerns have arisen as to the detection precision for small defects that static data can offer, due to their relatively dull susceptibility to undersized damage or the evolution of deterioration.

Damage Index Analysis

NDE using the concept of *damage index* has shown some encouraging prospects. Ihn and Chang [2002] developed a *built-in* cost-effective diagnostic system to monitor crack growth in aircraft structures. In their approach, the damage index was non-dimensionally defined as time integration of power scatter spectra density at a specified frequency

$$Damage-Index=\left[\frac{\int_{t_i}^{t_f}\left|S_{ss}(\omega,t)^2\cdot dt\right|}{\int_{t_i}^{t_f}\left|S_{bs}(\omega,t)^2\cdot dt\right|}\right]^{1/2} \tag{2.1}$$

where S_{ss}, S_{bs} and ω denote the spectral densities of scatter signal, baseline signal and selected frequency, respectively, in the time range concerned $[t_i, t_f]$. With damage-scatter information, Equation (2.1) serves as an indicator to calibrate damage.

More generally, various damage indices have been introduced. Keilers and Chang [1993, 1995a] developed a *comparator* using a *weighted quadratic objective function* to compare measured and calculated structural responses, also referred to as the

Figure of Merit (FOM) method. Similar to Equation (2.1), FOM was used in frequency domains to calibrate damage. The technique was then validated by detecting delamination in a composite beam [Keilers and Chang, 1995b] and locating impact source [Choi *et al*, 1994; Choi and Chang, 1996]. Tracy and Chang [1996] and Seydel and Chang [1999a, 1999b] respectively developed their own comparators and damage indices for determination of impact location and history. Yan and Yam [2002] established one-dimensional correlation between *Maximum Energy Variation* (MEV) and damage length, by which a crack in composite plate was successfully identified. Wolfinger *et al* [1998] found that the delamination area correlated with a self-defined damage index, *Effective Value of Signal*, which permitted classification of impacts and evaluation of damage location in a fibre-composite plate with bolts. Dupont *et al* [1999] demonstrated that another damage index, *High-Frequency Root Mean Square* (HF-RMS) of signal, was sensitive to damage occurrence, location and severity. Valdes and Soutis [2001] quantitated delamination size using a damage index, *Time of Flight* (TOF), from acquired stress wave signals. Kim *et al* [2003] derived a damage index based on changes in modal strain energy and applied it to localise sites of damage in a beam. Though performing well in the case studies cited here, methods using the damage index concept require analytically complicated models and benchmarking, and satisfactory prediction can be obtained for relatively simpler structures only.

Other Techniques

Model-based NDE techniques also include some specific methods developed to accommodate particular applications. Worden *et al* [2003a, 2003b,] presented a detection method for machine components, described as *Novelty Detection*. Application on a metallic aircraft wingbox [Worden *et al*, 2003c] demonstrated good performance of such a method. Pai and Jin [2000] and Ghoshal *et al* [2000] developed an approach to pinpoint crack location using operational deflection shapes

(ODSs) measured by a scanning laser vibrometer, whose principle relied on the fact that cracks introduced new boundaries and consequently changed ODSs at boundaries. Sohn *et al* [2000] proposed a NDE technique with a statistical process control algorithm, known as *X-bar control chart*, based on an auto-regressive (AR) model, which was proved effective to vibration test data acquired from a concrete bridge with progressively damaged columns.

2.4 Elastic Wave-Based NDE for Composites

One tendency imposed on new generation composite structures is to systematically syncretise structural functionalities with self-damage detection, and even self-rehabilitation, which is the so-called *cost-effective* functional composite system [Ye *et al*, 2003]. The traditional NDE approaches introduced above, whether model-based or not, seem unlikely to match such a strategy. Since 1990, novel methods taking advantage of elastic waves, also described in model-based NDE, have exponentially gained preference from major engineering communities for their uncontroversial capability in linking detection precision with application universality, to act as competitive substitutes to conventional NDE tools. For example, rather than removing insulation and using a single probe to inspect point-to-point an insulated long pipe, one can use a guided wave probe at a single location, leave the insulation intact, and check the entire pipe system instantaneously by simply examining reflected wave signals.

> *One decade from now on, the guided wave inspection programs will be commonplace.*
>
> Joseph L. Rose [1999]

The earliest utility of elastic waves in ultrasonic frequency ranges for NDE purposes can be dated back to blemish detection for ships or undersea vehicles in the 19^{th} century (known as a prototype of Sonar technology). Essential development was

driven with introduction of such a technique for medical applications during World War II. In the 1950s, Firestone and Ling re-examined this topic at the request of *Sperry Products*, Inc. (a well-known supplier of NDE services) for damage inspection in sheet metals [Chimenti, 1997]. In their research, the definition of *Lamb wave* was first introduced, which nowadays serves as the widely accepted terminology for guided waves in thin traction-free plates.

With mature understanding of elastic waves in one-dimensional structures, NDE techniques for flexible beams or rods have been well developed [Ma and Pine, 2001]. Based on damage type, methods can be roughly grouped as crack or notch detection for metals [Lakshmanan and Pines, 1997; Biemans *et al*, 1999; Grondel *et al*, 2002; Kim and Kim, 2000, 2001; Fromme and Sayir, 2002; Ihn and Chang, 2002] and delamination or crack detection for composite beams [Guo and Cawley, 1992, 1993a, 1993b; Islam and Craig, 1994; Lakshmanan and Pines, 1997; Purekar *et al*, 1998; Kessler *et al*, 2002a, 2002b; Perel and Palazotto, 2002; Wang and Rose, 2001]. From the perspective of mechanisms they can also be categorised as longitudinal vibration-based [Seemann, 1996; Palacz and Krawczuk, 2002] or transverse vibration-based [Kim and Kim, 2000, 2001]. The majority of the relevant studies have focused on the case of open cracks, where the nonlinearity due to crack closing or material nonlinearity, if any, was neglected, in parallel with some studies considering closed cracks [Chati *et al*, 1997]. But results indicate that consideration of a crack as an open crack rather than a closed crack gives a better prediction of crack size [Chati *et al*, 1997].

Lamb waves, elastic waves in plate-like structures (to be specified in a forthcoming chapter), was first found useful for NDE of composites by Worlton in 1960 [Kessler, 2002], and their applications have doubled since the 1980s. Lamb waves are able to propagate over a relatively long distance even in materials with high attenuation ratios, such as CF/EP laminated composites, and a broad area can thus be examined

with only a few transducers. Meanwhile, the entire thickness of the laminate can be interrogated by virtue of various vibration patterns of Lamb waves, offering the possibility to detect internal damage as well as surface defects.

Tang and Henneke [1991] used Lamb waves to quantify the axial stiffness reduction in a laminated composite plate. Similarly, the reduction in cross-ply laminate due to transverse crack was evaluated by Toyama *et al* [2003]. Seale *et al* [1998] used Lamb waves to detect fatigue damage and thermal damage in composites. Benz *et al* [2003] localised a notch in a plate structure based on laser source-generated Lamb wave signal in a time–frequency space. Paget *et al* [2003] proposed a method to track impact damage for aerospace composite plates aided by an advanced signal-processing technique. Tan *et al* [1994] identified delaminations of different sizes with Lamb waves, and discussed the sensitivity of wave probes to detectable damage sizes.

Most representatively, Chang [1995], and Wang and Chang [1999] reported a practical damage identification approach using Lamb waves generated by distributed piezoelectrics. Lemistre and Balageas [2001] successfully detected delamination in CF/EP composite structures by analysing damage-scattered Lamb waves. Badcock and Birt [2000] established a relation between attenuation of symmetric Lamb wave and residual energy for different impacts, which contributed to identification of impact damage. Kessler *et al* [2002a, 2002b] also presented a Lamb wave-based detection approach for composite structures and an optimisation technique for the shape of piezoelectric actuators.

Damage detection using elastic waves has also been extended to more complex structures, such as sandwich structures [Kwon and Wojcik, 1998; Jensen and Irgens, 1999; Castaings and Hosten, 2001b; Osmont *et al*, 2002; Yam *et al*, 2003] and honeycomb structures [Thwaites and Clark, 1995]. All of these pilot studies have

consolidated the essential role of elastic waves in developing quicker, more accurate and economical NDE techniques for various engineering practices.

Regardless of their excellent ability to overcome the shortcomings of traditional NDE techniques, methodologies based on elastic waves, particularly Lamb waves, still present some thorny issues, which can considerably limit their successful application unless effective amelioration is found. Basically, elastic waves in composite structures are highly intractable. With very fast propagation velocity, reflected waves from geometric boundaries may easily hide damage-scattered wave components. Thus, to ensure precision, the structure under inspection should be relatively large, and meanwhile the effective detection area relatively small. Multiple wave modes are usually engaged in elastic waves, which also interfere with signal understanding. Under such circumstances, efficient signal processing/interpretation is of vital importance.

2.5 Non-Model-Based *vs.* Model-Based

Based on the discussion above, a comparison between non-model-based and model-based NDE techniques for composite structures is summarised in Table 2.1.

Non-model-based

Non-model-based NDE techniques usually feature exactness, convenience, speed, and independence of complicated analytical models. The detection is locally conducted, facilitating investigation on a focused region and ensuring high sensitivity to different damage sizes. Results are explicit, intuitive and easy to interpret in most cases. Among these techniques, ultrasonics seems most effective for general purposes, while acoustic emission is simplest in triangulating defect location.

Detectable damage types by these methods are detailed in Table 2.2 [Tan *et al*, 1995].

Table 2.1 Comparison of major NDE techniques for composite structures

	Method	Merits	Shortcomings	Applications
Non-model-based	***Visual inspection & tapping***	Quick, no cost, no preparation	Very rough, experience required	Rough detection; large damage in simple structure
	Ultrasonics	Sensitive, intuitive, reliable & exact, good penetrability	Time, money & labor consuming, probe needed, out-of-service required	Small damage, large thickness; difficult for online application; simple and flat structure
	Acoustic emission	Surface mountable, good coverage	Passive, not exact, complex results, fast damping	For location detection only, small structures only
	Eddy-current	Surface mountable, most sensitive	Expensive, complex results, safety hazard, large power source needed	For composite structures; not yet mature; offline applications
	Radioscopy	Exact, intuitive, easy to understand	Expensive, safety hazard	Offline detection only
	Infrared thermography	Exact, sensitive	Expensive, image processing needed	Small structure, laboratory only
Model-based	***Modal Data***	Convenient, cheap, quick, good coverage	Susceptible to boundaries and environment; insensitive to small defects; benchmark needed; low accuracy	Good for large structures; good for presence detection
	Impedance	Low cost	Less precision; incapable of distant defect detection	Real-time detection; damage near sensor
	Static parameters	Cost-effective, convenient	Insensitive to small or varying defects; complex model, benchmark needed	For defect and material property changes
	Damage Index	Cost-effective	Complex model and benchmark needed	Delamination; good for location detection
	Elastic Wave	Cost-effective, fast, exact, repeatable	Sophisticated signal processing required	Universal

Table 2.2 Detectable damage types by major non-model-based NDE techniques

Damage Type	Ultra-sonics	Radio-graphy	Eddy-Current	Acoustic Emission	Thermo-graphy	Optical holography
Voids, porosity	Yes	Yes	No	No	Some	Some
Debonding	Yes	Some	No	Some	Yes	Yes
Delamination	Yes	Some	No	Some	Yes	Yes
Impact damage	Yes	Yes	Yes	No	some	some
Resin variations	Yes	Some	No	No	No	No
Broken fibres	Yes	Some	Yes	Yes	No	No
Fibre misalignment	Yes	Yes	Yes	No	No	No
Resin cracks	Yes	Some	No	No	No	No
Cure variations	Yes	Some	No	No	Yes	Yes
Inclusions	Yes	Yes	No	No	Some	No
Moisture	Yes	Some	No	No	Yes	No

However, none of these non-model-based NDE approaches are mature enough to be used independently in practice [Kessler, 2002] or for online detection. There are several reasons. Firstly, when locally conducted, the entire structure has to be rigorously and slowly scanned, which becomes impractical for large structures with complicated geometry. *A priori* knowledge about the possible vicinity of damage is helpful, but that is not always available. Secondly, these techniques usually require the whole structure, or at least portion of it, to be readily accessible, to ensure that the probe (such as X-ray or ultrasonic probes) is functional. Thus in most cases a temporary downtime or even disassembly of components from main structures may be required. Finally, instruments and equipment involved in this category are generally costly and bulky. Because of these shortcomings, non-model-based NDE approaches can be most effective for *offline* damage assessment. Most likely a

combination of several types would be able more efficiently to capture arbitrary forms of damage in composite materials.

Model-based

Basically, model-based NDE approaches perform the comparison between measured structural parameters before and after damages is incurred, and feature low cost and ease of implementation. Most importantly, they potentially permit *online* detection without the need to terminate normal system operation. Meanwhile, globally conducted measurement points can be customised for user convenience.

In particular, modal data (frequency, mode shapes, etc.) exhibit extra cost-efficiency for civil engineering communities. These data are well able to reflect global properties of a structure. But in contrast, damage known as a local phenomenon may not significantly influence global responses. In fact, studies [Staszewski *et al*, 1999a, 2000; Yam *et al*, 2002] have shown that modal data probably are not responsive to damage until it reaches a notable level (usually greater than *10%* of the entire structure). Pandey *et al* [1991] also demonstrated that delamination in a composite structure can cause frequency shift, but the maximum shifts occur only where the wavelength approximates the size of debonding.

Damping properties are generally far more sensitive to delamination than stiffness, which suggests that damping is a better indicator, especially for small and medium crack length [Zou *et al*, 2000]. Though effective for some cases, damping is a complex factor. On the other hand, change in mass is least responsive to damage [Zou *et al*, 2000], and accordingly not ideal for damage detection.

Intact structures are usually required as benchmarks, though some attempts have been made to be independent of them [Stubbs and Kim, 1996]. However, it is not

always possible to provide benchmarks in engineering practice. Extra storage for benchmark data can become a major concern for large or complicated civil structures. Additionally, modal data are egregiously susceptible to changes in boundary conditions and environmental factors, even temperature or humidity. Thus the damage-induced shift may be severely overshadowed by such interference.

Other model-based NDE techniques, generally speaking, can play an effective role in detecting certain types of damage with various levels of complexity. However, electrical/mechanical impedance, static parameters and damage indices seem incapable of providing sufficient and quantitative information to describe small or growing defects, and their individual implementation is not reliable [Shen and Sharpe, 1998].

Compared with other techniques, elastic wave-based methods exhibit outstanding advantages in offering more sensitive and cost-effective detection. For example, with the same size of sensor, smaller damage can be detected by wave-based approaches (refer to Figure 2.2); and for the same damage size, less power is required by such a method (refer to Figure 2.3). In summary, elastic wave-based damage detection is characterised by:

(1) ability to inspect large structures, e.g. a pipe system;
(2) ability to inspect the entire cross sectional area of structures, *100%* coverage over a fairly long length;
(3) no need for complicated and expensive insertion/rotation devices, no need for motion of sensing devices during inspection;
(4) excellent sensitivity to many defects; high identification precision;
(5) ability to inspect tubing or piping under water, coating or insulation, but without any loss of sensitivity;
(6) lower energy consumption, greater cost-effectiveness.

But as commented before, the practical utility of this technique must be guaranteed by sophisticated signal processing and interpretation software.

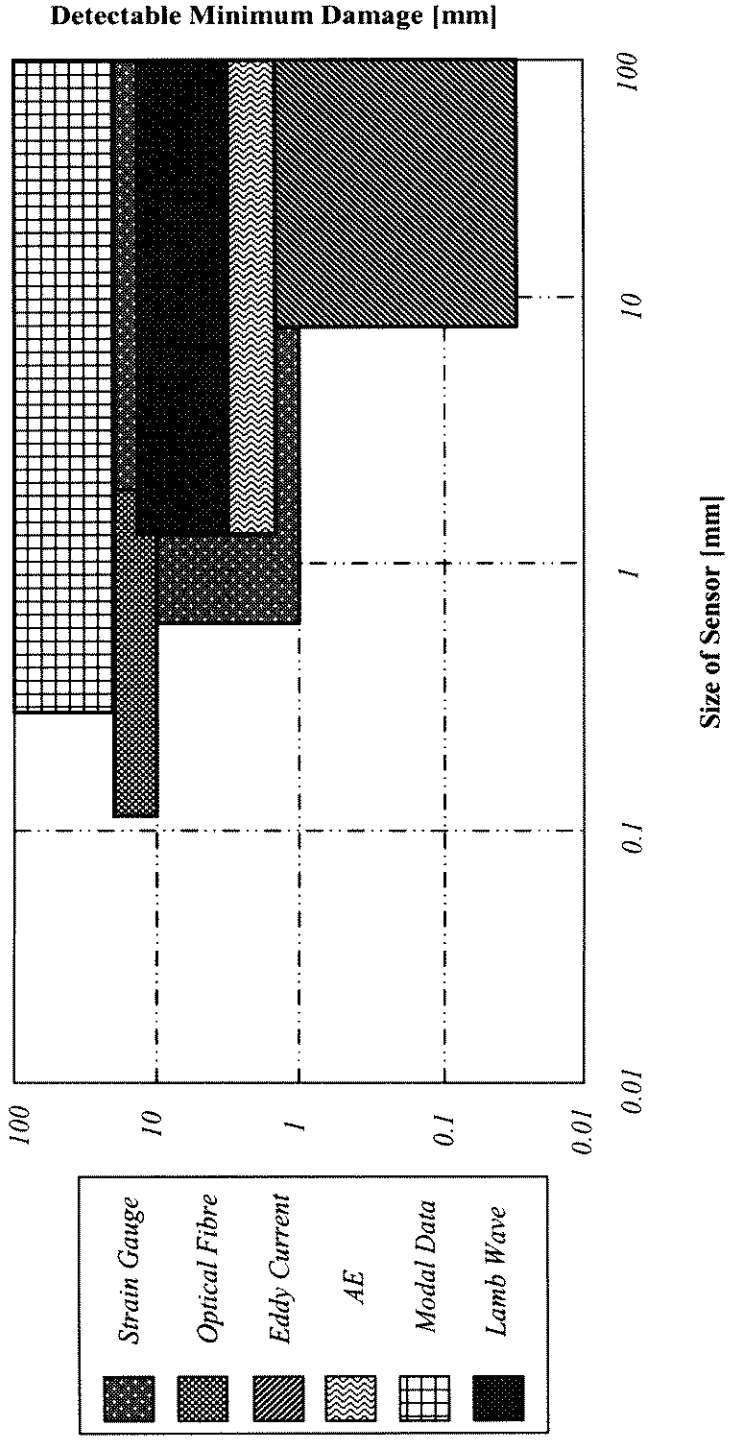

Figure 2.2 Comparison of elastic wave-based NDE with other methods: size of detectable minimum damage *vs.* size of actuator [Kessler and Spearing, 2002]

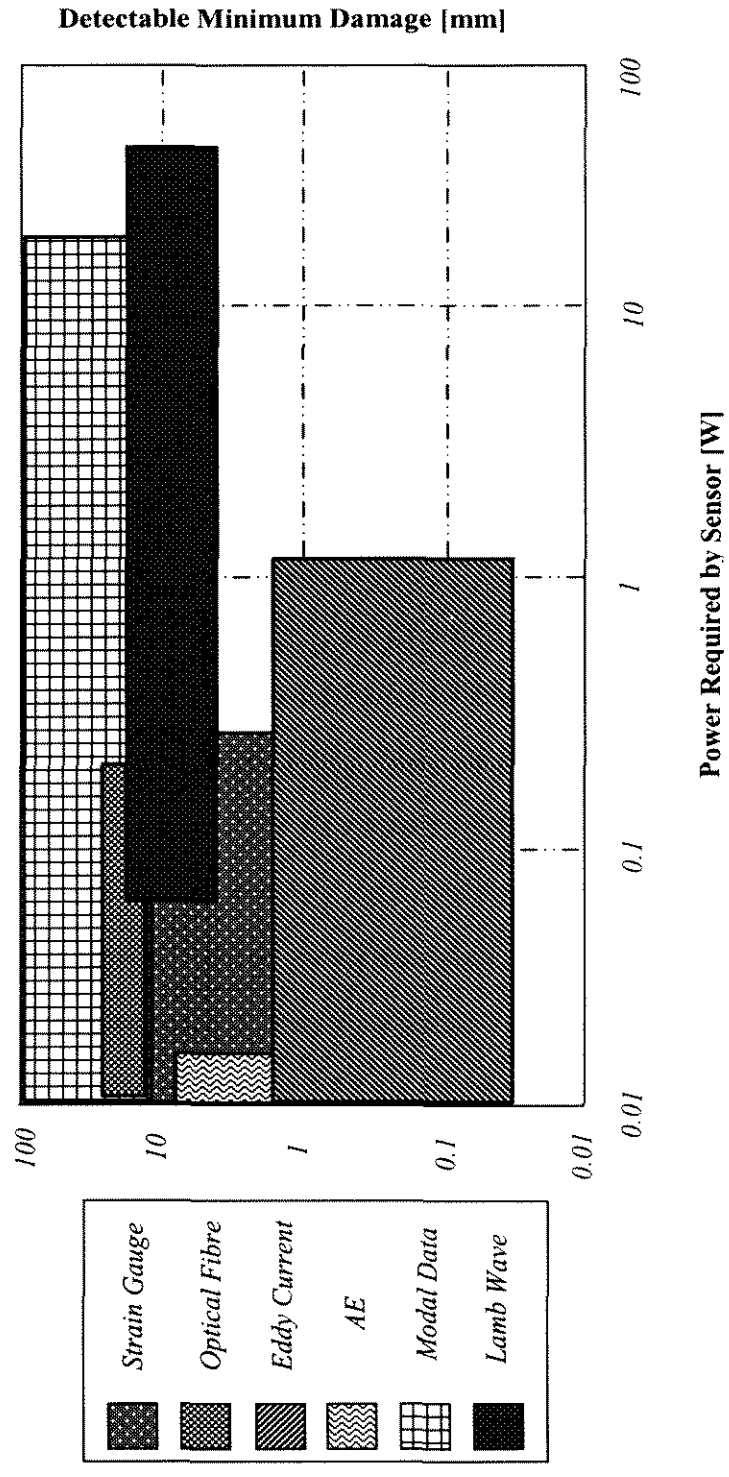

Figure 2.3 Comparison of elastic wave-based NDE with other methods: size of detectable minimum damage *vs.* power required for excitation source [Kessler and Spearing, 2002]

2.6 Sensor Technology for NDE

Systems endowed with autonomous diagnosis ability are known as smart structures. More generally, a smart structure is literally described as an integrity that senses its internal state/external environment, and consequently responds in a certain manner [Chiu *et al*, 2000]. The primary advantages of smart structures are cost-saving and significant service-life extension. One key issue implied by the definition is the sensing capability. Analogous to the nervous system of human beings, a sensing network is essential for practical introduction of damage detection in composite structures. As a basic unit in a sensing network, a sensor converts physical responses into electrical or optical signal identifiable for data acquisition hardware [Mathworks, 2001a]. Sensor technology, an interdisciplinary technology, is seen as an integral element in the overall development of NDE, spanning areas of physics, chemistry, materials, molecular biology, manufacturing, electronics and signal processing. General sensor technology also covers R&D for actuating devices.

Basically, sensing devices for NDE purposes require (1) a certain resistance to general environmental injury, (2) a life of at least *5-10* years, (3) simple and easy handling and attachment [Mathworks, 2001a]. For higher performance, they should feature smaller size, lighter mass, higher sensitivity, lower cost/power, more reliable and quick response to sudden changes, as well as easy integration. To cater for future trends, preferences also include remote control and data transmission, toughness for vibration and noise, little aging deterioration and less wire or even wireless state.

Sensor Type and Selection

Various sensing/actuation devices are available for different NDE purposes, including piezoelectrics, optical fibres, magnetostrictive/electrostrictive, electro-rheological fluids, and shape memory alloy/polymer, compared in Table 2.3.

Table 2.3 Sensors for NDE

Sensor	Applications/Features	Available Style
Ultrasonic probe	Flaw, distance & thickness detection, exact & efficient	Contact, air/ fluid-coupled
AE sensor	changes in physical property only, location detection, passive sensor	Attaching, embedding
Magnetic sensor	Crack or large deformation with magnetic leakage, soft magnetic piece, magnetic field required	Contact, attaching
Eddy-current transducer	Electromagnetic impedance detection, good for composites, too complicated, expensive	Attaching
Accelerometer	Acceleration detection, high-frequency response	Attaching
Strain gauge	Deformation detection, low-frequency response, possible to use in hostile environments, cheap	Attaching
Shape memory alloy	Active sensor, deformation detection, active control, large force, low-frequency response	Attaching, embedding
Laser interferometer	Derivation or displacement measuring, high precision, expensive	Contactless
Optical fibre	Deformation, temperature & location detection, line sensing, high precision, conformable, expensive	Embedding
Electro-magnetic acoustic transducer (EMAT)	Narrow band, avoidance of physical contact	Contact, attaching
Piezoceramics	Active sensor, vibration detection, high-frequency response, low driving force, cheap	Attaching, embedding
Piezoelectic paint and PVDF	vibration and/or crack detection, easy application for non-flat shapes, cheap	Attaching, embedding

There is no single principle in selecting sensors for a practical application. Typically, strain gauges are able to give localised measurement of deformation economically, but are applicable only for static or dynamic changes at a low rate. Acoustic emission (AE) sensors can be efficient in triangulating damage and monitoring propagation of a crack, but do not sense the damage unless it is propagating. Moreover, AE sensors are highly susceptible to noise interference during measurement. Fibre-optic sensors

can sense strain and vibration, but are difficult to fit into structures with complex geometry. These three devices are passive sensors.

In contrast, self-sensing devices, represented by piezoceramic materials, can be used as active sensors. Compared with passive sensors, they are more flexible and controllable. But used locally, a single sensor is unable to offer enough information for a complex damage, and a large number of sensors is often required to configure an active sensor network, ensuring completeness of acquisition.

Piezoelectric Sensors

The piezoelectric actuator/sensor shows an excellent capacity to satisfy the exigency of *online* NDE techniques. With regard to double piezoelectric effects, piezoelectrics can be fabricated to function as both actuator and sensor, permitting significant reduction in transducer number, electrical wiring and associated hardware. They are known for excellent mechanical strength, wide frequency response ranges, generation of relatively high voltage with a low current and favorable cost. The insignificant mass and volume make it possible for piezoelectrics to be distributed in a structure with only minor effects on structural mechanical properties. Compared with other sensors, piezoceramics are more favorable for cost-effective NDE techniques.

Crystals, ceramics and polymers are the major available forms of piezoelectrics. Modern techniques allow piezoceramics and piezo-polymer in arbitrary geometric configurations, e.g. plate, disk, ring, tube, etc. These sensors can be flexibly bonded onto or embedded into a composite structure. For instance, one recent publication reports work aimed at developing piezoelectric fibres integrative for composite materials [Ristic, 1994].

Chapter 3

Elastic Waves in Engineering Structures

3.1 Introduction

With a distinguished history, studies for the mechanism of elastic waves have been rigorously conducted for nearly two centuries, though their sophistication and utility for damage detection are still highly debated. For developing wave-based damage detection algorithms in this study, it is essential to understand wave propagation characteristics in engineering structures, in particular composite structures. In this chapter, the fundamentals of elastic waves in both homogeneous and anisotropic media, from one-dimensional to three-dimensional, are addressed, with a review of the major body of related studies.

Antecedents of this specialty are not hard to identify. It was Lord Rayleigh in 1889 who first explained wave propagation along a guided surface, and the wave discovered was then named after him (*Rayleigh wave*). After 1900, interest in waves gained momentum from geophysics. Following Rayleigh's work, Love and Lamb individually examined plate waves in 1911 and 1917, respectively, and established the theoretical relation between velocity dispersion and frequency for waves in homogenous plate in vacuum [Lowe, 1995]. In 1924, Stoneley discovered that waves travel along the interface between two different solids (*Stoneley Wave*) [Achenbach, 1973]. All these pioneering studies on elastic waves provided the basis for what is currently known as the *theory of elasticity* [Chimenti, 1997].

3.2 Elastic Waves in Engineering Structures

The elastic wave, a dynamic disturbance originating from forced motion of a portion in a deformable substance, (1) is highly susceptible to interference, e.g. discontinuities or boundaries, during propagation; (2) consumes a certain period of time to propagate from its excitation source to other areas; (3) is influenced by resistance to deformation due to material consistency and resistance to the motion due to the inertia of materials; and (4) carries kinetic and potential energy from consecutive motions of particles around positions of equilibrium. These four characteristics serve as the basic principia for the elastic wave-based damage detection algorithm developed in this study.

More specifically, waves that compulsorily require boundaries to keep propagation are referred to as guided waves [Achenbach, 1973]. Examples include waves in a rod, plate, tube, or multilayer structure. Guided waves often interact with boundaries by way of reflection and refraction.

3.2.1 Waves in One-Dimensional Structural Beam

In engineering design, many structural components are one-dimensionally simplified as a flexural beam or rod. Slaved to one spatial variable only, guided waves in a beam can be easily described without the encumbrance of geometrical complication. Three modes are generally available according to the particulate motion styles, i.e., *longitudinal*, *torsional* and *transverse* modes.

3.2.1.1 Longitudinal Mode

Considering an Euler-Bernoulli beam subjected to a longitudinal disturbance, the particles are energised to deviate around their positions of equilibrium along the axial

direction, and the induced wave is defined as *longitudinal mode*, as illustrated in Figure 3.1(a). Normal stress, $\sigma_x(t)$, is related to strain, $\varepsilon_x(t)$, as [Achenbach, 1973]

$$\sigma_x(t) = E \cdot \varepsilon_x(t) \tag{3.1}$$

where E is Young's modulus of the beam. Both strain and stress are dependent on only location, x, and time, t. For a single micro-element, in Figure 3.1, in the absence of lateral inertia, the governing equation of motion gives

$$\frac{\partial \sigma_x}{\partial x} = \rho \frac{\partial^2 u}{\partial t^2} \tag{3.2}$$

where u is the axial displacement under the excitation, and ρ denotes the mass density of beam. Deformation in the transverse direction is not prevented. Substituting Equation (3.2) into (3.1) yields

$$\frac{\partial^2 u}{\partial x^2} = \frac{1}{v^2} \cdot \frac{\partial^2 u}{\partial t^2}, \quad v = \sqrt{\frac{E}{\rho}} \tag{3.3}$$

where v is the wave propagation velocity.

3.2.1.2 Transverse Mode

Consider the same beam under a pure transverse disturbance perpendicular to the axis, as in Figure 3.1(b). Such an excitation induces particulate transverse displacement, referred to as *transverse mode* or *flexural mode*. With the assumption of the beam axis being the x-axis and neglecting any twisting effect, the governing motion equation can be expressed in terms of the lateral displacement $w(x,t)$ and rotation angle $\theta(x,t)$ [Bland, 1988; Doyle, 1997] upon introduction of the shear correction coefficient κ,

$$\kappa^2 c_s^2 [\frac{\partial^2 w}{\partial x^2} - \frac{\partial \theta}{\partial x}] - \frac{\partial^2 w}{\partial t^2} = 0$$

$$c_0^2 \frac{\partial^2 \theta}{\partial x^2} + \kappa^2 \frac{c_s^2}{q^2}[\frac{\partial w}{\partial x} - \theta] - \frac{\partial^2 \theta}{\partial t^2} = 0 \tag{3.4}$$

$$c_0 = \sqrt{E/\rho}\ ,\ c_s = \sqrt{G/\rho}\ ,\ q = \sqrt{I/A}\ ,\ \kappa = \pi/\sqrt{12}$$

where E, G, I, A and ρ denote the elastic modulus, shear modulus, second moment of area, cross-section area and mass density of the beam, respectively. Upon consideration of dispersion relations [Bland, 1988],

$$w = w_0 \cdot e^{-i(kx-\varpi t)}, \qquad \theta = \theta_0 \cdot e^{-i(kx-\varpi t)} \tag{3.5}$$

the eigen-roots (wavenumber) for Equation (3.4) are obtained

$$k_n = \pm\left[\frac{1}{2}\left(1+\frac{c_0^2}{\kappa^2 c_s^2}\right) \pm \sqrt{\left(\frac{c_0}{q\varpi}\right)^2 + \frac{1}{4}\left(1-\frac{c_0^2}{\kappa^2 c_s^2}\right)^2}\right]^{1/2} \cdot \frac{\varpi}{c_0} \tag{3.6}$$

$$(n = 1,\ 2,\ 3,\ 4)$$

The existence of four eigen-roots mathematically determines that four possible wave components are available synchronously. By considering all eigen-roots, the solution to Equation (3.4) can therefore be obtained as [Achenbach, 1973]

$$w(x,t) = [\sum A_1 e^{-ikx} + \sum A_2 e^{ikx} + \sum A_3 e^{-kx} + \sum A_4 e^{kx}] \cdot e^{i\varpi t} \tag{3.7}$$

In Equation (3.7), each term corresponds to one of the four possible wave modes, hereafter recognised as *positively propagating wave*, *negatively propagating wave*, *positively growing evanescent wave* and *negatively exponentially decaying wave*, respectively, depending on the propagation direction and properties.

3.2.1.3 Torsional Mode

In the absence of axial and radial disturbances, a *torsional mode* can be produced when a pure tangential loading is applied, as in Figure 3.1(c). This results in only tangential motion in the cross-section, vertical to the axis, formulated as [Rose, 1999]

$$\frac{\partial^2 u_\theta}{\partial r^2}+\frac{1}{r}\frac{\partial u_\theta}{\partial r}-\frac{u_\theta}{r^2}+\frac{\partial u_\theta}{\partial x^2}=\frac{1}{c_T^2}\frac{\partial^2 u_\theta}{\partial t^2} \tag{3.8}$$

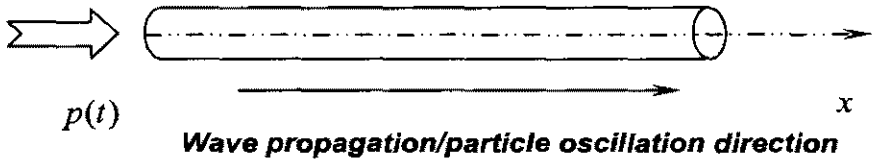

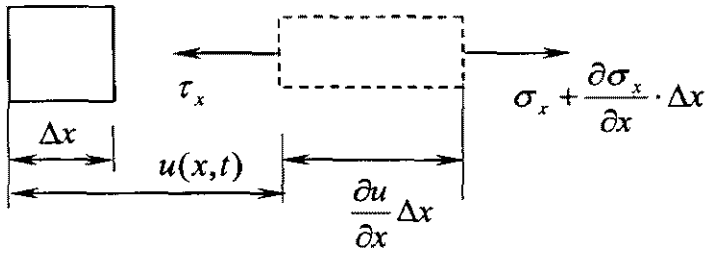

(a)

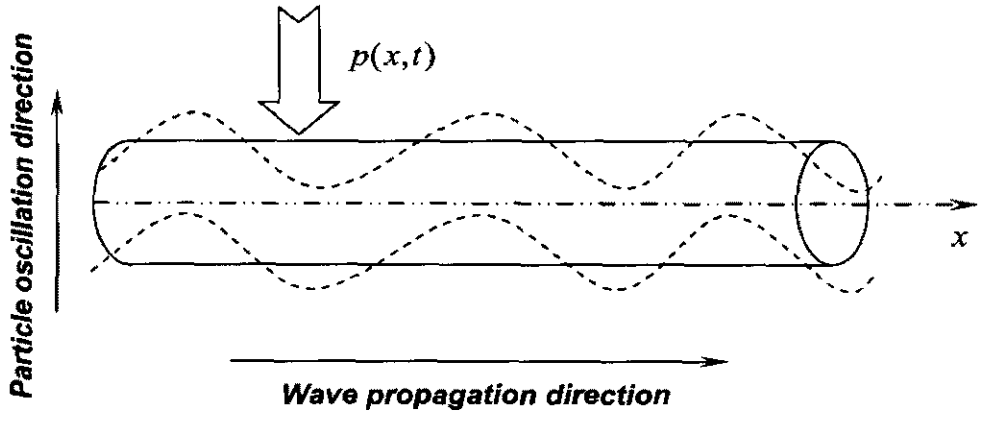

(b)

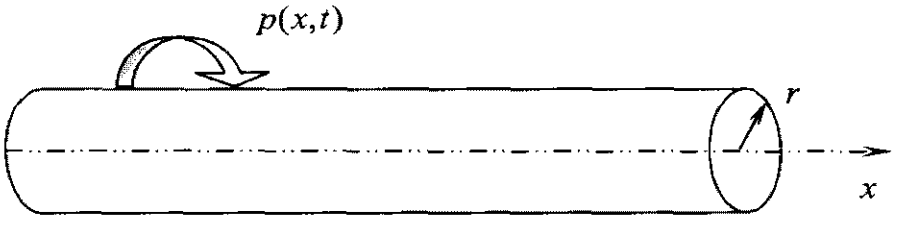

(c)

Figure 3.1 Wave propagation in one-dimensional structural beam or rod: (a) longitudinal mode; (b) transverse mode; (c) torsional mode

where $c_T = \sqrt{\mu/\rho}$ is the torsional wave speed. u_θ is the tangential displacement, with the radial coordinate, r, axis coordinate, x, and time, t. Applying boundary conditions, $\sigma_{rr} = \sigma_{rx} = \sigma_{r\theta} = 0$ at $r = a$ on Equation (3.8), leads to

$$u_\theta = \frac{1}{2} Bre^{i(kx-\omega t)} \tag{3.9}$$

where B is a constant. Equation (3.9) represents the lowest torsional mode, the amplitude of which is proportional to the rod radius (both u_r and u_x are zero). The lowest mode is non-dispersive, while the higher modes are predicted to be dispersive and their frequency spectra have the same shapes as those of plate wave [Rose, 1999].

3.2.2 Waves in Plate-Like Structures

Similarly, according to particle motion style, guided waves in plate-like structures can be [Bindal, 1999]:

Longitudinal Wave

Travelling through the medium as a series of alternate compressions and rarefactions, a *longitudinal wave* vibrates particles back and forth in the direction of wave propagation, as illustrated in Figure 3.2(a).

Transverse Wave

Transverse wave, also termed as *shear wave*, is generated by the vibration of particles perpendicular to wave propagation, as in Figure 3.2(b).

Rayleigh Wave

Also defined as *surface wave* and existing along the free surface of a semi-infinite (or very thick) solid, it decays exponentially in displacement amplitude with distance from the surfaces (see Figure 3.2(c)). The traction forces vanish on the boundary.

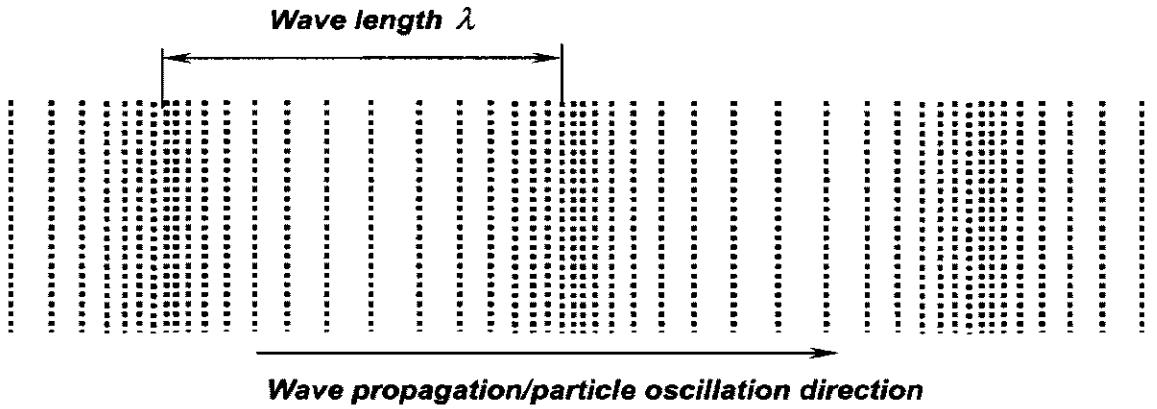

(a)

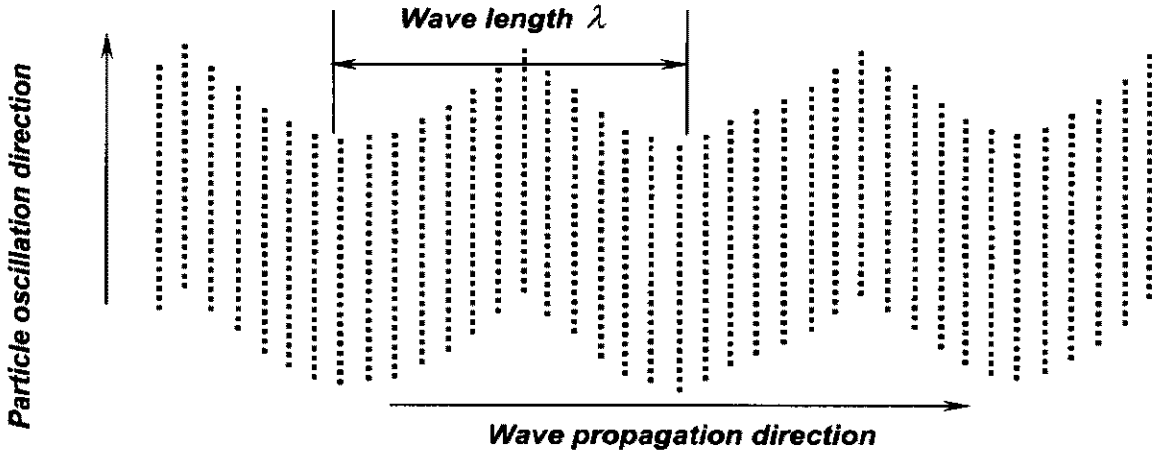

(b)

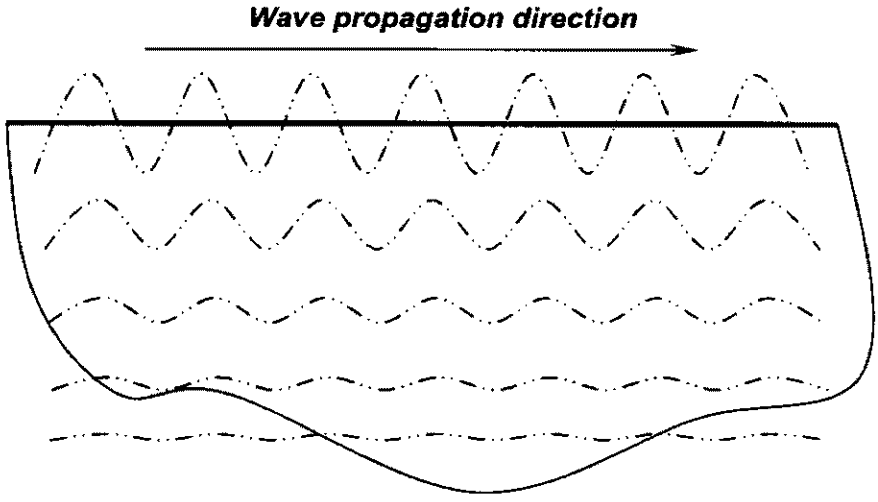

(c)

Figure 3.2 Guided waves in elastic medium: (a) longitudinal wave; (b) transverse wave; (c) Rayleigh wave; (d) Lamb wave; (e) Stonely wave; (f) Creep wave

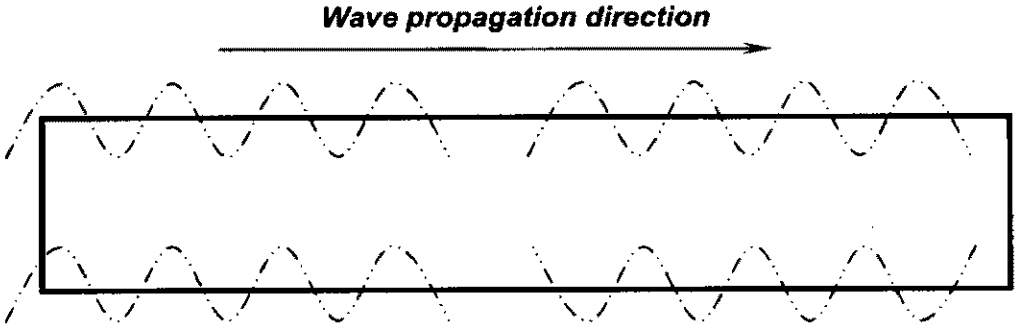

(d)

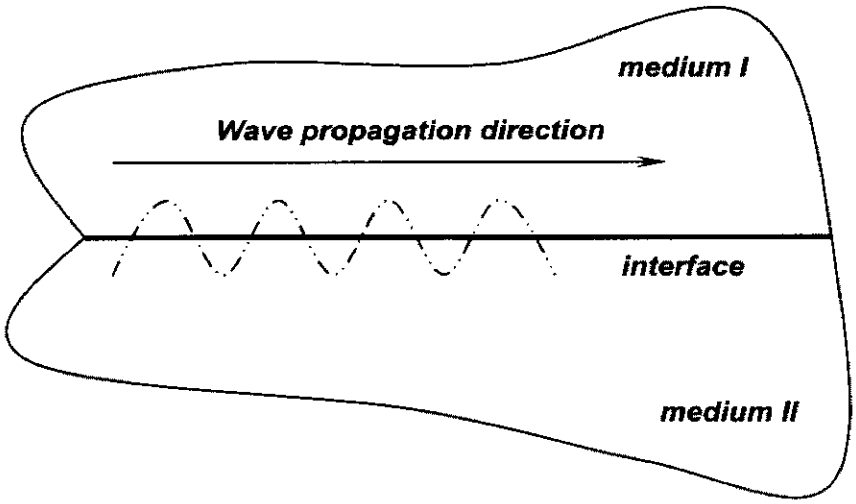

(e)

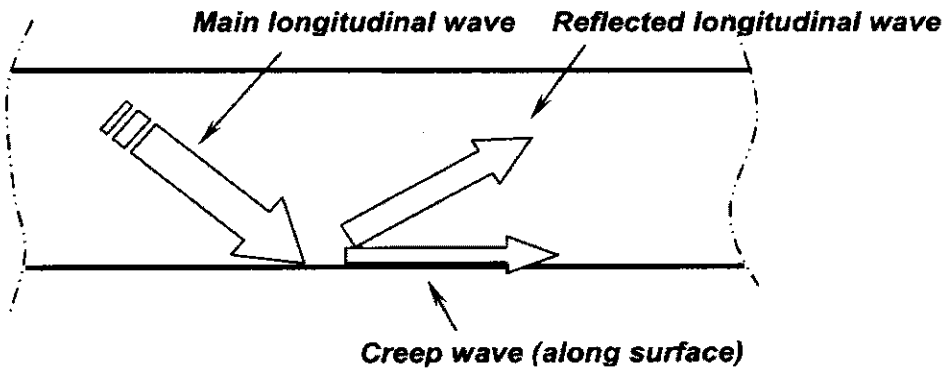

(f)

Figure 3.2 *Cont.*

Lamb Wave

Lamb wave, also known as *plate wave* propagating in a thin plate-like medium, is guided by the upper and lower free boundaries, where traction forces vanish, as shown in Figure 3.2(d). In most cases, infinite Lamb modes are available in a finite body and propagation characteristics vary with entry angle, excitation and structural geometry.

Stonely Wave

As a kind of wave existing at the interface between two media or in the neighbourhood of a free surface, the *Stonely wave* is explained in Figure 3.2(e). Continuity of traction and displacement should be met at the interface.

Creep Waves

Generated by refraction of longitudinal waves from a boundary with the same propagation velocity, *creep waves*, sometimes called *head waves*, have similar behavior to that of longitudinal waves (see Figure 3.2(f)).

In most cases, guided waves in plate-like structures are made up of a superposition of longitudinal and shear waves, but, because of boundaries, other modes may be induced simultaneously. Interaction with boundaries often results in mode conversion. Unlike bulky waves in an infinite medium, there is generally an infinite number of modes associated with a guided wave problem. It is the introduction of boundary conditions and multiple modes that make the guided wave problem difficult to handle.

Guided waves in plate with thickness of $2h$ (see Figure 3.3), regardless of mode, can generally be described using the theory of elasticity in a form of *Cartesian* tensor notation [Rose, 1999], as

$$\mu \cdot u_{i,jj} + (\lambda + \mu) \cdot u_{j,ji} + \rho \cdot f_i = \rho \ddot{u}_i \tag{3.10}$$

where u is the displacement field tensor, λ and μ are Lamé constants.

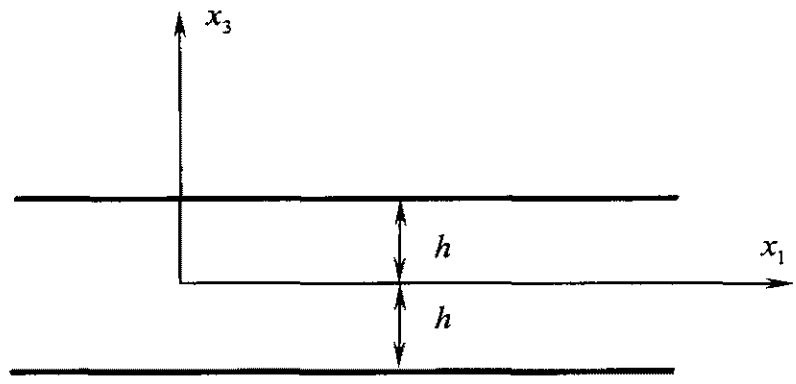

Figure 3.3 Plate (*2h* in thickness) in referred coordinate system

Equation (3.10) governs partial wave motion, which is sufficient to describe wave propagation in an infinite domain. But for a finite elastic medium, boundary conditions are compulsory. For plate with boundary conditions,

$$\sigma_{31} = \sigma_{33} = 0, \text{ at } x_3 = \pm d/2 = \pm h \ \textit{(for plane strain)}$$

a displacement potentials method [Achenbach, 1973; Rose, 1999] has been developed to obtain a general solution to Equation (3.10) as

$$\frac{\tan(qh)}{\tan(ph)} = \frac{4k^2 qp\mu}{(\lambda k^2 + \lambda p^2 + 2\mu p^2)(k^2 - q^2)} \tag{3.11}$$

where

$$p^2 = \frac{\omega^2}{c_L^{\,2}} - k^2, \ q^2 = \frac{\omega^2}{c_T^{\,2}} - k^2, \text{ and } k = \omega / c_p$$

k, c_L, c_T, ω are the wavenumber, velocities of longitudinal and transverse modes, wave circular frequency, respectively. Equation (3.11) generally describes guided waves in plate-like structures.

3.2.3 Waves in Anisotropic Multilayered Laminates

Waves in multilayered media are involved in a wide of situations, ranging from coating problems of plasma spray on turbine blade, diffusion/adhesively bonded structures, to ice detection for the windshield of aircraft. The increased acceptance of composite materials, whose direction-dependent mechanical properties classify them as typical anisotropic multilayered media, has motivated the relevant studies. Anisotropic properties introduce many interesting but complex phenomena in elastic wave propagation, e.g. direction-dependent speed, difference between phase and group velocities, wave skewing, and others which are somewhat more unique.

Considering an N-layered anisotropic plate, the displacement field, u, within each layer must satisfy Navier's displacement equations [Rose, 1999],

$$\mu^n \nabla^2 u^n + (\lambda^n + \mu^n)\nabla(\nabla \cdot u^n) = \rho^n \frac{\partial^2 u^n}{\partial t^2} \qquad (n = 1, 2, \cdots, 9) \qquad \textbf{(3.12)}$$

where ρ^i and λ^i, μ^i are density, Lamé constants for the i^{th} layer, respectively. The *Helmholtz* principle can be used to decompose the displacement field and achieve a general solution (see [Rose, 1999]).

Material viscoelasticity unavoidably interferes with wave characteristics. Attenuation in wave magnitude, variation in propagating velocity and change in wavenumber are commonly observed, effects which are known as *dispersion*. For the laminate under consideration, $N-1$ interfaces and two free surfaces are available, at which all boundary conditions must be met, leading to a comprehensive correlation from Equation (3.12) [Rose, 1999],

$$\left| A(\omega, k, \lambda^n, \mu^n, h_n) \right| = 0 \qquad \textbf{(3.13)}$$

Known as the *Dispersion Equation*, Equation (3.13) associates frequency ω with wavenumber k or plate geometry (h_n), for a given material (λ^n, μ^n). In an implicit expression, the dispersion equation has infinite roots [Rose, 1999]. Dispersion is a key concern throughout the present study, to be specified in following section regarding Lamb waves.

3.3 Lamb Waves in Laminated Composite Structures

3.3.1 Historical Retrospect

Introduced by Horace Lamb in 1917 in his milestone publication, '*On Waves in an Elastic Plate*' (Proc. R. Soc. London Ser. A. 93:114-128, 1917), Lamb waves can exist in plate-like thin plate with parallel free boundaries [Viktorov, 1967]. Lamb's discovery did not gain wide attention due to the extremely complicated nature of the equations, until 1945 when Osborne and Hart revisited this topic to analyse the interaction between steel plates and waves generated by underwater explosions. Then this intriguing topic was espoused by some great mathematicians such as Cauchy, Lamé, Green and Poisson. A comprehensive solution to Lamb waves was first established by Mindlin in 1950 [Lowe, 1995]. At the same time, equations for Lamb wave in a plate with an arbitrary number of flat layers were established by Thomson [Lowe, 1995].

Pioneer experimental studies on Lamb waves were parallelly carried out by Schoch in 1952, Worlton in 1961 and Frederick in 1962 [Chimenti, 1997]. Until the 1960s most experiments were performed specifically to evaluate Lamb's original theory. A renaissance occurred in the 1970s with the appearance of fast computational devices. Many issues that had previously been exceedingly complex could now be efficiently solved.

3.3.2 Fundamentals

As a typical type of elastic disturbance, Lamb waves can also be described by the general motion equation for waves established above, Equation (3.11). Mathematically comprised of the trigonometrics function *sine* and *cosine*, Equation (3.11) determines that two Lamb modes are synchronously available, i.e. *symmetric* and *anti-symmetric* modes, individually simplified as

$$\frac{\tan(qh)}{\tan(ph)} = -\frac{4k^2qp}{(k^2-q^2)^2}, \quad \textit{for symmetric modes} \qquad \textbf{(3.14a)}$$

$$\frac{\tan(qh)}{\tan(ph)} = -\frac{(k^2-q^2)^2}{4k^2qp}, \quad \textit{for anti-symmetric modes} \qquad \textbf{(3.14b)}$$

Equation (3.14), frequently referred to as the *Rayleigh-Lamb frequency equation*, presents the correlation between the propagation velocity of a Lamb wave and its frequency. In spite of its simplicity in appearance, the equation can be solved only by numerical simulation under most circumstances.

Physically, symmetric modes across the entire plate thickness are symmetric for u (horizontal), and anti-symmetric for w (vertical); and anti-symmetric modes are symmetric for w but anti-symmetric for u, as illustrated in Figure 3.4. Equation (3.14) also implies that Lamb waves, regardless of their mode, are dispersive (depending on propagation frequency).

In addition to Lamb waves, transverse (shear) motion was also observed in layers of finite thickness by Love in 1911. FEM simulation [Birt, 1998] confirmed such a conclusion, based on FEM models which allow particle motion in any direction. Tests [Percival and Birt, 1997; Lemistre *et al*, 1999; Badcock and Birt, 2000] have also demonstrated the existence of horizontal shear wave in the direction perpendicular to the plane of wave travel, besides the normal shear waves (vertical

shear mode) and Lamb waves. This wave is therefore named the *Shear Horizontal* (SH) wave or *Love* wave, and is displayed in Figure 3.5.

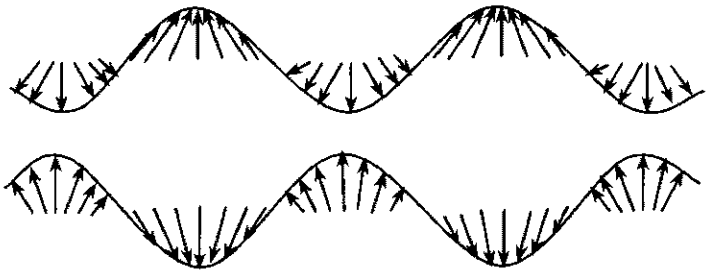

Compressional wave (symmetric Lamb mode)

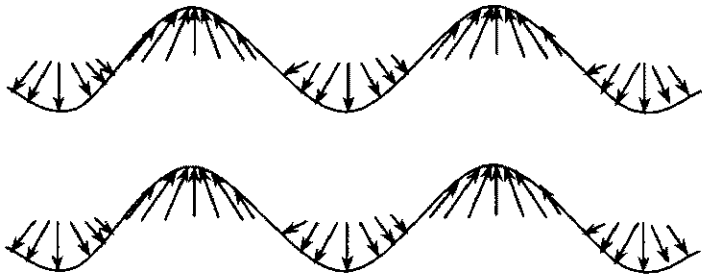

Flexural wave (anti-symmetric Lamb mode)

Figure 3.4 Symmetric and anti-symmetric Lamb wave modes

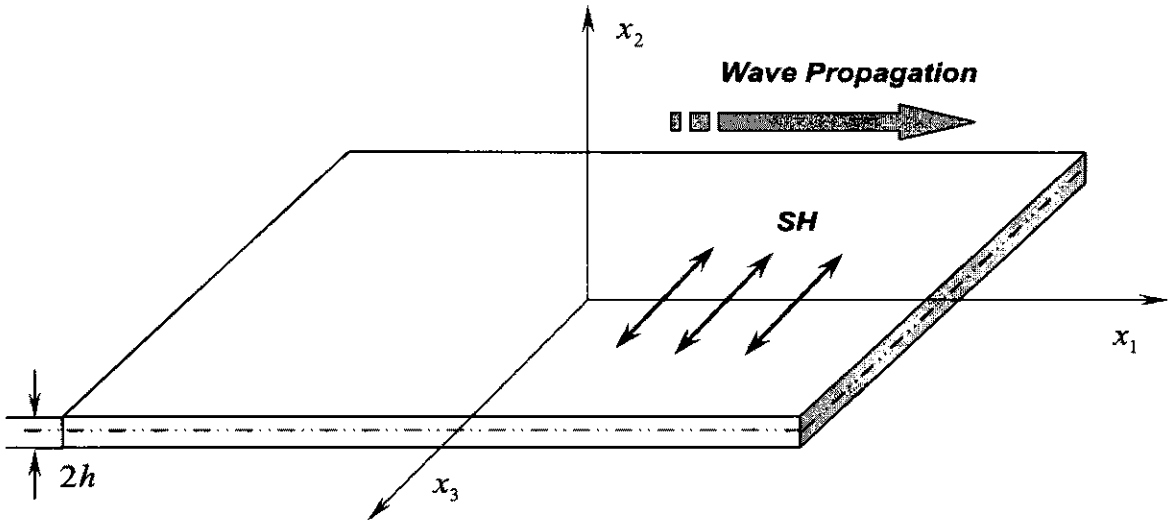

Figure 3.5 Horizontal shear (SH) mode in laminated structure

In Figure 3.5, the wave propagates along the x_1 direction, and the particle vibrates in the x_3 direction, which is caused by SH modes in a plane parallel to the surface of layers. Any mode in the SH family can be considered as a superposition of up- and down-reflecting bulk shear waves, polarised along x_3, with wavevectors lying in the $x_1 - x_2$ plane and inclined at such an angle that the system of waves satisfies traction-free boundary conditions on surfaces [Rose, 1999]. Analytically, *Love* mode can be governed by [Achenbach, 1973]

$$\frac{\partial^2 u_3}{\partial x_1^2} + \frac{\partial^2 u_3}{\partial x_2^2} = \frac{1}{c_T^2} \cdot \frac{\partial^2 u_3}{\partial t^2} \tag{3.15}$$

with the general solution under the boundary condition $\frac{\partial u_3}{\partial y} = 0$ at $y = 0$,

$$u_3 = [B_1 \sin(q_B x_2) + B_2 \sin(q_B x_2)] \cdot \exp[ik(x_1 - ct)] \tag{3.16}$$

$$q_B = k[(\frac{c}{c_T})^2 - 1]^{\frac{1}{2}}$$

B_1 and B_2 are constants. Like Lamb waves, basic Love modes exist only in the relatively low frequency ranges, and higher modes gradually appear with an increase of excitation frequency.

In this study, Lamb waves together with Love waves are employed in the proposed damage detection scheme, to be detailed in the following chapters.

3.3.3 Generation of Lamb Waves: A Review

In spite of many attractive traits, Lamb waves in anisotropic viscoelastic media are notoriously complicated. Based on Equation (3.11), multiple Lamb modes are simultaneously available with unique dispersive properties, even for the same mode but in different frequency scopes. Two technologies are therefore motivated for

generation of Lamb waves: (1) active generation of controllable Lamb waves, and (2) effective signal processing and interpretation (to be detailed in Chapter 4).

Lamb waves can be actively excited by a variety of means. With each possessing unique intrinsic advantages and disadvantages, these methods can be roughly summarised into four major categorises.

(1) *Ultrasonic probes*. Notable for excellent precision and controllability, ultrasonic probes coupled with angle-adjustable perspex wedges have dominated nondestructive evaluation (NDE) practice over the years [Alleyne and Cawley 1992b; Guo and Cawley 1992, 1994; Cawley and Alleyne, 1996; Percival and Birt, 1997], to generate and collect pure Lamb waves in accordance with the Snell's law [Bindal, 1999]. Without interference from multiple modes, the probe-excited Lamb wave permits explicit signal interpretation.

Such methods, though extensively successful, are nowadays challenged for their use in real-time NDE, where their access into in-service systems is somewhat problematic. Downtime is usually required to guarantee the probe operation. During manipulation, couplant, directionality and contact are some basic issues that may considerably influence detection effectiveness. Motivated by these obstacles, non-contact innovations, such as air-coupled [Castaings and Cawley, 1996; Castaings and Hosten, 2001a; Hosten *et al*, 2001] and fluid-coupled [Ghosh *et al*, 1998] transducers or electro-magnetic acoustic transducers (EMAT) [Guo *et al*, 1997; Legendre *et al*, 2000] were invented. However, air- or fluid-coupled transducers can suffer from the large differences in mechanical impedance between air/fluid and objects under detection. Additionally, being the diagnostic signal most extensively excited by ultrasonic probes, the narrowband pulse excitation, though it provides centralised incident energy, becomes less efficient for the detection of near-surface damage, where reflections from defects are limited within the wavelength of transmitted

ultrasonic pulse [Achenbach, 2000]. EMAT can be one effective way to generate SH-waves, but they are usually interfered with by the electrical conductivity of the objects to be inspected [Achenbach, 2000], and their effectiveness can be limited in certain frequency ranges. Meanwhile, the non-negligible mass/volume of probes, costly excitation establishment and complexity of device manufacture also reduce the practical applications of these ultrasonic probes to a certain extent.

(2) *Laser*. Non-contact excitation of Lamb waves via *Laser-Based Ultrasonics* (LBU) and acquisition using *Laser Interferometer* (LI) have recently appeared as a promising method for contactless NDE [Guo *et al*, 1997; Yoshimura *et al*, 1998; Ishak *et al*, 2001; Niethammer *et al*, 2001; Valle and Littles, 2002; Gao *et al*, 2003; Silva *et al*, 2003]. *Fabry–Perrot* interferometer and heterodyne interferometers are most frequently employed in this field. Flexibly controllable, LBU can be designed to be broadband or narrowband depending on actual applications, to satisfy different spatial resolution requirements. The exact detection that LBU can offer ranges from apparent defects to small cracks. LBU can be exceptionally effective for remote manipulation with easy scanning, exact calibration and applicability to curved surfaces or complicated geometry [Achenbach, 2000], and is applicable even in exigent environments where access is unfeasible. Besides, by using a short laser pulse, it is possible to excite a broad bandwidth signal with several Lamb modes in a single measurement, providing more opportunities to selectively use the most appropriate modes [Silva *et al*, 2003].

Nevertheless, subject to similar concerns as those encountered by probe-based methods, the application of LBU is clearly restrained in cost-effective real-time damage assessment systems, in which surveillance devices are expected to be economically integrated into the system without affecting the original structural integrity, because of its bulky and costly excitation equipment.

(3) *Piezoelectric elements*. Initially used for sensing devices such as accelerometers, or for active structural control, Piezoelectric Lead Zirconate Titanate (PZT) elements have delivered promising performance for damage detection since the 1980s [Keilers and Chang, 1995a, 1995b; Dupont *et al*, 1999; Lemistre and Balageas, 2001; Kessler *et al*, 2002a, 2002b], regarded as an important step towards intelligent structure techniques to fulfil online damage detection. A PZT element, shaped as a disc or tube, etc., is mass-less and volume-less, has low-power consumption, easy integration and activation, low acoustic impedance, wide frequency responses and low cost. PZT elements are particularly suitable to be easily integrated with structures with minor intrusion as *in-situ* wave generators or sensors. Using distributed PZT elements, transducer networks can be further tailored to realise multi-point measurements [Chang, 1995; Lemistre and Balageas, 2001].

Despite these merits, PZT generated-Lamb waves still present undesirable features. Multiple Lamb modes are induced simultaneously by a PZT element unless appropriate design and controls are used, which can obscure the signal explanation [Roh and Chang, 1995]. Additionally, PZT elements exhibit certain non-linear behaviour and hysteresis under large strains/voltages or at high-temperature, small force and displacement, brittleness, low fatigue life, etc. [Schulz *et al*, 1999].

(4) *Interdigital transducers*. Novel interdigital transducers, such as polyvinylidene fluoride (PVDF) piezoelectric polymer films, have been introduced to accommodate more versatile applications with reasonable cost [Monkhouse *et al*, 1997, 2000; Blanas and Das-Gupta, 1999]. Possessing higher internal damping features than common PZT ceramics, PVDF exhibits good ability to produce guided Lamb waves with controllable wavelength, by adjusting the space between interdigital electrodes deposited on transducer substrates [Monkhouse *et al*, 1997]. Soft and flexible, the interdigital PVDF can be geometrically shaped and permanently bonded onto or embedded into structures, adapting to curved surfaces or complicated geometry.

However, compared with PZT, PVDF displays certain insensitivity to structural dynamic responses and relatively weak driving forces, limiting applications to some extent. In addition, its performance is susceptible to environmental factors in relation to its glass transition temperature.

3.3.4 Analytical Study

Equation (3.13) associates frequency ω with wavenumber k and phase velocity c_p for Lamb waves, whose graphic descriptions are *frequency spectrum* and *dispersion curves*, respectively. Mathematically, for a given frequency, there are infinite wavenumbers satisfying Equation (3.13), either real or purely imaginary, which can be achieved by using an iterative root-finding method (such as Newton-Raphson) [Rose, 1999]. In brief, analytical approaches for Lamb wave dispersion characteristics are represented by the *Transfer Matrix* method (Thomson-Haskell method), the *Global Matrix* method [Lowe, 1995] and the *Effective Elastic Constant* method [Habeger *et al*, 1979].

Transfer Matrix Method

For a N -layer medium, it is sufficient to assume four waves at each layer: longitudinal/shear waves arriving from the '*upper*' interface and leaving the '*lower*' interface (L+, S+), and similarly, longitudinal/shear waves arriving from the '*lower*' interface and leaving the '*upper*' interface (L-, S-), as illustrated in Figure 3.6. Snell's law [Bindal, 1999] requires that all of these waves must share the same frequency and spatial properties along the x_1 direction at each interface, imposing the condition that all displacement and stress equations have the same ω and wavenumber.

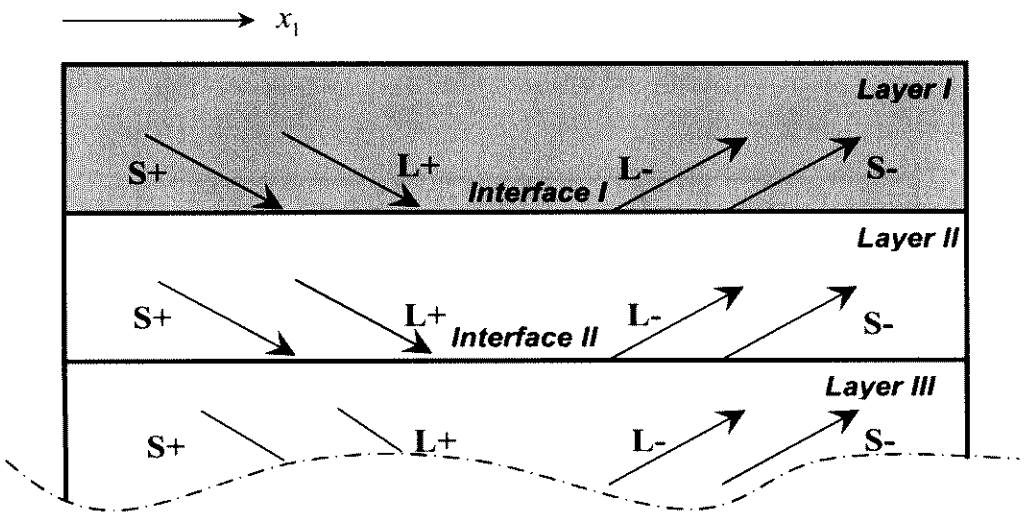

Figure 3.6 Waves in layered elastic medium

With such an assumption, the transfer matrix method works by condensing the multilayered system into a set of four equations relating the boundary conditions at the first interface to those at the last interface. In this process, the equations for intermediate interfaces are eliminated so that the fields in all of the layers can be described solely with regard to boundary conditions. The relation between wave frequency and wavenumber is therefore established in the form of a matrix, referred to as a *characteristic function*, which can be solved by the root loci approach [Lowe, 1995]. By such a technique, dispersion curves for a titanium sheet of *1.0mm* in thickness were obtained and are shown in Figure 3.7.

Global Matrix Method

The transfer matrix method becomes ill-conditioned and unstable when the plate thickness (d) is large and the frequency (f) is high, displaying the so-called '*large* $f \cdot d$ *problem*'. For these special cases, Knopoff developed an improved method, the *Global Matrix* method, in 1964 [Lowe, 1995]. Using a similar procedure for obtaining characteristic functions as the transfer matrix method, the global matrix method directly assembles a single matrix only, to seek for loci root. This method

remains numerically robust for any range of $f \cdot d$ values, and can be implemented simply but with a relatively slow convergence.

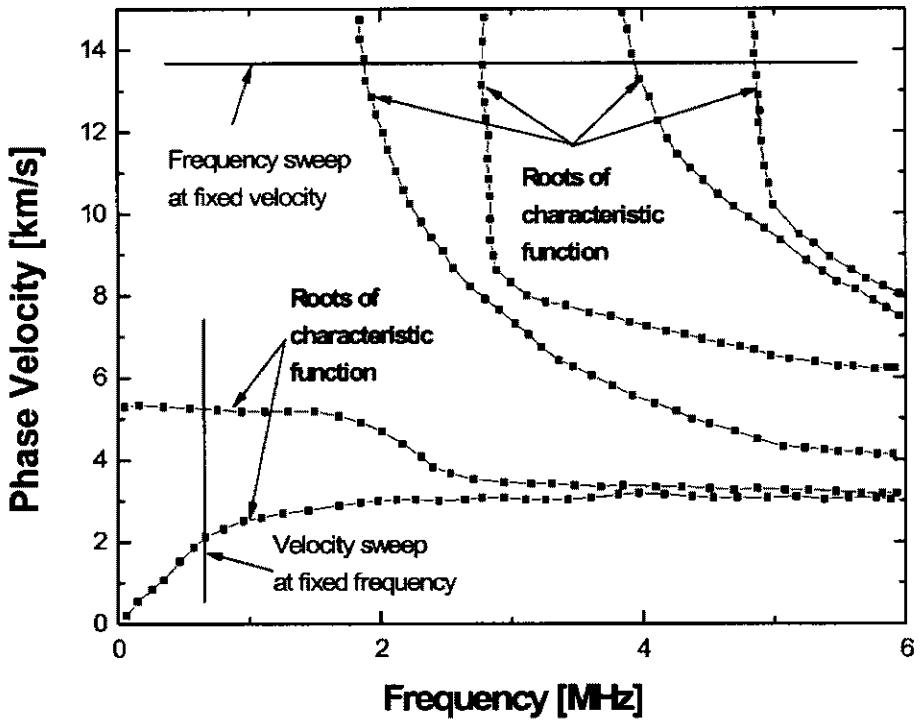

Figure 3.7 Dispersion curves for aluminium plate (thickness: *1.0mm*)

Other analytical approaches are also available. As one of the simplest methods to describe Lamb waves in anisotropic medium, the *Effective Elastic Constant* technique assumes composite plate to behave as a homogeneous orthotropic structure by neglecting its layered nature and deriving dispersion [Percival and Birt, 1997]. Additionally, Ghoshal *et al* [2002] examined the dispersion nature of asymmetric wave propagation in a glass epoxy panel using a passive acoustic wave model. Chien *et al* [1994] presented an analytical method to interrogate wave propagation in multilayered piezoelectric media. Aberg and Gudmundson [2000] developed their own micromechanical model for transient waves resulting from a fibre fracture and matrix cracking in a laminated composite beam.

3.3.5 FEM Simulations and Experimental Techniques

In parallel with analytical work, FEM simulation has been introduced into the study on the characteristics of Lamb waves in layered composites. Percival and Birt [1997] and Birt [1998] developed an FEM model to interrogate the dispersion nature of Lamb wave in carbon fibre (T800)/resin (924) composites. Their model allowed particle motion in any direction and hence successfully simulated the Love wave. The influence of different laminate layouts on Lamb wave dispersion was also evaluated in their work. Guo and Cawley [1992, 1993b] presented an FEM method in which uniform in-plane displacement was applied across the thickness of a laminate beam end to excite symmetric Lamb modes. Propagation of Lamb waves was then monitored by individually measuring vertical displacement [Alleyne and Cawley, 1991; Guo and Cawley, 1992] or horizontal displacement [Guo and Cawley, 1993b] in the area concerned, as shown in Figure 3.8. This method works well for one-dimensional structures.

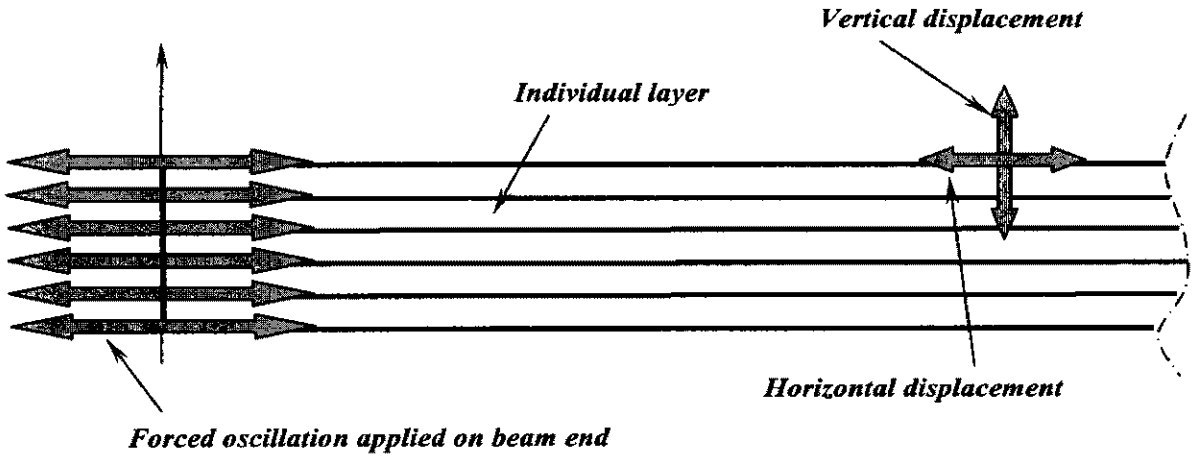

Figure 3.8 Lamb wave generation and monitoring [Guo and Cawley, 1992, 1993b]

Giurgiutiu *et al* [2001] evaluated the propagation of flexure and pressure waves through aluminium beams and plates under different excitation and boundary conditions, using a *4*-node shell element on the ANSYS platform, where a flexural

wave was excited by transient nodal rotations, while the pressure mode was generated by nodal translations. Moulin *et al* [2000] developed a coupled finite element–normal mode expansion approach, considering both bonded and embedded transducers. Such a method is able to deal with cases of multi-element transducers integrated into a composite structure. The influence of PZT dimension, position and excitation delay was also assessed. Issa *et al* [1994] proposed a self-adaptive finite element modelling technique for oblique ultrasonic waves. You and Lord [1991] analysed ultrasonic wave propagation using their *3-D* finite formulation.

Dispersion characteristics and interlaminar displacement/stress distribution are of greatest concern for the purpose of NDE. Dispersion curves of Lamb waves in aluminium plate and several typical CF/EP composite laminates obtained from FEM simulation [Percival and Birt, 1997] are displayed in Figure 3.9, compared with those from an effective elastic constant model. From FEM, propagation velocities are observed to be closely associated with the algebraic product of frequency and laminate thickness, but independent of laminate configuration. Fundamental symmetric and anti-symmetric modes are synchronously available in any frequency range, while higher order modes gradually appear as an increase in frequency.

Particle displacement u, v, and w, respectively along the x_1, x_2, and x_3 directions (referring to Figure 3.3), and normal stress component σ_{zz}, shear stress components σ_{zx} and σ_{zy} throughout the laminate thickness, under an excitation frequency of *1MHz*, are compared and shown in Figures 3.10 and 3.11, respectively, via Percival and Birt's model.

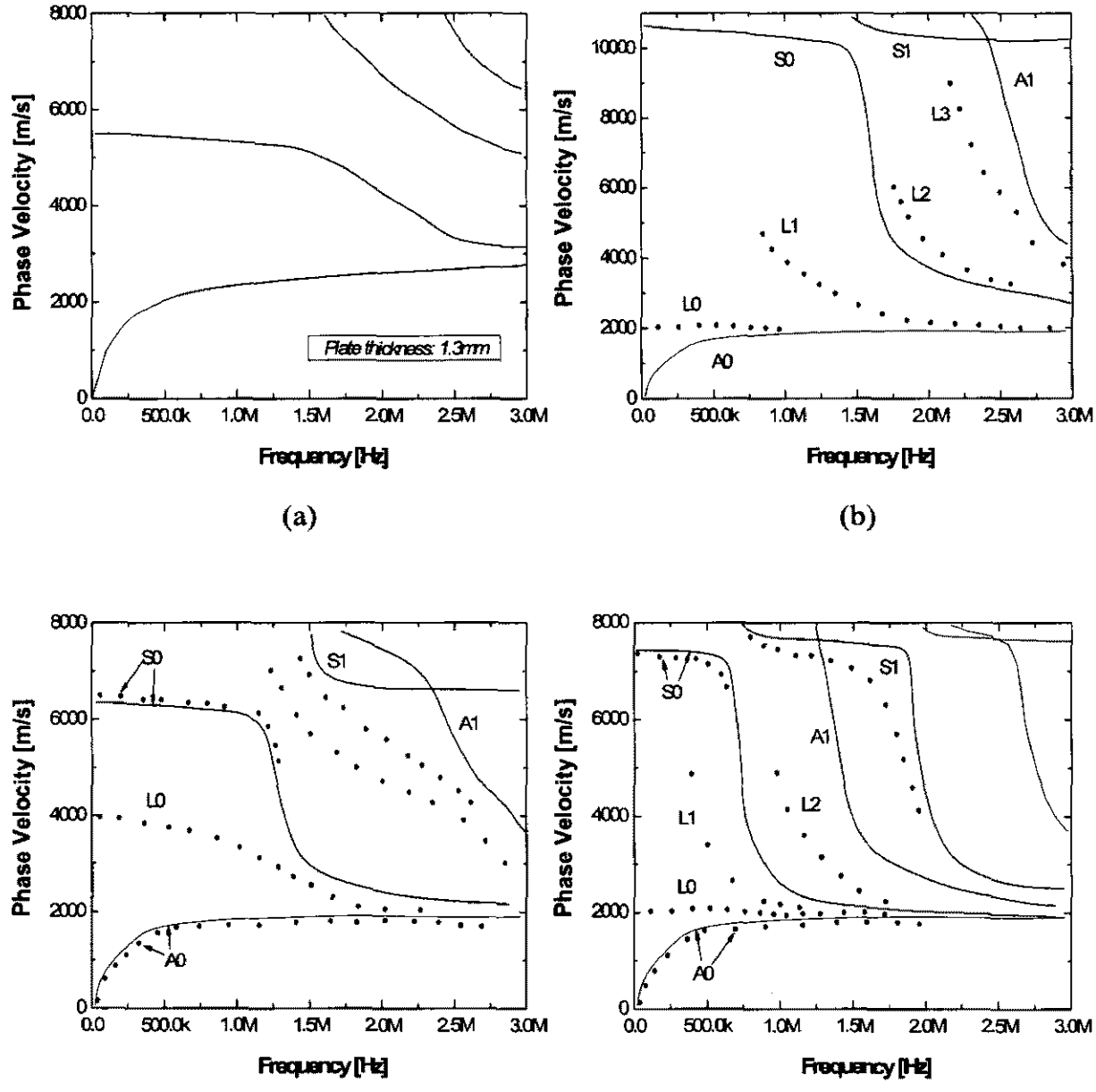

(*solid line: effective elastic constant model; dotted line: FEM model*)

Figure 3.9 Dispersion curves for (a) aluminium plate; (b) *8*-ply unidirectional laminate; (c) *8*-ply $[45/-45/0/90]_s$ quasi-isotropic laminate; (d) *16*-ply $[0/90]_{4s}$ cross-ply laminate

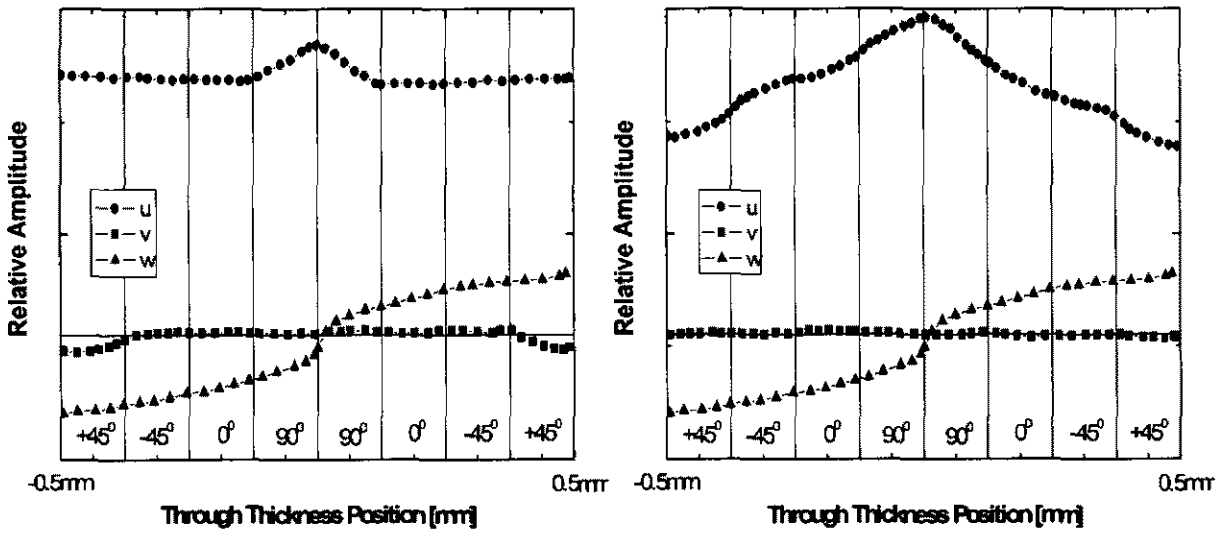

Figure 3.10 Particle displacement throughout laminate thickness of (a) *8*-ply $[45/-45/0/90]_s$ quasi-isotropic laminate; (b) *16*-ply $[0/90]_{4s}$ cross-ply laminate

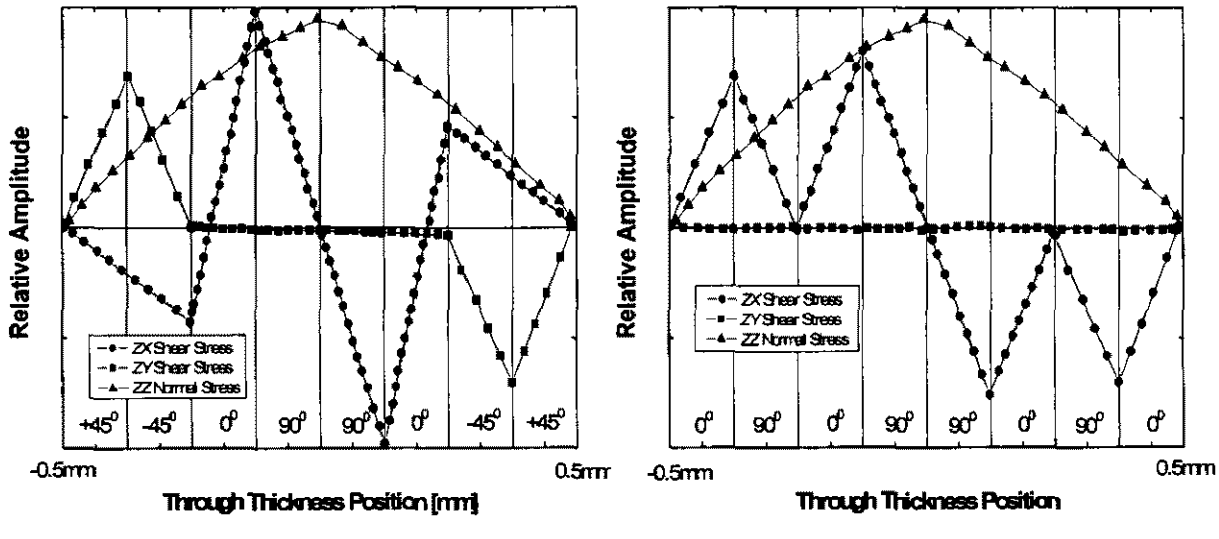

Figure 3.11 Stress distribution throughout laminate thickness of (a) *8*-ply $[45/-45/0/90]_s$ quasi-isotropic laminate; (b) $[0/90]_{4s}$ *16*-ply cross-ply laminate

From Figure 3.10, it can be seen that most particle motion for the anti-symmetric mode is along the z-direction, while for the symmetric mode it is along the x-direction. In Figure 3.11, shear stress, σ_{zx}, has an anti-symmetric distribution centred about the plate neutral plane, while normal stress, σ_{zz}, is symmetric regarding the neural plane and dominant through the thickness. Both particle motion along the y-direction and σ_{zy} stress are zero throughout the thickness. Figures 3.10 and Figure 3.11 illustrate well the behaviour of particle displacement and interlaminar stress under excitation, and on that basis the Lamb modes and parameters most sensitive to structural damage can be chosen and used for NDE.

Parallel experimental techniques have also been developed. In some cases they are probably the only or most effective ways to evaluate wave propagation. Though not the initial researchers but the most fruitful, Guo and Cawley [1992, 1993a, 1993b, 1994], Alleyne and Cawley [1992a, 1992b] and Birt and Percival [1997] individually presented their abundant findings. In most of their research, angle-variable ultrasonic probes were employed to produce pure Lamb modes and monitor their propagation. Innovatively, some *in-situ* damage detection techniques using integrative piezoelectrics were also developed [Lemistre *et al*, 1999; Wang and Chang, 2000]. For example, Gaul and Hurlebaus [1999] successfully determined the history of an external transient force applied on a structure by analysing responses directly measured by distributed piezoelectric elements. In these representative studies, piezoelectric elements exhibit advantageous performance in configuring flexible sensor networks.

Chapter 4

Signal Processing and Interpretation Technique

4.1 Introduction

Condition-based damage detection relies on *changes* of structure parameters measured from sensors [Chang, 2002a]. One great challenge in the principle is determining *what* changes to look for and *how* to identify them. Appropriately exploring captured signals and extracting essential information become a prime concern, predominating the feasibility and precision that a damage detection technique can offer.

Though promising for NDE, elastic waves, particularly Lamb waves, present several awkward features in complex structures, limiting their virtual utility in cost-effective damage detection techniques: (1) in practice, sensors and structures under surveillance may operate in noisy or fluctuant environments, where the acquired wave signals can be severely impaired by diverse disturbances, such as random electrical or mechanical noise; (2) in both experimental tests and numerical simulations, interference from natural structural vibrations, especially low-frequency modes, may obscure the damage-induced wave components in signals; (3) compared with waves excited by angle-variable ultrasonic probes coupled with angle-adjustable perspex wedge, multiple modes of wave exist simultaneously when a piezoelectric

element is used directly as actuator for wave generation, and their dispersion behaviour is notoriously complicated; (4) adoption of high-resolution data acquisition guarantees precision of identification, but it unavoidably leads to a bulky amount of data to serialise the sampling, burdening signal processing.

All these factors undoubtedly weaken the sensitivity of elastic waves to structural damage, and lower detection precision. For this reason, a signal processing technique for elastic wave-based damage detection is first developed in this study.

4.2 Signal Processing Techniques for NDE: A Review

Signals, functions containing a number of parameters of interest [Boashash, 1992], allow ascertainment of properties of the source and the medium. Actions applied on the acquired signal constitute signal processing, and further understanding is known as signal identification [Picinbono, 1988]. For NDE purposes, a wide variety of signal processing methods are currently available. Amongst them, time-series analysis, frequency analysis and time-frequency analysis are the most common.

4.2.1 Time Domain Analysis

Most signals in a NDE test come with a time-dependent history of electric field, magnetic field, pressure or voltage, etc. Regarded as a continuous propagation of energy, E, a time-dependent signal $f(t)$ can be formulated as [Boashash, 1992],

$$E = \int_{t\geq 0} |f(t)|^2 \, dt \tag{4.1}$$

where $|f(t)|^2$ is defined as the energy density per unit time at t, and thus $|f(t)|^2 \cdot \Delta t$ denotes fractional energy in the time interval Δt at time t.

In earlier stage of NDE, analysis in the time domain was the only means to study a signal. Such analysis can detect damage status both globally and locally [Thwaites and Clark, 1995]. However, except some successful applications in location detection [Sohn and Farrar, 2001; Yam *et al*, 2003], such an analysis cannot separate defect-scattered composition appropriately from a raw signal containing all parts with different frequencies. Quantitative identification may not be straightforward.

4.2.2 Frequency Domain Analysis

To obtain better understanding, it is often preferable to examine a signal in the frequency domain, viz. *Fourier Transform* (FT). One of the most influential and powerful tools in signal processing, FT mathematically transforms a time-dependent signal, $f(t)$, from the time space into the frequency space [Boashash, 1992] by

$$F(\omega) = \int_{-\infty}^{+\infty} f(t) \cdot e^{-j\omega t} dt \qquad \textbf{(4.2a)}$$

where ω and j are the angular frequency ($\omega = 2\pi \cdot f$) and unit complex, respectively. $F(\omega)$ is the Fourier counterpart of $f(t)$. Equation (4.2a) uniquely illustrates the signal as the summation of a series of simple waveforms, $e^{j\omega t}$, with different amplitudes $|F(\omega)|$, frequencies ω and phases $\angle S(\omega)$. Inversely, it has

$$s(t) = \frac{1}{2\pi} \int_{-\infty}^{+\infty} F(\omega) \cdot e^{j\omega t} d\omega \qquad \textbf{(4.2b)}$$

Similarly, signal energy can be expressed in the frequency domain as

$$E = \frac{1}{2\pi} \int_{-\infty}^{+\infty} |F(\omega)|^2 d\omega \qquad \textbf{(4.3)}$$

where $|F(\omega)|^2$ is analogously defined as the energy density per unit frequency at ω, and $|F(\omega)|^2 \cdot \Delta\omega$ is the fractional energy in the frequency interval $\Delta\omega$ at ω. Considering conservation of energy and combining Equations (4.1) and (4.3) lead to

$$E = \int_{t\geq 0} |f(t)|^2 dt = \frac{1}{2\pi} \int_{-\infty}^{+\infty} |F(\omega)|^2 d\omega \qquad (4.4)$$

Derived from Fourier transform, *Fast Fourier Transform* (FFT) speeds up this transform by convolution and correlation [Chan, 1995]. FFT-based explanation reveals signal features that are difficult or impossible to discern in the time domain. The effectiveness of FT or FFT analyses, especially for large structures in civil engineering, has been demonstrated by numerous successful applications [Wu *et al*, 1992; Keilers, 1997, 1998; Kawiecki, 1998; Blanas and Das-Gupta, 1999].

The most serious drawback for the frequency domain analysis is the loss of temporal information during transforming. Although signal compositions with different eigen-frequencies can be separated, their history is hidden. This may not be a major concern for stationary signals, but it is critical for dynamic signals.

4.2.3 Time-Frequency Domain Analysis

Analysis in either the time or frequency domain alone seems inadequate for quantitative identification of a non-stationary signal, which necessitates a combination of the time domain with the frequency domain. Many time-frequency algorithms have been developed [Prosser *et al* 1999]. All of them can be mathematically generalised as [Boashash, 1992]

$$P(t,\omega) = \frac{1}{2\pi} \int_{\delta} \int_{\tau} \int_{\theta} e^{-i\theta t - i\tau\omega - i\theta\delta} \phi(\theta,\tau) \cdot f^*(\delta - \frac{\tau}{2}) \cdot f(\delta + \frac{\tau}{2}) d\delta \cdot d\lambda \cdot d\theta \qquad (4.5)$$

where $P(t,\omega)$ is the energy intensity at time t and frequency ω of signal $f(t)$. f^* denotes the complex conjugate of f. $\phi(\theta,\tau)$ is a function depending on $f(t)$. *Short-Time Fourier Transform* (STFT), *Winger-Ville* distribution (WVD), and wavelet transform (WT) analysis are several important examples deriving from Equation (4.5).

Short-Time Fourier Transform (STFT) Analysis

Introduced by Dennis Gabor in 1946 [Mathworks, 2001d], short-time Fourier transform (STFT) aims at correcting the deficiency of Fourier or FFT transform for non-stationary signals. STFT applies the basic Fourier transform on a small piece of signal around a specific time ('*short time*') by neglecting the rest of signal. The operation is then continuously performed by moving this short time interval along the time axis. Mathematically, this is actualised by multiplying a window function, $r(t)$, with the time-series signal around time t, [Boashash, 1992]

$$f(t-\tau)_{STFT} = f(t)\cdot r(t-\tau), \quad (time\ domain) \tag{4.6a}$$

$$F(\omega)_{STFT} = F(\omega) * R(\omega), \quad (frequency\ domain) \tag{4.6b}$$

where $R(\omega)$ is the Fourier pair of $r(t)$ and symbol * denotes convolution. For the entire signal, relation expands to

$$F(\tau,\omega)_{STFT} = \frac{1}{2\pi}\int_{-\infty}^{+\infty} f(t)\cdot r(t-\tau)e^{-i\omega t}dt \tag{4.7}$$

Equation (4.7) maps a time-dependent signal into a two-dimensional representation with *time* and *frequency*, viz. *STFT spectrographic analysis*. For a specific time, t, the energy density in STFT spectra becomes

$$\rho_{STFT}(t,\omega) = \left|F(\varpi)\right|_t^2 \tag{4.8}$$

and the totality of energy, E, over time-frequency for the signal, is

$$E = \int_{-\infty}^{+\infty}\rho(t,\omega)_{STFT}\cdot dt\cdot d\varpi = \left|\frac{1}{2\pi}\int_{-\infty}^{+\infty} f(t)\cdot r(t-\tau)e^{-i\omega t}dt\right|^2 \tag{4.9}$$

$$= \iint_t \left|f(t)\right|^2 dt = \iint_\omega \left|F(\omega)\right|^2 d\omega$$

With successful applications [Li and Ma, 1997; Kim and Kim, 2001], STFT achieves a reasonable compromise between *time* and *frequency*, offering full information

about *when* and *at what* frequencies an event happens. Nevertheless, due to the unalterable window size in Equation (4.6), satisfactory precision along both time- and frequency-axes cannot usually be synchronously obtained.

Winger-Ville Distribution (WVD) Analysis

A flexible choice of the window size is therefore attractive. Setting an arbitrary function $\phi(\theta,\tau)=1$ in Equation (4.6) leads to

$$P(t,\omega)=\int_{\tau}\bar{f}(t-\frac{\tau}{2})\cdot f(t+\frac{\tau}{2})\cdot e^{-i\tau\omega}d\tau \qquad \textbf{(4.10)}$$

Defined as the *Winger-Ville* distribution (WVD) transform, Equation (4.10) provides better resolution than STFT. But such a signal processing method requires a higher sampling rate (usually at least four times higher than the highest frequency in a signal) to avoid aliasing [Mathworks, 2001e]. Meanwhile, undesirable negative values may occur between two strong signal components, or between strong and weak components, which do not have physical meaning but can lead to erroneous explanation [Wang, 2001]. Additionally, WVD lacks sensitivity when applied directly to raw signals, and changes in short duration or low magnitude may not always be detected. Although some variants of WVD analysis have been developed to overcome these disadvantages, e.g. *Choi-Williams* analysis [Kim and Kim, 2001; Lee *et al*, 2001], the technique is still not very suitable for practical damage detection [Wang and McFadden, 1993].

Some other time-frequency signal processing methods for NDE also include reassigned spectrographic analysis [Valle, 2001], cepstrum investigation [Dalpiaz *et al*, 2000; Zheng and Wang, 2001], blind deconvolution [Zheng *et al*, 2001] and cyclostationary processes [Rubin and Sidahmed, 1997], or statistical model [Martin *et al*, 1990], auto-regressive [Sohn *et al*, 2000] and probability analyses [Achenbach *et al*, 1997], which can play certain roles in specific cases.

4.3 Wavelet Transform Technique

In historical perspective, wavelet transform is a fresh approach, though its mathematical underpinnings can be dated back to the work of Joseph Fourier in the *19th* century. The first record of the term '*wavelet*' appears in a thesis by Alfred Haar in 1909 [Mathworks, 2001e]. The concept of wavelet in its present theoretical fashion was established by Jean Morlet in the 1950s, and its modern algorithm was perfected by Stephane Mallat in 1988. Since then, research on wavelets has become active internationally. In particular, Ingrid Daubechies, Ronald Coifman and Victor Wickerhauser, etc., have made essential contributions to their practical applications. From geophysics, biomedicine, to offshore petroleum exploration and movie industry, the wavelet transform technique plays an indispensable role, indeed, wherever signal or image processing is engaged.

It was probably Daubechies [1990] and Newland [1994a, 1994b] who first introduced the wavelet transform technique into studies of vibrational signals in the early 1990s, and they found it of undeniable advantage for singularity detection in signals. Nowadays, wavelet transform-based signal processing enjoys a burgeoning popularity in the NDE industry [Abbate *et al*, 1997; Liu *et al*, 1997; Samuel and Pines, 1997; Hou *et al*, 1998, 2000; Staszewski 1998; Staszewski *et al*, 1999b; Okafor and Dutta, 2000; Peng and Chu, 2003], covering signal purification, spectrographic analysis, and signal/image compression.

4.3.1 Fundamentals

In brief, a *wavelet* is a waveform with limited duration, whose average amplitude equals zero. Like STFT, wavelet transform maps a time-dependent signal into a two-dimensional representation with dual parameters, *scale* and *time*. During transforming, *scale* rather than *frequency* is used. Though *scale* is directly associated

with the *reciprocal of frequency* ($1/f$), it is acknowledged that the wave energy allocation for a variable signal can be more conveniently understood using the parameters *time* and *scale*, for more intuitive explanation than the time-frequency domain [Mathworks, 2001e]. They are reciprocally associated by

low scale ⇔ *compressed wavelet* ⇔ *rapidly changing* ⇔ *high frequency*

high scale ⇔ *stretched wavelet* ⇔ *slowly changing* ⇔ *Low frequency*

In addition to this replacement, *sampling point* (SP) is adopted in the present study instead of *time point* (TP), to expedite data processing.

$$\text{Time Point} = \frac{\text{Sampling Point}}{\text{Sampling Rate}}$$

Exhibited in time-frequency space, *when* and *where* the discontinuity or singularity in a signal can be therefore determined. Examination of a dynamic signal can be concentrated in a localised fragment to display hidden characteristics such as trends, breakdown points or discontinuities, and self-similarity.

There are two types of wavelet transform, namely *continuous wavelet transform* (CWT) and *discrete wavelet transform* (DWT). Generally, CWT is particularly effective for signal analysis and visualisation, while DWT is more effective in signal denoising, filtration, compression and extraction.

4.3.2 Continuous Wavelet Transform (CWT)

Fundamentally, with the basic orthogonal wavelet transform function, $\Psi(t)$, a time-dependent wave signal, $f(t)$, acquired from sensors, is converted into a quadratic expression using the dual parameters *scale* a, and *time* b [Hou *et al*, 2000]:

$$W(a,b)=\frac{1}{\sqrt{a}}\int_{-\infty}^{+\infty} f(t)\cdot\Psi^{*}(\frac{t-b}{a})\,dt \tag{4.11}$$

Operation by Equation (4.11) is CWT and $W(a,b)$ is the *CWT coefficient*. $\Psi^{*}(t)$ denotes the complex conjugate of $\Psi(t)$. Conversely, the signal can also be reconstructed via inverse continuous wavelet transform:

$$f(t)=\frac{1}{C_{\Psi}}\int_{-\infty a>0}^{+\infty}\int^{+\infty} W(a,b)\cdot\frac{1}{\sqrt{a}}\cdot\Psi\left(\frac{t-b}{a}\right)\cdot\frac{1}{a^{2}}\,da\cdot db \tag{4.12}$$

where C_{ψ} is a constant depending on $\Psi(t)$, determined by,

$$C_{\Psi}=\int_{0}^{+\infty}\frac{|\Psi(\omega)|^{2}}{\omega}\cdot d\omega$$

In terms of Equations (4.9), (4.11) and (4.12), the energy allocation for the signal $f(t)$ in the time-scale domain is then derived as [Picinbono, 1988]:

$$E=\int_{-\infty}^{+\infty}\int_{a\geq 0}^{+\infty}|W(a,b)|^{2}\,da\cdot db \tag{4.13}$$

where $|CWT(a,b)|^{2}$, referred to as a *scalogram*, permits the description of the signal in the form of wave energy over the time-scale space, i.e. *spectrographic analysis*. Though wavelet transform does not produce a direct time-frequency view, it is not a weakness but a strength of the time-frequency analysis [Mathworks, 2001e], where *scale* can be connected with *frequency* by determining the value at which a scalogram reaches its maximum [Qu, 1994].

As an illustration, the signal acquired by a piezoceramic sensor attached on a flexural alloy beam bearing a perpendicular crack (to be detailed in Chapter 8), is shown in Figure 4.1(a). With CWT-based spectrographic analysis applied, its energy allocation spectrum is displayed in Figure 4.1(b).

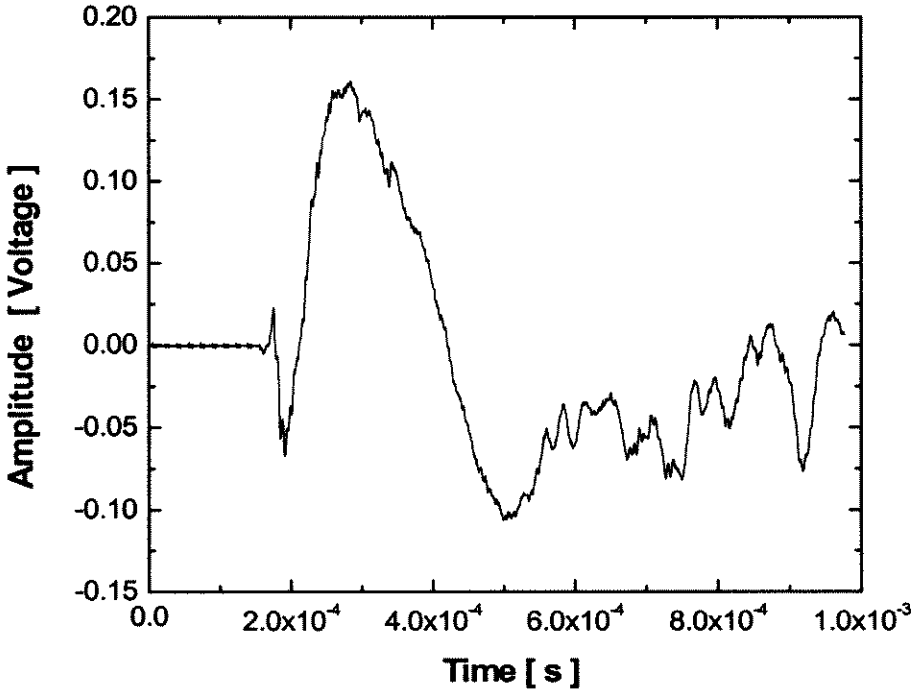

(a)

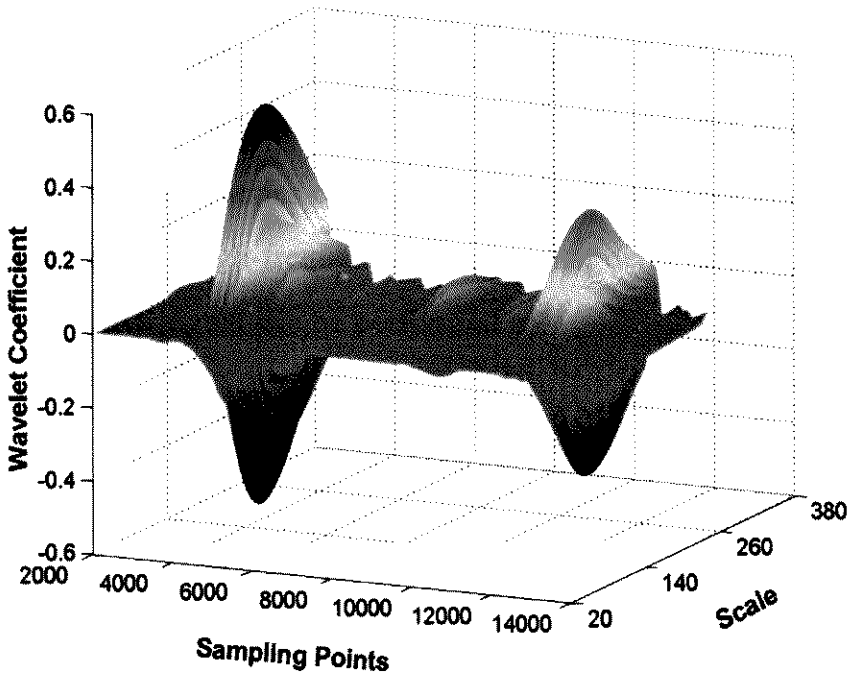

(b)

Figure 4.1 CWT-based spectrographic analysis, (a) raw signal, and (b) energy spectrum

Research [Yan and Yam, 2002] has demonstrated that the CWT-based spectrographic analysis is able to detect *0.01–0.1%* variation in selected parameters for crack detection, while this value is normally over *10%* for modal-based methods.

4.3.3 Discrete Wavelet Transform (DWT)

To calculate wavelet coefficients at every scale point is computationally expensive. For simplification, Equation (4.11) is executed only at discretised *scale* and *time* using dyadic variables m and n, i.e. DWT [Chui, 1997]:

$$a = a_0^m \quad \text{and} \quad b = na_0^m b_0, \qquad m, n \in Z \tag{4.14a}$$

$$DWT(m,n) = a_0^{-\frac{m}{2}} \int f(t) \cdot \Psi(a_0^{-m} t - nb_0) \cdot dt \tag{4.14b}$$

where a_0 and b_0 are constants determining sampling intervals along the *time* and *scale* axes, respectively. Equation (4.14) decomposes signals into associated scopes with relatively higher and lower frequencies. Paradigmatically, decomposition in a three-level architecture is outlined in Figure 4.2, where the signal $f(t)$ is hierarchically represented by a series of *approximations* (low-frequency components, denoted by A) and *details* (high-frequency components, denoted by D). Inversely, reconstruction of the wave signal can be performed by

$$f(t) = c \sum_m \sum_n C_{mn}(t) \cdot DWT(m,n) \tag{4.15a}$$

$$C_{mn}(t) = a_0^{-\frac{m}{2}} \Psi(a_0^{-m} t - nb_0) \tag{4.15b}$$

where c is a constant in correlation with $\Psi(t)$. The time-dependent function $C_{mn}(t)$ is the *DWT coefficient*. The more densely the decomposition is conducted, the higher the resolution that is achieved. Theoretically, decomposition can proceed successively until the individual details consist of only a single sample point or pixel. In practice, a suitable number of levels should be determined by evaluating the

nature of a signal. After applying orthogonal DWT analysis to the example signal in Figure 4.1(a), its decomposed first ten levels are displayed in Figure 4.3.

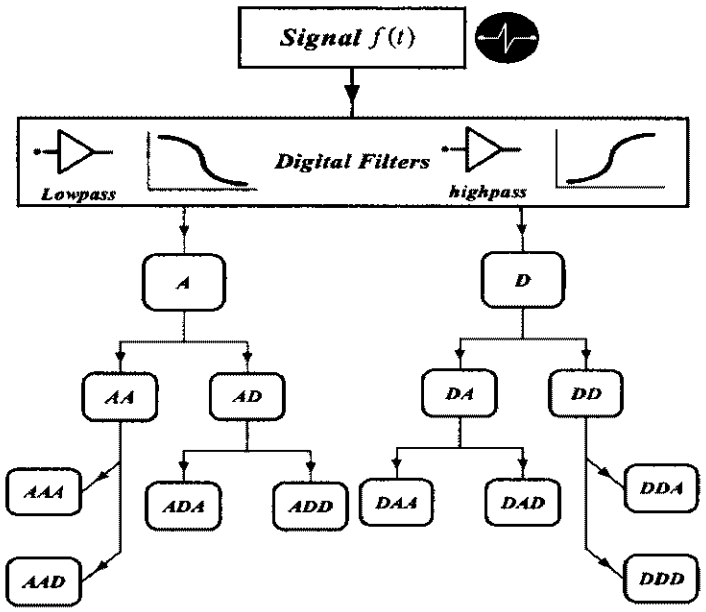

$$f(t) = AAA + AAD + ADA + ADD + DAA + DAD + DDA + DDD$$

Figure 4.2 Principle of DWT-based digital filter design with *3*-level architecture

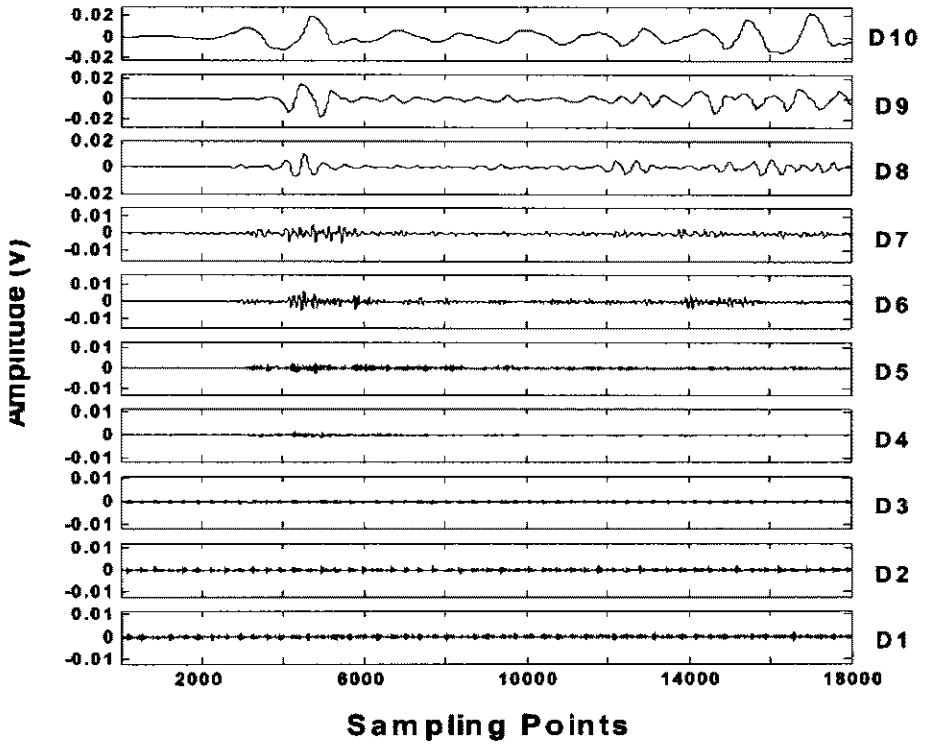

Figure 4.3 *Details* from levels *1* to *10* via DWT analysis for signal in Figure 4.1(a)

4.4 Intelligent Signal Processing and Pattern Recognition (ISPPR)

Considering the features of wave signals enumerated, an *intelligent signal processing and pattern recognition* (ISPPR) technique for wave-based damage detection is developed in this study, including units of signal purification, characteristic extraction, data compression, information mapping and pattern recognition.

4.4.1 Signal Purification

Digital filters (DF) with discretised frequency thresholds and ranges are built in virtue of DWT, to denoise the acquired raw wave signals and separate diverse wave components. In this approach, noise is defined as any component that is not part of the phenomena of interest, and may be generated by various factors such as electrical units in the system, environmental variation, structural natural vibration, and other unpredictable sources. Such noise is unavoidable even when precautions are taken preliminarily. From a mathematical perspective, a digital filter is recognised as a transfer function, with which the original signal, $f(t)$, is convolved and weighted by [Mathworks, 2001d]

$$f'(t) = f(t) * w(t) \tag{4.16}$$

where $f'(t)$ and $w(t)$ are the filtered signal and filter function, respectively, with representation in the Fourier domain,

$$F'(\omega) = F(\omega) \cdot W(\omega) = \frac{b_1 + b_2 e^{-j\omega(1)} + b_3 e^{-j\omega(2)} + \cdots + b_n e^{-j\omega(n-1)}}{a_1 + a_2 e^{-j\omega(1)} + a_3 e^{-j\omega(2)} + \cdots + a_n e^{-j\omega(m-1)}} \cdot W(\omega) \tag{4.17}$$

where $F'(\omega)$, $F(\omega)$ and $W(\omega)$ are Fourier transform counterparts corresponding to $f'(t)$, $f(t)$ and $w(t)$, respectively. a_i ($i = 1, 2, \cdots, m$) and b_i ($i = 1, 2, \cdots, n$) are the filter coefficients, and the maximum of m and n is the order of filter.

Low-pass and high-pass DF are designed in parallel in ISPPR to remove all extraneous components, as sketched in Figure 4.2. A low-pass DF admits lower frequency components in a signal but attenuates higher frequency components, in correlation with the designed cutoff frequency threshold, while a high-pass filter inhibits the lower frequency components in the wave signal.

During transforming, it can be seen that the orthogonal wavelet function, $\Psi(t)$, plays an important role. Wavelet functions widely employed for NDE purposes include *Haar*, *Daubechies*, *Biorthogonal*, *Coiflets*, *Symlets*, *Morlet*, etc. [Chan, 1995]. The choice of a wavelet function is really application-dependent. In particular, the *Daubechies* family (denoted by *dbN*, where *N* is the order), a series of compactly-supported orthonormal wavelets without mathematic expression, is chosen as the transfer function in this study, as it has been demonstrated to be most effective in the approach.

4.4.2 *Digital Damage Fingerprints* (DDF) and Characteristic Extraction

A typical signal acquisition procedure is depicted in Figure 4.4, where the object's physical attributes are sensed and transformed into a reduced set of features. One paramount concern in this procedure is how to '*discover*' effective signal characteristics.

The most effective characteristics of a signal are application-specific. However, the basic principle is to extract the characteristics that are most sensitive to alteration of damages. In ISPPR, specific spectrographic characteristics in both time and time-scale spaces are adopted as the basic signal features, which have been rigorously substantiated most susceptible to structural damage, as addressed hereinabove.

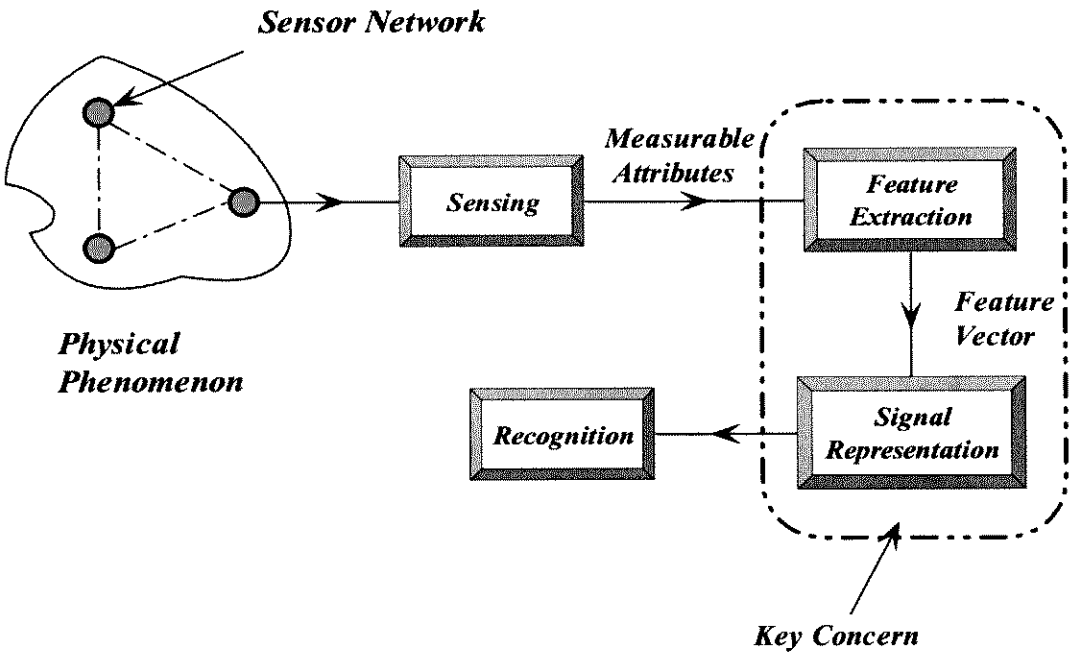

Figure 4.4 Principles of signal acquisition

To facilitate data processing in ISPPR, it is stipulated that the time points in the DF-filtered time-series signal and the time/frequency points in the energy allocation spectrum, at which the absolute magnitude of amplitude is simultaneously larger or smaller than those of contiguous time or time/frequency points anteriorly and posteriorly, are defined as '*characteristic points*', and the corresponding amplitudes are '*characteristic amplitudes*'. Both of these are *principal components* for the signal. While other extrinsic points are '*non-characteristic components*', as elucidated with a true signal fragment in Figure 4.5.

In ISPPR, *characteristic points*, *characteristic amplitudes*, and rising/attenuating durations within sampling periods of interest are discretely extracted from the filtered signals in the time domain. Similarly and in parallel, the *characteristic points*, *characteristic amplitudes*, and rising/attenuating durations along both the *time* and *scale* axes for each energy concentration within the time-scale region of interest are also extracted. A *feature vectors pair*, {*time*, *amplitude*} and {*time*, *frequency*,

amplitude}, is created to accommodate the extracted *principal components* for two domains, respectively. As an illustration, a set of typical DDF is presented in Appendix *A*.

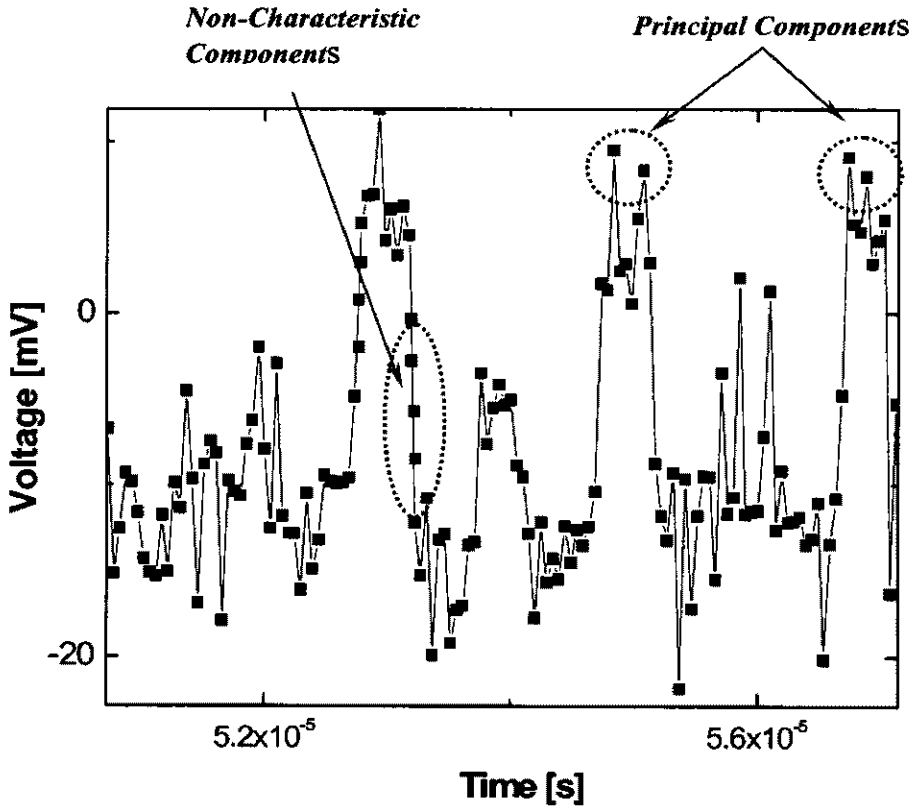

Figure 4.5 *Principal components* in a signal fragment

In engineering practices, where a certain number of actuators and sensors rather than a single device may be used to configure an actuator/sensor network, a series of *feature vectors pairs* can be obtained exclusively for each actuator-sensor path for a particular damage case.

To streamline the analysis, a concept is introduced, where these *feature vectors pairs* are arranged in sequence, referred to as '*digital damage fingerprints*' (DDF). DDF may be understood as a series of digitalised system behaviours or symptoms; accordingly, one particular damage case is uniquely defined with one set of DDF. For the purpose of damage detection, different damage cases can be personified as

'*crimes*' to a structure, and thus DDF functions as the record of characteristics for such a crime.

Using the concept of DDF and considering all the damage cases of interest, a damage parameter database (DPD) containing all the *feature vector pairs* is subsequently constructed for one type of damage in a structure, such as cracks or delaminations.

4.4.3 Data Compression

During wave signal acquisition, a large amount of data is usually produced. Of this, only the intrinsic characteristics in a filtered signal or energy spectrum are essential for signal interpretation. Other extrinsic data, inevitably contained to serialise the sampling, contribute virtually nothing to signal evaluation, which however takes tremendous computational time and effort. Additionally, detection effectiveness can be fairly jeopardised when high-dimensional data capacity is engaged. To maximise precision and effective computational capability, condensation of the acquired data but without loss of virtual characteristics is a necessity. A data compression unit is therefore developed in ISPPR.

Known to be a matter of judgement beyond mathematic capability, there is no clearly specified boundary at which the amount of acquired data becomes manageable for a system. Several data compression approaches are available [Levin and Lieven, 1998; Staszewski, 2002], roughly categorised as methods which eliminate redundancies in a signal [Staszewski, 2002], and those using linear and nonlinear transforms, such as *principal component analysis* (PCA) [Staszewski, 2002]. In ISPPR, data compression is conducted by gradually screening the *non-characteristic components* in the signal and constraining the signal to use *principal components* only.

4.4.4 Information Mapping

Completely or partially symmetric geometry or loading conditions are commonly available in a structure. To exploit this property, a mapping approach is additionally adopted in ISPPR to simplify signal processing.

In brief, wherever symmetric conditions are applicable, the signal DDF, orderly stored in the DPD for damage cases in a partial region of the entire structure to be inspected, are parallelly mirrored into other regions with regard to the available symmetric point, axis or plane, to figure out the mirror-images of other DDF. Integrating all possible DPDs, a comprehensive database for the overall structure can be established accordingly. Without sacrificing information that could possibly be acquired, the mapping approach strengthens the capacity of a damage detection technique under given conditions. Applications and restrictions of the mapping approach are addressed in the light of actual case studies in subsequent chapters.

4.4.5 Normalisation

In variable environments, robust data are desired to minimise any uncertainty in signal analysis. Normalisation with respect to varying operational and environmental conditions is an essential step towards avoidance of false positive indications [Farrar *et al*, 2001b].

For accurate DDF extraction in ISPPR, all the signals acquired from the piezoelectric sensor network are normalised before extraction and identification. Meanwhile, considering that actual signals usually suffer from DC deviation, the mean value of signal history is calculated by integrating amplitudes at each sampling point within the time period of interest, and then subtracted from the signal to remove such disturbances. The maximum absolute amplitude is captured to normalise the signal,

limiting all magnitudes to the range of [-1, +1]. An original signal acquired from a PZT sensor and normalised signal are compared in Figure 4.6.

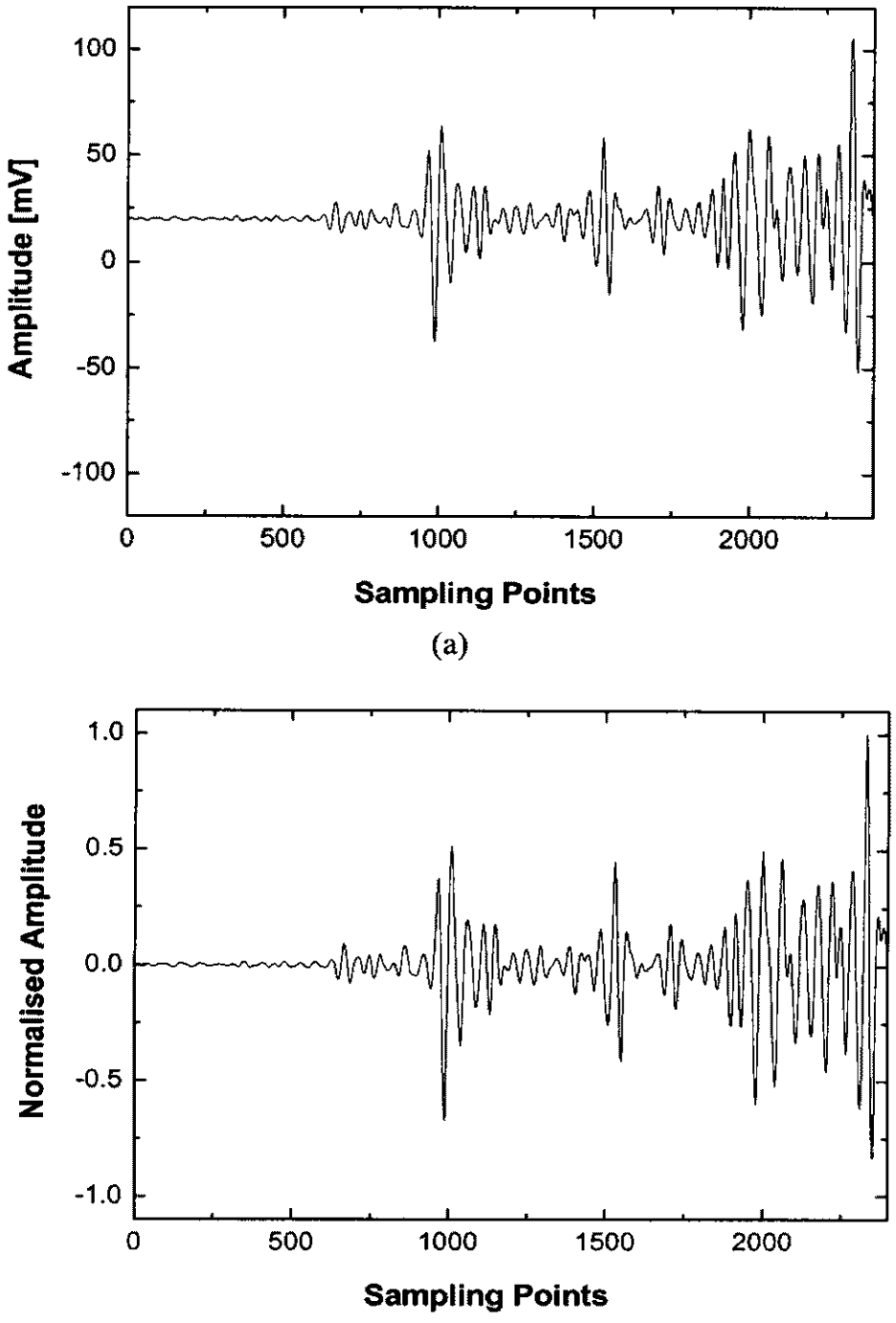

Figure 4.6 Signal normalisation, (a) raw signal and (b) normalised signal

4.4.6 Pattern Recognition

The identification of an individual object as a unique singleton class is defined as *pattern recognition* [Looney, 1997]. For damage detection, diverse damage cases are considered as different patterns that present various symptoms [Staszewski, 2002], and therefore identification is a problem of pattern recognition. In ISPPR, damage pattern recognition is fulfilled via an artificial neural network (ANN) technique, which is detailed in Chapter 6.

4.5 Actualisation of ISPPR: Signal Processing Package (SPP)

Signal processing package (SPP) software is developed to actualise the proposed ISPPR algorithm, whose schematic flowchart is shown in Figure 4.7. Commercial software *Matlab*® [Mathworks, 2002d, 2002e], which provides an interactive interface and rich graphical environment, is employed as the development framework for the SPP.

By way of illustration, a raw Lamb wave signal acquired from a piezoelectric transducer (sensor) surface-bonded on a quasi-isotropic CF/EP composite laminate, under excitation of *500kHz* by another transducer (actuator), is displayed in Figure 4.8(a). Applied with the digital bandpass filters designed in Section 4.4.1, the filtered wave component corresponding to the active excitation frequency (*500KHz*) is separated, as shown in Figure 4.8(b). Spectrographic analysis is conducted, and the wave energy spectrum is displayed in Figure 4.8(c).

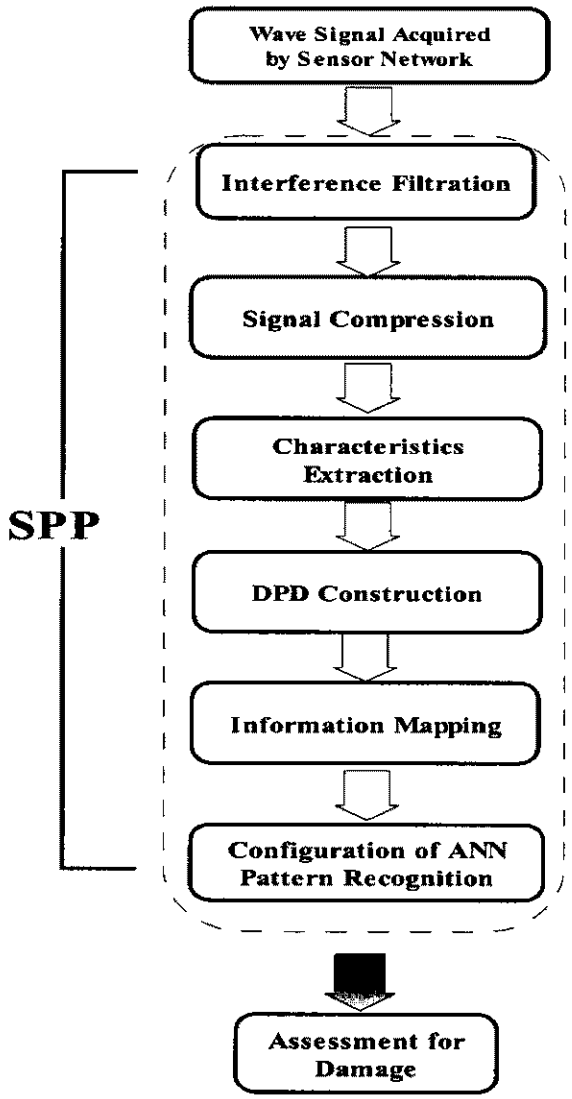

Figure 4.7 Flowchart for development of SPP

Applied with SPP, the signal further compressed in the time domain, and the compressed energy spectrum in the time-scale domain for the selected example signal are exhibited in Figures 4.8(d) and (e), respectively. DDF embedded in the wave signals are sequentially extracted, in Figures 4.8(f) and (g). From Figures 4.8(a) to (f) and (g), the raw Lamb wave signal, involving all the kinds of components, is now represented concisely and rationally, but without loss of connatural features. Containing the extracted DDF for all concerned actuator-sensor paths under a diversity of damage cases, the DPD is configured for the structure under inspection, and then used for damage pattern recognition.

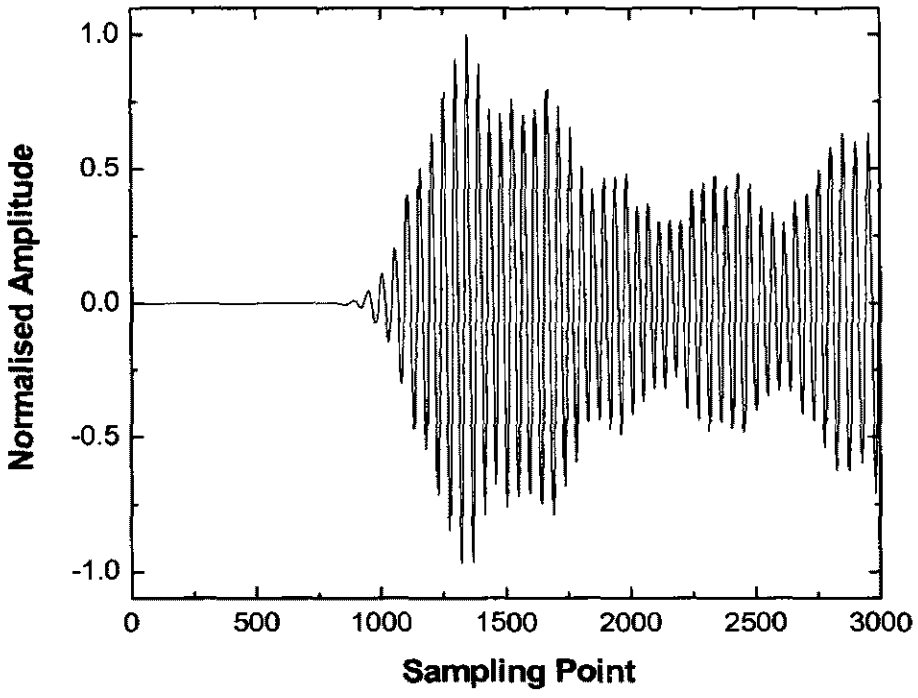

(a)

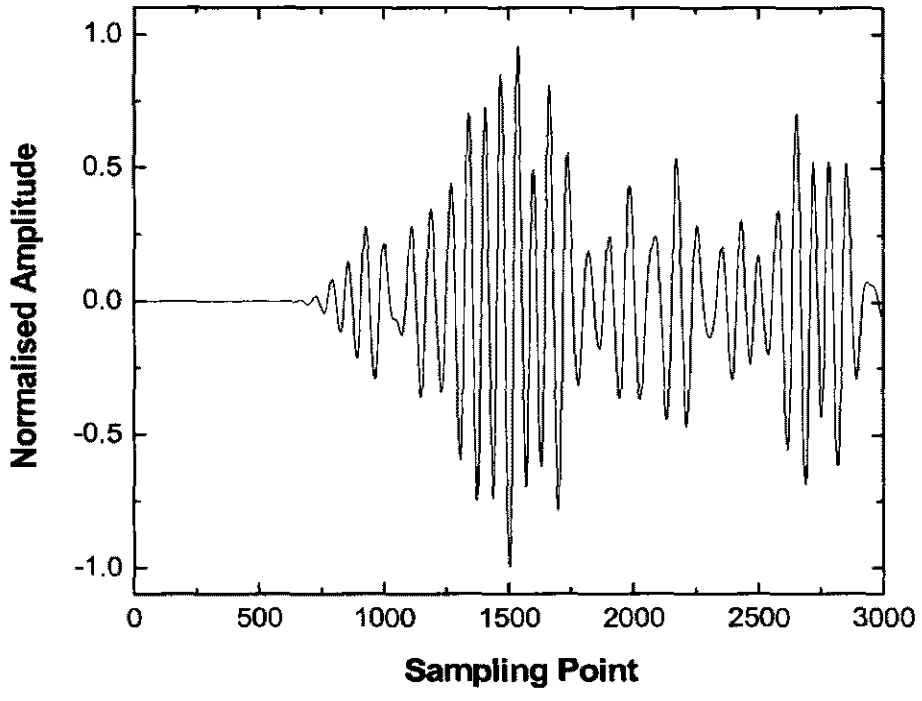

(b)

Figure 4.8 Signal processing by SPP: (a) original Lamb wave signal; (b) filtered signal of (a) in active excitation frequency band; (c) signal energy spectrum; (d) compressed signal in time domain; (e) compressed energy spectrum in time-scale domain; (f) DDF in time domain; (g) DDF in time-scale domain

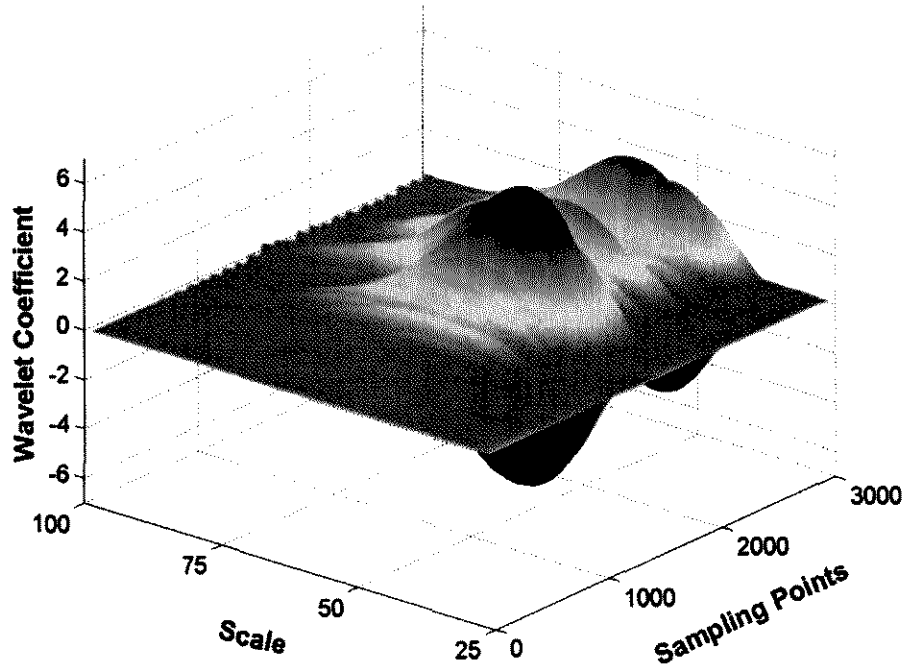

(c)

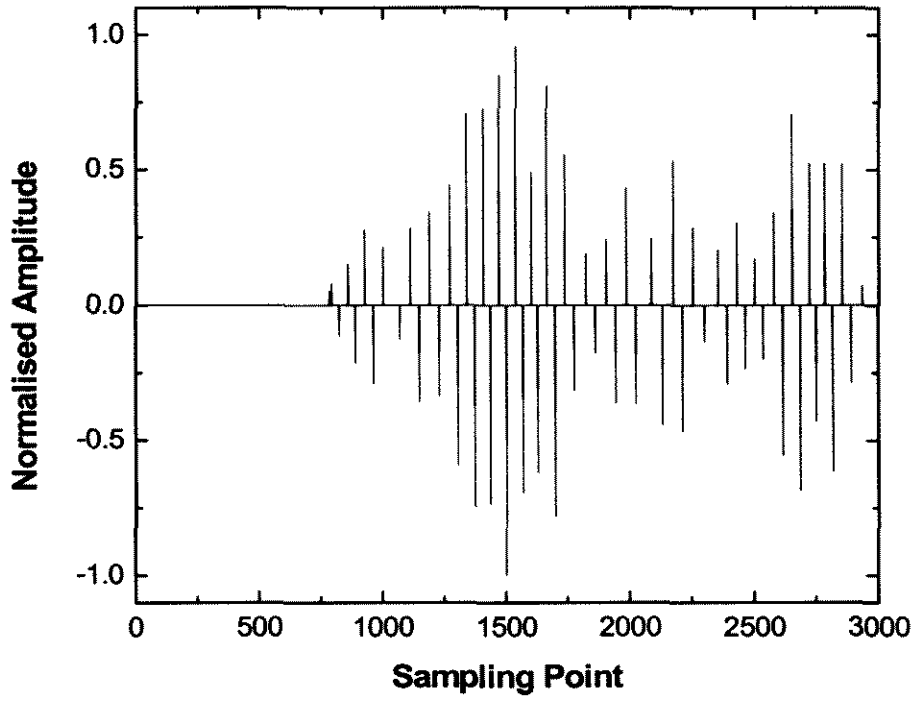

(d)

Figure 4.8 *Cont.*

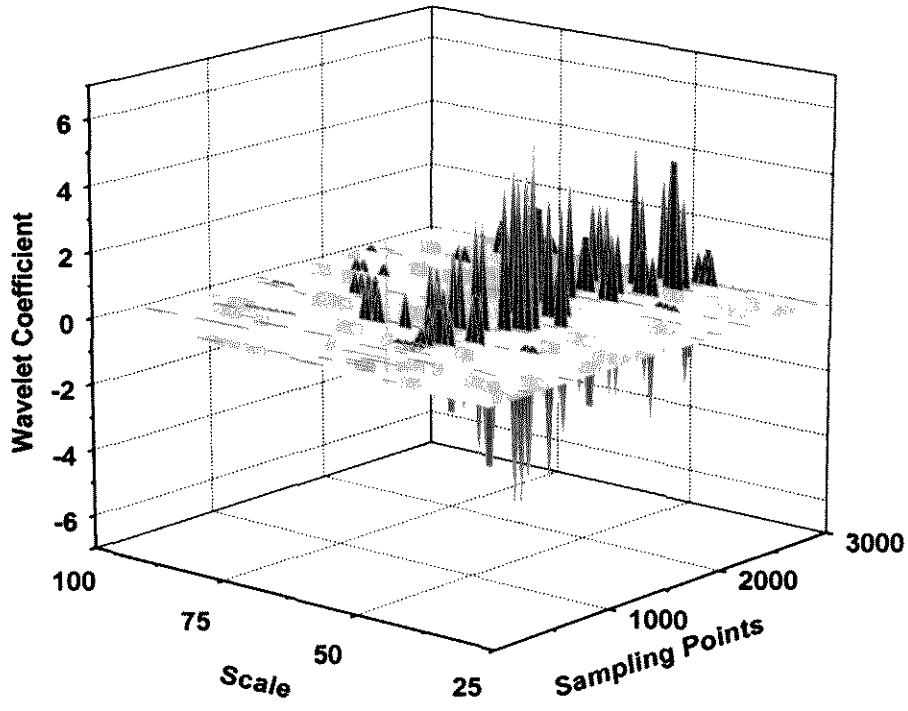

(e)

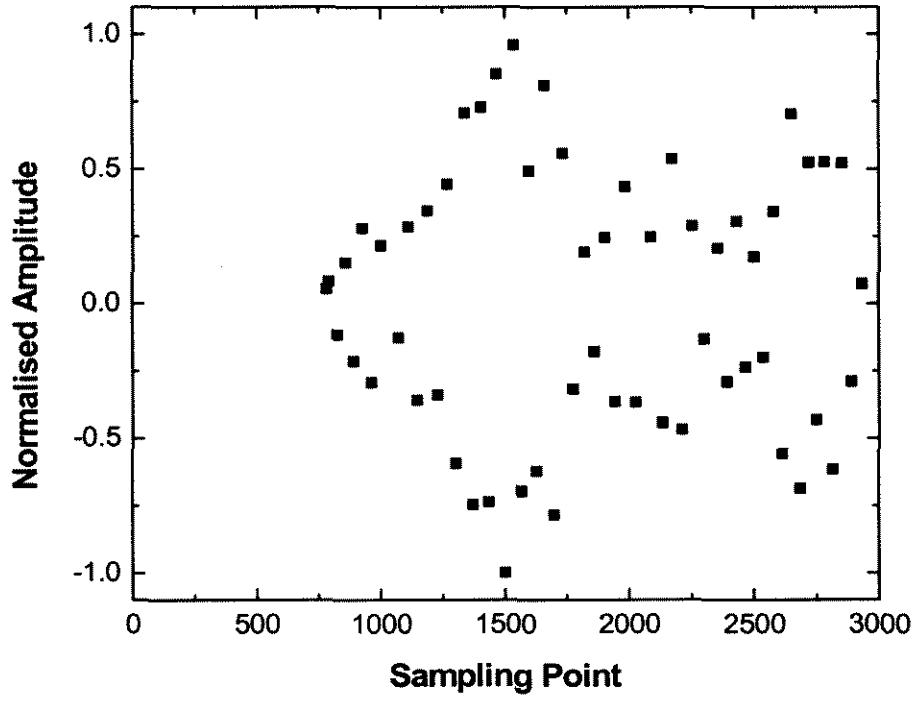

(f)

Figure 4.8 *Cont.*

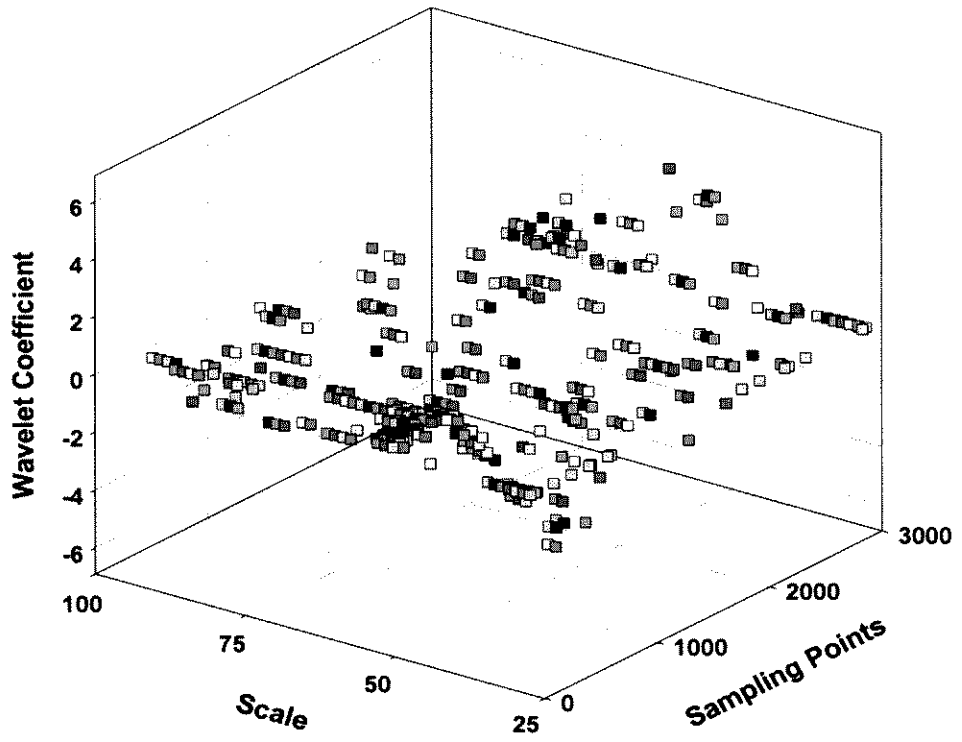

(g)

Figure 4.8 *Cont.*

4.5 Concluding Remarks

Problematic issues confronted in wave propagation-based damage detection are addressed. In the light of these difficulties, various signal processing and identification techniques, roughly grouped as analyses in time, frequency and joint time-frequency domains, are reviewed in this chapter.

An efficient signal processing and interpretation algorithm is expected to extract essential yet concise characteristics from acquired raw wave signals, and to assist the prognostic or diagnostic evaluation for structural health status. To meet this requirement, and an intelligent signal processing and pattern recognition (ISPPR) technique is developed and actualised by a signal processing package (SPP), taking advantage of wavelet transform and artificial neural algorithms (the latter is detailed

in subsequent chapters). As the essential unit in a damage detection approach, SPP functions signal filtration, characteristics extraction, data compression, information mapping and pattern recognition.

In ISPPR, novel concepts, *digital damage fingerprints* (DDF) and a damage parameter database (DPD), are developed. Such concepts are able to extract the essential characteristics of raw signals acquired from an active sensor network, digitise them into identifiable information for analysis and decision-making, and consequently quantify a damage case in a complex structure using only characteristic data. The effectiveness of ISPPR will be demonstrated by actual case studies in the following chapters.

Chapter 5

Elastic Waves in Defective Composite Structures and Damage Detection Scheme

5.1 Introduction

A study on the propagation characteristics of elastic waves in defective CF/EP composite structures containing delamination is conducted in this chapter with aid of the developed SPP. An FEM modelling technique for quasi-isotropic CF/EP composite laminate containing delamination and coupled with piezoelectric sensor/actuator is developed. The interaction between delamination and fundamental Lamb modes is evaluated. In parallel with FEM analysis, experimental verification is also carried out. Based on the phenomena observed, a damage locating scheme is established, while quantitative identification techniques for damage size, shape and orientation are detailed in subsequent chapters.

5.2 FEM Modelling Technique for NDE: A Review

For the purposes of NDE, FEM modelling techniques for defective composite structures, particularly for those containing delamination, have been well developed over years.

Most commonly, delamination occurring through the width in a composite beam, parallel to the beam surfaces along both the span and thickness directions, can be one-dimensionally simplified into four separate component segments, each of which can be modelled with beam elements [Majumdar and Suryanarayan, 1988; Islam and Craig 1994; Ostachowicz *et al*, 2002], as sketched in Figure 5.1(a).

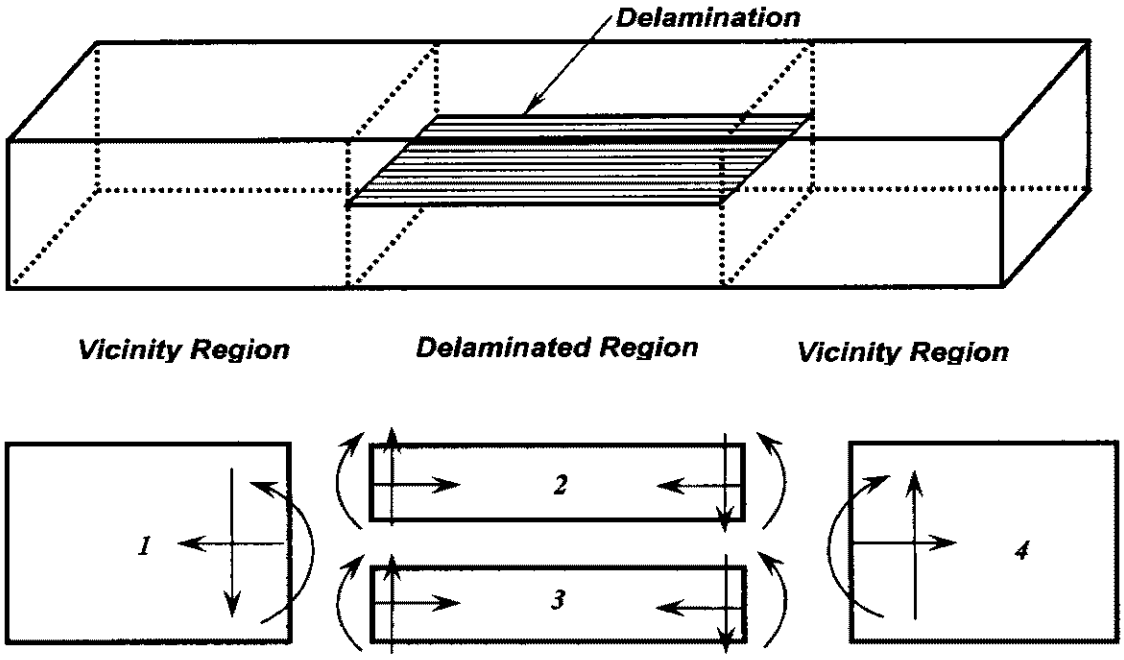

(a)

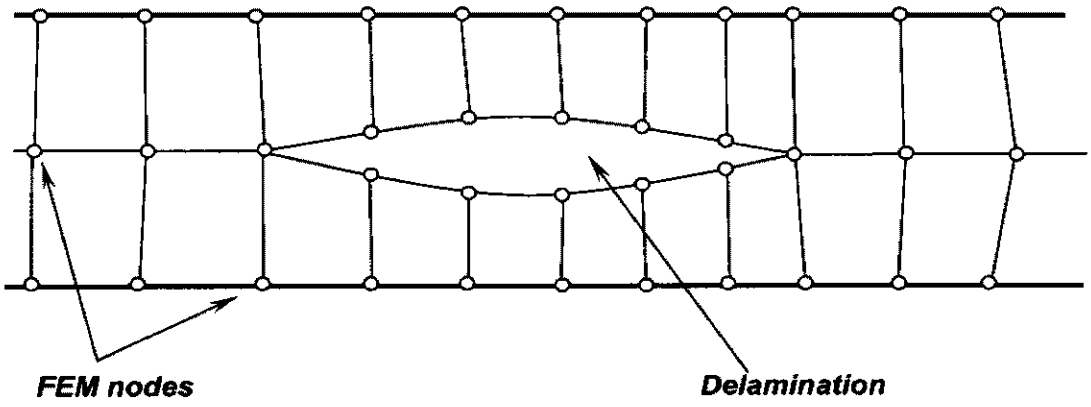

(b)

Figure 5.1 *1*-D delamination models by (a) [Majumdar and Suryanarayan, 1988; Islam and Craig, 1994; Ostachowicz *et al*, 2002] and (b) [Guo and Cawley, 1992, 1993a]

Continuity conditions of transverse displacements, slopes, bending moments and shear forces, as well as axial displacements and forces, are applied. The solution for the entire beam can be obtained by considering four separate components, with boundary conditions at the ends of integral segments and continuity conditions at the junctions between integral and delamination regions. Such a simple FEM model works well for detection of delamination in composite beams.

Tracy and Pardoen [1989] developed a similar model and introduced two extra assumptions: (1) extensional and bending stiffnesses are uncoupled; (2) the effect of contact between delaminated free surfaces is included, i.e., the sections above and below the delamination are constrained to vibrate together. This model has been shown to predict well stiffness degradation and structural natural frequencies of composite beams with delamination. Also focused on natural frequencies, mode shapes and modal damping, a modelling approach for composite beams based on laminate mechanics has been developed [Saravanos and Hopkins, 1996], where the kinematic assumptions allow for in-plane and out-of-plane relative motion between the delaminated parts. This approach can handle multiple delaminations. Its unique merit is that it considers the effect of damping.

Guo and Cawley [1992, 1993b] presented another FEM model for composite beams containing delamination (see Figure 5.1(b)), where FEM nodes across the interface are separated by a small distance. This '*zero volume*' delamination does not remove any mass. Other methods for one-dimensional through-width delaminations in composite beams also include models presented by Purekar *et al* [1998], by Gadelrab [1996] using five-node elements, and by Pines [1997] based on continuum mechanics.

To interrogate the scattering of ultrasonic waves in infinite isotropic solids two-dimensionally, a finite element model with absorbing boundary conditions was

developed by Kishore *et al* [2000], which is able to simulate complex mode-conversion when pulse interacts with flaw. It highlights the fact that if the scattering object is a void, such as a delamination, part of the incident energy will be converted to radiate energy in all directions and surface wave 'creep' around the cavity.

Using a more complex approach, Razi and Kobayashi [1993] created a three-dimensional model to investigate the growth of delamination based on a criterion using strain energy release rate. In their study, the delaminated area was modelled with coincident nodes and gap elements between these nodes to prevent overlapping of coincident surfaces, as shown in Figure 5.2, where the predicted shapes via such a method and the actual delamination zones are also compared and good agreement is observed. Similar work was also presented by Wisnom and Chang [2000], in which duplicated nodes and interface elements were used to model the splitting and delamination zone in a notched cross-ply laminate in terms of interface modelling technique. The model accurately assessed development of a narrow triangular delamination zone, and established the extent of splitting as a function of applied tensile stress.

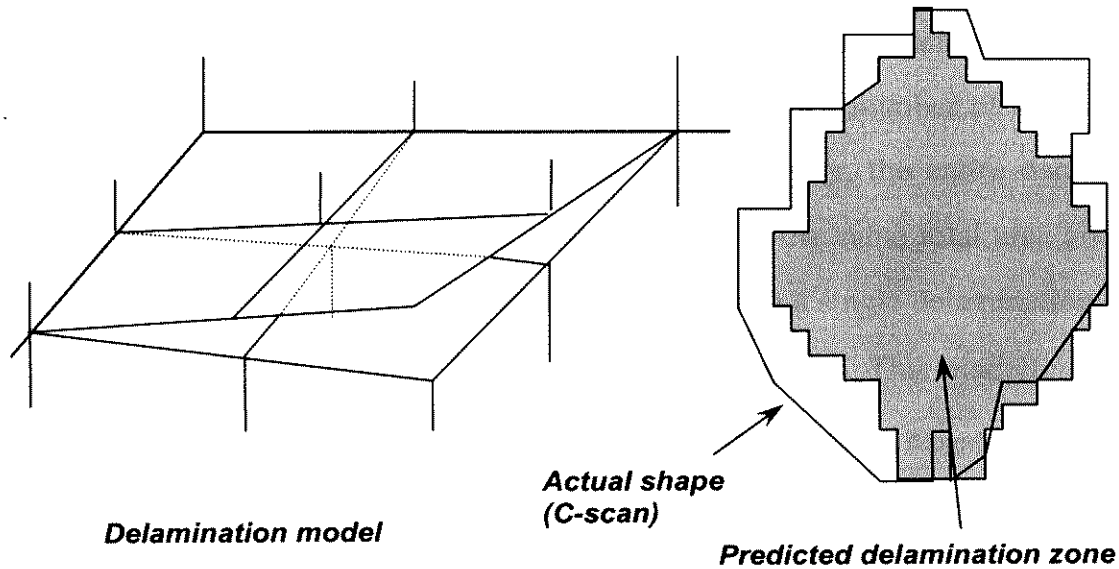

Figure 5.2 *3*-D delamination model and practical validation [Razi and Kobayashi, 1993]

Shah *et al* [1994] developed a quasi-three-dimensional model for a piezo layer embedded in composite laminate containing a delamination using eight-noded iso-parametric elements, as shown in Figure 5.3. Performed two-dimensionally but allowing a degree of freedom in the third direction, this model lowered the computational memory/time requirements, and simulated well the stress distribution and electric response of the piezo layer.

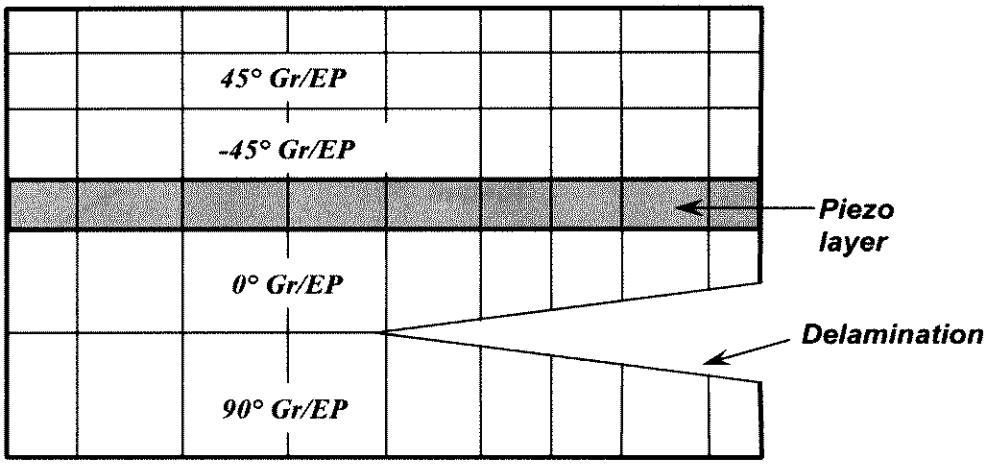

Figure 5.3 Delamination model for PZT-embedded composites [Shah *et al*, 1993]

Olsson [2001] developed a peanut-shaped three-dimensional delamination model. The delaminations were joined by matrix cracks to form a number of separate sub-laminates of irregular shape and thickness. For simplicity, the entire damage was represented by n equivalent circular delaminations of the same total area and outer boundary. Damage growth was assumed to initiate with a single delamination ($n=1$) and increase to a saturated number (n_{max}) of delaminations. This modelling method is particularly suitable for large-impact damage. Meanwhile based on layer-wise theory, Barbero and Reddy [1991] modelled delaminations by jump discontinuity conditions at interfaces, where displacements in adjacent layers remained independent, allowing for separation and slope. Their results showed good performance in studying multiple delaminations through the thickness of the plate.

Clark [1989] proposed a model based on the discreet observation of impact tests, as depicted in Figure 5.4. In his model, two adjacent, non-parallel plies, say *45°* and *-45°*, were considered under compact. This model successfully predicted a delamination in a 56-ply $[+/-45/0_2]_{7s}$ CF/EP laminate. However, such a model is applicable for point loading only and is unable to provide quantitative predictions. To overcome this shortcoming, Finn and Springer [1993] developed another model using interface principles, to estimate locations, shapes and sizes of delaminations in composite laminates subjected to either transverse static loads or penetrating (low velocity) impact.

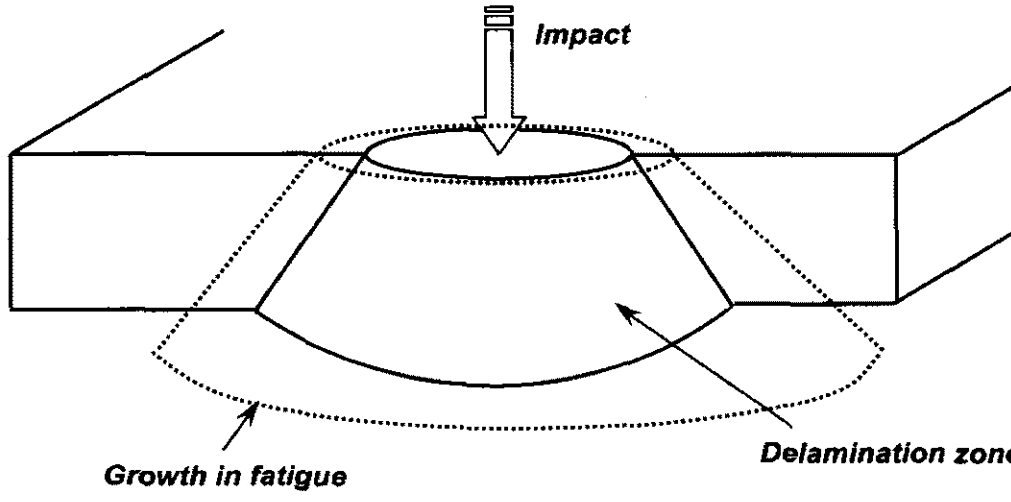

Figure 5.4 Model of impact-induced delamination [Clark, 1989]

Other modelling techniques worthy of mention also include that developed by Williams and Vaziri [2001] using *LS-DYNA3D*, where the damage took the form of disc-like cracks oriented parallel or normal to the fibre direction. In such a manner, symmetry of the lamina was preserved throughout damage evolution. Davis *et al* [1994] modelled delamination as the loss of flexural stiffness due to fibre fracture under impact, using an in-house FEM code FE77 at Imperial College. Though confined to a small region, the loss of stiffness was sufficient to soften the area around the indent. A FEM model was also created to predict initiation of damage and extent of final damage by Choi and Chang [1992], using their own damage criteria.

Finite element modelling of wave propagation is usually associated with modelling techniques for piezoelectrics-coupled structures. Further information on this specific topic can be found in [Ha *et al*, 1991; Chee *et al*, 1998, 1999; Chattopadhyay *et al*, 1999; Fukunaga *et al*, 2002; Perel and Palazotto, 2002].

5.3 FEM Modelling and Simulation for Lamb Waves in Delaminated Composites

A FEM modelling technique for piezoelectrics-coupled quasi-isotropic CF/EP composite laminate containing a delamination is developed in this study. The interaction between fundamental Lamb wave modes and delamination is evaluated.

5.3.1 Model of Actuator

Single PZT Activation

Considering a PZT-coupled composite laminate, a perfect bonding condition between them is applied to ensure strain continuity at interfaces. The electro-mechanical constitutive mutuality, with regard to direct and converse piezoelectric effects, for a single piezoelectric disc in free status, is [Lin and Yuan, 2001],

$$\begin{Bmatrix} Q_1 \\ Q_2 \\ Q_3 \\ \varepsilon_{11} \\ \varepsilon_{22} \\ \varepsilon_{33} \\ \varepsilon_{23} \\ \varepsilon_{13} \\ \varepsilon_{12} \end{Bmatrix} = \begin{bmatrix} p_1 & 0 & 0 & 0 & 0 & 0 & 0 & d_{15} & 0 \\ 0 & p_1 & 0 & 0 & 0 & 0 & d_{15} & 0 & 0 \\ 0 & 0 & p_3 & d_{31} & d_{31} & d_{33} & 0 & 0 & 0 \\ 0 & 0 & d_{31} & c_{11} & c_{12} & c_{13} & 0 & 0 & 0 \\ 0 & 0 & d_{31} & c_{12} & c_{11} & c_{13} & 0 & 0 & 0 \\ 0 & 0 & d_{33} & c_{13} & c_{13} & c_{33} & 0 & 0 & 0 \\ 0 & d_{15} & 0 & 0 & 0 & 0 & c_{55} & 0 & 0 \\ d_{15} & 0 & 0 & 0 & 0 & 0 & 0 & c_{55} & 0 \\ 0 & 0 & 0 & 0 & 0 & 0 & 0 & 0 & c_{66} \end{bmatrix} \cdot \begin{Bmatrix} E_1 \\ E_2 \\ E_3 \\ \sigma_{11} \\ \sigma_{22} \\ \sigma_{33} \\ \sigma_{23} \\ \sigma_{13} \\ \sigma_{12} \end{Bmatrix} \quad \textbf{(5.1)}$$

where orthogonal components Q_i and E_i (i=1, 2, 3) are the electric displacement (charge/area) and electric field (voltage/length), respectively. σ_{ij} and ε_{ij} are stresses and strains in the PZT disc actuator. Constants d_{ij}, p_i and c_{ij} represent the piezoelectric strain constants, dielectric permittivity and compliance constants, respectively. Provided the poling direction is perpendicular to the surface of the PZT disc, Equation (5.1), in the absence of in-plane external electric fields ($E_1 = E_2 = 0$), is simplified in the polar coordinate system (see Figure 5.5(a)),

$$Q_3 = p_3 E_3 + d_{31}(\sigma_r + \sigma_\theta) \tag{5.2a}$$

$$\sigma_r = \frac{E_{PZT}}{1-\nu^2_{PZT}}[(\varepsilon_r + \nu_{PZT}\varepsilon_\theta) - (1+\nu_{PZT})\cdot d_{31}E_3] \tag{5.2b}$$

$$\sigma_\theta = \frac{E_{PZT}}{1-\nu^2_{PZT}}[(\varepsilon_\theta + \nu_{PZT}\varepsilon_r) - (1+\nu_{PZT})\cdot d_{31}E_3] \tag{5.2c}$$

where σ_r / ε_r and $\sigma_\theta / \varepsilon_\theta$ are radial and tangential stress/strain components in the polar coordinate system, respectively. E_{PZT} and ν_{PZT} denote Young's modulus and Poisson's ratio of the PZT disc, respectively.

For a free thin piezoelectric disc of h_{PZT} in thickness, in-plane strains, ε_{r-PZT} and $\varepsilon_{\theta-PZT}$, are generated when an external voltage V is applied,

$$\varepsilon_{r-PZT} \doteq \varepsilon_{\theta-PZT} = d_{31}E_3 = \frac{d_{31}}{h_{PZT}}\cdot V = \Pi \tag{5.3}$$

Introducing the strain continuity condition at the interface ($\varepsilon^i_{r-PZT} = \varepsilon^i_{r-LMT} = \varepsilon^i_r$ and $\varepsilon^i_{\theta-PZT} = \varepsilon^i_{\theta-LMT} = \varepsilon^i_\theta$, while superscript i denotes variables at the interface between the PZT disc and composite laminate), Equation (5.2b) can be rewritten as

$$\sigma^i_{r-PZT} = \frac{E_{PZT}}{1-\nu^2_{PZT}}[(\varepsilon^i_r + \nu_{PZT}\varepsilon^i_\theta) - (1+\nu_{PZT})\cdot d_{31}E_3] \tag{5.4}$$

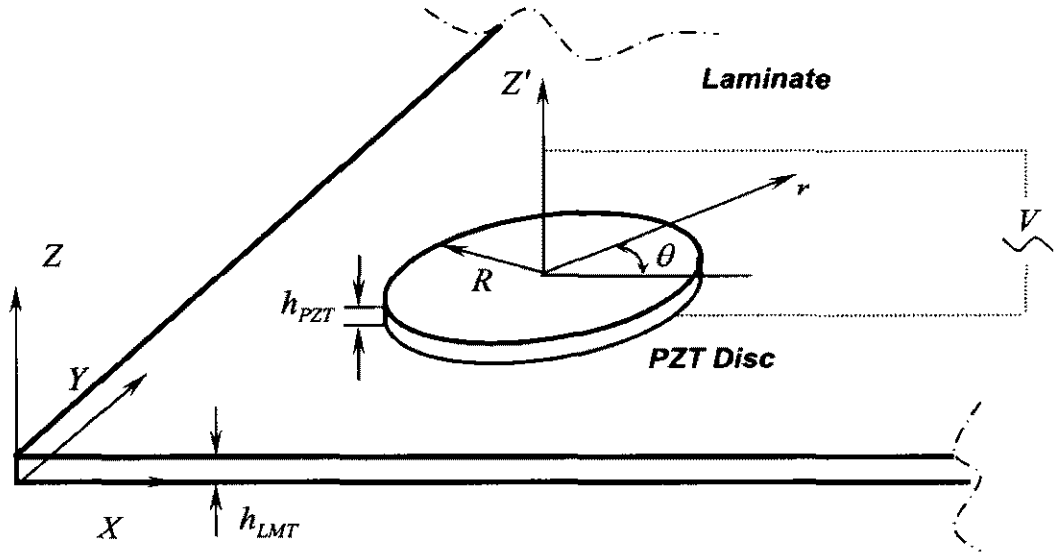

(a)

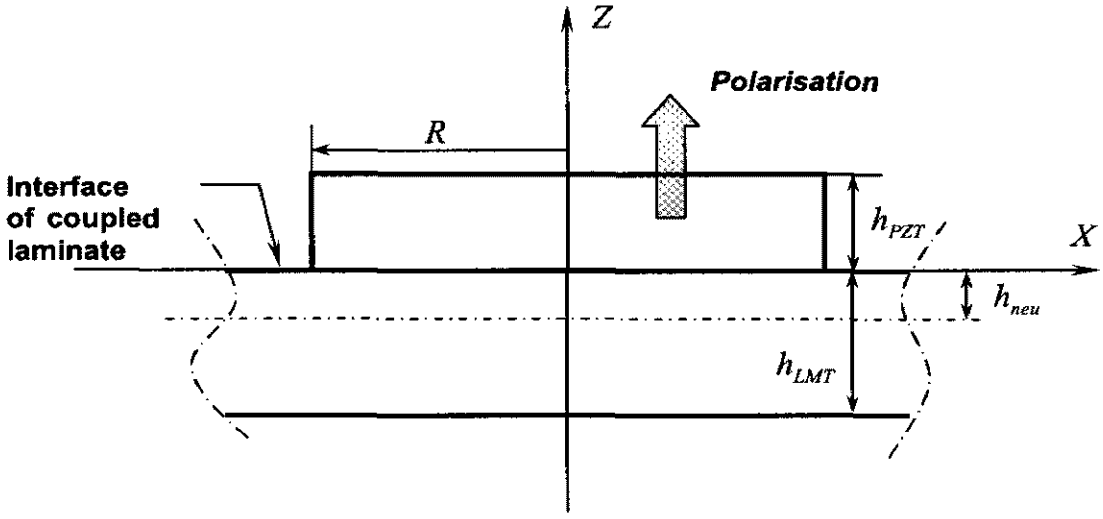

(b)

Figure 5.5 Model of PZT actuator/sensor: (a) PZT disc in the polar coordinate system; (b) single-PZT-coupled laminate system; (c) stress/strain distribution throughout thickness for single-PZT-coupled laminate system; (d) stress/strain distribution throughout thickness for double-PZT-coupled laminate system

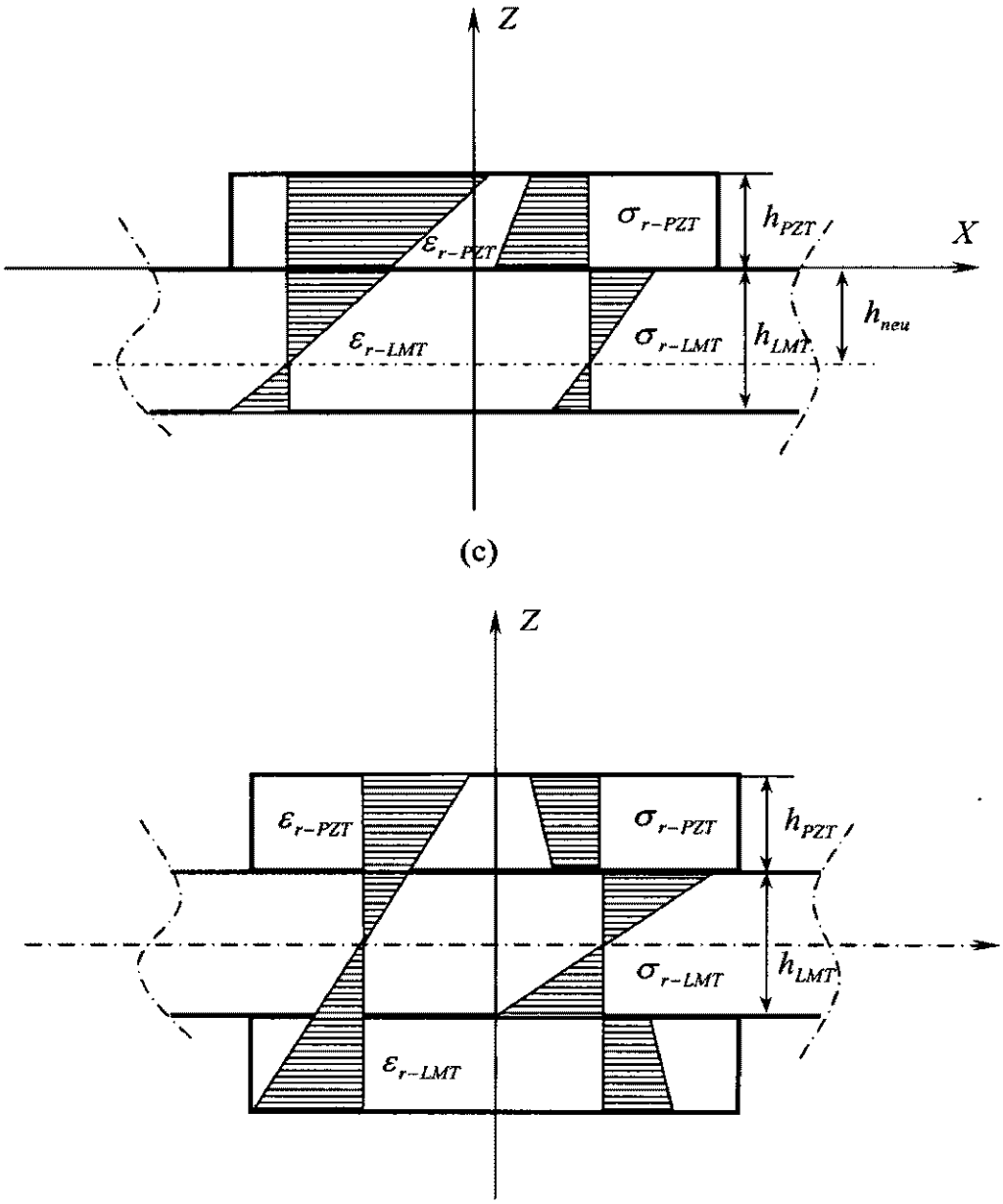

Figure 5.5 *cont.*

Laterally depicted in Figure 5.5(b), the z -axis in the referred polar coordinate system originates from the interface, and h_{neu} denotes the distance between the abscissa plane and neutral plane of the PZT-coupled laminate. Considering that both the PZT disc and the laminate are thin, classic lamination theory is applicable and the strain distribution in the laminate and PZT disc can be assumed linear across their own thickness, as

$$\sigma_{r-LMT} = \frac{\sigma^i_{r-LMT}}{h_{neu}} \cdot (h_{neu} + z) \qquad (-h_{LMT} \le z \le 0) \tag{5.5a}$$

$$\sigma_{r-PZT} = \frac{1-\nu_{LMT}}{1-\nu_{PZT}} \cdot \frac{E_{PZT}}{E_{LMT}} \cdot \frac{\sigma^i_{r-LMT}}{h_{neu}} \cdot (h_{neu} + z) - \frac{E_{PZT}}{1-\nu_{PZT}} \cdot \Pi \quad (0 \le z \le h_{PZT}) \tag{5.5b}$$

as graphically explained in Figure 5.5(c), where subscript *LMT* represents corresponding variables and constants for the laminate.

Applying equilibrium of moments and force regarding neutral plane,

$$\int_{-h_{LMT}}^{0} 2\pi r \sigma_{r-LMT} \cdot z \cdot dz + \int_{0}^{h_{PZT}} 2\pi r \sigma_{r-PZT} \cdot z \cdot dz = 0 \tag{5.6a}$$

$$\int_{-h_{LMT}}^{0} 2\pi r \sigma_{r-LMT} \cdot dz + \int_{0}^{h_{PZT}} 2\pi r \sigma_{r-PZT} \cdot dz = 0 \tag{5.6b}$$

yields stresses of the laminate and PZT actuator at the interface,

$$\sigma^i_{r-PZT} = \widetilde{A} \cdot \frac{E_{PZT}}{E_{LMT}} \widetilde{D} \cdot \Pi - \frac{E_{PZT}}{1-\nu_{PZT}} \cdot \Pi = \widetilde{E} \cdot \Pi \tag{5.7a}$$

$$\sigma^i_{r-LMT} = \widetilde{D} \cdot \Pi \tag{5.7b}$$

where

$$\widetilde{A} = \frac{1-\nu_{LMT}}{1-\nu_{PZT}}$$

$$\widetilde{B} = 2E_{LMT}E_{PZT}h_{LMT}h_{PZT} \cdot (1-\nu_{LMT}) \cdot (2h^2_{LMT} + 3h_{LMT}h_{PZT} + 2h^2_{PZT})$$

$$\widetilde{C} = \frac{E^2_{LMT}h^4_{LMT}(1-\nu_{PZT})^2 + E^2_{PZT}h^4_{PZT}(1-\nu_{LMT})^2}{(1-\nu_{PZT})}$$

$$\widetilde{D} = \frac{E_{LMT}E_{PZT}h_{PZT}(4E_{LMT}h^3_{LMT} + 3E_{LMT}h^2_{LMT}h_{PZT} + \widetilde{A}E_{PZT}h^3_{PZT})}{\widetilde{B} + \widetilde{C}}$$

$$\widetilde{E} = (\widetilde{A} \cdot \frac{E_{PZT}}{E_{LMT}} \widetilde{D} - \frac{E_{PZT}}{1-\nu_{PZT}})$$

Substituting Equation (5.7) into Equation (5.2) leads to the strain of the PZT actuator at the interface. For a small PZT disc ($\varepsilon_r^i \approx \varepsilon_\theta^i = \varepsilon^i$), equivalent radial elastic deformation, d_r , along the disc circumference, is achieved by integrating the interface strain

$$d_r = \int_0^R \varepsilon^i dr = R \cdot \frac{d_{31}}{h_{PZT}} [\frac{\widetilde{E}(1-\nu_{PZT})}{E_{PZT}} + 1] \cdot V \qquad \textbf{(5.8)}$$

It is implied that the resultant equivalent radial displacement along the circumference of a PZT disc actuator is proportional to the applied external voltage, whose scale factor is determined by Equation (5.8).

Dual PZT Activation

A similar principle is applied for the case of dual PZT activation (see Figure 5.5(d)), where the resulting neutral plane for the PZT-coupled laminate is consistent with the neutral plane of the laminate, and the stress symmetrically distributes with regard to the neutral plane as [Lin and Yuan, 2001]

$$\sigma_{r-LMT} = \frac{2\sigma^i_{r-LMT}}{h_{LMT}} \cdot z \qquad (0 \le z \le h_{LMT}/2) \qquad \textbf{(5.9a)}$$

$$\sigma_{r-PZT} = \widetilde{A} \cdot \frac{E_{PZT}}{E_{LMT}} \cdot \frac{2\sigma^i_{r-LMT}}{h_{LMT}} \cdot z - \frac{E_{PZT}}{1-\nu_{PZT}} \cdot \Pi \quad (0 \le z \le h_{PZT}) \qquad \textbf{(5.9b)}$$

as described in Figure 5.5(d). The equilibrium of moments regarding the neutral plane can therefore be simplified as

$$\int_0^{h_{LMT}/2} 2\pi r \sigma_{r-LMT} \cdot z \cdot dz + \int_{h_{LMT}/2}^{h_{LMT}/2z+h_{PZT}} 2\pi r \sigma_{r-PZT} \cdot z \cdot dz = 0 \qquad \textbf{(5.10)}$$

which gives the stress of the laminate at the interface

$$\sigma^{i}_{r-LMT} = \widetilde{F} \cdot V \tag{5.11}$$

$$\widetilde{F} = \frac{6d_{31}h_{LMT}E_{PZT} \cdot (h_{LMT} + h_{PZT})}{(1-\nu_{PZT}) \cdot [h^3_{LMT} + 2\widetilde{A} \cdot \frac{E_{PZT}}{E_{LMT}} \cdot h_{PZT}(3h^2_{LMT} + 4h^2_{PZT} + 6h_{LMT}h_{PZT})]}$$

Substituting Equation (5.11) into Equation (5.9a) and integrating the strain at the interface results in

$$d_r = \int_0^R \varepsilon^i dr = \widetilde{F} \cdot \frac{R \cdot (1-\nu_{LMT})}{E_{LMT}} \cdot V \tag{5.12}$$

Serving the similar function to Equation (5.8), Equation (5.12) determines the scale proportional factor for activation under dual PZT disc actuators.

Based on Equations (5.8) and (5.12), actuator models are developed (see Figure 5.6), with which various Lamb wave modes can be generated by applying uniform radial displacement constraints in the *x-y* plane to stimulate desirable Lamb modes in the composite laminate.

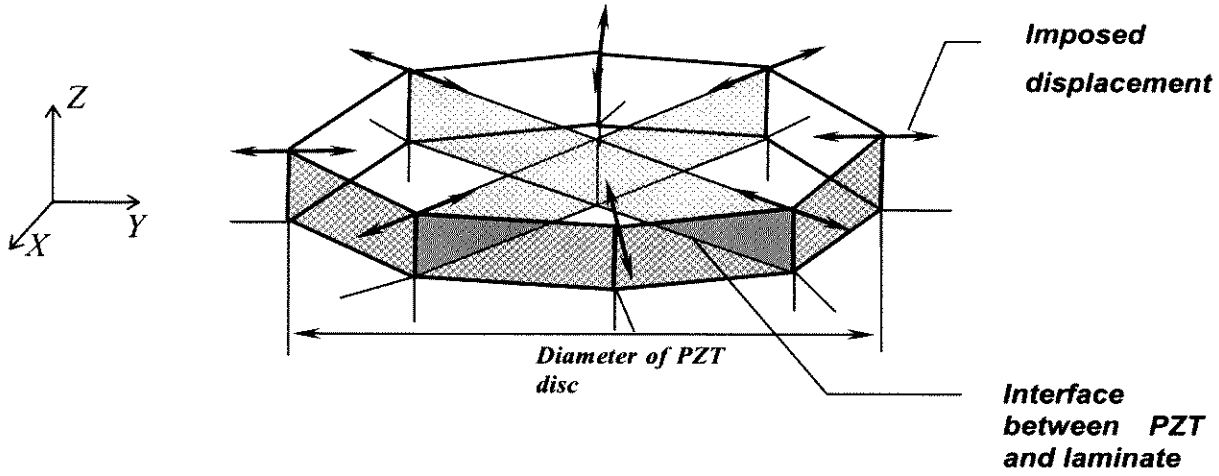

Figure 5.6 Actuator model with applied displacement constraints

5.3.2 Model of Sensor

A model for PZT disc sensor bonded on composite laminate is developed. Considering deformation in the x'-y' plane only, the constitutive relation, Equation (5.1), for a PZT disc sensor of R in radius and h_{PZT} in thickness, can be simplified in its local polar coordinate system $r'-\theta'-z'$, in the absence of an external electric field [Lin and Yuan, 2001],

$$Q = d_{31}(\sigma_{r'} + \sigma_{\theta'}) = \frac{d_{31}E_{PZT}}{1-\nu_{PZT}}(\varepsilon_{r'} + \varepsilon_{\theta'}) \tag{5.13}$$

where r' and θ' are the local polar coordinates. Electric charges, Θ, accumulated on both surfaces of PZT disc sensor, can be defined in terms of applied external voltage,

$$\Theta = \frac{1}{4\pi}\iiint \nabla \cdot Q \cdot dV \tag{5.14}$$

Substituting Equations (5.13) into (5.14) and applying Gauss' theorem leads to

$$\Theta = \frac{d_{31}E_{PZT}}{4\pi(1-\nu_{PZT})}\iint(\varepsilon_{r'} + \varepsilon_{\theta'}) \cdot r' \cdot dr' \cdot d\theta' \tag{5.15}$$

Regarded as a capacitor with a capacitance of C, the PZT disc sensor induces the output voltage V_{otp} under the deformation

$$V_{otp} = \frac{\Theta}{C} = \frac{\Theta \cdot h_{PZT}}{\pi K_3 p_0 R^2} \tag{5.16}$$

where K_3 and p_0 represent the relative dielectric constant and the dielectric permittivity of the free PZT disc, respectively. Combining Equations (5.15) and (5.16) yields

$$V_{otp} = \frac{d_{31}E_{PZT}h_{PZT}}{4\pi K_3 p_0 R^2(1-\nu_{PZT})}\iint(\varepsilon_{r'} + \varepsilon_{\theta'}) \cdot r' \cdot dr' \cdot d\theta' \tag{5.17}$$

Compared with the laminate, the PZT disc sensor is geometrically small ($\varepsilon_{r'} \approx \varepsilon_{\theta'} \approx \varepsilon_{cen}$, and ε_{cen} is the strain at the centre of PZT disc). Equation (5.17) then becomes

$$V_{otp} = \widetilde{G} \cdot \varepsilon_{cen}, \qquad \widetilde{G} = \frac{d_{31} E_{PZT} h_{PZT}}{4\pi K_3 \varepsilon_0 (1 - \nu_{PZT})} \tag{5.18}$$

This indicates that for a PZT disc sensor, the output voltage induced due to geometrical deformation is directly proportional to the central strain of the PZT sensor with the factor of $\widetilde{G}$. Based on Equation (5.18), the PZT sensor output responses, in the form of induced output voltage, can be achieved with the sensor model by calculating the strain at the PZT sensor centre [Tracy and Chang, 1998].

5.3.3 Model of Delamination

Considering reality, a delamination is assumed to be geometrically elliptical in this study, but allowed arbitrary axis length, orientation and interlaminar position. In the delamination region, a volume-split is shaped and enveloped by two isolated surfaces sharing the same boundary, on which FEM nodes are symmetrically allocated, as depicted in Figure 5.7. The maximum distance between two delaminated surfaces, h, is determined depending on the individual case.

A surface contact algorithm provided by the ABAQUS/EXPLICIT® FEM package [Hibbitt, Karlsson & Sorensen Inc., 2003] is adopted to process the contact problem arising from delamination, primarily relaxing restrictions on surfaces which may come into contact. The contact algorithm permits a small relative sliding displacement and arbitrary rotation of two delaminated surfaces. Both the upper and lower surfaces are defined using an element-based deformable surface, allowing interaction between two surfaces in the normal direction without mutual penetration.

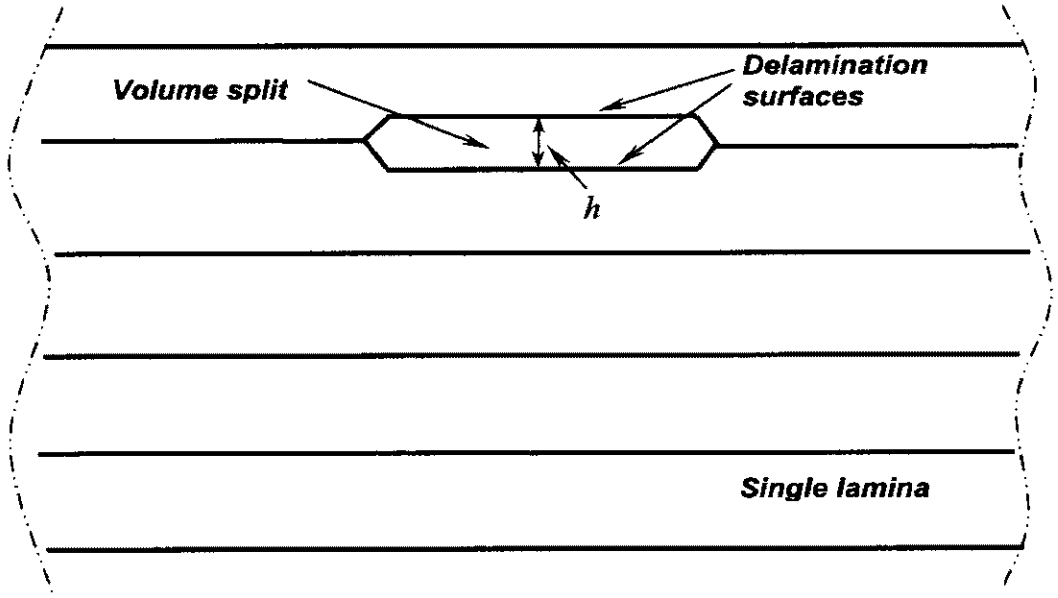

Figure 5.7 Cutaway view of delamination model

5.3.4 Elastic Properties

A three-dimensional fibre/matrix model based on micromechanics [Gommers *et al*, 1996] is employed to derive the elastic properties for chosen CF/EP composite materials (F584, *Hexcel*®). In the model, it is presumed

$$E_{11} = \Omega_f E_{f11} + \Omega_m E_m; \qquad E_{22} = E_{33} = \frac{E_m}{1-\sqrt{\Omega_f}(1-\frac{E_m}{E_{f22}})}$$

$$G_{12} = G_{13} = \frac{G_m}{1-\sqrt{\Omega_f}(1-\frac{G_m}{G_{f12}})}; \qquad G_{23} = \frac{G_m}{1-\sqrt{\Omega_f}(1-\frac{G_m}{G_{f23}})} \qquad \textbf{(5.19)}$$

$$\nu_{12} = \nu_{13} = \Omega_f \nu_{f12} + \Omega_m \nu_m; \qquad \nu_{23} = \frac{E_{22}}{2G_{23}} - 1$$

where subscripts f and m denote fibre and matrix, respectively. Ω, G, E and ν are volume percentage, shear modulus, Young's modulus and Poisson's ratio, respectively. Subscript *11* is the fibre direction. In general, these formulae predict the in-plane elastic constants quite well, except for axial shear modulus which is

normally underestimated [Gommers *et al*, 1996]. Assuming there are no voids in the composite materials, the density is defined using

$$\rho = \Omega_f \cdot \rho_f + \Omega_m \cdot \rho_m \tag{5.20}$$

Based on the elastic properties of individual fibre and matrix [Hexcel Co., 2001] detailed in Tables 5.1, effective elastic properties for single unidirectional lamina are determined using Equations (5.19) and (5.20), summarised in Table 5.2.

Table 5.1 Elastic properties for composite material (F584, *Hexcel*®) [Hexcel Co., 2001]

(a) carbon fibre

Volume Fraction [%]	E_{f11} [GPa]	E_{f22} [GPa]	G_{f12} [GPa]	G_{f23} [GPa]	ν_{f23} [GPa]	ρ_f [g/m^3]
0.555	276	17.3	11.24	6.056	0.25	1835

(b) epoxy matrix

Volume Fraction [%]	E_m [GPa]	G_m [GPa]	ν_m [GPa]	ρ_m [g/m^3]
0.445	4.14	1.532	0.35	1219

Table 5.2 Estimated effective elastic properties for single CF/EP lamina

E_{11} (GPa)	E_{22} (GPa)	E_{33} (GPa)	G_{12} (GPa)	G_{13} (GPa)	G_{23} (GPa)	ν_{12}	ν_{13}	ν_{23}	ρ_m [g/m^3]
153.67	9.49	9.49	4.26	4.26	3.44	0.295	0.295	0.381	1528

5.3.5 Model of Delaminated Composite Laminate

Two quasi-isotropic CF/EP (T650/F584) composite laminates (*475mm* × *475mm* × *1.275mm*) with a configuration of $[45/-45/0/90]_s$ are considered. One pair of laminate edges is fixed-supported, as shown schematically in Figure 5.8. Four PZT discs, acting as both actuators and sensors, are presumed to be located along laminates diagonally *65mm* away from two neighboring edges, numbered counterclockwise as *P1*, *P2*, *P3* and *P4* from the lower left. Two laminates are modelled without and with damage as benchmark and defective laminates, respectively. In the latter, an elliptic delamination (semi-major axis: *15mm*, semi-minor axis: *10mm*, angle between major axis and *0°* fibre direction: *135°*, centre position: *276mm* to left and *299mm* to bottom edges of laminate, delaminated area: *0.25%* of total surficial area of laminate) between the 1^{st} and the 2^{nd} layers is introduced.

Full-scale FEM models for the specified laminates are created using *8*-node three-dimensional brick elements on the PATRAN® platform, symbolised by *FEM-UD1*# and *FEM-UD2*# for the benchmark and defective laminates, respectively. It is clear that the delamination is a complicated *3-D* pattern, and highly refined finite element description with laminar-thick elements is adopted to capture all the stress/strain components. Ensuring precision, *8* layers are divided along the laminate thickness to characterise each unidirectional lamina individually, leading to approximate *100,000* solid brick elements for the simulation. The ichnography of the FEM model and the vicinity of delaminated area are displayed in Figure 5.9, where more than *10* nodes exist within one wavelength [Alleyne and Cawley, 1991, 1992b; Bull, 1996].

The delamination model (Section 5.3.3) is employed to simulate the delamination, as shown in Figure 5.10. PZT actuator/sensor models (Sections 5.3.1 and 5.3.2) are invoked, where a uniform radial displacement in the *x-y* plane, following a *5*-cycle sinusoidal toneburst windowed with the *Hanning* function at a central frequency of

0.5MHz, is applied on the actuator model to generate Lamb waves. Wave propagation is simultaneously monitored at a sample rate of *20.48MHz* by the sensor model.

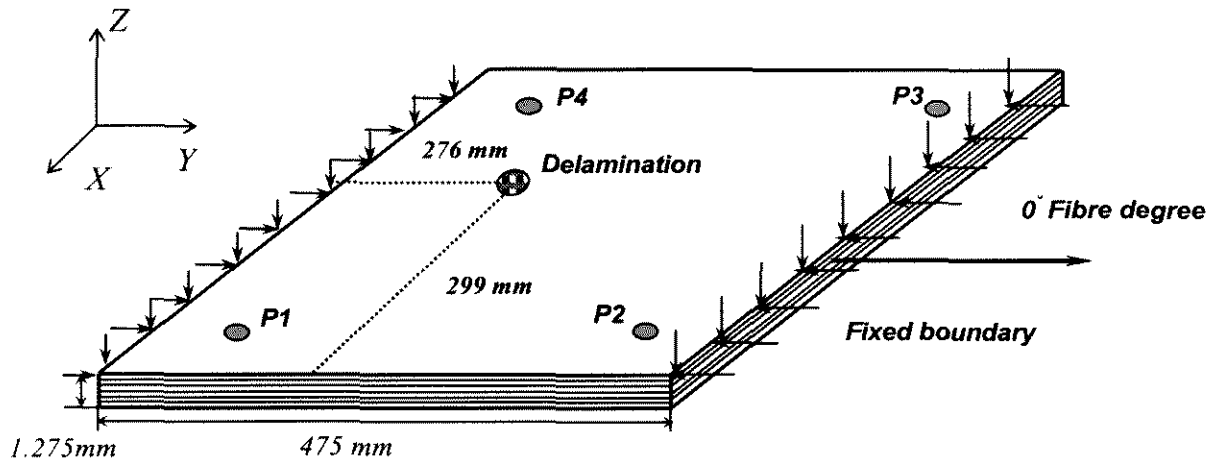

Figure 5.8 *8*-layer $[45/-45/0/90]_s$ quasi-isotropic composite laminate containing a delamination

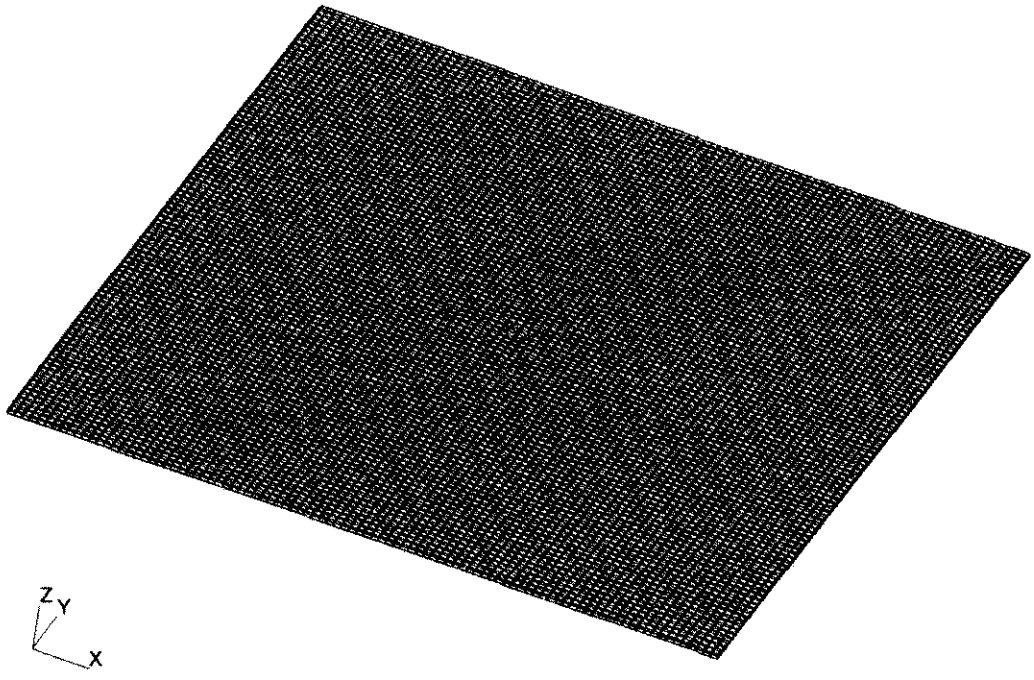

(a)

Figure 5.9 FEM Model for *8*-layer $[45/-45/0/90]_s$ quasi-isotropic CF/EP composite laminate; (a) overall model, (b) partial magnification near delaminated area

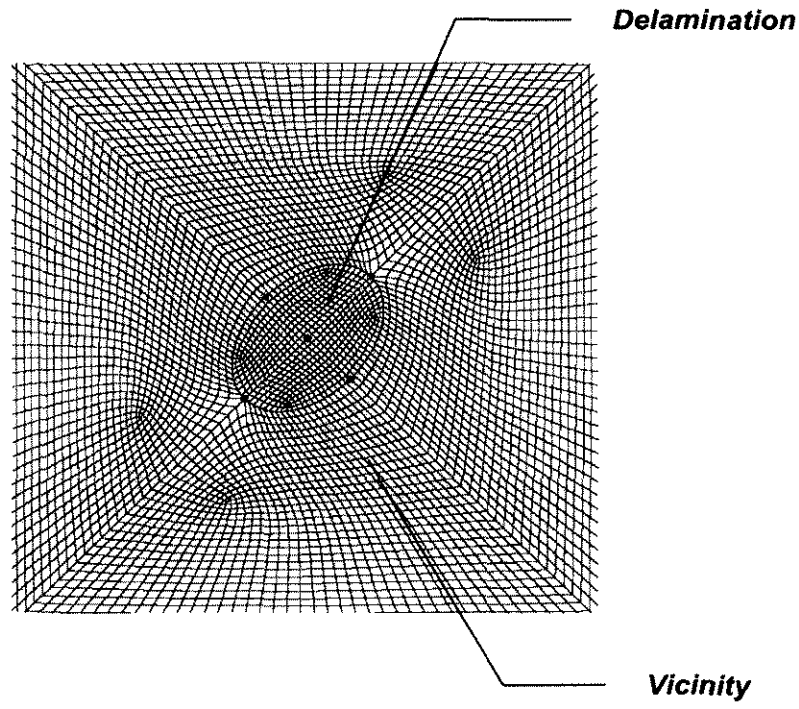

(b)

Figure 5.9 *Cont.*

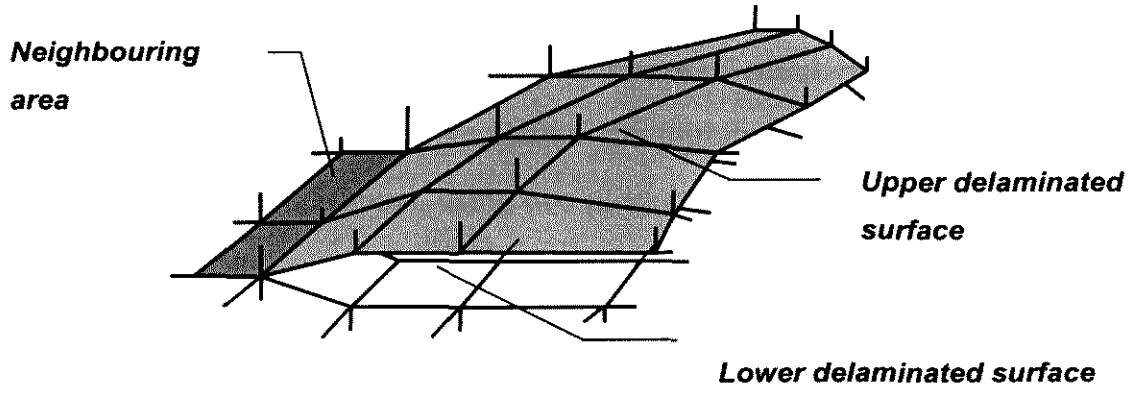

Figure 5.10 Delamination model

5.3.6 Dynamic Simulation and Results

The dynamic simulation is accomplished on a supercomputer (physically installed at the *Australian National University*) using the ABAQUS/EXPLICIT® FEM code. The step of calculation time is controlled to be less than the ratio of the minimum distance of any two adjoining nodes to the maximum wave velocity.

Actively generated by the actuator model, visualised wave propagation in *FEM-UD1#* at several representative times is captured in Figure 5.11. Meanwhile, a typical moment of the Lamb wave produced by the PZT actuator model in *FEM-UD2#* is displayed in Figure 5.12 for comparison (note that the vertical displacement in the figures is magnified for illustration, but not proportionately accurate), where delamination-imposed disturbance on the wave propagation can be clearly observed.

5.4 Experimental Validation

The FEM simulation was then experimentally verified. Two quasi-isotropic CF/EP composite laminates with the same materials (T650/F584), configuration $[45/-45/0/90]_s$ and geometry ($475mm \times 475mm \times 1.275mm$), made from unidirectional (UD) prepreg were manufactured. For the purpose of comparison, a delamination of the same shape and size in FEM simulation was introduced in one of the laminates to serve as the defective specimen, using two pieces of *UPLEX©-R-25* film of $25\mu m$ in thickness during fabrication, while the other was kept intact, symbolised by *EXP-UD1#/UD2#*, respectively. Meanwhile, two T650/F593 $[(0/90)/(-45/45)/(90/0)]_s$ quasi-isotropic CF/EP laminates made from plain woven fabric (WF) prepreg were also made, denoted by *EXP-WF1#/WF2#* for the benchmark and the one containing a delamination, respectively. Configurations of the specimens are summarised in Table 5.3.

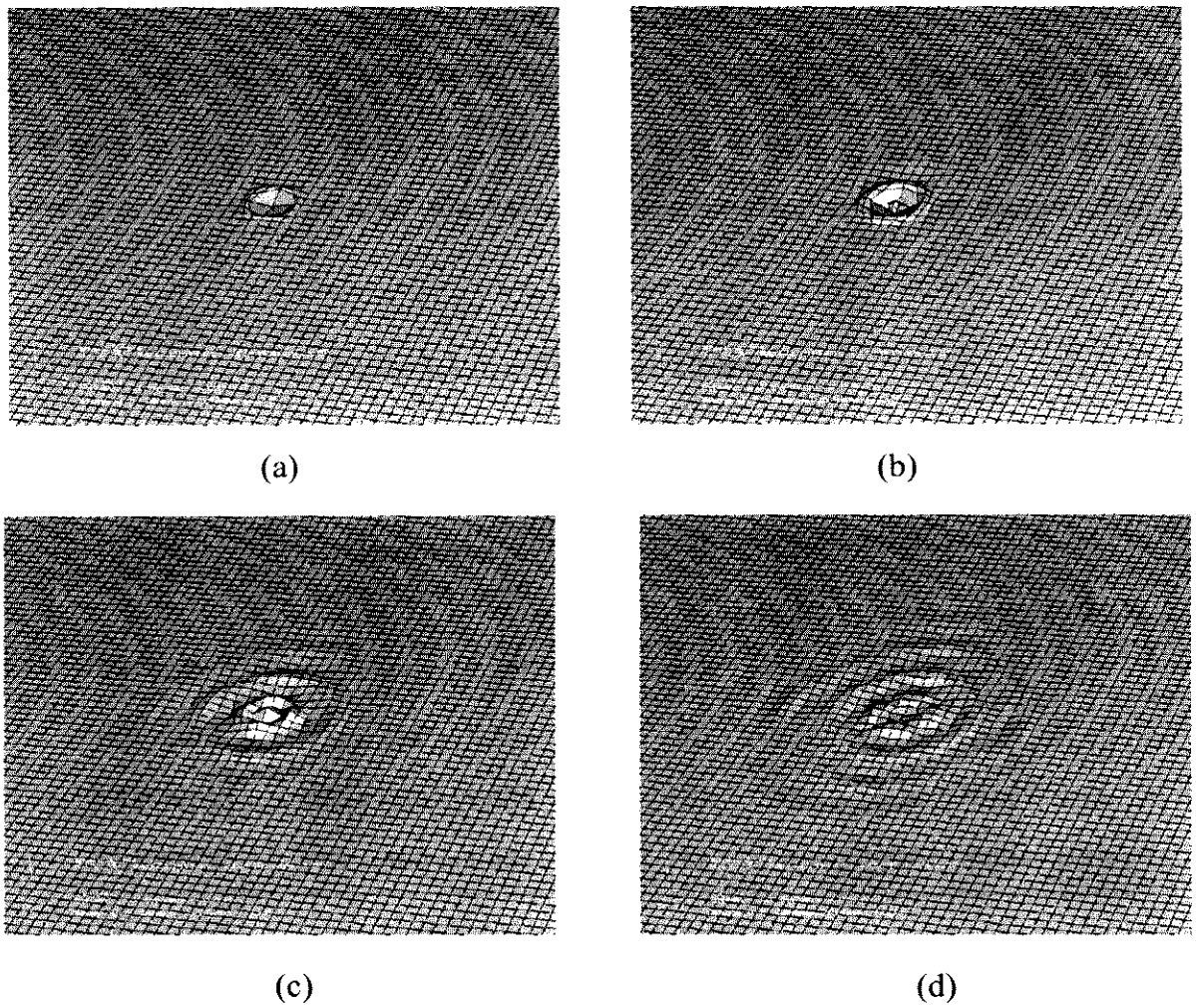

Figure 5.11 Lamb wave generated by PZT actuator model at (a) 3.5^{th}; (b) 6.0^{th}; (c) 8.5^{th}; (d) 12.0^{th} microsecond

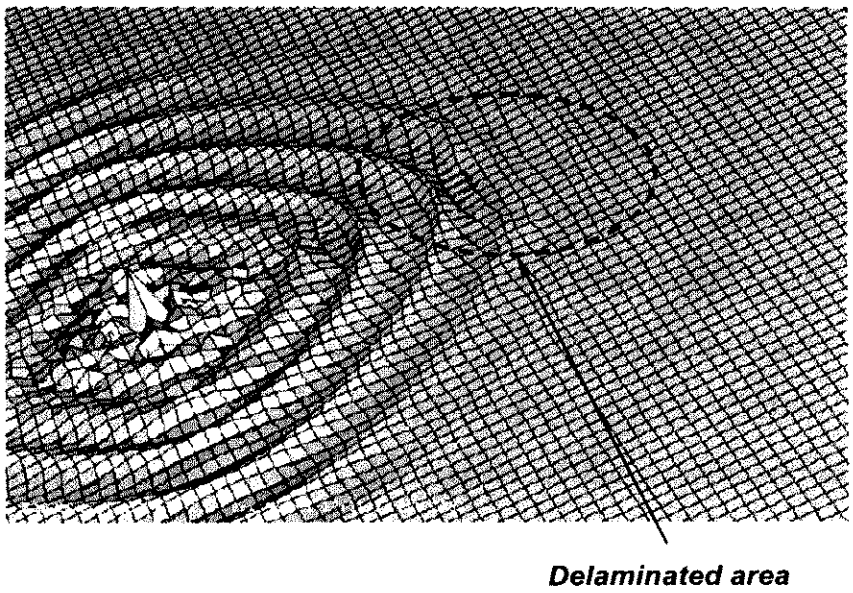

Figure 5.12 Lamb wave propagation in delaminated area

PZT wafers (*PI© PIC151*) of *6.9mm* in diameter and *0.5mm* in thickness were selected. Amplified and modulated excitation conditions, in accordance with the FEM simulation, were applied on each PZT wafer in turn to generate Lamb waves. Wave signals were acquired via each actuator-sensor path at the sample rate of *20.48MHz*.

Table 5.3 Configuration of specimens

(Unit: *mm*)

Specimen No.	Geometric Dimension (mm)	Simulated delamination					
		α	β	ϕ	ξ	ζ	θ
EXP-UD1#	480 × 480 × 1.275	N/A	N/A	N/A	N/A	N/A	N/A
EXP-UD2#	480 × 480 × 1.275	15	10	135	276	299	0.25
EXP-WF1#	480 × 480 × 1.454	N/A	N/A	N/A	N/A	N/A	N/A
EXP-WF2#	480 × 480 × 1.454	17	12	45	268	190	0.18

α : semi-major axis β : semi-minor axis ϕ : angle between the major axis and 0° fibre direction

ξ / ζ : vertical distance to left/bottom edges from the centre of delamination

θ : percentage of delaminated area (%) in laminate

5.5 Signal Processing and Discussion

Signal Processing and Interpretation

Signal acquisition was well replicable in both the simulations and experiments. As representative paradigms, captured signals for *FEM-UD1#/UD2#* and *EXP-UD1#/UD2#*, via actuator-sensor path *P1-P3*, are displayed in Figure 5.13. Their frequency spectra via FFT are compared in Figure 5.14. Certain nuances of difference can be observed between the signals of the benchmark and defective laminates, either in the time or the frequency domain. However, none of them is sufficient for quantitative damage identification.

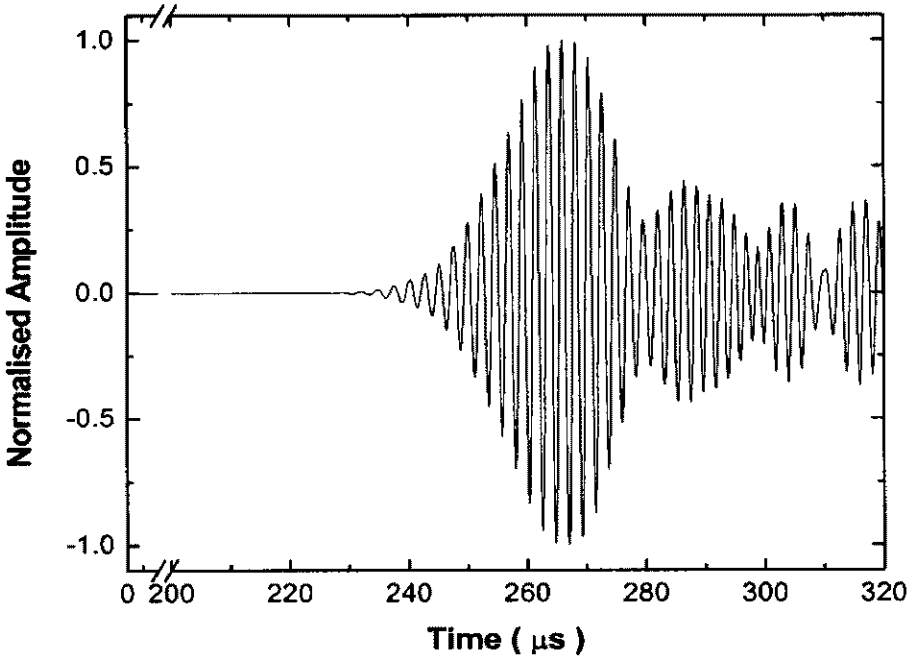

(a)

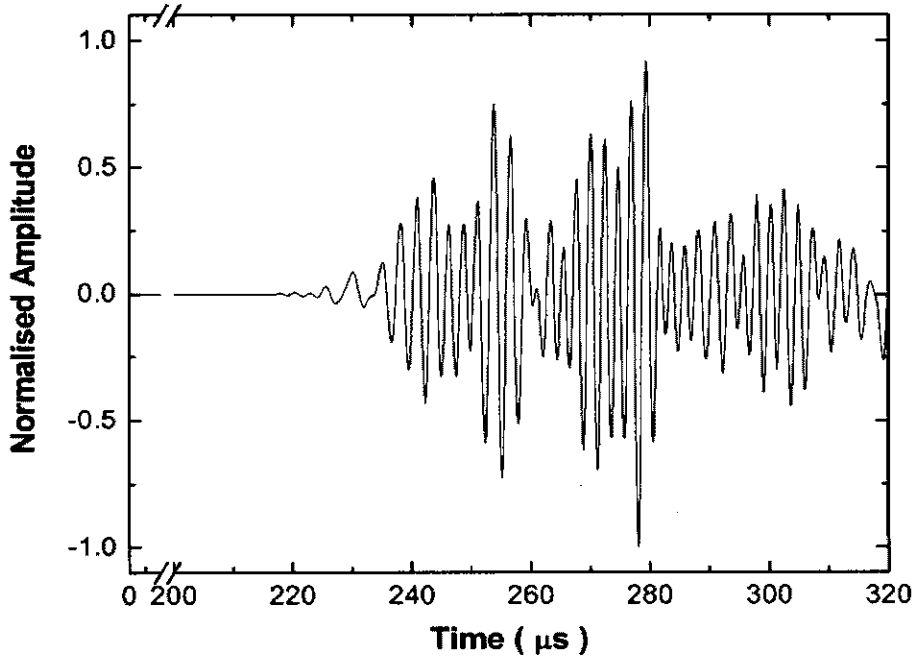

(b)

Figure 5.13 Raw Lamb wave signals acquired via *P1-P3* for (a) benchmark *FEM-UD1*$^{\#}$; (b) defective *FEM-UD2*$^{\#}$; (c) benchmark *EXP-UD1*$^{\#}$; (d) defective *EXP-UD2*$^{\#}$

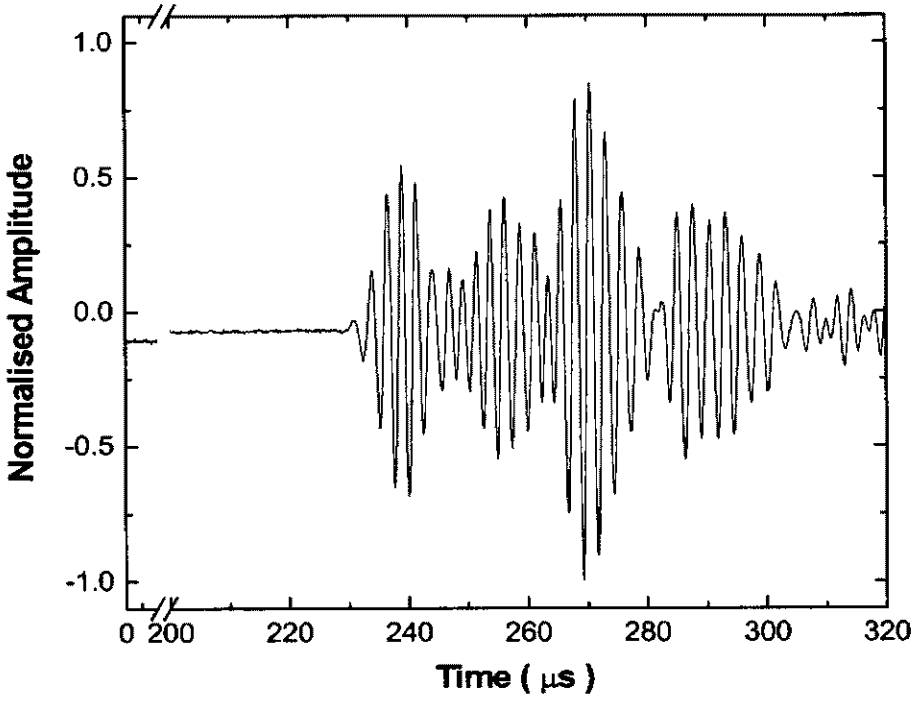

(c)

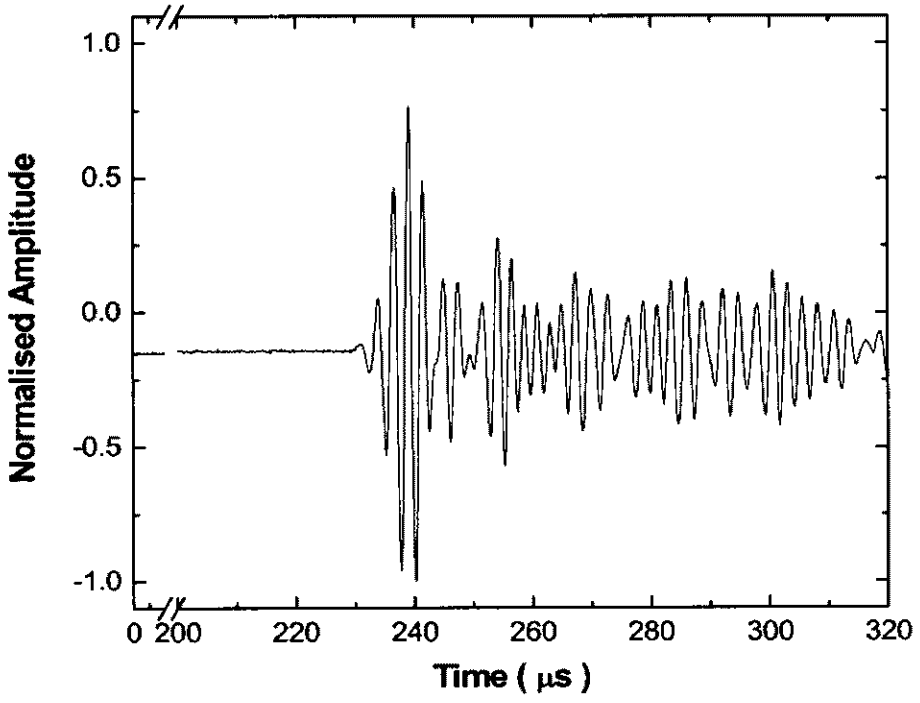

(d)

Figure 5.13 *Cont.*

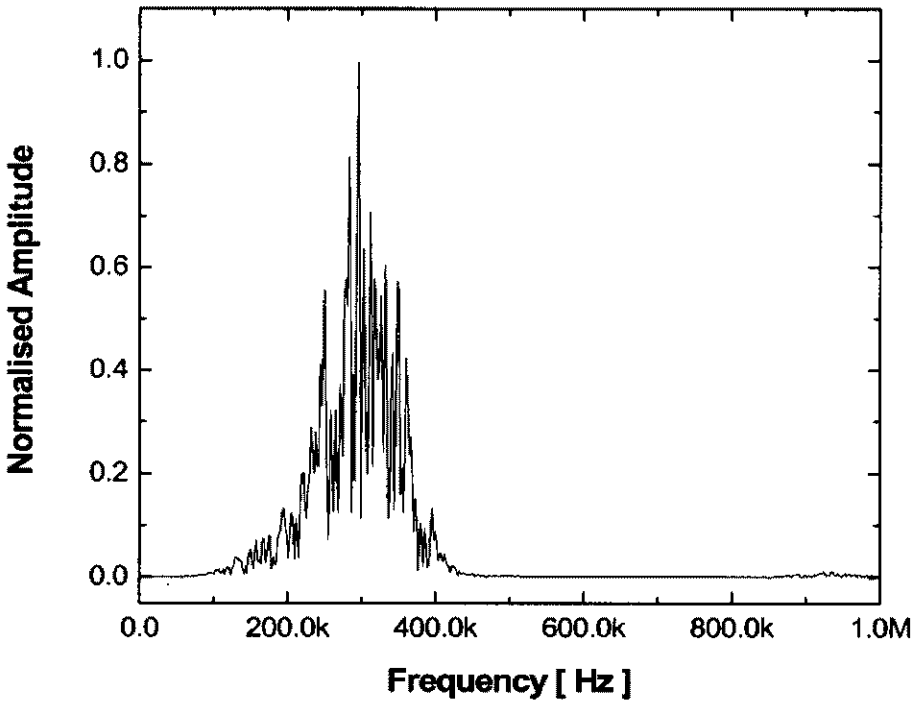

(a)

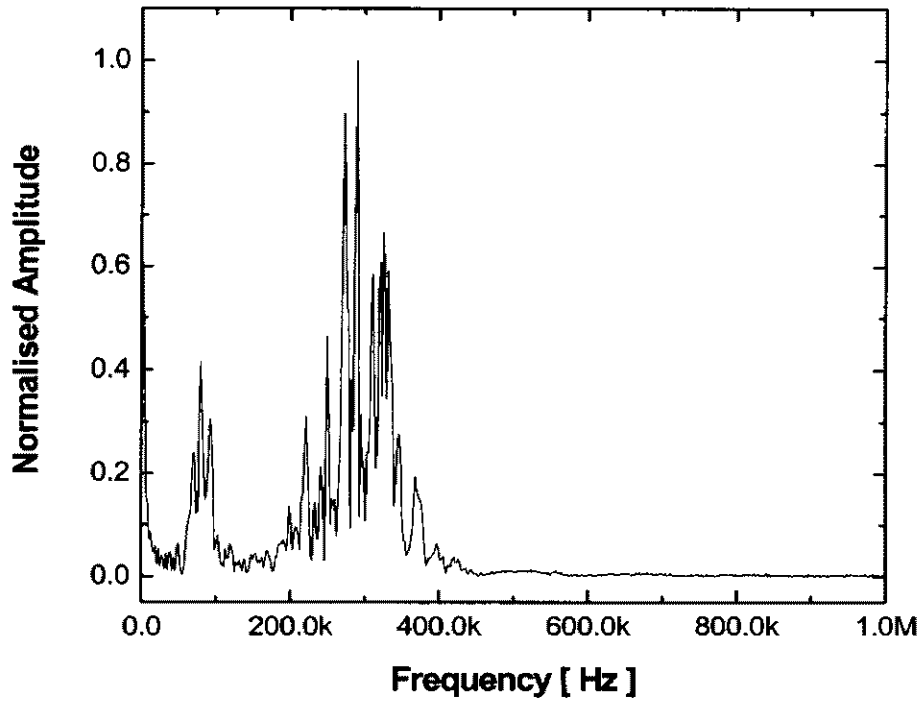

(b)

Figure 5.14 FFT spectra for signals in Figure 5.13: (a) benchmark *EXP-UD1*$^{\#}$; (b) defective *EXP-UD2*$^{\#}$

Using the signal processing package (SPP), digitally filtered signals corresponding to active excitation (*500kHZ*) are separated from raw signal (see Figure 5.15), where the basic symmetric Lamb mode, S_0, and the basic horizontal shear (SH) mode, S_0', together with the reflected components from laminate edges, denoted by S_{0ref}, can be observed in sequence). For identification only the first few wave components are useful and the rest may be corrupted by multiple boundary reflections.

Mode conversion induced by the existence of delamination is noticeable in the signals for the defective laminates. Compared with the benchmark laminates, extra wave components between S_0 and S_{0ref} are detected in Figures 5.15 (b) and (d), which is recognised as the delamination-induced basic shear mode, S'_{0Delam}. The appearance order of wave components in a signal is deterministically dependent on the relative locations among defect, boundaries and sensors. Other damage-induced modes are unexploitable because their propagation velocities are either too high to be identified or too low to be sampled in the specific time period.

Further, *2*-D and *3*-D spectrographic analyses based on CWT are also performed via SPP. Results for selected signals are compared in Figure 5.16. In both *2*-D and *3*-D energy spectra, a defect-caused shear wave, S'_{0Delam}, can be visually detected. Similar phenomena have also been observed for FEM simulations and experiments on laminates made from woven fabric prepreg, which are detailed elsewhere [Su *et al*, 2002].

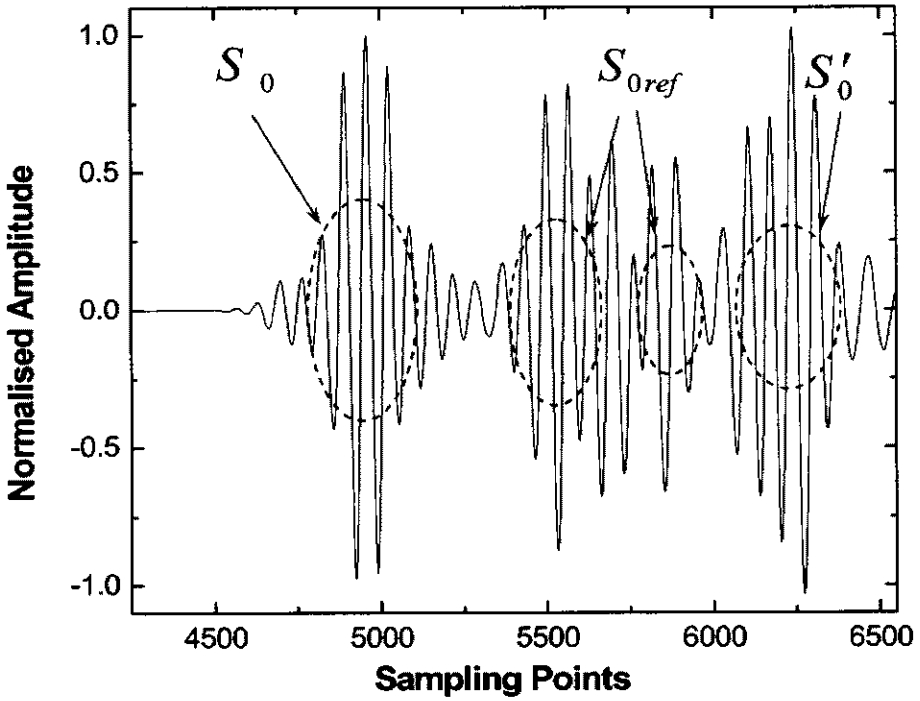

(a)

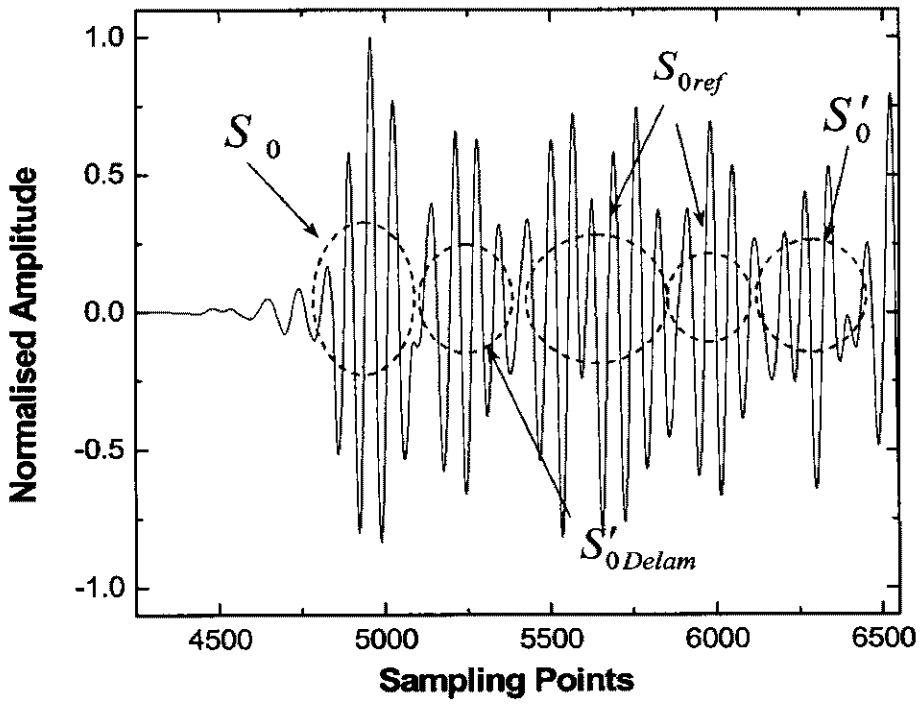

(b)

Figure 5.15 DWT-filtered signals in time domain for (a) benchmark *FEM-UD1*$^{\#}$; (b) defective *FEM-UD2*$^{\#}$; (c) benchmark *EXP-UD1*$^{\#}$; (d) defective *EXP-UD2*$^{\#}$

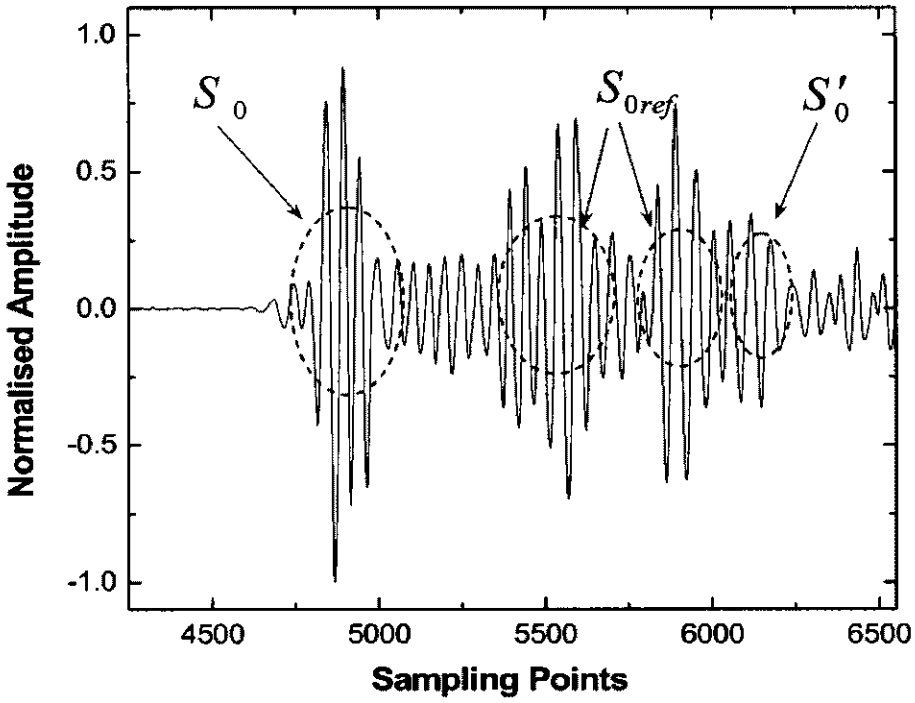

(c)

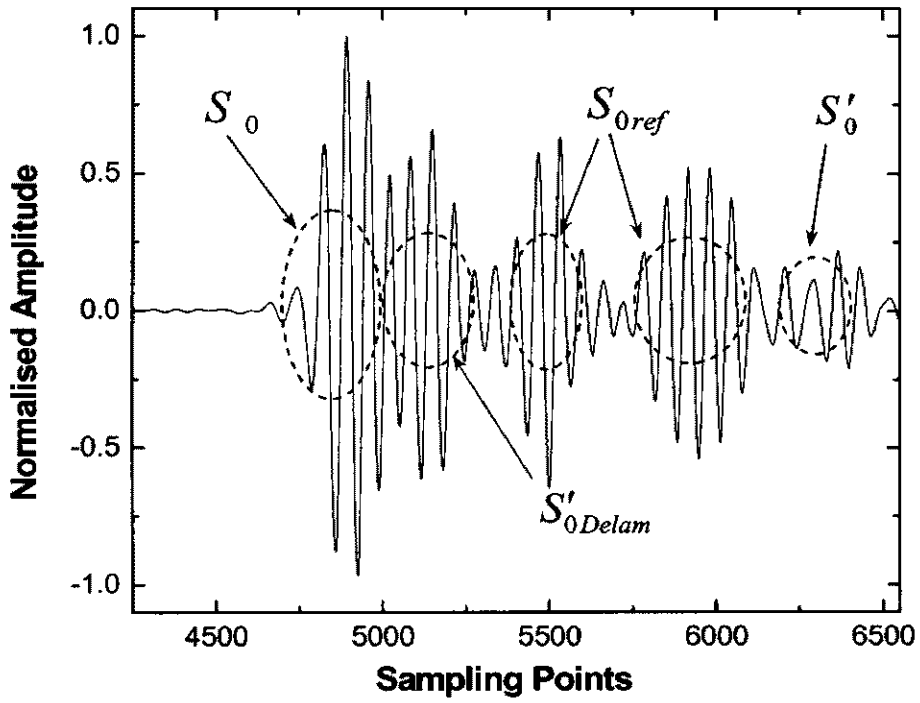

(d)

Figure 5.15 *Cont.*

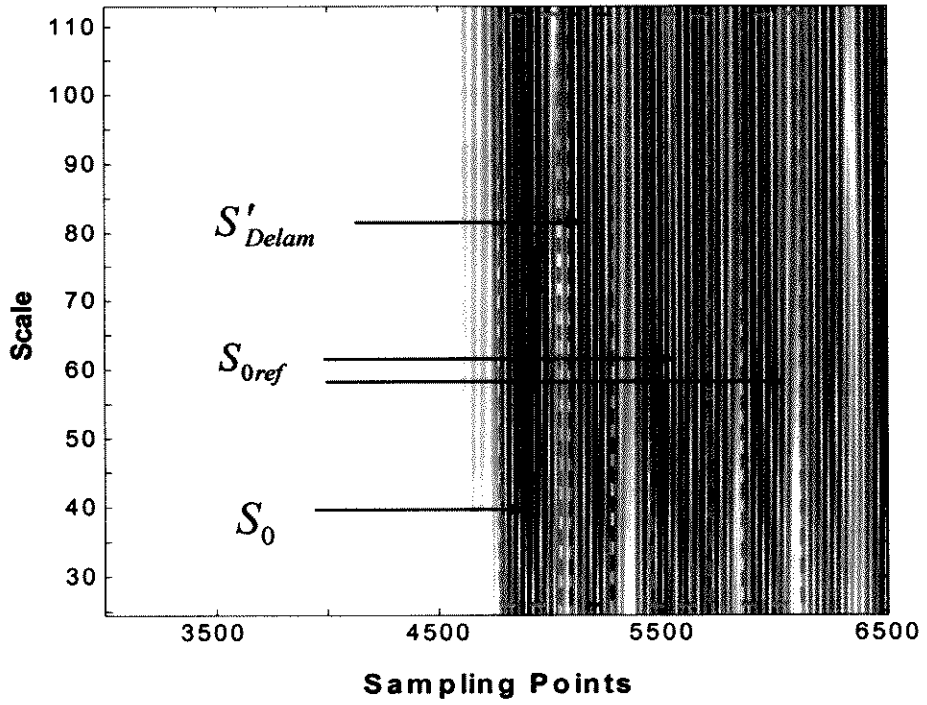

(a)

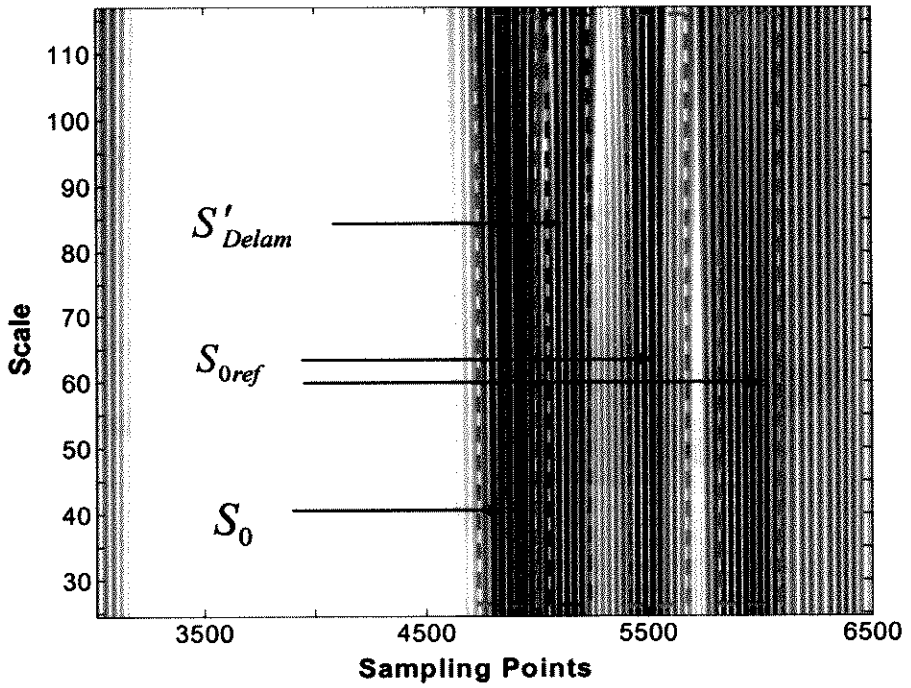

(b)

Figure 5.16 CWT spectrographic analysis in time-scale domain: (a) *2*-D spectrum for *FEM-UD2*$^{\#}$; (b) *2*-D spectrum for *EXP-UD2*$^{\#}$; (c) *3*-D spectrum for *FEM-UD2*$^{\#}$; (d) *3*-D spectrum for *EXP-UD2*$^{\#}$

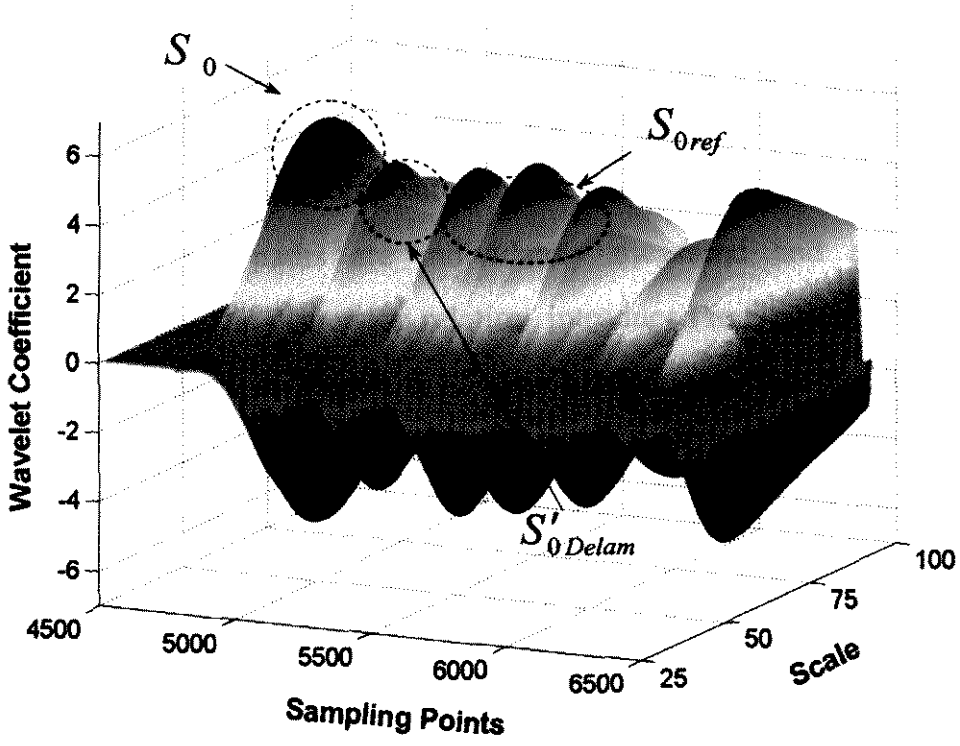

(c)

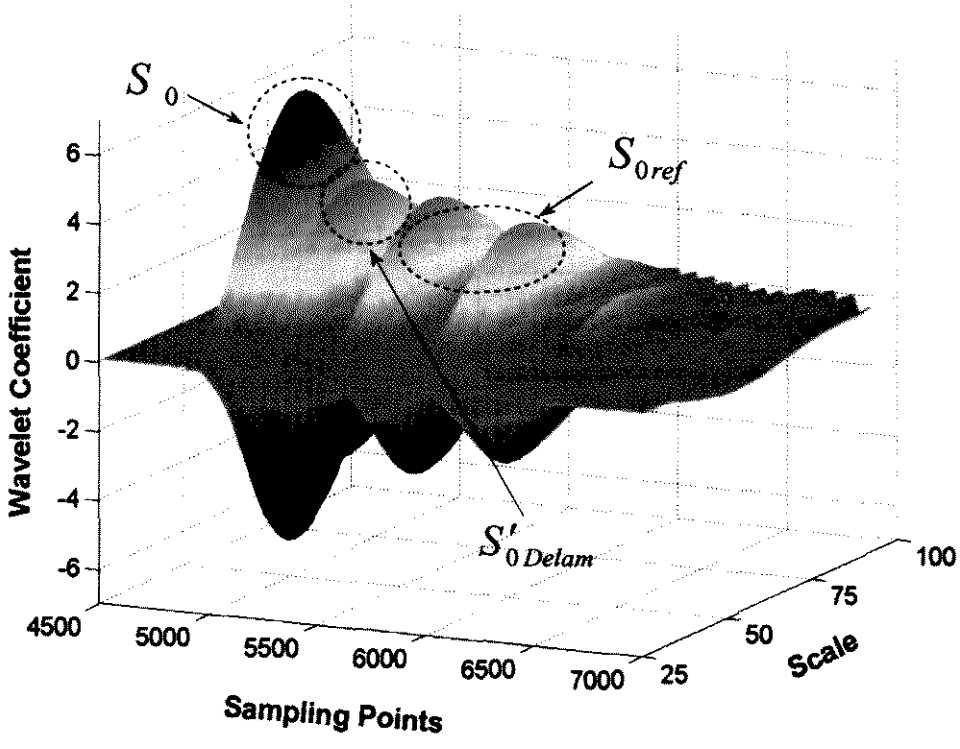

(d)

Figure 5.16 *Cont.*

Dispersion Natures

Expanding the above experiment in a sweep frequency range from *0.05MHz* to *2.0MHz*, the dispersion characteristics for Lamb waves in quasi-isotropic $[0/-45/45/90]_s$ CF/EP (T650/F584) composite laminates are studied. Wave velocities via different actuator-sensor paths are individually measured and averaged upon purification using SPP. The dispersion relation, introduced in Section 3.3, for chosen laminates is diagrammed in Figure 5.17. For comparison, the dispersion curves simulated by FEM and analytically calculated using the *effective elastic constant* method [Percival and Birt, 1997] are also contrasted in Figure 5.17, denoted by different symbols.

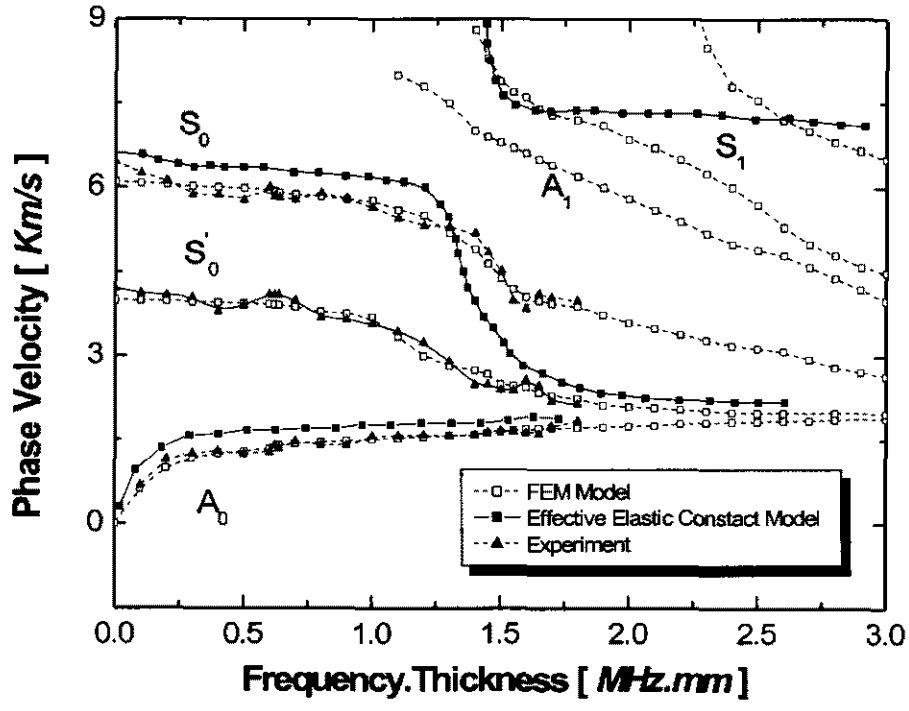

Figure 5.17 Dispersion curves for Lamb waves in *8*-ply quasi-isotropic CF/EP (T650/F584) composite laminate

Good correlation between FEM and experiments has been observed. Both reveal that symmetrical and anti-symmetrical modes are synchronously available without the

application of active control, and their phase/group velocities are dependent on the algebraic product of the laminate thickness and the central frequency. A low-frequency region (*<1.0MHz·mm*) exists for the present structure, in which the fundamental anti-symmetric Lamb mode, A_0, symmetric Lamb mode, S_0, and the lowest order shearing mode, S_0', exhibit reasonably non-dispersive behaviour. Higher order modes appear gradually with increase in frequency.

During dispersion, distortion of the wave signal (deviation of waveform and frequency from original diagnostic signal) could not be avoided. Different diagnostic waveforms, *1*-cycle, *3*-cycle, *5*-cycle, *7*-cycle and *10*-cycle windowed toneburst as well as pulse excitation, at different central frequencies, from *0.15MHz* to *1.0MHz*, are examined. The results show that the signal-to-noise ratio (SNR) increases as the signal central frequency increases, and the high SNR benefits signal identification. However, high frequency weakens the capability of Lamb waves to propagate in the composites. Meanwhile, it is noticed that a high cycle number of toneburst may lower the risk of signal distortion, but an accompanying superposition of multiple wave modes occurs due to the large bandwidth, also leading to confusion in signal interpretation. As an example from experiment, the Lamb wave signals acquired by a PZT sensor *485mm* away from PZT actuator, under pulse-excitation at a central frequency of *0.5 MHz* and *10*-cycle *Hanning* windowed toneburst at a central frequency of *0.35 MHz*, are processed with SPP and displayed in Figure 5.18, where distortion of the incident pulse excitation is evident in (a), while immersion and superposition of multiple Lamb modes inevitably appears in (b). Both the distortion and superposition can make it problematic to extract useful diagnostic components. In experiments, satisfactory resolution and accuracy can be met for the present system when a *5*-cycle toneburst in the central frequencies of *0.3-0.5 MHz* is adopted.

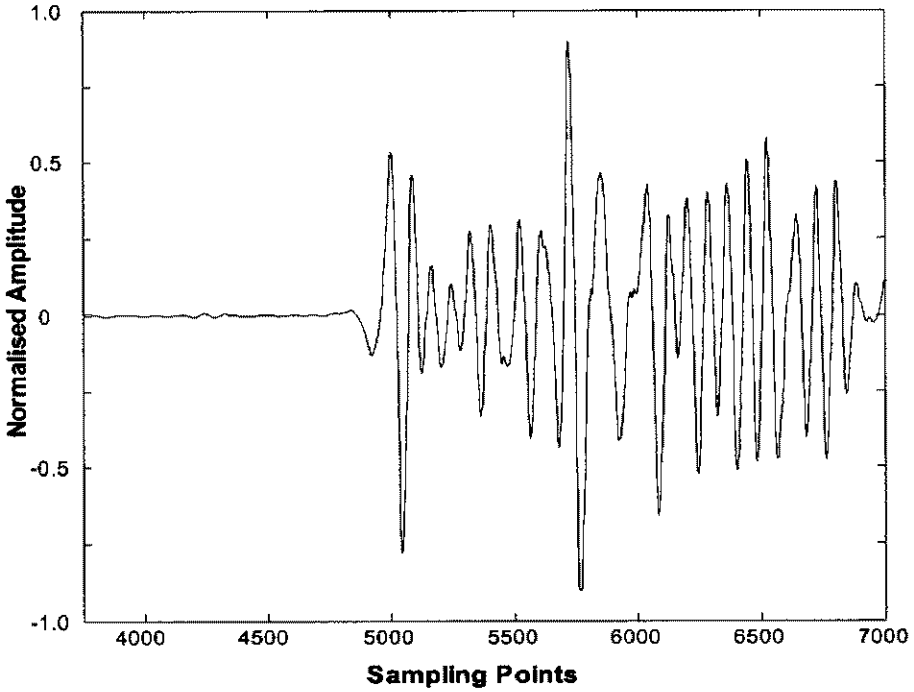

(a)

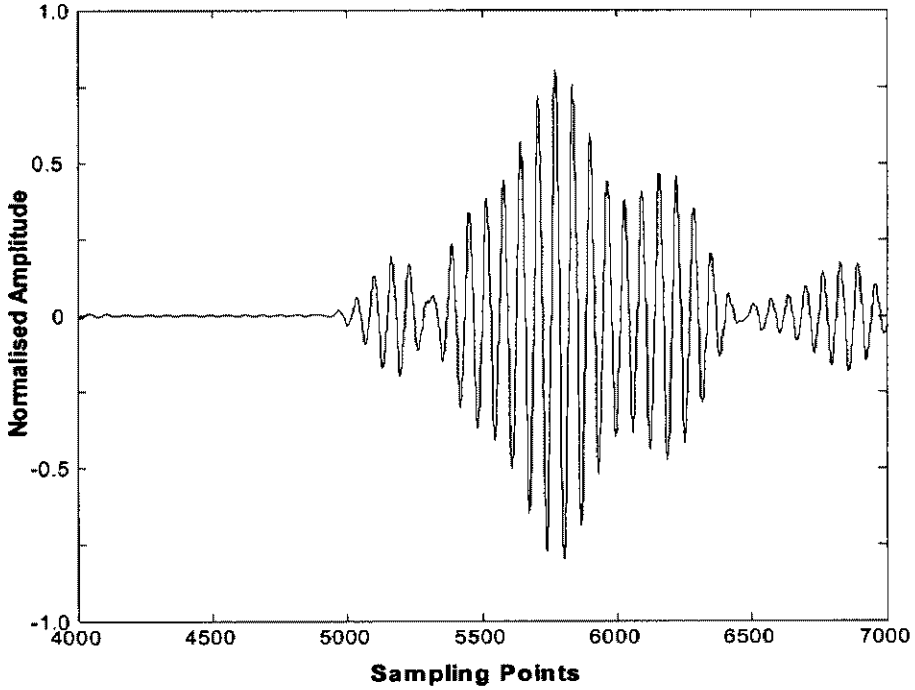

(b)

Figure 5.18 Signals under different excitations: (a) excited by pulse at *0.5MHz*; (b) excited by *10*-cycle toneburst at *0.35MHz*

5.6 Elastic Wave-Based Damage Identification

Both the numerical simulation and experimental validation demonstrate that elastic waves are highly sensitive to the presence, location and degree of structural damage. Their normal propagation characteristics can be significantly influenced by such damage, leading to scattering, i.e. reflection/transmission, and mode conversion. Various damage locations and severities may cause exclusive scattering phenomena. Based on these findings, a damage identification scheme is proposed in this study. Two independent approaches are included, based respectively on *forward* (logical) and *inverse* (anti-logical) analyses. The former is derived directly from experimental signals (for damage location detection only), and addressed in the following section, while the latter (applicable for all damage parameters) is illuminated by artificial intelligence techniques, and is addressed in subsequent chapters.

5.6.1 Forward (*Logical*) Method

For damage triangulation, the time lags among wave components of interest in a filtered signal and energy spectrum are captured. For the damaged laminate described in previous sections, if transducer *P1* acts as an actuator, and the damage centre locates at (x, y) (in the coordinate system where the actuator is at the origin and the X-axis is parallel to the lower edge of the laminate), a set of nonlinear equations can be established with regard to the relative distances among transducers and damage:

$$\frac{L_{A-D}}{V_{S_0}} + \frac{L_{D-S}}{V_{S'_{0\,Delam}}} - \frac{L_{A-S}}{V_{S_0}} = T_{1-i}, \qquad (i = 2, 3, 4) \qquad \textbf{(5.21)}$$

where L_{D-S}, L_{A-D} and L_{A-S} represent distances between the damage centre (x, y) and the i^{th} sensor, the selected actuator *P1* and the damage centre, actuator *P1* and the i^{th} sensor, respectively. $V_{S'_{0\,Delam}}$ and V_{S_0} are the measured velocities of modes,

S'_{0Delam} and S_0, respectively. T_{1-i} denotes the experimentally acquired time lag via path P_1-P_i. In the referred Cartesian coordinate system, it is

$$L_{D-S} = \sqrt{(x - x_i)^2 + (y - y_i)^2}$$

$$L_{A-D} = \sqrt{x^2 + y^2}$$

$$L_{A-S} = \sqrt{x^2{}_i + y^2{}_i}$$

$$(i = 2, 3, 4) \qquad \textbf{(5.22)}$$

where (x_i, y_i) represents the coordinates of the i^{th} transducer in the current coordinate system. In practice, some actuator-sensor paths are unexploitable because multiple reflections of waves from boundaries may spoil the damage-induced wave components in the sampled signals.

Analogously, a non-linear system consisting of four equation sets is established after the four coordinate systems are introduced individually, in which each PZT actuator in turn is at the origin of its reference systems. A mathematic optimal method based on a graphic searching technique [Gaul and Hurlebaus, 1999; Mathworks Inc., 2001c] is then applied to solve the nonlinear system.

Additionally, preliminary searching for the approximate delamination location is executed to expedite the overall process of identification, suggesting an initial point for starting damage searching. In such a step, the whole laminate is assumed to be quartered evenly and the delamination is assumed to locate individually at the central position in each quadrant, respectively. An FEM simulation is performed to calculate the relevant structural responses via actuator-sensor paths of interest under each presumed situation. A comparison between these simulated signals and experimentally acquired signals is conducted, and the least discrepancy indicates the quadrant in which the damage is most likely to have occurred.

5.6.2 Validation

The delamination searching procedure is schematically explained in Figure 5.19 for specimen detailed in Table 5.3. The signal acquired via each individual actuator-sensor path contributes to the construction of one equation in the non-linear equation system based on Equations (5.21) and (5.22), whose root locus indicates the possible damage locations, denoted by the dash-and-dot line in the figure. The intersection of loci from all available actuator-sensor paths is the most likely position for damage to have occurred.

The diagnosis results are summarised in Table 5.4. It is clear that detection errors decrease with an increase in the number of actuator-sensor path involved, while *4* paths contribute the minimum mathematic requirement to the solution of the nonlinear equation system. However, the more paths employed, the more time is consumed in experimental measurement. It is noted that satisfactory accuracy can be ensured with half of the total actuator-sensor paths engaged.

Table 5.4 Diagnostic results and estimation errors

(Unit: *mm*)

Specimen	Based on 4 Paths		Based on 6 Paths		Based on 8 Paths	
	Diagnostic result *	Relative Error	Diagnostic result *	Relative Error	Diagnostic result *	Relative Error
EXP-UD2#	(312, 266)	13.0%	(293, 316)	6.8%	(262, 313)	4.8%
EXP-WF2#	(311, 218)	16.5%	(249, 204)	7.7%	(285, 201)	6.9%

* *The vertical distances away from the left and bottom edges of the laminates, respectively*

Recognised as a typical forward analysis, the proposed locating algorithm can serve as a qualitative method to locate delaminations in composite structures.

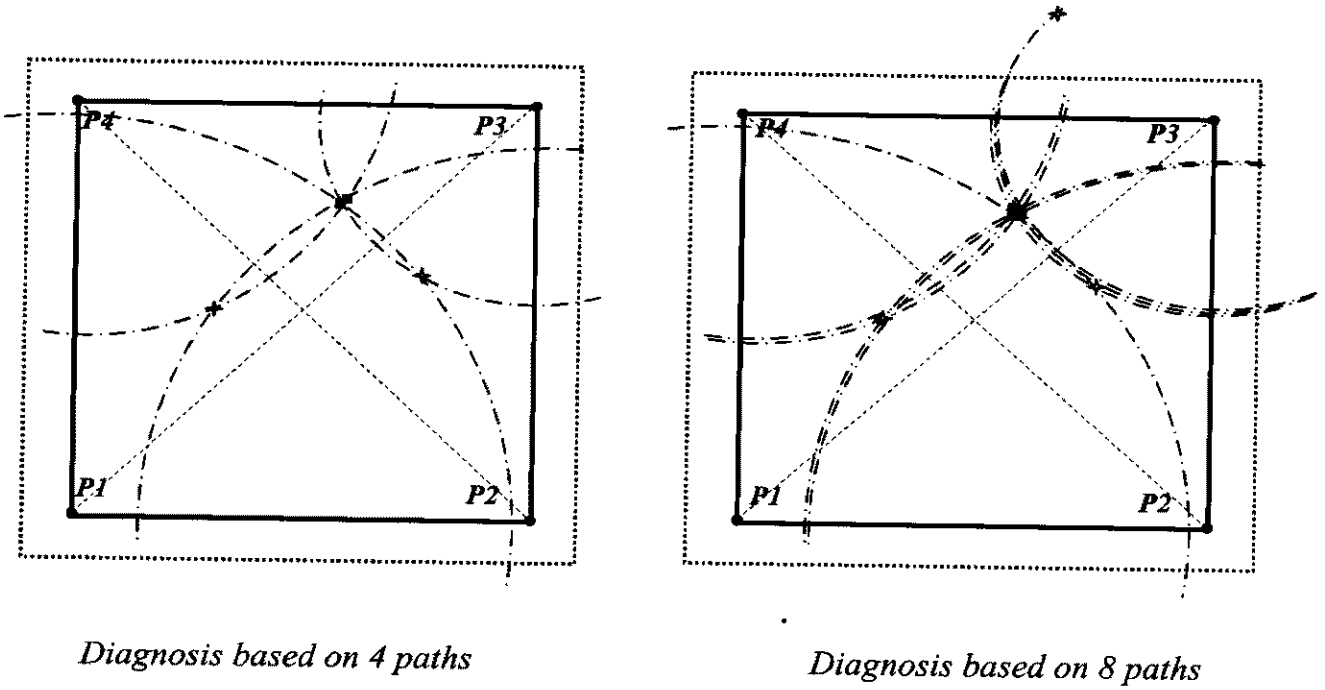

Diagnosis based on 4 paths *Diagnosis based on 8 paths*

(a)

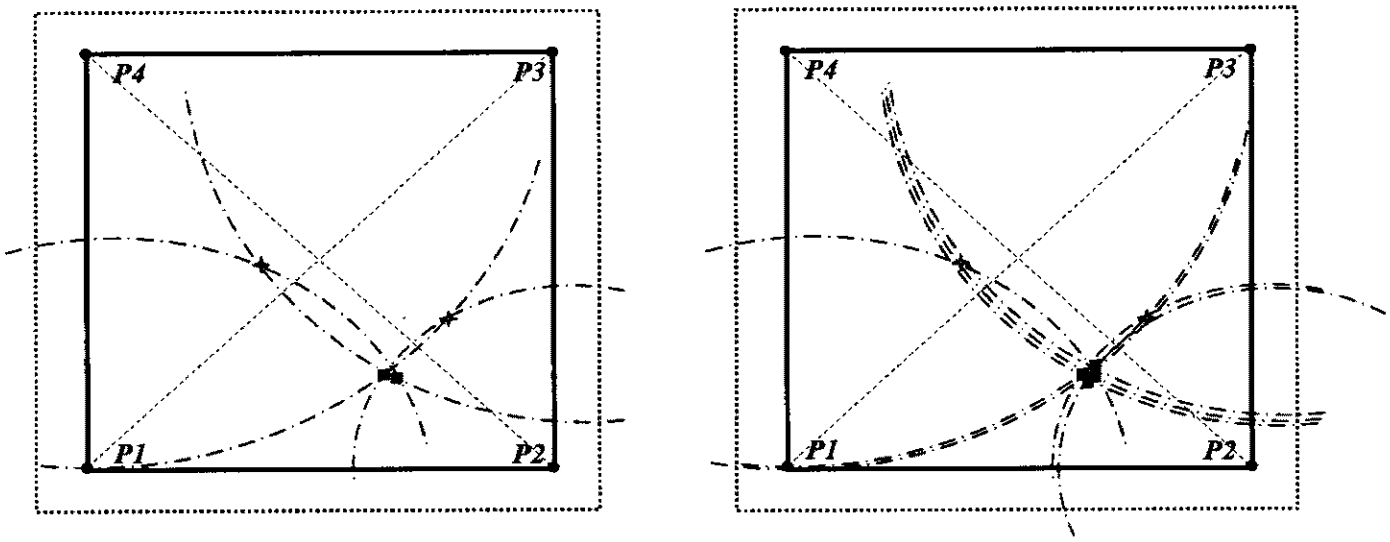

Diagnosis based on 4 paths *Diagnosis based on 8 paths*

(b)

■: *Diagnosis results* ✦: *Accompanying pseudo-results* ····· *Actual laminate frame*

——— *Coordinate axes* – · – · – *Intercurrent lines for solving nonlinear system*

Figure 5.19 Detection of delamination location for (a) specimen *EXP-UD2*$^{\#}$; (b) specimen *EXP-WF2*$^{\#}$

5.7 Concluding Remarks

Elastic wave propagation in delaminated CF/EP composite structures is studied using FEM methods. Modelling techniques for piezoelectric devices (actuator/sensor) and delamination are specifically developed, which are substantiated to perform well in simulating reality. A surface algorithm adopted in the simulation is shown to be effective in handling problems arising from delamination. The FEM results are then validated by experiments, and good correlation between them is achieved.

Actual case studies show that satisfactory diagnosis can be achieved by analysing damage-scattering signals using signals after appropriate signal processing and identification. However, strong reliance of estimation accuracy on excitation waveforms and bandwidth is observed. Appropriate excitation conditions can ensure Lamb wave signals with good non-dispersive behavior.

An elastic wave-based damage detection algorithm for CF/EP composite structures is proposed using a *forward* (logical) method, which is validated by triangulating a delamination. Identification errors are noticed to be dependent on the number of actuator-sensor paths involved for diagnosis, and satisfactory precision can be achieved when half of the total actuator-sensor paths are taken into account. But the information that this process can offer is yet not adequate for identification of damage shape and size.

Benchmarks are introduced in both FEM simulation and experimental verification, to avoid any disturbance from boundary effects. During comparison between benchmark and defective laminates, or between FEM simulation and experiment, certain distinctions or incomplete agreement can be observed in addition to the delamination-induced extra wave components. These phenomena are attributed to differences in boundary conditions, imperfect similarity of two individual laminates

in manufacture or discrepancy of theoretical emulation with laboratory measurement. For detection based on *forward* (logical) analysis, information from the benchmark is essential, which limits the practical utility and precision of identification. Methods independent of benchmarks are developed using artificial neural network techniques in the following chapters.

Chapter 6

Solution to Damage Detection:

Inverse Pattern Recognition

6.1 Introduction

The solution to an engineering problem can be either *forward* or *inverse*. Relatively easier, a *forward* analysis can be conduced logically, and in most cases the solution is unique. In contrast, an *inverse* problem may be difficult to solve by rational means, and the solution can be uncertain or ambiguous. Damage detection is known as a typical and highly complicated *inverse* pattern recognition problem.

Tremendous efforts have been directed towards this issue. Statistical modelling, syntactic method and artificial intelligence are three major approaches in this regard. Relying first on probabilistic models developed on deterministic and stochastic theories, the principle of the former two approaches is an iterative comparison between theoretical results and practically captured signals, to pursue the case that fits best. These applications are limited to relatively simple cases.

Since the 1990s, with the aid of progressive advances in neuroscience and high capable computing devices, artificial intelligence (AI) technology, defined as the simulation of human intelligence so as to efficiently use the right piece of '*knowledge*' at a given step toward solving a problem [Konar, 2000], has rapidly

emerged as one of the most promising alternatives to deal with diverse and complex *inverse* engineering problems. Represented by *expert systems* (knowledge-based system), *fuzzy logic*, *inductive learning*, *genetic algorithms* and *artificial neural networks*, AI technology now has a wide range of applications, including pattern recognition, classification, function approximation, signal/image processing and system identification. Particularly, inspired by psychological and neurophysiologic principia, artificial neural network (ANN), a novel information processing approach, inherently displays strong capability in adaptability, parallelism and robustness.

As a key unit in the Intelligent Signal Processing and Recognition (ISPPR), an inverse pattern recognition technique taking advantage of an ANN algorithm is developed in this chapter.

6.2 ANN Fundamentals

Emulating the human brain's mechanisms, an artificial neural network (ANN) operates as a parallel computational model to authentically explore the connection between a series of reasons (*inputs*) and consequences (*outputs*) for a given system. A well-trained ANN is able to predict outcomes under an unknown stimulus according to pre-accumulated knowledge, while avoiding interrogating intricate constitutive relations or establishing a complicated model.

The attempt to make a general computing '*engine*' was first proposed by Charles Babbage in the 19^{th} century. This became the conceptual basis for today's ANN technique [Anderson, 1995]. In 1950, abstract computational models of intelligence appeared, and consequently simple learning algorithms were invented in the 1960s. Substantial development of such a concept stemmed from introduction of the personal computer, culminating in the evolution of ANNs in last decade [Mehra and Wah, 1992].

A typical ANN is illustrated in Figure 6.1, composed of one input layer, single or several neural processing layers and one output layer.

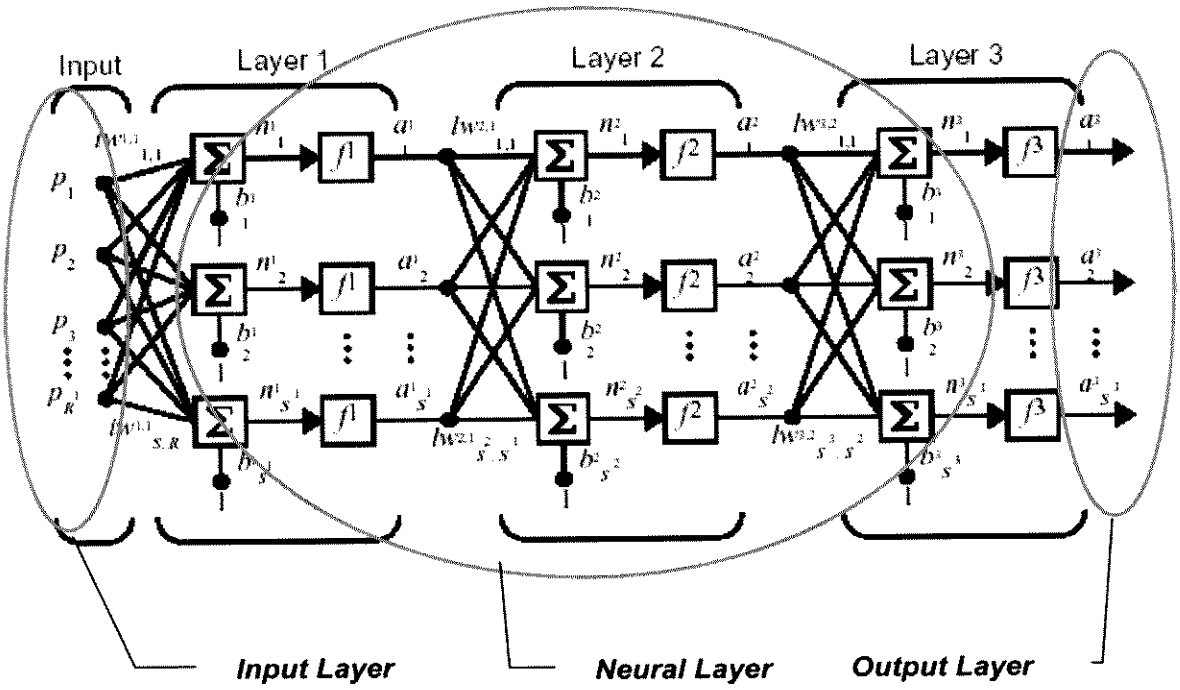

Figure 6.1 An artificial neural network

In the figure (where two processing layers are involved), R input elements are arranged in an R-dimensional vector, $\vec{p}$, (*input vector*,). S^1 and S^2 computing units are respectively hosted in two processing layers to simulate neurons of the human brain, and are therefore identified as '*neurons*'. The output layer accommodates S^3 output variables, to form the *output vector*, $\vec{o}$. Each neuron is weighted by an adjustable variable (defined as a *weight* and denoted by w), and offset by a constant (defined as *bias* and abbreviated by b) [Fausett, 1994].

In the network, the i^{th} neuron summates all the weighted input elements and their biases to output the scalar output a_i, which then acts the input for the next layer. Considering all neurons, this mathematic operation can be simplified by introducing a *weight matrix* [Mehra and Wah, 1992]

$$W = \begin{bmatrix} w_{1,1} & w_{1,2} & \cdots & w_{1,R} \\ w_{2,1} & w_{2,2} & \cdots & w_{2,R} \\ \vdots & \vdots & \vdots & \vdots \\ w_{S,1} & w_{S,2} & \cdots & w_{S,R} \end{bmatrix} \tag{6.1}$$

In the weight matrix, a row index indicates the destination neuron of the weight, and a column index denotes the source for that weight. Similarly, all the biases are hosted in the *bias vector*, $\vec{b}$. Various layers in the network are associated by different transfer functions, f. Thus the output for each layer can be obtained by

$$\vec{a}_i = \vec{f}_i(\vec{w}_i \cdot \vec{a}_i + \vec{b}_i), \quad (i = 1, 2, 3) \tag{6.2}$$

Both w and b are adjustable, so that the network exhibits some interesting behaviors by iterative training. The training procedure can be understood as seeking a set of most suitable weights to negotiate all provided inputs and corresponding outputs by comparing output with desirable targets.

Neural processing layers in an ANN are also referred to as *hidden layers*. Several typical transfer functions are employed in this study, including *hard-limit*, *linear*, *tan-sigmoid* and *log-sigmoid* [Karayiannis and Venetsanopoulos, 1993], as diagrammed in Figure 6.2.

The *hard-limit* transfer function imposes the output of each neuron with either *0* (when the input argument is less than *0*) or *1* (when the argument is greater than or equal to *0*), which works well for classification decisions in ANN architecture of a single layer in. The *linear* transfer function faithfully sets the output equal to the input, but that output may be far from '*0*' or '*1*'. The *sigmoid* function, including *tag-sigmoid* and *log-sigmoid*, squashes the output in the range [-1, 1] and [0, 1], respectively, which is commonly used in backpropagation networks. Based on the choice of transfer function, an ANN can be categorised as perceptron (*hard-limit*), liner filter (*linear*), and backpropagation (*sigmoid*).

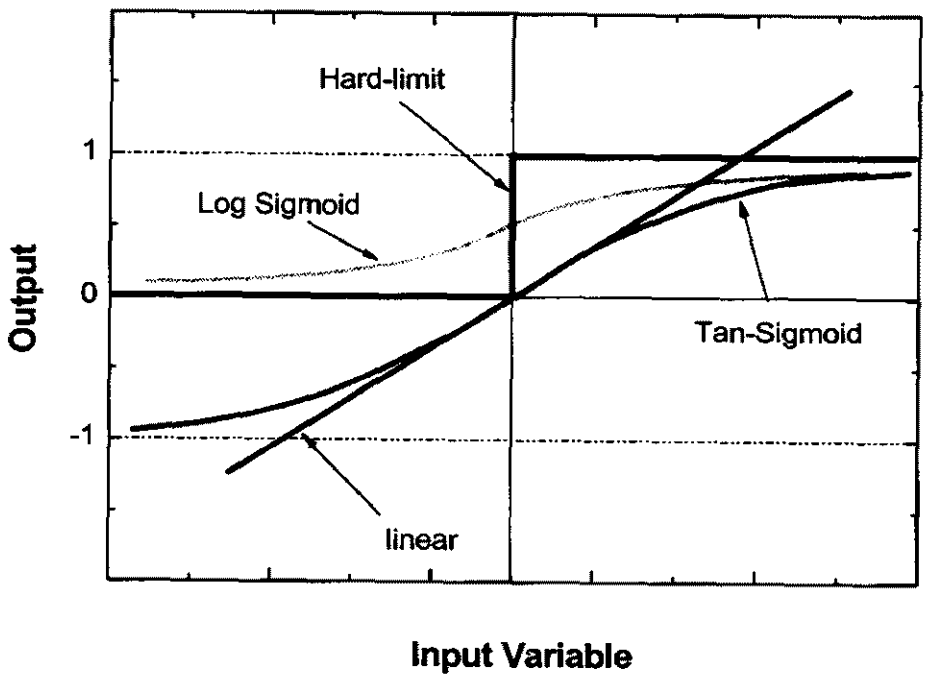

Figure 6.2 ANN transfer functions used in neural network

6.3 Feedforward Backpropagation ANN

As one of the closest simulations by far to human behaviour, the feedforward backpropagation neural network (BP-ANN) was first designed by Rumelhart, Hinton and Williams in 1986, and then actualised by David Parker in 1986 at *MIT* and Yann Le Cun in 1986 at *AT&T Bell Laboratory* [Anderson, 1995]. Numerous successful applications have substantiated its excellent performance in pattern recognition even for highly complicated systems, where traditional modelling or analysis is unavailable or difficult.

In brief, standard backpropagation is a gradient descent algorithm. The network weights are moved in the direction of negative gradient [Mathworks Inc., 2001b]. The term *backpropagation* refers to such a gradient computing manner, while *feedforward* describes the direction of information flow from input to output. During ANN training, target vectors are referred until matched with network outputs with

acceptable error. The feedforward architecture can provide excellent computational efficiency, and a well-trained BP-ANN is adept at inferring general rules or predicting consequences from specific examples such as new inputs that have never been examined, or reorganising invariance from complex high-dimensional inputs. It is the generalisation property of BP-ANN that makes it possible to train a network using just a representative set of input/target pairs, rather than all possible cases, but achieving good ratiocination.

BP-ANN Basics

Iteratively balancing weights in all neural processing layers is personified as '*learning*' and '*training*', which constitute the behaviour that accumulates experience and strengthens network performance. Two contrast learning rules, *unsupervised* and *supervised*, are commonly adopted for BP-ANN training. *Unsupervised* learning is performed straightforward regardless of the outputs, and is suitable for clustering analysis or identification of data groups [Mathworks Inc., 2001b]. *Supervised* training adjusts weights based on the discrepancies between the targets and actual network outputs after each iteration, as illustrated in Figure 6.3. Guaranteed by successive feedback, *supervised* training certainly excels at achieving higher precision. In the present study, the *supervised* training algorithm is always used.

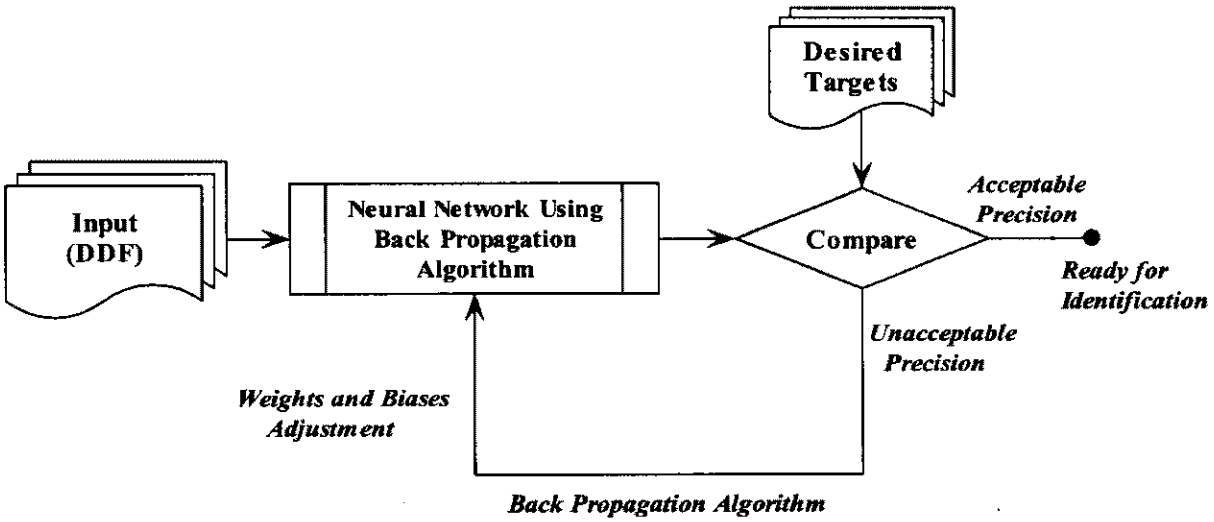

Figure 6.3 Algorithm of error backpropagation (BP) training

An error function, *mean square error* (MSE), is introduced to indicate network performance. Serving as a criterion, MSE is formulated as

$$MSE = \frac{1}{N}\sum_{i=1}^{N}\left[t(i) - o(i)\right]^2 \tag{6.3}$$

where $t(i)$ and $o(i)$ are the target and output vectors for every iteration, respectively, while N denotes the element's number in the target vector. Equation (6.3) calibrates the network capability in real time. Monitored by MSE, error backpropagation learning is conducted by

$$x_{k+1} = x_K - \alpha_k \cdot g_K \tag{6.4}$$

where x_K and g_K are the vectors representing the current weights/biases and gradient components, respectively. K represents the present iteration number, while α_K denotes a positive constant increment in training, described as '*learning rate*'. Training is not terminated unless the maximum estimation error is controlled with less than the desirable precision. Representatively, a typical ANN training progress, reflected by the MSE versus training iteration, is displayed in Figure 6.4.

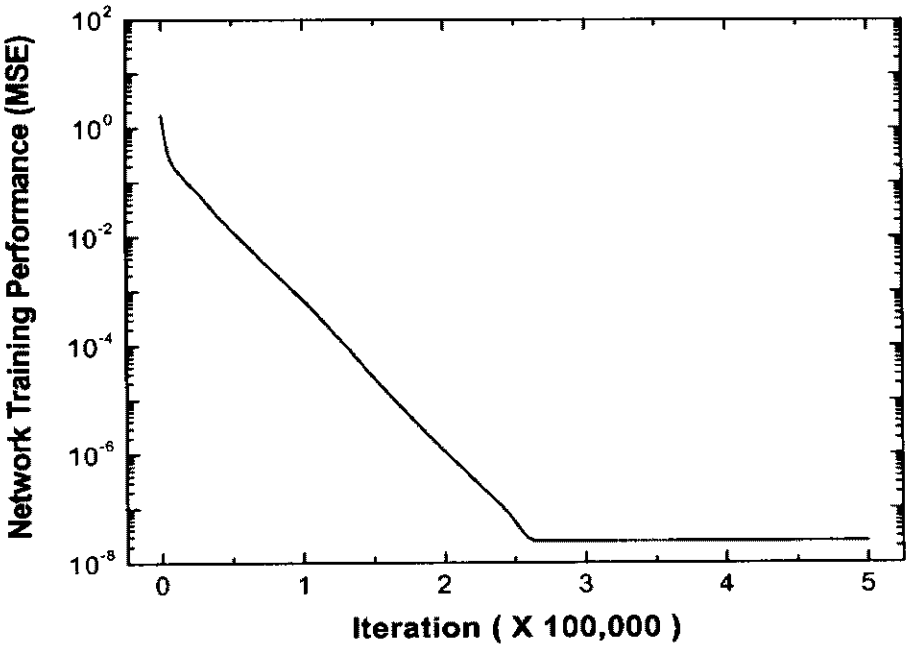

Figure 6.4 Network training history

BP-ANN Training Algorithms

For actual implementation, variants of the basic backpropagation algorithm are commonly used to enhance the capabilities of BP-ANN, roughly classified as *incremental mode* and *batch mode*. In incremental mode, the gradient is computed and the weights are updated after each input is applied to the network. In batch mode, the weight and bias are changed after an entire set (batch) of inputs are applied for training. In this study, the batch training mode is used due to its excellence in negotiating convergence precision at a fast rate. In batch mode, the training algorithms to be used in the following study are: *batch gradient descent with momentum mode*, *variable learning rate batch mode*, *resilient backpropagation*, *conjugate gradient mode* and *scaled conjugate gradient mode*. In particular, the scaled conjugate gradient (SCG) algorithm is most computationally efficient, since it avoids time-consuming line searches [Mathworks Inc., 2001b].

BP-ANN Enhancements

Though effective for most applications, the performance of a normal backpropagation neural network is still subject to a number of unpredictable factors. For instance, inappropriate choice of initial training conditions can lead to unstable and imprecise convergence, because of its gradient-descent nature. For this reason, some enhancements are introduced for the BP-ANN training. These are mostly heuristic modifications with the goals of increasing convergence speed, avoiding local minima, and improving generalisation.

It has been mathematically demonstrated [Hassoun, 1995] that both the convergence speed and precision of an ANN can be significantly influenced by the initial values of weights. This issue becomes paramount when a single hidden layer is adopted in the feedforward network. The weights are usually initialised to small zero-mean random values, because large weights tend to result in premature saturation of the

training and insensitivity of the network to the learning process. In this study, this is achieved by setting the initial weights of unit i to be of the order of $1/\sqrt{f_i}$, where f_i is the number of inputs for unit i, which proves very effective.

Before training, it is often useful to scale the inputs and targets so that they always fall within a specified range. For all the neural networks developed in this study, the input, output, and target variables are normalised by the possible maximum absolute value, so as to fall in the range [-1, 1]. Whenever new inputs are fed into the trained network, they are normalised.

6.4 ANN for Damage Detection

Crucially relying on neural network configuration, an actual engineering system probably cannot be faithfully represented by a small size network, while on the other hand, the convergence and stability of network training may be sacrificed if an oversize network configuration is designed. Both are liable to yield erroneous identification. In reality, no cardinal doctrines are available for a given system in determining the most appropriate network size and architecture, but a suitable configuration is usually achieved based on reiterative trial and experience.

Architecture

Pioneer work [Browne, 1997; Mathworks Inc., 2001b] suggests that any continuous system with an m - to n-dimensional mapping can be smoothly portrayed using an ANN with two hidden processing layers. On this basis, neural networks in feedforward architecture, consisting of two neural hidden layers, are developed in this study for damage detection. One of them is shown in Figure 6.5.

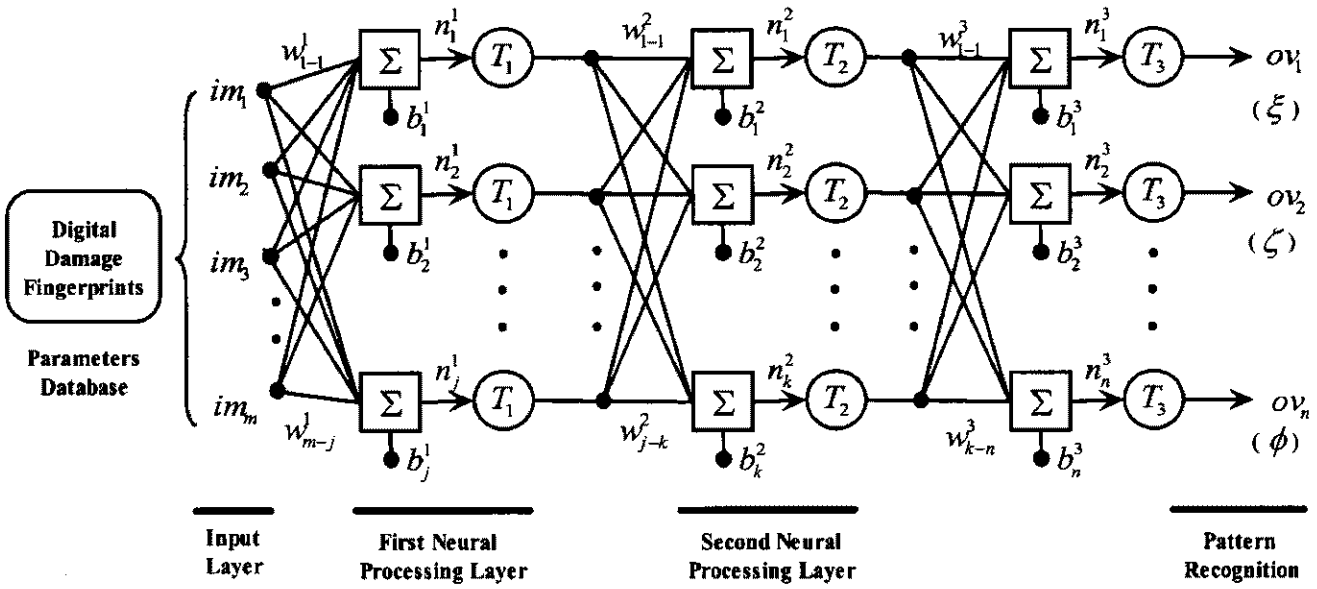

Figure 6.5 A typical ANN developed for damage detection in this study

This example ANN features one input layer with m input elements (im), two processing layers, respectively possessing J and K computing elements, and one output layer containing n output variables (ov). The variables m, n, J and K are dependent on actual applications. Mathematically, the i^{th} output variable in the designed network is defined by

$$ov_i = T_3\left(\left(\sum_{q=1}^{K} w_{q-i}^3 \cdot T_2\left(\left(\sum_{r=1}^{J} w_{r-q}^2 \cdot T_1\left(\left(\sum_{p=1}^{m} w_{p-r}^1 \cdot im_p\right) + b_r^1\right)\right) + b_q^2\right)\right) + b_i^3\right)$$

$$(i = 1, 2, \cdots, n) \qquad \textbf{(6.5)}$$

where im_p denotes the p^{th} input element, w_{p-q}^r $(r = 1, 2, 3)$ represents the weight joining the p^{th} input element/neuron in the r^{th} layer with the q^{th} neuron/output variable in the next layer. Similarly, b_q^i is the bias for the q^{th} element in i^{th} layer ($q = 1, 2, \cdots, J/K/n$ for the first/second-processing/output layer), while T_i is the transfer function to bridge different layers in the neural network.

I/O Variables

In major NDE approaches based on ANN, various structural characteristics in the single time or frequency domain, or static parameters are normally employed for training the networks due to their simplicity of capture. These parameters include mode shape [Tsou and Shen, 1994; Yun and Bahng, 2000] and natural frequencies [Chaudhry and Ganino, 1994; Islam and Craig, 1994; Okafor *et al*, 1996; Chang *et al*, 1999; Yun and Bahng, 2000; Zang and Imregun, 2001], or combined modal information [Chang *et al*, 2000]; displacement [Chen *et al*, 1995; Barai and Pandey, 1996; Yoshimura *et al*, 1998], acceleration spectra [Wu *et al*, 1992] or combined parameters of displacement, velocity and acceleration [Zu and Wu, 2001]; applied force [Rhim and Lee, 1995], or static parameters, such as strain [Hwu and Liang, 1998, 2001; Liang and Hwu, 2001], strain history [Maseras-Gutierrez *et al*, 1998; Staszewski *et al*, 2000], auto-correlation function [Zubaydi *et al*, 2002], impedance [Lopes *et al*, 1999], etc.

However, these modal and time-series data or static parameters have relatively low susceptivity to undersized damage or to the evolution of deterioration in a single time or frequency domain as addressed in Chapters 4 and 5.

It has been shown in Chapter 5 that the spectrographic characteristics of elastic waves in the time-scale domain are more sensitive to structural damage than modal, temporal or static features. In terms of the signal processing package (SPP) developed in Chapter 4, these characteristics are extracted as *digital damage fingerprints* (DDF), stored in the damage parameters database (DPD). The DPD is then used as input data for ANN training in this study, as highlighted in Figure 6.5.

The network outputs are herein set as the parameterised damage indices, i.e. damage presence (*0* or *1*), central position (ξ and ζ, in the referred coordinate system),

semi-major/minor axis (α / β), and orientation (ϕ, the angle between the major axis and $x-$axis in the referred coordinate system, $0 \le \phi < \pi$), based on the assumption of damage being elliptic.

Training Algorithm and Transfer Function

Supervised training using error-backpropagation (BP) algorithms, scaled conjugate gradient (SCG), is adopted. It has been pointed out [Mathworks Inc., 2001b] that a BP-ANN, in which neural layers are connected with a sigmoid and a linear transfer function, is capable of approximating any system with finite number of discontinuities. In this regard, two sigmoid transfer functions, defined as (refer also to Figure 6.2)

$$f(\Omega) = \frac{1}{1+e^{-\Omega}} \tag{6.6}$$

are used to associate the input layer with the first processing layer, and between the two processing layers in the designed ANN. Meanwhile a linear transfer function,

$$f(\Omega) = \alpha \cdot \Omega \tag{6.7}$$

where α denotes a preset constant in the linear relation, links the second processing layer with the output layer.

Design and training of the ANN is accomplished on commercial software *MATLAB*® platform (Release 12.0) [Mathworks Inc., 2001b]. The constructed ANN is then incorporated into the ISPPR developed in Chapter 4, acting as the unit of *inverse* pattern recognition. Schematically, the basic flowchart for the whole process of damage detection using ISPPR is outlined in Figure 6.6, and is to be elaborated by actual case studies in the following chapters.

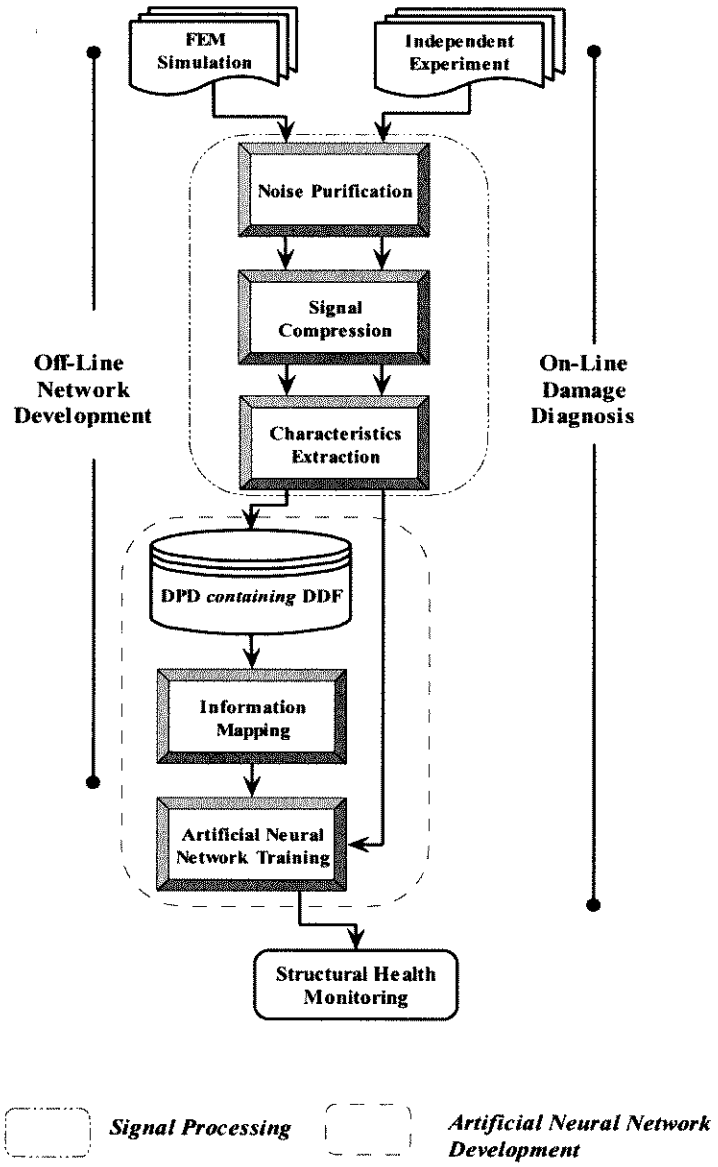

Figure 6.6 Principle for proposed artificial neural network-based damage detection

6.5 Concluding Remarks

The ANN technique is employed in this study to perform damage detection, an *inverse* pattern recognition problem. For this purpose, the fundamentals of ANN are briefly introduced. In diverse ANNs, feedforward error-backpropagation (BP) networks with supervised training algorithm show uncontroversial cost-efficiency in

mapping a complicated system. Multi-layer networks are designed, and then trained using the preliminarily constructed DPD, accommodating DDF extracted from Lamb wave signals.

As the successor of work in Chapter 4, the designed ANN is incorporated into the ISPPR. Validation of the proposed damage detection methodology is implemented in the chapters that follow.

Chapter 7

Actualisation of Damage Detection:

Active Online Diagnosis System

7.1 Introduction

Based on the work in Chapters 4-6, an *active online structural health diagnosis* (AO-SHD) system is configured, supported by the intelligent signal processing and pattern recognition (ISPPR). The system consists of a *built-in transducer network*, *signal generation subsystem* (SGS), *data acquisition subsystem* (DAS) and, most importantly, *central control/analysis subsystem* (CCAS).

Defined as the continuous monitoring of structural responses to the loading environment in order to diagnose the onset of anomalous structural behavior [Moyo and Brownjohn, 2002], a *structural health monitoring* (SHM) system is an integrity possessing capabilities of signal acquisition, validation and technical data analysis. Relying on condition-based changes, SHM is applicable to both predictable and unpredictable working conditions [Chang, 2002b], greatly benefiting overall improvement in structure reliability and facilitating life-cycle management decisions [Hall, 1999; Balageas, 2002].

The SHM technology comprehensively involves material science, sensor/actuator and manufacture techniques, computation and information processing, etc. At a

sophisticated level, a complete SHM system hierarchically performs the following tasks with increasing difficulty [Worden *et al*, 2003a]:

Level 1 (Occurrence detection): qualitative indication of damage occurrence;
Level 2 (Localisation): quantitative assessment of damage position;
Level 3 (Degree evaluation): quantitative estimation of damage severity;
Level 4 (Reliability prediction): prediction of structural safety, e.g. residual life.

An SHM system that can operate in real-time is referred to as *online-SHM*. Such a system can quickly or online access the health status for in-service structures while without terminating their normal operation. In addition, it should also have (1) a reliable active actuator/sensor network; (2) efficient signal excitation and faithful data acquisition subsystems; (3) exact and fast signal processing/identification algorithms; and (4) economical system components.

Efforts directed towards the development of cost-effective SHM systems, particularly for composite structures, have increased in the past decade. Representatively, research teams from *Stanford* [Chang *et al*], the *French Aeronautics and Space Research Center* (ONERA) [Balageas and Lemistre], *MIT* [Kessler and Spearing], Imperial College [Cawley, Soutis and Staszewski] and the *University of Sydney* [Ye *et al*] are known for their reputable contributions. Their various SHM systems, though developed on different theoretical bases, have demonstrated potential for engineering applications.

In addition to the above, Al-Khalidy *et al* [1997] have developed an SHM system aimed at fatigue damage detection for civil infrastructures. Wang *et al* [1998] configured a modal data-based system and validated it on large structures. Wolfinger *et al* [1998] proposed a similar monitoring system for detection of impact damage in reinforced composite materials using acoustic emission signals. Dupont *et al* [1999],

Samuel and Pines [1997], Osmont *et al* [2002], Sung *et al* [2000] and Valdes and Soutis [2001] have also individually presented various SHM systems using distributed PZT transducers.

Though there is a considerable distance from laboratory research to engineering practice, it is worthy of note that as a valuable step in this direction, few SHM techniques have also been commercialised at this stage, such as the system developed by *Acellent Technologies* Ltd. [Boller, 2001]. *Structural Monitoring Systems* Ltd. has also introduced its SHM products into the engineering market in Australia.

7.2 Development of AO-SHD System

7.2.1 Basics

Basically, an SHM system comprises a host computer with integrated signal processing/interpretation software, signal excitation/acquisition hardware and sensors. In some cases, communication devices or equipment are also required for data/command transmission between users and inaccessible or remote sites.

Host Computer

Accommodating previously developed software, the host computer in a SHM system serves as the controller for signal excitation/acquisition, and the analysis unit for damage assessment. Additionally, it functions to record and transfer data so that it is PC-identifiable, and/or to communicate with remote computers.

Transducer (Actuator/Sensor)

Like the sensory cells disseminated all over the human body, transducers (actuator/sensor) in a SHM system play roles of signal activation and information collection. An efficient transducer is expected to faithfully deliver designed motion (as actuator), and accurately sense local or global structural responses (as sensor).

Signal Generation and Acquisition

Signal generation and data acquisition units act as the link between the transducer network and the host computer, transferring commands to each actuator and returning sampled data from each sensor to the host computer.

Communication

A characteristic of new generation of SHM systems is that their advanced communication capabilities allow surveillance in more demanding circumstances, such as outer aerospace. Possible communication devices include modem, telephone line, satellite, telemetry, internet, radio link or cellular connection.

An AO-SHD system consisting of all the basic components is developed in this study, following the development principles outlined in Figure 7.1.

7.2.2 Multi-Point Active Actuator/Sensor Network

According to the excitation source, an actuator/sensor network can be either *passive* or *active*, as compared in Figure 7.2. In passive sensing, structural responses, naturally induced due to uncontrollable or unpredictable sources, are collected, such as the deformation of a bridge under certain traffic flow and wind. Such a sensing scenario can be fulfilled inexpensively and easily. In contrast, active actuating/sensing approach measures structural responses under a particular purpose, using controllably generated excitation. Obviously, active sensing is able to offer more flexible and exact monitoring than the passive method.

Two commercial sensor network products, *SMART Layer®* and *HELP layer®*, are now available. *SMART Layer®* (also known as the *Stanford Multi-Actuator-Receiver Transduction Layer*), jointly produced by *Stanford University* and *Acellent®*

Technologies, Ltd., integrates a certain number of distributed piezoceramics into a dielectric film. Unlike *SMART Layer®* that generates and measures stress waves, *HELP layer®* (*Hybrid Electromagnetic Performing Layer*), developed by ONERA, is based on the interaction between electromagnetic field and structural abnormality. Mechanical damage, as well as thermal defects, can be diagnosed due to their observable influence on electromagnetic properties [Lemistre *et al*, 2003].

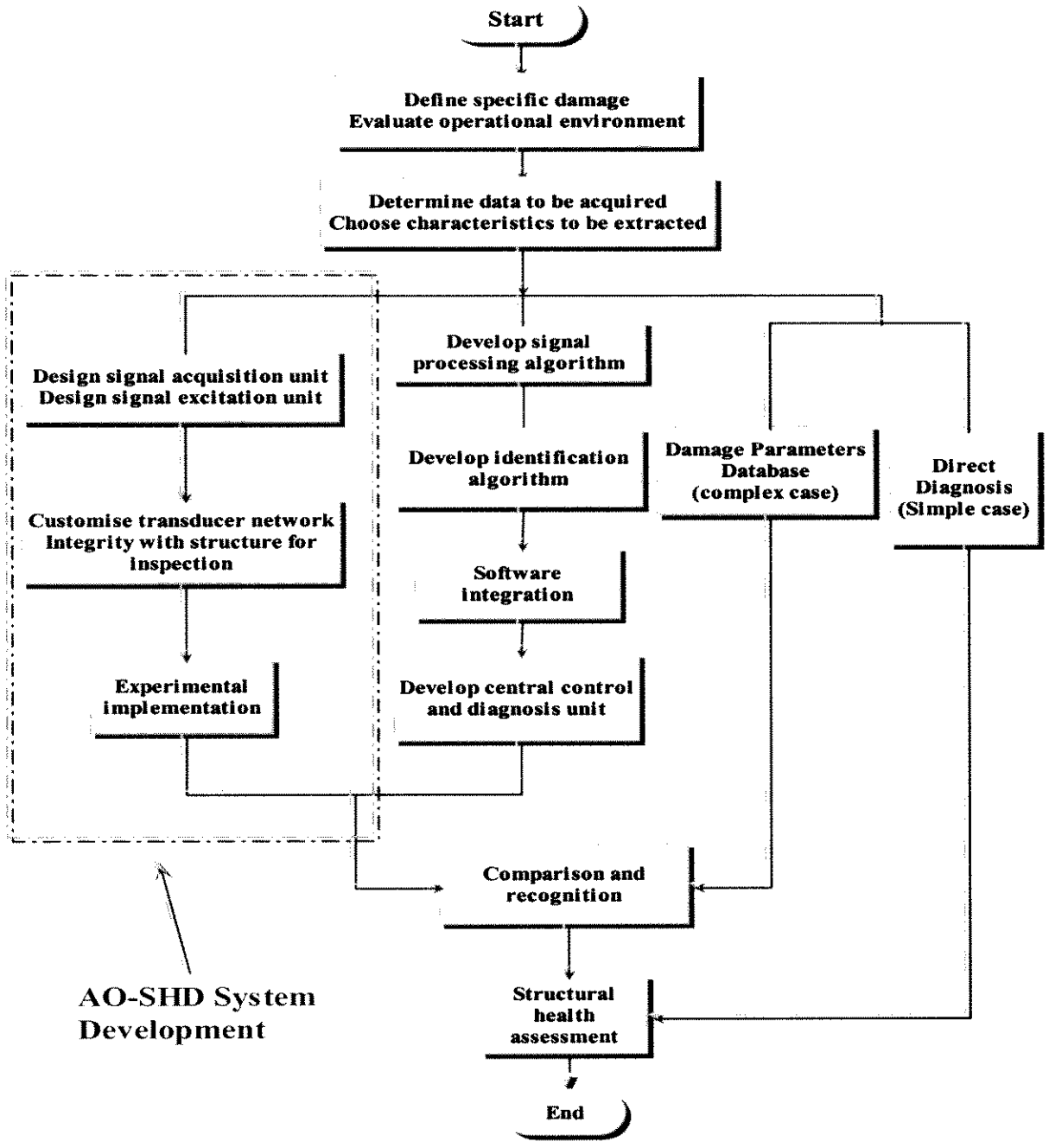

Figure 7.1 Development of the AO-SHD system

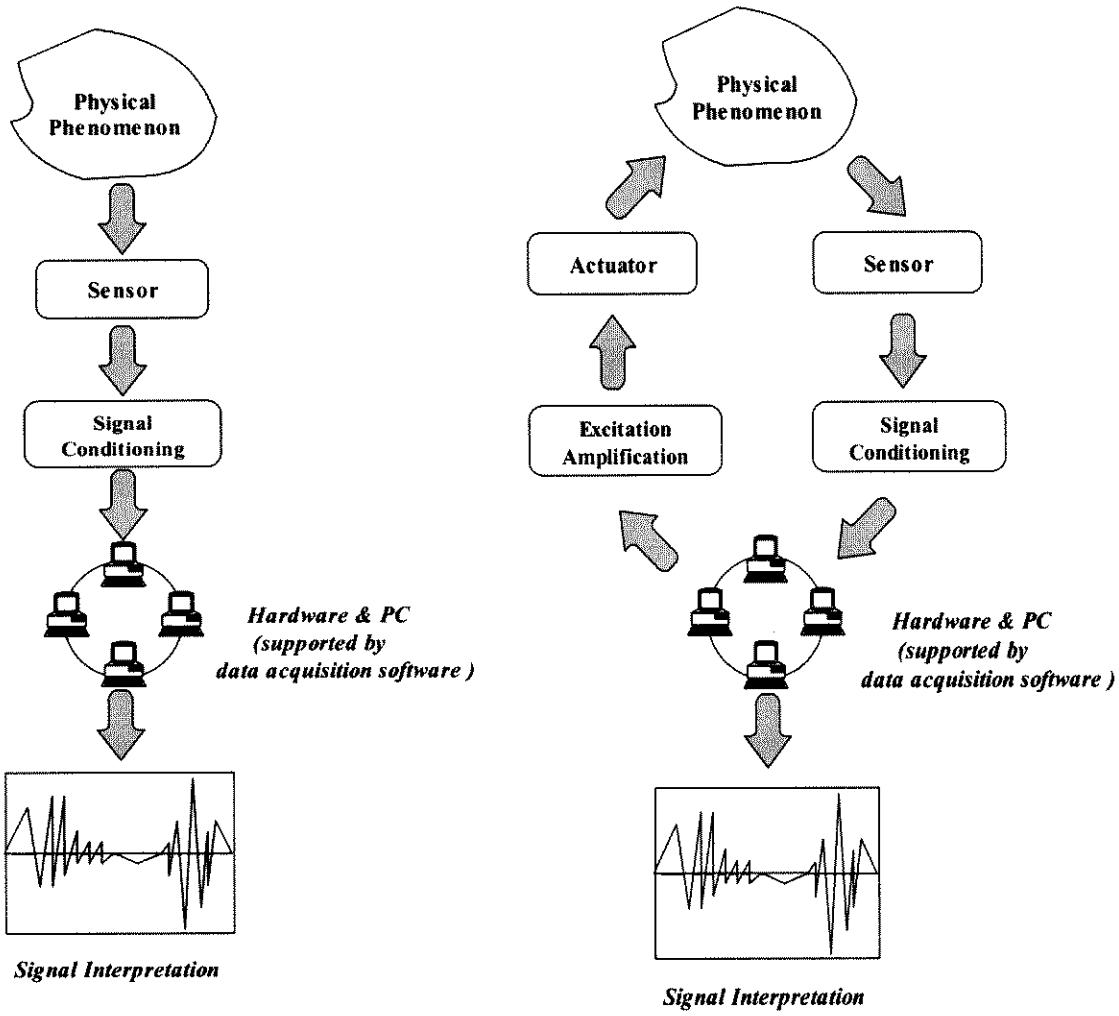

Figure 7.2 (a) Passive sensing; (a) active actuating/sensing

7.2.2.1 Transducer Design

As introduced in Section 2.6, a variety of smart materials are selectable for NDE transducers. Piezoelectric Lead Zirconate Titanate (PZT) seems most cost-effective for generating and collecting elastic waves without inducing noticeable integrity degradation on host structures. Commercial PZT disks (*PI© PIC151*), with the mechanical properties listed in Table 7.1 are chosen in the work, following an optimal criterion [Kessler *et al*, 2002a],

$$2R = \frac{v_{wave}}{f} \cdot (n + \frac{1}{2}) = \lambda_{wave} \cdot (n + \frac{1}{2}), \qquad (n = 0, 1, 2\ldots) \qquad \textbf{(7.1)}$$

where R is the radius of the PZT disk; v_{wave}, f and λ_{wave} are the wave velocity (circa *6000m/s* in quasi-isotropic CF/EP laminates for the fundamental symmetric Lamb mode), frequency (controlled at *0.5MHz* in this study) and wavelength of the relevant Lamb mode, respectively.

Considering the relation between PZT disk size and detectable damage area (Figure 2.2), PZT disks are shaped with a diameter of *6.9mm* diameter. Such criterion-based shaping is able to minimise geometric effect and consequently avoid uneven wave propagation. The PZT disks are trimmed to *0.5mm* in thickness to trade off the desired excitation force and unpolarised voltage limit, permitting an unpolarised voltage limit of *125~150V* (it was observed by Wang and Chang [1999] that the maximum voltage applied to PZT without unpolarising effect is *250-300V/mm*).

Table 7.1 Material properties of PZT transducer [PI Ceramic, 1994]

Product Name	*PI 151*
Geometry	ϕ : *6.9 mm*, h_{PZT} : *0.5 mm*
Density	*7.80 g/cm*^{3}
Poisson's ratio	*0.31*
Charge constant d_{31}	*-170x10*$^{-12}$ *m/V*
Charge constant d_{33}	*450x10*$^{-12}$ *m/V*
Relative dielectric constant K_3	*1280*
Dielectric permittivity P_0	*8.85x10*$^{-12}$*Fm*$^{-1}$
Elastic constant E	*72.5 GPa*

7.2.2.2 Standard Sensor Unit (SSU)

In practice, structures to be inspected are geometrically diverse. Traditional transducer allocation, where the distribution of actuators/sensors and signal excitation/acquisition must be individually configured for each application, is unlikely to provide an expedient cost-effective solution. Motivated by methods adopted in the automobile industry for standardised accessories and parts, a sensor network approach based on concept of *standard sensor unit* (SSU) is developed.

Here, *4* PZT disks are collocated to encircle a square area of *172.5mm* × *172.5mm* (the value is determined by most of the actual applications in this study) and controlled by a signal excitation/acquisition circuit. Such a design is nominated as *standard sensor unit* (SSU), and is illustrated in Figure 7.3(a). In SSU, two-way switches are attached to each PZT wafer, enabling every PZT transducer to act as both the actuator and sensor. Theoretically, a total of *6* actuator-sensor pairs, viz. *12* actuator-sensor paths, can be offered by one SSU. Paradigmatically, an active sensor network involving several SSUs, customised for a non-regular geometric entity, is schematically configured in Figure 7.3(b).

Serving as the basic unit in a transducer network, SSU is collocable. Via this concept, diverse transducer networks can be conveniently customised by appropriately assembling SSUs, to flexibly accommodate different geometries and boundary conditions. The distributed multi-point architecture also contributes to the enhancement of signal-to-noise ratio (SNR). Meanwhile, since each SSU is independent from the others, such a network is robust for signal excitation and acquisition.

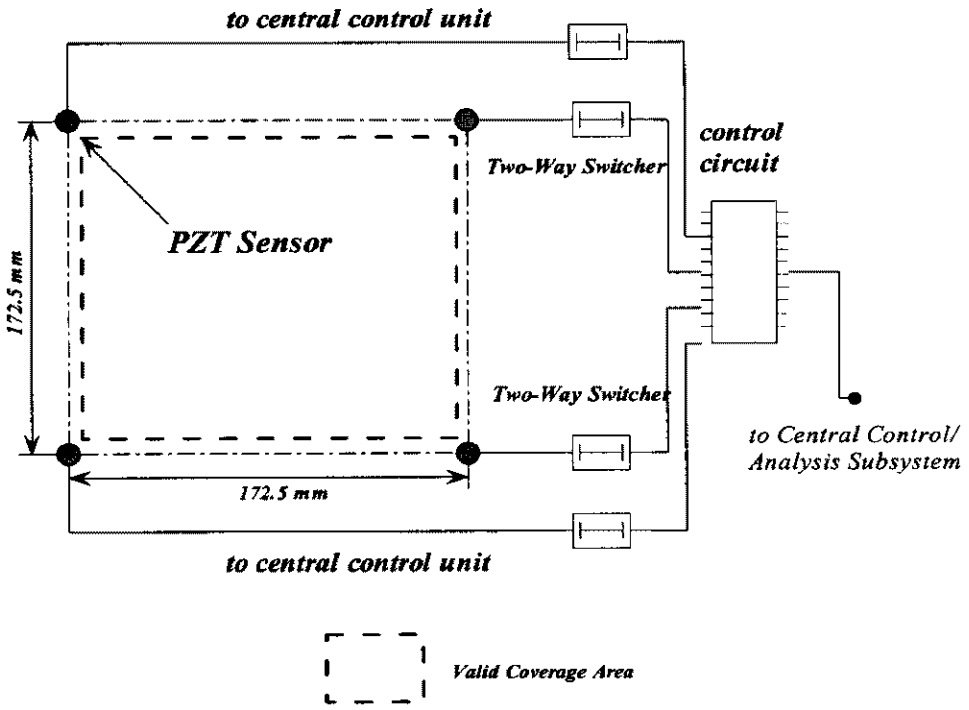

CCIU is to be detailed in Section 7.2.5

(a)

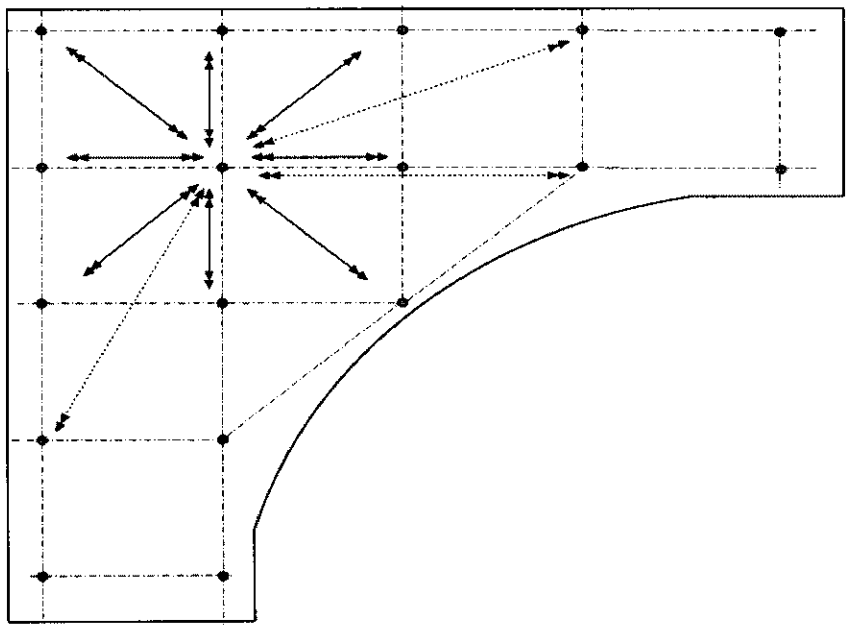

(b)

Figure 7.3 Active actuator/sensor network: (a) a *standard sensor unit* (SSU); (b) customised network for a geometrically non-regular structure

7.2.2.3 Multi-Point Active Actuator/Sensor Network

In a network, several SSUs can be employed, which may own conterminous actuator-sensor paths. Under such a circumstance, the number of PZT transducers is minimised by keeping only one transducer at joint of SSUs, as in the example in Figure 7.4, where *9* SSUs (*16* instead of $4 \times 9 = 36$ transducers) are used.

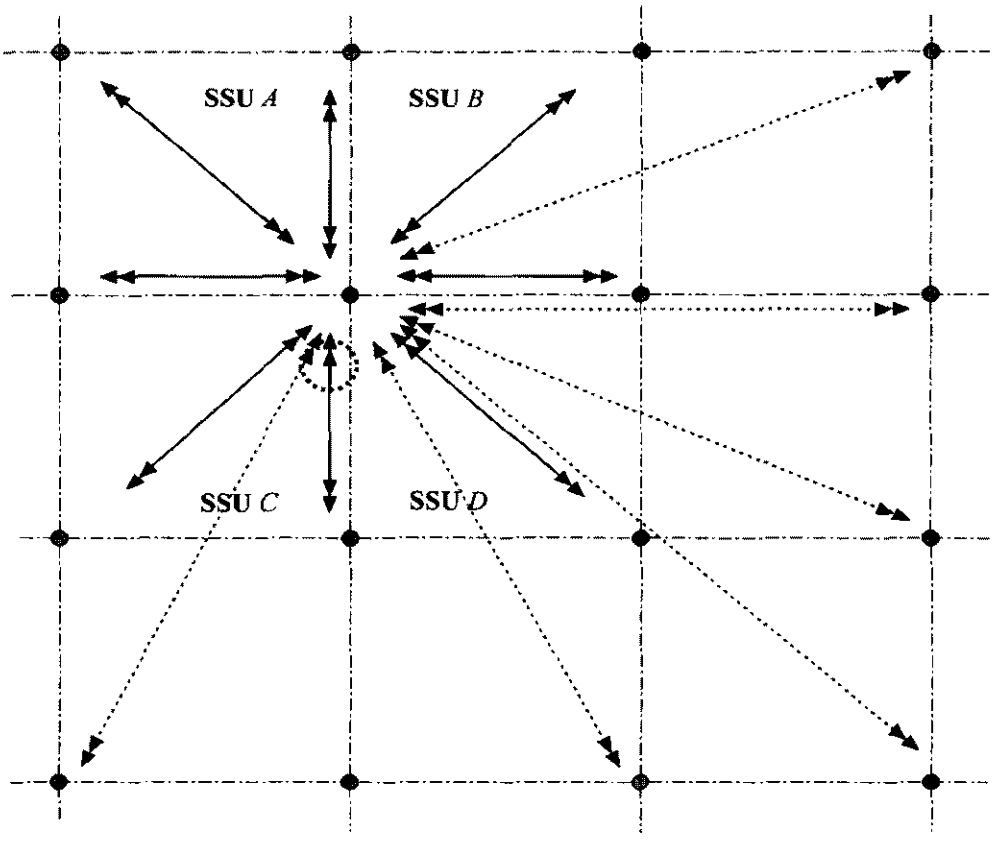

Figure 7.4 Actuator/sensor network using *9* SSUs

By way of elucidation, a PZT transducer located in the second row is chosen as the actuator. Synchronously belonging to SSUs *A*, *B*, *C* and *D*, the selected transducer performs standard excitation/acquisition for each SSU (denoted by solid lines with double arrowheads), and also additional excitation/acquisition for neighbouring SSUs (denoted by dotted lines with double arrowheads). The additional signal acquisition is aimed at improving efficiency with a limited number of PZT transducers. All the standard and additional excitation/acquisition is conducted in sequence mastered by a central control circuit.

7.2.3 Signal Generation Subsystem (SGS)

Performing excitation generation and transmission, a signal generation system bridges control units with actuators. In the study, development of the signal generation subsystem (SGS) covers (1) hardware design and implementation, and (2) diagnostic signal construction. The SGS is able to provide user-defined signal excitation with arbitrary waveform and frequency.

SGS Design and Implementation

The principium for SGS design is diagrammed in Figure 7.5.

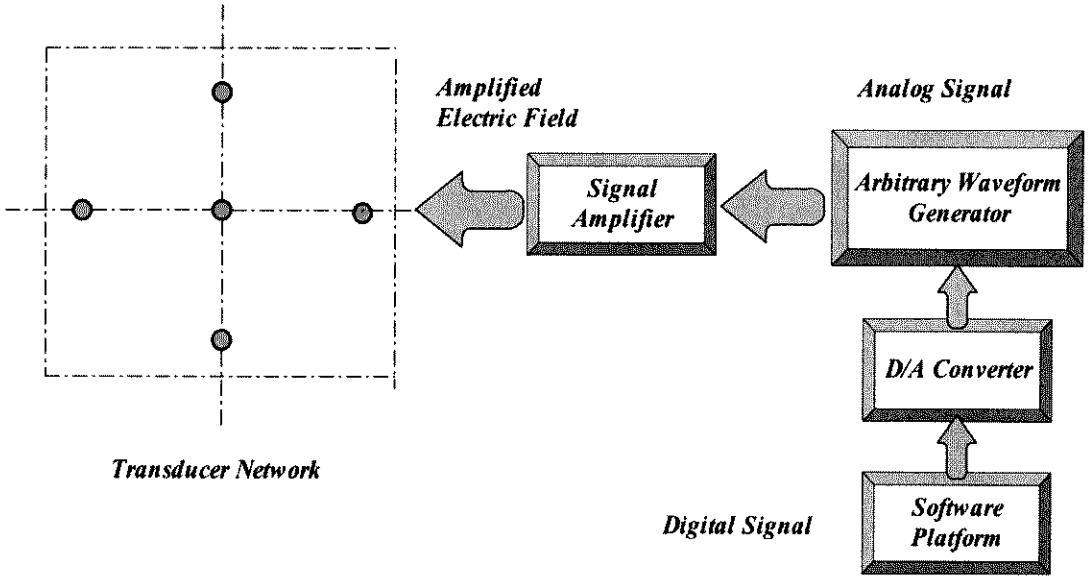

Figure 7.5 Principium of SGS design

The digital signal is programmed and excited by an arbitrary waveform generator (*Agilent© E1441*), and transferred into the corresponding analog signal by a *built-in* D/A converter. The analog signal is downloaded into a PZT signal amplifier (*PiezoSys© EPA-104*), and then applied on each PZT actuator in the transducer network.

Diagnostic Signal Construction

As a basic feature in an active system, the excitation signal can be flexibly controllable. Generated via the SGS, the signal most frequently used in this study, a 5-cycle toneburst modulated by the *Hanning* window function, is formulated as [Mathworks, 2001d],

$$h(x) = \frac{1}{2}[1 - \cos(2\pi \frac{x}{n+1})], \ (x = 1,2,\cdots n) \qquad \textbf{(7.2a)}$$

with the corresponding Fourier counterpart in the frequency domain,

$$H(\omega) = \{\frac{1}{2}W_R(\omega) + \frac{1}{4}[W_R(\omega - \frac{2\pi}{N-1}) + W_R(\omega + \frac{2\pi}{N-1})]\} \cdot e^{-j(\frac{N-1}{2})\omega} \qquad \textbf{(7.2b)}$$

where W_R is the characteristic function for rectangular waveform. The constructed diagnostic signal is shown in Figure 7.6. In the FFT spectrum, excitation energy is observed to concentrate within a narrow frequency band, efficiently reducing the wave dispersion effect and accordingly benefiting signal interpretation.

7.2.4 Data Acquisition Subsystem (DAS)

A data acquisition unit, collecting signals from both structure and environment, plays important roles in determining the accuracy and precision that a SHM system can offer. In a closed data acquisition loop, a sensor, such as a microphone or probe, senses analog signal, and transports and converts the signal into digital bits by an A/D converter for host computer identification.

In this study, development of the data acquisition subsystem (DAS) involves (1) selection of sensor, and design of sensor number/locations (optimal *versus* redundant) (see Sections 2.6 and 7.2.2); and (2) software/hardware design. More general considerations also include sampling algorithms, system calibration and variability qualification, as well as long-term reliability [Ye *et al*, 2003]. Dual-

channel synchronous sampling with adjustable sampling rate (up to *20.48MHz*) is supported by the control software in DAS.

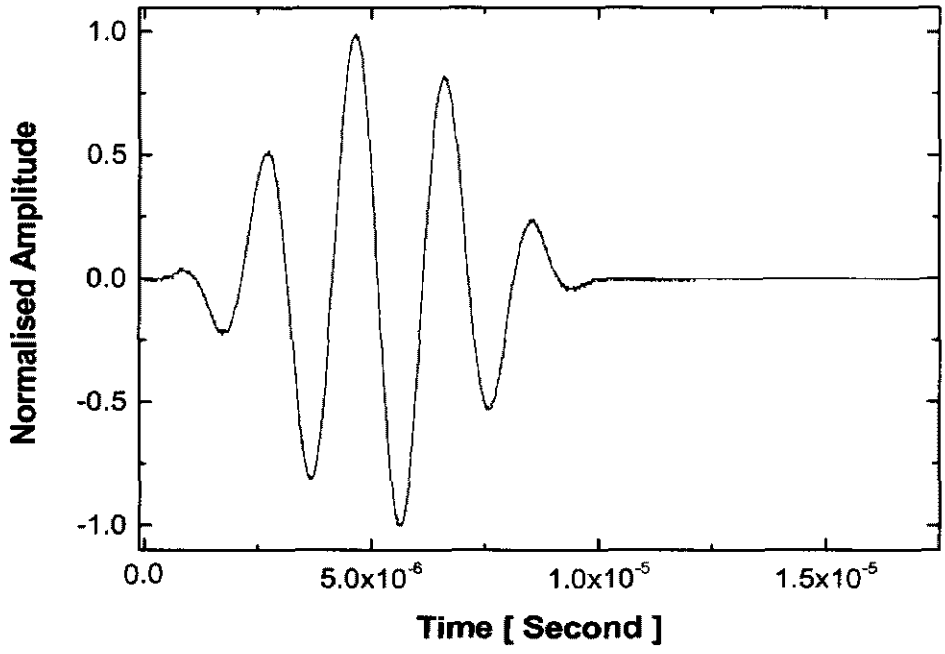

(a)

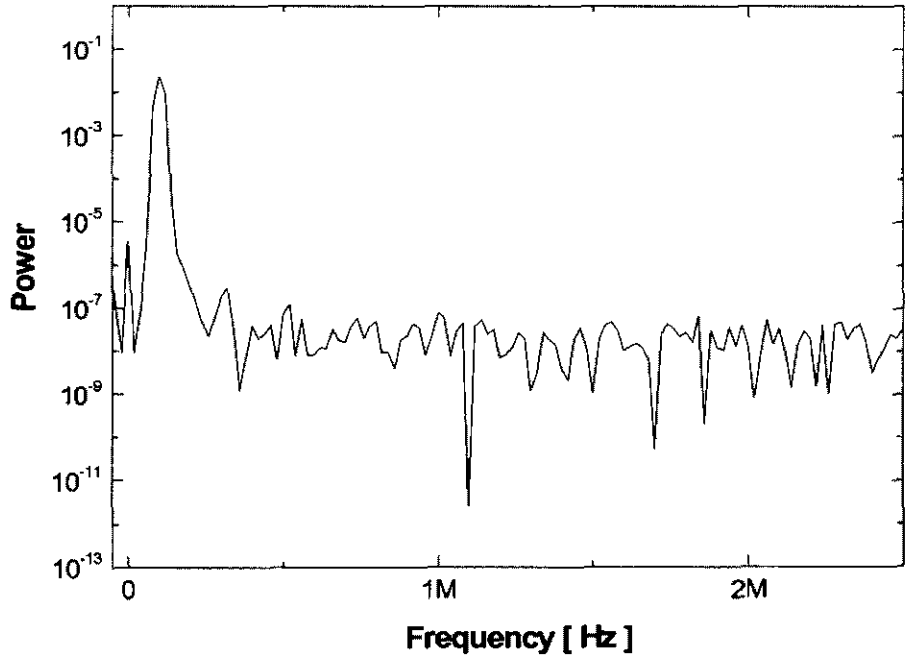

(b)

Figure 7.6 Diagnostic wave (*5*-cycle *Hanning* window modulated toneburst) constructed by SGS: (a) in time domain; (b) in frequency domain

The DAS proposed in this study is diagrammed in Figure 7.7, where a digitizer (*Agilent© E1437A*) is employed to perform signal acquisition through *IEEE-488* bus, with an adjustable sampling rate up to *20.48MHz*, and to digitise acquired signals. Allowing for incompatibility between signals and acquisition hardware, the signal is conditioned prior to transmission to computer, which is conducted by a signal conditioner (*Agilent© E3242A*) in the DAS, including amplification, filtering, electrical isolation and multiplexing [Mathworks, 2001a].

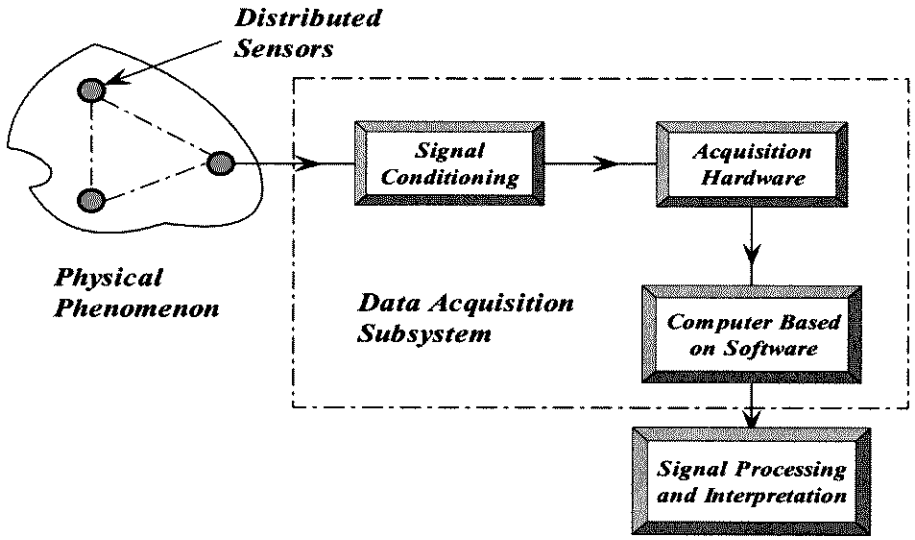

(a)

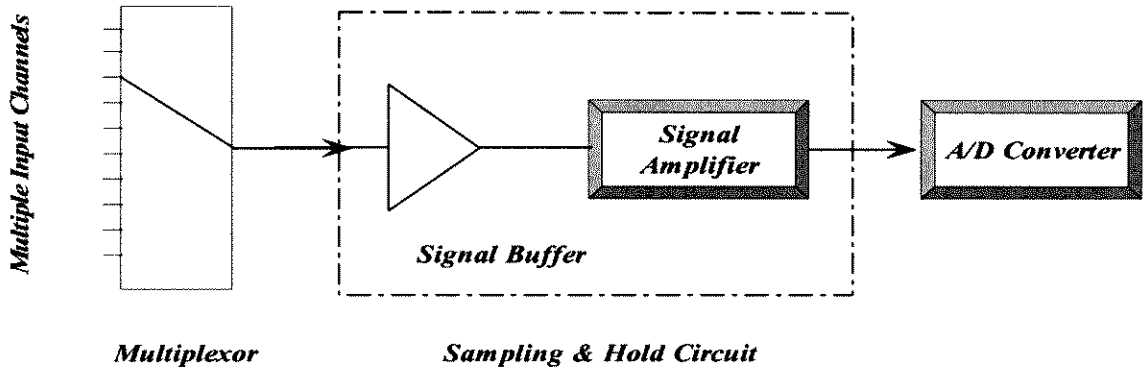

(b)

Figure 7.7 Principles of data acquisition: (a) DAS; (b) sampling unit

In DAS, a signal conditioner usually generates a few micro-volts of internal noise, limiting the signal resolution to this level. The amount of noise added to the signal depends on the bandwidth of the input amplifier. To reduce internal noise, an amplifier with a bandwidth that closely matches the bandwidth of the input signal is adopted. Meanwhile, shielded cables, kept as short as possible, are used to screen electrical and other environmental noises. Both the SGS and the DAS are developed on the *Agilent© VXI* signal simulation/acquisition platform.

7.2.5 Central Control/Analysis Subsystem (CCAS)

Being the pivotal unit in AO-SHD system, the central control/analysis subsystem (CCAS) comprehensively integrates diagnosis controller and signal processing/interpretation. In-house software is developed on *NI Labview©* (Version: *5.6, National Instrument Co.*) and *HP VEE©* (Version: *4.0, Hewlett-Packard Co.*) platforms to fulfill the designed functionalities. Such software interactively invokes *Agilent® Virtual Instrument Software Architecture* (VISA) and *Agilent® Standard Instrument Control Library* (SICL) [Agilent, 2000], to access the SGS and DAS. The interfaces for control of the SGS and DAS are displayed in Figure 7.8.

In addition to function of control, CCAS also acts as the interpreter for acquired signals and offers diagnosis and identification, by integrating signal processing package (SPP), damage parameters database (DPD) and the well-trained artificial neural network (see Chapters 4 and 6).

7.2.6 Active Online Structural Health Diagnosis (AO-SHD) System

Incorporating the CCAS, SGS, DAS and transducer networks, an *active online structural health diagnosis* (AO-SHD) system is then configured, shown

schematically in Figure 7.9. The configuration of hardware involved in the system is summarised in Appendix *B*. Biomimetic principles are introduced, whose philosophy is illustrated in Figure 7.10. Herein, the active multi-point actuating/sensing network simulates the nervous/muscular system of human body. The central control/analysis subsystem functions as an expert system similar to the 'human brain centre'.

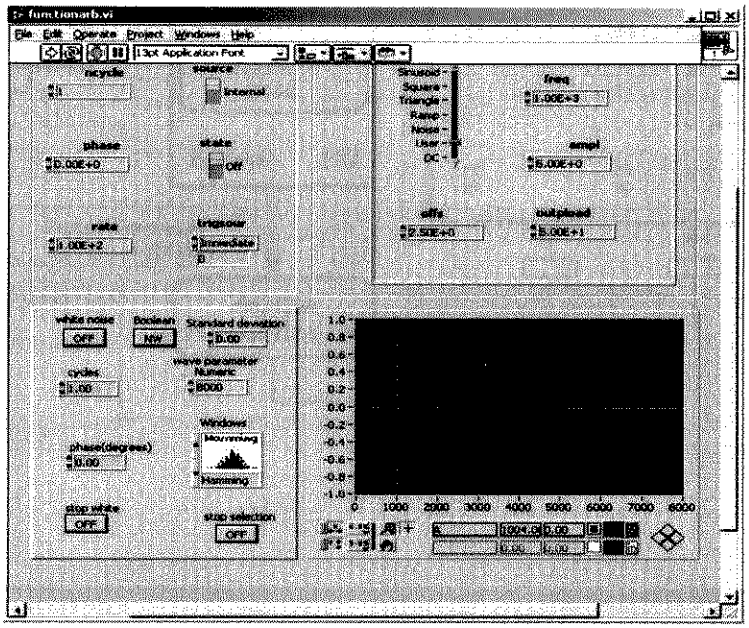

(a)

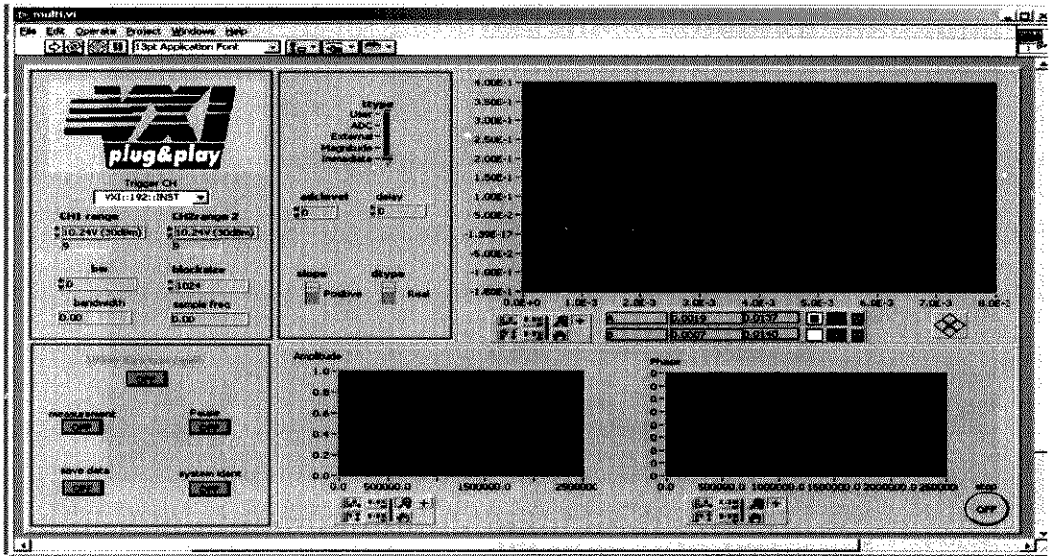

(b)

Figure 7.8 In-house software interfaces of (a) arbitrary signal generation control for SGS; (b) dual-channel data acquisition for DAS

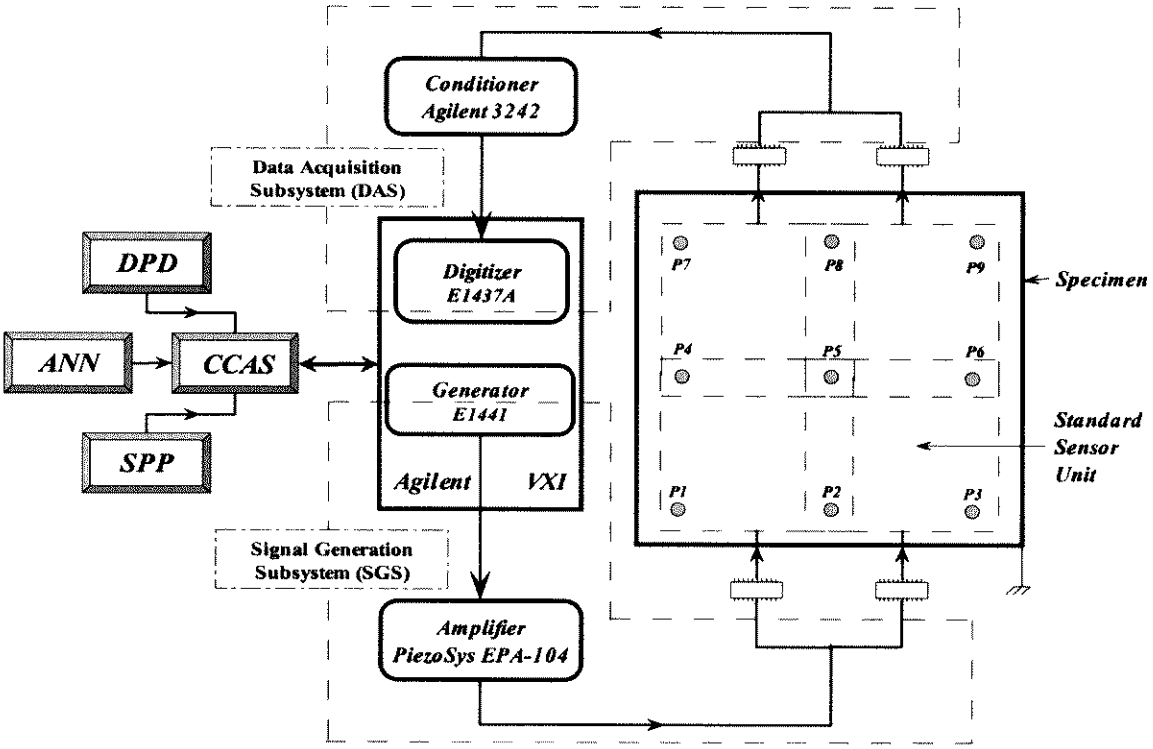

(a)

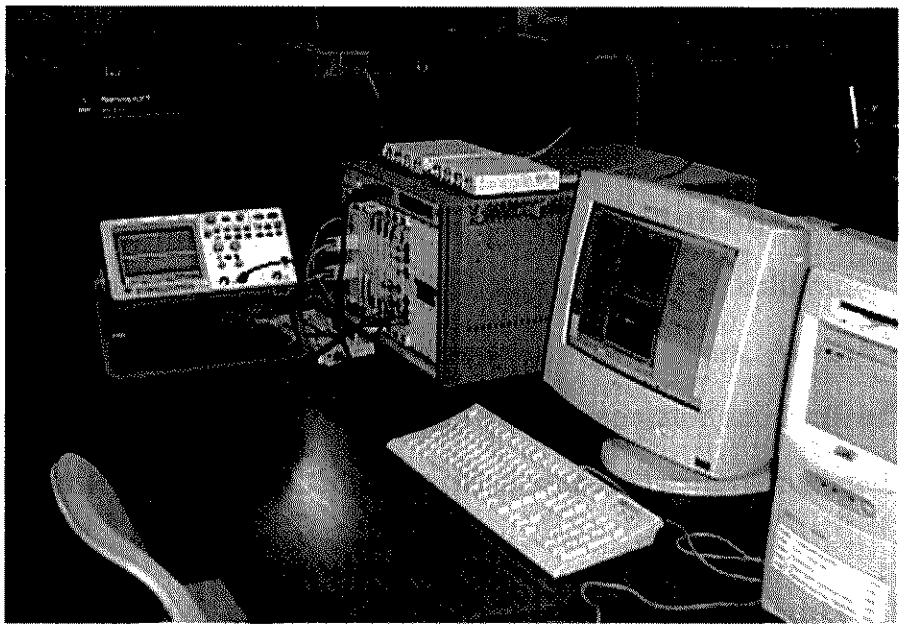

(b)

Figure 7.9 *Active Online Structural Health Diagnosis* (AO-SHD) System: (a) schematic description; (b) in-field photo

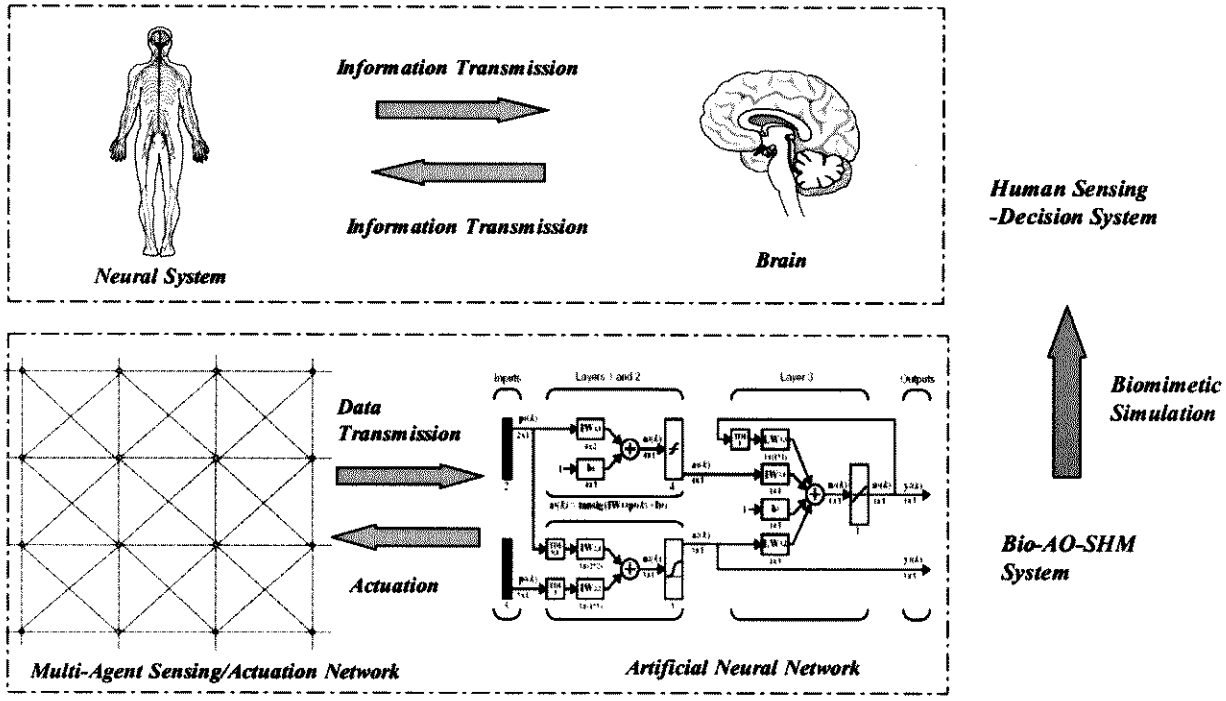

Figure 7.10 Biomimetic philosophy-inspired SHM system

7.3 System Calibration and Testing

7.3.1 System Calibration

A specified code is developed on the *NI Labview*© platform to calibrate the configured AO-SHD system before its actual application. The calibration includes zero setting, correction of instrument offset and drift (gain errors, AD/DA converter offset drift, voltage offset, etc.). A *HP*® *3310A* signal generator and *Agilent*® *54620A* oscilloscope (commercially calibrated) are used as standard calibrating benchmarks.

Calibration circuits for SGS and DAS are designed, as shown in Figures 7.11(a) and (b), respectively. In the former, a sweep of signals with same waveforms and frequencies is actively generated by both standard generator and SGS, and applied on a standard PZT actuator-sensor pair. Signal differences, collected and compared by the standard oscilloscope, are then fed back for correction. Similarly, various signals

generated by the standard generator are simultaneously acquired by both the oscilloscope and DAS, and the differences are then fed back for amendment. Calibration is repeated until satisfactory precision is met.

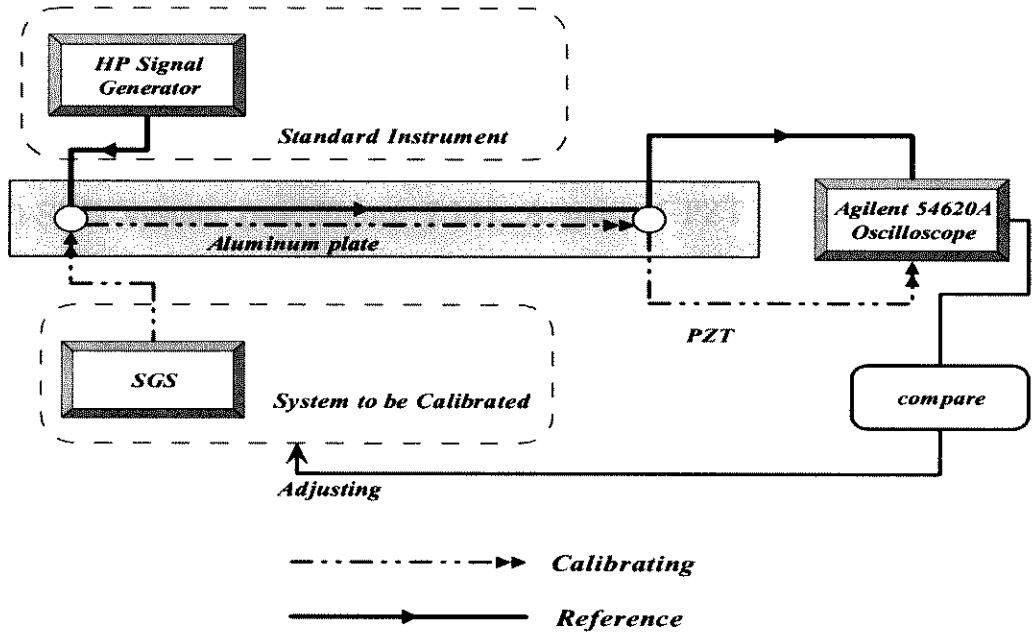

(a)

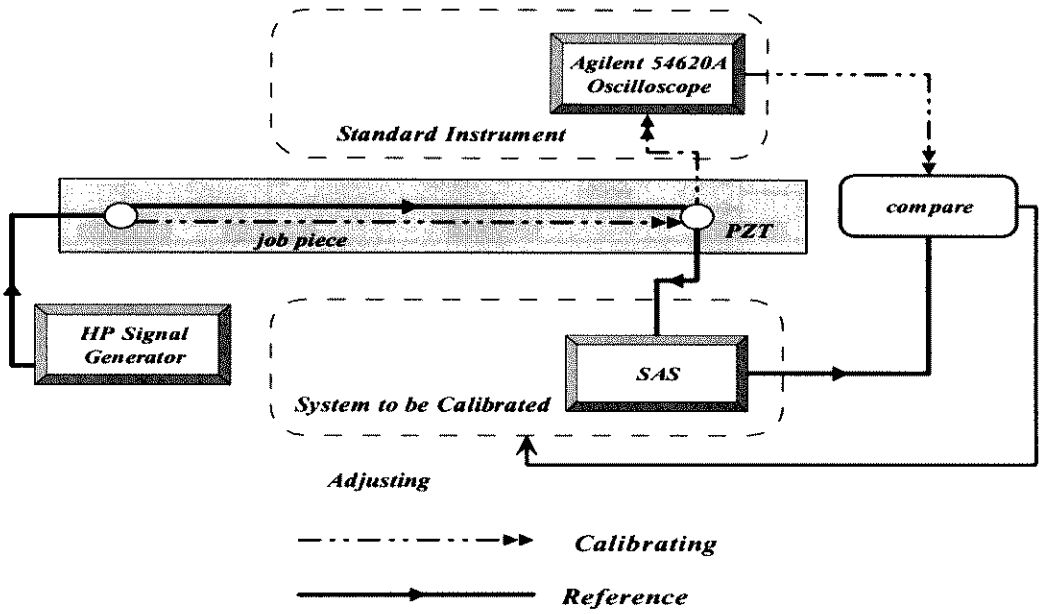

(b)

Figure 7.11 System calibration establishment for (a) SGS; (b) DAS

7.3.2 System Testing

The developed AO-SHD system is then validated by stimulating desired fundamental Lamb wave modes.

7.3.2.1 Setup Configuration

An active excitation control circuit is additionally designed and instrumented with the AO-SHD system (see Figure 7.12). A pair of PZT discs, functioning as an actuator-unit, are symmetrically surface-bonded at the same position on opposite sides of an *8*-layer $[45/-45/0/90]_s$ CF/EP (T650/F584) laminate plate. Three PZT discs are located along a straight line, *100mm*, *200mm* and *250mm* away from the actuator, serving as sensors. All PZTs are kept far away from laminate edges to preclude boundary effects.

The diagnostic signal (see Figure 7.6) is stimulated by the SGS to provide an external electric field with *60* V_{PP} (peak-to-peak). Signal acquisition is performed by the DAS. The SPP developed in Chapter 4 is employed to assist signal interpretation.

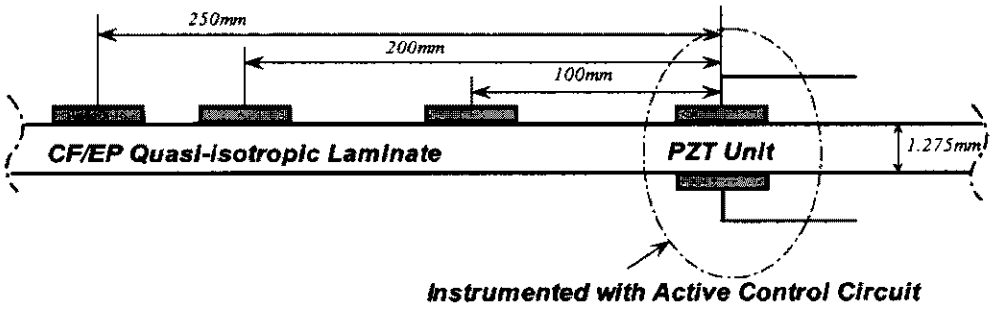

(a)

Figure 7.12 Control circuit for selective generation of Lamb mode: (a) partition of actuators and sensors; (b) control circuit

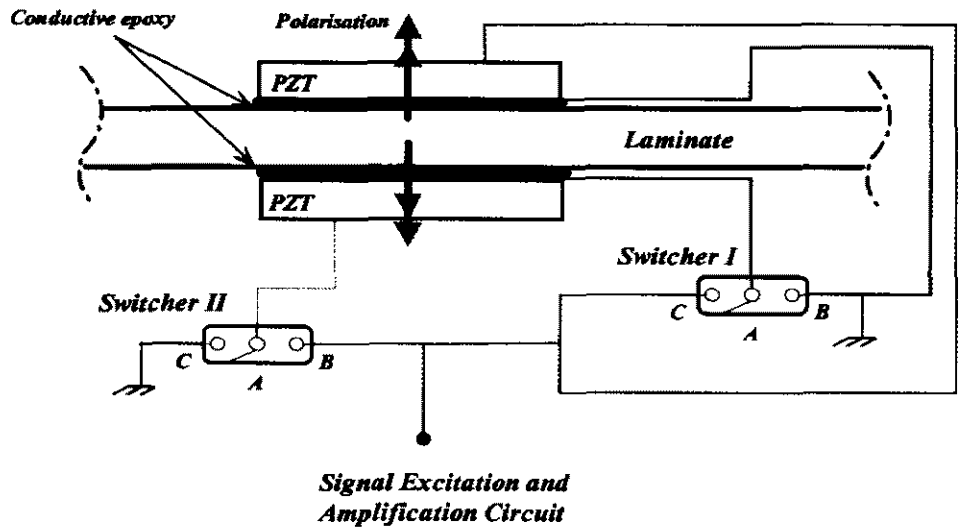

Case A: Single electric field excitation

Case B: Symmetric electric fields excitation

Case C: Anti-symmetric electric fields excitation

(b)

Figure 7.12 *Cont.*

7.3.2.2 Selective Excitation of Basic Lamb Modes

Case A: A single PZT actuator, located on the upper laminate surface, is energised (Terminal *B* in switcher *I* and Terminal *C* in switcher *II* are simultaneously activated in the additional control circuit, Figure 7.12). An external electric field, parallel to the PZT polarised direction, is therefore applied. Processed by the SPP, the energy spectrum for the signal acquired by the sensor located *100mm* away, as a typical example, is displayed in Figure 7.13(a), where the symmetric Lamb mode, S_0, shear mode, S_0', and anti-symmetric mode, A_0, are observed.

Case B: Dual PZTs are energised in-phase (Terminals *B* are simultaneously activated in both switchers). Symmetric electric fields, parallel to the polarised direction, are synchronously applied on the upper and lower PZT wafers. The energy spectrum for

the signal acquired by the sensor located *100mm* away is exhibited in Figure 7.13(b), where symmetric Lamb mode, S_0, is obvious with an enhanced magnitude in amplitude, indicating stronger incident wave energy centralised on the symmetric mode. Meantime, the shear mode, S_0', and anti-symmetric mode, A_0, are considerably weaker.

Case C: Dual PZTs are energised out-of-phase (Terminals *C* are simultaneously activated in both switchers). Anti-symmetric electric fields, parallel to the polarised direction, are applied on both PZT wafers simultaneously. The energy spectrum for the signal acquired by the same sensor as used above is compared in Figure 7.13(c), in which the shear mode, S_0', and anti-symmetric mode, A_0, are observed to dominate the overall wave energy, while the symmetric Lamb mode with a small magnitude is reasonably suppressed.

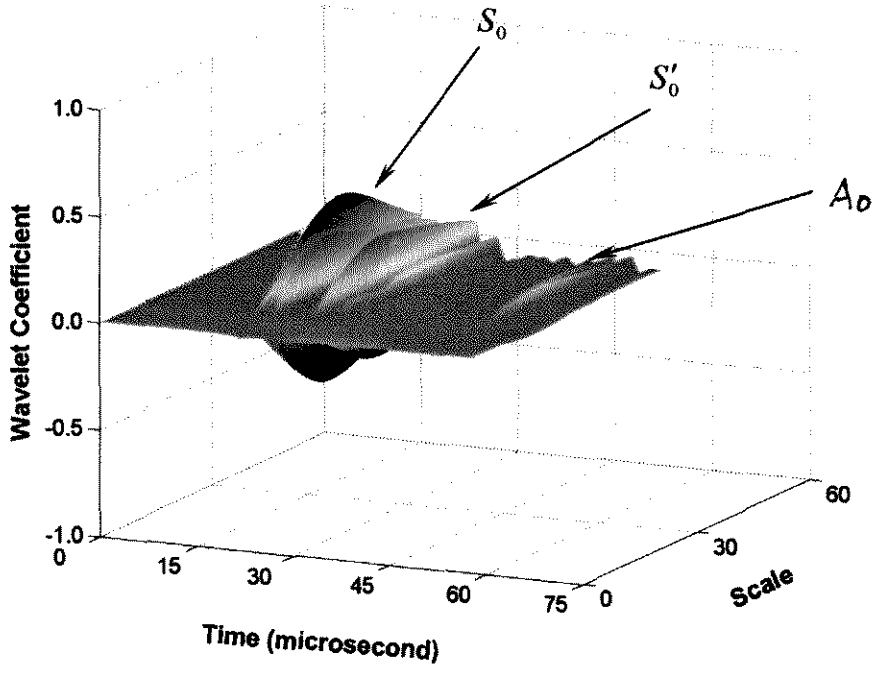

(a)

Figure 7.13 Energy spectra for actively generated Lamb modes (*from experiment*) under excitation: (a) Case A; (b) Case B; (c) Case C

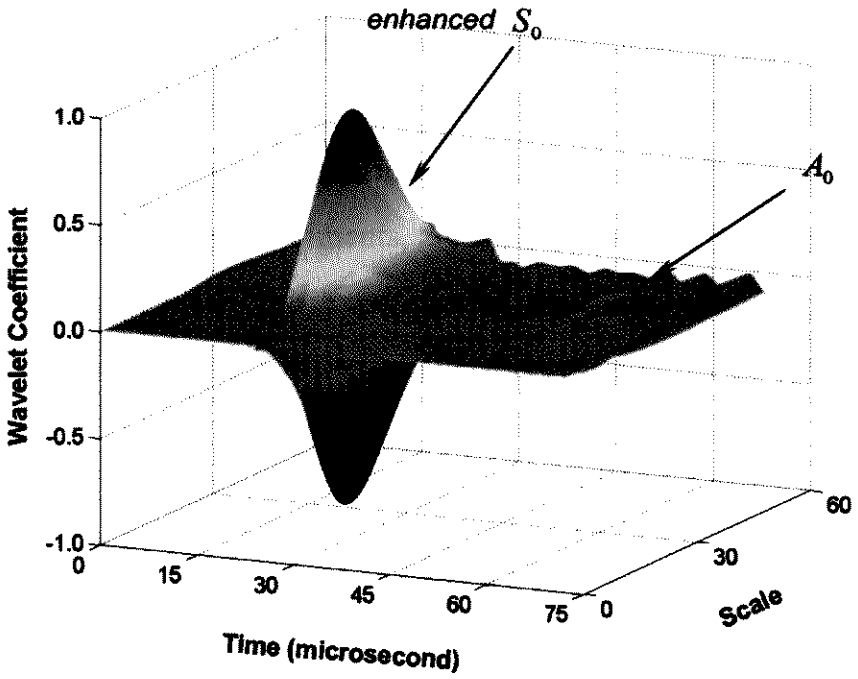

(b)

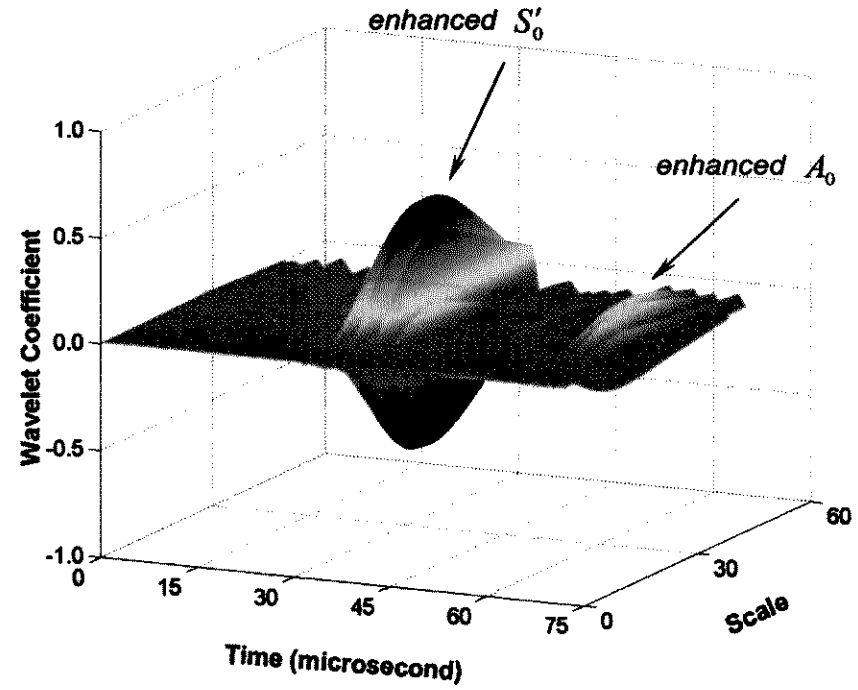

(c)

Figure 7.13 *Cont.*

7.3.2.3 Numerical Validation

In parallel with experiments, numerical simulations based on the dynamic FEM modelling developed in Section 5.3 are used for verification. Energy allocation spectra for signals numerically obtained, under individual excitation cases in accordance with those in the experiments, are shown in Figure 7.14. Good agreement has been achieved between the experimental measurements (Figure 7.13) and numerical simulations (Figure 7.14), upon signal processing via the SPP.

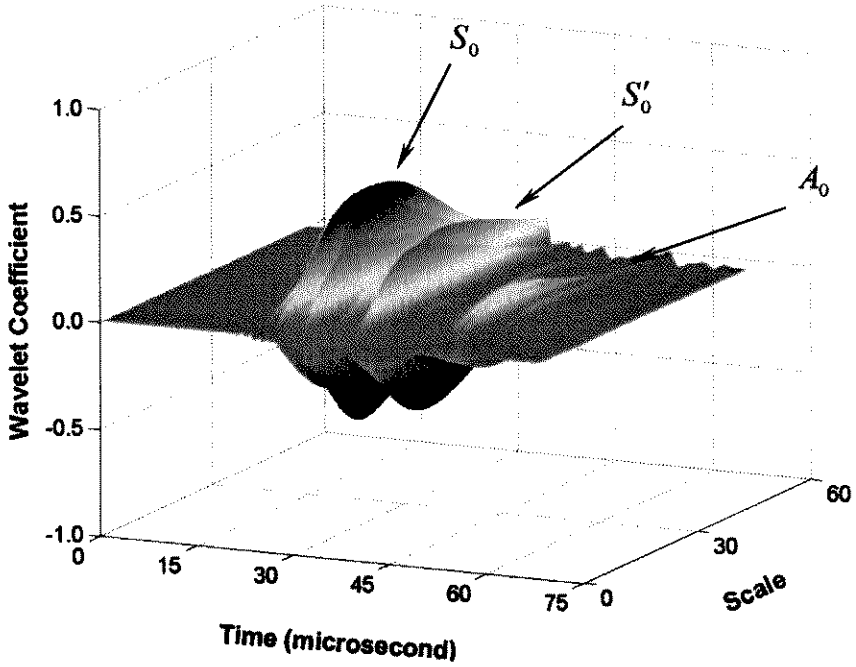

(a)

Figure 7.14 Energy spectra for actively generated Lamb modes (*from FEM simulation*) under excitation: (a) Case A; (b) Case B; (c) Case C

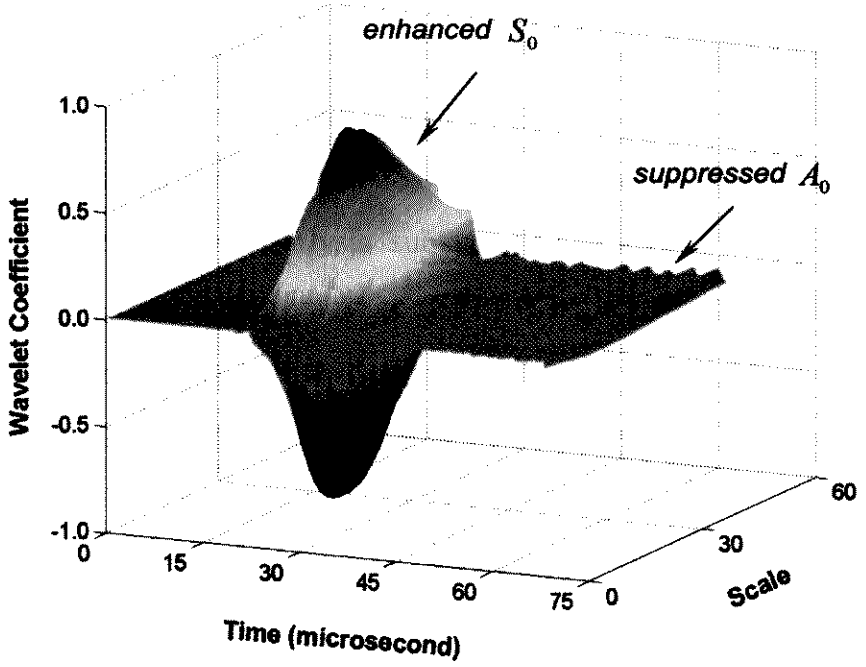

(b)

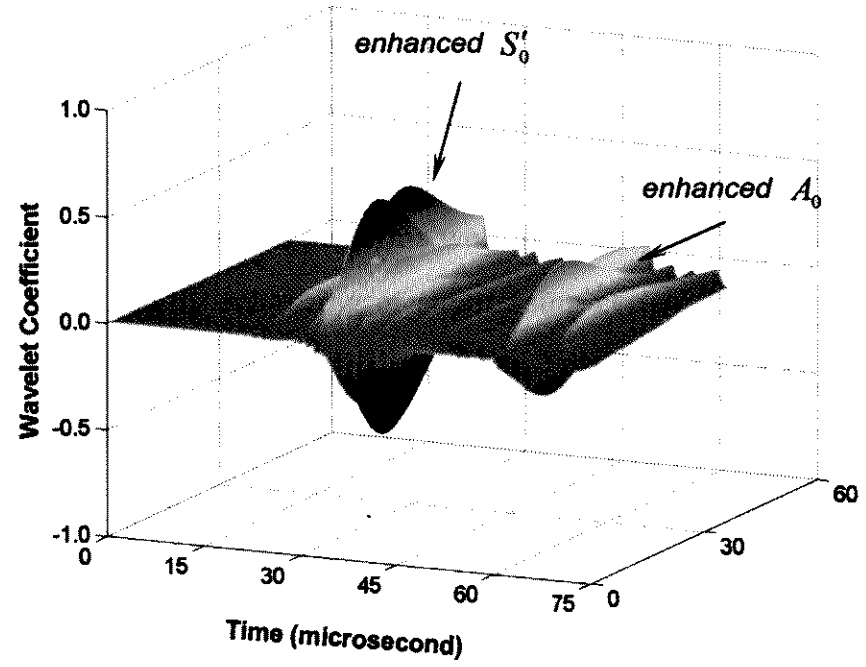

(c)

Figure 7.14 *Cont.*

7.4 Concluding Remarks

An AO-SHD system is configured based on the work in previous chapters. It includes an active multi-point actuator/sensor network using distributed piezoelectric discs, a signal generation subsystem (SGS), a data acquisition subsystem (DAS), and particularly, a central control/analysis subsystem (CCAS). The key unit, CCAS, incorporates a signal processing package (SPP) (Chapter 4), a constructed damage parameters database (DPD) and a designed ANN (Chapter 6), to actualise the designed diagnosis algorithms. The system is then calibrated before application.

A novel concept of *standard sensor unit* (SSU) is introduced to facilitate actuator/sensor network design and improve robustness. Such an approach easily negotiates different structural geometries and boundary conditions.

The system is then validated by selectively generating desirable single symmetric and anti-symmetric modes in a quasi-isotropic CF/EP composite laminate. The FEM modelling technique developed in Chapter 5 is also employed for validation, and good agreement is achieved. It is concluded that (1) the configured AO-SHD system, including hardware and software, performs well in the chosen case studies; (2) pure waves can be generated by enhancing or suppressing certain Lamb modes; and (3) the PZT actuator and sensor models developed in Section 5.3 simulate reality well. The AO-SHD system is further evaluated in the following chapters by three actual case studies.

Chapter 8

Identification of Crack Growth in a Structural Beam

8.1 Introduction

A one-dimensional structure, such as a flexible beam or a rod in a truss system, serves as a basic component in a weight-carrying system. But its stiffness can be reduced significantly with the occurrence of damage. This damage, such as a transverse crack in metal alloy or matrix crack/delamination in a composite beam, can originate from internal manufacture defects or external impact, and develop further under fatigue loading. As an essential step toward complicated structures, assessment of damage in one-dimensional structures has generated much interest.

As a case study to validate the proposed damage detection technique and the AO-SHD system, diagnostic monitoring of transverse crack growth in an aluminium alloy structural beam is described in this chapter. (Detection of delamination in composite beams, regarded as a special case of delamination in composite plates, can be referred to Chapter 10.)

8.2 Damage Model

Consider a uniform Euler-Bernoulli beam bearing a transverse crack, perpendicular to the beam axis and with an increasing depth, H_d, as shown in Figure 8.1.

Following the derivation in Section 3.2.1.2, its motion under transverse excitation can be described as [Achenbach, 1973; Bland, 1988]

$$w(x,t) = [\sum A_1 e^{-ikx} + \sum A_2 e^{ikx} + \sum A_3 e^{-kx} + \sum A_4 e^{kx}] \cdot e^{i\omega t} \qquad \textbf{(8.1)}$$

Each term in Equation (8.1) respectively corresponds to one possible wave mode in the beam, recognised in order as *positively propagating wave*, *negatively propagating wave*, *positively growing evanescent wave* and *negatively exponentially decaying wave*.

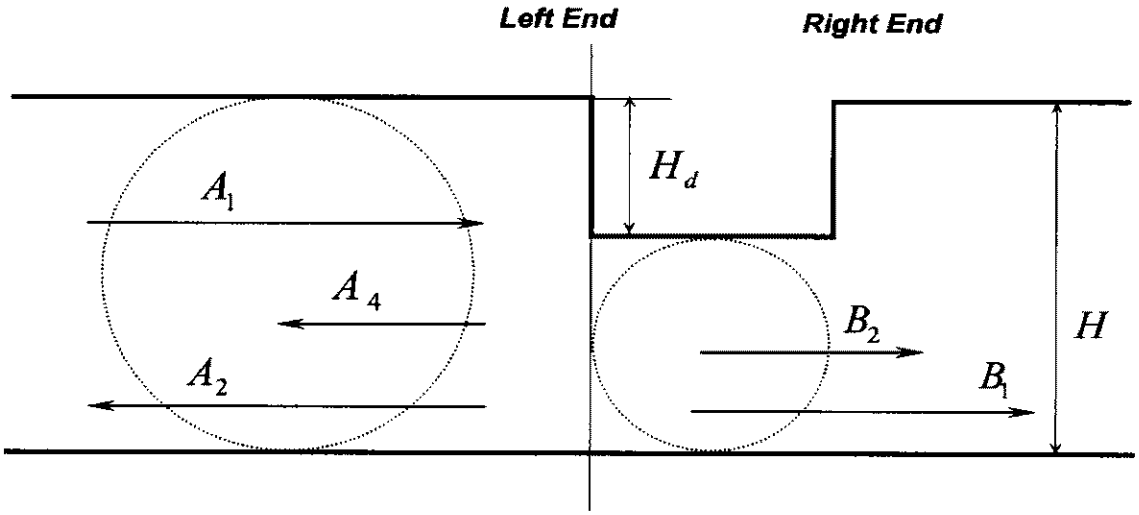

Figure 8.1 Damage model

With the damage shown in Figure 8.1, Equation (8.1) is modified using two equations before (denoted by w_-) and after (denoted by w_+) the left damage end, respectively,

$$w_-(x,t) = [\sum A_1 e^{-ik_1 x} + \sum A_2 e^{ik_1 x} + \sum A_4 e^{k_1 x}] \cdot e^{i\omega t} \qquad \textbf{(8.2a)}$$

$$w_+(x,t) = [\sum B_1 e^{-ik_2 x} + \sum B_2 e^{-k_2 x}] \cdot e^{i\omega t} \qquad \textbf{(8.2b)}$$

The three terms in Equation (8.2a) correspond to the *incident wave*, *reflected propagating wave* and *reflected exponentially decaying wave*; and the two terms in Equation (8.2b) are the damage-induced *positively propagating wave* and *growing*

attenuating wave, respectively. Note that the wave components A_4 and B_2 disappear very quickly due to exponential decaying. Using the continuity and compatibility conditions at the left damage end,

$$w_{-}(x,t) = w_{+}(x,t), \qquad \frac{\partial w_{-}(x,t)}{\partial x} = \frac{\partial w_{+}(x,t)}{\partial x},$$

$$EI_1 \frac{\partial w_{-}^2(x,t)}{\partial^2 x} = EI_2 \frac{\partial w_{+}^2(x,t)}{\partial^2 x}, \qquad EI_1 \frac{\partial w_{-}^3(x,t)}{\partial^3 x} = EI_2 \frac{\partial w_{+}^3(x,t)}{\partial^3 x} \tag{8.3}$$

the reflection ratio, Ref , is obtained

$$\text{Ref} = \frac{A_2}{A_1} = \frac{-iI_1^2 k_1^4 + 2I_1 I_2 k_1^3 k_2 + 2iI_1 I_2 k_1^2 k_2^2 - 2I_1 I_2 k_1 k_2^3 - iI_2^2 k_2^4}{I_1^2 k_1^4 + 2I_1 I_2 k_1^3 k_2 + 2I_1 I_2 k_1^2 k_2^2 + 2I_1 I_2 k_1 k_2^3 + I_2^2 k_2^4} \tag{8.4}$$

$$I_1 = \frac{l \cdot H^3}{12}, \quad I_2 = \frac{l \cdot (H - H_d)^3}{12}$$

where l, H and H_d represent the width and depth of the beam cross-section and damage depth, respectively. Equation (8.4) theoretically associates the damage depth, H_d, with the reflection ratio, as calibrated in Figure 8.2.

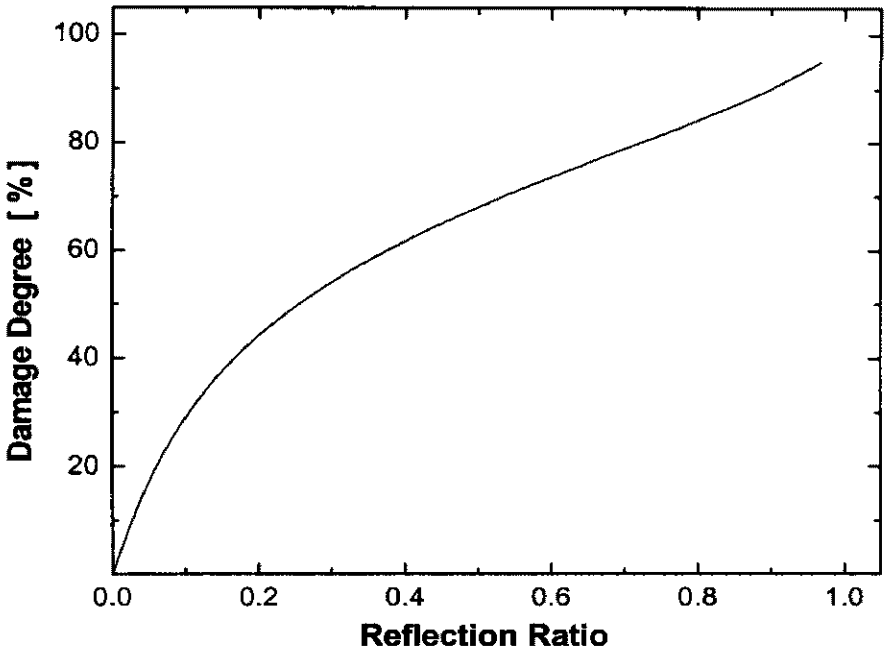

Figure 8.2 Theoretical relation between reflection ratio and damage degree

8.3 Quantitative Diagnosis Scheme

8.3.1 Determination of Damage Location

Structural damage scatters the incident wave into reflected and transmitted components, both of which carry information about the damage. Two key concerns in this regard are (1) correct recognition of reflected wave components/energy, and (2) measurement of time lag among the wave components concerned.

Using the signal processing package (SPP), acquired signals under excitation are decomposed into discretised frequency ranges by digital bandpass filters, and transformed into time-scale space by spectrographic analysis. To obtain higher precision, time lags between incident and damage-induced waves in the filtered signal (in the time domain), and incident and damage-induced energy in the energy spectrum (in the time-scale domain), are simultaneously captured. The reflection source (damage) can thus be triangulated with the known wave propagation velocity.

8.3.2 Determination of Damage Severity

Lemma

Considering a three-dimensional energy spectrum in the time-scale domain via spectrographic analysis, the magnitude of any wave energy ridge in this spectrum, symbolised by A_{ridge}, along the scale axis at an arbitrary time point, can be obtained using the *root-mean-square* (RMS) method [Wolfram Co., 1999; Kim and Kim, 2000],

$$A_{ridge} = \sqrt{\frac{W_1^2 + W_2^2 + \cdots + W_N^2}{N}} \tag{8.5}$$

where W_i ($i=1,\cdots,N$) is the i^{th} wavelet coefficient along the scale axis at the chosen time point, whilst N denotes the total number of discretised points, which is determined by the selected wavelet transform.

Similarly, for two energy ridges in one spectrum, A_{ridge1} and A_{ridge2}, at different time points t_1 and t_2 respectively, their amplitude ratio can be defined, if the same wavelet transform function and precision are chosen, as

$$\left(\frac{\mathrm{A}_{\mathrm{ridge1}}}{\mathrm{A}_{\mathrm{ridge2}}}\right)=\sqrt{\frac{W_1^{\,2}+W_2^{\,2}+\cdots+W_N^{\,2}\,|_{t=t_1}}{W_1^{\,2}+W_2^{\,2}+\cdots+W_N^{\,2}\,|_{t=t_2}}} \tag{8.6}$$

When N is sufficiently large, Equation (8.6) becomes

$$\left(\frac{\mathrm{A}_{\mathrm{ridge1}}|_{t_1}}{\mathrm{A}_{\mathrm{ridge2}}|_{t_2}}\right)^2=\frac{\int_{S_{\min}}^{S_{\max}} W^2|_{t=t_1}\cdot da}{\int_{S_{\min}}^{S_{\max}} W^2|_{t=t_2}\cdot da} \tag{8.7}$$

where a is the variable *scale*. Derived from the basic definition of wavelet transform (see Section 4.3.1), it yields

$$E \propto \int_{Min}^{Max} \left|W(a,b)_{b=t}\right|^2 da \tag{8.8}$$

where b is variable *time*. For two given energy components, E_1 and E_2, over the time-scale domain, at different time points, t_1 and t_2, it has

$$\frac{E_1}{E_2}=\frac{\int_{Min}^{Max}\left|W(a,b)_{b=t_1}\right|^2 da}{\int_{Min}^{Max}\left|W(a,b)_{b=t_2}\right|^2 da} \tag{8.9}$$

On the other hand, the energy ratio can also be expressed by [Picinbono, 1988]

$$\frac{E_{t=t_1}}{E_{t=t_2}} = \frac{|f_1(t)|^2{}_{t_1}}{|f_2(t)|^2{}_{t_2}} \tag{8.10}$$

where $f(t)$ represents the acquired signal. Combining Equations (8.9) and (8.10), the energy ratio for two wave components, at specific time points, t_1 and t_2 respectively, is derived

$$\frac{E_{t=t_1}}{E_{t=t_2}} = \frac{\int_{Min}^{Max} |W(a,b)_{b=t_1}|^2 da}{\int_{Min}^{Max} |W(a,b)_{b=t_2}|^2 da} = \frac{|f_1(t)|^2{}_{t_1}}{|f_2(t)|^2{}_{t_2}} \tag{8.11}$$

Compared with Equation (8.7), the reflection ratio, Ref , can be therefore achieved

$$\text{Ref} = \frac{|f(t_1)|}{|f(t_2)|} = \left| \left(\frac{\text{A}_{\text{ridge1}}|_{t_1}}{\text{A}_{\text{ridge2}}|_{t_2}} \right) \right| \tag{8.12}$$

Determination of Crack Depth

Equation (8.12) indicates that the reflection ratio, Ref , is equivalent to the RMS ratio of their related continuous wavelet coefficients along the scale axis at the time points, corresponding to the maximum energy concentration in the time-scale domain. Based on this, the depth of the crack can be calibrated in terms of Figure 8.2 by interpolating the RMS ratio experimentally obtained from an unknown damage case.

8.3.3 Experimental Implementation

The AO-SHD system is employed to obtain RMS values for unknown damage cases. A defective aluminum alloy beam (cross-section: *10mm* × *10mm*, Young's modulus: *72.4GPa*, density: *2.69g/cm*^{3}) with fixed ends, is considered, as in Figure 8.3. A transverse crack across the entire width of the beam with a *0.15mm* span along the

beam axis, is created using a diamond saw. The damage depth, H_d, increases from *1* to *8mm* with a step of *1 mm*, simulating crack growth.

In the majority of existing studies, either relatively complicated excitation sources, such as laser-based ultrasonic (LBU), or imprecise hand operations were adopted for generation of the diagnostic signal. For this simple case, a pendulum force hammer, controlled by the signal generation subsystem (SGS) in the AO-SHD system, is used as the excitation source to generate an impact energy at a constant level of *0.4J*. A piezoceramic disk (*20mm* × *10mm* × *1mm*, *PI® 151*), with the properties summarised in Table 7.1, is chosen as the sensor and surface-mounted on the beam with silver-epoxy adhesive (*Farnell®*). Signal acquisition is performed via DAS at a sample rate of *20.48 MHz*.

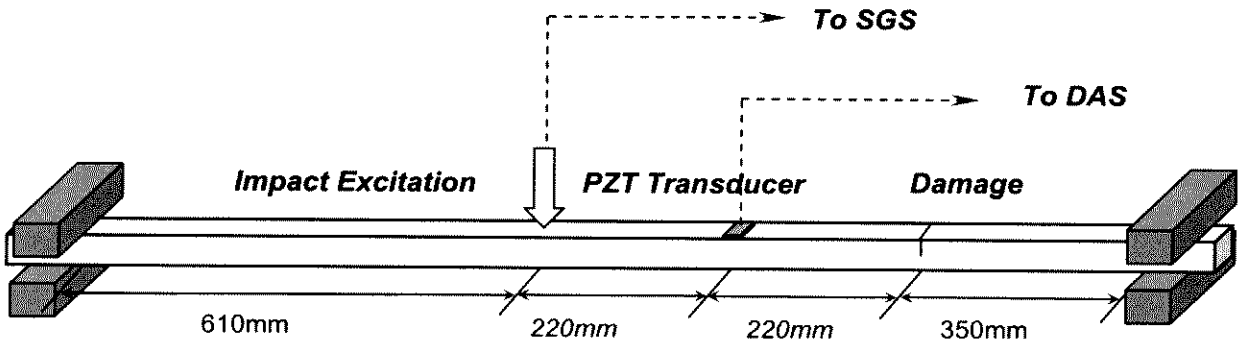

Figure 8.3 Experiment setup

As mentioned in Chapter 3, under imperfect transverse excitation, longitudinal and transverse wave modes exist simultaneously. The propagating velocities for each possible mode are therefore required. In this case, velocities for the longitudinal and transverse waves in aluminum alloy are measured using a multi-point PZT sensor architecture (see Figure 8.4), and processed by SPP. The average velocities measured experimentally and calculated theoretically are compared in Table 8.1.

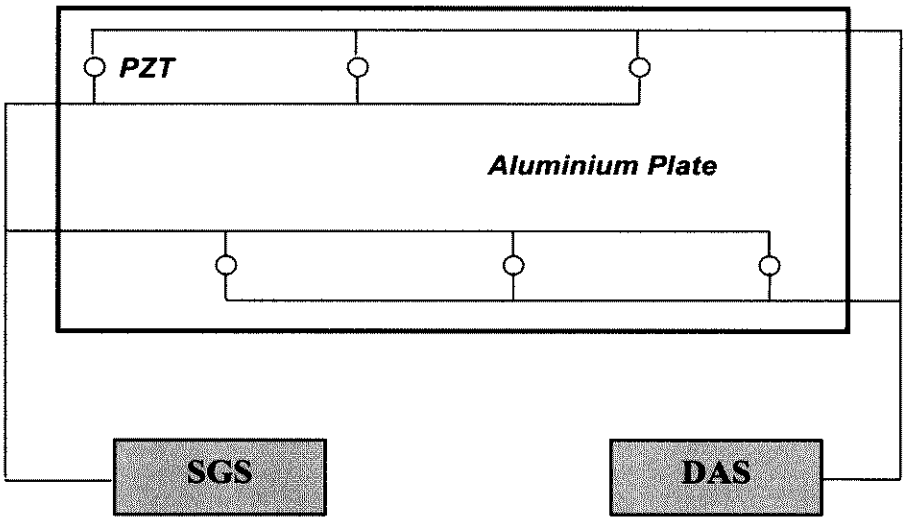

Figure 8.4 Multi-point PZT sensor network for wave velocity measurement

Table 8.1 Wave velocities in aluminium alloy

Wave Mode	Measured (*m/s*)	Calculated* (*m/s*)
Longitudinal Wave	6365	6314
Transverse Wave	3205	3180

$$* \; c_L = \sqrt{\frac{E}{\rho}} \cdot \sqrt{\frac{1-\mu}{(1+\mu)\cdot(1-2\mu)}}, \; c_T = \sqrt{\frac{E}{\rho}} \cdot \sqrt{\frac{1}{2(1+\mu)}}$$

8.3.4 Signal Processing and Interpretation

Inevitably, introduction of impact excitation comes at the cost of rich responses scattered in a wide frequency scope. The signals for different damage severities are sampled experimentally. As typical examples, the acquired wave signals for *4mm* and *6mm*-depth cracks, and their corresponding frequency spectra are shown in Figures 8.5 and 8.6, respectively.

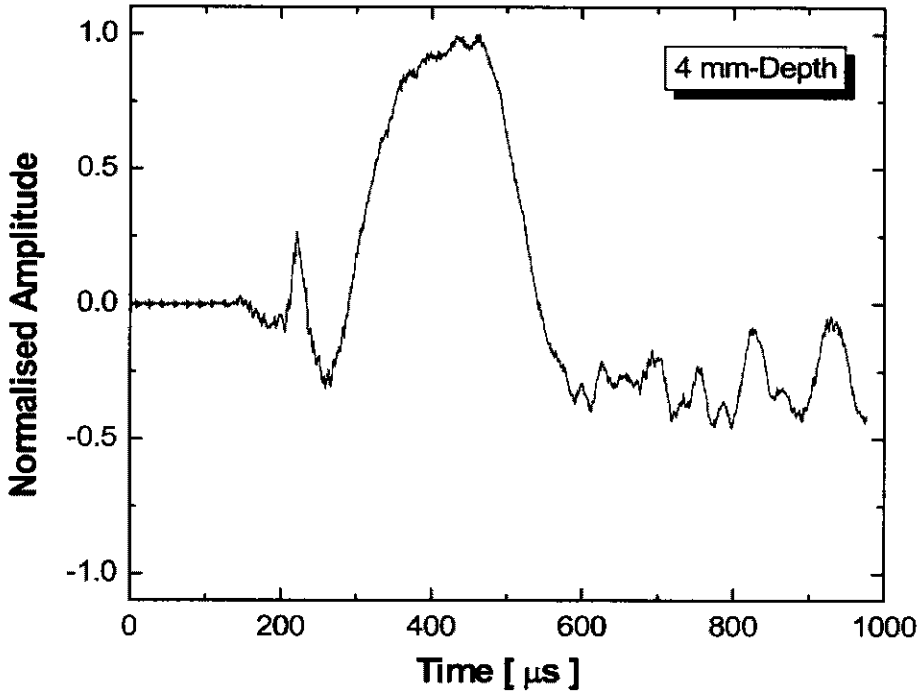

(a)

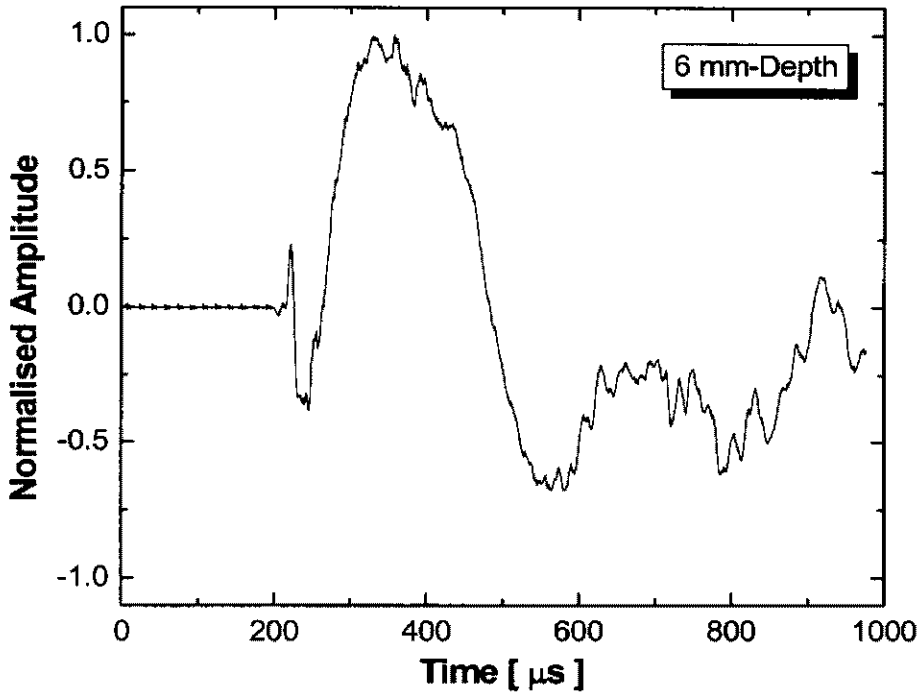

(b)

Figure 8.5 Raw wave signals for (a) *4mm* crack; (b) *6mm* crack

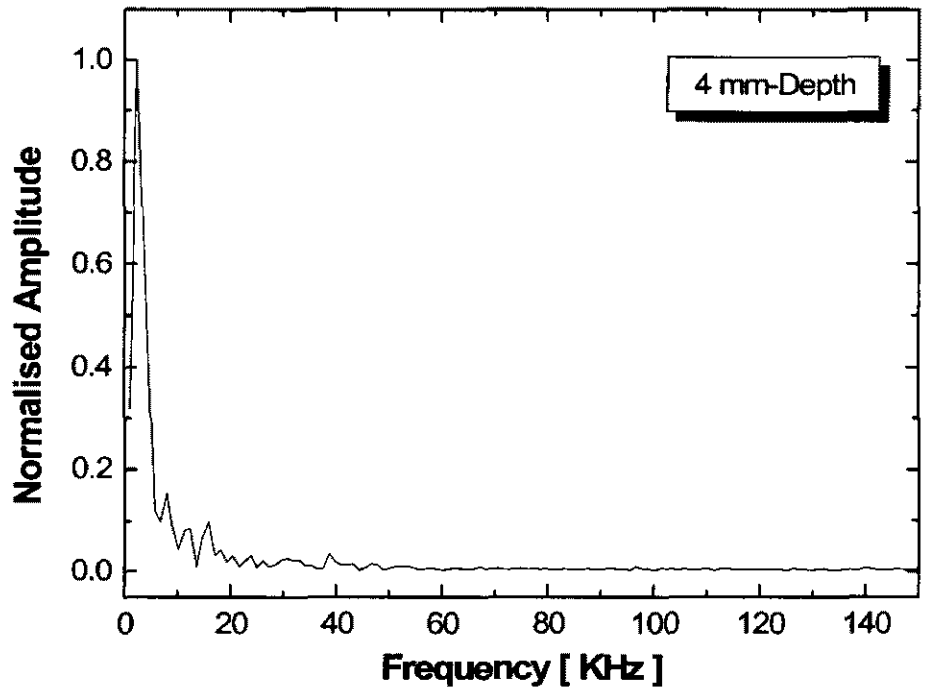

(a)

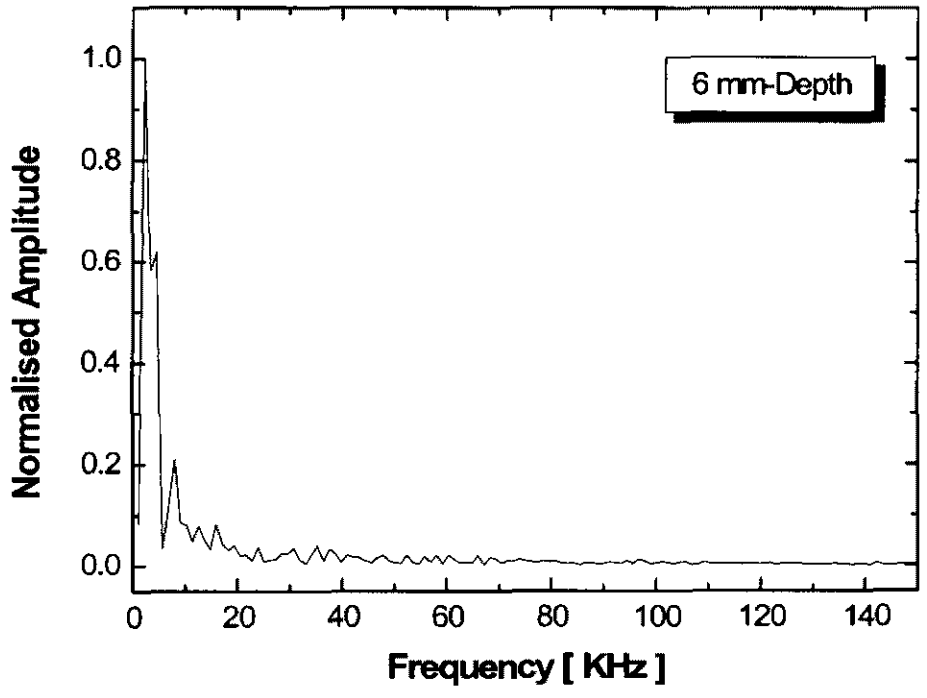

(b)

Figure 8.6 FFT spectra of signals in Figure 8.5 for (a) *4mm* crack; (b) *6mm* crack

Differences are noticed between the signals under different damage severities, but neither is sufficiently clear for accurate diagnosis, because of interference by low-frequency structural vibration and various noise.

Simple beam theory [Gere, 2002] is preliminarily used to calculate the first several order structural eigen-frequencies, so that disturbance from structural natural vibration can be filtered. Applied with frequency bandpass filters in the SPP, where *Daubechies* function, $\Psi(a,b)$, at level *4* (*db4*) is chosen as the wavelet transform function, purified stress wave components for *4mm*-depth crack, as a paradigm, from levels *1* to *10*, and the distribution of DWT coefficients are displayed in Figures 8.7(a) and (b), respectively, where the grayscale indicates wave energy density. The darker the grayscale appears, the stronger the wave energy is. Obvious energy concentration can be noticed clearly from level *5*, while at level *8* the spectrogram exhibits major impact energy.

The filtered signals at level *8* (*db4-8*) for selected damage cases are displayed in Figure 8.8. The first wave peak originates from the incident energy (transverse wave), followed by the first reflected wave due to the crack as well as other reflected components from left/right boundaries and multi-reflected waves from the damage. The time lags among the related wave component peaks are then captured to locate the crack.

2-D and *3*-D energy spectra are achieved by SPP, respectively displayed in Figure 8.9 and Figure 8.10 for selected signals, where damage-induced extra energy is detected between the incident energy and first reflected energy from the boundary. In the experiment, stronger energy reflection from the crack is noticed as the crack size increases because of expansion of the valid reflection area.

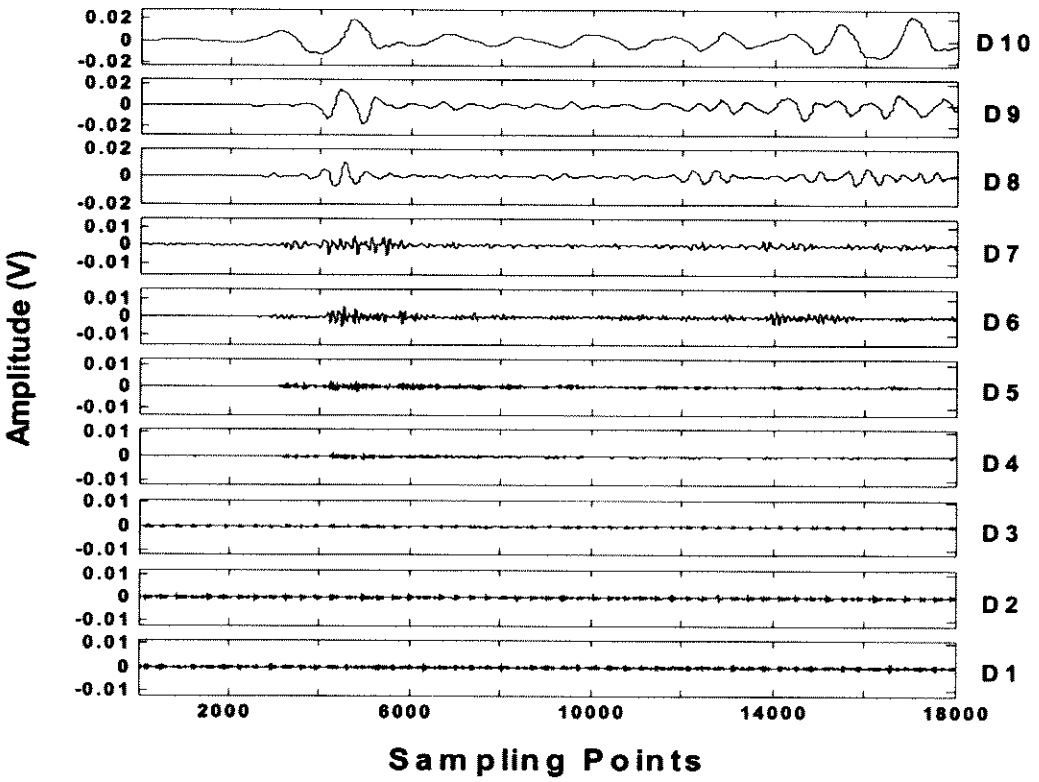

(a)

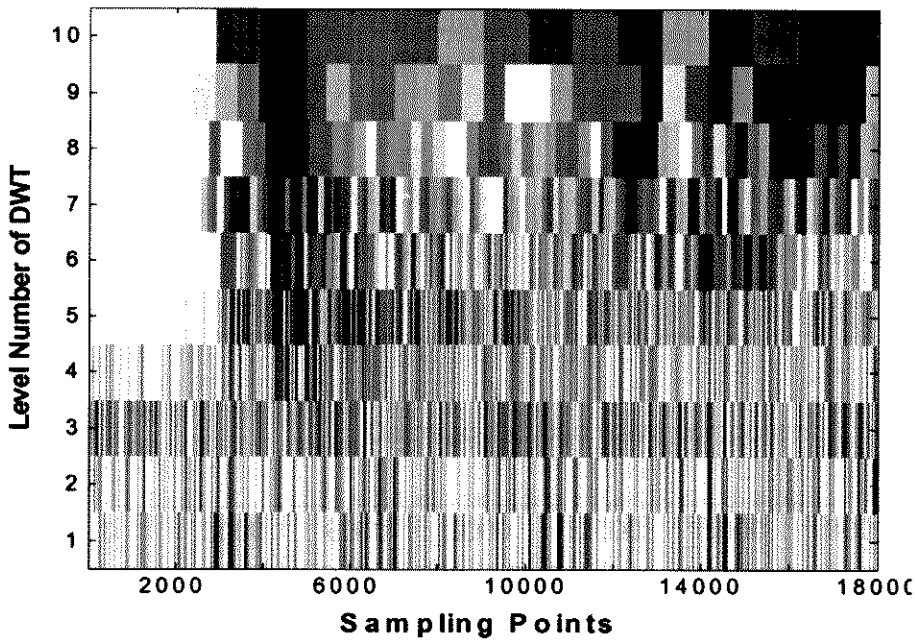

(b)

Figure 8.7 DWT analysis for *4mm*-depth crack: (a) details from levels *1* to *10*; (b) distribution of DWT coefficients

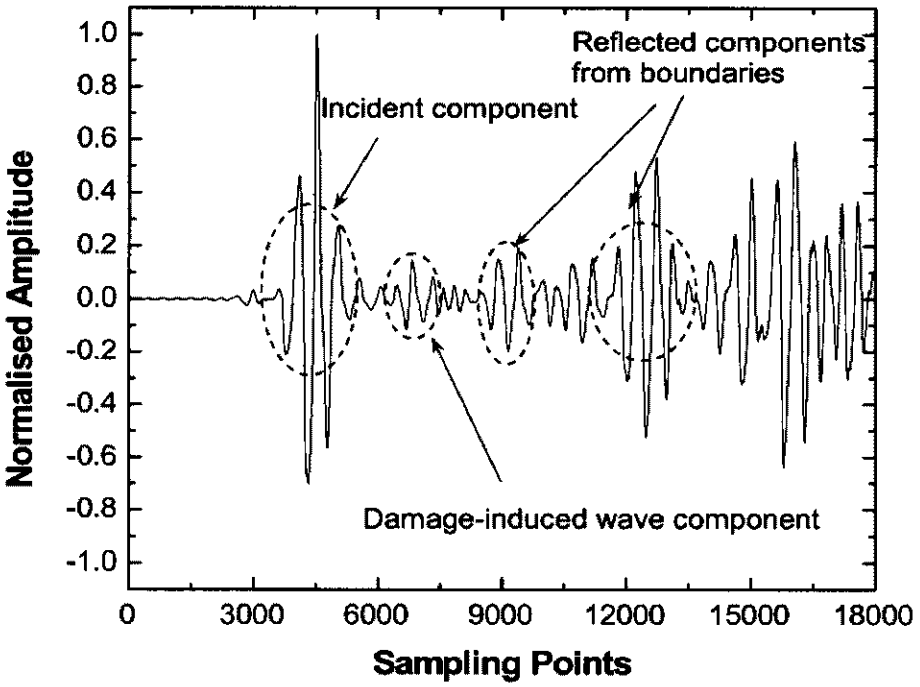

(a)

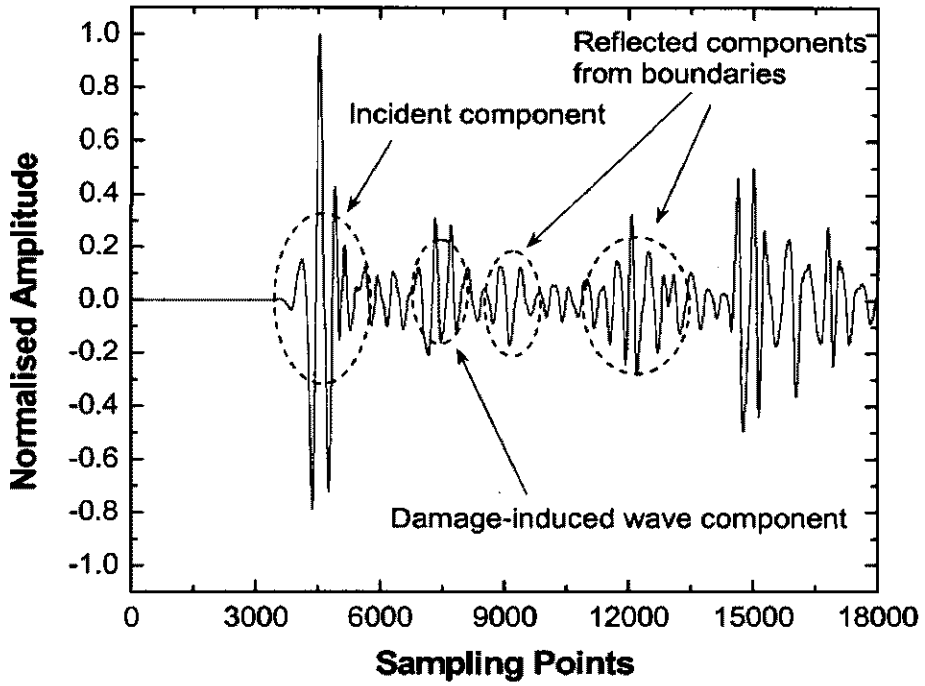

(b)

Figure 8.8 Filtered signal component at level *8* for (a) *4mm* crack; (b) *6mm* crack

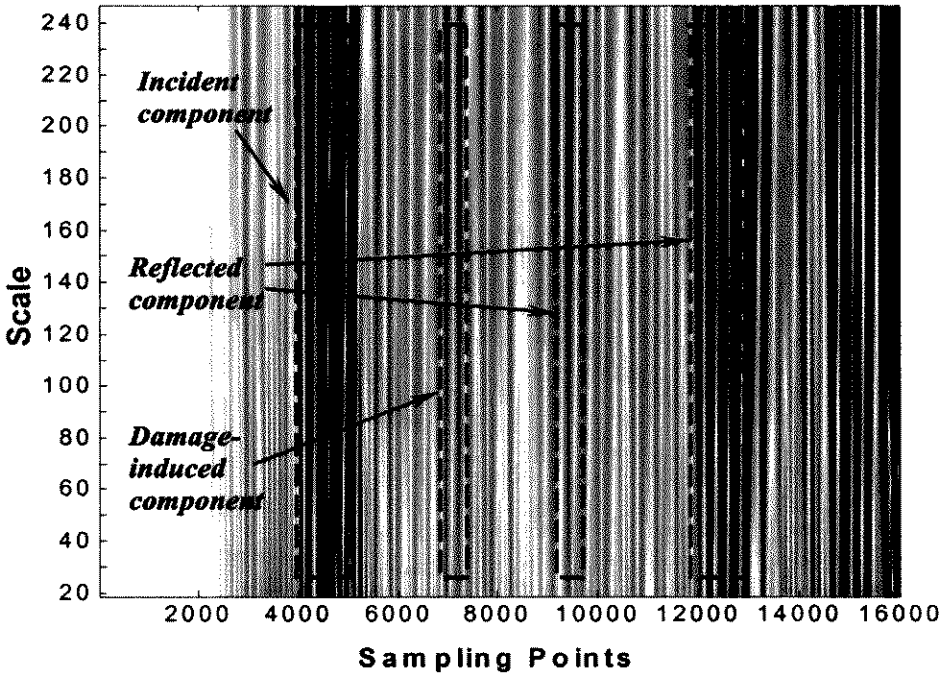

(a)

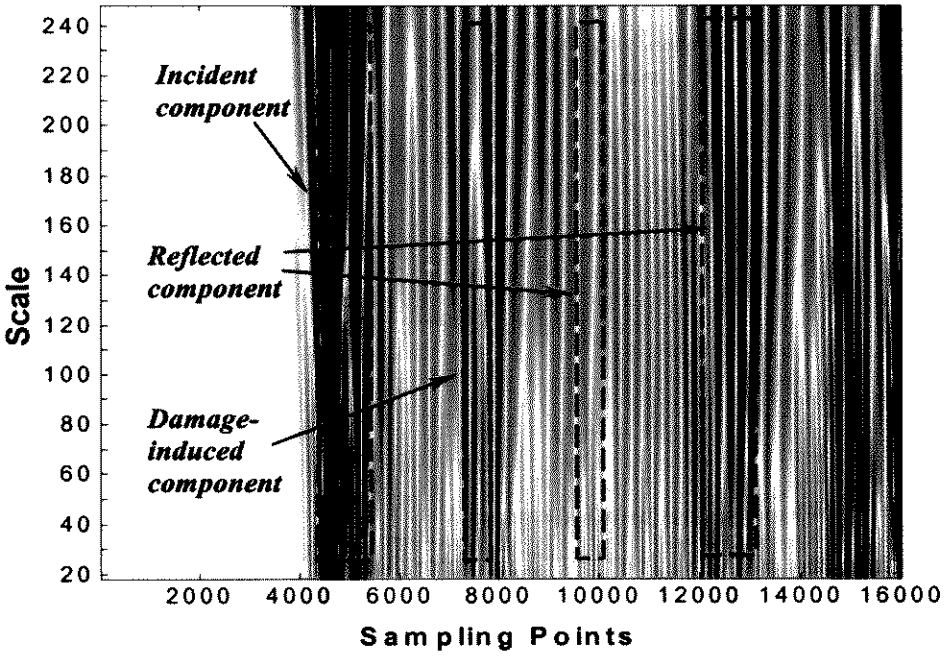

(b)

Figure 8.9 *2*-D energy spectra for (a) *4mm* crack; (b) *6mm* crack

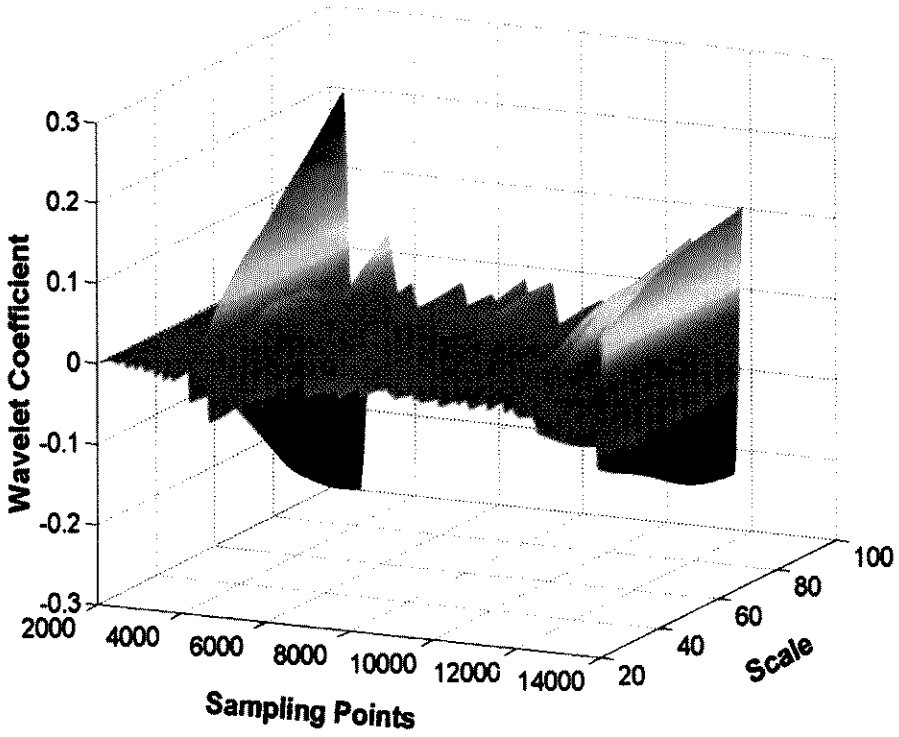

(a)

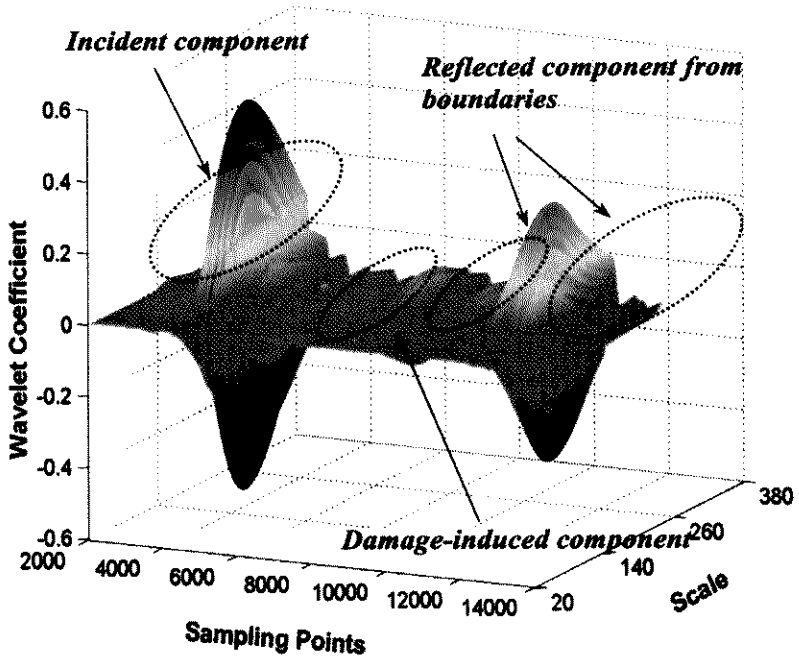

(b)

Figure 8.10 *3*-D energy spectra for (a) *4mm* crack; (b) partial magnification of (a); (c) *6mm* crack; (d) partial magnification of (c)

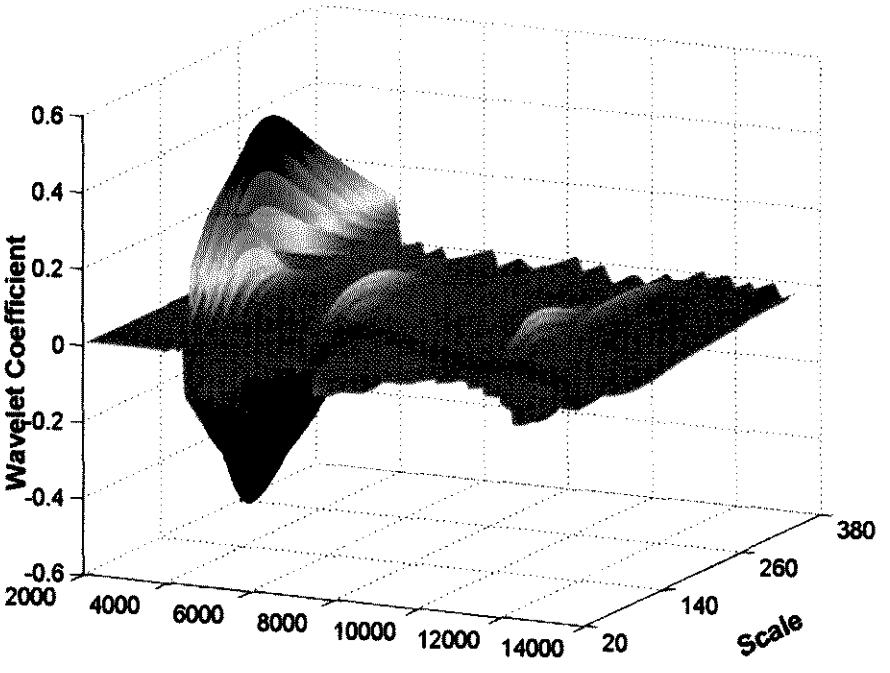

(c)

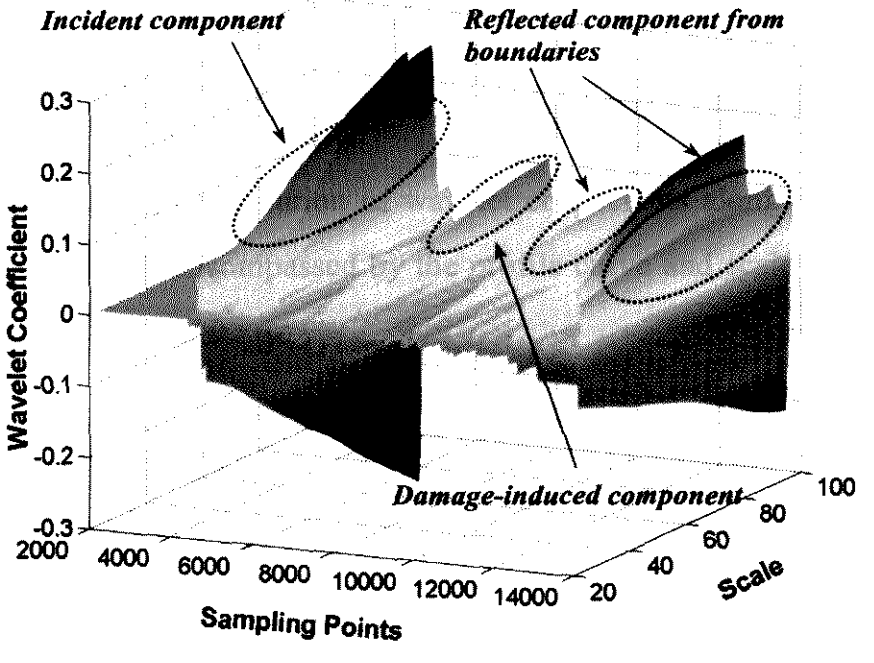

(d)

Figure 8.10 *Cont.*

8.3.5 Damage Diagnosis

Ridges of incident energy and reflected-energy from the *4mm* to *6mm*-depth crack in the spectra at *characteristic points* (see Section 4.4.2) are anatomised along the scale axis, and compared in Figure 8.11.

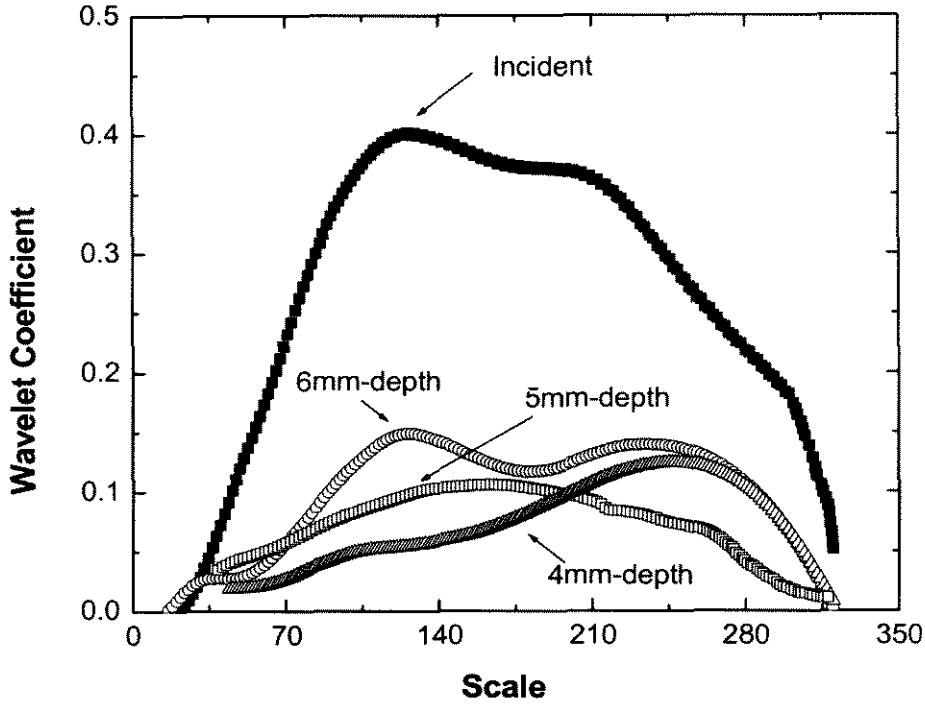

Figure 8.11 Profile curves of CWT coefficients under different degrees of damage

In this figure, a crestiform distribution of wavelet coefficients along the scale axis can be observed. The area encompassed by the profile curve and scale axis expands with an increase in crack length.

Equation (8.12) demonstrates that the RMS ratio of wavelet coefficients for incident energy to damage-induced energy in the profile curves is equivalent to the reflection coefficient. Based on this observation, two approaches are employed to calculate the reflection coefficient, namely the RMS method and the integration method [Kim and Kim, 2000; Wolfram, 1999]. Furthermore, damage severity can be determined by interpolating the calculated reflection ratio in Figure 8.2. Diagnostic results for several typical degrees of damage are compared with actual values in Table 8.2.

Table 8.2 Diagnostic results and estimation errors

Actual Damage Degree	Location Diagnosis (*mm*)		Degree Diagnosis (*mm*)			
	Calculated Value*	Abs. Error (%)	Calculated Value by RMS	Abs. Error (%)	Calculated Value by Integration	Abs. Error (%)
1mm	373	6.57	1.073	7.30	1.073	7.30
2mm	336	4.00	2.100	5.00	2.104	5.20
3mm	341	2.57	3.150	5.00	2.853	4.90
4mm	359	2.57	3.832	4.20	4.161	4.03
5mm	340	2.86	5.115	2.30	4.862	2.76
6mm	357	2.00	6.123	2.05	6.141	2.35
7mm	355	1.14	6.404	8.51	7.642	9.17
8mm	346	1.14	6.200	22.50	6.152	23.10

* *The actual damage position is 350mm away from the right end of the beam*

8.4 Discussion

Credibility of predictions is charted in Figure 8.12. Both Table 8.2 and Figure 8.12 indicate that the identification accuracy for crack location, regardless of the actual damage severity, is acceptable with high credibility. The precision for damage severity identification increases with crack size and maintains until the crack size approaches *6 mm* approximately (*60-70%* of the entire beam cross-section). Considerable errors occur when the crack size exceeds *65%* of the beam height. This is attributed to inapplicability of the basic hypotheses for model development in terms of simple beam theory. Under such a circumstance, the twisting effect cannot be neglected, leading to inapplicability of the continuity and compatibility conditions.

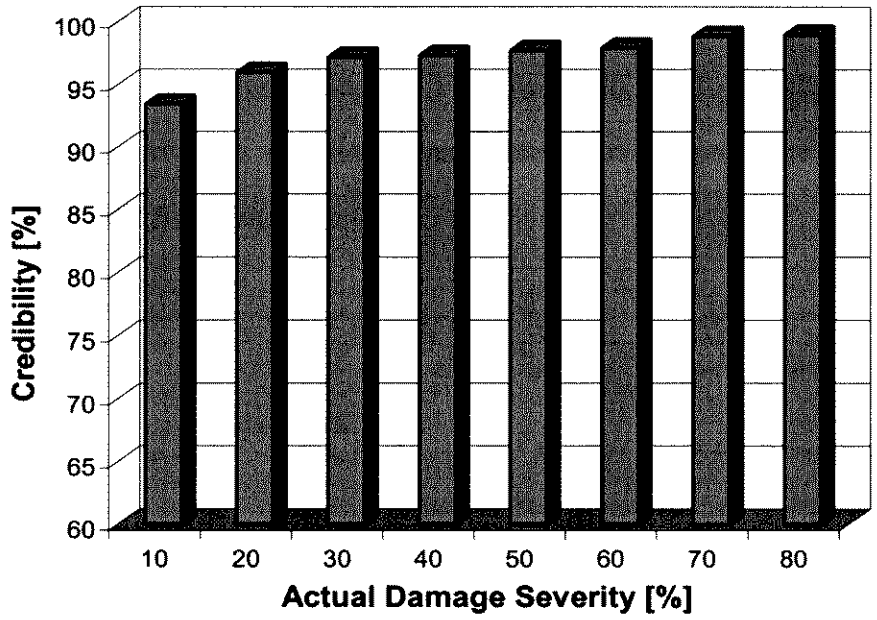

(a)

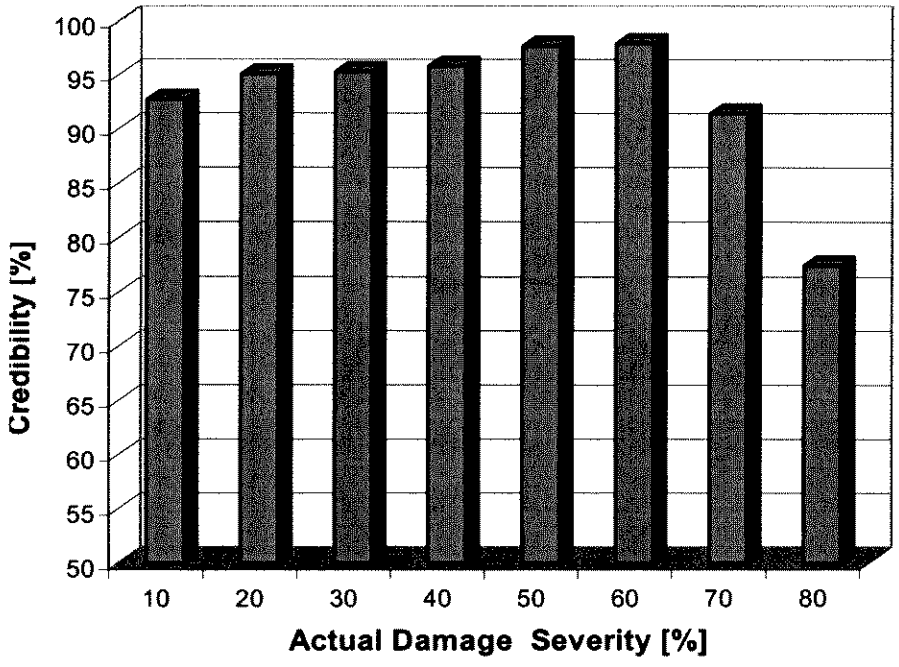

(b)

Figure 8.12 Credibility of identification for (a) damage location; (b) damage degree

In the preceding discussion, a rectangular cross-section is considered for the beam model. Since the derivation in Section 8.2 is not geometry-dependent, the model is also applicable for other shapes. For instance, the corresponding reflection coefficient derived for a circular cross-section, as shown in Figure 8.13, can be obtained by modifying Equation (8.4),

$$I_1 = \frac{\pi \cdot R^4}{4}$$

$$I_2 = \frac{1}{4}\sqrt{r^2-(R-H_d)^2}\cdot(6H_d{}^2R - 2H_d{}^3 - 5H_dR^2 + R^3)$$

$$+\frac{1}{4}r^4 \cdot \arctan\frac{(R-H_d)\sqrt{R^2-(R-H_d)^2}}{(2R-H)\cdot H} + \frac{\pi R^4}{8} \qquad \textbf{(8.13)}$$

where H_d still denotes the damage depth and R represents the radius of the circular cross-section.

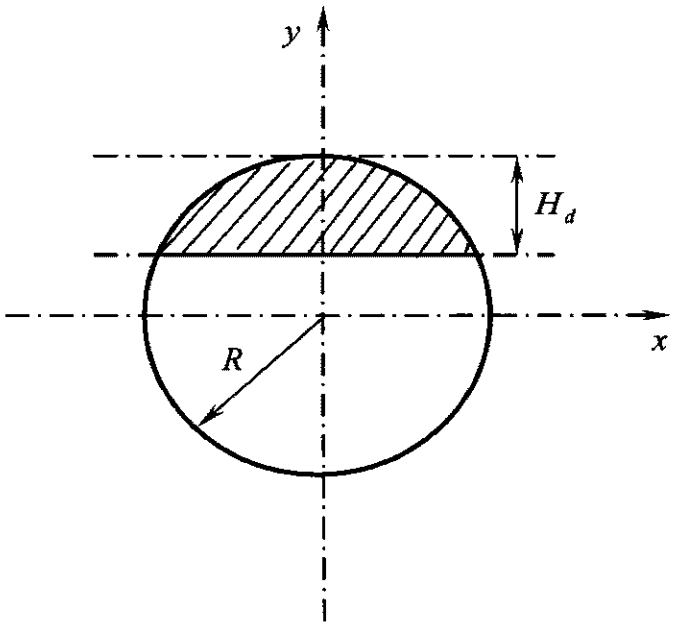

Figure 8.13 Circular cross-section (*shadow denotes the damaged area*)

It is important to maintain sufficient distance between the excitation source and structural boundaries to ensure that the damage-induced wave would not be interfered with waves reflected from boundaries. One possible solution to this concern is to reduce the frequency bandwidth of excitation energy. For an accurate damage diagnosis, based on the wave velocity and the maximum sampling rate of the AO-SHD system, the minimum distance between signal excitation source and PZT sensor, and the distance between PZT sensor and crack should be no less than *200 mm* for the current structure.

8.5 Concluding Remarks

The performance of the proposed damage identification scheme and configured AO-SHD system are evaluated by quantitatively assessing a crack with an increasing depth in an aluminum alloy structural beam, in correlation with impact response analysis.

A simple and controllable impact excitation source is adopted for the generation of diagnostic stress waves. The accompanying broadband interference from impact excitation is effectively suppressed by the SPP. The sensitivity of the identification algorithm is evaluated, and results indicate that identification accuracy depends on the actual severity of the damage. Unacceptable error occurs only when the damage is very severe (over *65%* of the cross-section area of the beam). Such a large scale of destruction is not normally of interest to structural health monitoring. For SHM purposes, the developed method and system work well.

Chapter 9

Identification of Through-Hole in CF/EP Composite Laminate

9.1 Introduction

Let us return to the *Columbia* tragedy cited in Chapter 1. Investigation [NASA-CAIB, 2003] revealed that its disassembly was directly attributable to a through-hole occurring in the leading edge (carbon-carbon composites) of the left wing, induced by the impact of a flying foam block during launching. Actually, composite structures used in aircraft are normally susceptible to unexpected flying objects during their flight, e.g. stone, hail, bird, potentially leading to through-hole type damage. This type of damage interrupts the structural geometry and weight-carrying pathway, and accordingly reduces the strength, stiffness and system stability. Although they are visible, quick or online detection for the sudden appearance of through-holes is yet not an easy process for in-service composite structures.

Pardo De Vera and Guemes [1998] identified the change in structural frequency with the occurrence of through-hole type damage, which was then applied to the detection of a hole in piezoelectrics-embedded glass/epoxy composites. Culshaw *et al* [1998] established a relationship between hole size and reflection coefficients using an optical fibre detector. Kishore *et al* [2000] developed a FEM model to simulate the scattering of a Lamb wave by a hole. Ghosh *et al* [1998] configured a water-coupled probe setup to detect vertical and horizontal holes in large aluminium plate, and

concluded that symmetric Lamb mode S_0 is more sensitive than anti-symmetric mode A_0 for hole type damage. Hwu and Liang [1998, 2001] quantitatively defined the holes existing in a composite plate based on measured static strains, and further expanded their method to holes with different geometries, such as square or triangle.

In this chapter, quantitative assessment for through-hole type damage in quasi-isotropic CF/EP composite laminates is conducted, serving as the second case study to validate the proposed damage identification technique and AO-SHD system.

9.2 Development of Damage Parameters Database (DPD)

In this study, full-scale three-dimensional FEM simulation is employed for the development of a damage parameters database (DPD).

9.2.1 Modelling of Composite Laminate with Hole

8-ply quasi-isotropic CF/EP (T650/F584) composite laminates in a stacking sequence of $[45/-45/0/90]_s$, measuring *475mm* × *475mm* × *1.275mm* and with a pair of clamped opposite edges, are considered. As an illustration, one such laminate is schematically depicted in Figure 9.1. Four standard sensor units (SSUs), involving nine distributed circular piezoelectric discs (see Table 7.1), are used to customise an active actuator/sensor network, which is surface-bonded on the laminate. The sensors are *65mm* away from the neighbouring edge(s) or at the plate centre, numbered with *Pi* (i *=1, 2, ···, 9*). With regard to dual piezoelectric effects (i.e. actuating and sensing), a total of *36* actuator-sensor pairs, i.e. *72* actuator-sensor paths, are provided by such a network. For convenience of approach, the whole laminate is factitiously quartered and denoted counterclockwise by *Zone-1*, *Zone-2*, *Zone-3* and

Zone-4 from the lower left quadrant. An elliptic through-thickness hole with certain geometric identity occurs discretionarily in *Zone-3* of the laminate.

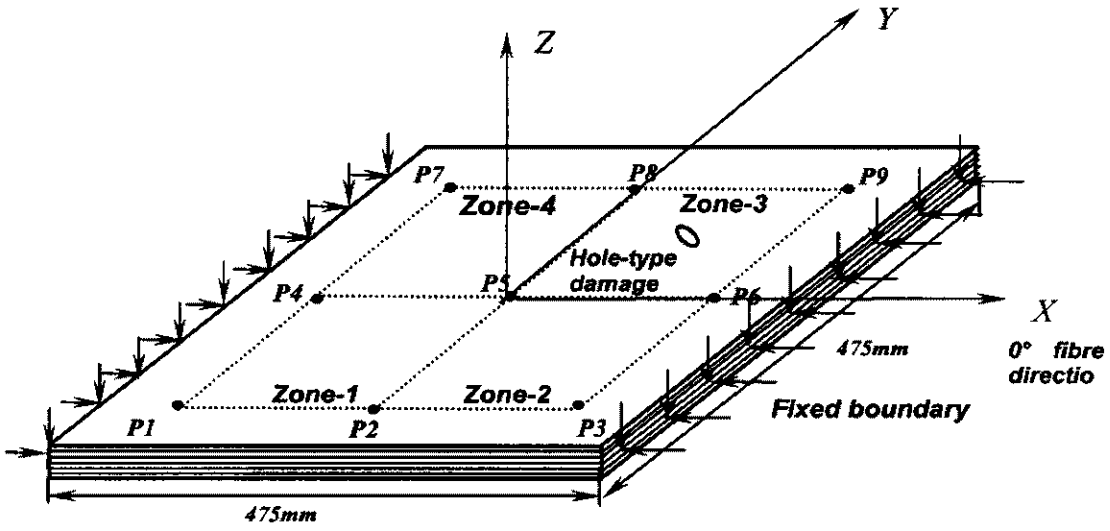

Figure 9.1 Quasi-isotropic CF/EP composite laminate with a hole-type damage

The modelling technique developed in Chapter 5 is employed. A full-scale FEM model for the selected defective laminate is created using *8*-node consolidated brick elements on the PATRAN® platform [MSC Software, 2001], whose ichnography is shown in Figure 9.2. It was found sufficient to model the laminate as an orthotropic plate by giving the overall elastic properties determined from classical laminate theory (see Section 5.3.4), assuming that the transverse shear stiffness of the laminate is close to the in-plane shear stiffness of the unidirectional ply [Diamanti *et al*, 2002]. The FEM mesh is particularly densified in the damage vicinity, where more than *10* FEM nodes are ensured to exist per Lamb wavelength.

Excitation, a *Hanning* window-modulated *5*-cycle sinusoid toneburst at a central frequency of *500KHz* (referring to Figure 7.6), is simulated by a PZT actuator model (see Section 5.3.1) as the diagnostic signal. Dynamic simulation is accomplished on a *SUN Blade® 1000* workstation platform (dual processors at *900MHz* and *2G* RAM), using the ABAQUS/EXPLICIT® FEM code. The step of calculation time is

controlled to be less than the ratio of the minimum distance of any two adjoining nodes to the maximum wave velocity, while the Lamb wave signals are acquired at a sampling rate of *20.48MHz* by the PZT sensor model (see Section 5.3.2).

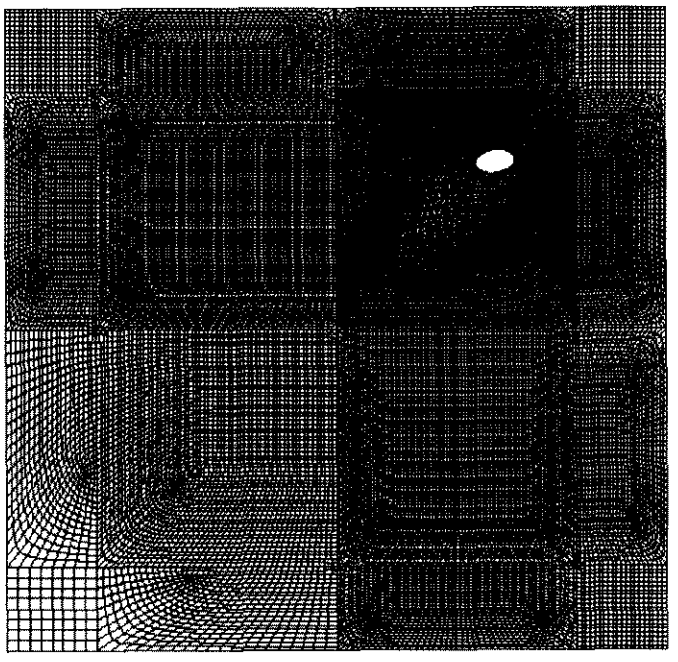

(a)

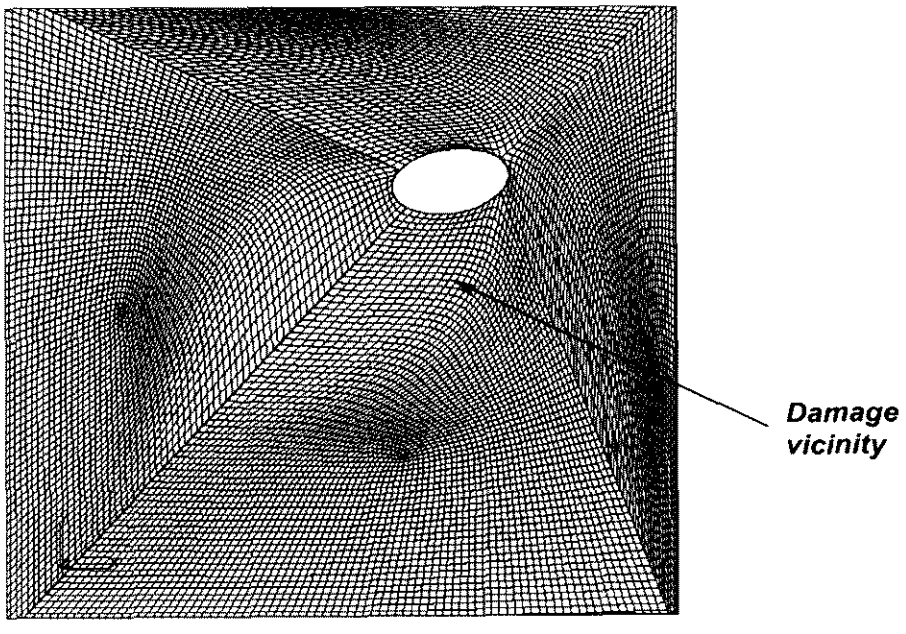

(b)

Figure 9.2 FEM model for defective laminate: (a) ichnography of model; (b) partial magnification in damage vicinity

Analogously, a variety of defective laminates, each bearing one through-hole with exclusive location and geometric identity, are individually modelled. In this procedure, the damage is selected stochastically by virtue of a subroutine in the SPP, which is programmed using a standard random function in the FORTRAN library [Microsoft, 1995]. For each damage case in *Zone-3*, only the actuator-sensor paths passing through this region, including *P2-P9/P9-P2*, *P3-P8/P8-P3*, *P4-P9/P9-P4*, *P6-P7/P7-P6* and *P5-P9/P9-P5*, *P6-P8/P8-P6*, are of interest, where propagation of Lamb waves is significantly scattered by the existence of damage.

9.2.2 Signal Processing and DDF Extraction

SPP is applied on each numerically acquired Lamb wave signal to extract *digital damage fingerprints* (DDF) for each presumed damage case. As an example, an originally acquired Lamb signal via a diagonal actuator-sensor path *P4-P8* for a typical damage case, and its DDF are displayed in Figure 9.3.

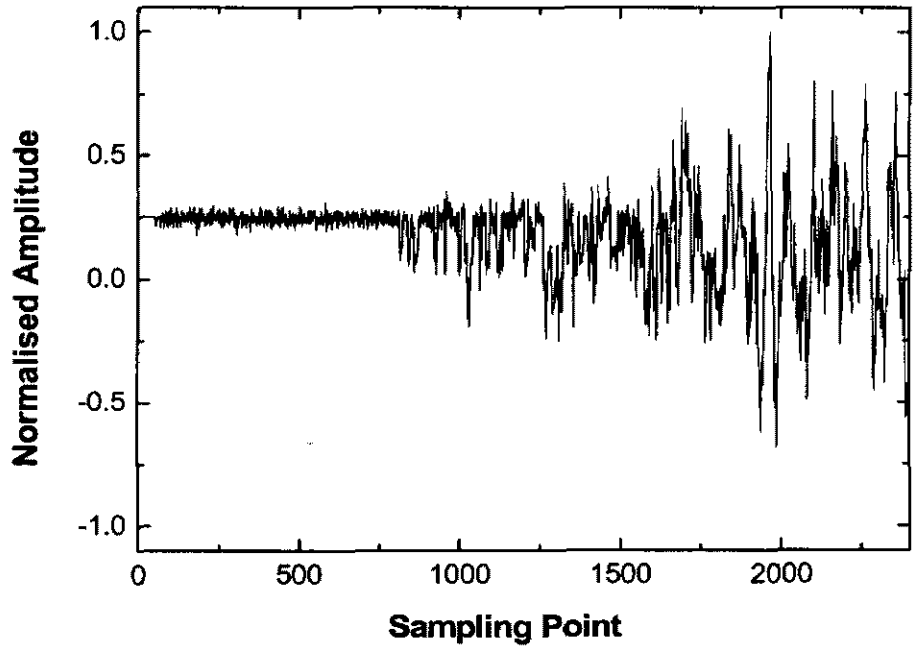

(a)

Figure 9.3 DDF extraction by SPP: (a) original Lamb wave signal; (b) DDF in time domain corresponding to excitation frequency range; (c) DDF in time-scale domain

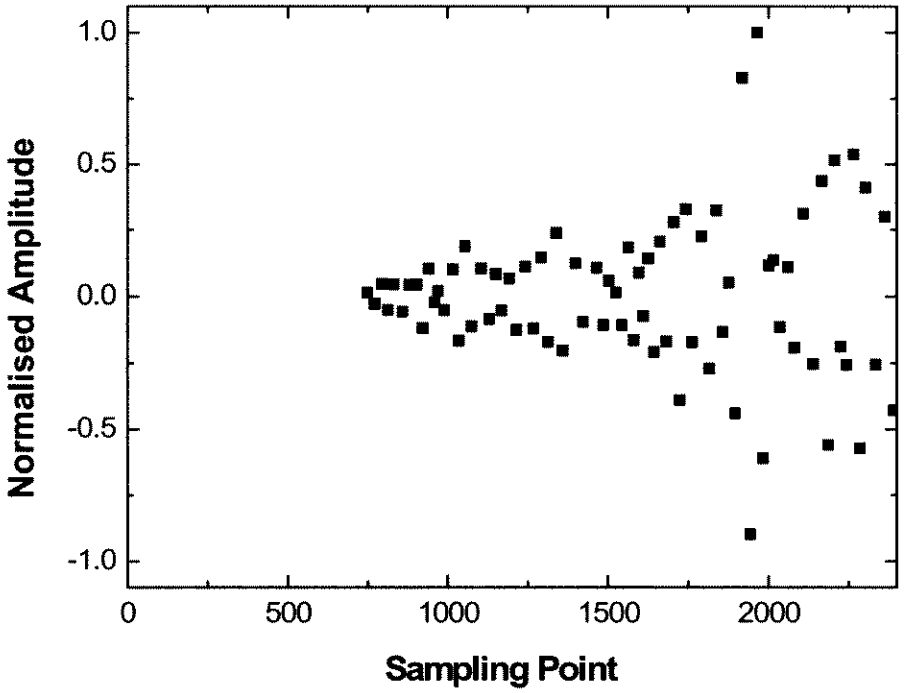

(b)

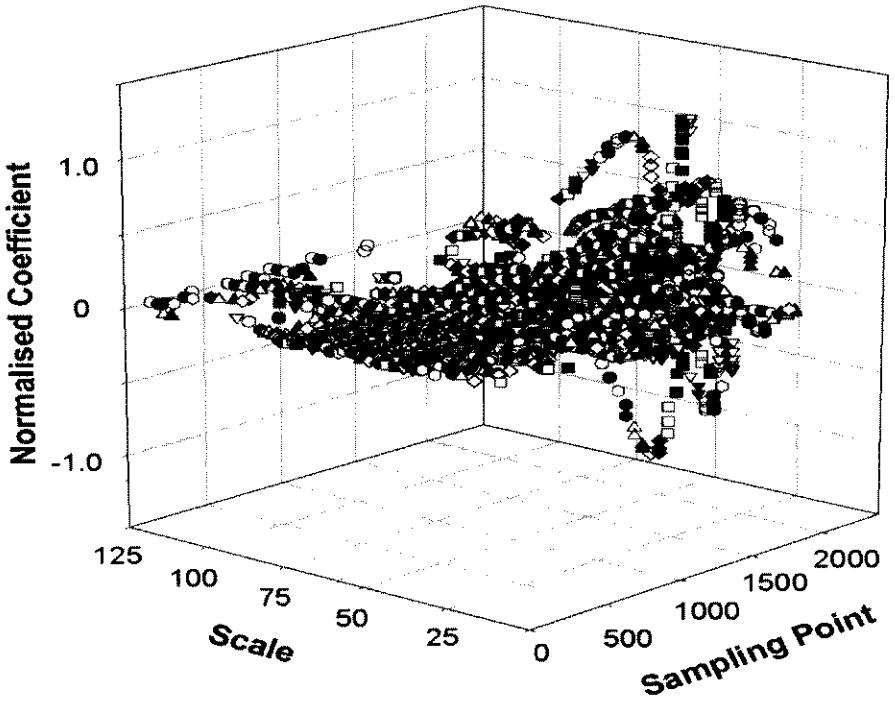

(c)

Figure 9.3 *Cont.*

9.2.3 Construction of DPD

Symmetric geometry is applicable. For simplification and without losing generality, all the damages cases are confined in the region *Zone-3*, for database development. Up to *120* damage cases, selected by the random function in SPP, are assumed in *Zone-3*. Containing the extracted DDF for all the actuator-sensor paths concerned under all the presumed damage cases, the DPD is constructed.

The information mapping unit in the SPP is invoked to figure out the DDF in other quadrants, to avoid reduplicative modelling and analyses while not sacrificing the amount of information that could possibly be acquired. In this step, the available DDF for *Zone-3* are symmetrically mirrored into other quadrants, with regard to the horizontal and longitudinal axes of the coordinate system. Four parallel sub-databases hosting the relevant DDF, respectively pertaining to four zones, are created. It is worth emphasising that adoption of the mapping technique for this case is guaranteed by the dense damages assumed and the structural symmetry.

9.3 Customisation and Training of ANN

The ANN designed in Section 6.4 is customised. A feedforward neural network with *4*-layer architecture is established, including an input layer, two neural processing layers respectively possessing *36* and *14* neurons, and an output layer (see Figure 6.5).

Following the DDF extraction criteria (Section 4.4.2), *900* and *1800* DDF in the time and time-frequency domains, respectively, are extracted for each simulated damage case. An accompanying *target vector* is established with *6* damage indices, i.e. damage presence (*0/1*), central position (ξ, ζ), semi-major/minor axis (α / β), and orientation (ϕ). All the variables in the ANN are normalised. *120* damage cases in

Zone-3 lead to *120* sets of DDF and relevant target vectors. Hosted in the DPD, these DDF are then used to train the ANN.

A *Supervised* training algorithm (Section 6.3) is adopted, and the network training is fulfilled on a PC platform (Pentium® *IV 1.6GHZ/512M*). Training convergence is monitored in real-time to calibrate network performance ($MSE = 1 \times 10^{-10}$ in this study) as shown in Figure 9.4. An exponentially accelerated improvement in convergence is obvious with an increase in iteration at the initial training stage, indicating the prompt approach of the network outputs to the anticipated targets. Although a slight instability may occur locally, as shown partially in Figure 9.4(b), successive amendment occurs. Subdued convergence is sustained in spite of an increase of iteration after *250,000*, implying that the network training reaches stabilisation.

9.4 Validation

9.4.1 Specimen Preparation

Three $[45/-45/0/90]_s$ quasi-isotropic laminates (*475mm* × *475mm* × *1.275mm*) are fabricated using CF/EP (T650/F584) unidirectional (UD) prepreg in an autoclave at a curing temperature of *180°*. Through-hole type defects, as shown in Table 9.1, are introduced in each laminate using a solid carbide helical router [Jahanmir *et al*, 1999], symbolised by $SP1^{\#}$, $SP2^{\#}$ and $SP3^{\#}$, respectively. The laminates are fabricated with the same boundary conditions, consistent with the FEM simulation.

9.4.2 Customisation of Active Actuator/Sensor Network

An active actuator/sensor network with four SSUs is configured based on the concept of *standard sensor unit* (SSU), and instrumented with the AO-SHD system (see Figure 9.5). The tailored actuator/sensor network is able to offer *72* actuator-sensor

paths, though for the current structural geometry some of them are unexploitable. In the network, only *8* PZTs are energised, where the PZT disk located furthest from the defective zone is not considered because of its minimal contribution to damage identification.

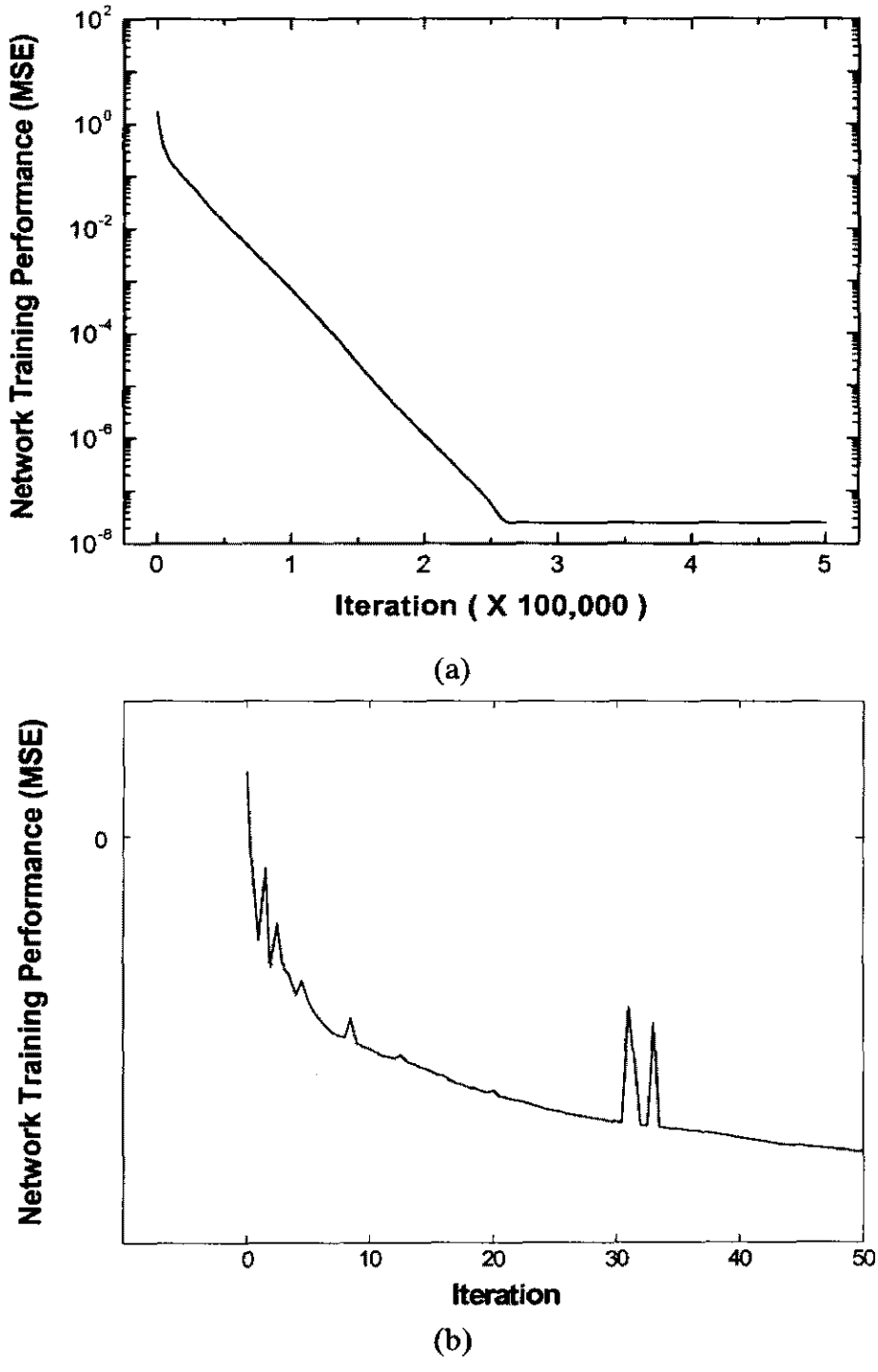

Figure 9.4 ANN training: (a) convergence history; (b) initial training stage

Table 9.1 Configuration of specimens

(unit: *mm*)

Specimen No.	Geometric Dimension	Damage Indices					
		To Left[1]	To Btm.[2]	Major Axis	Minor Axis	Orit. (°)[3]	Zone
SP1#	475 × 475 × 1.275	269	192	17	11	175	2
SP2#	475 × 475 × 1.275	172	272	19	12	135	4
SP3#	475 × 475 × 1.275	330	353	25	18	40	3

1. Vertical distance to the left edge from the centre of damage (mm)
2. Vertical distance to the bottom edge from the centre of damage (mm)
3. Included angle between major axis and 0° fibre (°)

9.4.3 Damage Diagnosis

The damage locating technique, preliminarily developed in Section 5.6, is invoked to find the zone where the actual damage exists, and thus the DPD exclusively for this zone can be used to provide detailed damage identification.

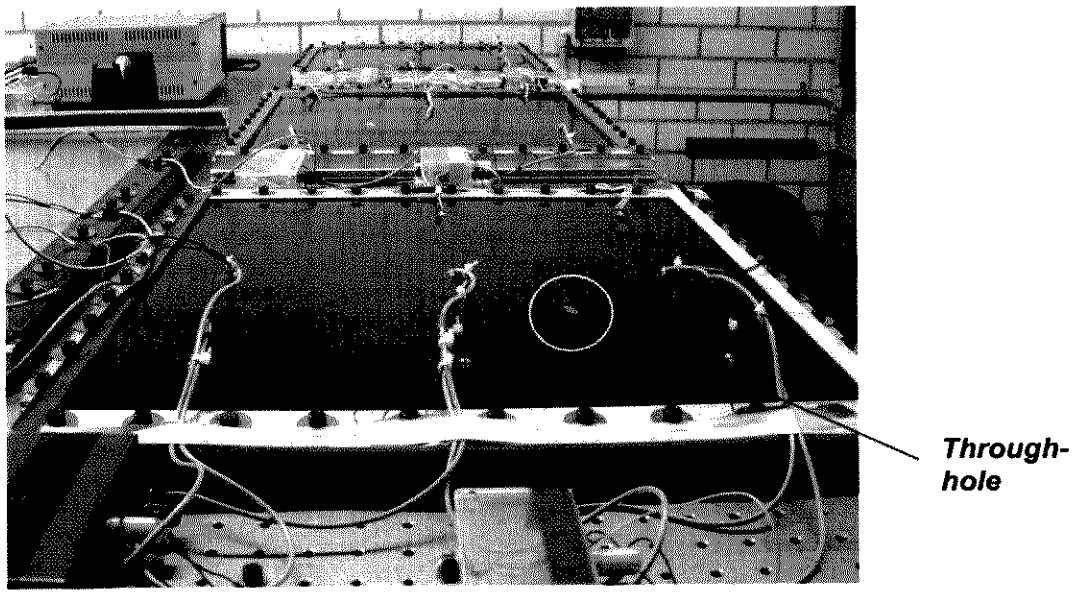

Figure 9.5 Instrumented specimen (quasi-isotropic CF/EP laminate) with active sensor network

Lamb wave propagation is monitored in real-time by the AO-SHD system via the actuator-sensor paths concerned, under the same excitation condition and sampling rate as in the DPD development. Using the SPP, DDF are extracted for each signal and fed into the CCAS (see Section 7.2.5) to perform online quantitative damage assessment. As a representative example, the diagnosis results for specimen *SP3#* are compared with the actual damage in Figure 9.6. The complete identification results for specimens *SP1-3#*, based on the DDF extracted from *100* damage patterns among a total of *120*, are summarised in Table 9.2.

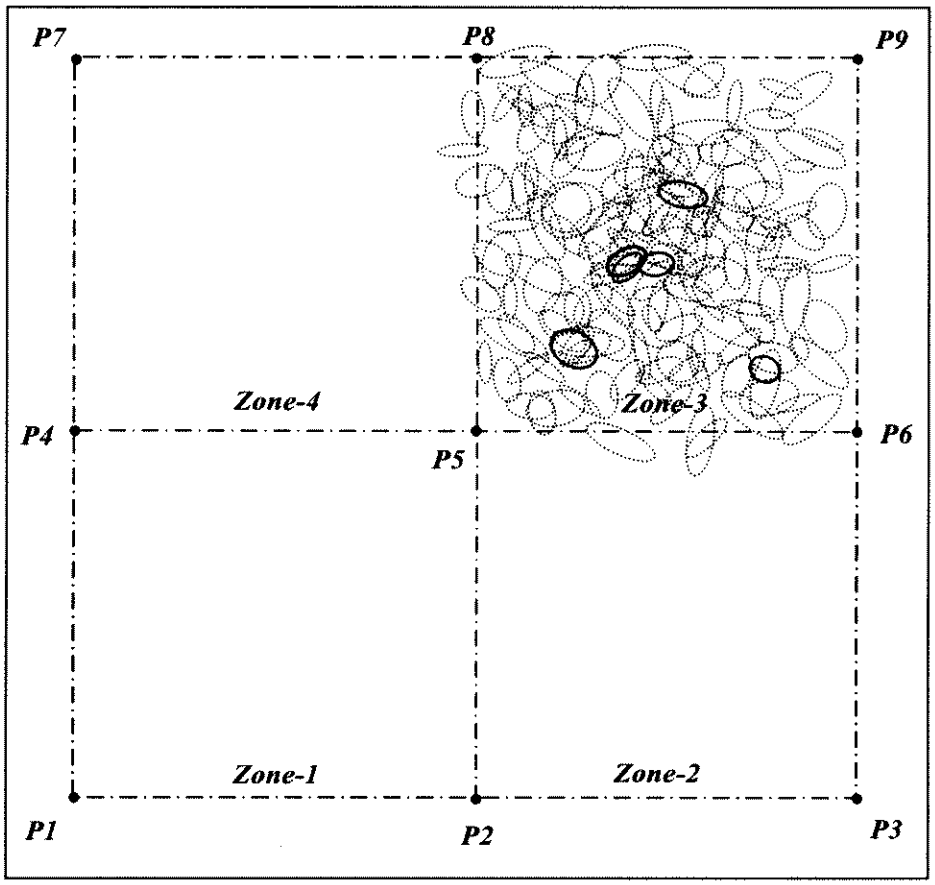

ANN basic configuration: 2 neural processing layers with 36 and 14 neurons, respectively
PZT network: 8 energised PZT transducers; Training function: scaled conjugate gradient (SCG)-based backpropagation

(a)

Figure 9.6 Diagnostic results from ANN trained with DDP: (a) whole laminate of *SP3#*; (b) partial magnification of *Zone-3*

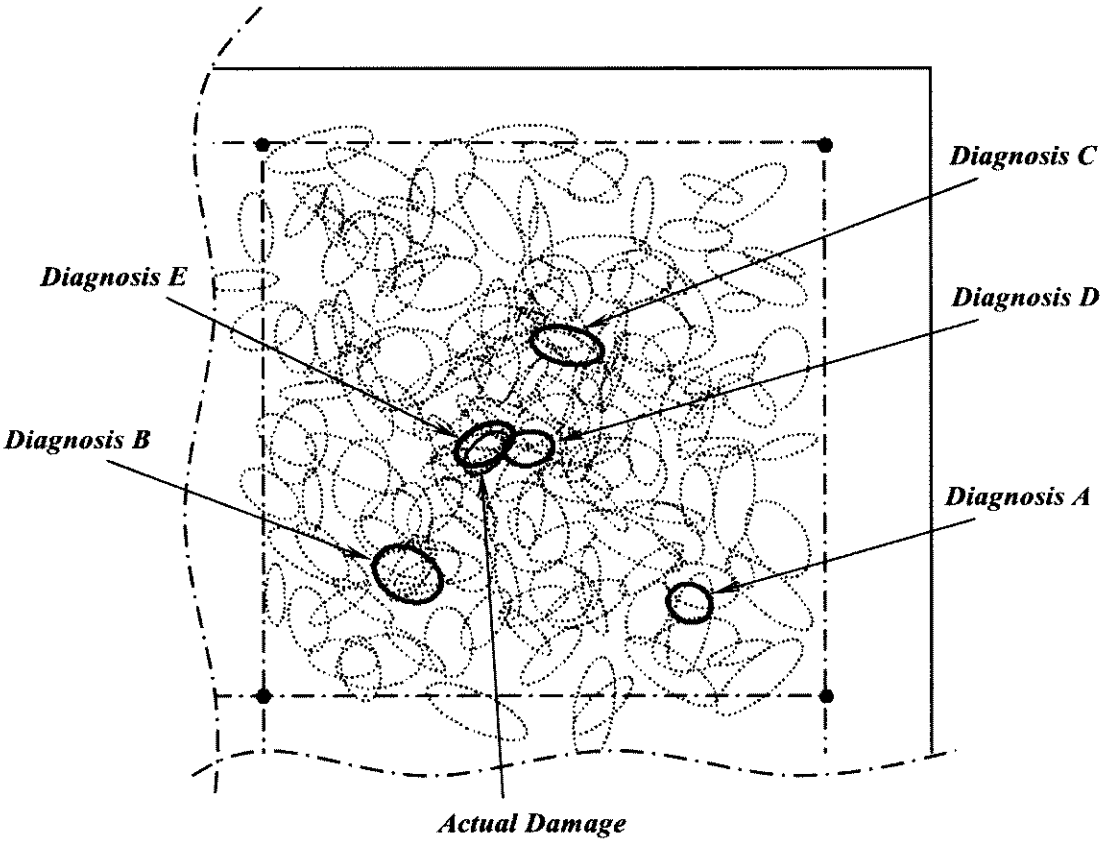

Diagnosis A/B/C/D/E: Identification using 20/30/40/60/80 damage patterns for sub-database training

(b)

Figure 9.6 *Cont.*

Table 9.2 Diagnostic results

Specimen No.	Absolute Estimation Errors (%)		
	(ξ, ζ)	(α, β)	ϕ
SP1#	(5.7, 3.2)	(6.0, 5.0)	8.5
SP2#	(4.7, 5.2)	(6.1, 4.8)	5.5
SP3#	(5.0, 3.7)	(2.8, 3.5)	4.1

ξ : $x-$coordinate of damage centre; ζ : $y-$coordinate of damage centre;
α : semi-major axis (mm); β : semi-minor axis (mm);
ϕ : Included angle between major axis and 0° fibre (^{o})

9.5 Discussion

The diagnostic results for selected specimens indicate that excellent quantitative predictions for damage presence, location, geometry and orientation have been achieved using the developed system. The maximum estimation error occurs in the prediction of orientation, but it still falls in an acceptable range ($\pm 9.5\%$). For further investigation, the dependence of identification precision on different network configurations is evaluated.

Training Pattern

As one of the key factors in network capability, the training pattern predominantly determines the precision of the network. Insufficient training can certainly lead to misleading predictions, while superfluous training unavoidably comes at the cost of demanding computational requirements.

20, 50, 80, 100, 120 stochastic damage cases are respectively used for network training. The ANNs consequently developed, represented by *ANN-T-20, ANN-T-50, ANN-T-80, ANN-T-100* and *ANN-T-120*, are individually evaluated. The complete diagnostic results for specimen *SP1-3*$^{\#}$ using different ANNs, together with their corresponding CPU time consumed for *offline* network training, are summarised in Table 9.3. From Figure 9.6(b), it is evident that the ANN ratiocination progressively approaches the actual damage, subject to the training patterns. To assist understanding, identification accuracy histograms are shown in Figure 9.7, where prediction error decreases with an increase in training patterns, while it stabilises after *80* damage patterns. No significant improvement in precision can be observed when *ANN-T-100* and *ANN-T-120* are used, compared with *ANN-T-80*. Conclusively, for the present system, satisfactory detection can be accomplished if up to *80-100* damage cases in one zone of the entire laminate are used for the DPD development.

Basically, the more training patterns are taken into account, the more accurate diagnosis for all damage parameters can be expected. But some impairment in identification of damage orientation is noted for *ANN-T-120*, from which is considered that the ANN has been overtrained. Additionally, more than double the computing time is consumed with a non-linear increase rate.

Table 9.3 Diagnoses based on different amounts of training patterns

DPD	Spec. No.	Absolute Prediction Error (%)					Max. Error (%)	Approx. Time*
		ξ	ζ	α	β	ϕ		
DPD-T-20	SP1#	21.6	23.3	21.7	27.9	32.0	32.0	3.2
	SP2#	24.8	19.9	23.0	20.4	39.5	39.5	
	SP3#	26.0	17.1	19.2	25.3	35.5	35.5	
DPD-T-50	SP1#	17.5	13.5	17.4	15.5	27.7	27.7	5.1
	SP2#	17.8	9.8	14.2	16.6	24.0	24.0	
	SP3#	15.7	11.0	12.3	14.1	26.5	26.5	
DPD-T-80	SP1#	6.5	3.5	6.9	5.8	9.2	9.2	8.3
	SP2#	5.8	6.3	7.2	4.3	4.0	7.2	
	SP3#	6.5	3.1	4.6	3.8	4.3	6.5	
DPD-T-100	SP1#	5.7	3.2	6.0	5.0	8.5	8.5	13.5
	SP2#	4.7	5.2	6.1	4.8	5.5	6.1	
	SP3#	5.0	3.7	2.8	3.5	4.1	5.0	
DPD-T-120	SP1#	5.3	3.7	4.8	4.8	9.1	9.1	17.2
	SP2#	4.7	5.2	6.1	4.7	5.4	5.4	
	SP3#	5.0	3.0	2.8	3.0	8.1	8.1	

ANN configuration: 2 neural processing layers (36/14 neurons); 8 energised PZT transducers; SCG-based backpropagation training; preset training MSE: 1×10^{-8}*; Approximate time consumed for the ANN training based on a PC with configuration of Pentium® IV 1.6G/512M RMA.*

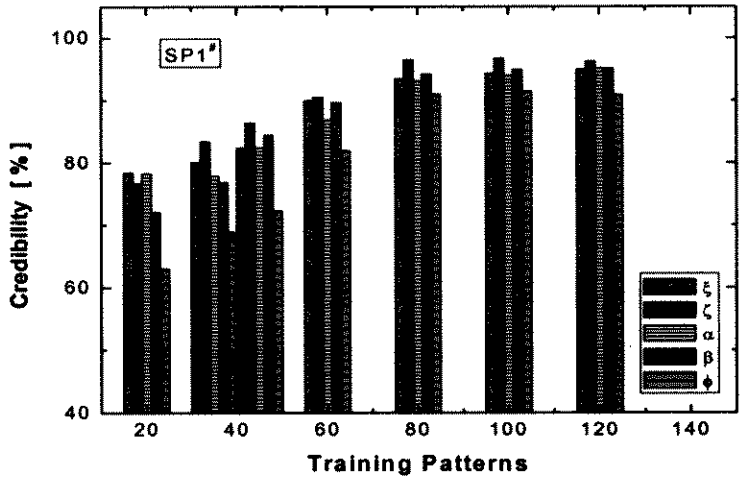

(a)

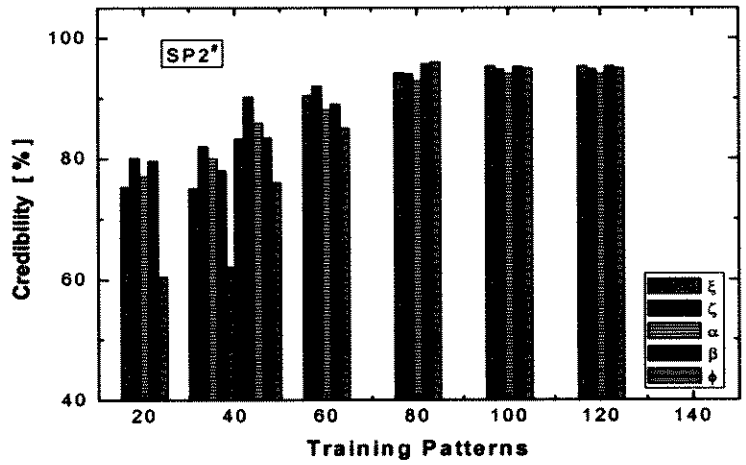

(b)

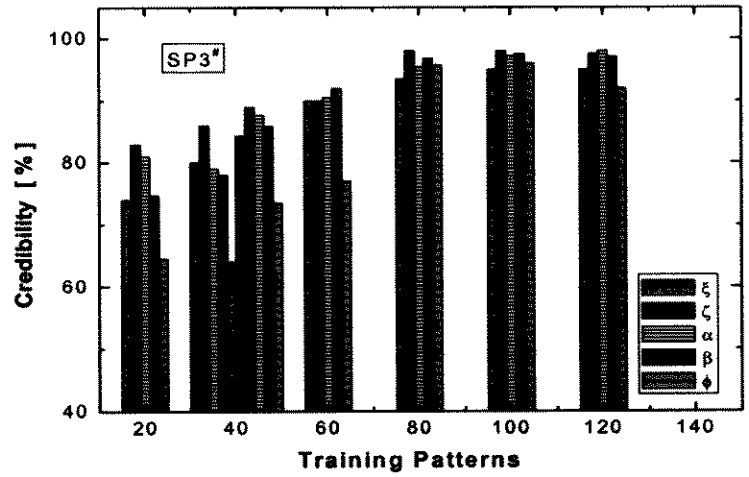

(c)

Figure 9.7 ANN identification accuracy for (a) *SP1*#; (b) *SP2*#; (c) *SP3*#

Transducer Number

The dependence of ANN precision on the number of SSU and amount of input information is evaluated. Three transducer networks, respectively possessing *4* (*P5, P6, P8, P9*), *6* (plus *P2* and *P4*) and *8* (plus *P3* and *P7*) activated PZT disks in the tailored actuator/sensor network, are used for DPD development. Individually, signals are acquired via *4* (*P5-P9/P9-P5* and *P6-P8/P8-P6*), *8* (plus *P2-P9/P9-P2* and *P4-P9/P9-P4*), and *12* (plus *P3-P8/P8-P3* and *P6-P7/P7-P6*) actuator-sensor paths for each damage case. Three input feature vectors with the capacity of *900*, *1800* and *2700* elements can thus be created when the same amount of DDF is extracted, and employed to develop three ANNs, represented by *ANN-P-04*, *ANN-P-06* and *ANN-P-08*. Their diagnoses for specimen $SP3^{\#}$ under the current network architecture, training functions and training patterns (*80* damage patterns for one quadrant) are collated in Table 9.4.

Table 9.4 Identification precision for $SP3^{\#}$ using different transducer networks

Number of Energised PZT Transducers		4 (DPD-P-04)	6 (DPD-P-06)	8 (DPD-P-08)
Relative Identification Error (%)	ξ	18.7	9.4	6.5
	ζ	16.8	8.2	3.1
	α	24.5	17.5	4.6
	β	29.1	21.6	3.8
	ϕ	27.6	17.6	4.3

2 neural processing layers (36/14 neurons); 80 damage patterns in Zone-3
SCG-based backpropagation training; preset training MSE: 1×10^{-8}

It is apparent that the adoption of more PZT sensors, i.e. more input information, uncontroversially leads to more precise identification, while much more computational memory and time will be consumed. Section 5.6.2 demonstrated that *4* PZT transducers could ensure satisfactory detection for the location of damage based

on a *forward* analysis, but are deficient in providing exact description for damage geometry. The current case study confirms that identification based on *inverse* analysis by virtue of the ANN relying on information collected from *4* transducers is unlikely to be adequate to quantitate both damage location and geometry. An ANN using *6* PZT transducers, i.e. *8* actuator-sensor paths, can give an approximate prediction for damage presence and location, but it is inadequate to depict the damage geometry exactly. The ANN using *8* PZT transducers (*12* actuator-sensor paths) is found sufficient to achieve excellent identification precision for all the damage parameters.

Training Function

In the above discussion, the ANN is trained using the *scaled conjugate gradient* (SCG)-based error-backpropagation algorithm, denoted by *ANN-SCG*. For comparison, performances of ANNs using other popular training functions, including *basic gradient descent* (BGD), *gradient descent with momentum* (GDM), *with adaptive learning rate* (GDA), *with combined momentum* and *adaptive learning rate* (GDMA), *resilient back-propagation* (RBP) and *Levenberg-Marquardt* (LM) algorithms [Mathworks, 2001b], are also evaluated. Their corresponding trained ANNs are represented by *ANN-BGD*, *ANN-GDM*, *ANN-GDA*, *ANN-GDMA*, *ANN-RBP* and *ANN-LM*, respectively. Each ANN is kept the same with regard to other network configurations (*80* damage patterns used and *8* energised PZT transducers).

During evaluation, an attempt to use the database *ANN-LM* for the current system is found not cost-effective due to its exigent demand for computational memory. The capabilities of other ANNs are compared in Figure 9.8, with their convergence speed and prediction precision. From Figures 9.6-9.8, it is clear that the ANN using the SCG-based backpropagation algorithm achieves both fast convergence and satisfactory precision. Subsequently, *ANN-BGD* is considered an alternative with

acceptable accuracy, although more training time is consumed in reaching network convergence. With slow convergence, *ANN-GDM* achieves good identification of damage location but has a relatively poor capability for identifying damage geometry. In contrast, databases *ANN-GDA*, *ANN-GDMA* and *ANN-RBP* meet convergence much more quickly than other ANNs, but their diagnosis precision is poor, or acceptable for only some damage parameters. Briefly, the consolidated neural network capabilities via different training functions for the present detection are summarised in Table 9.5.

Figure 9.5 Overall capabilities of ANNs using different training algorithms

DPD	Convergence Speed [1]	Memory Requirement	Identification Performance
ANN-SCG	Medium	Medium	Very good identification for all damage parameters
ANN-BGD	Slow	Low	Good identification for most damage parameters
ANN-RBP	Fast	Low	Poor identification for damage location
ANN-GDM	Slow	Low	Poor identification for damage geometry
ANN-GDMA	Fast	Medium	Acceptable identification for partial parameters
ANN-GDA	Fastest	Medium	Poor identification
ANN-LM [2]	Medium	Huge	N/A

[1] *time to reach preset convergence precision*

[2] *only suitable for small-scale analysis and unsuccessful for the present system*

Altogether, compared with other backpropagation (BP) algorithms, SCG-based training avoids computationally expensive linear searching for convergence and thus exhibits a good balance between identification precision and training convergence speed. In practice, no clear guideline exists for selecting a training function toward a specific system, so efficiency and convergence speed may differ slightly in different cases.

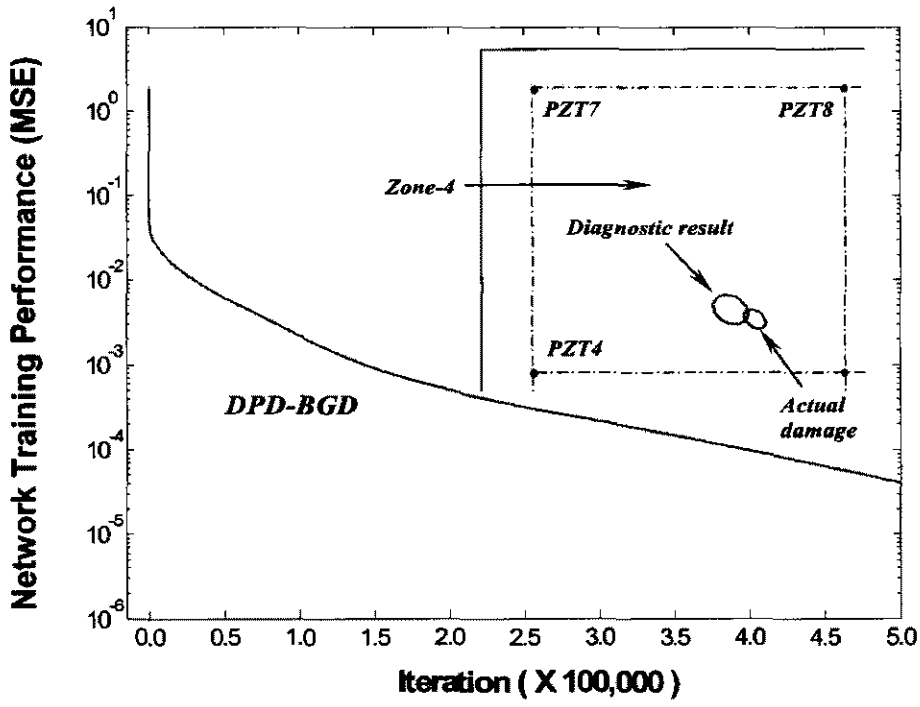

(a)

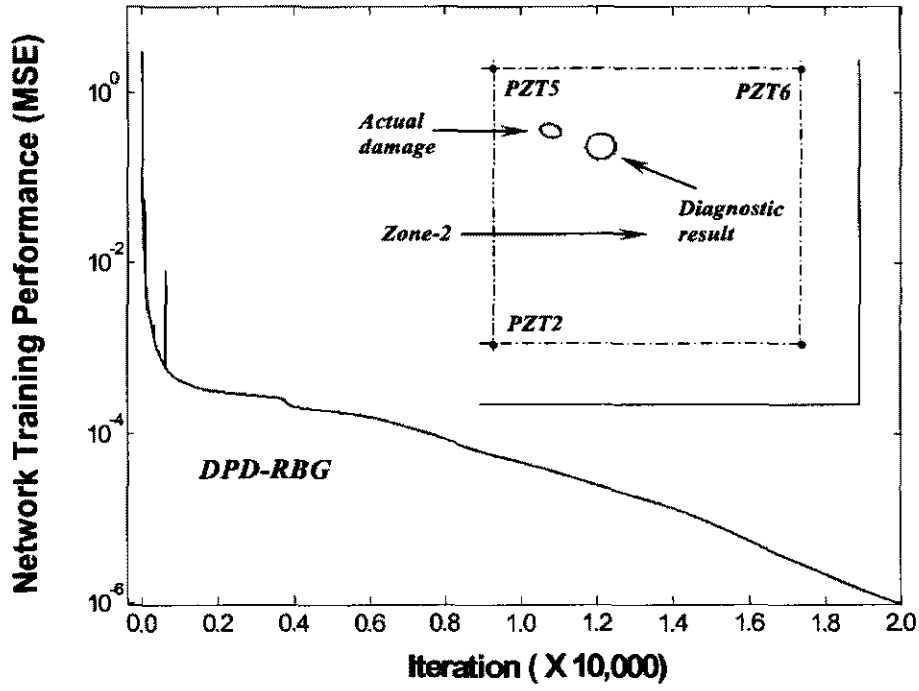

(b)

Figure 9.8 Convergence speed and precision for different ANNs: (a) *DPD-BGD* for *SP2*#; (b) *DPD-RBP* for *SP1*#; (c) *DPD-GDM* for *SP2*#; (d) *DPD-GDMA* for *SP3*#; (e) *DPD-GDA* for *SP1*#

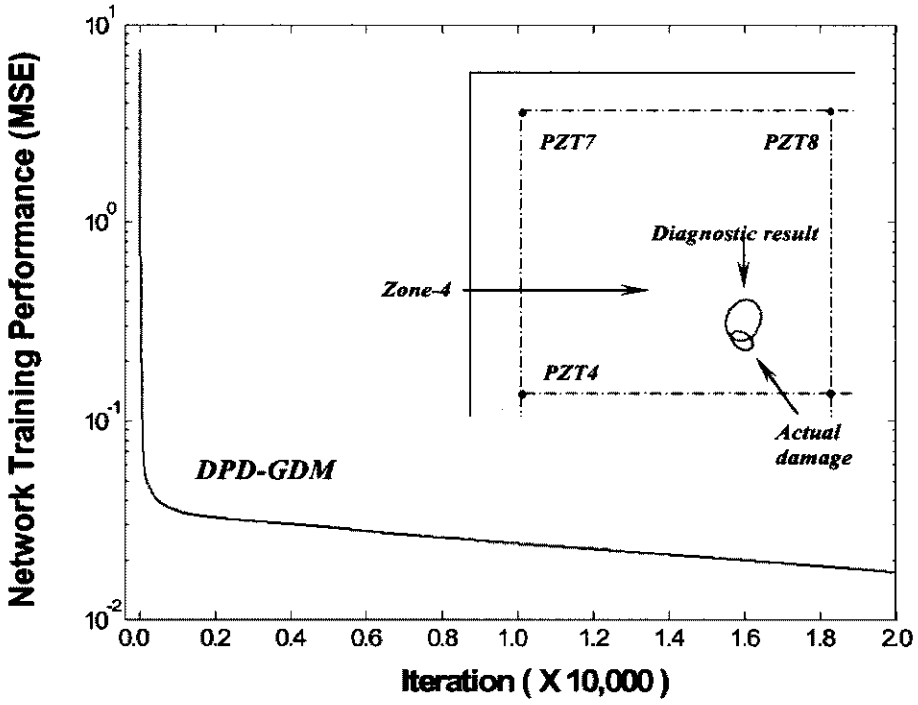

(c)

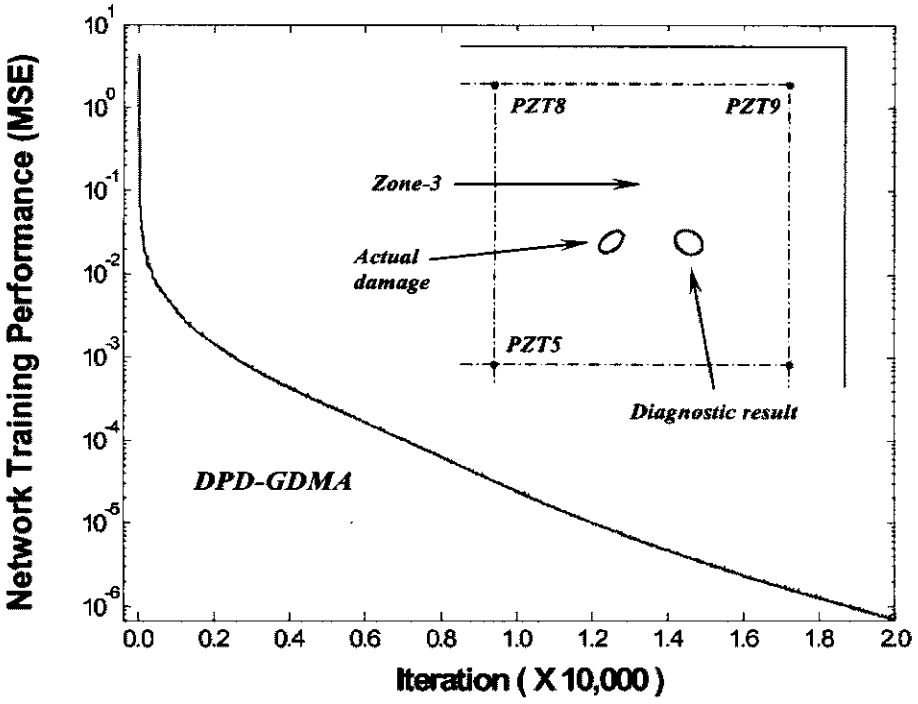

(d)

Figure 9.8 *Cont.*

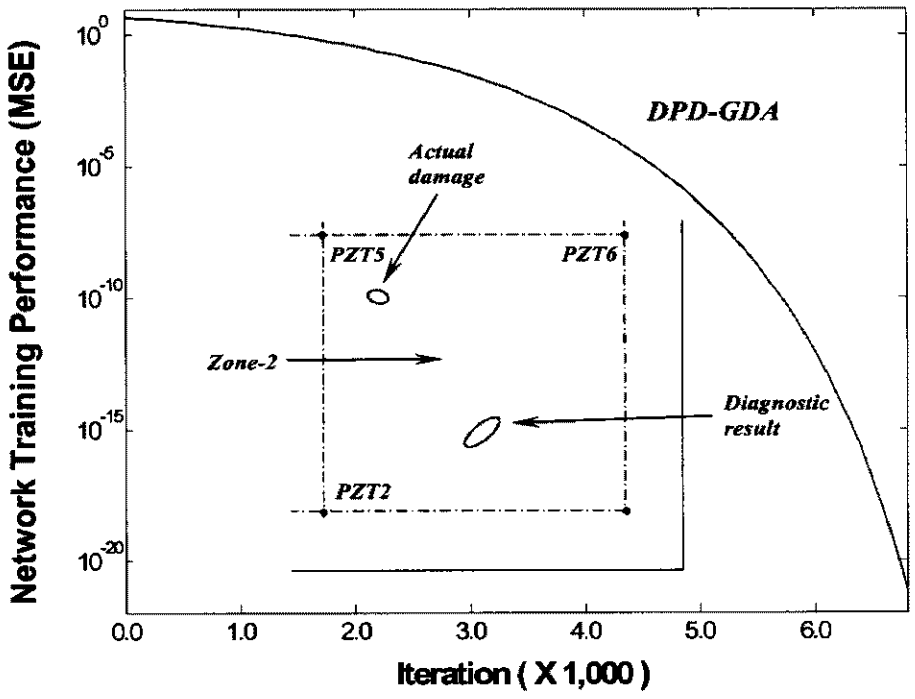

(e)

ANN basic configuration: 2 neural processing layers with 36 and 14 neurons, respectively; PZT network: 8 energised PZT transducers; Training patterns: 80 damage patterns in Zone-3

Figure 9.8 *Cont.*

Network Architecture

As noted earlier, an engineering system can probably not be represented faithfully by a small sized network, while on the other hand, convergence and stability for network training may be sacrificed with an oversize network. Three ANNs characterised by different network architectures are parallelly constructed, featuring *20/8*, *36/14* and *50/30* neurons in the first/second processing layers, represented by *ANN-A-2008*, *ANN-A-3614* and *ANN-A-5030*, respectively. Their convergence speeds versus training iterations, under the given training conditions (SCG-based training function, *80* damage patterns used in one quadrant and *8* energised PZT transducers), are displayed in Figure 9.9(a); and their relevant damage identification results for specimen *SP1-3*$^{\#}$ are diagrammed in Figure 9.9(b).

An interesting phenomenon can be observed, in that both *ANN-A-2008* and *ANN-A-5030* are relatively slow to reach convergence compared with *ANN-A-3614*, implying that insufficient neurons in the processing layer may lead to difficulty in achieving convergence with satisfactory precision; and superfluous neurons can also lead to unforeseen reduction in precision, additionally entailing bulky network architecture and certainly more computational costs. Like other factors, the most appropriate number of neurons in a network varies with different applications. To obtain an adequate yet efficient architecture is beyond mathematical capability, and the best configuration can usually be achieved based on reiterative trials and experience, although research [Tao, 1997] suggests that the neuron number can be approximately determined by

$$i = \sqrt{m+n} + A \tag{9.1}$$

where i, m and n are the numbers of neurons, input elements and output targets, respectively. A denotes an empirical constant, commonly ranging from *4* to *8* depending on actual applications.

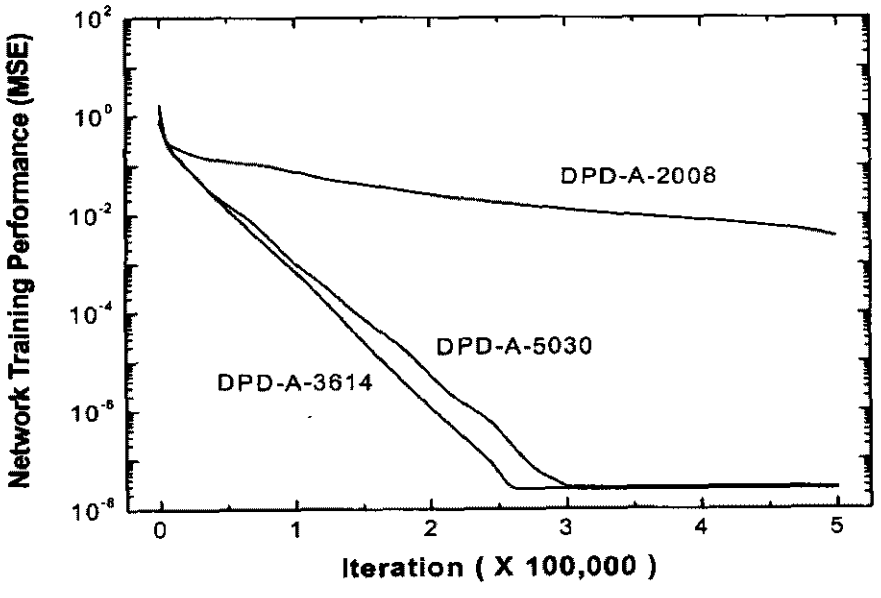

(a)

PZT network: 8 energised PZT transducers; Training patterns: 80 damage patterns in one quadrant; Training function: Scaled Conjugate Gradient (SCG)-based backpropagation

Figure 9.9 Comparison of different network architectures: (a) convergence history and stability; (b) diagnostic precision

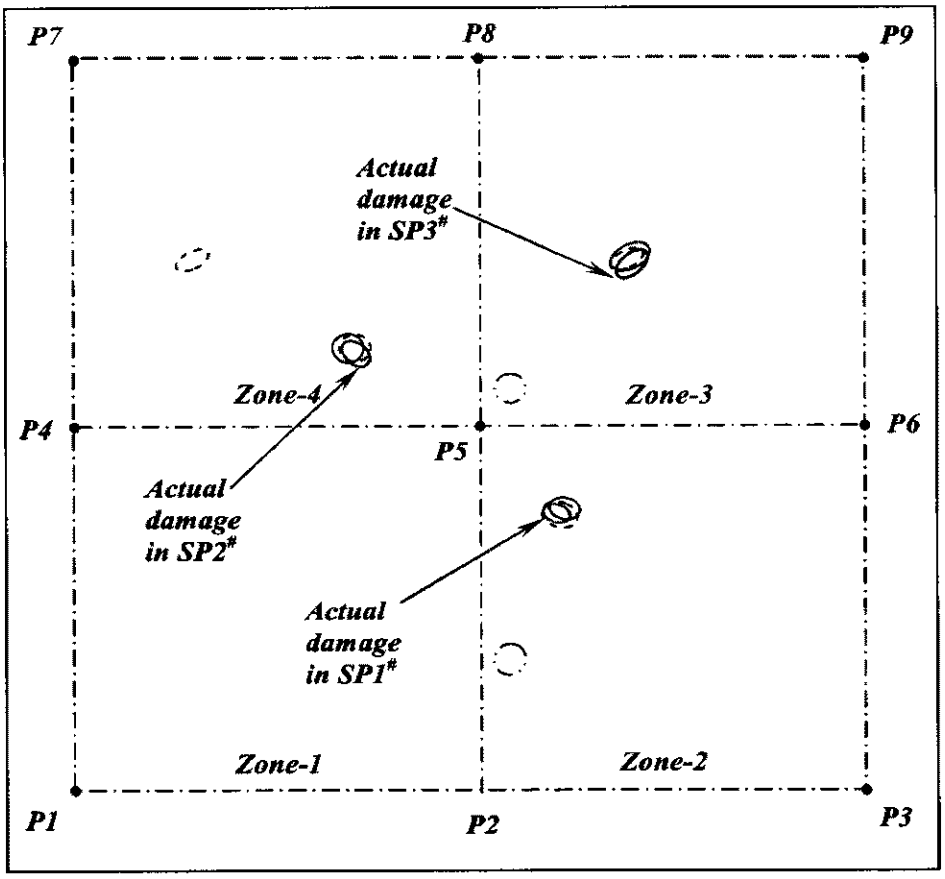

Actual damage; Diagnostic results by DPD-A-3614

Diagnostic results by DPD-A-5030; Diagnostic results by DPD-A-2008

(b)

Figure 9.9 *Cont.*

Damage Severity

Different levels of damage are introduced for validation (specimen *SP1-3*#), as summarised in Table 9.1. It can be seen that good diagnoses for all the chosen damage levels are obtained using the well-trained neural network, although a relatively unfavorable deviation of assessment for smaller amounts of damage is noticed under insufficient training. Unlike the experiment-based detection approaches, in which more severe damage normally leads to more tractable signal discrimination and thus more accurate prediction, identification based on the ANN is dependent on the accumulated DDF in the DPD. More precise results can be

achieved when the actual damage falls into the ranges involving more damage patterns during training. From the results, it is concluded that the current system has a stronger ability to estimate damage location and geometric identity, but a somewhat weaker ability to identify damage orientation, especially when the angle is close to the critical values (0 or π), although rapid amelioration appears as the training patterns increase.

Robustness

Filtered by the SPP, the inputs for ANN training are free of noise. For comparison, the raw dynamic responses obtained directly from simulation for two randomly chosen damage cases involving various disturbances in broadband, together with the processed noise-free DDF for the other *78* damage cases, are mixed as the inputs for ANN training. The network consequently configured, denoted by *ANN-NOISE*, and the network without artificial disturbance, *ANN-NOSFR*, are compared in Figure 9.10 by their diagnostic results.

No evident negative impact on identification using *ANN-NOISE* can be noted, which suggests that for a small amount of perturbance among the massive number of DDF, good robustness and fault tolerance can still be anticipated for a well-trained ANN. In fact, in addition to noise-filtered DDF, the original raw structural dynamic responses, involving diverse interference, can also be used directly for DPD development, where the various disturbances can be regarded as one part of the input information for ANN training. However, this exponentially and unnecessarily increases the capacity of input vector and incurs more training time.

As a complicated high-order non-linear system, the development of the most suitable ANN is tied to a diversity of comprehensive diatheses. Other than the major factors

discussed above, validity and accuracy of an ANN also depend on choice of initial weights and biases, order of input elements, transfer function, etc.

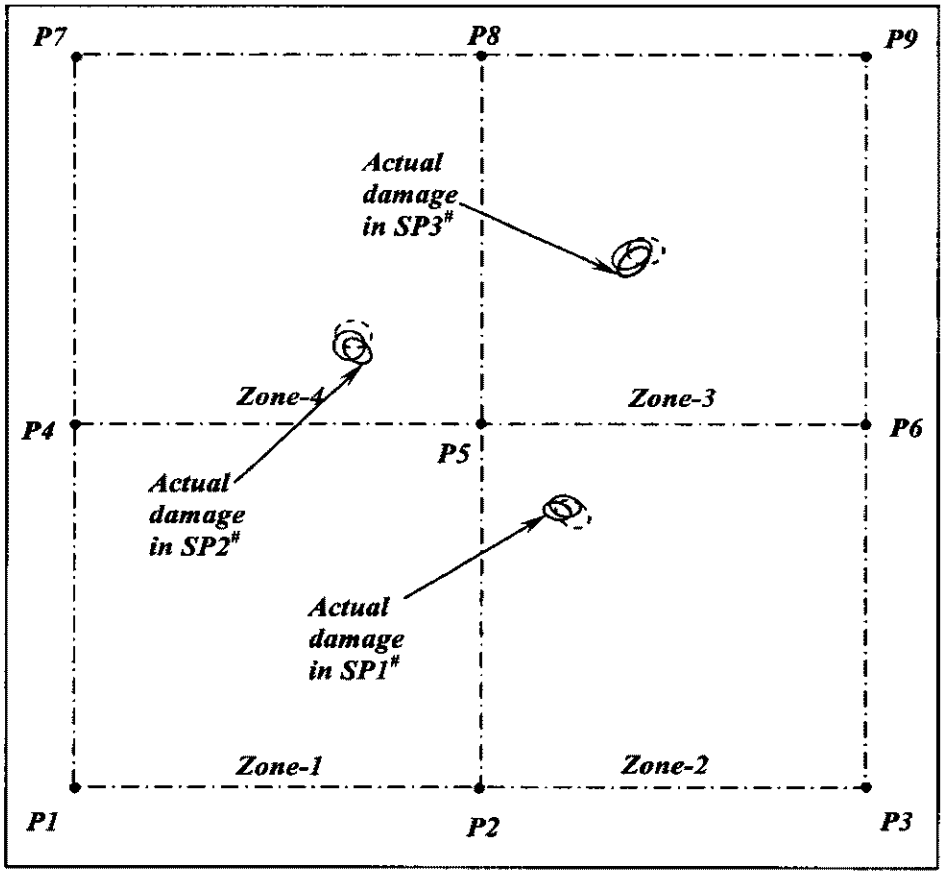

Figure 9.10 Diagnostic results of ANNs with/without noise disturbances

9.6 Concluding Remarks

Validation of the proposed damage detection algorithm and the AO-SHD system is conducted using a case study of quantitatively identifying through-hole type damage in quasi-isotropic CF/EP (T650/F584) composite structures. Excellent diagnosis for damage parameters (presence, location, geometry and orientation) is achieved.

During system development, identification efficiency and accuracy are noted to be dependent on the multiformity of neural network configurations. For investigation, a diversity of ANNs are constructed with different network architectures, neuron numbers, training patterns, PZT transducer numbers, and training functions. Based on this testing, the following conclusions can be drawn:

(1) based on the developed DPD, a feedforward artificial neural network (ANN) with two neural processing layers using the error-backpropagation algorithm exhibits excellent capability to define damage parameters using extracted DDF;
(2) an over-trained network may contribute to improvement of identification precision (but not always for all the damage parameters), however, at the expense of massive extra computational time and cost. For the present case, *80-100* damage cases, assumed in one-fourth of the whole laminate for network training, are found sufficient yet with affordable computational effort;
(3) the utility of *8* PZT transducers can offer sufficient information for exactly quantitative recognition;
(4) various training functions may lead to different efficiency and convergence speeds. Among popular functions, the SCG-based BP algorithm is found most effective to achieve fast training with high precision;
(5) the effectiveness and convergence speed of the ANN are also noted to rely on the number of neurons in the processing layer. For the current structure, *36/14* neurons allocated in the first/second layers, are shown to be most cost-effective;
(6) a well-trained neural network possesses a certain robustness and fault tolerance, capable of tolerating a small amount of unintended disturbance in training information;
(7) although substantial time is inevitably spent on the *offline* development of the DPD and training of the ANN, the diagnosis of actual damage can be performed instantly *online* with a well-developed ANN.

Chapter 10

Identification of Delamination in CF/EP Composite Laminate

10.1 Introduction

Delamination, appearing as the debonding of adjoining plies, is probably the most common but most hazardous defect in carbon fibre-reinforced composites. It can be induced in manufacture, through the accumulation of small defects, or as a result of accidental impact during service [Voyiadjis, 1993]. In a delaminated region, the mismatch in Poisson ratios between plies causes large out-of-plane interlaminar stresses near the ply interfaces, to balance the bending moment along the thickness direction. Furthermore, the redistribution of such stresses can also lead to additional stresses in areas around the delamination under fatigue loadings, expanding the original delamination area. The occurrence of delamination plays a major role in lowering structural strength and stiffness or damping properties, consequently downgrading system integrity and reliability.

As one of the hottest topics in the NDE community, delamination detection has attracted much interest (see reviews in Chapters 3 and 5). In this chapter the aim is to examine the effectiveness of the proposed damage detection technique and the AO-SHD system for identifying delamination in three-dimensional CF/EP composite laminates.

10.2 Development of Damage Parameters Database (DPD)

As with the DPD development for through-hole damage in the previous chapter, dynamic FEM simulation is used to achieve *digital damage fingerprints* (DDF) for delaminated CF/EP composite structures and construct DPD.

10.2.1 Modelling of Composite Laminates with Delamination

Consider an *8*-ply $[45/-45/0/90]_s$ quasi-isotropic CF/EP composite laminate, measuring *490 mm* × *490 mm* × *1.27mm*, as schematically shown in Figure 10.1. All edges are clamped supported. As in the approach in Chapter 9, the whole laminate is presumed to be quartered, denoted counterclockwise by *Zone-1*, *Zone-2*, *Zone-3* and *Zone-4* from the lower-left quadrant. Without losing generality, an elliptic delamination is presumed to occur between the first and second laminae in *Zone-1*. Four standard sensor units (SSUs), involving nine piezoelectric disks, are tailored and surface-bonded on the laminate. Each PZT disk is *70mm* away from the neighboring edge(s) or at the plate centre, numbered with *Pi* ($i = 1, 2, \cdots, 9$).

Commercial composite materials (T650/F584) [Hexcel Co., 2001] with properties listed in Table 5.1 are considered. In terms of the modelling techniques for delamination and PZT actuator/sensor given in Section 5.3, full-scale FEM models for the delaminated laminates are created using *8*-node three-dimensional brick elements on the PATRAN® platform.

To accommodate the actual laminate configuration, *8* layers are divided along the laminate thickness in *Zone-1* to characterise each unidirectional lamina individually. The FEM mesh is particularly densified therein, where more than *10* FEM nodes are

guaranteed to exist per Lamb wavelength. Distant fields (e.g. *Zone-2, 3, 4* for damage occurring in *Zone-1*), modelled for geometric completeness but not virtually contributing to the identification, are simplified by choosing consolidated single layer *8*-node brick elements [Diamanti *et al*, 2002] as used in Chapter 9. For each single layer, elastic properties, derived on a micro-mechanics model (Section 5.3.4), are adopted.

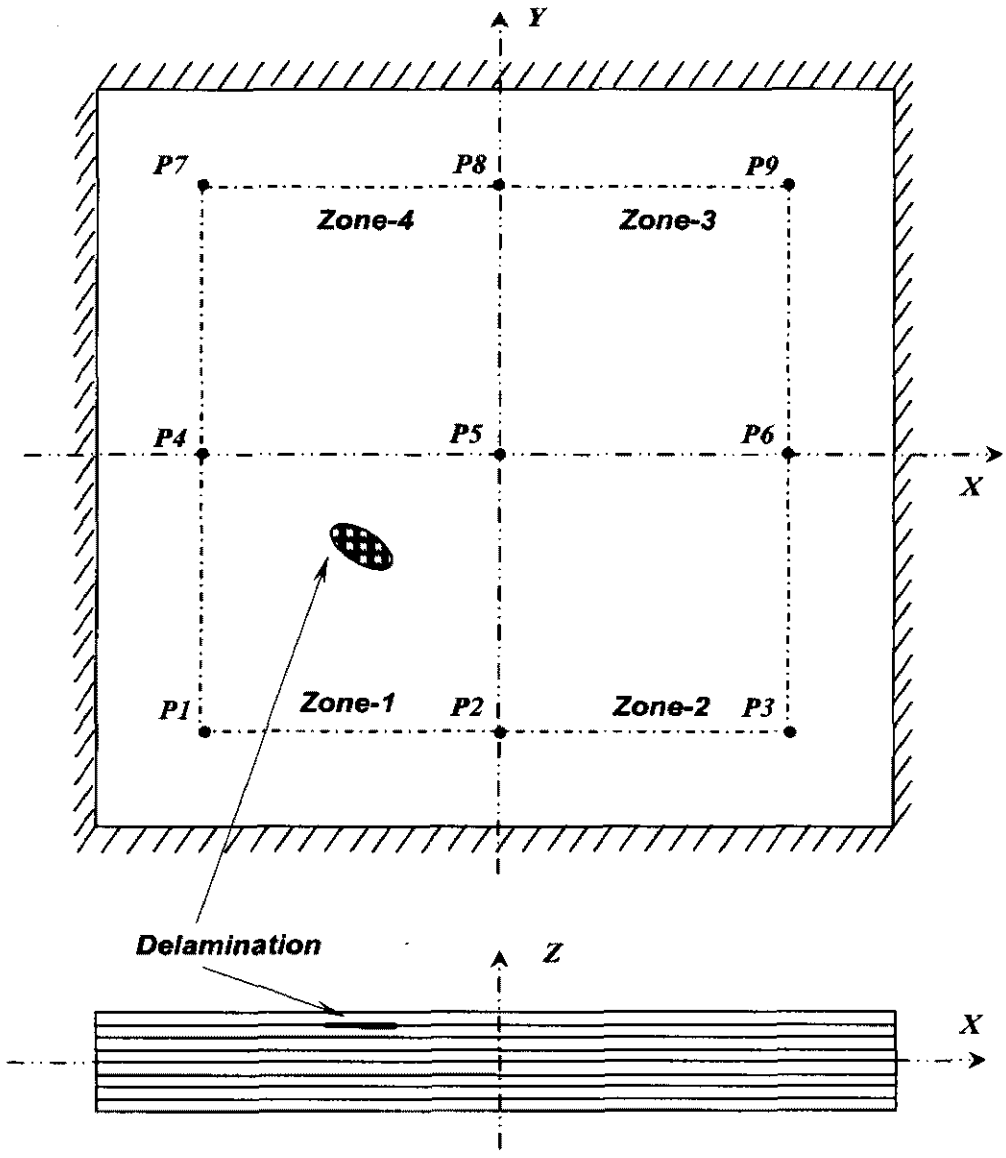

Figure 10.1 Composite laminate with a delamination

Under such a circumstance, degrees of freedom (DoF) are incompatible at conterminous edges among four zones. A multi-point constraints (MPC) technique [Hibbitt, Karlsson & Sorensen, Inc., 2003] is invoked to harmonise different DoF among *Zone-1* (*8*-layer *3*-D brick elements) with other zones (*1*-layer *3*-D brick elements). As explained in Figure 10.2, MPC constrains each DoF at nodes p and q to be interpolated linearly from DoF at nodes a and b, whose linear relation is represented by scale of shadow. Such a measure makes it possible to connect models with different mesh density while without eliminating any DoF.

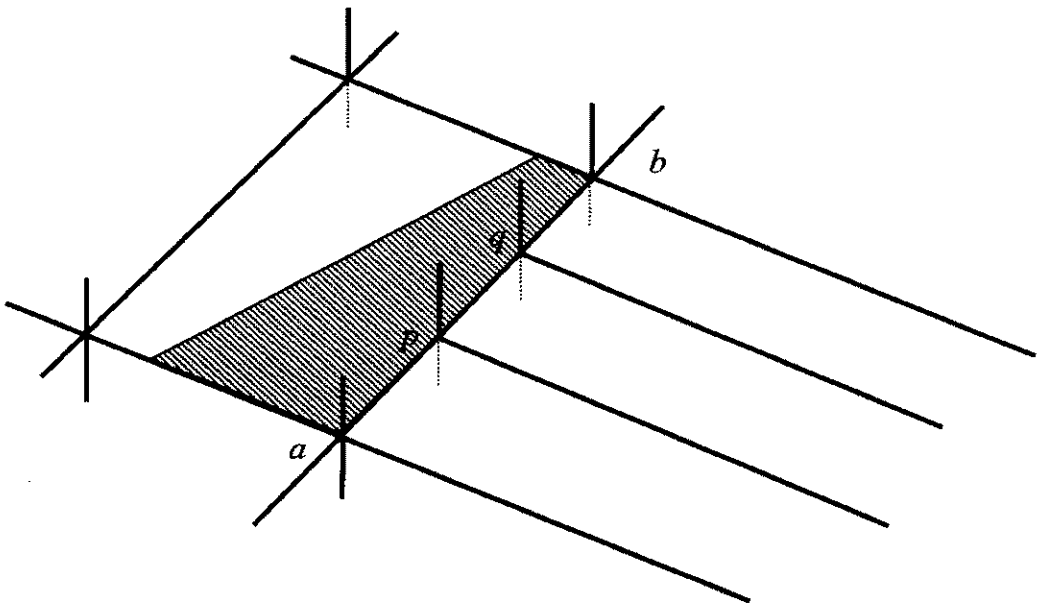

Figure 10.2 MPC technique

The FEM model developed is displayed in Figure 10.3. In the model, a total of *120,000* three-dimensional solid elements with *420,000* DoF are engaged. The particular mesh description for a delamination region can be found in Figures 5.7, 5.9 and 5.10.

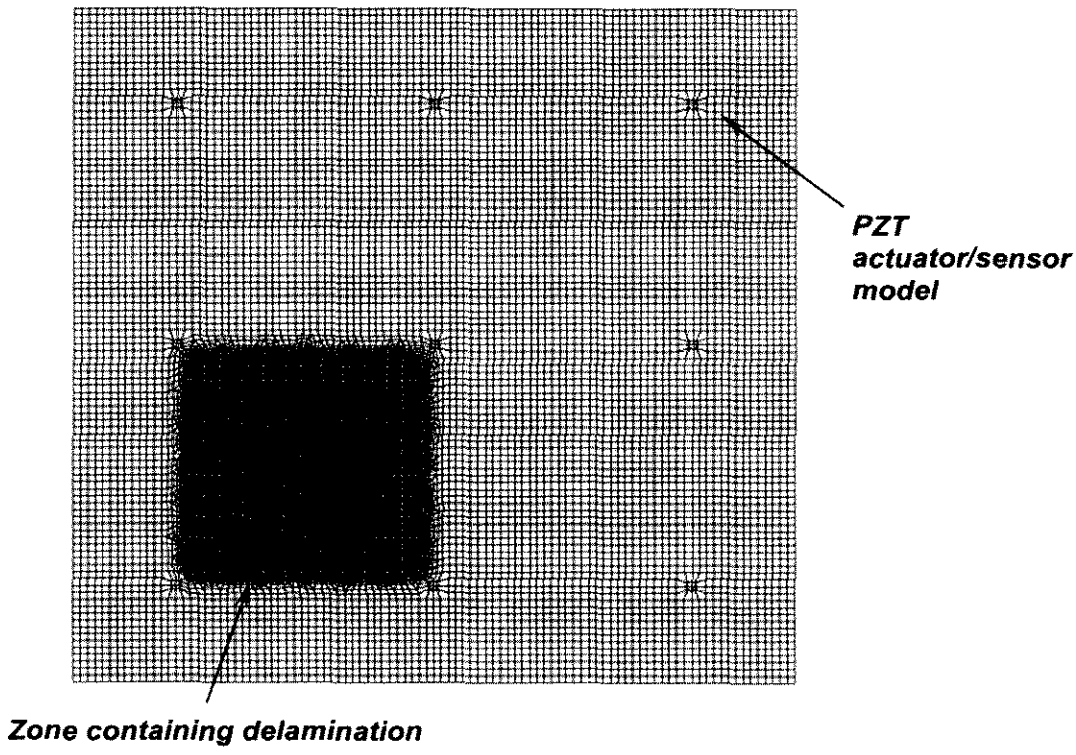

(a)

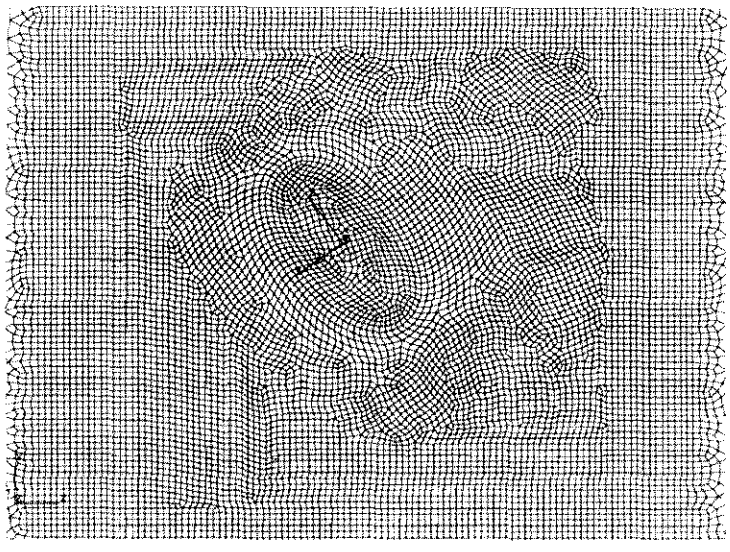

(b)

Figure 10.3 FEM model for delaminated laminate: (a) ichnography of model; (b) partial magnification for *Zone-1*

10.2.2 Parameterised Modelling Technique (PMT)

For data accumulation in the DPD, a variety of defective laminates, each bearing one delamination with exclusive location and geometric identity, is required. However, it is clearly not practical and economical to develop complicated FEM models for each damage case individually. The effectiveness of the proposed identification technique could be strongly challenged due to the massive amount of work required for database development. Motivated by this constraint, a parameterised FEM modelling technique is developed.

Commercial FEM software PATRAN® [MSC Software, 2001] provides a development environment, *Patran Command Language* (PCL), to customise specific applications, perform variational modelling, and integrate self-developed programs into commercial ones. A computational code is built on the PCL platform to realise parameterised modelling [Huang *et al*, 2004]. Such a technique permits the development of FEM models for complicated structures in terms of just several simple characteristic parameters provided by the user. Paradigmatically, for the composite laminate under inspection, these parameters include three-dimensional geometric definition, material properties and boundary conditions; for delamination, they are location, interlaminar position, shape, size, and orientation; for PZT actuator/sensor, they are location, material properties, geometry, and intensity of applied electrical field. Additionally, FEM mesh density along three dimensions, element genus, etc. can also be specified.

With the provided parameters, the PMT is able to customise an FEM model automatically and expeditiously. Research [Huang *et al*, 2004] reveals that over *90%* of computational effort and time can be saved via such a technique. Further, modelling errors are also avoided or at least minimised.

By using PMT, up to *100* individual cases are considered, where each laminate contains one unique delamination in *Zone-1*, generated by the random program in the signal processing package (SPP) introduced in Section 9.2.1 (allowing arbitrary location, length of major/minor axes, orientation and interlaminar position). FEM models are created by simply changing parameters, and properly transformed into ABAQUS/EXPLICIT® for dynamic analysis.

Similarly, a *Hanning* window-modulated *5*-cycle sinusoid toneburst at a central frequency of *500KHz* (referring to Figure 7.6), is stimulated by the actuator model as the diagnostic signal. Dynamic FEM simulation is accomplished on a *SUN Blade® 1000* workstation (dual processors at *900MHz* and *2G* RAM). The step of calculation time is controlled to be less than ratio of the minimum distance of any two adjoining nodes to the maximum wave velocities, while Lamb wave signals are acquired at a sampling rate of *20.48MHz* by the sensor model. For damage in *Zone-1*, only the actuator-sensor paths directly passing through this region, including *P1-P8/P8-P1*, *P1-P6/P6-P1*, *P2-P7/P7-P2*, *P4-P3/P3-P4* and *P1-P5/P5-P1*, *P2-P4/P4-P2*, are of interest.

10.2.3 Signal Processing and DDF Extraction

The SPP is applied to the acquired Lamb wave signals to extract DDF. By way of illustration, one raw wave signal acquired via a diagonal actuator-sensor path *P1-P8* for a damage case arbitrarily chosen, with its DDF in the time domain corresponding to active excitation frequency (*500kHz*), and DDF in the time-scale space, are displayed in Figure 10.4.

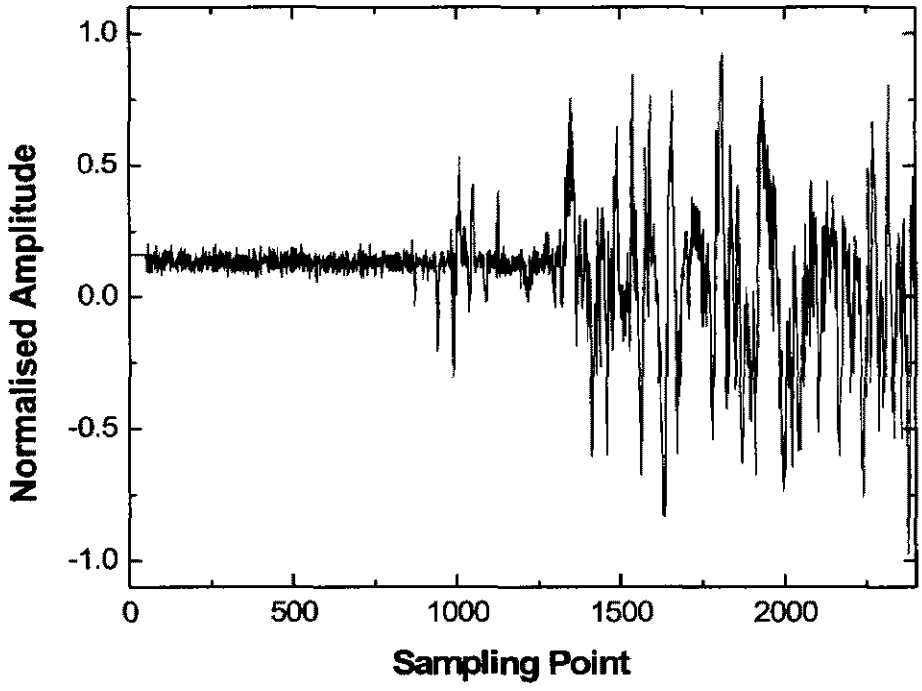

(a)

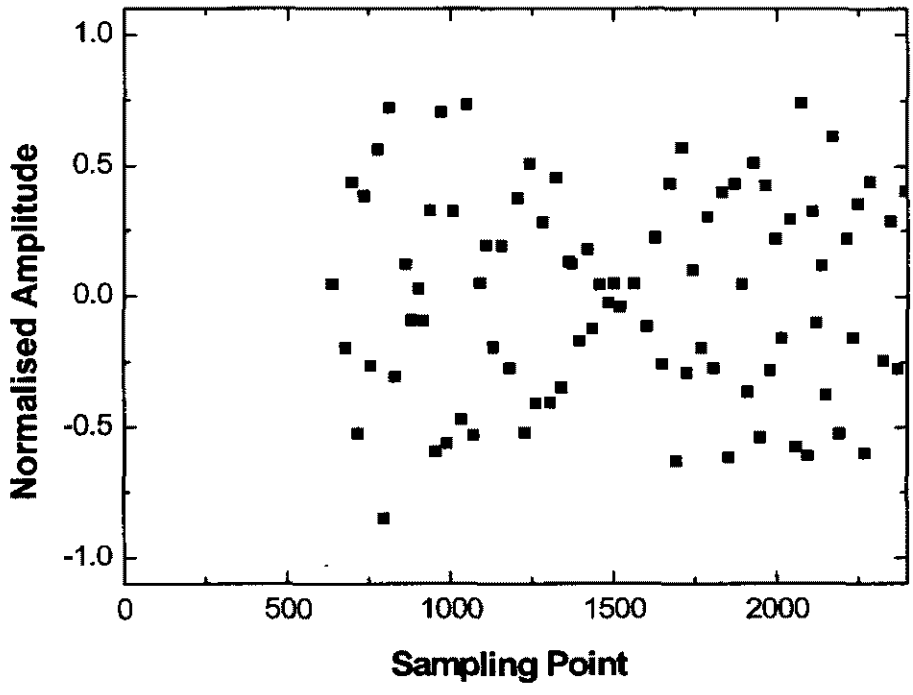

(b)

Figure 10.4 Signal processing by SPP: (a) original Lamb wave signal; (b) DDF in time domain; (c) DDF in time-scale domain

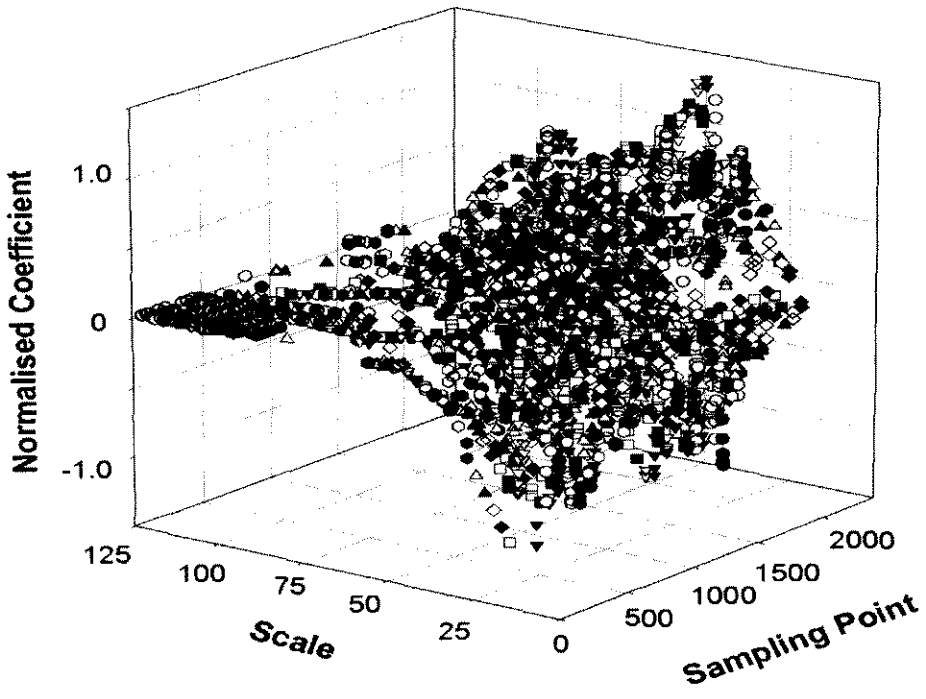

(c)

Figure 10.4 *Cont.*

10.2.4 Construction of DPD

The DPD for delamination in quasi-isotropic CF/EP laminate is constructed, containing the extracted DDF for all the relevant actuator-sensor paths under all the damage cases considered. Since symmetric geometry and excitation conditions are applicable, for simplification and without losing generality, all the damage cases are confined to region *Zone-1* during database development. *100* damage cases in *Zone-1* lead to *100* sets of DDF. The mapping technique in the SPP is then employed to achieve DDF for the other quadrants of the laminate. Four parallel sub-databases hosting the relevant DDF, respectively pertaining to the four zones, are configured. It is emphasised again that the feasibility of the mapping technique adopted here is guaranteed by the assumption of dense damage cases during database development.

10.3 Customisation and Training of ANN

The artificial neural network (ANN) designed in Section 6.4 is customised for this case study, consisting of two hidden neural processing layers (see Figure 6.5), containing *50/22* neurons in the first/second processing layers. The ANN is then trained using the constructed DPD.

8 PZT transducers are energised for damage cases occurring in *Zone-1*, where the furthest transducer *P9* (see Figure 10.1) is not considered due to the minor influence of damage on the wave signals emitted from it. Assisted by SPP and following DDF extraction criteria (Section 4.4.2), one set of DDF, extracted from the Lamb wave signal from each actuator-sensor path, consists of *50* temporal data items and *50* corresponding crestal amplitudes in the time domain, and *50* sets of temporal and frequency data, as well as *50* corresponding energy crestal magnitudes in the time-frequency domain. *8* PZT transducers, that is, *12* concerned actuator-sensor paths, can offer *3000* DDF for each damage case. *100* sets of accompanying target vectors are established for the chosen *100* damage cases, hosting *6* damage indices, namely damage presence (*0/1*), central position (ξ and ζ), semi-major/minor axis (α / β), and orientation (ϕ). All the variables in the network are normalised.

The supervised training algorithm, introduced in detail in Section 6.3, is adopted. Network training is performed on a PC platform (Pentium® *IV 2.4GHZ, 256M* RAM), as recorded in Figure 10.5 ($MSE = 1 \times 10^{-10}$ in this study), where it can be seen that the ANN stabilises at circa *2,300,000* iterations.

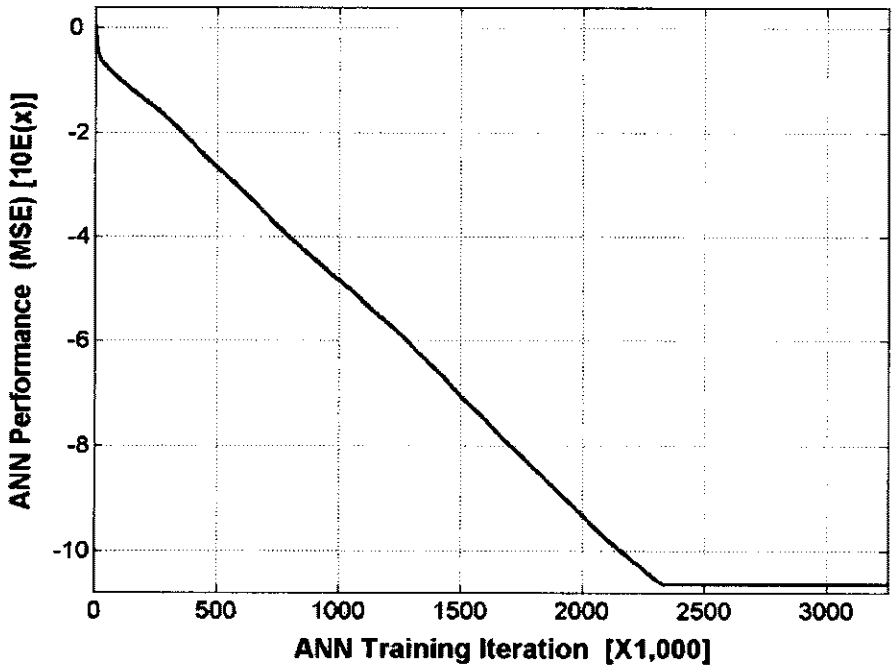

Figure 10.5 ANN training

10.4 Validation

10.4.1 Specimen Preparation

The trained ANN is evaluated by identifying actual delaminations in *8*-ply $[45/-45/0/90]_s$ quasi-isotropic CF/EP (T650/F584) laminates. Configuration of specimens is summarised in Table 10.1, symbolised by *SP1*$^{\#}$ and *SP2*$^{\#}$, respectively. Delaminations are introduced using two pieces of *UPLEX*©*-R-25* film of $25\mu m$ in thickness during hand-lay-up. The laminates are then applied with boundary conditions consistent with the FEM simulations.

10.4.2 Customisation of Active Actuator/Sensor Network

Four SSUs are involved in customising an actuator/sensor network on each specimen in accordance with DPD development (see Figure 10.6), which is able to offer a total

of *72* actuator-sensor paths. The network is then instrumented with the AO-SHD system.

Table 10.1 Configuration of specimens

Specimen No.	Geometric Dimension	Damage Indices						
		To Left[1] [*mm*]	To Btm[2] [*mm*]	α [*mm*]	β [*mm*]	ϕ_3 [°]	Zone	Delam Area
SP1#	490 × 490 × 1.27	100	192	25	19	75	1	0.62%
SP2#	490 × 490 × 1.27	349	272	28	15	150	3	0.55%

1. Vertical distance to the left edge from centre of the damage (mm)
2. Vertical distance to the bottom edge from centre of the damage (mm)
3. Included angle between major axis and 0° fibre (°)

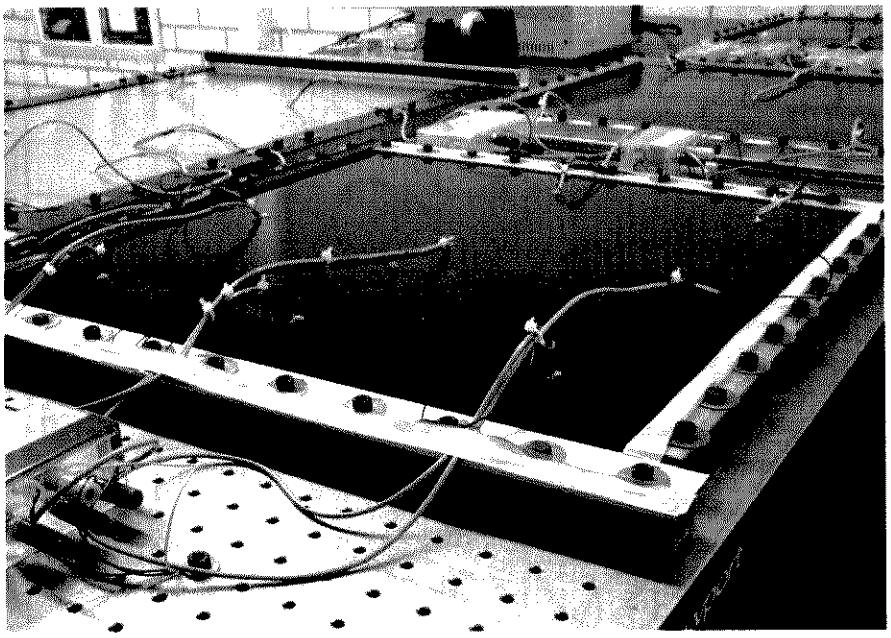

Figure 10.6 Instrumented specimen (quasi-isotropic CF/EP laminate) with active sensor network

10.4.3 Damage Diagnosis

As with the detection of through-hole type damage in Chapter 9, the damage location technique initially developed in Section 5.6 is applied first to determine the zone where damage exists. The DPD for the detected zone is then invoked to offer quantitative identification of delamination. The same diagnostic signal, in accordance with DPD development, is activated and applied to each PZT disk in turn to generate the Lamb wave. The acquired Lamb wave signals are processed with the SPP, to extract the DDF and *feature vector*, which are then fed into the ANN for diagnosis.

The diagnostic results for the selected laminates are shown in Figure 10.7, compared with the actual damage.

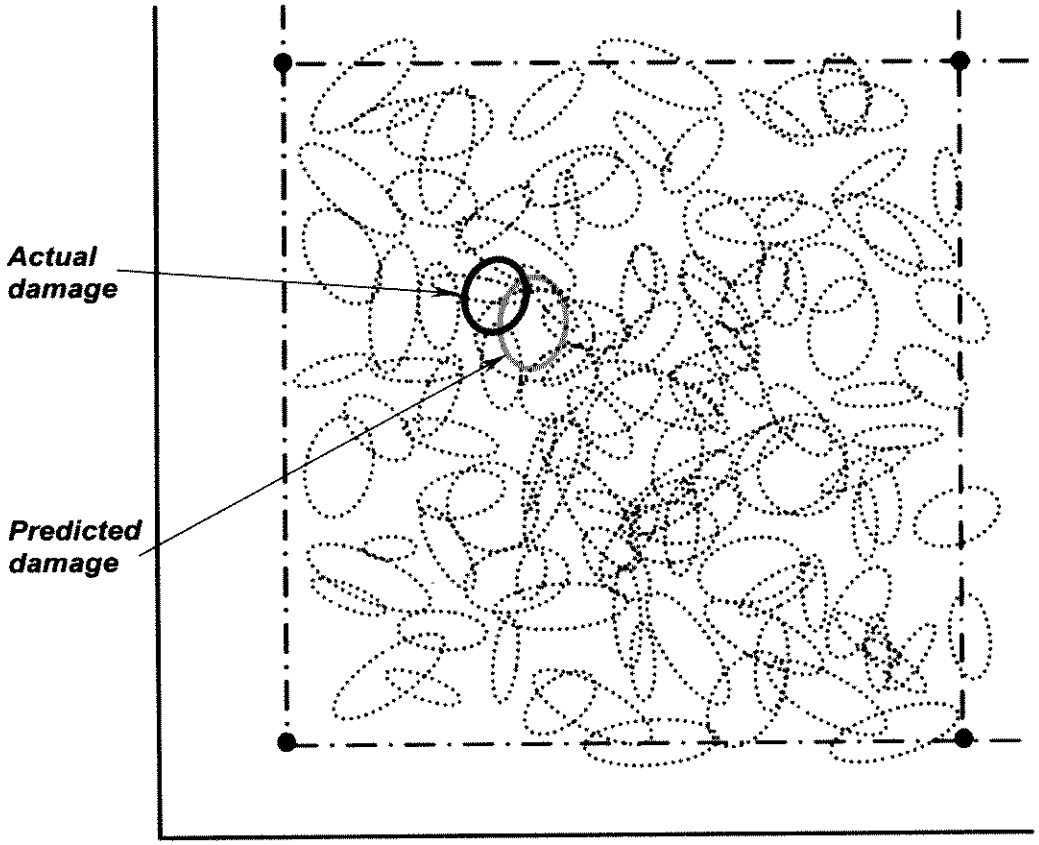

(a)

Figure 10.7 Diagnostic results for (a) $SP1^{\#}$; (b) $SP2^{\#}$

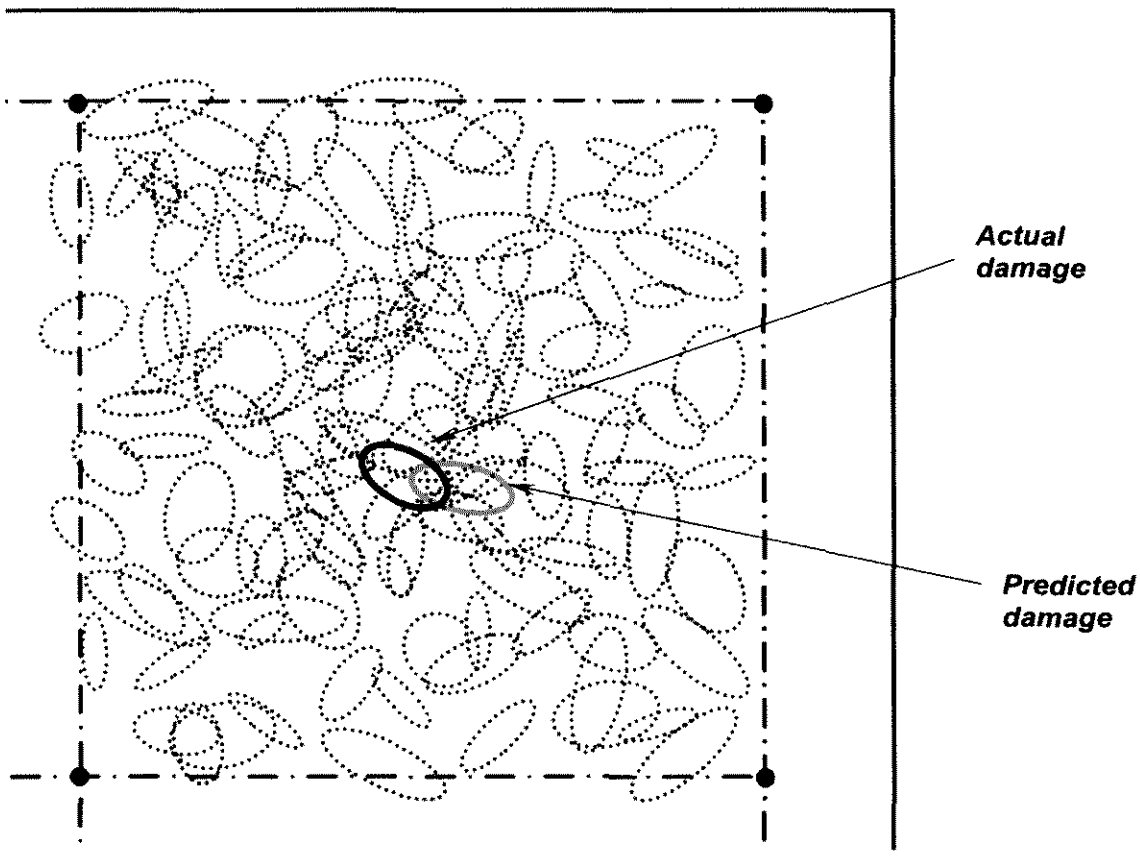

(b)

Figure 10.7 *Cont.*

10.4.4 Discussion

Results (see Figure 10.7) indicate that excellent quantitative predictions for presence, location, geometry and orientation of delamination in CF/EP composite laminates have been achieved in terms of the current neural network. The maximum estimation error occurs for delamination geometry and orientation, but it still falls in an acceptable range.

As discussed in Chapter 9, one of the deterministic factors to qualify ANN capability is the training pattern that predominantly masters precision of identification. Insufficient training certainly leads to misleading predictions, while superfluous

training unavoidably entails demanding computational requirements. Although more training patterns certainly lead to good identification, no significant improvement in precision can be observed when training patterns increase beyond a certain level (*100* in the present case study).

The results predicted by the well-trained ANN, as shown in Figure 10.7, do not superpose any damage pattern used during network training, which implies that the results are ratiocinated, rather than just finding the fittest patterns from the DPD. Precision of dentification also depends on various network configurations (input amount, training functions, network architecture, etc.), as discussed in the previous chapter.

10.5 Concluding Remarks

The proposed damage detection methodology and AO-SHD system are validated by identifying delaminations in quasi-isotropic CF/EP (T650/F584) composite structures, with tailored piezoelectric transducer networks. A DPD for delamination is constructed and an artificial neural network is customised. Quantitative diagnosis for delamination parameters (presence, location, geometry and orientation) has been achieved.

During DPD development, the parameterised modelling technique (PMT) greatly reduces time and effort in modelling and analysing, and it enhances the versatility and efficiency of the proposed method, making structural health monitoring feasible for complicated structures.

Chapter 11

Conclusions and Recommendations for Future Research

11.1 Concluding Remarks

In this study, the propagation characteristics of elastic waves, particularly Lamb waves, in an aluminium alloy structure containing a transverse crack and in quasi-isotropic CF/EP composite laminates bearing through-hole or delamination, were evaluated in terms of analytical derivation, FEM simulation and experimental validation. Results indicate that spectrographic characteristics of elastic waves in the time-scale domain are highly sensitive to the existence and degree of structural damage. Based on this observation, a quantitative damage detection algorithm was established. An *intelligent signal processing and pattern recognition* (ISPPR) algorithm was developed to fulfill the proposed detection scheme, actualised by software *signal processing package* (SPP).

In ISPPR, *wavelet transform* (WT) and *artificial neural network* (ANN) techniques are adopted to facilitate damage identification, a complicated *inverse* problem. It has been demonstrated that WT-based digital filters and spectrographic analysis are able to effectively eliminate broadband interference from various noise in signals, providing legible explanation for wave behaviour. The concept of *digital damage fingerprints* (DDF) was established, for the purpose of forming a pattern to describe

the filtered signals and their energy spectra, using digitalised and concise characteristic information. Hosting the extracted DDF, damage parameters databases (DPDs) for through-hole damage and delamination in CF/EP (T650/F584) composite structures were constructed. Additionally, an information mapping technique was proposed in ISPPR, which was also substantiated to significantly enhance the capability of the identification technique with limited data.

Another major contribution of this work concerns the establishment of the concept *standard sensor unit* (SSU). Such a concept is able to customise an active actuator/sensor network conveniently and promptly, to cater for engineering structures with various geometries and boundary conditions.

Modelling techniques for transverse crack in aluminium beams, interlaminar delamination and through-hole damage in CF/EP composite laminate, as well as piezoelectric actuator/sensors were developed. Effective elastic properties based on a micromechanical model, contact surface and multi-point constraint (MPC) algorithms in FEM simulation were also proven effective in this study. Experimental validation correlated very well with FEM results. The *parameterised modelling technique* (PMT) developed in this study exhibits powerful ability to make repetitious modelling for a complex engineering system feasible with minimal human manipulation, thus exponentially improving the efficiency and accuracy of the proposed damage detection scheme.

Supported by ISPPR, an *active online structural health diagnosis* (AO-SHD) system was configured on the *VXI* instrument platform with a tailored active actuating/sensing network, to implement damage assessment in real time. Validation of the identification algorithm and the AO-SHD system was then undertaken by actual case studies of detecting transverse crack growth in an aluminium alloy structural beam, and through-hole and delamination in quasi-isotropic CF/EP

(T650/F584) composite structures. Excellent quantitative diagnosis for damage parameters (presence, location, geometry and orientation) was achieved, verifying the capability of the ISPPR and the system developed.

Sensitivity of the proposed method to sensor numbers was evaluated. Results indicate that utility of *8* PZT transducers offers sufficient information to guarantee exact recognition for the chosen case studies in CF/EP composite laminates with economical and rational effort, while *4* PZT sensors can locate a delamination approximately but seem to be ineffective at providing quantitative identification of damage geometry and degree.

During ANN training, it was noted that a wide range of factors could influence network performance. A feedforward ANN with an architecture of two neural processing layers exhibits excellent capability to correlate damage parameters with structural dynamic parameters. Clearly, the number of training pattern plays an essential role in determining detection accuracy. Based on the results, training patterns, roughly covering the region where damage is most likely to occur but not necessarily to be considered with different orientation and geometrical shapes at the same location, were found to be sufficient to meet normal damage detection requirements. Massive training patterns do not always significantly improve ANN performance. In fact, from the study, a greater number of training cases can even lead to a decrease in prediction accuracy when ANN training has reached saturation. The scaled conjugate gradient (SCG)-based error-backpropagation (BP) algorithm performs well in negotiating network convergence and identification precision. In addition to the major factors delineated above, the network architecture may also affect convergence speed to some extent. Although it is beyond mathematic capability to select the most appropriate network configuration, some criteria can still be followed, which have been summarised in the discussion. Interestingly, a well-trained neural network seems to possess a certain robustness and fault tolerance,

capable of tolerating a small amount of disturbance in training input. This feature greatly benefits the SHM in practical environments.

11.2 Problematic Issues and Recommendations for Future Research

Inverse identification inherently involves the themes of searching, solvability and uniqueness. In spite of the promising results reported herein, problematic issues were also observed during the study, which need to be addressed in future work.

Firstly, the detection algorithm relying on the ANN technique is generally focused on one type of damage under given structural properties and geometry, which is naturally confined and not applicable to other kinds of damage or structures, or to multiple damage situations. One major concern evoked in this respect is to improve the versatility of an ANN with possibly less extra effort. To develop a universal damage information database applicable to various types of damage, structural properties, geometric identities and working conditions, would certainly lead to burdensome work and expensive computation, which is understood to be unfeasible and uneconomical. Moreover, as demonstrated in this study, the capability of the neural network may not be guaranteed with such bulky architecture. Considering the practical reality, several ANNs, exclusively contributing to the identification of one kind of damage in structures concerned, can be constructed and further integrated to perform comprehensive structural health monitoring. As a step towards resolving this issue, an information mapping technique can be helpful in reducing input effort.

Secondly, in this study, numerical simulations were used to produce DDF for network training, but higher identification precision can be expected by including actual experimental data for rectification during network training.

Flexible configurations of the active actuator/sensor network show promise. But optimisation of the number, location, and scale of the actuator/sensor network is another interesting topic worth exploring. With regard to the sensor network, interests also include improvement of cost-efficiency, integration with various systems, and combination of multiple sensor types, e.g. fibre optical sensor, so as to exploit their unique advantages. To accommodate future field applications, remote control and data transmission, less wire or even a wireless network would also be preferred. In particular, less ambitious but more attainable wireless actuating/sensing is now emerging as a full-fledged engineering discipline [Liu and Tomizuka, 2003].

The effects of damage on a structure can be classified as linear or nonlinear. A linear damage situation is defined as one in which the initially linear-elastic structure remains linear-elastic after damage. The majority of the work in this field concerns linear damage detection only, because in most cases SHM targets the identification of damage initiation only. In contrast, a nonlinear damage situation is defined as one in which the initially linear-elastic structure behaves in a nonlinear manner after damage. One example of nonlinear damage is the formation of a fatigue crack that opens and closes under normal operating vibration. A robust damage-detection method should be applicable for both types of situation.

Multiple damage detection is another intriguing subject, which contra-indicates uniqueness of detection techniques. Some encouraging issues associated with the present study also include the repair and/or rehabilitation of damaged components, sensitivity study, etc., which were not addressed here.

Bibliography

Abbate, A., Koay, J., Frankel, J., Schroeder S. C. and Das P. (1997). Signal detection and noise suppression using a wavelet transform signal processor: application to ultrasonic flaw detection, IEEE Transactions on Ultrasonics, Ferroelectrics and Frequency Control, **44**, 14-25.

Aberg, M. and Gudmundson, P. (2000). Micromechanical modeling of transient waves from matrix cracking and fibre fracture in laminated beams, International Journal of Solids and Structures, **37**, 4083-4102.

Achenbach, J. D. (1973). Wave Propagation in Elastic Solids, North-Holland Publishing Company, Amsterdam.

Achenbach, J. D. (2000). Quantitative nondestructive evaluation, International Journal of Solids and Structures, **37**, 13-27.

Achenbach, J. D., Moran, B. and Zulfiqar, A. (1997). Techniques and instrumentation for structural diagnostics, Structural Health Monitoring (ed. 1), edited by Chang, F.-K., Technomic Publishing Co, Lancaster, 179-190.

Agilent Co. (2000). User's Manual for *VXI* Instrument.

Airbus Co. (2003). www.airbus.com.

Al-Khalidy, A., Noori, M., Hou, Z., Yamamoto, S., Masuda, A. and Sone, A. (1997). Health monitoring systems of linear structures using wavelet analysis, Structural Health Monitoring (ed. 1), edited by Chang, F.-K., Technomic Publishing Co, Lancaster, 164-175.

Alleyne, D. and Cawley, P. (1991). A 2-dimensional Fourier transform method for the quantitative measurement of Lamb modes, Review of Progress in Quantitative Nondestructive Evaluation, edited by Thompson, D. O. and Chimenti, D. E., **10A**, 201-208.

Alleyne, D. N. and Cawley, P. (1992a). Optimisation of Lamb wave inspection techniques, NDT & E International, **25**(1), 11-22.

Alleyne, D. N. and Cawley, P. (1992b). The interaction of Lamb waves with Defects, IEEE Transactions on Ultrasonics, Ferroelectrics and Frequency Control, **39**(3), 381-397.

Anderson, J. A. (1995). An Introduction to Neural Networks, MIT Press, Cambridge.

Ayres, J. W., Lalande, F., Chaudhry, Z. and Rogers, C. A. (1998). Qualitative impedance-based health monitoring of civil infrastructures, Smart Materials and Structures, **7**, 599-605.

Badcock, R. A. and Birt, E. A. (2000). The use of 0-3 piezocomposite embedded Lamb wave sensors for detection of damage in advanced fibre composites, Smart Materials and Structures, **9**, 291-297.

Balageas, D. L. (2002). Structural health monitoring R&D at the "European Research Establishments in Aeronautics" (EREA), Aerospace Science and Technology, **6**, 159-170.

Banaszak D., Dale G. A., Watkins, A. N. and Jordan, J. (1999). An optical technique for detecting fatigue cracks in aerospace structures, Presented at the 24th Dayton-Cincinnati Aerospace Science Symposium, 9 April, Dayton, OH.

Barai, S. V. and Pandey, P. C. (1996). Time-delay neural networks in damage detection of railway bridges, Advances in Engineering Software, **28**, 1-10.

Barbero, E. J. and Reddy, J. N. (1991). Modelling of delamination in composite laminates using a layer-wise plate theory, International Journal of Solids and Structures, **28**(3), 373-388.

Benmedakhene, S., Kenane, M. and Benzeggagh, M. L. (1999). Initiation and growth of delamination in glass/epoxy composites subjected to static and dynamic loading by acoustic emission monitoring, Composites Science and Technology, **59**, 201-208.

Benz, R., Niethammer, M., Hurlebaus, S. and Jacobs, L. J. (2003). Localization of notches with Lamb waves, Journal of the Acoustical Society of America, **114**(2), 677-685.

Biemans, C., Staszewski, W. J., Boller, C. and Tomlinson, G. R. (1999). Crack detection in metallic structures using piezoceramic sensors, Key Engineering Materials, **167-168**, 112-121.

Bindal, V. N. (1999). Transducers for Ultrasonic Flaw Detection, Narosa Press, New Delhi.

Birt, E. A. (1998). Damage detection in carbon-fibre composites using ultrasonic Lamb waves, Insight, **40**(5), 335-339.

Blanas, P. and Das-Gupta, D. K. (1999). Composite piezoelectric sensors for smart composite structures, Proceedings of the 10th International Symposium on Electrets, Athens, Greece, 731-734.

Blanas, P., Rigas, E. and Das-Gupta, D. K. (1999). Health monitoring of composite structures using composite piezoelectric transducers, Structural Health Monitoring (ed. 2), edited by Chang, F.-K., Technomic Publishing Co, Lancaster, 635-642.

Bland, D. R. (1988). Wave Theory and Applications, Clarendon Press, Oxford.

Boashash, B. (1992). Time-Frequency Signal Analysis: Methods and Applications, Longman Cheshire Press, Melbourne.

Boeing Co. (2003). www.boeing.com.

Boller, C. (2001). Ways and options for aircraft structural health management, Smart Materials and Structures, **10**, 432-440.

Browne, A. (1997). Neural Network Analysis, Architectures and Applications, Institute of Physics Publishing Co., London.

Bull, J. W. (1996). Numerical Analysis and modelling of Composite Materials, Blackie Academic & Professional, London.

Castaings, M. and Cawley, P. (1996). The generation, propagation, and detection of Lamb waves in plates using air-coupled ultrasonic transducers, Journal of the Acoustical Society of America, **100**(5), 3070-3077.

Castaings, M. and Hosten, B. (2001a). Lamb and SH waves generated and detected by air-coupled ultrasonic transducers in composite material plates, NDT & E International, **34**, 249-258.

Castaings, M. and Hosten, B. (2001b). The propagation of guided waves in composite sandwich-like structures and their use for NDT, Review of Progress in Quantitative Nondestructive Evaluation, edited by Thompson, D. O. and Chimenti, D. E., **20**, 999-1006.

Cawley, P. (1984). The impedance method of non-destructive inspection, NDT International, **17**(2): 59-65

Cawley, P. and Alleyne, D. (1996). The use of Lamb waves for the long range inspection of large structures, Ultrasonics, **34**, 287-290.

Chan, Y. T. (1995). Wavelet Basic, Kluwer Academic Publishers, Boston.

Chance, J., Tomlinson, G. R. and Worden, K. (1994). A simplified approach to the numerical and experimental modeling of the dynamics of a cracked beam, Proceedings of the 12th International Modal Analysis Conference, 778–785.

Chang, C. C., Chang, T. Y. P. and Xu, Y. G. (2000). Structural damage detection using an iterative neural network, Journal of Intelligent Material Systems and Structures, **11**, 32-42.

Chang, F.-K. (1995). Built-in damage diagnosis for composite structures,

Proceedings of 10th International Conference on Composite Materials, Whistler, Canada.

Chang, F.-K. (2002a). Introduction to health monitoring: context, problems, solutions, talk on the 1st European Pre-Workshop on Structural Health Monitoring, 9, July, 2002, Paris, France.

Chang, F.-K. (2002b). Ultra reliable and super safe structures for the new century, Proceedings of the 1st European Workshop on Structural Health Monitoring, edited by Balageas, D., 10-12, July, 2002, Paris, France, 3-12.

Chang, T. Y. P., Chang, C. C. and Xu, Y. G. (1999). Updating structural parameters: an adaptive neural network approach, Structural Health Monitoring (ed. 2), edited by Chang, F.-K., Technomic Publishing Co, Lancaster, 379-389.

Chati, M., Rand, R. and Mukherjee, S. (1997). Modal analysis of a cracked beam, Journal of Sound and Vibration, **207**(2), 138-169.

Chattopadhyay, A., Nam, C. and Dragomir-Daescu, D. (1999). Delamination modelling and detection in smart composite plates, Journal of Reinforced Plastics and Composites, **18**(17), 1557-1572.

Chaudhry, Z. and Ganino, A. J. (1994). Damage detection using neural networks: an initial experimental study on debonded beams, Journal of Intelligent Material Systems and Structures, **5**, 585-589.

Chee, C. Y. K., Tong, L. and Steven, G. P. (1998). A review on the modelling of piezoelectric sensors and actuators incorporated in intelligent structures, Journal of Intelligent Material Systems and Structures, **9**, 3-19.

Chee, C. Y. K., Tong, L. and Steven, G. P. (1999). A mixed model for composite beams with piezoelectric actuators and sensors, Smart Materials and Structures, **8**, 417-432.

Chen, H. M., Qi, G. Z., Yang, J. C. S. and Amini, F. (1995). Neural network for structural dynamic model identification, Journal of Engineering Mechanics, **121**, 1377-1381.

Chen, Y. and Swamidas, A. S. J. (1994). Dynamic characteristics and modal parameters of a plate with a small growing surface crack, Proceedings of the 12th International Modal Analysis Conference, 1155–1161.

Chien, H.-T., Sheen, S.-H. and Raptis, A. C. (1994). Theoretical studies of wave propagation in multilayered piezoelectric media. Review of Progress in Quantitative Nondestructive Evaluation, edited by Thompson, D. O. and Chimenti, D. E., **13**, 219-226.

Chimenti, D. E. (1997). Guided waves in plates and their use in materials characterization, Applied Mechanics Reviews, **50**(5), 247-284.

Chiu, W. K., Galea, S. C., Koss, L. L. and Rajic, N. (2000). Damage detection in bonded repairs using piezoceramics, Smart Materials and Structures, **9**, 466–475.

Choi, H. Y. and Chang, F.-K. (1992). A model for predicting damage in graphite/epoxy laminated composites resulting from low-velocity point impact, Journal of Composite Materials, **26(14)**, 2134-2169.

Choi, K. and Chang, F.-K. (1996). Identification of impact force and location using distributed sensors, AIAA Journal, **34**(1), 136-142.

Choi, K., Keilers, Jr. C. K. and Chang, F.-K. (1994). Impact Damage detection in composite structures using distributed piezoceramics, Proceedings of the 35th AIAA/ASME/ASCE/AHS Conference on Structural Dynamics and Materials, 118-124.

Chou, J.-H. and Ghaboussi, J. (2001). Genetic algorithm in structural damage detection, Computers and Structures, **79**, 1335-1353.

Chui, C. K. (1997). Wavelets: a Mathematical Tool for Signal Processing, SIAM, Philadelphia.

Clark, G. (1989). Modelling of impact damage in composite laminates, Composites, **20**(3), 209-214.

Culshaw, B., Pierce, S. G. and Staszewski, W. J. (1998). Condition monitoring in composite materials: an integrated systems approach, Proceedings of Institute of Mechanical Engineers, **212**, 189-201.

Cunha, J. and Perreux, D. (1998). Method for damage evaluation of laminated composite materials by using model updating techniques in dynamics, Journal of Engineering Materials and Technology, **120**(3), 256-260.

Dalpiaz, G., Rivola, A. and Rubini, R. (2000). Effectiveness and sensitivity of vibration processing techniques for local fault detection in gears, Mechanical systems and signal processing, **14**(3), 387-412.

Daubechies, I. (1990). The wavelet transform, time-frequency localization and signal analysis, IEEE Transactions on Information Theory, **36**(5), 961-1005.

Davis, G. A. O., Zhang, X., Zhou, G. and Watson, S. (1994). Numerical modelling of impact damage, Composites, **25**(5), 342-350.

Diamanti, K., Hodgkinson, J. M. and Soutis, C. (2002). Damage detection of composite laminates using PZT generated Lamb waves, Proceedings of the 1st

European Workshop on Structural Health Monitoring, edited by Balageas, D., 10-12, July, 2002, Paris, France, 398-405.

Doebling, S. W. (1995). Measurement of Structural Flexibility Matrices for Experiments with Incomplete Reciprocity, Ph. D. Dissertation, Department of Aerospace Engineering Sciences, University of Colorado, Boulder, CO, CU-CAS-95-10.

Doebling, S. W., Farrar, C. R., Prime, M. B. and Shevitz, D. W. (1996). Damage identification and health monitoring of structural and mechanical systems from changes in their vibration characteristics: a literature review, Los Alamos Report, LA-13070-MS.

Doyle, J. F. (1997). Wave Propagation in Structures, Springer-Verlag, New York.

Dupont, M., Osmont, D., Gouyon, R. and Balageas, D. L. (1999). Permanent monitoring of damaging impacts by a piezoelectric sensor based integrated system, Structural Health Monitoring (ed. 2), edited by Chang, F.-K., Technomic Publishing Co, Lancaster, 561-570.

Farrar, C. R., Doebling, S. W. and Nix, D. A. (2001a). Vibration-based structural damage identification, Philosophical Transactions of the Royal Society of London, Series A: Mathematical Physical and Engineering Sciences, **359**, 131-149.

Farrar, C. R. and Jauregui, D. A. (1998a). Comparative study of damage identification algorithms applied to a bridge: I. experiment, Smart Materials and Structures, **7**, 704-719.

Farrar, C. R. and Jauregui, D. A. (1998b). Comparative study of damage identification algorithms applied to a bridge: II. numerical study, Smart Materials and Structures, **7**, 720-731.

Farrar, C. R., Sohn, H. and Worden, K. (2001b). Data normalisation: a key for structural health monitoring, Structural Health Monitoring (ed. 3), edited by Chang, F.-K., CRC Press, Boca Raton, 1229-1239.

Fausett, L. (1994). Fundamentals of Neural Networks, Architectures, Algorithms and Applications, Prentice Hall, Inc., Englewood Cliffs.

Finn, S. R. and Springer, G. S. (1993). Delaminations in composite plates under transverse static or impact loads - a model, Composite Structures, **23**, 177-190.

Fritzen, C.-P. and Bohle, K. (2001). Application of model-based damage identification to a seismically loaded structure, Smart Materials and Structures, **10**: 452-458.

Fromme, P. and Sayir, M. B. (2002). Detection of cracks at rivet holes using guided waves, Ultrasonics, **40**, 199-203.

Fukunaga, H., Hu, N. and Chang, F.-K. (2002). Structural damage identification using piezoelectric sensors, International Journal of Solids and Structures, **39**, 393-418.

Gadelrab, R. M. (1996). The effect of delamination on the natural frequencies of a laminated composite beam, Journal of Sound and Vibration, **197**(3), 283-292.

Gao, W., Glorieux, C. and Thoen, J. (2003). Laser ultrasonic study of Lamb waves: determination of the thickness and velocities of a thin plate, International Journal of Engineering Science, **41**, 219-228.

Gaul, L. and Hurlebaus, S. (1999). Wavelet-transform to identify the location and force-time-history of transient load in a plate, Structural Health Monitoring (ed. 2), edited by Chang, F.-K., Technomic Publishing Co, Lancaster, 851-860.

Gere, J. M. (2002). Mechanics of materials, Cheltenham, Eng., Nelson Thorn's.

Ghosh, T., Kundu, T. and Karpur, P. (1998). Efficient use of Lamb modes for detecting defects in large plates, Ultrasonics, **36**, 791-801.

Ghoshal, A., Martin, W. N. and Schulz, M. J. (2002). Simulation of asymmetric Lamb wave propagation for health monitoring, Proceedings of the 1st European Workshop on Structural Health Monitoring, edited by Balageas, D., 10-12, July, 2002, Paris, France, 365-373.

Ghoshal, A., Sundaresan, M. J., Schulz, M. J. and Pai, P. F. (2000). Structural health monitoring techniques for wind turbine blades, Journal of Wind Engineering and Industrial Aerodynamics, **85**, 309-324.

Giurgiutiu, V., Bao, J. and Zhao, W. (2001). Active sensor wave propagation health monitoring of beam and plate structures, Proceedings of SPIE (International symposium on smart structures and material), **4327**, 234-245.

Giurgiutiu, V. and Rogers, C. A. (1998). Recent advancements in the Electro-Mechanical (E/M) impedance method for structural health monitoring and NDE, Proceedings of SPIE on Smart Structures and Materials, **3329**, 536-550.

Goldfine, N., Washbaugh, A., Schlicker, D. and Zilberstein, V. (2000). Application of MWM-Array Eddy Current Sensor to Corrosion Mapping, Proceedings of 4th International Aircraft Corrosion Workshop.

Goldfine, N., Washbaugh, A. and Walrath, K. (1999). Conformable eddy current sensors and methods for gas turbine inspection and health monitoring, Gas Turbine Materials Technology, 105-114.

Gommers, B., Verpoest, I. and Houtte, P. V. (1996). Modelling the elastic properties of knitted fabric-reinforced composites, Composites Science and Technology, **56**, 685-694.

Gorl, E. and Link, M. (2001). Identification of damage parameters of a full-scale steel structure damaged by seismic loading, Smart Materials and Structures, **10**, 459-465.

Gray, J. and Tillack. G.-R. (2001). X-ray imaging methods over the last 25 years – new advances and capabilities, Review of Progress in Quantitative Nondestructive Evaluation, edited by Thompson, D. O. and Chimenti, D. E., **20**, 1443-1450.

Green, W. A. and Green, E. R. (2000). Elastic waves in fibre composite laminates, Ultrasonics, **38**, 228-231.

Grondel, S., Delebarre, C., Assaad, J., Dupuis, J.-P. and Reithler, L. (2002). Fatigue crack monitoring of riveted aluminium strap joins by Lamb wave analysis and acoustic emission measurement techniques, NDT & E International, **35**, 137-146.

Guo, N. and Cawley, P. (1992). Lamb waves for the NDE of Composite Laminates, Review of Progress in Quantitative Nondestructive Evaluation, edited by Thompson, D. O. and Chimenti, D. E., **11**, 1443-1450.

Guo, N. and Cawley, P. (1993a). Lamb wave propagation in composite laminates and its relationship with acousto-ultrasonics, NDT & E International, **26**(2), 75-84.

Guo, N. and Cawley, P. (1993b). The interaction of Lamb waves with delaminations in composite laminates, Journal of the Acoustical Society of America, **94**(4), 2240-2246.

Guo, N. and Cawley, P. (1994). Lamb wave reflection for the quick nondestructive evaluation of large composite laminates, Materials Evaluation, **52**, 404-411.

Guo, Z., Achenbach, J. D. and Krishnaswamy, S. (1997). EMAT generation and laser detection of single Lamb wave modes, Ultrasonics, **35**, 423-429.

Ha, S.-K., Keilers, C. and Chang, F.-K. (1991). Analysis of laminated composites containing distributed piezoelectric ceramics, Journal of Intelligent Material Systems and Structures, **2**(1), 59-71.

Habeger, C. C., Mann, R. W. and Baum, G. A. (1979). Ultrasonic plate waves in paper, Ultrasonics, **17**, 57-62.

Hall. S. R. (1999). The effective management and use of structural health data, Structural Health Monitoring (ed. 2), edited by Chang, F.-K., Technomic Publishing Co, Lancaster, 265-275.

Hassoun, M. H. (1995). Fundamentals of Artificial Neural Networks, MIT Press, Cambridge.

Hemez, F. M. (1993). Theoretical and Experimental Correlation between Finite Element Models and Modal tests in the Context of Large Flexible Space Structures, Ph. D. Dissertation, Department of Aerospace Engineering Sciences, University of Colorado, Boulder, CO.

Hexcel Co. (2001). Datasheet for T650/F584 composite materials.

Hibbitt, Karlsson & Sorensen Inc. (2003). ABAQUS User's Manual, Ver. 6.2.4.

Hoskin, B. C. and Baker, A. A. (1986). Composite Materials for Aircraft Structures, American Institute of Aeronautics and Astronautics, New York.

Hosten, B., Castaings, M., Tretout, H. and Voillaume, H. (2001). Identification of composite materials elastic moduli from Lamb wave velocities measured with single sided, contactless ultrasonic method, Review of Progress in Quantitative Nondestructive Evaluation, edited by Thompson, D. O. and Chimenti, D. E., **20**, 1023-1030.

Hou, Z. (2003). Application of electronic shearing speckle pattern interferometry, Presentation on University of Sydney.

Hou, Z., Noori, M. and Amand, R. St. (2000). Wavelet-based approach for structural damage detection, Journal of Engineering Mechanics, **126**, 677-683.

Hou, Z., Noori, M., Amand, R. St., Hu, J., Al-Khalidy, A., Baker, M., Yamamoto, S., Masuda, A. and Sone, A. (1998). Damage detection using wavelet approach and its application for on-line health monitoring, Proceedings of the 2nd World Conference on Structural Control, June 28-July 1, 1998, Kyoto, Japan, 2351-2358.

Huang, N., Ye, L. and Su, Z. (2004). Parameterised modelling technique and its application in structural health monitoring, Proceedings of 4th Asian-Australasian Conference on Composite Materials, 6-9, July, 2004, Sydney, Australia (accepted).

Hurlesbaus, S., Gaul, L. and Jacobs, L. J. (2001). Localization of acoustic emission signals in a fatigue specimen using laser ultrasonic, Structural Health Monitoring (ed. 3), edited by Chang, F.-K., CRC Press, Boca Raton, 1219-1228.

Hwu, C. B. and Liang, Y. C. (1998). Crack identification by artificial neural network, Key Engineering Materials, **145-149**, 405-410.

Hwu, C. B. and Liang, Y. C. (2001). Hole/crack identification by static strains from multiple loading modes, AIAA Journal, **39**(2), 315-323.

Ihn, J.-B. and Chang, F.-K. (2002). A smart patch for monitoring crack growth in metallic structures underneath bonded composite repair patch, Proceedings of the 16th American Society for Composites.

Ishak, S. I., Liu, G. R., Shang, H. M. and Lim, S. P. (2001). Locating and sizing of delamination in composite laminates using computational and experimental methods, Composites, Part B, **32**, 287-298.

Islam, A. S. and Craig, K. C. (1994). Damage detection in composite structures using piezoelectric materials, Smart Materials and Structures, **3**, 318-328.

Issa, C. A., Balasubramaniam, K. and Srirengan, K. (1994). Adaptive finite element modeling of oblique ultrasonic NDE waves, Review of Progress in Quantitative Nondestructive Evaluation, edited by Thompson, D. O. and Chimenti, D. E., **13**, 85-92.

Jahanmir, S., Ramulu, M. and Koshy, P. (1999). Machining of Ceramics and Composites, Marcel Dekker, New York.

Jensen, A. E. and Irgens, F. (1999). Thickness vibrations of sandwich plates and beams and delamination detection, Journal of Intelligent Material Systems and Structures, **10**, 46-55.

Jih, C. J. and Sun, C. T. (1993). Prediction of delamination in composite laminates subjected to low velocity impact, Journal of Composite Materials, **27**(7), 684-701.

Karayiannis, N. B. and Venetsanopoulos, A. N. (1993). Artificial Neural Networks: Learning Algorithms, Performance Evaluation and Applications, Kluwer Academic, Boston.

Kawiecki, G. (1998). Feasibility of applying distributed piezotransducers to structural damage detection, Journal of Intelligent Material Systems and Structures, **9**(3), 189-197.

Keilers, Jr. C. H. (1997). Identifying composite delaminations using built-in sensors and actuators, AIAA Journal, **97**, 1707-1716.

Keilers, Jr. C. H. (1998). Search strategies for identifying a composite plate delamination using built-in transducers, Journal of Intelligent Material Systems and Structures, **9**, 883-891.

Keilers, Jr. C. H. and Chang, F.-K. (1993). Damage detection and diagnosis of composites using built-in piezoceramics, Proceedings of SPIE on Smart Structures and Materials, Albuquerque, New Mexico, USA, **1917**, 1009-1019.

Keilers, Jr. C. H. and Chang, F.-K. (1995a). Identifying delamination in composite beams using built-in piezoelectrics: part I - experiments and analysis, Journal of Intelligent Material Systems and Structures, **6**, 649-663.

Keilers, Jr. C. H. and Chang, F.-K. (1995b). Identifying delamination in composite beams using built-in piezoelectrics: part II - an identification method, Journal of Intelligent Material Systems and Structures, **6**, 664-672.

Kessler S. S. (2002). Piezoelectric-based In-Situ Damage Detection of Composite Materials for Structural Health Monitoring Systems, Massachusetts Institute of Technology, Ph.D. Thesis.

Kessler, S. S. and Spearing, S. M. (2002). In-situ sensor-based damage detection of composite materials for structural health monitoring, Presentation on SDM-02.

Kessler, S. S., Spearing, S. M. and Atalla, M. J. (2002a). In-situ damage detection of composites structures using Lamb wave methods, Proceedings of the 1st European Workshop on Structural Health Monitoring, edited by Balageas, D., 10-12, July, 2002, Paris, France, 374-381.

Kessler, S. S., Spearing, S. M. and Soutis, C. (2002b). Damage detection in composite materials using Lamb wave methods, Smart Materials and Structures, 11, 269–278.

Kim, H. M. and Bartkowicz, T. J. (1993). Damage detection and health monitoring of large space structures, Sound and Vibration, **27**(6), 12–17.

Kim, J.-T., Ryu, Y.-S., Cho, H.-M. and Stubbs, N. (2003). Damage identification in beam-type structures: frequency-based method vs mode-shape-based method, Engineering Structures, **25**, 57-67.

Kim, Y. Y. and Kim, E. H. (2000). A new damage detection method based on a wavelet transform, Proceedings of the 18th IMAC, San Antonio, Texas, U.S.A., 1207-1212.

Kim, Y. Y. and Kim, E. H. (2001). Effectiveness of the continuous wavelet transform in the analysis of some dispersive elastic waves, Journal of the Acoustical Society of America, **110**(1), 1-9.

Kishore, N. N., Sridhar, I. and Iyengar, N. G. R. (2000). Finite element modelling of the scattering of ultrasonic waves by isolated flaws, NDT & E International, **33**, 297-305.

Konar, A. (2000). Artificial Intelligence and Soft Computing: Behavioral and Cognitive Modeling of the Human Brain. CRC Press LLC.

Kwon, Y. W. and Wojcik, G. W. (1998). Impact study of sandwich composite structures with delamination, Journal of Composite Materials, **32**(5), 406-430.

Lan, H. F., Ko, J. M. and Wong, C. W. (1998). Localization of damaged structural connections based on experimental modal and sensitivity analysis, Journal of Sound and Vibration, **210**, 91-115.

Lakshmanan, K. A. and Pines, D. J. (1997). Modeling damage in rotorcraft flexbeams using wave mechanics, Smart Materials and Structures, **6**, 383-392.

Lee, S. U., Robb, D. and Besant, C. (2001). The directional Choi-Williams distribution for the analysis of rotor-vibration signals, Mechanical Systems and Signal Processing, **15**(4), 789-811.

Legendre, S., Massicotte, D., Goyette, J. and Bose, T. K. (2000). Wavelet-transform-based method of analysis for Lamb-wave ultrasonic NDE signals, IEEE Transactions on Instrumentation and Measurement, **49**, 524-530.

Lemistre, M. and Balageas, D. (2001). Structural health monitoring system based on diffracted Lamb wave analysis by multiresolution processing, Smart Materials and Structures, **10**, 504-511.

Lemistre, M. and Balageas, D. (2002a). A new concept for SHM applied to composite materials, part I: theoretical considerations, Proceedings of the 1st European Workshop on Structural Health Monitoring, edited by Balageas, D., 10-12, July, 2002, Paris, France, 493-499.

Lemistre, M. and Balageas, D. (2002b). A new concept for SHM applied to composite materials, part II: experimental validation, Proceedings of the 1st European Workshop on Structural Health Monitoring, edited by Balageas, D., 10-12, July, 2002, Paris, France, 500-507.

Lemistre, M., Gouyon, R., Kaczmarek, H. and Balageas, D. (1999). Damage localization in composite plates using wavelet transform processing on Lamb wave signals, Structural Health Monitoring (ed. 2), edited by Chang, F.-K., Technomic Publishing Co, Lancaster, 861-870.

Lemistre, M., Placko, D. and Balageas, D. L. (2003). Evaluation of the performances of the *HELP layer*® SHM system using both DPSM simulations and experiments, Structural Health Monitoring (ed. 4), edited by Chang, F.-K., DEStech Publications, Lancaster, pp. 903-910.

Levin, R. I. and Lieven, N. A. J. (1998). Dynamic finite element model updating using neural networks, Journal of Sound and Vibration, **210**, 593-607.

Li, C. J. and Ma, J. (1997). wavelet decomposition of vibrations for detection of bearing-localized defects, NDT & E International, **30**(3), 143-149.

Liang, Y. C. and Hwu, C. (2001). On-line identification of holes/cracks in composite structures, Smart Materials and Structures, **10**, 599-609.

Lichtenwalner, P. F., Dunne, J. P., Becker, R. S. and Baumann, E. W. (1997). Active damage interrogation system for structural health monitoring, Proceedings of SPIE, **3044**, 186-194.

Lim, T. W. (1995). Structural damage detection using constrained eigenstructure assignment, Journal of Guidance, Control, and Dynamics, **18**(3), 411–418.

Lin, X. and Yuan, F. G. (2001). Diagnostic Lamb waves in an integrated piezoelectric sensor/actuator plate: analytical and experimental studies, Smart Materials and Structures, **10**, 907-913.

Liu, B., Ling, S.-F. and Meng, Q. (1997). Machinery diagnosis based on wavelet packets, Journal of Vibration and Control, **3**, 5-17.

Liu, S. C. and Tomizuka, M. (2003). Vision and strategy for sensors and smart structures technology research, Structural Health Monitoring (ed. 4), edited by Chang, F.-K., DEStech Publications, Lancaster, Lancaster, 42-52.

Looney, C.G. (1997). Pattern Recognition Using Neural Networks, (1997), Oxford University Press, New York.

Lopes, Jr. V., Park, G., Cudney, H. H. and Inman, D. J. (1999). Smart structures health monitoring using artificial neural network, Structural Health Monitoring (ed. 2), edited by Chang, F.-K., Technomic Publishing Co, Lancaster, 976-985.

Lowe, M. J. S. (1995). Matrix Techniques for modelling ultrasonic waves in multilayered media, IEEE Transactions on Ultrasonics, Ferroelectrics and Frequency Control, **42**(4), 525-542.

Lu, C.-J. and Hsu, Y.-T. (1999). Application of wavelet transform to structural damage detection, Proceedings of the 17th International Modal Analysis Conference, 908-914.

Luong, M. P. (1998). Fatigue limit evaluation of metals using an infrared thermographic technique, Mechanics of Materials, **28**, 155-163.

Ma, J. and Pine, D. J. (2001). A comparison of modal and wave-based damage detection approaches for one-dimensional structures, Structural Health Monitoring (ed. 3), edited by Chang, F.-K., CRC Press, Boca Raton, 967-979.

Majumdar, P. M. and Suryanarayan, S. (1998). Flexural vibrations of beams with delaminations, Journal of Sound and Vibration, **125**, 441-461.

Mamishev, A. V., Lesieutre, B. C. and Zahn, M. (1998). Optimization of multi-wavelength interdigital dielectrometry instrumentation and algorithms, IEEE Transactions on Dielectrics and Electrical Insulation, **5**, 408-420.

Martin, H. R., Ismall, F. and Sakuta, A. (1990). New statistical approach for gear damage detection, Proceedings of the 2nd International Machinery Monitoring and Diagnostics Conference, Los Angeles, U.S.A., 329-334.

Maseras-Gutierrez, M. A., Staszewski, W. J., Found, M. S. and Worden, K. (1998). Detection of impacts in composite materials using piezoceramic sensors and neural networks, Proceedings of SPIE on Smart Structures and Materials, **3329**, 491-497.

Mathworks Inc. (2001a). Data Acquisition Toolbox User's Guide, Ver. 2.0.

Mathworks Inc. (2001b). Neural Network Toolbox User's Guide, Ver. 4.0.

Mathworks Inc. (2001c). Optimisation Toolbox User's Guide, Ver. 2.0.

Mathworks Inc. (2001d). Signal Processing Toolbox User's Guide, Ver. 6.0.

Mathworks Inc. (2001e). Wavelet Transform User's Guide, Ver. 1.0.

Mehra, P. and Wah, B. W. (1992). Artificial Neural Networks: Concepts and Theory, IEEE computer Society Press, Washington.

Mickens, T., Schulz, M., Sundaresan, M. and Ghoshal, A. (2003). Structural health monitoring of an aircraft joint, Mechanical Systems and Signal Processing, **17**(2), 285-303.

Microsoft Co. (1995). FORTRAN Power Station, Ver. 4.0.

Monkhouse, R. S. C., Wilcox, P. D. and Cawley, P. (1997). Flexible interdigital PVDF transducers for the generation of Lamb waves in structures, Ultrasonics, **35**, 489-498.

Monkhouse, R. S. C., Wilcox, P. W, Lowe, M. J. S., Dalton, R. P. and Cawley, P. (2000). The rapid monitoring of structures using interdigital Lamb wave transducers, Smart Materials and Structures, **9**, 304-309.

Moulin, E., Assaad, J., Delebarre, C., Grondel, S. and Balageas, D. (2000). Modeling of integrated Lamb waves generation systems using a coupled finite element normal modes expansion method, Ultrasonics, **38**, 522-526.

Moyo, P. and Brownjohn, J. M. W. (2002). Detection of anomalous structural behaviour using wavelet analysis, Mechanical Systems and Signal Processing, **16**, 429-445.

MSC Software (2001). Patran User's Manual, Ver. 2001.

NASA Columbia Accident Investigation Board (NASA-CAIB). (2003). *Columbia* Accident Report.

NASA (2003). www.nasa.gov.

Newland, D. E. (1994a). Wavelet analysis of vibration, part I: theory, Journal of Vibration and Acoustics, **116**, 409-416.

Newland, D. E. (1994b). Wavelet analysis of vibration, part II: wavelet maps, Journal of Vibration and Acoustics, **116**, 417-425.

Niethammer, M., Jacobs, L. J., Qu, J. and Jarzynski, J. (2001). Time-frequency representations of Lamb waves, Journal of the Acoustical Society of America, **109**(5), 1841-1847.

Okafor, A. C., Chandrashekhara, K. and Jiang, Y. P. (1996). Delamination prediction in composite beams with built-in piezoelectric devices using modal analysis and neural network, Smart Materials and Structures, **5**, 338-347.

Okafor, A. C. and Dutta, A. (2000). Structural damage detection in beams by wavelet transforms, Smart Materials and Structures, **9**, 906-917.

Olsson, R. (2001). Analytical prediction of large mass impact damage in composite laminates, Composites, Part A, **32**, 1207-1215.

Osmont, D., Barhoncel, D., Devillers, D. and Dupont, M. (2002). Health monitoring of sandwich plates based on the analysis of the interaction of Lamb waves with damages, Proceedings of the 1st European Workshop on Structural Health Monitoring, edited by Balageas, D., 10-12, July, 2002, Paris, France, 336-343.

Ostachowicz, W., Krawczuk, M., Cartmell, M. and Gilchrist, M. (2002). Detection of delaminations using spectral finite elements, Proceedings of the 1st European Workshop on Structural Health Monitoring, edited by Balageas, D., 10-12, July, 2002, Paris, France, 374-381.

Paget, C. A., Grondel, S., Levin, K. and Delebarre, C. (2003). Damage assessment in composites by Lamb waves and wavelet coefficients, Smart Materials and Structures, **12**, 393-402.

Pai, P. F. and Jin, S. (2000). Locating structural damage by detecting boundary effects, Journal of Sound and Vibration, **231**(4), 1079-1110.

Palacz, M. and Krawczuk, M. (2002). Analysis of longitudinal wave propagation in a cracked rod by the spectral element method, Computers and Structures, **80**, 1809-1816.

Pandey, A. K. and Biswas, M. (1994). Damage detection in structures using changes in flexibility, Journal of Sound and Vibration, **169** (1), 3–17.

Pandey, A. K. and Biswas, M. and Samman, M. M. (1991). Damage detection from changes in curvature mode shapes, Journal of Sound and Vibration, **145**: 321-332.

Pardo De Vera, C. and Guemes, J. A. (1998). Embedded self-sensing piezoelectric for damage detection, Journal of Intelligent Material Systems and Structures, **9**(11), 876-882.

Park, K. C., Reich, G. W. and Alvin, K. F. (1998). Structural damage detection using localised flexibilities, Journal of Intelligent Material Systems and Structures, **9**, 911-919.

Peng, Z. K. and Chu, F. L. (2003). Application of the wavelet transform in machine condition monitoring and fault diagnostics: a review with bibliography, Mechanical Systems and Signal Processing (in press).

Percival, W. J. and Birt, E. A. (1997). A study of Lamb wave propagation in carbon-fibre composites, Insight, **39**, 728-735.

Perel, V. Y. and Palazotto, A. N. (2002). Finite element formulation for dynamics of delaminated composite beams with piezoelectric actuators, International Journal of Solids and Structures, **39**, 4457-4483.

Peterson, L. D., Doebling, S. W. and Alvin, K. F. (1995). Experimental determination of local structural stiffness by disassembly of measured flexibility matrices, Proceedings of the 36th AIAA/ASME/ASCE/AHS/ASC Conference on Structures, Structural Dynamics, and Materials, AIAA-95-1090-CP, 2756–2766.

PI Ceramic (1994). Data sheet for PI-151 materials.

Picinbono, B. (1988). Principles of Signals and Systems: Deterministic Signals, Artech House, London.

Pines, D. J. (1997). The use of wave propagation for structural damage identification, Structural Health Monitoring (ed. 1), edited by Chang, F.-K., Technomic Publishing Co, Lancaster, 665-677.

Pohl, J., Herold, S., Mook, G. and Michel, F. (2001). Damage detection in smart CFRP composites using impedance spectroscopy, Smart Materials and Structures, **10**, 834-842.

Pojl, H., Mook, G., Michel, F. (2000). Health monitoring of smart CFRP-structures, Proceedings of the 15th World Conference on Nondestructive Testing, Roma, Italy, 15-21 October.

Prosser, W. H., Seale, M. D. and Smith, B. T. (1999). Time-frequency analysis of the dispersion of Lamb modes, Journal of the Acoustical Society of America, **105**(5), 2669-2676.

Purekar, A., Lakshmanan, K. A. and Pines, D. J. (1998). Detecting delamination

damage in composite rotorcraft flexbeams using the local wave response, Proceedings of SPIE, **3329**, 523-535.

Qu, J. (1994). Elastic waves scattering by interface cracks, Review of Progress in Quantitative Nondestructive Evaluation, edited by Thompson, D. O. and Chimenti, D. E., **13**, 53-60.

Ratcliffe, C. P. (1997). Damage detection using a modified Laplacian operator on mode shape data, Journal of Sound and Vibration, **204**(3), 505-517.

Razi, H. and Kobayashi, A. S. (1993). Delamination in cross-ply laminated composite subjected to low-velocity impact, AIAA Journal, **31**(8), 1498-1502.

Rhim, J. and Lee, S. W. (1995). A neural network approach for damage detection and identification of structures, Computational Mechanics, **16**, 437-443.

Ristic, L. (1994). Sensor Technology and Devices, Artech House, Boston.

Roh, Y.-S. and Chang, F.-K. (1995). Effect of impact damage on Lamb wave propagation in laminated composites, Proceedings of ASME on Dynamic Responses and Behavior of Composites, 127-138.

Rose, J. L. (1999). Ultrasonic waves in solid media, Cambridge University Press, New York.

Rose, J. L. (2000). Guided wave nuances for ultrasonic nondestructive evaluation, IEEE Transactions on Ultrasonics, Ferroelectrics, and Frequency Control, **47**(3), 575-583.

Rubin, R. and Sidahmed, M. (1997). Diagnostics of gear systems using the spectra correlation density of the vibration signal, Proceedings of the Symposium on Fault Detection, Supervision and Safety for Technical Processes, Hull, U.K., 977-982.

Sage I., Badcock R., Humberstone L., Geddes N., Kemp M. and Bourhill, G. (1999). Triboluminescent damage sensors, Smart Materials and Structures, **8**, 504-510.

Salvia, M. and Abry, J.-C. (2002). Damage mechanisms characterisation of CFRP using electrical resistance, talk on the 1st European Pre-Workshop on Structural Health Monitoring, 9, July, 2002, Paris, France.

Samuel, P. and Pines, D. (1997). Health monitoring/damage detection of a rotorcraft planetary geartrain system using piezoelectric sensors, Proceedings of SPIE, **3041**, 44-53.

Sanayei, M. and Onidepe, O. (1991). Damage assessment of structures using static test data, AIAA Journal, **29**, 1174-1179.

Saravanos, D. A. and Hopkins, D. A. (1996). Effects of delaminations on the damped dynamic characteristic of composite laminates: analysis and experiments, Journal of Sound and Vibration, **195**, 977-993.

Scarponi, C. and Briotti, G. (2000). Ultrasonic technique for the evaluation of delaminations on CFRP, GFRP, KFRP composite materials, Composites, Part B, **31**, 237-243.

Schulz, M. J., Pai, P. F. and Abdelnaser, A. S. (1996). Frequency response function assignment technique for structural damage identification, Proceedings of the 14th International Modal Analysis Conference, 105–111.

Schulz, M. J., Pai, P. F. and Inman, D. J. (1999). Health monitoring and active control of composite structures using piezoceramic patches, Composites, Part B, **30**, 713-725.

Seale, M. D., Smith, B. T. and Prosser, W. H. (1998). Lamb wave assessment of fatigue and thermal damage in composites, Journal of the Acoustical Society of America, **103**(5), 2416-2424.

Seemann, W. (1996). Transmission and reflection coefficients for longitudinal waves obtained by a combination of refined rod theory and FEM, Journal of Sound and Vibration, **198**(5), 571-587.

Seydel, R. E. and Chang, F.-K. (1999a). Implementation of a real-time impact identification technique for stiffened composite panels, Structural Health Monitoring (ed. 2), edited by Chang, F.-K., Technomic Publishing Co, Lancaster, 225-233.

Seydel, R. E. and Chang, F.-K. (1999b). Real-time impact identification of stiffened composite panels, Proceedings of SPIE on Smart Structures and Integrated Systems, Newport Beach, California, 295-305.

Shah, D. K., Chan, W. S. and Joshi, S. P. (1994). Delamination detection and suppression in a composite laminate using piezoceramic layers, Smart Materials and Structures, **3**, 293-301.

Shen, J. Y. and Sharpe, Jr. L. (1998). An overview of vibration-based nondestructive evaluation techniques, Proceedings of SPIE, **3397**, 117-128.

Shen, M. H. H. and Grady, J. E. (1992). Free vibration of delaminated beams, AIAA Journal, **30**: 1361-1370.

Shi, Z. Y., Law, S. S. and Zhang, L. M. (1998). Structural damage localization from modal strain energy change, Journal of Sound and Vibration, **218**(5), 825-844.

Shih, J.-H. and Mal, A. K. (1999). Acoustic emission from impact damage in cross-ply composites, Structural Health Monitoring (ed. 2), edited by Chang, F.-K., Technomic Publishing Co, Lancaster, 209-217.

Silva, M. Z., Gouyon, R. and Lepoutre, F. (2003). Hidden corrosion detection in aircraft aluminum structures using laser ultrasonics and wavelet transform signal analysis, Ultrasonics, **41**, 301-305.

Smith, S. W. and Beattie, C. A. (1991), Model correlation and damage location for large space truss structures: secant method development and evaluation, NASA, CR-188102.

Soeiro F. J. and Hajela, P. (1993). Damage detection in composite materials using identification technique, Journal of Aerospace Engineering, **6**: 363-380.

Sohn, H., Czarnecki, J. J. and Farrar, C. R. (2000). Structural Health Monitoring using Statistical Process Control, Journal of Structural Engineering, ASCE, **126**(11), 1356-1363.

Sohn, H. and Farrar, C. R. (2001). Damage diagnosis using time series analysis of vibration signals, Smart Materials and Structures, **10**, 1-6.

Staszewski, W. J. (1998). Structural and mechanical damage detection using wavelets, The Shock and Vibration Digest, **30**(6), 457-472.

Staszewski, W. J. (2002). Intelligent signal processing for damage detection in composite materials, Composites Science and Technology, **62**, 941-950.

Staszewski, W. J., Biemans, C., Boller, C. and Tomlinson, G. R. (1999a). Impact damage detection in composite structures - recent advances, Structural Health Monitoring (ed. 2), edited by Chang, F.-K., Technomic Publishing Co, Lancaster, 754-763.

Staszewski, W. J., Pierce, S. G., Worden, K. and Culshaw, B. (1999b). Cross-wavelet analysis for Lamb wave damage detection in composite materials using optical fibres, Key Engineering Materials, **167-168**, 373-380.

Staszewski, W. J., Worden, K., Wardle, R. and Tomlinson, G. R. (2000), Fail-safe sensor distributions for impact detection in composite materials, Smart Materials and Structures, **9**, 298-303.

Stubbs, N. and Kim, J.-T. (1996). Damage localization in structures without baseline modal parameters, AIAA Journal, **34**(8), 1644-1649.

Stubbs, N., Kim, J.-T. and Topole, K. (1992). An efficient and robust algorithm for damage localization in offshore platforms, Proceedings of ASCE the 10th Structures Congress, 543–546.

Su, Z., Ye, L. and Bu, X. (2002). Identification of delamination in woven fabric composite laminates using surface-bonded piezoelectrics, Proceedings of

International Conference of Structural Integrity and Fracture, 25-28, September, Perth, WA, Australia, 415-420.

Sung, D.-U., Oh, J.-H., Kim, C.-G. and Hong, C.-S. (2000). Impact monitoring of smart composite laminates using neural network and wavelet analysis, Journal of Intelligent Material Systems and Structures, **11**, 180-190.

Talbot, D. (2003). Boeing's flight for survival, Technology Review, September, 35-44.

Tamiatto, C., Krawczak, P., Pabiot, J. and Laurent, F. (1998). Integrated sensors for in-service health monitoring of Glass/Resin composites, Journal of Advanced Materials, **30**, 32-37.

Tan, K. S., Guo, N., Wong, B. S. and Tui, C. G. (1994). Experimental evaluation of delaminations in composite plates by the use of Lamb waves, Composites Science and Technology, **53**, 77-84.

Tan, K. S., Guo, N., Wong, B. S. and Tui, C. G. (1995). Comparison of Lamb waves and pulse echo in detection of near-surface defects in laminate plates, NDT & E International, **28**(4), 215-223.

Tandon, N. and Choudhury, A. (1999). A review of vibration and acoustic measurement methods for the detection of defects in rolling element bearings, Tribology International, **32**, 469-480.

Tang, B. and Henneke, II. E. G. (1991). Lamb-wave monitoring of axial stiffness reduction of laminated composite plates, Materials Evaluation, **47**, 928-934.

Tao, B. Q. (1997). Smart Materials and Structures, Defense Industry Publishing Co, Beijing.

Thwaites, S. and Clark, N. H. (1995). Non-destructive testing of honeycomb sandwich structures using elastic waves, Journal of Sound and Vibration, **187**(2), 253-269.

Thyagarajan, S. K., Schulz, M. J., Pai, P. F. and Chung, J. (1998). Detecting structural damage using frequency response functions, Journal of Sound and Vibration, **210**(1): 162-170.

Todoroki, A., Tanaka, Y. and Shimamura, Y. (2000). Smart delamination monitoring of graphite/epoxy laminates using electric resistance change with response surfaces, Proceedings of the 2nd Asian-Australasian Conference on Composite Materials, 1041-1046.

Toyama, N., Noda, J. and Okabe, T. (2003). Quantitative damage detection in cross-ply laminates using Lamb wave method, Composites Science and Technology, **63**, 1473-1479.

Tracy, J. J. and Pardoen, G. C. (1989). Effect of delamination on the natural frequencies of composite laminates, Journal of Composite Materials, **23**, 1200-1215.

Tracy, M. and Chang, F.-K. (1996). Identifying impact load in composite plates based on distributed piezoelectric sensor measurements, Proceedings of SPIE on Smart Structures and Materials, **2717**, 231-236.

Tracy, M. and Chang, F.-K. (1998). Identifying impacts in composite plates with piezoelectric strain sensors, part I: theory, Journal of Intelligent Material Systems and Structures, **9**, 920-928.

Tsou, P. and Shen, M.-H. H. (1994). Structural damage detection and identification using neural networks, AIAA Journal, **32**(1), 176-183.

Valdes, S. H. D. and Soutis, C. (1999). Delamination detection in composite laminates from variations of their modal characteristics, Journal of Sound and Vibration, **228**, 1-9.

Valdes, S. H. D. and Soutis, C. (2001). A structural health monitoring system for laminated composites, Proceedings of DETC, Pittsburgh, PA, U.S.A., 2013-2021.

Valle, C. (2001). On characterizing multi-mode, dispersive Lamb waves, Review of Progress in Quantitative Nondestructive Evaluation, edited by Thompson, D. O. and Chimenti, D. E., **20B**, 1047-1052.

Valle, C. and Littles, Jr. J. W. (2002). Flaw localization using the reassigned spectrogram on laser-generated and detected Lamb modes, Ultrasonics, **39**, 535-542.

Vecchio, A. and Auweraer, H. V. D. (2001), An experimental validation of a model-based approach in damage detection and localization, Structural Health Monitoring (ed. 3), edited by Chang, F.-K., CRC Press, Boca Raton, 957-966.

Viktorov, I. A. (1967). Rayleigh and Lamb Wave, Physical theory and Applications, Plenum Press, New York.

Voyiadjis, G. Z. (1993). Damage in Composite Structures, Elsevier, Amsterdam.

Wahab, M. M. A., Roeck, G. D. and Peeters, B. (1999), Parameterization of damage in reinforced concrete structures using model updating, Journal of Sound and Vibration, **228(4)**: 717-730.

Waldron, K., Ghoshal, A., Schulz, M. J., Sundaresan, M. J., Ferguson, F., Pai, P. F. and Chung, J. H. (2002). Damage detection using finite element and laser operational detection shapes, Finite Elements in Analysis and Design, **38**, 193-226.

Wang, C. and Chang, F.-K. (2003). Imaging method for in-situ structural health monitoring, private communication.

Wang, C. and Rose, L. R. F. (2001). Wave reflection and transmission in beams containing delamination and inhomogeneity, private communication.

Wang, C. S. and Chang, F.-K. (1999). Built-In diagnostics for impact damage identification of composite structures, Structural Health Monitoring (ed. 2), edited by Chang, F.-K., Technomic Publishing Co, Lancaster, 613-621.

Wang, C. S. and Chang, F.-K. (2000). Diagnosis of impact damage in composite structures with built-in piezoelectrics network, Proceedings of SPIE, **3990**, 13-19.

Wang, M. L., Heo, G. and Satpathi, D. (1998). Health monitoring system for large structural systems, Smart Materials and Structures, **5**, 606-661.

Wang, Q. and Deng, X. (1999). Damage detection with spatial wavelets, International Journal of Solids and Structures, **36**, 3443-3468.

Wang, W. J. (2001). Wavelet for detecting mechanical faults with high sensitivity, Mechanical Systems and Signal Processing, **15**(4), 685-696.

Wang, W. J. and McFadden, P. D. (1993). Early detection of gear failure by vibration analysis, part I: calculation of he time-frequency distribution, Mechanical Systems and Signal Processing, **7**, 193-203.

Wegman, R. F. (1989). Nondestructive test method for structural composites, SAMPE Handbook, Vol. **1**, Society for the Advancement of Materials and Process Engineering.

Williams, K. V. and Vaziri, R. (2001). Application of a damage mechanics model for predicting the impact response of composite materials, Computers and Structures, **79**, 997-1011.

Wisnom, M. R. and Chang, F.-K. (2000). Modelling of splitting and delamination in notched cross-ply laminates, Composites Science and Technology, **60**, 2849-2856.

Wolfinger, C., Arendts, F. J., Friedrich, K. and Drechsler, K. (1998). Health-monitoring-system based on piezoelectric transducers, Aerospace Science and Technology, **6**, 391-400.

Wolfram Co. (1999). Mathematica User's Manual, Ver. 4.0.

Wong, B. S., Guan, T. C. and King, L. M. (1993). Mechanical impedance inspection of composite structures, British Journal of NDT, **35**, 3-9.

Worden, K., Manson, G. and Allman, D. (2003a). Experimental validation of a structural health monitoring methodology: part I. novelty detection on a laboratory structure, Journal of Sound and Vibration, **259**(2), 323-343.

Worden, K., Manson, G. and Allman, D. (2003b). Experimental validation of a structural health monitoring methodology: part II. novelty detection on a GNAT aircraft, Journal of Sound and Vibration, **259**(2), 345-363.

Worden, K., Manson, G. and Allman, D. (2003c). Experimental validation of a structural health monitoring methodology: part III. damage location on an aircraft wing, Journal of Sound and Vibration, **259**(2), 365-385.

Wu, X., Ghaboussi, J. and Garrett, Jr. J. H. (1992). Use of neural networks in detection of structural damage, Computers and Structures, **42**(4), 649-659.

Yam, L. H., Li, Y. Y. and Wong, W. O. (2002). Sensitivity studies of parameters for damage detection of plate-like structures using static and dynamic approaches, Engineering Structures, **24**, 1465-1475.

Yam, L. H., Yan, Y. J. and Jiang, J. S. (2003). Vibration-based damage detection for composite structures using wavelet transform and neural network identification, Composite Structures, **60**, 403-412.

Yan, Y. J. and Yam, L. H. (2002). Online detection of crack damage in composite plates using embedded piezoelectric actuators/sensors and wavelet analysis, Composite Structures, **58**, 29-38.

Ye, L., Lu, Y. and Su, Z. (2003). Advanced composites and artificial intelligence techniques for new generation aircraft structures, submitted to Mechanics of Materials.

Yoshimura, S., Yagawa, G., Oishi, A. and Yamada, K. (1998). Neural network based inverse analysis for defect identification with laser ultrasonics, Key Engineering Materials, **145-149**, 443-452.

You, Z. and Lord, W. (1991). A 3-D finite element formulation for ultrasonic NDE, Review of Progress in Quantitative Nondestructive Evaluation, edited by Thompson, D. O. and Chimenti, D. E., **10A**, 233-240.

Yun, C.-B. and Bahng, E. Y. (2000). Substructural identification using neural networks, Computers and Structures, **77**, 41-52.

Zahn M. (1998). Optical, electrical and electromechanical measurement methodologies of fields, charge and polarization in dielectrics, IEEE Transactions on Dielectrics and Electrical Insulation, **5**, 627-650.

Zang, C. and Imregun, M. (2001). Structural damage detection using artificial neural networks and measured FRF data reduced via principal component projection, Journal of Sound and Vibration, **242**(5), 813-827.

Zhang, Z. and Aktan, A. E. (1995). The damage indices for constructed facilities, Proceedings of the 13th International Modal Analysis Conference, 1520–1529.

Zheng, G. T., Buckley, M. A., Kister, G. and Fernando, G. F. (2001). Blind deconvolution of acoustic emission signals for damage identification in composites, AIAA Journal, **39**:1198-1205.

Zheng, G. T. and Wang, W. J. (2001). A new cepstral analysis procedure of recovering excitations for transient components of vibration signals and applications to rotating machinery condition monitoring, Transactions of the ASME, **123**:222-229.

Zou, Y., Tong, L. and Steven, G. P. (2000). Vibration-based model-dependent damage (delamination) identification and health monitoring for composite structures - a review, Journal of Sound and Vibration, **230**, 357-378.

Zu, B. and Wu, Z. (2001). Neural-networks-based structural health monitoring strategy with dynamic responses, Structural Health Monitoring (ed. 3), edited by Chang, F.-K., Technomic Publishing Co, Boca Raton, 1418-1427.

Zubaydi, A., Haddara, M. R. and Swamidas, A. S. J. (2002). Damage identification in a ship's structure using neural networks, Ocean Engineering, **29**, 1187-1200.

Appendix *A*

A Set of Typical DDF (Partial) for Delamination

	A11M	A12M	A13M	A14M	A15M	A16M	A17M	A18M	A19M	A20M	A21M	A22M	A23M	A2
1	0.43333	0.39298	0.25033	0.38289	0.24167	0.42237	0.42368	0.42588	0.46228	0.43991	0.47851	0.39693	0.40746	0.
2	-0.0223	-0.03462	0.01722	0.07315	0.03417	0.03131	0.02759	0.0304	0.02082	0.01793	0.01888	0.00707	0.01777	0.
3	0.44298	0.40395	0.26842	0.39211	0.25088	0.43684	0.43333	0.43465	0.47895	0.44868	0.48772	0.40395	0.41754	0.
4	[illegible]	[illegible]	[illegible]	[illegible]	[illegible]	[illegible]	[illegible]	[illegible]	[illegible]	[illegible]	[illegible]	[illegible]	[illegible]	-0.
	A19M	A20M	A21M	A22M	A23M	A24M	A25M	A26M	A27M	A28M	A29M	A30M	A31M	A2
83	0.79781	0.91053	0.71404	0.74551	0.89693	0.70658	0.88246	0.78377	0.79386	0.74825	0.69211	0.78026	0.65746	0.
84	-0.54261	-0.2418	0.28825	-0.14363	-0.39651	0.32687	-0.17973	-0.04356	0.35727	-0.42193	-0.10932	0.38944	0.09224	0.
85	0.8057	0.9193	0.72237	0.75833	0.90877	0.7136	0.89079	0.79167	0.80482	0.75746	0.69912	0.79123	0.66866	0.
86	0.49596	0.19933	-0.20169	0.15758	0.41829	-0.36576	0.13309	0.06307	-0.4318	0.48036	0.20574	-0.39302	-0.10387	0.
	A37M	A38M	A39M	A40M	A41M	A42M	A43M	A44M	A45M	A46M	A47M	A48M	A49M	A5
1	0.53684	0.46535	0.4114	0.31009	0.3614	0.39386	0.4364	0.40351	0.43202	0.24912	0.42456	0.50658	0.56623	0.
2	-0.01156	0.02819	-0.02247	-0.03939	-0.02489	-0.04296	-0.02608	-0.02293	-0.03792	-0.02067	0.0303	0.01233	-0.03224	-0.
3	0.54956	0.47412	0.42281	0.32018	0.3693	0.40877	0.44561	0.41096	0.44079	0.25702	0.43333	0.51535	0.57237	0.
4	0.06173	-0.05899	0.0689	0.07866	0.04987	0.09175	0.05041	0.0462	0.03594	0.05758	-0.05024	-0.03258	0.03332	0.
5	0.55877	0.48202	0.43333	0.32851	0.37675	0.41754	0.45395	0.41798	0.46009	0.26579	0.44211	0.52325	0.57939	0.
6	-0.13572	0.06724	-0.13514	-0.07966	-0.05371	-0.19972	-0.08537	-0.06017	-0.02192	-0.07969	0.03451	0.08378	-0.09697	-0.
7	0.56754	0.48991	0.44386	0.3364	0.38421	0.42588	0.46228	0.42544	0.46754	0.27675	0.45395	0.53114	0.58728	0.
8	0.13947	-0.06648	0.14357	0.04713	0.08152	0.35539	0.09922	0.14413	0.0419	0.08783	-0.02601	-0.13213	0.15586	0.
9	0.57544	0.49693	0.45395	0.35351	0.39342	0.43377	0.47368	0.43465	0.47544	0.28553	0.46272	0.53947	0.59605	0.
10	-0.03787	0.0364	-0.16631	-0.05389	-0.10382	-0.42304	-0.0705	-0.21036	-0.05673	-0.13133	0.03594	0.11141	-0.14861	-0.
11	0.59254	0.50877	0.46184	0.36228	0.40614	0.44298	0.48421	0.44649	0.48465	0.29386	0.47982	0.54781	0.60658	0.
12	-0.0706	0.05527	0.13609	0.07052	0.13175	0.27419	0.08183	0.23752	0.03732	0.14111	-0.07064	-0.02704	0.13932	0.
13	0.60132	0.51754	0.46842	0.37018	0.41667	0.45526	0.49518	0.4557	0.50044	0.30482	0.48904	0.55439	0.61535	0.
14	0.15831	-0.13558	-0.10805	-0.06859	-0.15676	-0.28123	-0.08106	-0.24944	-0.03896	-0.10398	0.12994	-0.01983	-0.20628	-0.
15	0.61053	0.52851	0.47544	0.37807	0.42588	0.46447	0.50395	0.46667	0.50965	0.31447	0.49912	0.56491	0.62281	0.
16	-0.14137	0.11651	0.10847	0.07696	0.27665	0.27533	0.10039	0.25005	0.03968	0.11214	-0.12732	-0.02895	0.24594	0.
17	0.62237	0.53991	0.48289	0.39605	0.43465	0.475	0.51228	0.47588	0.51667	0.32193	0.50965	0.57412	0.63026	0.
18	0.11411	-0.09507	-0.07098	-0.2161	-0.36335	-0.36772	-0.07704	-0.3673	-0.03699	[illegible]	0.0894	-0.21622	-0.	
19	0.63026	0.55746	0.48947	0.40482	0.44649	0.48289	0.52368	[illegible]	[illegible]	[illegible]	[illegible]	[illegible]	[illegible]	0.
20	-0.10419	0.08873	0.01338	0.36351	0.38686	0.38582	[illegible]	[illegible]	[illegible]	[illegible]	[illegible]	[illegible]	[illegible]	[illegible]
21	0.63816	0.56579	0.49518	0.4136	0.4557	[illegible]	[illegible]	[illegible]	[illegible]	[illegible]	[illegible]	[illegible]	[illegible]	[illegible]
22	0.07021	-0.12817	-0.02715	-0.3087	[illegible]	[illegible]	[illegible]	[illegible]	[illegible]	[illegible]	[illegible]	[illegible]	[illegible]	[illegible]
23	0.64781	0.57368	0.50395	[illegible]	[illegible]	[illegible]	[illegible]	[illegible]	[illegible]	[illegible]	[illegible]	[illegible]	[illegible]	[illegible]
24	-0.05694	0.13103	[illegible]	[illegible]	[illegible]	[illegible]	[illegible]	[illegible]	[illegible]	[illegible]	[illegible]	[illegible]	[illegible]	[illegible]

Appendix *B*

Glance of AO-SHD System Configuration

	Equipment/ Model	Manufacturer	Description/ Configuration	Software	Functionality
SGS	E1441 Modulus	Agilent© Technologies	Arbitrary Function Generator, Otp: 10V	Inhouse Control Software	Excitation Generation
	Signal Amplifier (EPA-104)	Piezo Systems, Inc.	Freq. range: DC-300KHz Otp. range: ±200 V	N/A	Excitation Amplification
DAS	E3242A Modulus	Agilent© Technologies	Voltage Sensitivity: <0.006pC/V	Inhouse Software	Signal Conditioning
	E1437A Modulus	Agilent© Technologies	Max. Sampling rate: 20MHz, Dual Channel	Inhouse Software	Signal Acquisition
	Oscilloscope (54620A)	Agilent© Technologies	Sample Rate: 200MSa/S	N/A	Acquisition Monitoring
CCAS	HP (Vectra VL600)	PIII733/256M	Central Control & Analysis	SPP (ISPPR)	SHM Control & Diagnosis
Sensor	PZT (PI 151)	PI Ceramic (Germany)	Referring to Table 7.1	N/A	Senor & Actuator

Publications Arising from this Work

Chapter

Su, Z. and Ye, L., Lamb Wave Scattering in Defective Quasi-isotropic CF/EP Composite Laminates with Active Sensor Network, in *Multi-scale Modelling of Composite Material Systems - the Art of Predictive Damage Modelling*, edited by Soutis, C. (*to be published in 2004 by Woodhead Publishing Ltd.*).

Referred Journal Papers

1. Su, Z., Ye, L. and Bu, X. 2002. 'A damage identification technique for CF/EP composite laminates using distributed piezoelectric transducers', *Composite Structures*, **57**:465-471.
2. Su, Z. Ye, L., Bu, X. and Wang, X. 2003. 'Quantitative assessment of damage in a structural beam based on wave propagation by impact excitation', *Structural Health Monitoring: An International Journal*, **2**(1):27-40.
3. Su, Z. and Ye, L. 2003. 'Selective generation of Lamb wave modes and their propagation characteristics in defective composite laminates', *Journal of Materials: Design and Applications*, **218**:95-110.
4. Bu, X., Ye, L. and Su, Z. 2003, 'Active control for a flexible smart beam using a system identification technique based on ARMAX model', *Smart Materials and Structures*, **12**(5):845-850.
5. Su, Z. and Ye, L. 2003. 'Fundamental Lamb mode-based delamination detection for CF/EP composite laminates using distributed piezoelectrics', *Structural Health Monitoring: An International Journal*, **3**(1):43-68.
6. Su, Z. and Ye, L. 2003. 'Lamb wave-based identification technique for delamination in composite laminates using artificial neural algorithm', *Composite Structures*, (in press).
7. Su, Z. and Ye, L. 2003. 'Lamb wave propagation-based damage identification for quasi-isotropic CF/EP composite laminates using artificial neural algorithm, Part I: methodology and database development', *Journal of Intelligent Material Systems and Structures*, (in press).

8. Su, Z. and Ye, L. 2003. 'Lamb wave propagation-based damage identification for quasi-isotropic CF/EP composite laminates using artificial neural algorithm, Part II: implementation and validation', *Journal of Intelligent Material Systems and Structures*, (in press).
9. Su, Z. and Ye, L. 2003. 'Digital damage fingerprints for structural health monitoring of composite structures based on artificial neural network', *Composite Structures*, (in press)
10. Su, Z. and Ye, L. 2003. 'An intelligent signal processing and patterns recognition technique for defect identification using active sensor network', *Smart Materials and Structures*, (in press).
11. Su, Z. and Ye, L. 2003. 'Quantitative damage prediction for composite laminates based on wave propagation and artificial neural algorithm', *Structural Health Monitoring: An International Journal*, (in press).
12. Ye, L., Lu, Y. and Su, Z. 2003. 'Advanced composites and artificial intelligence techniques for new generation aircraft structures', submitted to *Mechanics of Materials*.
13. Wang, X., Foliente, G., Su, Z. and Ye, L. 2004, 'Multilevel decision fusion in a distributed active sensor network for structural damage detection', submitted to *Structural Health Monitoring: An International Journal*.

Conferences:

14. Su, Z., Ye, L., Bu, X., Mai, Y-W. and Wang, X. 2002. 'A damage identification approach based on stress wave propagation', in *Proceedings of the 3rd Australasian Congress on Applied Mechanics*, edited by Zhang, L, Tong, L. and Gal, J., 20-22, Feb, 2002, Sydney, Australia, Singapore: Word Scientific, pp. 183-188.
15. Su, Z., Ye, L. and Bu, X. 2002. 'Evaluation of delamination in laminated composites based on Lamb wave modes: FEM simulation and experimental verification', in *Proceedings of the 1st European Workshop on Structural Health Monitoring*, edited by Balageas, D., 10-12, July, 2002, Paris, France, Lancaster: DEStech Publications, pp. 328-335.

16. Su, Z., Ye, L. and Bu, X. 2002. 'Identification of delamination in woven fabric composite laminates using surface-bonded piezoelectrics', *in Proceedings of International Conference of Structural Integrity and Fracture*, edited by Dyskin, A.V. *etc.*, 25-28, September, 2002, Perth, WA, Australia, pp. 415-420.
17. Su, Z. and Ye, L. 2003. 'Artificial neural algorithm-based damage assessment for laminated composite structures using distributed actuators/sensors', in *Proceedings of the 5th International Symposium on Advanced Composites*, edited by Paipetis, A. S., 5-7, May, 2003, Corfu, Greece.
18. Su, Z. and Ye, L. 2003. 'Guided wave-based inverse identification technique for damages in CF/EP composites using artificial neural algorithm', in *Proceedings of the 14th International Conference on Composite Materials (ICCM-14)*, San Diego, USA, 14-18, July, 2003.
19. Su, Z. and Ye, L. 2003. 'A signal processing and interpretation technique for Lamb-wave-based damage diagnosis using digital damage fingerprints extracted from an actuator/sensor network', in *Proceedings of the 4th International Workshop on Structural Health Monitoring*, edited by Chang, F.-K., 15-17, Sep, 2003, Stanford, California, USA., 1300-1307.
20. Huang, N., Ye, L. and Su, Z. 2004. 'Parameterised modelling technique and its application in structural health monitoring', in *Proceedings of the 4th Asian-Australasian Conference on Composite Materials*, 6-9, July, 2004, Sydney, Australia.
21. Lu, Y., Ye, L. and Su, Z. 2004, 'Lamb wave-based damage detection for aluminium alloy structure using active sensor network', in *Proceedings of the 2nd European Workshop on Structural Health Monitoring*, 7-9, July, 2004, Munich, Germany.
22. Choi, Y.-G., Ye, L., Su, Z. and Chen, Z.-R. 2004. 'Quantitative nondestructive evaluation for composites beaming using piezoelectrics', in *Proceedings of the 4th Asian-Australasian Conference on Composite Materials*, 6-9, July, 2004, Sydney, Australia.
23. Wang, X., Su, Z., Ye, L. and Foliente, G. 2004, 'Information fusion in distributed sensor network for structural damage detection', in *Proceedings of the 4th Asian-*

Australasian Conference on Composite Materials, 6-9, July, 2004, Sydney, Australia.

24. Wang, X., Foliente, G., Su, Z. and Ye, L. 2004, 'Bayesian Inference for Structural Damage Identification with a Distributed Sensor Network, submitted to *The 2nd Australasian Workshop on Structural Health Monitoring, Dec. 2004, Melbourne, Australia.*
25. Lu, Y., Ye, L. and Su, Z. 2004, 'Crack Locating for Aluminium Plate Based on Lamb Wave Propagation', in *Proceedings of the 11th International Conference on Fracture*, 20-25, March, 2005, Turin, Italy.

Selective generation of Lamb wave modes and their propagation characteristics in defective composite laminates

Z Su and L Ye*
Laboratory of Smart Materials and Structures (LSMS), Centre for Advanced Materials Technology (CAMT), School of Aerospace, Mechanical and Mechatronic Engineering, University of Sydney, Australia

Abstract: Techniques for the generation of Lamb waves with purpose of non-destructive inspection (NDI) were briefly reviewed. An active excitation control circuit was designed and instrumented with an online damage diagnosis system, by which the desired fundamental symmetric Lamb mode, shear mode and antisymmetric mode can be selectively stimulated. A signal processing and identification algorithm in the time-scale domain, using spectrographic analyses based on the wavelet transform technique, was developed to assist the wave signal interpretation. The proposed excitation methodology was applied to the study of the dispersion and propagation characteristics of Lamb waves in quasi-isotropic CF/EP composite laminates with delamination. For validation, numerical simulations were conducted in parallel with experimental investigations.

Keywords: Lamb wave, wave excitation, fibre-reinforced composite, wavelet transform, finite element method, damage detection

1 INTRODUCTION

Lamb waves, guided elastic waves propagating in plate-like structures with free surface boundaries, have emerged as a competent tool for non-destructive inspection (NDI) of engineering structures, combining high precision and universal accessibility. Lamb waves were first used as a means of damage detection in 1960 by Worlton [1], and their mechanisms have been rigorously investigated in the past two decades and widely introduced into virtual applications. Lowe [2] and Habeger *et al.* [3] developed transfer and global matrix methods to evaluate the dispersion characteristics of Lamb waves in multilayered structures, Percival and Birt [4] and Alleyne and Cawley [5] interrogated Lamb wave propagation using numerical simulations, while experiment verifications were individually conducted by Guo and Cawley [6–8] and Birt [9]. Representatively, Cawley *et al.* in the United Kingdom [5–8, 10], Chang *et al.* in the United States [11, 12] and Balageas *et al.* in France [13, 14] have made substantial achievements in Lamb wave-based NDI techniques for composite structures. All these studies have shown the potential of Lamb waves for diverse NDI practices. However, in spite of many attractive traits, the propagation of Lamb waves in anisotropic viscoelastic media is notoriously complicated. In most cases, multiple Lamb modes synchronously exist, and moreover their dispersive properties throughout the medium thickness are not identical, even for the same mode but in different frequency ranges. Two challenging technologies are essential to streamline the practical actualization of Lamb waves:

(a) active generation of controllable Lamb modes,
(b) efficient signal processing and interpretation.

The present studies are aimed at an active Lamb wave excitation approach using distributed piezoelectric lead zirconate titanate (PZT) transducers, with which the desirable Lamb modes can be selectively generated. For this, a control circuit was established and a signal identification algorithm based on the wavelet transform technique was developed in order to improve the Lamb wave signal interpretation. The methodology was then applied to examine the relationship between Lamb waves and composite delamination. In addition, numerical simulations for the designed activation establishment and propagation characteristics of

The MS was received on 23 April 2003 and was accepted after revision for publication on 6 August 2003.

**Corresponding author: Laboratory of Smart Materials and Structures, Centre for Advanced Materials Technology, School of Aerospace, Mechanical and Mechatronic Engineering, University of Sydney, NSW 2006, Australia.*

Lamb waves in delaminated composite laminates were performed in parallel.

2 GENERATION OF LAMB WAVES: A BRIEF REVIEW

Lamb waves can be expediently and efficiently activated by a variety of methods with intrinsic advantages and disadvantages. These methods can be roughly summarized into four major categories:

1. *Ultrasonic probes*. Notable for excellent precision and controllability, ultrasonic probes coupled with angle-adjustable perspex wedges have been dominantly employed in NDI practice over the years [4–8, 15, 16] to generate and collect pure Lamb waves in accordance with Snell's law [17]. Without the interference of multiple modes, the probe-excited Lamb wave enables an effective yet explicit signal interpretation, and consequently exhibits a high reliability for damage assessment. Such methods, though extensively successful, have been incrementally challenged for their flexibility in real-time signal generating and monitoring, where accessing the in-service systems is somewhat problematic. In most circumstances, a temporary downtime of the structures under inspection is required to guarantee the operation of probes. During manipulation, directionality and contact are among basic issues that may considerably influence the detection effectiveness. Motivated by this, substituent non-contact devices, such as air-coupled [18, 19] and fluid-coupled [20] transducers or electromagnetic acoustic transducers (EMATs) [21, 22], were invented. However, air- or fluid-coupled transducers can suffer from a relatively low efficiency because of the large differences in mechanical impedances between the air/fluid and the objects under detection. As for EMATs, they are severely restricted by the applicable frequency ranges, and their functionality may be fairly limited by the electrical conductivity of the objects to be inspected [23]. On the other hand, being the diagnostic signal most extensively excited by ultrasonic probes, the narrow-band pulse excitation, though capable of providing centralized incident energy, becomes less efficient for the detection of near-surface damage, where the reflections from the defects are limited within the wavelength of the transmitted ultrasonic pulse [23]. Meanwhile, the non-neglectable mass/volume of probes, costly excitation establishment and complication in device manufacturing also reduce the practicability of these ultrasonic probes to a certain extent.
2. *Laser*. Non-contact excitation of Lamb waves via laser-based ultrasonics (LBU) and acquisition using a laser interferometer has recently appeared as a promising method for contactless NDI [21, 24–27]. Flexibly controllable, the LBU can be designed to be broadband or narrow-band, depending on the application, providing excellent spatial resolution. The exact detection that the LBU can offer ranges from apparent defects to small cracks. An LBU can be exceptionally effective for remote manipulation, with easy scanning, exact calibration and applicability to curved surfaces or complicated geometric identities [23], and it is even applicable in exigent environments where access is unfeasible. Nevertheless, faced with similar issues to those encountered by probe-based methods, the use of LBU in cost-effective real-time damage assessment systems, in which surveillance devices are expected to be economically integrated into the system without modifying the original structural integrity, is clearly restricted by its bulky and costly excitation equipment.
3. *Interdigital transducers*. Alternatively, interdigital transducers, such as polyvinylidene fluoride (PVDF) piezoelectric polymer films, are introduced to cater for more versatile applications with favourable cost [28–30]. Possessing higher internal damping features than other common ceramics, PVDF exhibits good ability to produce guided Lamb waves with specific wavelength by controlling the space between interdigital electrodes deposited on the transducer substrates [28]. Soft and flexible, the interdigital PVDF may be shaped and permanently bonded onto or embedded into structures, adapting to the curved surfaces or complicated geometry. In contrast to piezoceramics, PVDF usually exhibits a certain insensitivity to structural dynamic responses and a relatively weak driving power, limiting its applications to some cases. In addition, its performance is highly susceptible to the environmental temperature in relation to its glass transition temperature.
4. *Piezoelectric elements*. Initially used for sensing devices, such as accelerometers, or for active structural control, PZT elements have been increasingly used for damage detection since the 1980s [12–14, 31–35], regarded as an important step towards intelligent structure techniques to fulfil designed functions. A PZT element, shaped as a disc, a tube, etc., has characteristics of massless, volumeless, low-power consumption, easy integration and activation, low acoustic impedance, wide frequency responses and low cost. With a good affinity, PZTs are easily surface bonded on structures, with minor intrusion, as *in situ* wave generators or sensors. The transducer network can be tailored, using distributed PZT elements, to realize multipoint measurements [35]. However, in spite of the above merits, PZT-generated Lamb waves still present some problematical issues. Most intricate, multiple Lamb modes are simultaneously induced by piezoelectric elements if appropriate design and implementation are not carried out, which fairly obscures the signal explanation. Additionally, PZT elements usually exhibit non-linear behaviour and hysteresis under large strains or high temperature, small driving force and displacement, brittleness, low fatigue life [36].

IMPLEMENTATION OF SELECTIVE LAMB MODES

3.1 Set-up configuration

Piezoelectric lead zirconate titanate wafers (PI© PIC151) of 6.9 mm diameter, with the material parameters listed in Table 1, were selected on the basis of an optimal criterion [37] as below, so as to lower the geometric effect and consequently avoid uneven propagation

$$2R = \frac{v}{f}\left(n + \frac{1}{2}\right) = \lambda\left(n + \frac{1}{2}\right), \qquad n = 0, 1, 2, \ldots \tag{1}$$

where R is the radius of the PZT disc, v is the propagating velocity of the Lamb wave modes (ca 6000 m/s for the fundamental symmetric Lamb mode), f is their frequency (controlled at 0.5 MHz in this study) and λ is their wavelength. The PZT discs were trimmed to 0.5 mm in thickness to trade off the desired excitation force and unpolarized voltage limit, permitting an unpolarized voltage limit of 125–150 V.

A control circuit for the selective generation of desirable Lamb modes was designed and is shown in Fig. 1. A pair of PZT wafers, functioning as an actuator unit, were symmetrically surface bonded at the same location on both sides of an eight-layer $[45/-45/0/90]_s$ CF/EP laminate plate (T650/F584) with the properties detailed in Table 2. Meanwhile, three PZT wafers were allocated on the laminate surface along a straight line, 100, 200 and 250 mm away from the actuator, serving as the sensors. All the PZT wafers were kept far away from the laminate edges to preclude boundary effects. The control circuit was instrumented by an active online damage diagnosis system established in previous studies [33, 34], as outlined in Fig. 2. The incident diagnostic signal, a five-cycle sinusoid toneburst windowed with a Hanning function at a central excitation frequency of 0.5 MHz, was stimulated by Agilent© E1441 on the NI Labview© platform, shown in Fig. 3a, and then amplified to 60 V_{PP} (peak to peak) by a PZT amplifier (PiezoSys© EPA-104). Its corresponding frequency spectrum, achieved via fast Fourier transform (FFT), is displayed in Fig. 3b, in which the excitation energy can be seen to concentrate within a narrow frequency band, efficiently reducing the wave propagation dispersion and benefiting the signal interpretation. Signal acquisition was performed using an Agilent© E1437A digitizer at a sampling rate of 20.48 MHz via IEEE-488 after conditioned by Agilent© E3242A.

Table 1 Material properties of PZT transducer

Product name	PI 151
Geometry	ϕ 6.9 mm, h_{PZT} 0.5 mm
Density	7.80 g/cm^3
Poisson's ratio	0.31
Charge constant d_{31}	170×10^{-12} m/V
Charge constant d_{33}	450×10^{-12} m/V
Relative dielectric constant K_3	1280
Dielectric permittivity P_0	8.85×10^{-12} F/m
Elastic constant E	72.5 GPa

3.2 Signal processing algorithm

As commented upon in section 2, the interpretation of Lamb waves generated by a piezoelectric element can be hindered by the confusion of multiple Lamb modes and wave dispersion. Meanwhile, diverse interferences, such as structural natural vibration patterns or broadband noises, are also inevitably contained in the sampled signals, which complicate the extraction of signal characteristics. For this, a signal processing and identification algorithm was developed using time–frequency spectrographic analyses implemented by the continuous wavelet transform (CWT) and discrete wavelet transform (DWT) techniques [38–40].

Fundamentally, applied with a basic wavelet transfer function $\Psi(t)$ (Daubechies in this study), the signal $f(t)$ acquired from a PZT sensor was convened into a quadratic expression using parameter scale, a, and time, b, via CWT analysis as

$$W(a, b) = \frac{1}{\sqrt{a}}\int_{-\infty}^{+\infty} f(t)\Psi^*\left(\frac{t-b}{a}\right) \mathrm{d}t \tag{2}$$

where $W(a, b)$ is defined as the continuous wavelet coefficient and $\Psi^*(t)$ denotes the complex conjugate of $\Psi(t)$. Conversely, the signal could be successively reconstructed via an inverse wavelet transform

$$f(t) = \frac{1}{C_\Psi}\int_{-\infty}^{+\infty}\int_{a>0}^{+\infty} W(a, b)\frac{1}{\sqrt{a}}\Psi\left(\frac{t-b}{a}\right)\frac{1}{a^2}\,\mathrm{d}a\,\mathrm{d}b \tag{3}$$

where C_Ψ is a constant depending on $\Psi(t)$. Based on equations (2) and (3), the energy distribution of the wave signal over the time-scale domain was derived

$$E = \int_0^{+\infty}\int_0^{+\infty} |W(a, b)|^2\,\mathrm{d}a\,\mathrm{d}b \tag{4}$$

where $|\mathrm{CWT}(a, b)|^2$, referred to as the scalogram, indicates the wave energy density over the time-scale domain. For simplification, equation (2) was also performed at discrete scale and time using dyadic variables m and n, namely DWT analysis

$$a = a_0^m \quad \text{and} \quad b = na_0^m b_0, \qquad m, n \in Z \tag{5a}$$

$$\mathrm{DWT}(m, n) = a_0^{-m/2}\int f(t)\Psi(a_0^{-m}t - nb_0)\,\mathrm{d}t \tag{5b}$$

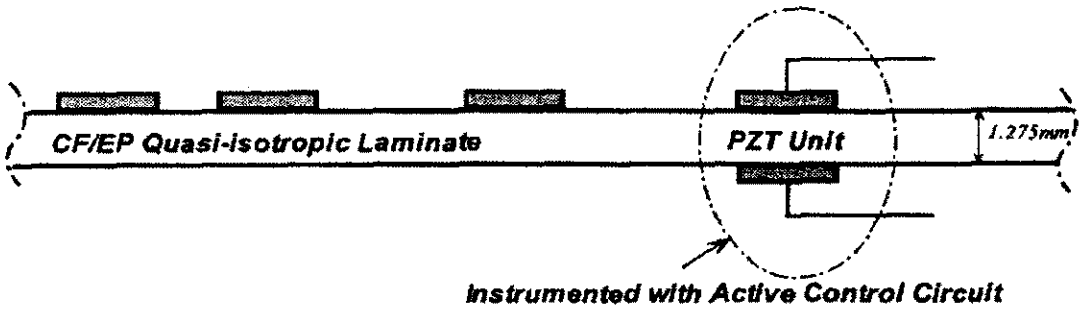

(a)

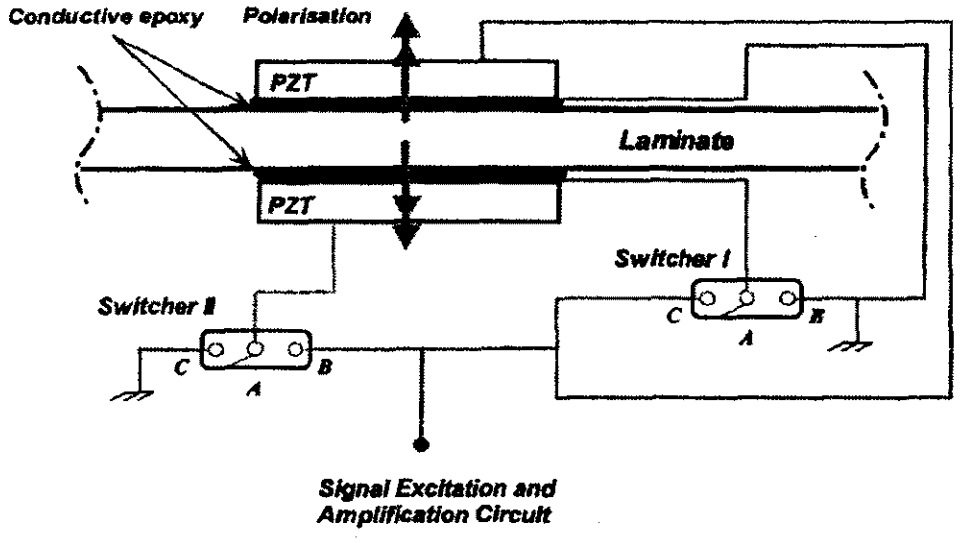

Case A: Single electric field excitation

Case B: Symmetric electric fields excitation

Case C: Anti-symmetric electric fields excitation

(b)

Fig. 1 Control circuit for generation of the selective Lamb mode: (a) PZT generator unit and sensors; (b) control circuit

where a_0 and b_0 are constants determining the sampling intervals along the time and frequency axes respectively. Similarly, the signal could be inversely reconstructed by

$$f(t) = c \sum_m \sum_n C_{mn}(t)\mathrm{DWT}(m, n) \tag{6a}$$

$$C_{mn}(t) = a_0^{-m/2} \Psi(a_0^{-m} t - nb_0) \tag{6b}$$

where c is a constant in correlation with $\Psi(t)$.

Based on equation (6), a series of bandpass filters with discrete initial thresholds and frequency ranges was built, with which the one-dimensional time dependent wave signals were decomposed into associated frequency bands. Lamb wave components pertaining to the active excitation were separated and extracted without diverse interferences. Meanwhile, taking

Table 2 Properties of T650/F584 CF/EP composites

Fibre product name	Matrix product name	Fibre volume (%)	Matrix volume (%)	Laminate density (kg/m^3)
T650/35-12K	F584	56	44	1528

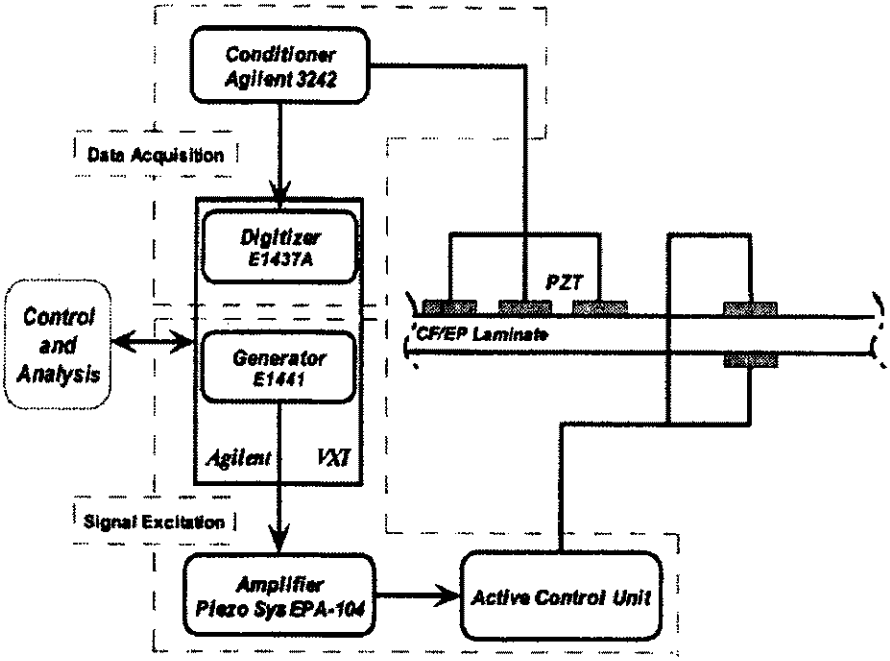

Fig. 2 Active online damage diagnosis system [34]

advantage of equation (4), the acquired signals were further examined in the time-scale space, where the propagation of Lamb waves could be intuitively characterized by the illustration of energy spectra. A program was developed using the processing algorithm for exact location of the characteristic times/frequencies and capturing of their corresponding magnitudes in the filtered wave signal and energy spectra.

3.3 Activation of basic Lamb modes

Multiphase switchers were introduced into the control circuit, shown in Fig. 1b, for selective excitation of the desirable Lamb modes:

1. Case A: a single PZT actuator, located on the upper laminate surface, was energized (terminal B in switcher I and terminal C in switcher II were simultaneously activated). An external electric field, parallel to the PZT polarized direction, was applied. For illustration, the raw signal acquired by the sensor located 100 mm away and its visualized energy allocation in the time-scale domain, obtained through the signal identification algorithm, are displayed in Fig. 4a, where the symmetric Lamb mode, S_0, shear mode, S_0', and antisymmetric mode, A_0, are observed.
2. Case B: dual PZTs were in-phase energized (terminals B were simultaneously activated in both switchers). Symmetric electric fields, parallel to the polarized direction, were synchronously applied on the upper and bottom PZT wafers. Similarly, the raw signal acquired by the sensor located 100 mm away and its energy allocation in the time-scale domain are exhibited in Fig. 4b. A symmetric Lamb mode, S_0, of enhanced amplitude is noted, indicating that a stronger wave energy is centralized on the symmetric mode. Meanwhile, the shear mode, S_0', and antisymmetric mode, A_0, are considerably weaker.
3. Case C: dual PZTs were out-phase energized (terminals C were simultaneously activated in both switchers). Antisymmetric electric fields, parallel to the polarized direction, were synchronously applied on both PZT wafers. The raw signal acquired by the same sensor used above and its energy allocation are compared in Fig. 4c. The shear mode, S_0', and antisymmetric mode, A_0, are observed to dominate the overall wave energy, while with a small magnitude, the symmetric Lamb mode is reasonably suppressed.

3.4 Dispersive nature of Lamb waves in the composites

The dispersion characteristics of Lamb waves in the multilayered medium are some of the pivotal concerns for the development of guided wave-based damage detection techniques. Lamb waves are known to have a great ability to propagate over a relatively long distance without significant attenuation in the wave amplitudes, even in materials with a high attenuation ratio, such as CF/EP laminated composites. However, dispersion phenomena with variation in wave velocity are commonly observed, which complicates the analysis and signal interpretation.

By means of the proposed selective generation method for Lamb wave modes and the signal processing algorithm, the dispersion nature of fundamental Lamb modes in an eight-layer quasi-isotropic CF/EP laminate (T650/F584) were experimentally characterized. Wave velocities for symmetric and antisymmetric Lamb modes, excited by the generation circuit, at a sweep frequency ranging from 0.1 to 1.5 MHz

were generated by applying uniform radial displacement raints in the x–y plane, in correlation with the excitation al voltages, to simulate excitation case A, or by individually applying in-phase or out-phase constraints in the dual PZT configuration to emulate excitation cases B or C.

4.2 Sensor model

The model for the PZT sensor was created in parallel. Considering the deformation in the x'–y' plane only, the constitutive relation, equation (7), for a PZT sensor of radius R and thickness h_{PZT} can be simplified in its local polar coordinate system r'–θ'–z', in the absence of external electric fields, as [41]

$$Q = d_{31}(\sigma_{r'} + \sigma_{\theta'}) = \frac{d_{31}E_{PZT}}{1 - \nu_{PZT}}(\varepsilon_{r'} + \varepsilon_{\theta'}) \tag{19}$$

where r' and θ' are the local polar coordinates. On the other hand, the electric charges, Θ, accumulated on both surfaces of the PZT sensor can be defined in terms of the externally applied voltage as

$$\Theta = \frac{1}{4\pi}\int\int\int \nabla Q \, dV \tag{20}$$

Substituting equation (19) into equation (20) and applying Gauss' theorem leads to [41]

$$\Theta = \frac{d_{31}E_{PZT}}{4\pi(1 - \nu_{PZT})}\int\int(\varepsilon_{r'} + \varepsilon_{\theta'})r' \, dr' \, d\theta' \tag{21}$$

Regarded as a capacitor of capacitance C, the PZT sensor induces the output voltage, V_{otp}, under the deformation

$$V_{otp} = \frac{\Theta}{C} = \frac{\Theta h_{PZT}}{\pi K_3 p_0 R^2} \tag{22}$$

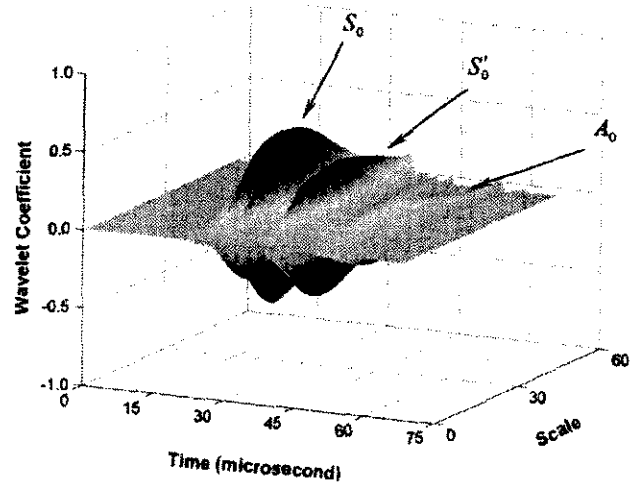

(a)

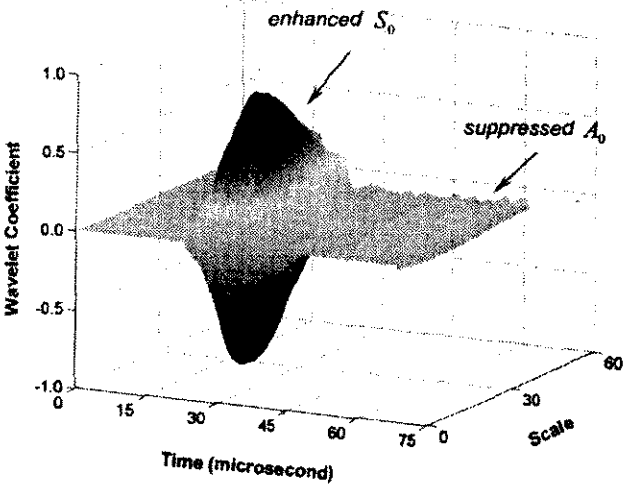

(b)

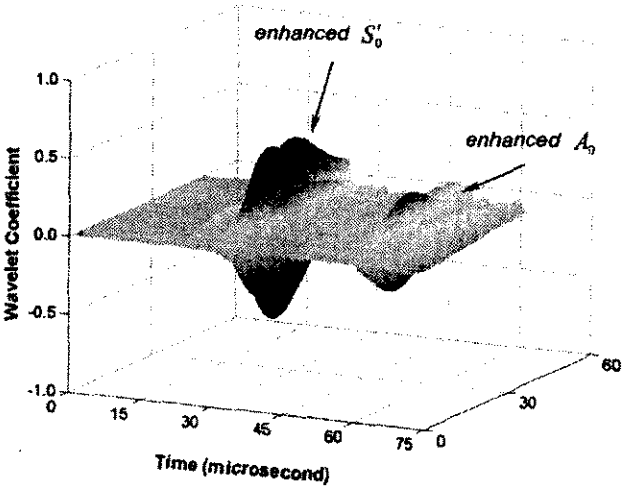

(c)

Fig. 9 Energy distribution spectrum for selectively generated Lamb modes (from FEM simulation): (a) excitation case A; (b) excitation case B; (c) excitation case C

where K_3 and p_0 represent the relative dielectric constant and the dielectric permittivity of a free PZT sensor respectively (Table 1). Combining equations (21) and (22) yields

$$V_{otp} = \frac{d_{31}E_{PZT}h_{PZT}}{4\pi K_3 p_0 R^2(1-\nu_{PZT})}\int\int(\varepsilon_{r'}+\varepsilon_{\theta'})r'\mathrm{d}r'\mathrm{d}\theta' \quad (23)$$

Compared with the laminate, the PZT sensor is geometrically small ($\varepsilon_{r'} \approx \varepsilon_{\theta'} \approx \varepsilon_{cen}$, where ε_{cen} is the strain at the centre of the PZT disc), and equation (23) can accordingly be simplified as [41]

$$V_{otp} = \tilde{G}\varepsilon_{cen} \quad (24)$$

where

$$\tilde{G} = \frac{d_{31}E_{PZT}h_{PZT}}{4\pi K_3\varepsilon_0(1-\nu_{PZT})}$$

This indicates that the output voltage for a PZT sensor, induced by geometrical deformation, is directly proportional to the central strain of the PZT sensor with a factor $\tilde{G}$. Based on equation (24), the PZT sensor output responses, in the form of induced output voltage, were achieved by the sensor model through calculating the strain at the PZT sensor centre.

4.3 Numerical simulation

Using the developed PZT actuator and sensor models, three-dimensional dynamic FEM simulation was accomplished employing ABAQUS/EXPLICIT® code. The relevant properties for the piezoelectric element can be found in Table 1. An eight-layer $[45/-45/0/90]_s$ CF/EP quasi-isotropic composite laminate (T650/F584) was modelled using eight-node solid brick elements with effective elastic properties,

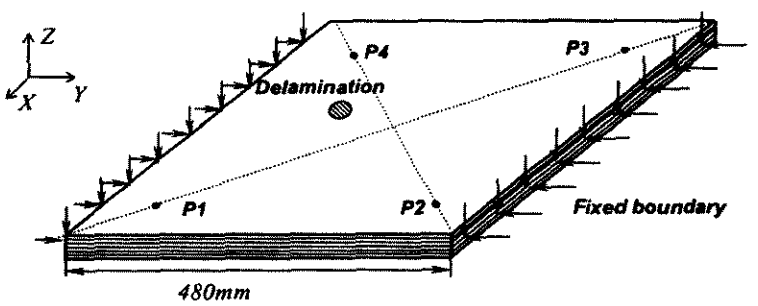

(a)

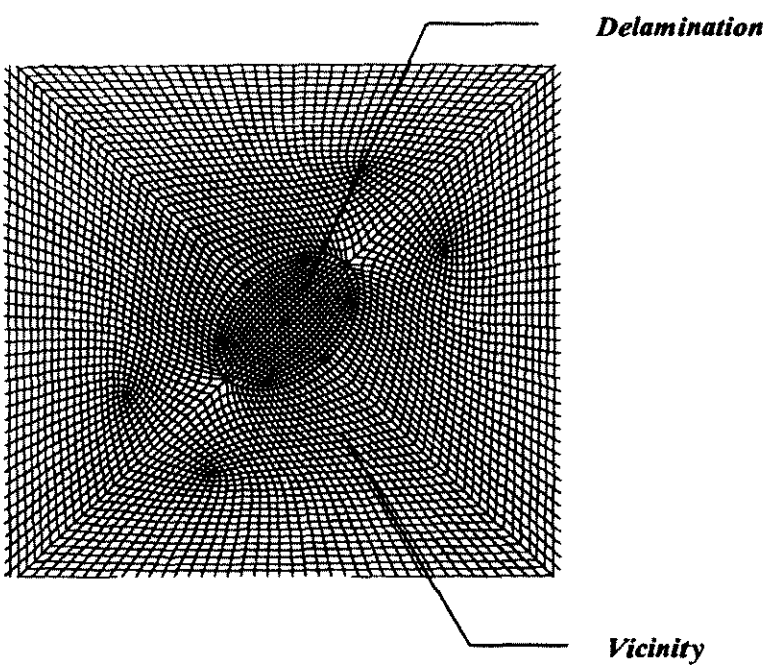

(b)

Fig. 10 Instrumented CF/EP laminate containing a delamination: (a) schematic description; (b) FEM model for vicinity of delamination

calculated using classical laminate theory from those of the unidirectional lamina [35], in Table 3, obtained from a micromechanics model [42].

Actively generated by the actuator model, visualized wave propagation from three-dimensional dynamic FEM simulations in the selected composite laminate at several representative times is plotted in Fig. 8. The energy allocations in the time-scale domain for signals numerically calculated for individual excitation cases (cases A, B and C) in accordance with experiments are compared in Fig. 9. Similar energy allocation (characteristic time and energy distribution) between the experimental measurements (Fig. 4) and numerical simulations (Fig. 9) can be observed upon application of the developed signal processing algorithm.

5 LAMB WAVE PROPAGATION IN DEFECTIVE LAMINATES

5.1 Specimen preparations and experimentation

Schematically depicted in Fig. 10a, two eight-layer [45/-4 0/90]$_s$ CF/EP quasi-isotropic laminates (T650/F584) with pair of clamped edges, shaped at 480 mm × 480 mm 1.275 mm, were manufactured using a unidirectional (UI prepreg (Table 3) in an autoclave at 180 °C under 600 kl pressure. In one laminate, an artificial delamination w introduced by inserting two elliptic UPLEX©-R-25 film (thickness 25 μm) between the first and the second laye (semi-major axis: 15 mm, semi-minor axis: 10 mm, ang

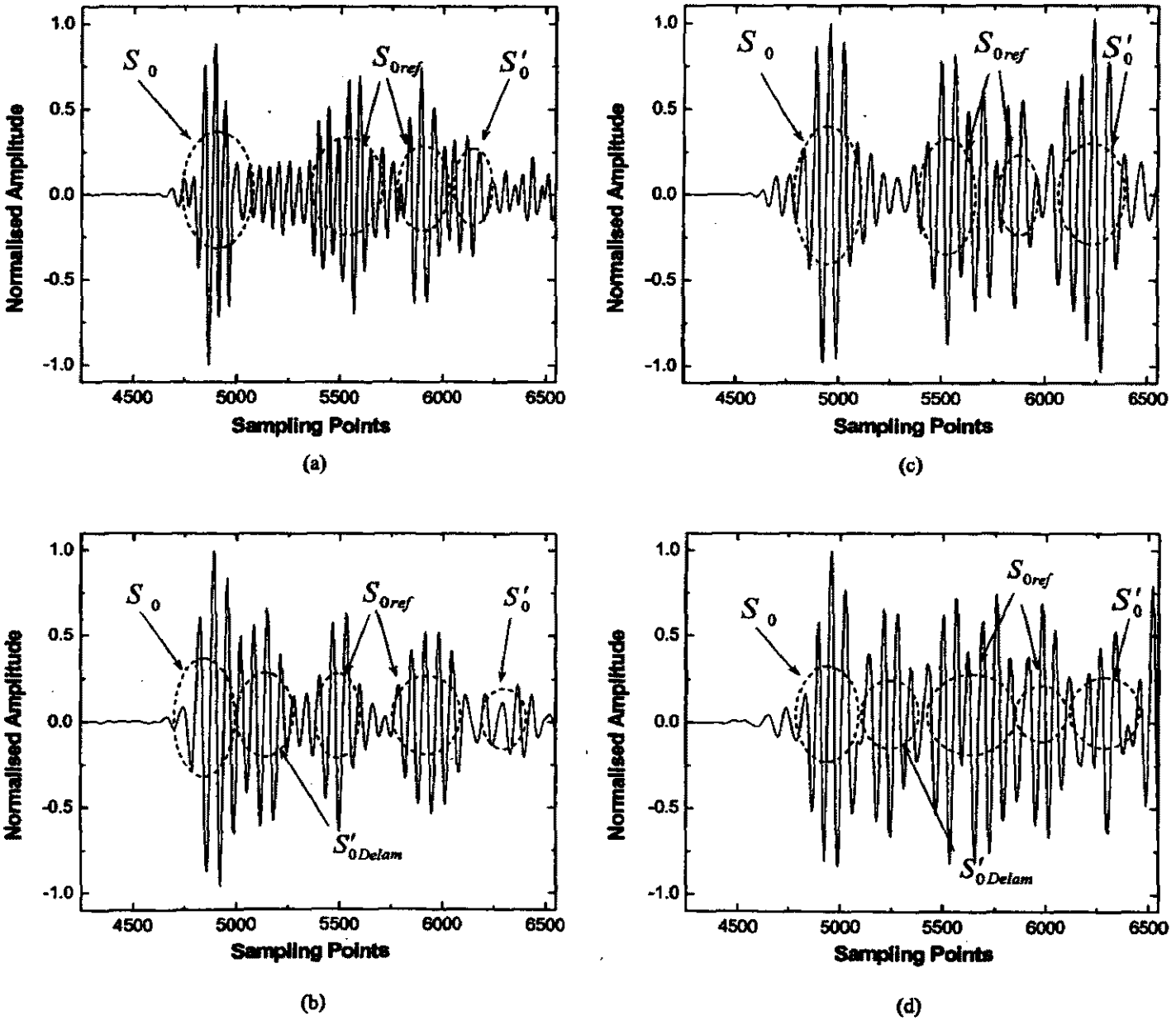

Fig. 11 DWT analysis processed signal acquired via actuator–sensor path P1–P3: (a) benchmark laminate from experiment; (b) delaminated laminate from experiment; (c) benchmark laminate from simulation; (d) delaminated laminate from simulation

between the major axis and 0° fibre direction: 135°, centre position: 276 and 299 mm away from the left and bottom edges of the laminate respectively). Another laminate was kept defect free as a benchmark for comparison. Four piezoelectric (PZT) discs, acting as both actuators and sensors, were bonded on the upper surface of each laminate, 65 mm away from the two neighbouring laminate edges and numbered counterclockwise P1, P2, P3 and P4 from the bottom left one. A diagnostic Lamb wave at the central excitation frequency of 0.5 MHz was activated by the designed control circuit. Signal acquisition was accomplished by an active online damage diagnosis system developed in a previous study [34].

5.2 Signal interpretation

The acquired signals were then identified using the signal processing algorithm described in section 3.2. The DWT-filtered wave signals for the benchmark and defective laminates, experimentally acquired through one actuator–sensor path P1–P3, corresponding to the incident excitation frequency, are displayed in Fig. 11a and b respectively. Their relevant energy allocation spectra in the time-scale domain are compared in Fig. 12. The fundamental symmetric Lamb mode, S_0, and basic shear mode, S_0', together with the reflected components from the boundaries, denoted by $S_{0\text{ref}}$, can be observed for both benchmark and delaminated

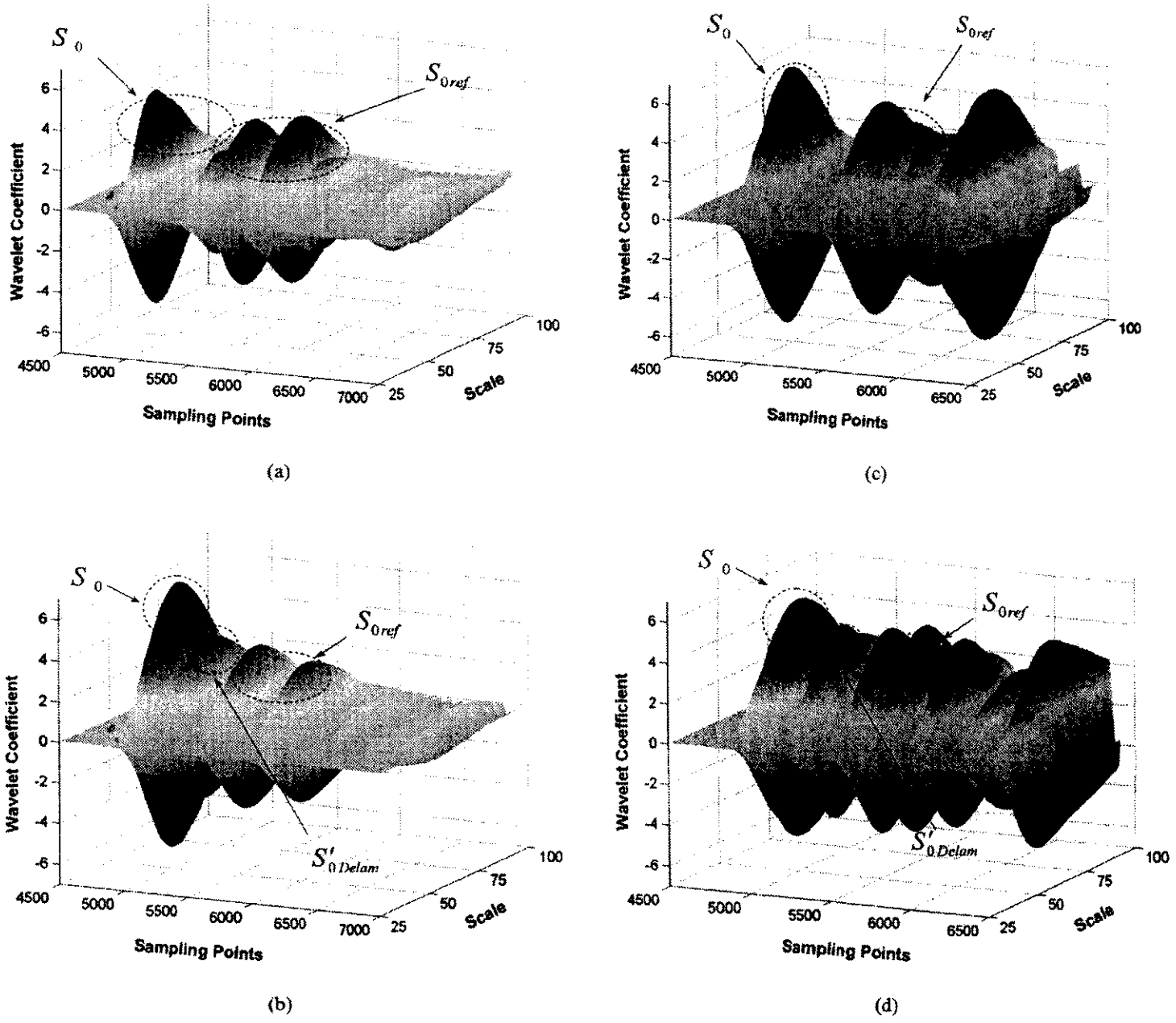

Fig. 12 Wave energy spectra for signal acquired via actuator–sensor path P1–P3: (a) benchmark laminate from experiment; (b) delaminated laminate from experiment; (c) benchmark laminate from simulation; (d) delaminated laminate from simulation

laminates. Compared with the benchmark laminate, extra wave components between S_0 and S_{0ref} are detected in Figs 11b and 12b, which are recognized as the delamination-induced basic shear mode, denoted by S'_{0Delam}. Based on the spectrographic analyses, the quantitative damage prediction can be fulfilled by capturing the variation in the energy spectra using a searching algorithm based on the artificial neural network technique, detailed in other work by the present authors [35].

For substantiation, FEM simulations were conducted in parallel. A previously developed modelling technique for the laminated CF/EP composite structures containing delamination [43] was employed. The FEM model for the vicinity of the delaminated area in the defective laminate is shown in Fig. 10b. The corresponding filtered signal and energy spectra are compared in Figs 11c and 12c for benchmark laminates and in Figs 11d and 12d for delaminated laminates. Good correlation, particularly the characteristic time and frequency for wave energy concentration in both time and time-scale spaces, was found between the numerical simulations and experimental measurements upon application of the proposed signal processing algorithm.

6 CONCLUSION

The practical utilization of Lamb waves for NDI purposes may be impeded by their complicated multimode and dispersive nature. An approach for active generation of selective Lamb wave modes in a CF/EP composite laminate was designed, by which the desirable single symmetric and antisymmetric modes can be individually stimulated. A signal processing and identification algorithm was devised using wavelet transform techniques in order to assist the filtration and interpretation of signal characteristics. Modelling techniques for PZT actuators and sensors were established and applied for the numerical simulation of Lamb wave generation and propagation in the chosen composite laminates. Good agreement between experimentation and FEM prediction has been achieved. The methodology was then implemented to investigate the propagation characteristics of Lamb waves in flawless and delaminated composite laminates. The results show that the utilization of Lamb waves and the interpretation of wave signals can be considerably facilitated by enhancing or suppressing certain Lamb modes via the proposed approach.

ACKNOWLEDGEMENTS

Z. Su would like to thank the Department of Education Science and Training (DEST), Australia for the financial support of an International Postgraduate Research Scholarship (IPRS), and the University of Sydney for an International Postgraduate Award (IPA).

REFERENCES

1 **Worlton, D. C.** Experimental confirmation of Lamb waves at megacycle frequencies. *J. Appl. Phys.*, 1961, **32**, 967–971.
2 **Lowe, M. J. S.** Matrix techniques for modeling ultrasonic waves in multilayered media. *IEEE Trans. Ultrasonics, Ferroelectrics and Freq. Control*, 1995, **42**, 525–541.
3 **Habeger, C. C., Mann, R. W.** and **Baum, G. A.** Ultrasonic plate waves in paper. *Ultrasonics*, 1979, **17**, 57–62.
4 **Percival, W. J.** and **Birt, E. A.** A study of Lamb wave propagation in carbon-fibre composites. *Insight*, 1997, **39**, 728–735.
5 **Alleyne, D. N.** and **Cawley, P.** The interaction of Lamb waves with defects. *IEEE Trans. Ultrasonics, Ferroelectrics and Freq. Control*, 1992, **39**, 381–397.
6 **Guo, N.** and **Cawley, P.** The interaction of Lamb waves with delamination in composite laminates. *J. Acoust. Soc. Am.*, 1993, **94**, 2240–2246.
7 **Guo, N.** and **Cawley, P.** Lamb wave propagation in composites and its relationship with acousto-ultrasonics. *NDT & E Int.*, 1993, **26**, 75–84.
8 **Guo, N.** and **Cawley, P.** Lamb wave reflection for the quick nondestructive evaluation of large composite laminates. *Mater. Evaluation*, 1994, **52**, 404–411.
9 **Birt, E. A.** Damage detection in carbon-fibre composites using ultrasonic Lamb waves. *Insight*, 1998, **40**, 335–339.
10 **Alleyne, D. N.** and **Cawley, P.** Optimisation of Lamb wave inspection techniques. *NDT & Int.*, 1992, **25**, 11–22.
11 **Wang, C. S.** and **Chang, F.-K.** Built-in diagnostics for impact damage identification of composite structures. In *Structural Health Monitoring* (Ed. F. -K. Chang), 2nd edition, 1999, pp. 612–621 (Technomic, Lancaster).
12 **Keilers Jr, C. H.** and **Chang, F.-K.** Identifying delamination in composite beams using built-in piezoelectrics. Part II: an identification method. *J. Intell. Mater. Syst. and Struct.*, 1995, **6**, 664–672.
13 **Dupont, M., Osmont, D., Gouyon, R.** and **Balageas, D. L.** Permanent monitoring of damaging impacts by a piezoelectric sensor based integrated system. In *Structural Health Monitoring* (Ed. F.-K. Chang), 2nd edition, 1999, pp. 561–570 (Technomic, Lancaster).
14 **Lemistre, M. B.** and **Balageas, D. L.** A new concept for structural health monitoring applied to composite materials. In Proceedings of the 1st European Workshop on *Structural Health Monitoring* (Ed. D. Balageas), France, Paris, 10–12 July 2002, pp. 493–507.
15 **Tan, K. S., Guo, N., Wong, B. S.** and **Tui, C. G.** Experimental evaluation of delaminations in composite plates by the use of Lamb waves. *Composites Sci. and Technol.*, 1995, **53**, 77–84.
16 **Tan, K. S., Guo, N., Wong, B. S.** and **Tui, C. G.** Comparison of Lamb waves and pulse echo in detection of near-surface defects in laminate plates. *NDT & E Int.*, 1995, **28**, 215–223.
17 **Bindal, V. N.** *Transducers for Ultrasonic Flaw Detection*, 1999 (Narosa Publishing House, New Delhi).
18 **Castaings, M.** and **Cawley, P.** The generation, propagation, and detection of Lamb waves in plates using air-coupled ultrasonic transducers. *J. Acoust. Soc. Am.*, 1996, **100**, 3070–3077.
19 **Hosten, B., Castaings, M., Tretout, H.** and **Voillaume, H.** Identification of composite materials elastic moduli from Lamb wave velocities measured with single sided, contactless ultrasonic method. In *Review of Progress in Quantitative Nondestructive Evaluation* (Eds D. O. Thompson and D. E. Chimenti), 2001, Vol. 20B, pp. 1023–1030 (Plenum, New York).

20 **Ghosh, T., Kundu, T.** and **Karpur, P.** Efficient use of Lamb modes for detecting defects in large plates. *Ultrasonics*, 1998, **36**, 791–801.

21 **Guo, Z., Achenbach, J. D.** and **Krishnaswamy, S.** EMAT generation and laser detection of single Lamb wave modes. *Ultrasonics*, 1997, **35**, 423–429.

22 **Legendre, S., Massicotte, D., Goyette, J.** and **Bose, T. K.** Wavelet-transform-based method of analysis for Lamb-wave ultrasonic NDE signals. *J. IEEE Trans. Instrum. and Measmt*, 2000, **49**, 524–530.

23 **Achenbach, J. D.** Quantitative nondestructive evaluation. *Int. J. Solids and Struct.*, 2000, **37**, 13–27.

24 **Yoshimura, S., Yagawa, G., Oishi, A.** and **Yamada, K.** Neural network based inverse analysis for defect identification with laser ultrasonics. *Key Engng Mater.*, 1998, **145–149**, 443–452.

25 **Niethammer, M., Jacobs, L. J., Qu, J.** and **Jarzynski, J.** Time–frequency representations of Lamb waves. *J. Acoust. Soc. Am.*, 2001, **109**, 1841–1847.

26 **Ishak, S. I., Liu, G. R., Shang, H. M.** and **Lim, S. P.** Locating and sizing of delamination in composite laminates using computational and experimental methods. *Composites: Part B*, 2001, **32**, 287–298.

27 **Valle, C.** and **Littles Jr, J. W.** Flaw localization using the reassigned spectrogram on laser-generated and detected Lamb modes. *Ultrasonics*, 2002, **39**, 535–542.

28 **Monkhouse, R. S. C., Wilcox, P. W.** and **Cawley, P.** Flexible interdigital PVDF transducers for the generation of Lamb waves in structures. *Ultrasonics*, 1997, **35**, 489–498.

29 **Blanas, P.** and **Das-Gupta, D. K.** Composite piezoelectric sensors for smart composite structures. In Proceedings of 10th International Symposium on *Electrets*, Athens, Greece, 22–24 September 1999, pp. 731–734.

30 **Monkhouse, R. S. C., Wilcox, P. W., Lowe, M. J. S., Dalton, R. P.** and **Cawley, P.** The rapid monitoring of structures using interdigital Lamb wave transducers. *Smart Mater. and Struct.*, 2000, **9**, 304–309.

31 **Gaul, L.** and **Hurlebaus, S.** Wavelet-transform to identify the location and forces-time-history of transient load in a plate. In *Structural Health Monitoring* (Ed. F.-K. Chang), 2nd edition, 1999, pp. 851–860 (Technomic, Lancaster).

32 **Lemistre, M.** and **Balageas, D.** Structural health monitoring system based on diffracted Lamb wave analysis by multiresolution processing. *Smart Mater. and Struct.*, 2001, **10**, 504–511.

33 **Su, Z., Ye, L.** and **Bu, X.** Quantitative assessment of structural damage by impact response. Accepted by *Structural Health Monitoring*.

34 **Su, Z.** and **Ye, L.** A damage identification technique for CF/EP composite laminates using distributed piezoelectric transducers. *Composite Struct.*, 2002, **57**, 465–471.

35 **Su, Z.** and **Ye, L.** Lamb wave propagation-based damage identification for quasi-isotropic composite laminates using artificial neural algorithm. Part II: implementation and validation. Submitted to *J. Intell. Mater. Syst. and Struct.*

36 **Schulz, M. J., Pai, P. F.** and **Inman, D. J.** Health monitoring and active control of composite structures using piezoceramic patches. *Composites: Part B*, 1999, **30**, 713–725.

37 **Kessler, S. S., Spearing, S. M.** and **Atalla, M. J.** In-situ damage detection of composites structures using Lamb wave. In Proceedings of 1st European Workshop on *Structural Health Monitoring* (Ed. D. Balageas), Paris, France, 10–12 July 2002, pp. 374–381.

38 **Boashash, B.** *Time-Frequency Signal Analysis*, 1992 (Longman Cheshire, Melbourne).

39 **Flandrin, P.** *Time-Frequency/Time-scale Analysis*, 1999 (Academic Press, San-Diego).

40 *Wavelet Toolbox: For Use with Matlab (User's Guide). Ver.1.0*, 2002 (The Mathworks, Inc.).

41 **Lin, X.** and **Yuan, F. G.** Diagnostic Lamb waves in an integrated piezoelectric sensor/actuator plate: analytical and experimental studies. *Smart Mater. and Struct.*, 2001, **10**, 907–913.

42 **Gommers, B., Verpoest, I.** and **Houtte, P. V.** Modelling the elastic properties of knitted-fabric-reinforced composites. *Composites Sci. and Technol.*, 1996, **56**, 685–694.

43 **Su, Z., Ye, L.** and **Bu, X.** Evaluation of delamination in laminated composites based on Lamb wave modes: FEM simulation and experimental verification. In Proceedings of 1st European Workshop on *Structural Health Monitoring* (Ed. D. Balageas), Paris, France, 10–12 July 2002, pp. 328–335.

ELSEVIER

Composite Structures 57 (2002) 465–471

COMPOSITE STRUCTURES

www.elsevier.com/locate/compstruct

A damage identification technique for CF/EP composite laminates using distributed piezoelectric transducers

Zhongqing Su [a], Lin Ye [a,*], Xiongzhu Bu [a,b]

[a] *Centre for Advanced Materials Technology (CAMT), School of Aerospace Mechanical and Mechatronic Engineering, The University of Sydney, Building J07, Sydney, NSW 2006, Australia*

[b] *School of Mechanical Engineering, Nanjing University of Science and Technology, 210094, China*

Abstract

In this study, a damage identification approach was developed for carbon fibre/epoxy composite laminates with localized internal delamination. Propagation of the Lamb wave in laminates and its interaction with the delamination were examined. The fundamental symmetric Lamb wave mode, S_0, and the lowest order shear wave mode, S_0', were chosen to predict damage location. A real-time active diagnosis system was therefore established. This technique uses distributed piezoelectric transducers to generate and monitor the ultrasonic Lamb wave with narrowband frequency. The two-way switches were employed to minimize the number of transducers. A signal-processing scheme based on the time–frequency spectrographic analysis was utilised to extract useful diagnostic information. Also, an optimal identification method was applied on damage searching procedure to reduce errors and obtain the diagnostic results promptly. Experiments were conducted on [0/−45/45/90]$_s$ CF/EP laminates to verify this diagnosis system. The results obtained show that satisfactory detection accuracy could be achieved.

Keywords: Structural health monitoring; Fibre-reinforced composite; Lamb wave; Signal processing; Smart structures

1. Introduction

Impact-induced damage is perhaps one of the most common defectives in carbon fibre reinforced composite laminates, which may result in a substantial impairment of structural integrity. Delamination, the most familiar impact damage in composite structures, plays a major role in inhibiting the further widespread application of laminated composites in practice. Particularly, its location and extent are of vital difficulty to predict in most cases. In the past two decades, both researchers and engineers have been pursuing effective techniques to detect the occurrence of delamination and to estimate its position at the early stage so as to reduce the risk of further catastrophic failure. Recently, vast of research indicates that non-destructive evaluation techniques based on the Lamb wave propagation offer one possible solution to this concern [1–11].

The Lamb wave in ultrasonic domain has the ability to propagate a relatively long distance in laminated composites, and a wide section can therefore be interrogated with a small number of transducers. In addition, the appearance of Lamb wave-caused interlaminar stresses makes the detection through the entire laminate thickness applicable, which affords a potential to detect the internal defects as well as the surface defects. For example, Tang and Henneke [1] proposed a monitoring technique for the stiffness reduction in laminated composite plates based on the Lamb wave; Guo and Cawley [2,3] examined the interaction between the ultrasonic Lamb wave and the delamination in terms of both numerical and experimental approaches; Tan et al. [4] developed a damage detection method for composites using ultrasonic probes. In most approaches, probes were usually used for the generation and collection of the Lamb wave due to good accessibility, with which the damage identification can be fulfilled conveniently and accurately. However, in most circumstances, a temporary out-of-service of the structure is required, ensuring the function of probes. As know, this confines the further application for on-line damage diagnosis. On the other hand, the advanced composite structures in aerospace industry are expected to be involved with built-in actuator/sensor networks to enhance the performance

* Corresponding author. Tel.: +61-2-9351-4798; fax: +61-2-9351-3760.

E-mail address: ye@aeromech.usyd.edu.au (L. Ye).

0263-8223/02/$ - see front matter
PII: S0263-8223(02)00115-0

and to reduce the operation and maintenance costs. For this target, innovations have been made in the past few years, in which piezoelectric elements instead of conventional probes are employed directly to facilitate a simple and reliable on-line damage detection with low expenditure. Wang and Chang [5] discussed the damage detection technique based on the Lamb wave generated by ultrasonic transmitter, and Lemistre et al. [6] reported a structural defect identification method using piezoelectrics.

The present work aims at developing a practical and effective real-time damage identification technique for CF/EP composite laminates, with which the structural health status can be in-service monitored. In this study, distributed piezoelectrics were involved into the structure during manufacturing to minimize the interference on the structural integrity. In correlation with the study on the propagation characteristics of Lamb wave in composites, a diagnosis system was developed. The feasibility of this system was then verified by applying it to quasi-isotropic laminates for the locating of delamination.

2. Characteristics of the Lamb wave in composites

Compared with the components produced by ultrasonic probes, the Lamb wave generated by the fixed piezoelectrics unavoidably contains multi-modes in plate-like laminated structure simultaneously due to the exclusive attenuation mechanism, which can be basically divided into two categories depending on the particulate motion, viz. symmetrical and asymmetrical modes. Additionally, the vibrational patterns and dispersive properties through the plate thickness are not identical for each mode, even for the same mode but in the different frequency domains, making the study for Lamb wave more intractable. Percival and Birt [7] verified that the dispersive characteristics of Lamb wave depend on both the plate thickness and frequency. In their study, an inhouse FEM software and a numerical simulation approach based on the effective elastic properties were developed to calculate the dispersive curves for typical composite laminates.

In this work, the propagation of Lamb wave in $[0/-45/45/90]_s$ quasi-isotropic CF/EP laminates within the frequency domain, ranging from 0.05 to 1.5 MHz, was investigated first. Four piezoelectric transducers were fixed on the laminates to establish 6 pairs of totally 12 actuator-sensor paths in order to characterise the wave velocity for different modes. The dispersive curve experimentally measured is plotted in Fig. 1, while the curve theoretically calculated by FEM [8] is also comparatively displayed, denoted by triangle and square symbols respectively. In Fig. 1, the fundamental asymmetric Lamb mode, A_0, symmetric Lamb mode, S_0, and

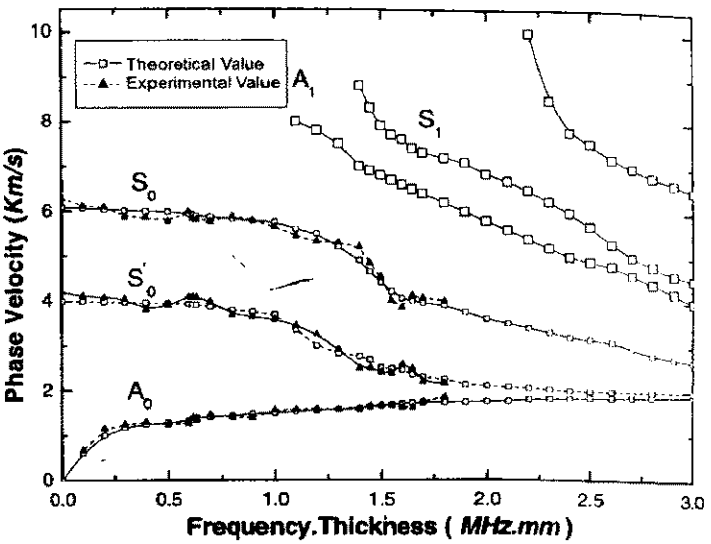

Fig. 1. The dispersive curve for quasi-isotropic CF/EP laminates.

the lowest order SH (shear mode) wave mode, S_0', can be observed in low frequency region, while the higher order modes appear gradually with an increase of frequency. The dispersive curve implies that at least two Lamb modes are available synchronously and their phase/group velocity is dependent on the algebraic product of the laminate thickness and the mode central frequency. Nevertheless, a low-frequency domain (<1.0 MHz mm) can be noticed in the dispersive curve, where the fundamental Lamb wave modes and the lowest order shear wave mode exhibit reasonably non-dispersive behavior. In this research, the fundamental symmetric Lamb mode, S_0, and the internal defect-induced lowest order SH mode, S_0', are utilised for the diagnosis.

3. Configuration of experiment

An active real-time diagnosis system was developed in this work, whose schematic description is given in Fig. 2. In this system, piezoelectric lead zirconate titanate (PZT) wafers (ϕ: 6.9 mm, thickness: 0.5 mm) acted as both actuators and sensors with the aid of two-way switches. *Agilent® E1441* arbitrary waveform generator was used to produce 5-cycle toneburst with *Hanning* window at a central frequency of 0.5 MHz. The simulated diagnostic signal was then applied on each PZT wafer after amplified with the PZT amplifier (*PiezoSys® EPA-104*) to generate ultrasonic Lamb wave. Response signals were conditioned by *Agilent® E3242A* and acquired via *E1437A* digitizer at a sampling rate of 20.48 MHz; Sampled signals were transmitted into the central control unit (CCU) for further analyses; All the diagnosis control and signal analyses were performed by CCU, supported on the *NI Labview©* and *Matlab©* platforms.

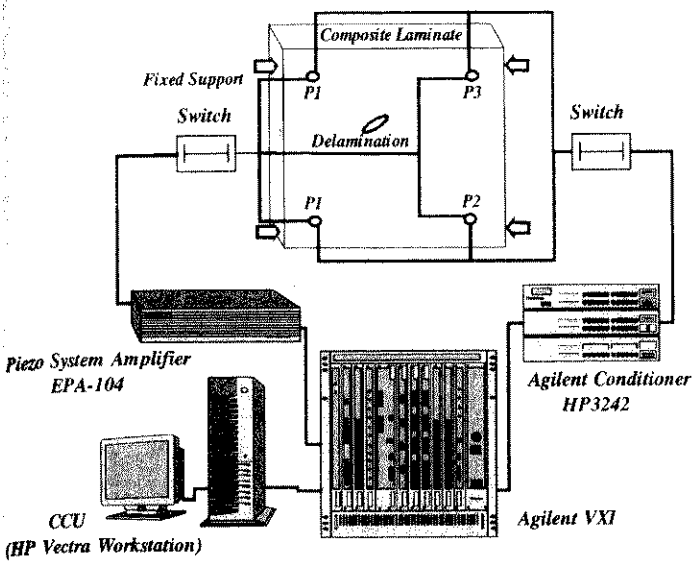

Fig. 2. Configuration of proposed diagnosis system.

The validity of this system was then verified by applying it to $[0/-45/45/90]_s$ CF/EP laminates (*HEXCEL*© *F854*). For comparison, two laminates ($480 \times 480 \times 1.275\ mm^3$) without/with pre-treated internal defect were manufactured, which are hereafter recognised as the benchmark laminate and the defective laminate. An elliptic *UPLEX*©*-R*-25 film (thickness: 25 μm, semi-major axis: 15 mm, semi-minor axis: 10 mm, angle between semi-major axis and 0° fibre direction: 135°) was inserted at interfaces between the 1st and the 2nd layer, simulating the common impact-induced delamination. The centre of the artificial delamination lies 276 and 299 mm respectively away from the left edge and bottom edge of the laminates. Response signals were sampled for each actuator-sensor path in experiment.

In Fig. 2, four PZT wafers are denoted counterclockwise by *P1*, *P2*, *P3* and *P4* respectively from the bottom-left one. Each transducer locates 65 mm away from two neighboring edges. Thus, totally 12 pairs of actuator-sensor path are theoretically available. In experiment, each laminate was fixed-supported on one pair of its parallel edges while another pair was free.

4. Signal processing and damage diagnosis

Sampling signals for the benchmark laminate and the defective laminate via actuator-sensor paths *P1–P3* and *P2–P4*, as typical paradigms, are displayed in Figs. 3 and 4, respectively. Containing the structural vibration components and diverse bandwidth noises, the acquired raw signals can hardly be used directly for the diagnosis. Wavelet transform-based time–frequency spectrographic analyses were employed to extract the useful diagnostic information [12–18]. In this study, both the discrete wavelet transform (DWT) analysis and continuous wavelet transform (CWT) analysis were performed for the signal processing to effectively diminish the influence of broadband noises. *Daubechies* function $\Psi(a,b)$ at level 4 (*db4*) was chosen as the transform function and applied with the CWT transform [14],

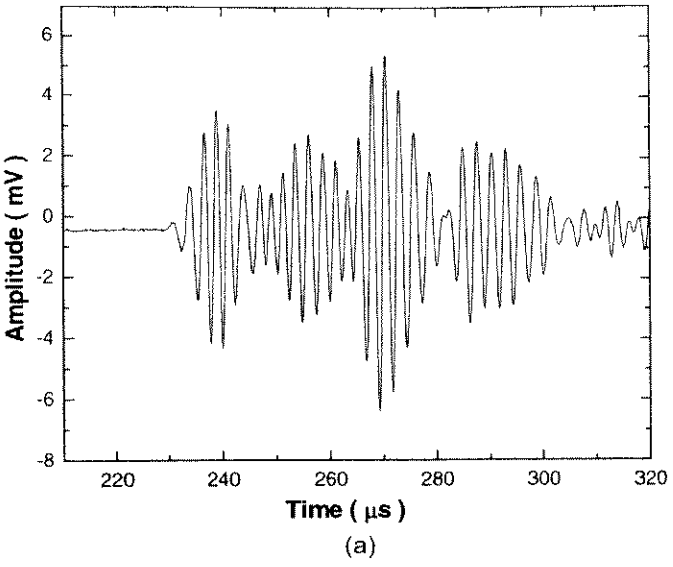

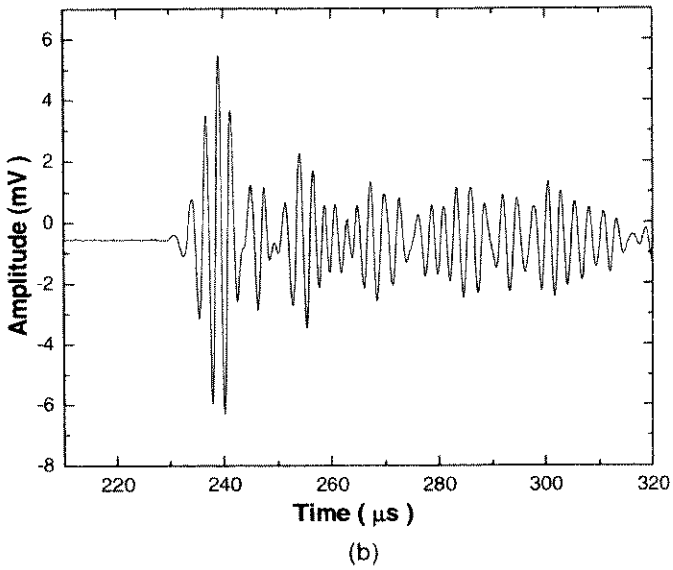

Fig. 3. Sampled signals via actuator-sensor path *P1–P3*: (a) the benchmark laminate, (b) the defective laminate.

$$W(a,b) = \frac{1}{\sqrt{a}} \int_{-\infty}^{+\infty} f(t)\Psi^*\left(\frac{t-b}{a}\right) \mathrm{d}t \tag{1}$$

where $W(a,b)$ denotes the continuous wavelet coefficient. a and b are the scale parameter and the translation parameter, respectively. $f(t)$ represents arbitrary sampled signal, while $\Psi^*(t)$ denotes the complex conjugate of $\Psi(t)$. Furthermore, the CWT analysis can be simplified by calculating the wavelet coefficients at discretized scale, i.e., the DWT analysis, with which the sampled signal can be broken down into low-resolution compo-

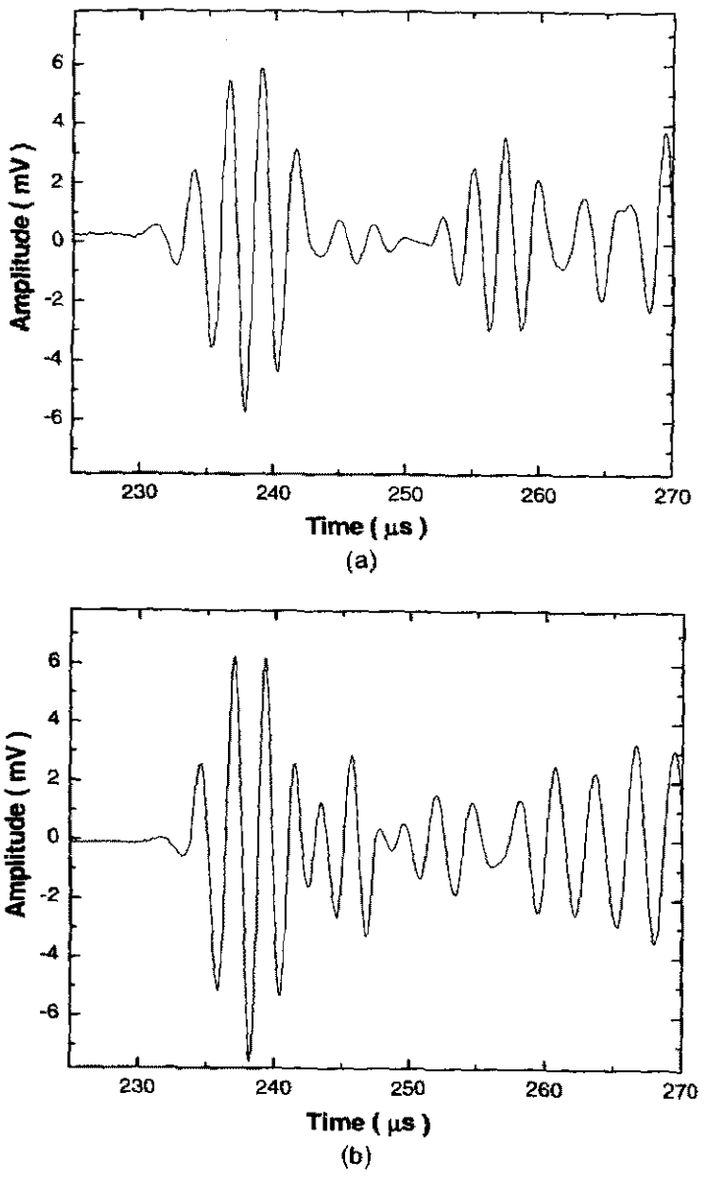

Fig. 4. Sampled signals via actuator-sensor path *P2–P4*: (a) the benchmark laminate, (b) the defective laminate.

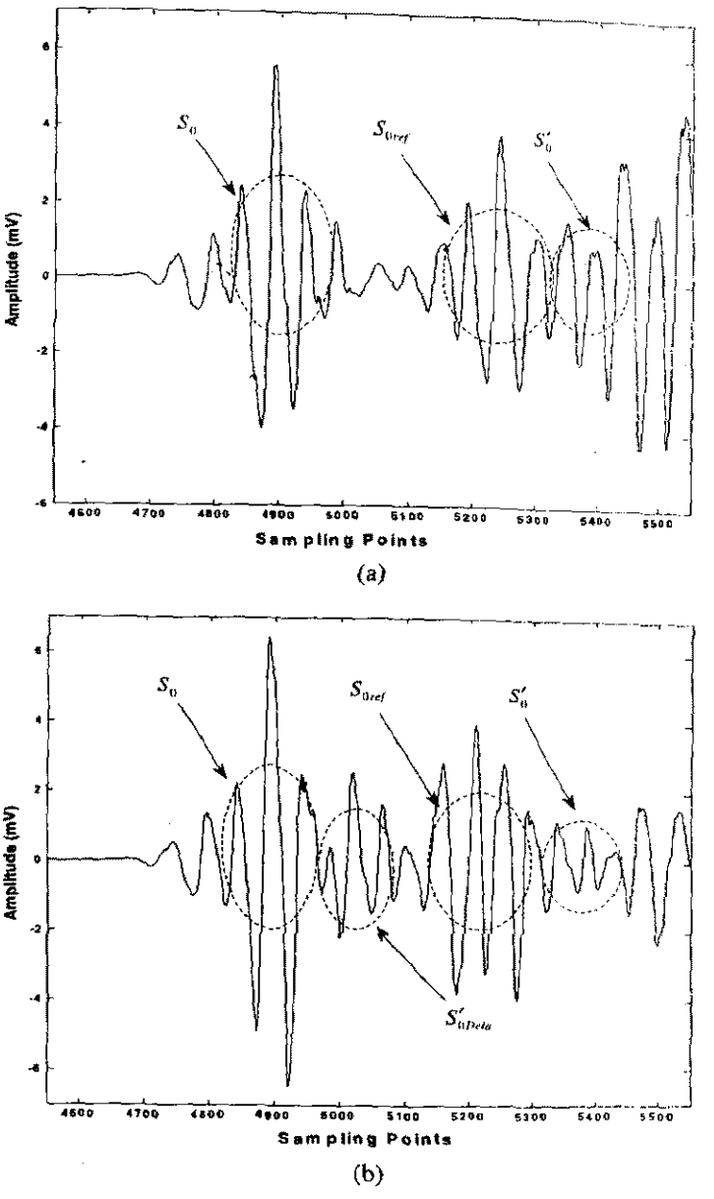

Fig. 5. DWT analytical results for signals via actuator-sensor path *P1–P3*: (a) the benchmark laminate, (b) the defective laminate.

nents. In addition, derived from Eq. 1, the total energy for sampling signal can be yielded as [14]:

$$E = C \int_{-\infty}^{+\infty} \int_{-\infty}^{+\infty} |W(a,b)|^2 \frac{da\,db}{a^2} \tag{2}$$

It indicates that the wavelet coefficient $W(a,b)$ can reflect the distribution of wave energy over the time and frequency domain.

The analytical results by DWT at the 5th level for signals shown in Figs. 3 and 4 are displayed and illustrated in Figs. 5 and 6, respectively. With the aid of DWT analysis, the fundamental symmetric Lamb modes, S_0, and the lowest order shear wave mode, S'_0, as well as their corresponding reflected waves from the boundaries which are herein denoted as S_{0ref} and S'_{0ref}, can be observed in the analysed signals in Fig. 5(a) and Fig. 6(a), corresponding to the benchmark laminate.

Paralleled with the analysed signals for the benchmark laminate, extra wave components can be noticed in analysed signals corresponding to the defective laminate via the same actuator-sensor paths, which are contrastively shown in Figs. 5(b) and 6(b). The extra component in signal is recognised as the induced lowest order shear wave mode S'_0 due to the existence of delamination, denoted as S'_{0Delam}. Other delamination-induced wave modes, S_{0Delam} and A_{0Delam}, are unexploitable because their propagation velocities are either too high to be separated or too low to be sampled. For identification, only first several wave components in sampled signals are useful.

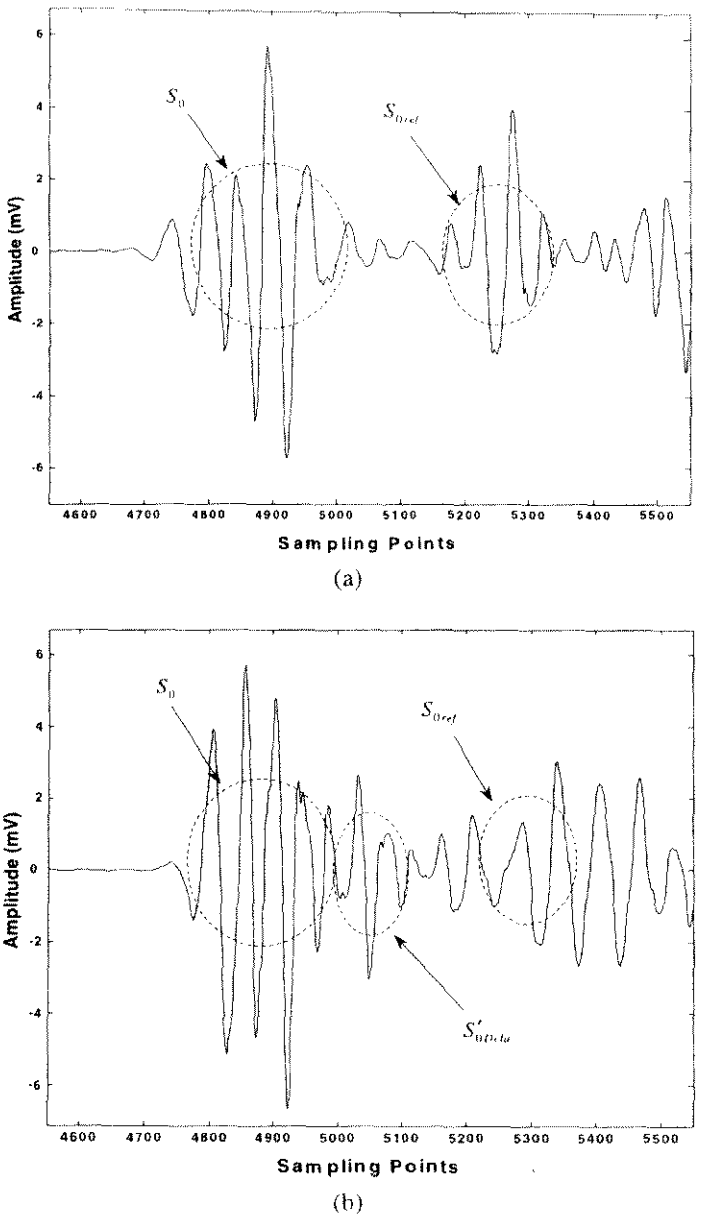

Fig. 6. DWT analytical results for signals via actuator-sensor path *P2–P4*: (a) the benchmark laminate, (b) the defective laminate.

Meanwhile, full-scale spectrographic analyses by CWT were also performed for the sampled signals. As example, 2D spectra of the raw signals for the benchmark laminate and the defective laminate via actuator-sensor path *P1–P3* are displayed in Fig. 7. In the spectra, the wavelet coefficients, represented by descending grayscale, reveal the distribution of wave energy density, deploying the local perturbations in the signals. More intuitively, 3D spectrum for the defective laminate is shown in Fig. 8. By virtue of DWT and CWT analyses, the damage can be located by calculating the related time lags upon consideration of multi-mode velocities [13].

A rough estimation for the possible delamination locations was preliminarily executed to expedite the

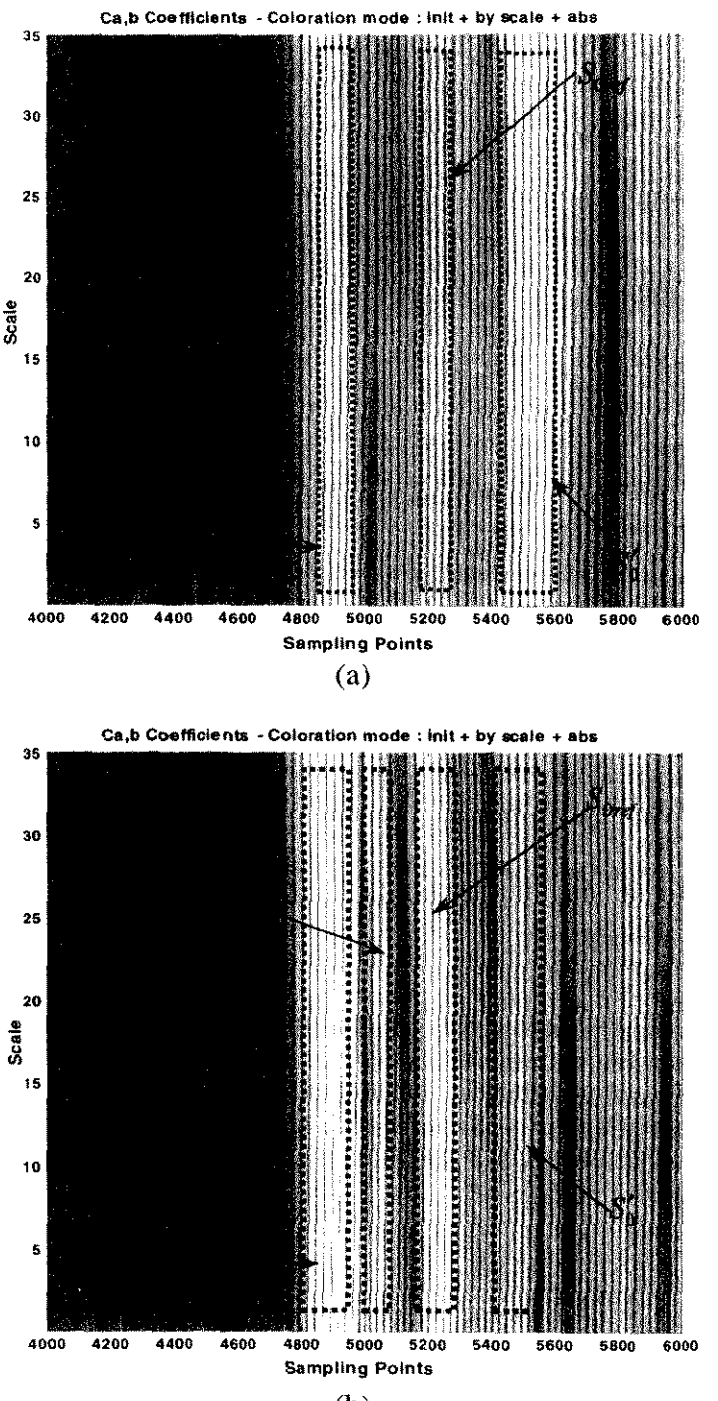

Fig. 7. 2D CWT spectra for signals via actuator-sensor path *P1–P3*: (a) the benchmark laminate, (b) the defective laminate.

diagnosis, approximately offering an initial position for the damage searching. It was found that the damage searching and identification could be consequently simplified by such initial estimation. During the searching procedure, the transducer *P1* is initially assumed as the origin of the coordinate system with the X axis paralleling with the bottom edge of the laminate, and a set of non-linear equations involving the position parameters for the delamination centre can be therefore

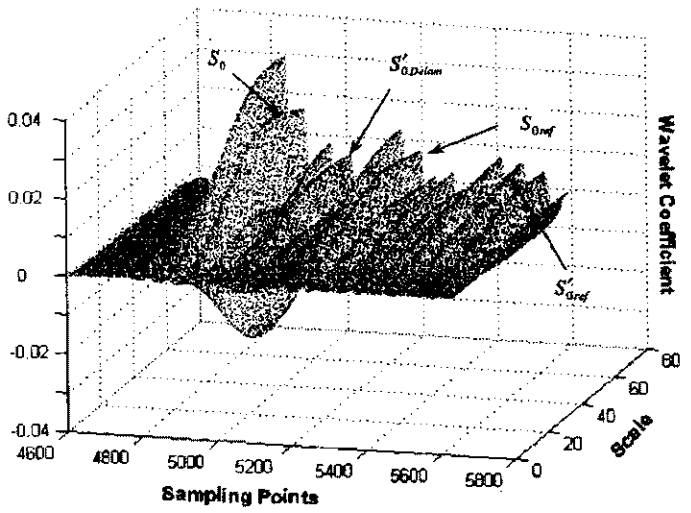

Fig. 8. 3D CWT spectrum for signals via actuator-sensor path *P1–P3* for the defective laminate.

etup in correlation with the geometric relationships among the locations of transducers and damage. The non-linear equations corresponding to the transducer *P1* can be given as [6,9],

$$\frac{\sqrt{(x-x_i)^2+(y-y_i)^2}}{V_{S'_{0\mathrm{Delam}}}}+\frac{\sqrt{x^2+y^2}}{V_{S_0}}-\frac{\sqrt{x_i^2+y_i^2}}{V_{S_0}}=T_{1-i}\quad(i=2,3,4) \tag{3}$$

where (x,y) denotes the coordinates of delamination centre in the current reference frame, and (x_i,y_i) represents the coordinates of the ith transducer. $V_{S'_{0\mathrm{Delam}}}$ and V_{S_0} are the velocities of wave modes $S'_{0\mathrm{Delam}}$ and S_0, respectively; while T_{1-i} is the measured time lag via actuator-sensor path *P1–Pi*.

Analogously, total four sets of the non-linear equations can be established upon four coordinate systems introduced, in which each PZT actuator takes turn to be nominated as the origin of the reference frames respectively. Further, an optimisation based on a graphic approach is then applied to solve the non-linear systems [13], fulfilling a prompt diagnosis with high accuracy. The whole searching procedure is schematically explained in Fig. 9. The dash-dot-lines represent the intercurrent lines generated by the searching algorithm, with which the proposed non-linear systems can be solved graphically, facilitating an accurate locating for the damage centre.

The results show that the diagnostic errors are dependent on the total number of the actuator-sensor paths involved for identification. The errors decrease with the increase of the path number for evaluation, while four paths are the minimum mathematic requirement to solve the nominated non-linear system sets for the location of delamination. However, the more the paths are taken into account, the more CCU computing time is consumed. In practice, a compromise between expected accuracy and affordable time/cost should be sychronised in accordance to the actual requirement.

5. Conclusion

An identification approach for delamination locating in laminated composites based on the Lamb wave propagation was proposed. The fundamental symmetric Lamb mode and the lowest order shear wave mode were identified. An active diagnosis system using built-in piezoelectrics was consequently developed and applied to quasi-isotropic CF/EP composite laminates to verify the feasibility and capability. Wavelet transform-based

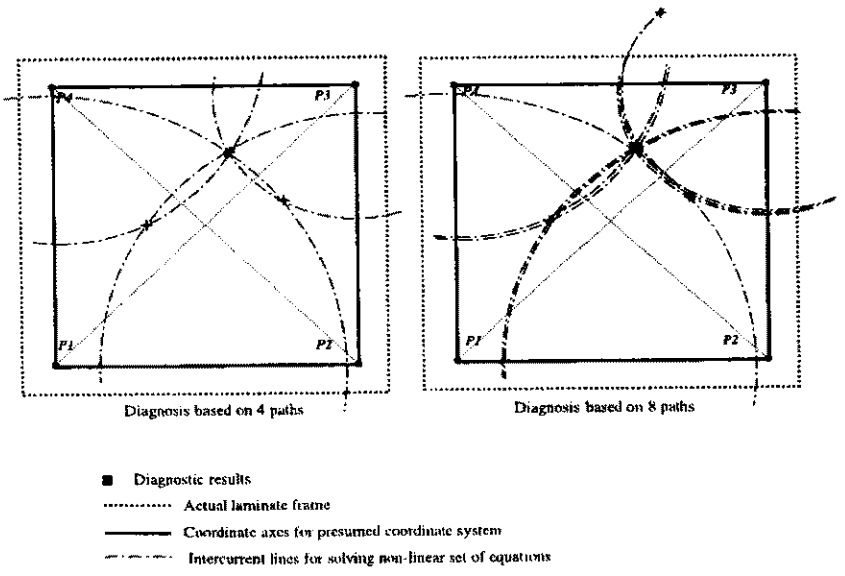

Fig. 9. Delamination locating procedure.

signal processing technique was employed in the identification scheme to suppress the diverse noises. It is shown that good diagnostic results can be achieved. Further studies will focus on the development of identification technique for the extent of delamination.

References

[1] Tang B, Henneke EG. Lamb-wave monitoring of axial stiffness reduction of laminated composite plates. Mater Eval 1991;47:928–34.

[2] Guo N, Cawley P. The interaction of Lamb wave with delaminations in composite laminates. J Acoust Soc Am 1993;94:2240–6.

[3] Guo N, Cawley P. Lamb wave reflection for the quick nondestructive evaluation of large composite laminates. Mater Eval 1994;52:404–11.

[4] Tan KS, Guo N, Wong BS, Tui CG. Experimental evaluation of delaminations in composite plates by the use of Lamb waves. Compos Sci Technol 1995;53:77–84.

[5] Wang CS, Chang F-K. Built-in diagnostics for impact damage identification of composite structures. In: Chang F-K, editor. Structural Health Monitoring. Lancaster: Technomic; 1999. p. 612–21.

[6] Lemistre M, Guoyon R, Kaczmarek H, Balageas D. Damage localization in composite plates using wavelet transform processing on Lamb wave signals. In: Chang F-K, editor. Structural Health Monitoring. Lancaster: Technomic; 1999. p. 861–70.

[7] Percival WJ, Birt EA. A study of Lamb wave propagation in carbon-fibre composites. Insight 1997;39:728–35.

[8] Badcock RA, Birt EA. The use of 0–3 piezocomposite embedded Lamb wave sensors for detection of damage in advanced fibre composites. J Smart Mater Struct 2000;9:291–7.

[9] Gaul L, Hurlebaus S. Wavelet-transform to identify the location and force–time-history of transient load in a plate. In: Chang F-K, editor. Structural Health Monitoring. Lancaster: Technomic; 1999. p. 851–60.

[10] Legendre S, Massicotte D, Bose TK. Wavelet-transform-based method of analysis for Lamb-wave ultrasonic NDE signals. J IEEE 2000;49:524–30.

[11] Hou Z, Noori M, Amand RS. Wavelet-based approach for structural damage detection. J Eng Mech 2000;126:677–83.

[12] Abbate A, Koay J, Frankel J, Schroeder SC, Das P. Signal detection and noise suppression using a wavelet transform signal processor: application to ultrasonic flaw detection. J IEEE 1997; 44:14–25.

[13] Su ZQ, Ye L, Xiong ZB. Lamb wave based delamination identification approach for fibre reinforced composite laminates, in preparation.

[14] Chan YT. Wavelet Basic. Boston: Kluwer Academic Publishers; 1995.

[15] Charles H, Keilers J. Identifying delamination in composite beams using built-in piezoelectrics: Part I—experiments and analysis. J Intel Mater Syst Struct 1995;6:649–63.

[16] Rose JL. Ultrasonic waves in solid media. Cambridge: Cambridge University Press; 1999.

[17] Chakraborty G, Mallil AK. Wave propagation in and vibration of a traveling beam with and without non-linear effects. J Sound Vib 2000;236:277–90.

[18] Doyle JF. Wave propagation in structures. second ed. New York: Springer-Verlag; 1997.

SHM
Structural Health Monitoring

Quantitative Assessment of Damage in a Structural Beam Based on Wave Propagation by Impact Excitation

Zhongqing Su,[1] Lin Ye,[1,*] Xiongzhu Bu[2], Xiaoming Wang[3] and Yiu-Wing Mai[1]

[1]*Centre for Advanced Materials Technology (CAMT), School of Aerospace, Mechanical and Mechatronic Engineering, The University of Sydney, NSW 2006, Australia*
[2]*School of Mechanical Engineering, Nanjing University of Science and Technology, 210094, P.R. China*
[3]*CSIRO Infrastructure Systems Engineering, Highett, VIC 3190, Australia*

A damage identification system involving a surface-attached piezoelectric transducer was developed in this study in correlation with an elastic wave propagation model. A signal processing and identification algorithm in the time–frequency domain based on the wavelet transform technique was proposed to suppress the diverse broadband interferences and effectively extract useful diagnostic information from the acquired raw impact responses, facilitating a prompt yet accurate structural health assessment. The developed system was then validated by applying it to a defective metal beam bearing a transverse crack with an increasing depth that simulates the crack growth. It is shown that the monitoring for the variable damage severity in the one-dimensional structure can be fulfilled quantitatively and exactly using this technique.

Keywords structural health monitoring (SHM) · wave propagation · impact response · signal processing · wavelet transform

Introduction

Great interest in the structural health monitoring with possibly less intrusion is increasing throughout the aerospace, mechanical and civil engineering communities. In the past decade, more demanding requirements for the identification accuracy and applicability as well as the operating/maintenance cost have considerably motivated the development of effective and economical structural health monitoring (SHM) techniques and damage diagnosis systems, leading to significant achievements in this area [1–19]. In particular, the detection approaches based on the elastic wave propagation have been attracting more and more attentions from both researchers and engineers, regarded as one of the most promising solutions to the quantitative assessment of the structural deterioration and the prevention for catastrophic failure.

On the other hand, signal processing is a key point to make an identification scheme applicable

*Author to whom correspondence should be addressed.
E-mail: ye@aeromech.usyd.edu.au

Vol 2(1): 0027–40
[1475-9217 (200303) 2:1;27–40; 10.1177/145792103029779]

and understandable. As known, neither traditional time-series nor frequency-spectrum analysis is capable of exhibiting the essence of signal at the full length, so that much useful diagnostic information may be lost. However, such an issue can be ameliorated with the aid of wavelet transform-based analysis in the time–frequency space, through which the time-dependent signal can be decomposed into the time and frequency domains simultaneously, and thus the characteristic details hidden in signal, such as trends, breakdown points or discontinuities, can be fully revealed. While probably Daubechies [1] and Newland [2] first systematically introduced the wavelet transform technique into the vibrational signal analyses in the early 1990s, it is in the past couple of years that the wavelet transform-based analyses have been widely applied into the structural damage detection. Actually, in its brief history, the wavelet transform technique has been proven to be a powerful analytical tool for signal processing, emerging as a substantial auxiliary implement for the system identification. Combined with the investigation on signals in the time–frequency space via the wavelet transform, elastic wave propagation-based detection approaches make the quantitative evaluation for structural health status more efficient and reliable. Kim et al. [3] reported their model and a signal-processing method for the identification of a fixed damage in a one-dimensional structure; Samuel et al. [4] accomplished a damage detection for a rotorcraft geartrain system; meanwhile Sung et al. [5] developed an impact monitoring technique for a composite structure using wavelet transform technique; and Kim et al. [6] thoroughly investigated the effectiveness of wavelet transform in the analysis for dispersive elastic waves; while other different analytical models and identification approaches have also been widely reported [7–19].

Damage growth, such as the extension of a crack in the metal alloy, is a common phenomenon for engineering structures in practice, which may result in the lethal malfunction of the whole system. It is therefore of vital importance to monitor the damage growth and consequently apply with appropriate remediation to minimise the risk of further structural destruction. The objective of the present research focuses on the development of a continuous monitoring scheme for the damage growth in one-dimensional structure. For this purpose, a damage diagnosis system incorporated with a piezoelectric transducer, in correlation with an elastic wave propagation model, was developed. The validity of this system was then investigated by applying it to a metal beam bearing a transverse crack with an increasing depth, simulating the damage growth. It is shown that the damage parameters, including the damage presence, location and its variable severity, can be identified promptly and accurately using this technique.

Model for Damage Identification

Consider a uniform Euler–Bernoulli beam owning a transverse crack-shaped damage perpendicular to the beam axis with an increscent depth, H_d, as depicted in Figure 1. With the assumption of the beam axis being the x-axis and neglecting the twisting effect, the motion equation for the Euler–Bernoulli beam can be expressed in terms of the lateral displacement $w(x,t)$ and the rotation angle $\theta(x,t)$ [20] upon the introduction of shear correction parameter κ,

$$\kappa^2 c_s^2\left[\frac{\partial^2 w}{\partial x^2}-\frac{\partial \theta}{\partial x}\right]-\frac{\partial^2 w}{\partial t^2}=0 \tag{1a}$$

$$c_0^2\frac{\partial^2 \theta}{\partial x^2}+\kappa^2\frac{c_s^2}{q^2}\left[\frac{\partial w}{\partial x}-\theta\right]-\frac{\partial^2 \theta}{\partial t^2}=0 \tag{1b}$$

$$c_0=\sqrt{E/\rho},\quad c_s=\sqrt{G/\rho},\quad q=\sqrt{I/A},\quad \left[\kappa=\pi/\sqrt{12}\right] \tag{1c}$$

where, E, I, A and ρ denote the elastic modulus, second moment of area, cross-section area and mass density of the beam, respectively.

Upon the consideration of the dispersion relations,

$$w=w_0\cdot e^{-i(kx-\varpi t)},\quad \theta=\theta_0\cdot e^{-i(kx-\varpi t)} \tag{2}$$

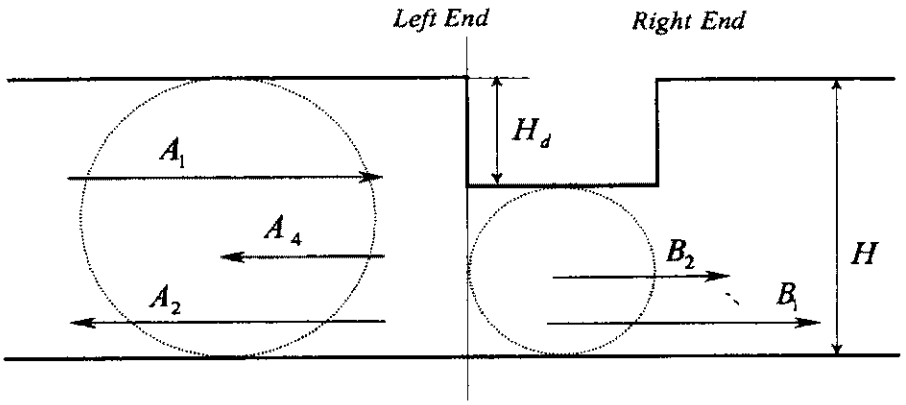

Figure 1 Damage model for diagnosis based on wave propagation.

the eigen roots (wavenumber) for Equation (1) can be yielded as,

$$k_n = \pm\left[\frac{1}{2}\left(1+\frac{c_0^2}{\kappa^2 c_s^2}\right) \pm \sqrt{\left(\frac{c_0}{q\varpi}\right)^2 + \frac{1}{4}\left(1-\frac{c_0^2}{\kappa^2 c_s^2}\right)^2}\right]^{1/2} \times \frac{\varpi}{c_0}, \quad (n=1,2,3,4) \tag{3}$$

Mathematically, the existence of four eigen roots determines that four propagating wave components are possibly available synchronously in the Euler–Bernoulli beam. The general solution to Equation (1) can be further expressed with a summation of four terms as below,

$$w(x,t) = \left[\sum A_1 e^{-ikx} + \sum A_2 e^{ikx} + \sum A_3 e^{-kx} + \sum A_4 e^{kx}\right] \cdot e^{i\varpi \cdot t} \tag{4}$$

where each term is respectively corresponding to one of the wave modes, which is hereafter recognised as the positively propagating wave, the negatively propagating wave, the positively growing evanescent wave or the negatively exponentially decaying wave, respectively, depending on their propagating direction and properties.

In Equation (4), the coefficient of exponential represents the amplitude of each wave component, which may be a complex. With the occurrence of a damage, Equation (4) yields two propagating equations before and after the left damage end (referring to Figure 1), respectively, denoted with w_- and w_+,

$$w_-(x,t) = \left[\sum A_1 e^{-ik_1 x} + \sum A_2 e^{ik_1 x} + \sum A_4 e^{k_1 x}\right] \cdot e^{i\varpi \cdot t} \tag{5a}$$

$$w_+(x,t) = \left[\sum B_1 e^{-ik_2 x} + \sum B_2 e^{-k_2 x}\right] \cdot e^{i\varpi \cdot t} \tag{5b}$$

where, the three terms in Equation (5a) correspond to the incident wave, reflected propagating wave and reflected exponentially decaying wave, respectively, which are induced by the interaction between the incident wave and the damage; while the two terms in Equation (5b) are recognised as the damage-induced positively propagating wave and growing attenuating wave, respectively. Note that the wave components A_4 and B_2 disappear very quickly due to exponentially decaying.

Applied with the continuity and compatibility conditions [3],

$$w_-(x,t) = w_+(x,t), \quad \frac{\partial w_-(x,t)}{\partial x} = \frac{\partial w_+(x,t)}{\partial x}$$

$$\begin{bmatrix} EI_1 \dfrac{\partial w_-^2(x,t)}{\partial^2 x} = EI_2 \dfrac{\partial w_+^2(x,t)}{\partial^2 x} \\ EI_1 \dfrac{\partial w_-^3(x,t)}{\partial^3 x} = EI_2 \dfrac{\partial w_+^3(x,t)}{\partial^3 x} \end{bmatrix} \tag{6}$$

the reflection ratio at the damage surface can be obtained as,

$$R=\frac{A_2}{A_1}$$
$$=\frac{-iI_1^2k_1^4+2I_1I_2k_1^3k_2+2iI_1I_2k_1^2k_2^2-2I_1I_2k_1k_2^3-iI_2^2k_2^4}{I_1^2k_1^4+2I_1I_2k_1^3k_2+2I_1I_2k_1^2k_2^2+2I_1I_2k_1k_2^3+I_2^2k_2^4} \quad (7a)$$

$$I_1=\frac{l\cdot H^3}{12}, \qquad I_2=\frac{l\cdot(H-H_d)^3}{12} \quad (7b)$$

where l and H denote the width and depth of the cross-section of the beam, respectively; while H_d represents the depth of the damage. Equation (7) implies that the depth of damage, H_d, can be therefore determined with a given reflection ratio. The relationship between the reflection ratio and the damage degree (H_d/H) for the present system was theoretically calibrated and shown in Figure 2.

Diagnosis Scheme

Daubechies function, $\Psi(a,b)$, at level 4 (db4) was chosen as the wavelet transform function, which was demonstrated most effective in this study to cater for the resolution requirement on the present problem compared with other

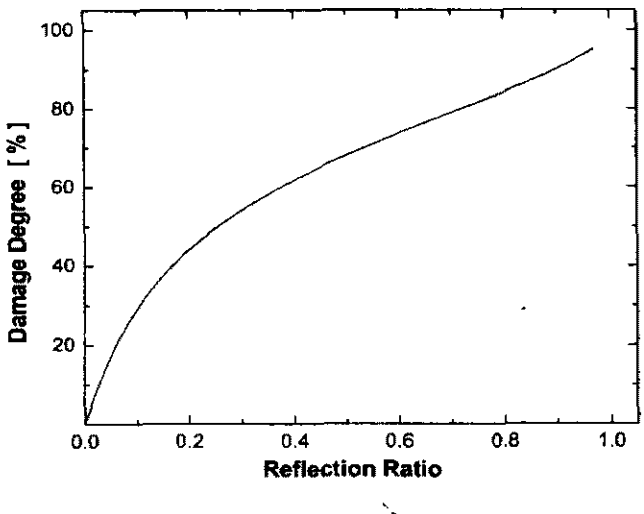

Figure 2 Theoretical relationship between reflection ratio and damage degree.

transform functions. $\Psi(a,b)$ was then applied with the Continuous Wavelet Transform (CWT) [21,22],

$$W(a,b)=\frac{1}{\sqrt{a}}\int_{-\infty}^{+\infty}f(t)\cdot\Psi^*\left(\frac{t-b}{a}\right)dt \quad (8)$$

where $W(a,b)$ denotes the continuous wavelet coefficient, which reflects the energy distribution of the signal over the time-scale domain. a and b are the scale and translation parameter, respectively. While $f(t)$ represents an arbitrary sampled signal; and $\Psi^*(t)$ denotes the complex conjugate of $\Psi(t)$. Contrarily, if the transform is invertible, the inverse wavelet transform exists,

$$f(t)=\frac{1}{C_\Psi}\int_{-\infty}^{+\infty}\int_{a>0}^{+\infty}W(a,b)\cdot\frac{1}{\sqrt{a}}\cdot\Psi\left(\frac{t-b}{a}\right)\cdot\frac{1}{a^2}da\cdot db \quad (9)$$

where $C\Psi$ is a constant that depends on $\Psi(t)$.

Practically, the CWT analysis can be simplified by calculating the wavelet coefficients only at discretised scale, namely, the Discretised Wavelet Transform (DWT) [21,22]. The sampled signal can be therefore decomposed into a series of Approximations and Details via DWT analysis, characterising the time-dependent signal in independently assorted frequency ranges.

The time–scale or time–frequency domain analysis offers a capability to quantitate the local perturbation or singularity in signal. In this study, the damage parameters (i.e., the location and severity), regarded as singularity involved in the signal, were determined using the CWT and DWT spectrographic analyses. In more detail, the damage location diagnosis was performed by calculating the time difference between the incident wave component and damage-induced wave component along the time axis within the discreted frequency scope pertaining to the impact excitation via the DWT analysis, or the time difference between incident wave energy concentration and damage induced-wave energy concentration in spectra through the CWT analysis. While the damage severity was calibrated upon the relation with the reflection ratio (see Figure 2), in which the reflection ratio was theoretically

proven to be equivalent to the root-mean-square (RMS) ratio of their related continuous wavelet coefficients along the scale axis at the time points corresponding to the maximum energy concentration over the time-scale domain [3] (see Appendix), while the RMS ratio could be achieved by experimental approach.

Configuration of Diagnosis System

The damage diagnosis system based on a VXI platform, described schematically in Figure 3, consists of the Signal Generation Unit (SGU), Signal Acquisition Unit (SAU) and Central Control Unit (CCU). With a low acoustic impedance and a broadband response range, a piezoelectric lead zirconate titanate (PZT) element (PI® 151), with the properties summarised in Table 1, was chosen as the signal sensor and surface-mounted on the beam with silver–epoxy adhesive (Farnell®). Signal acquisition was performed via the Agilent® E1437A digitizer at a sampling rate of 20.48 MHz after conditioned by the Agilent® E3242A conditioner. Being the kernel of the system, CCU performed as both the controller and the interpreter, supported by an inhouse software developed on the NI Labview® platform.

In order to evaluate the effectiveness of the proposed model and identification scheme, the diagnosis system was then applied to a defective aluminum alloy beam (cross-section of 10 mm × 10 mm, Young's modulus of 72.4 GPa and density of 2.69 g/cm^3) with dual-end fixed-supported, sketched in Figure 4. A transverse crack, extending across the entire width of the beam with a 0.15 mm span along the beam axis, was previously made using a diamond saw. The damage depth, H_d, varies from 1 mm to 8 mm with a step of 1 mm. In most previous studies, relatively complicated excitation sources, such as PZT actuators, were chosen for the generation of a diagnostic

Table 1 Geometry and mechanical properties of PZT sensor.

Product Name	*PI 151*
Geometry	20 mm × 10 mm × 1 mm
Density	7.80 g/cm^3
Charge constant d_{31}	-170×10^{-12} m/V
Charge constant d_{33}	450×10^{-12} m/V
Elastic constant E_{11}	66.67 GPa
Elastic constant E_{33}	86.21 GPa

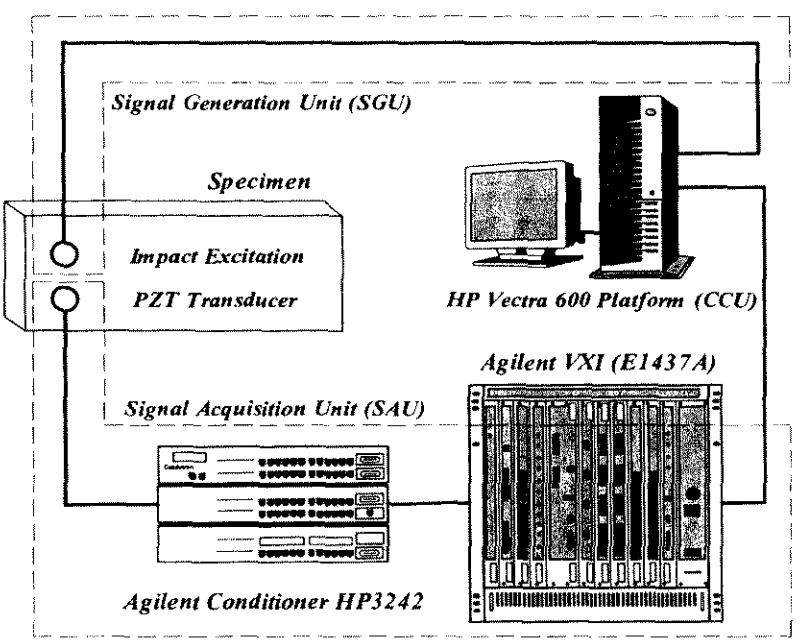

Figure 3 Configuration of identification system based on VXI platform.

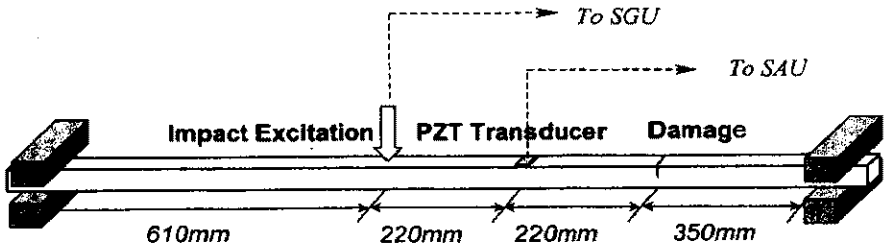

Figure 4 Configuration of experiment setup for a structural beam with damage.

signal. In the present study, a simple yet practical pendulum force hammer, controlled by the SGU to generate constant impact energy of 0.4 J, was used for the excitation of incident signal. It is of essence to keep a sufficient distance between the excitation spot and structural boundaries to ensure the reflected wave modes from the boundaries would not interfere the damage-induced wave component.

Table 2 Measured wave velocities in an aluminum alloy structural beam.

Wave Mode	*Measured* (m/s)	*Calculated** (m/s)
Longitudinal wave	6365	6314
Transverse wave	3205	3180

* $C_{Longitudinal} = \sqrt{E/\rho} \cdot \sqrt{(1-\mu)/(1+\mu)\cdot(1-2\mu)}$; $C_{Transverse} = \sqrt{E/\rho} \cdot \sqrt{1/2(1+\mu)}$; E: Elastic modulus, 72.4 GPa; ρ: Mass density, 2.69 g/cm^3; μ: Poisson's ratio, 0.33.

Signal Analysis

Inevitably, broadband responses will be induced by the impact excitation due to the wave dispersion, making the signal distinguish intractable. Meanwhile, muddled with the diverse noises and structural vibration patterns, the diagnostic information is usually ruined in the raw response signal. An improved signal processing and damage identification algorithm by virtue of CWT and DWT analysis based on the Matlab© mathematic platform [23] was hereby proposed to meliorate the identification.

In experiment, different wave components can simultaneously be observed. The propagating velocity for each possible wave is therefore required for the signal distinguish. The velocities measured experimentally and calculated theoretically are compared in Table 2. The response signals for different damage severities were sampled. As typical examples, the acquired structural response signals in the time domain for 4 mm and 6 mm-depth cracks, and their corresponding frequency spectra by the Fast Fourier Transform (FFT) analysis are shown in Figures 5 and 6, respectively. Interfered by the low-frequency structural vibration and various noises, only tiny differences can be noticed between the signals in the time or frequency domain, both of which can hardly be used directly for the accurate diagnosis. Spectrographic analyses based on the CWT and DWT techniques [24] were accordingly executed. A series of band filters with proposed threshold and different frequency scopes were designed and applied on the sampled signals to suppress the diverse interferences and effectively extract diagnostic components. Meanwhile, the Ansys© FEM software was employed to calculate the vibrational patterns of the structural beam, so that the components in the frequency scopes corresponding to the structural natural modals could be filtered. Thus the interrogation on the sampled signals can be concentrated in a specific frequency scope. On the other hand, in this study, the Sampling Point (SP) was hereafter introduced instead of the direct Time Point (TP) in CCU to expedite and facilitate the data processing procedure.

The DWT analytical results of the sampling signal for the 4 mm-depth crack, as a paradigm, from level 1 to level 10, and the distribution of its DWT coefficient are displayed in Figure 7, in which the DWT level refers to the different frequency ranges. The wave energy distribution is portrayed by the grayscale, and the darker the grayscale appears, the stronger the wave energy

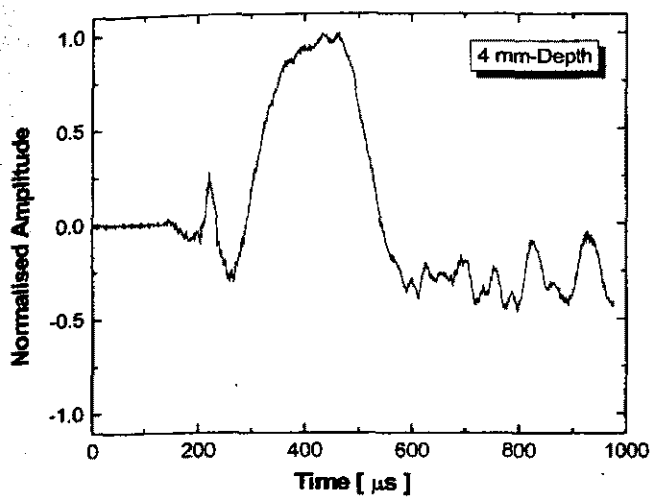

(a)

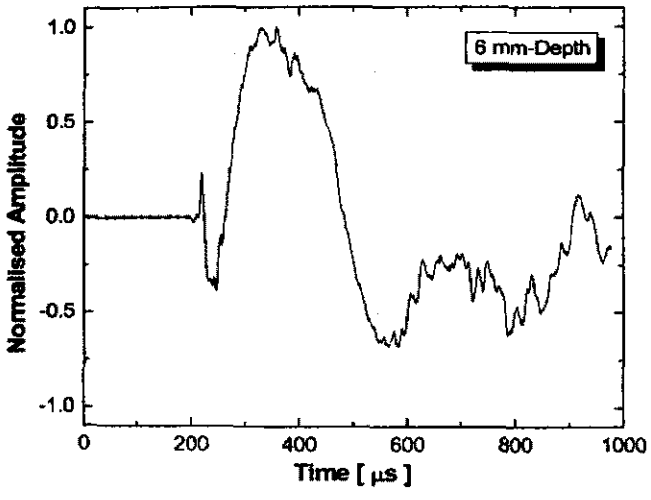

(b)

Figure 5 Sampled raw response signals in the time domain: (a) 4 mm-depth crack; (b) 6 mm-depth crack.

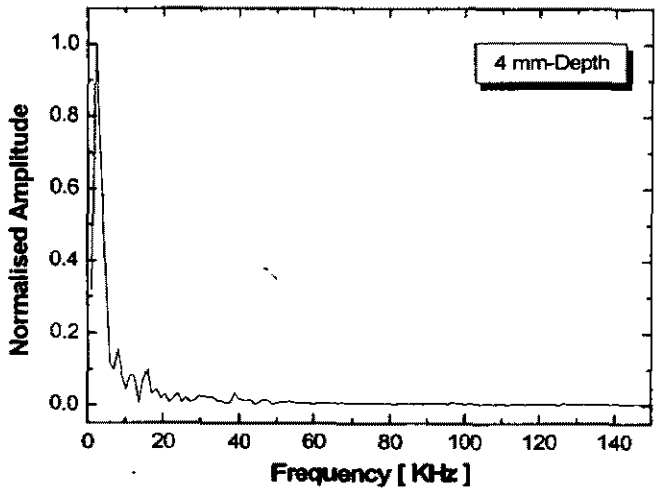

(a)

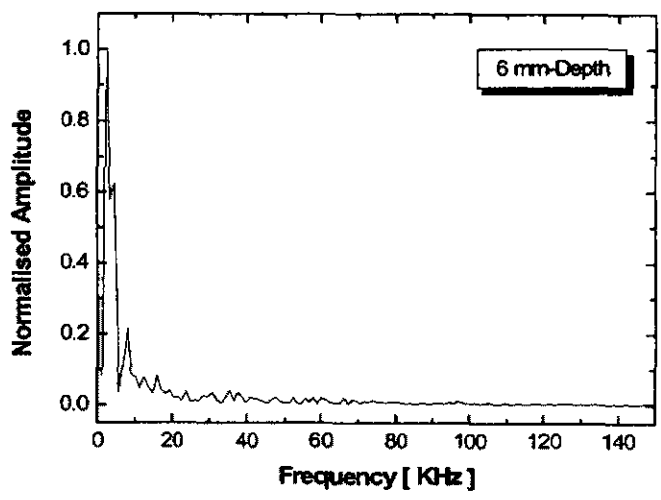

(b)

Figure 6 FFT analysis for signals in Figure 5: (a) 4 mm-depth crack; (b) 6 mm-depth crack.

is. The obvious energy concentration can be clearly noticed from level 5, while at level 8 the spectrogram well exhibits the response arisen from the impact excitation.

Particularly, the DWT analytical results at level 8 for 4 mm and 6 mm-depth cracks are displayed in Figure 8 for comparison. The first wave peak originates from the incident wave (transverse wave in this case), followed by the first reflected wave due to the crack as well as other reflected components from left/right boundaries or multi-reflected wave components from the damage. For the signal identification purpose, only the first several wave components in the sampling signal are useful while the others are not the concern. The time lags among the related wave components (peaks and wavefronts) were calculated to locate the crack.

Meanwhile, the 2D and 3D spectrographic analyses via CWT were performed. As instances, the 2D spectra for the paradigmatic sampling signals, shown in Figure 5, are displayed in Figure 9, where the grayscale reflects the density of wave energy over the time-scale domain, with the darker one indicating the higher energy. The damage-induced energy can be observed between

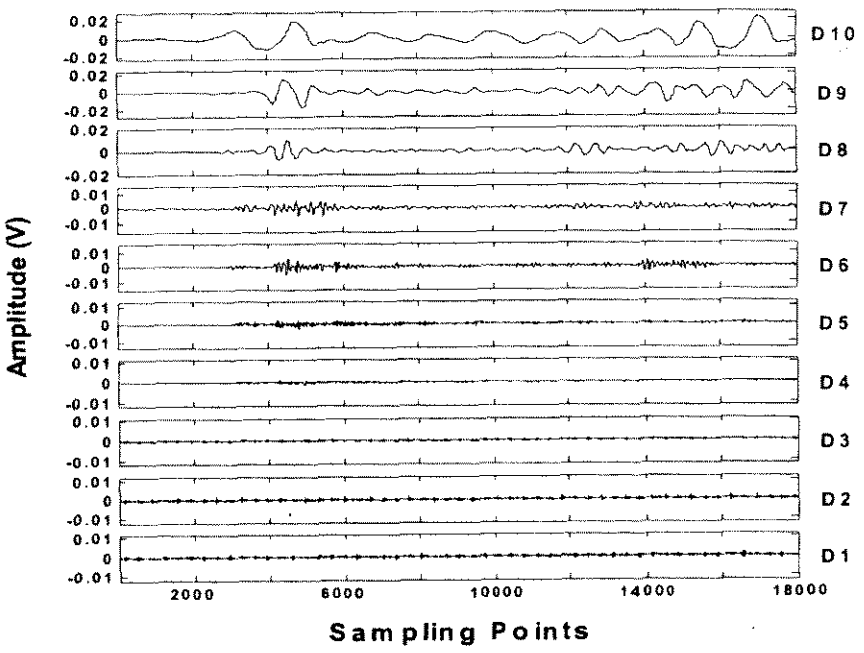

(a)

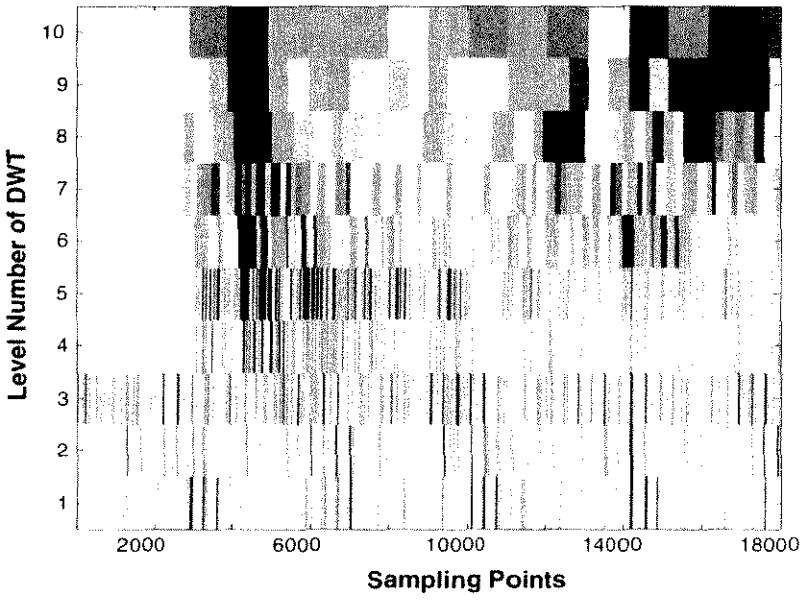

(b)

Figure 7 DWT analytical results of the sampled signal for 4 mm-depth crack: (a) details from level 1 to level 10; (b) distribution of DWT coefficients.

the incident energy and the first reflected energy from the boundary. More intuitively, the corresponding 3D spectrographic images for different damage severities and their partial magnification are displayed in Figure 10. In the 3D spectra, the intuitionistic ridges, relative to the CWT coefficients, also indicate the energy distribution. Similarly, the energy concentration induced by the damage can be visually observed in 3D spectra. From Figures 8–10, stronger energy

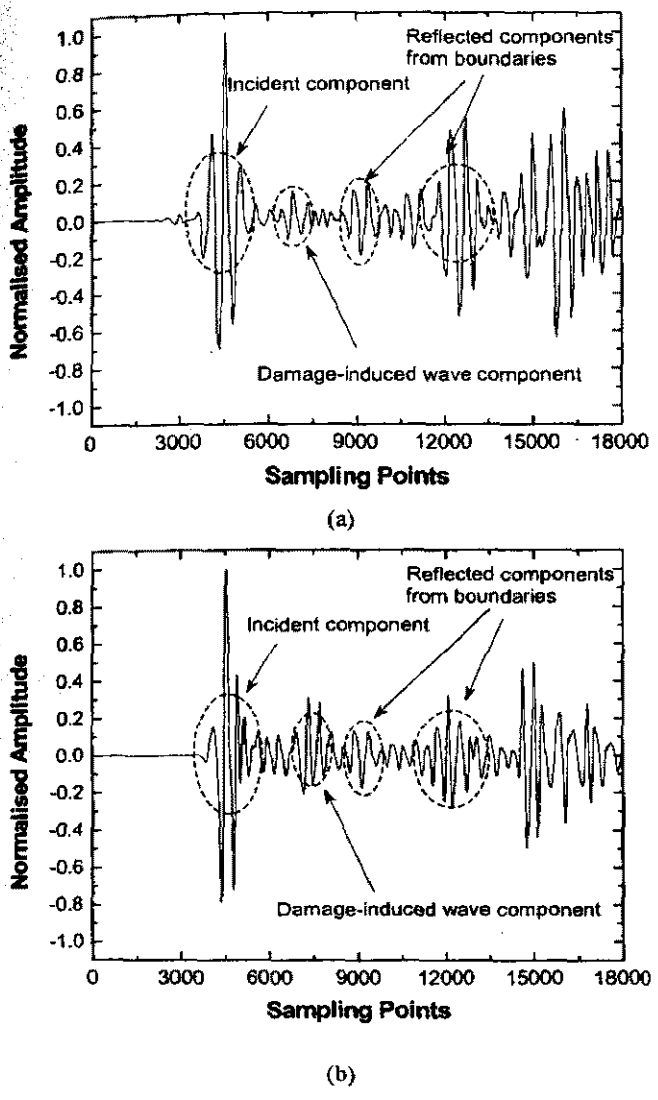

Figure 8 Detail at level 8 by DWT analysis for signals in Figure 5: (a) 4 mm-depth crack; (b) 6 mm-depth crack.

reflection from the crack can be noticed as the crack size increases because of the expansion of the valid reflection area. The resolution for sampling signal and identification accuracy for both the damage location and the severity are consequently improved. The full-scale CWT analyses are more wieldy of detecting local perturbations in signal.

Damage Diagnosis and Discussion

For diagnosis purpose, the energy ridges in the time-scale space at the time point, pertaining to the maximum energy concentration, are anatomised and investigated along the scale axis. The consequently anatomised profiles for the incident energy and induced-energy from 4 mm to 6 mm-depth crack are contrastively shown in Figure 11 as paradigms. In profile curves, a crestiform distribution of the wavelet coefficients along the scale axis within the assorted scale range can be observed. Two approaches were employed to calculate the magnitude of the distribution of wavelet coefficient in the profile curves, viz., RMS method [3] and integration method, so that the reflection ratio can be determined. Attention should be paid that the area encompassed by the profile curve and scale axis increases with the crack length from 1 mm to 8 mm. By virtue of the RMS value ratio of the wavelet coefficients for the incident energy to the damage-induced energy in the profile curves, the reflection ratio was calculated (Equation (A10)), leading to the determination of the damage severity (Figure 2). The damage diagnostic results achieved via the proposed identification scheme and the actual damage parameters are compared in Table 3.

Capability of the diagnoses for damage location and severity using the developed system was evaluated. The percentage diagnostic errors are listed in Table 3 and illustrated in Figure 12. The results imply that the identification accuracy for crack location, in spite of the actual damage severity, is acceptable with a high creditability. The precision of damage severity identification increases with the crack size and a satisfactory precision for the damage severity estimation is maintained until the crack size approaches 6 mm approximately when the transverse damage area occupies around 60–70% of the entire cross-section of the beam. Considerable errors occur when the crack size exceeds 70% of the height of the beam. This is attributed to the inapplicability of the basic hypotheses used in the Euler–Bernoulli beam theory, on which the model was developed. Under such a circumstance, the twisting effect cannot be neglected, leading to the inapplicability of the continuity and compatibility conditions.

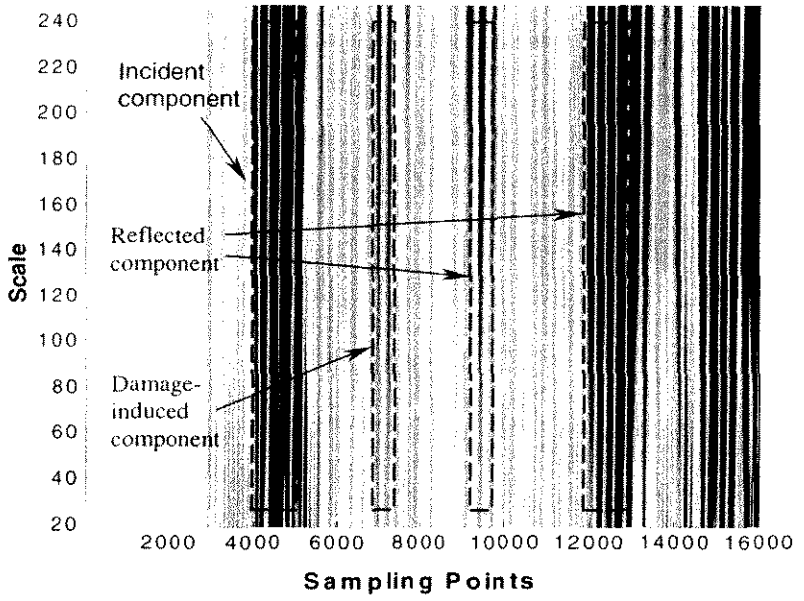

(a)

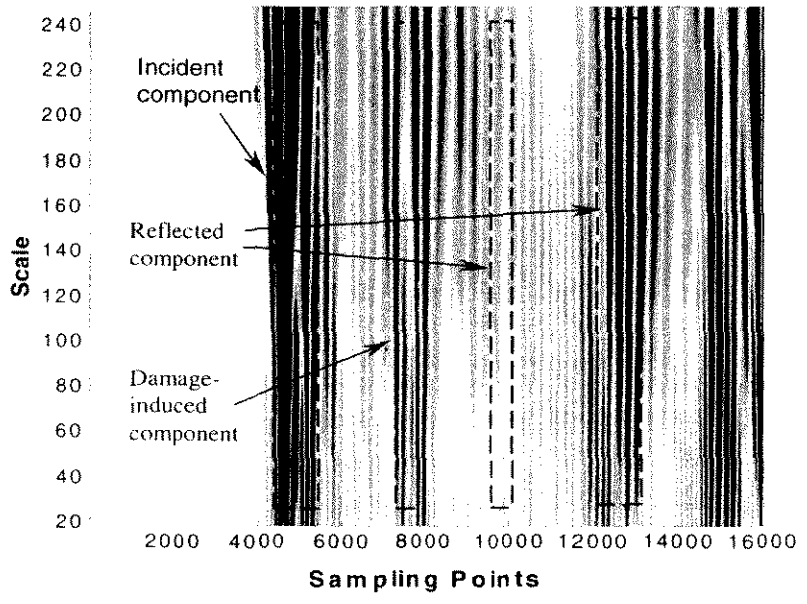

(b)

Figure 9 2D spectrographic analysis by CWT for signals in Figure 5: (a) 4 mm-depth crack; (b) 6 mm-depth crack.

Conclusion

An identification and monitoring scheme for structural damage in correlation with the impact response analysis has been developed, and its validity was examined experimentally through a quantitative diagnosis for the location and size of damage with an increasing depth in a one-dimensional structural beam. A simple and practical impact excitation source was used for the generation of diagnostic stress wave. The accompanying broadband interference of impact excitation was suppressed using an improved signal processing technique based on the wavelet

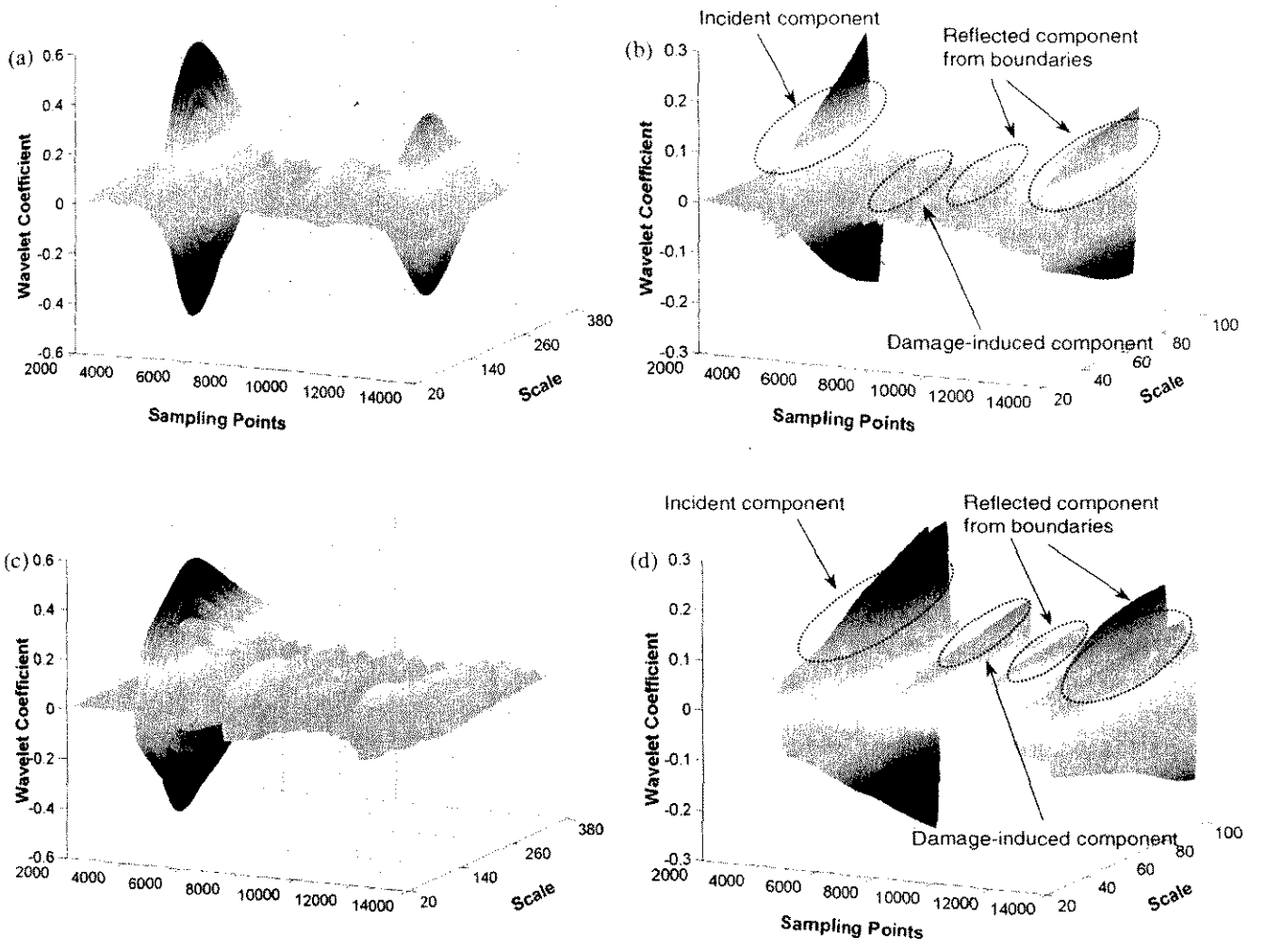

Figure 10 3D spectrographic analysis by CWT for signals in Figure 5: (a) 4 mm-depth crack; (b) partial magnification of (a); (c) 6 mm-depth crack; (d) partial magnification of (c).

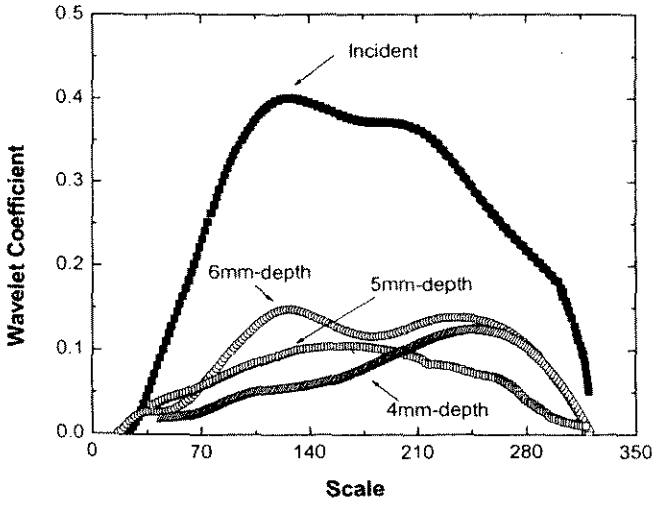

Figure 11 Profile curve of CWT coefficients for signals.

transform technique as well as a high-resolution data acquisition system, with which satisfactory diagnosis results have been achieved. The sensitivity of the identification algorithm was then evaluated. The experimental results indicate that the identification accuracy depends on the actual severity of the damage. Unacceptable error occurs only when the damage is very severe (the damage size is over 65% of the cross-sectional area of the beam). In practice, such a kind of large destruction is normally not the concern of the structural health monitoring.

Health monitoring techniques and identification systems for more complicated structures, such as laminated fibre composite plates, will be presented in forthcoming reports.

Table 3 Diagnosis results and relative percentage errors for a crack with variable depths in a beam.

Actual Damage Degree	*Location Diagnosis* (mm)		*Degree Diagnosis* (mm)			
	Calculated Value (To the Right End)*	*Minimum Error* (%)	*Calculated Value by RMS Method*	*Minimum Error* (%)	*Calculated Value by Integration Method*	*Minimum Error* (%)
1 mm	373	6.57	1.073	7.25	1.073	7.31
2 mm	336	4.00	2.100	4.90	2.104	5.19
3 mm	341	2.79	3.150	4.69	2.853	4.89
4 mm	359	2.65	3.832	4.17	4.161	4.02
5 mm	340	2.26	5.115	2.30	4.862	2.76
6 mm	357	2.05	6.123	2.05	6.141	2.35
7 mm	355	1.13	6.404	8.52	7.642	9.17
8 mm	346	1.02	6.200	22.5	6.152	23.1

*The actual damage position is 350 mm away from the right end of the beam.

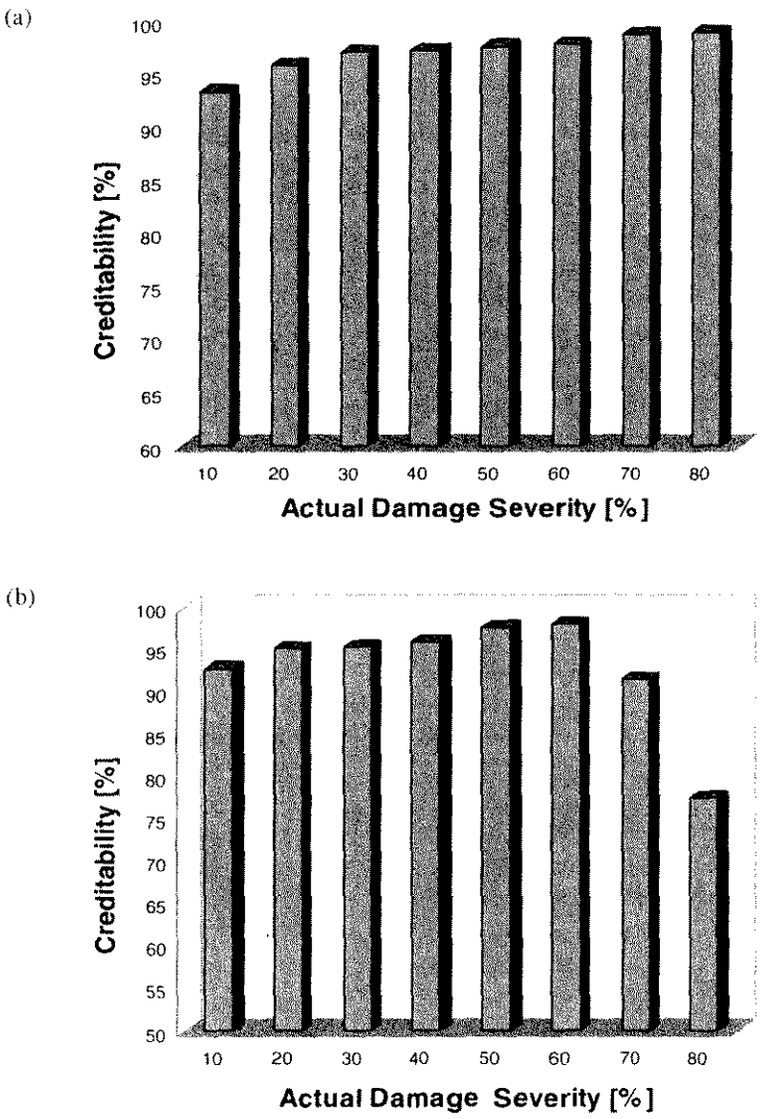

Figure 12 Credibility for proposed identification scheme: (a) for damage location diagnosis; (b) for damage degree diagnosis.

Acknowledgement

Z. SU would like to gratefully acknowledge the support of the International Postgraduate Research Scholarship (IPRS) from the Department of Education Science and Training (DEST), Australia, and the International Postgraduate Award (IPA) from the University of Sydney. While X. BU appreciates the support from the China Scholarship Council.

Appendix

Considering a 3D spectrum over the time-scale domain obtained via the CWT analysis, the magnitude of a wave energy ridge in this spectrum, denoted hereafter by A_{ridge}, along the scale axis at an arbitrary time point, can be calculated by RMS method [25],

$$A_{\text{ridge}} = \sqrt{\frac{W_1^2 + W_2^2 + \cdots + W_N^2}{N}} \tag{A1}$$

where $W_i (i = 1, N)$ is the ith wavelet coefficient on the profile curve along the scale axis, whilst N denotes the total number of discretised points, which is determined by the precision of the selected wavelet transform.

Similarly, as for two energy ridges in one spectrum, A_{ridge1} and A_{ridge2}, at different time points t_1 and t_2 respectively, their amplitude ratio can be defined as following if the same wavelet transform function and transforming precision are chosen,

$$\left(\frac{A_{\text{ridge1}}}{A_{\text{ridge2}}}\right) = \sqrt{\frac{W_1^2 + W_2^2 + \cdots + W_N^2|_{t=t_1}}{W_1^2 + W_2^2 + \cdots + W_N^2|_{t=t_2}}} \tag{A2}$$

When N is large enough, Equation (A2) is equivalent to,

$$\left(\frac{A_{\text{ridge1}}|_{t_1}}{A_{\text{ridge2}}|_{t_2}}\right)^2 = \frac{\int_{S_{\min}}^{S_{\max}} W^2|_{t=t_1} \cdot da}{\int_{S_{\min}}^{S_{\max}} W^2|_{t=t_2} \cdot da} \tag{A3}$$

where a represents the variable on the scale axis.

Meantime, derived from the definition of wavelet transform [21],

$$W(a,b) = \frac{1}{\sqrt{a}} \int_{-\infty}^{+\infty} f(t) \cdot \Psi^*\left(\frac{t-b}{a}\right) \cdot dt \tag{A4}$$

where $f(t)$ represents any time-dependent signal, its inverse wavelet transform exists,

$$f(t) = \frac{1}{C_\Psi} \int_{-\infty}^{+\infty} \int_{a>0}^{+\infty} W(a,b) \cdot \frac{1}{\sqrt{a}} \times \Psi\left(\frac{t-b}{a}\right) \cdot \frac{1}{a^2} da \cdot db \tag{A5}$$

where a is the scale parameter while b is the translation parameter, both of which are real number and a must be positive. C_Ψ is a constant and $\Psi^*(t)$ denotes the complex conjugate of $\Psi(t)$. Derived on Equations (A4) and (A5), the following proportional relation exists [21],

$$E \propto \int_{\text{Min}}^{\text{Max}} |W(a,b)_{b=t}|^2 da \tag{A6}$$

For two given energy components, E_1 and E_2, over time-scale domain, at different time points, t_1 and t_2, respectively, it exists,

$$\frac{E_1}{E_2} = \frac{\int_{\text{Min}}^{\text{Max}} |W(a,b)_{b=t_1}|^2 da}{\int_{\text{Min}}^{\text{Max}} |W(a,b)_{b=t_2}|^2 da} \tag{A7}$$

On the other hand, in the time domain, the energy ratio for two sampled signals is known to be equal to [21],

$$\frac{E_{t=t_1}}{E_{t=t_2}} = \frac{|f_1(t)|^2_{t_1}}{|f_2(t)|^2_{t_2}} \tag{A8}$$

Combining Equations (A7) and (A8), the energy ratio for two wave components, at specific time points, t_1 and t_2 respectively, can be

yielded as,

$$\frac{E_{t=t_1}}{E_{t=t_2}} = \frac{\int_{\text{Min}}^{\text{Max}} |W(a,b)_{b=t_1}|^2 da}{\int_{\text{Min}}^{\text{Max}} |W(a,b)_{b=t_2}|^2 da} = \frac{|f_1(t)|^2_{t_1}}{|f_2(t)|^2_{t_2}} \quad \text{(A9)}$$

Therefore, via Equations (A3) and (A9), the reflection ratio can be given:

$$\frac{|f(t_1)|}{|f(t_2)|} = \left| \left(\frac{A_{\text{ridge1}}|_{t_1}}{A_{\text{ridge2}}|_{t_2}} \right) \right| \quad \text{(A10)}$$

References

1. Daubechies, I. (1990). The wavelet transform, time-frequency localization and signal analysis. *Journal of IEEE Transactions on Information Theory, 36(5)*, 961–995.
2. Newland, D.E. (1994). Wavelet analysis of vibration, Part I: Theory. *Journal of Sound and Vibration, 116*, 409–416.
3. Kim, Y.Y. and Kim, E.H. (2000). A new damage detection method based on a wavelet transform. *Proceedings of 18th IMAC*. San Antonio, Texas, USA. pp. 1207–1212. 7–10 February.
4. Samuel, P. and Pines, D. (1997). Health monitoring/ damage detection of a rotorcraft planetary geartrain system using piezoelectric sensors. *SPIE, 3041*: 44–53.
5. Sung, D.U., Oh, J.H. and Kim, C.G. (2000). Impact monitoring techniques for smart composite laminates. *Proceedings of the Second Asian-Australasian Conference on Composite Materials*. Korea. pp. 1123–1128. 18–20 August.
6. Kim, Y.Y. and Kim, E.H. (2001). Effectiveness of the continuous wavelet transform in the analysis of some dispersive elastic waves. *J. Acoust. Soc. Am., 110(1)*, 1–9.
7. Chakraborty, G. and Mallik, A.K. (2000). Wave propagation and vibration of a traveling beam with and without non-linear effects, Part I: free vibration. *Journal of Sound and Vibration, 236*, 277–290.
8. Kawiecki, G. (1998). Feasibility of applying distributed piezo transducers to structural damage detection. *Journal of Intelligent Material Systems and Structures, 9(3)*, 189–197.
9. Zhou, Z., Noori, M. and Amand, R.S. (2000). Wavelet-based approach for structural damage detection. *Journal of Engineering Mechanics, 7*, 667–683.
10. Zou, Y., Tong, L. and Steven, G.P. (2000). Vibration-based model-dependent damage (delamination) identification and health monitoring for composite structures a review. *Journal of Sound and Vibration, 230*, 257–278.
11. Achenbach, J.D. (2000). Quantitative nondestructive evaluation. *International Journal of Solids and Structures, 37*, 13–27.
12. Wang, M.L., Heo, G. and Satpathi, D. (1998). Health monitoring system for large structural systems. *Smart Materials and Structures, 7*, 606–661.
13. Lakshmanan, K.A. and Pines, D.J. (1997). Modeling damage in rotorcraft flexbeams using wave mechanics. *Smart Materials and Structures, 6*, 383–392.
14. Vera, C.P.D. and Guemes, J.A. (1998). Embedded self-sensing piezoelectric for damage detection. *Journal of Intelligent Material Systems and Structures, 9(11)*, 876–887.
15. Wolfinger, C., Arendts, F.J. and Friedrich, K. (1996). Health-monitoring based on piezoelectric transducers. *Aerospace Science and Technology, 6*, 391–400.
16. Salawu, O.S. (1997). Detection of structural damage through changes in frequency: a review. *Engineering Structure, 19(9)*, 718–723.
17. Laura, P.A.A., Malfa, S.L. and Bambill, D.V. (1998). Monitoring structural health through changes in frequency. *Journal of Sound and Vibration, 212(5)*, 909–911.
18. Tracy, M. and Chang, F.-K. (1998). Identifying impacts in composite plates with piezoelectric strain sensors, Part I: Theory. *Journal of Intelligent Material Systems and Structures, 9(11)*, 920–927.
19. Boller, C. (2001). Ways and options for aircraft structural health monitoring. *Smart Materials and Structures, 10*, 432–440.
20. Doyle, J.F. (1997). *Wave propagation in structures*. Springer-Verlag, New York. 2nd Edn.
21. Chan, Y.T. (1995). *Wavelet basic*. Kluwer Academic Publishers, Boston. 1st Edn.
22. Chui, C.K. (1997). *Wavelets: a mathematical tool for signal processing*. SIAM, Philadelphia, 1st Edn.
23. The Mathworks Inc. (2000). Wavelet Toolbox: for Use with Matlab (User's Guide). Ver: 1.0.
24. Boashash, B. (1992). *Time-frequency signal analysis, Methods and applications*. 1st Edn. Longman Cheshire Press, Melbourne.
25. OriginLab Co. (2000). User's Guide, Ver: 6.1052.

SHM
Structural Health Monitoring

Fundamental Lamb Mode-based Delamination Detection for CF/EP Composite Laminates Using Distributed Piezoelectrics

Zhongqing Su and Lin Ye*

Laboratory of Smart Materials and Structures (LSMS),
Centre for Advanced Materials Technology (CAMT),
School of Aerospace, Mechanical and Mechatronic Engineering,
The University of Sydney, NSW 2006, Australia

A delamination detection scheme for the CF/EP composite laminates based on the Lamb wave propagation was proposed. The fundamental symmetric Lamb mode (S_0) and the delamination-induced basic shear mode (S_0') in an ultrasonic frequency range were utilised for locating the delamination. Both numerical simulation and experimental studies were performed to evaluate the propagation characteristics of Lamb waves in the composite laminates involving a delamination. An active online damage diagnosis system was established with a transducer network configured using distributed piezoelectrics. Bandpass filters were designed and spectrographic analyses in the time-scale space via wavelet transform technique were accomplished, to diminish diverse broadband interferences and consequently improve signal interpretation. Algorithm based on a graphic approach was introduced into the damage searching procedure to expedite the diagnosis and minimise the estimation errors. The proposed identification scheme and diagnosis system were then validated by detecting delaminations in CF/EP laminates made from unidirectional and woven fabric prepreg, respectively. Satisfactory prediction for the damage location has been achieved. Additionally, the influence of diagnostic waveforms and frequencies on the identification accuracy was also evaluated.

Keywords fibre-reinforced composite · structural health monitoring (SHM) · Lamb wave · finite element method (FEM) · wavelet transform

1 Introduction

Delamination, induced by the interlaminar stresses, is probably the most common internal defect in carbon fibre (CF)/epoxy (EP)-laminated composites, and it can originate and develop during manufacturing or as a result of accidental out-of-plane impact during service. The occurrence of delamination may considerably lower the strength, stiffness or damping properties of the composites and severely reduce the structural integrity and reliability. It is therefore momentous for engineers and researchers to pursue effective and reliable detection techniques, with which the delamination might be detected at its initial stage.

Conventional nondestructive evaluation (NDE) for structural criticality, such as C-scan

*Author to whom correspondence should be addressed.
E-mail: ye@aeromech.usyd.edu.au

Vol 3(1): 0043–68
[1475-9217 (200403) 3:1;43–68 10.1177/1475921704041874]

and radiographic inspection, or model-based methods, ranging from modal analyses to static parameters identification, are facing the challenge of compromise between satisfactory estimation accuracy and versatile applicability in practice. Motivated by this, innovations in NDE field have become an increasing concern over years, leading to intensive researches on the novel and improved techniques. Amongst them, Lamb wave-based detection approaches have been increasingly attracting noticeable preferences, encouraged for damage assessment with high precision requirement [1–13]. Generated and monitored by transducers expediently and efficiently, Lamb wave is able to propagate over a relatively long distance even in materials with high attenuation ratio, such as CF/EP laminated composites, and thus a broad area can be investigated with only a few transducers. Meanwhile, the entire thickness of the laminate may be interrogated in virtue of different vibration patterns of various Lamb modes, which affords possibility to detect the internal damages as well as the defects on the surface. In the majority of existing literatures [1–10], the ultrasonic probes were widely used for the generation and monitoring of Lamb waves for their excellent accessibility and accuracy. However, the further applications of ultrasonic probes for online detection may be hindered due to the poor affinity with practical engineering structures and the non-neglectable size and weight. Additionally, in most cases, a period of temporary out-of-service for the structures to be inspected is required to ensure the probes are operational. It is obvious that these deficiencies have considerably limited their applications, such as the health surveillance for in-service aircrafts, where the structural components are expected to combine the designed functions together with self-assessment and self-rehabilitation capabilities. Under such a circumstance, the integration of *in situ* transducers into the structures is regarded as a promising measure to feature the smart function for the real-time damage monitoring. Wang et al. [11] reported a practical damage identification approach using distributed piezoelectric devices; Lemistre et al. [12] successfully detected the structural damage using Lamb wave generated by piezoelectrics; while Gaul et al. [13] determined the history of an external transient force applied on a structure by analysing the responses measured by piezoelectric materials. In these studies, the piezoelectrics exhibit low acoustic impedance and wide frequency responses yet with minor intrusion into the structures, serving as a practical and reliable integrated signal transmitter.

On the other hand, the study upon characteristics of Lamb wave propagation in the laminated composites and the damage evaluation using numerical simulation have been rigorously explored for a couple of years, and related achievements are in a good supply [2,4–7,14–16]. Most of the related work, however, is limited in either one-dimensional or two-dimensional situations, in which the internal damage, a complicated three-dimensional pattern, usually has to be simplified with certain scenarios, leading to approximate simulations.

The efforts in this study are aimed at developing a delamination identification scheme for CF/EP composite structures based on the Lamb wave propagation. A detection algorithm using the wavelet transform technique was developed. The propagation properties of fundamental Lamb modes interacted with interlaminar delamination were examined through numerical and experimental analyses. For this, a full-scale three-dimensional finite element model was developed and structural dynamic analyses were performed. An active diagnosis system incorporated with piezoelectrics network was consequently established in accordance with the identification scheme, and it was then validated to locate delaminations in CF/EP laminates made from unidirectional and woven fabric prepreg, respectively.

2 Lamb Waves in the Composites

2.1 Propagation Characteristics of Lamb Wave in Laminated Composites

Lamb wave, a guided wave propagating in the plate-like structures, is known to be dispersive during propagation in the viscoelastic medium, whose properties rely on not only the material properties and structural geometry, but also the

excitation conditions. In most cases, more than two modes are synchronously available; and the vibration patterns and dispersive properties throughout the plate thickness are not identical for different modes, even for the same mode but in different frequency ranges. Practically, the angle-variable ultrasonic probes are normally employed to produce the pure and single Lamb mode in accordance with the Snell's law [17], shunning multiple modes. Compared with the components generated by ultrasonic probes, the Lamb waves induced by the piezoelectric elements directly, such as a PZT disk, unavoidably contain multi-modes simultaneously, which can be basically classified as *symmetrical* and *anti-symmetrical* modes, depending on the particulate motion patterns.

Dispersion characteristics of Lamb waves in the multilayered medium are some of the pivotal concerns for development of guided wave-based damage detection techniques. Lamb waves are known for owning a strong ability to propagate over a relatively long distance while without significant attenuation in the energy and wave amplitudes, even in the materials with a high attenuation ratio, such as CF/EP-laminated composites [17]. However, the dispersion phenomena with the variation in wave frequency were clearly observed, dependent on the structural thickness. The dispersive properties for fundamental Lamb wave modes in an 8-layers $[45/-45/0/90]_s$ CF/EP quasi-isotropic composite laminate were experimentally evaluated. In experiments, wave phase velocities for symmetric and anti-symmetric Lamb modes, excited by a PZT actuator in a sweep frequency ranging from 0.1 to 1.5 MHz with a step of 50 Hz, were measured individually by PZT sensors. The dispersion curves for fundamental Lamb waves in terms of wave phase velocities and excitation frequencies are plotted in Figure 1. Meanwhile the dispersion curves theoretically calculated using the method proposed by Percival et al. [2] are also included in Figure 1 for comparison. Good correlation between them can be noticed. The fundamental anti-symmetric Lamb mode, A_0, symmetric Lamb mode, S_0, and the lowest order shearing mode, S_0', are observed in the low frequency region, while higher order modes appear gradually with increase in frequency. The dispersion properties shown in Figure 1 indicate the presence of multiple Lamb modes in the laminated composite, whose phase/group velocities

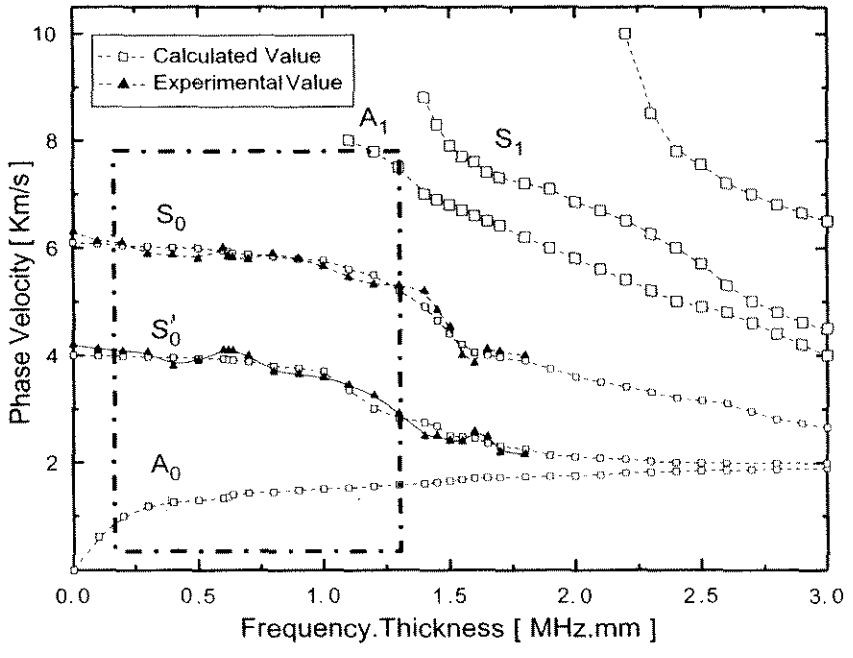

Figure 1 Dispersion properties for Lamb waves in an 8-ply quasi-isotropic CF/EP laminate.

are dependent on the algebraic product of the laminate thickness and the central excitation frequency. Whereas for the current structure, a low-frequency domain (< 1.2 MHz mm) exists, in which the fundamental modes exhibit reasonably non-dispersive behaviour. In the present work, the fundamental symmetric Lamb mode, S_0, and the defect-induced basic shear mode, S_0', were utilised for the damage detection.

2.2 Interaction between Lamb Modes and Internal Defect in the Composites

The interaction between fundamental Lamb modes and the interlaminar delamination in CF/EP $[45/-45/0/90]_s$ quasi-isotropic composite laminate was numerically investigated. A rectangular laminate ($480 \times 480 \times 1.275\,mm^3$) with an assumed elliptic delamination (semi-major axis: 15 mm, semi-minor axis: 10 mm, angle between the major axis and 0° fibre direction: 135°, centre position: 276 and 299 mm away from the left and bottom edges of the laminate, respectively, delaminated area: 0.25% of surficial area of laminate) between the 1st and the 2nd layers was considered. One pair of its edges were fixed-supported while the other pair were kept free. Four PZT disks, acting as both actuators and sensors, were located at the corners of a square route, 65 mm away from the two neighbouring laminate edges, counter-clockwise numbered with *P*1, *P*2, *P*3 and *P*4 from the bottom-left one, schematically delineated in Figure 2.

Full-scale three-dimensional FEM model with fine mesh description was created for the delaminated laminate on the PATRAN® platform [18], while the dynamic analyses were accomplished using ABAQUS/EXPLICIT® FEM code [19] using a super computer. Eight layers were divided along the laminate thickness to characterise each unidirectional lamina individually, leading to approximately 100,000 solid brick elements used for the simulation. The ichnographic FEM model for the vicinity of delaminated area is given in Figure 3(a), where more than 10 nodes exist within one wavelength. For comparison, modelling and numerical simulation for the laminate without artificial defect were also conducted. The time step adopted in dynamic calculation was controlled to be clearly less than the ratio of the minimum distance of any two adjoining FEM nodes to the maximum achievable wave velocity. A surface contact algorithm [19], permitting a small sliding relative displacement and arbitrary rotation of two delaminated surfaces, was introduced to process the contact problem arising from the delamination, sketched in Figure 3(b), which was proven in this study to be virtual in approximating the delamination. The technical information for the CF/EP composites considered in the simulation is listed in Table 1(a); while the mechanical properties for unidirectional laminae estimated using a micromechanics model [20] based on properties of constituents (carbon fibre and epoxy matrix), in accordance with the composite laminates used in the following experiments, were detailed in Table 1(b). In addition, PZT

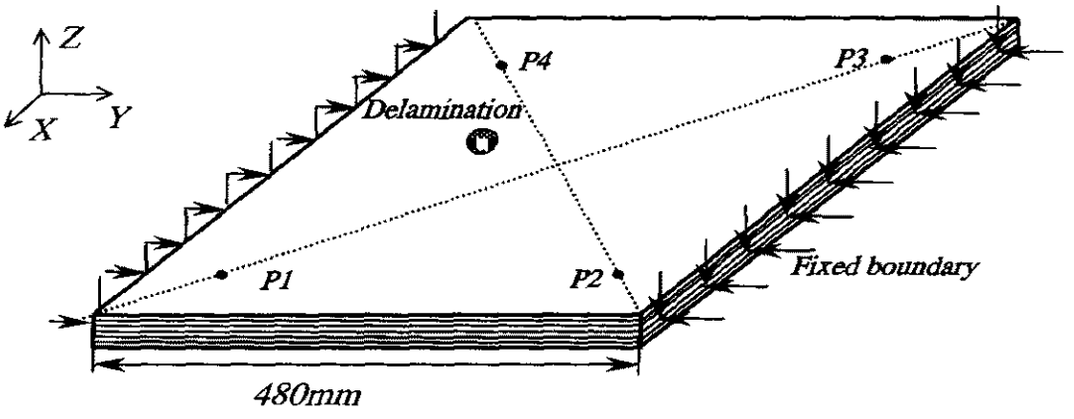

Figure 2 Composite laminate for numerical simulation.

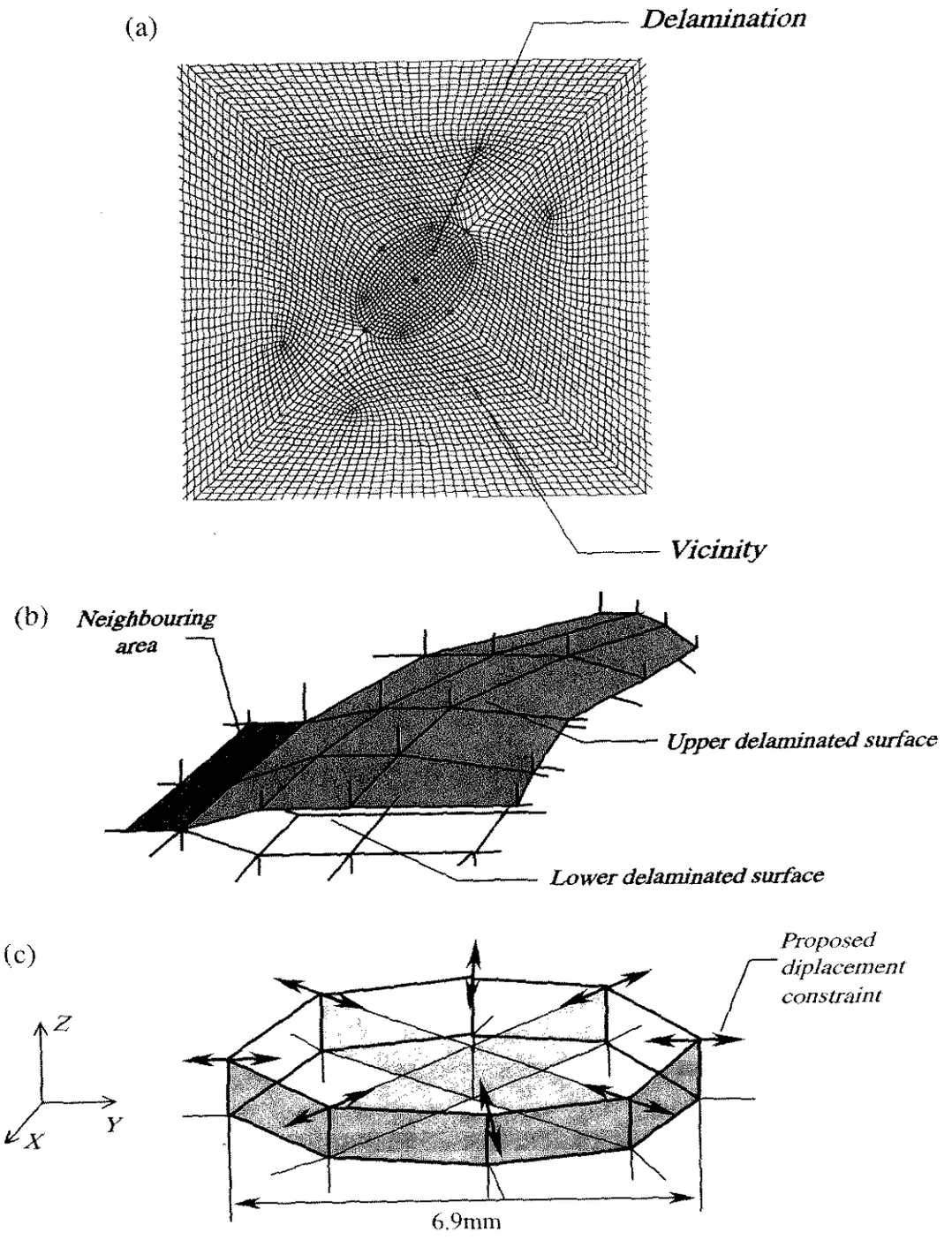

Figure 3 FEM modelling in numerical simulation: (a) mesh near delamination area; (b) contact surfaces for delamination; and (c) applied displacement constraints in the actuator area.

actuators/sensors were individually modelled [21]. A uniform radial displacement in the x–y plane, following a 5-cycle sinusoidal toneburst windowed with *Hanning* function at a central frequency of 0.5 MHz, was applied on the actuator model [21] to generate the Lamb modes, as described in Figure 3(c). The structural responses were dynamically monitored using the sensor model [21] at a

Table 1 Configurations of specimens

(a) Technical data for CF/EP composites used in simulation and experiment.

	Fibre Product Name	*Matrix Product Name*	*Fibre Fraction* (%)	*Matrix Fraction* (%)	*Laminate Density* (kg/m^3)	*Weave*	*Count Warp* × *Fill*
UD	T650/35-12K	F584	56	44	1528	N/A	N/A
WF	T300/3K	F593	48	52	1376	Plain	12.5 × 12.5

(b) Estimated elastic properties for unidirectional CF/EP lamina.

E_{11} (GPa)	E_{22} (GPa)	E_{33} (GPa)	G_{12} (GPa)	G_{13} (GPa)	G_{23} (GPa)	ν_{12}	ν_{13}	ν_{23}
153.67	9.49	9.49	4.26	4.26	3.44	0.295	0.295	0.381

(c) Geometric identities of laminates and delaminations (Unit: mm).

Specimen No.	*Geometric Dimension* (mm)	*Simulated Delamination*					
		α	β	ϕ	ξ	ζ	θ
UD1#	480 × 480 × 1.275	N/A	N/A	N/A	N/A	N/A	N/A
UD2#	480 × 480 × 1.275	15	10	135	276	299	0.25
WF1#	480 × 480 × 1.454	N/A	N/A	N/A	N/A	N/A	N/A
WF2#	480 × 480 × 1.454	17	12	45	268	190	0.18

α: semi-major axis; β: semi-minor axis; ϕ: angle between the major axis and 0° fibre direction; ξ: vertical distance to the left edge from centre of the delamination; ζ: vertical distance to the bottom edge from centre of the delamination; θ: percentage of delaminated area (%) in laminate.

sample rate of 20.48 MHz. Stereo-visualised plots from FEM for Lamb wave propagation in the delaminated composite plate with a time interval of 10 μs are shown in Figure 4, where the internal defect-imposed disturbance on the Lamb wave propagation can be clearly observed.

A series of bandpass filters with proposed thresholds were designed, introduced hereinafter, and applied on the simulated signals to screen the broadband noisy interferences and extract diagnostic components in the frequency scopes corresponding to the excitation. The filtered dynamic signals via actuator–sensor path *P*1–*P*3, as typical examples, for the composite laminates without/with delamination are displayed in Figure 5. Mode conversion induced by the existence of delamination is noticed in the signals for defective specimen. Compared with Figure 5(a), extra Lamb mode in the selected frequency scope is clearly observed in Figure 5(b), which is recognised as the damage-induced basic shear mode, hereafter denoted by $S'_{0\text{Delam}}$. Other damage-induced modes are unexploitable because their velocities are either too close to other actuator-generated wave modes in the limited sampling period, or too slow to be sampled in the specific time.

3 Signal Processing and Experimental Implementation

3.1 Wavelet Transform Principles

Muddled by the structural low-frequency vibration patterns and diverse broadband noise corruptions, the interpretation of both theoretically calculated structural responses and experimentally acquired signals are not straightforward for damage detection in either the time or frequency domain. An identification algorithm based on the spectrographic analysis in the time-scale space was developed using the *Discrete Wavelet Transform* (DWT) and *Continuous Wavelet Transform* (CWT) technique [22–26]. *Daubechies* function was chosen as the wavelet transform function, which was experimentally demonstrated in this study to be most effective for the present system compared with other transform functions.

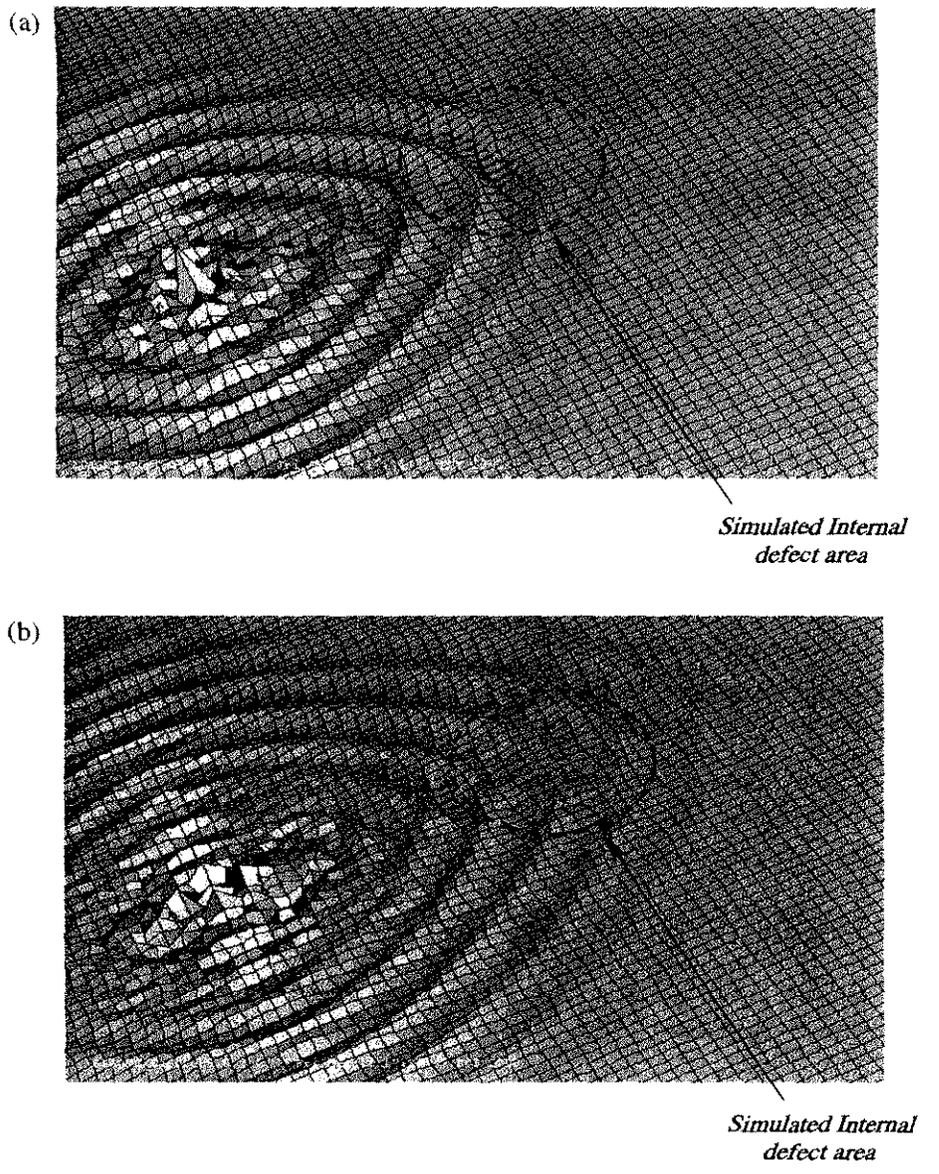

Figure 4 Defect-impacted disturbance on Lamb wave propagating in composite laminates: (a) at the 55th microsecond after excitation and (b) at the 65th microsecond after excitation.

Herein, for an arbitrary sampled signal $f(t)$, the discrete expression in the time-scale domain could be achieved by applying the selected basic wavelet function $\Psi(t)$ (*Daubechies* in this study) as [22],

$$a = a_0^m \text{ and } b = na_0^m b_0, \quad m, n \in Z \tag{1a}$$

$$DWT(m,n) = a_0^{-m/2} \int f(t) \cdot \Psi(a_0^{-m} t - nb_0) \cdot dt \tag{1b}$$

where a and b are the *scale* and *time* parameters, which were discreted by dyadic variables m and n, while a_0 and b_0 are constants determining the sampling intervals. Reversely, the signal could be reconstructed by [26],

$$f(t) = c \sum_m \sum_n C_{mn}(t) \cdot DWT(m,n) \tag{2a}$$

$$C_{mn}(t) = a_0^{-m/2} \Psi(a_0^{-m} t - nb_0) \tag{2b}$$

where c is a constant in correlation with $\Psi(t)$. Time-dependent function $C_{mn}(t)$, is defined as the

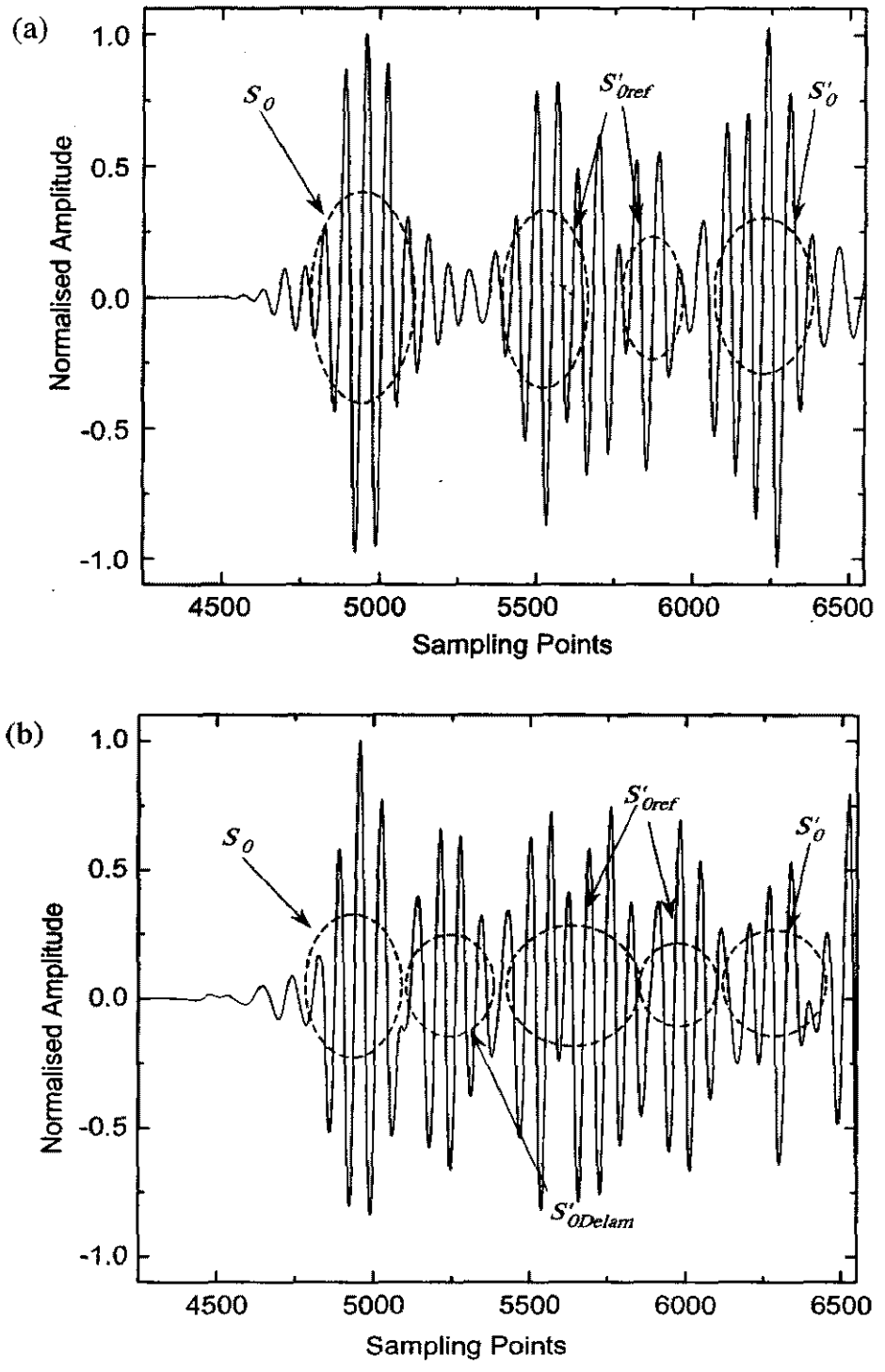

Figure 5 DWT analysis-processed structural responses via actuator–sensor path *P*1–*P*3 in simulation: (a) for laminate without delamination and (b) for laminate with delamination.

DWT coefficient, and the overline indicates the complex conjugate.

Based on Equations (1b) and (2), a series of bandpass filters with discreted initial thresholds and frequency scopes were established, with which the one-dimensional time-dependent wave signals were decomposed into associated band ranges according to frequency. Lamb wave components

pertaining to the excitation were therefore separated and characterised without diverse interferences.

Serialising Equation (1), signal $f(t)$ was converted into a quadratic description as [22],

$$CWT(a,b) = \frac{1}{\sqrt{a}} \int_{-\infty}^{+\infty} f(t) \cdot \overline{\Psi\left(\frac{t-b}{a}\right)} \cdot dt \qquad (3)$$

where $CWT(a,b)$ is defined as the *CWT wavelet coefficient*. Conversely, the signal was reconstructed via the inverse continuous wavelet transform,

$$f(t) = \frac{1}{C_\Psi} \int_{-\infty}^{+\infty} \int_{a>0}^{+\infty} CWT(a,b) \cdot \frac{1}{\sqrt{a}} \cdot \Psi\left(\frac{t-b}{a}\right) \cdot \frac{1}{a^2} da \cdot db \qquad (4)$$

where C_Ψ is a constant depending on $\Psi(t)$. Energy allocation for the wave signal was furthermore derived, in light of Equations (3) and (4) as,

$$E = \int_{-\infty}^{+\infty} \int_{a\geq 0}^{+\infty} |W(a,b)|^2 da \cdot db \qquad (5)$$

where $|CWT(a,b)|^2$, defined as the *scalogram*, indicates energy density in the time-scale domain. Based on Equations (3)–(5), the sampled signals were decomposed into two- and three-dimensional time-scale spaces with the intuitive illustration for the energy allocation, which offers a full display of the characteristics for acquired signals, more capable of detecting local perturbations in the signals. If the detected perturbation is not caused by the factors already known, such as a geometric boundary, it can be attributed to the existence of a damage. In the present study, the characteristic times for different Lamb modes in the time-scale space, at which the wave energy reached its maximum/minimum, were captured using a special program. The time differences among concerned Lamb modes, such as the one between incident and damage-reflected modes, were used to predict the damage location. In this study, identification of delamination location in the CF/EP composite laminates was conducted, while complete quantitative identification for damage severity using the energy allocation is reported elsewhere [27, 28].

In the above discussion, the spectrographic analyses were conducted in the time-scale domain, rather than the time–frequency space. The parameter *scale* (a) in Equations (1)–(5) is directly proportional to the *reciprocal of frequency* ($1/f$), depending on the selected wavelet transform function. It was found that the wave energy allocation could be more easily defined by representing the acquired signal into the time-scale domain [22, 29].

3.2 Configuration of Diagnosis System

An active online damage diagnosis system was established in accordance with the identification principle, sketched in Figure 6. It consists of Signal Excitation Unit (SEU), Signal Acquisition Unit (SAU) and Central Control Unit (CCU). A transducer network was designed using Piezoelectric Lead Zirconate Titanate (PZT) wafers, 6.9 mm in diameter and 0.5 mm in thickness, which was surface-bonded on each laminate and controlled by the SEU and SAU. Two-way switches were attached to SEU and SAU, making each PZT transducer function as both actuator and sensor, minimising the number of transducers and intrusion into the structure. While diagnostic signal, simulated by *Agilent© E1441* on *NI Labview©* platform, was applied on actuators through SEU after amplified to 60 V_{PP} (peak-to-peak) by a PZT amplifier (*PiezoSys© EPA-104*). Signal acquisition was performed via *Agilent© E1437A* digitizer at a sample rate of 20.48 MHz through *IEEE-488* bus; and the acquired signal was conditioned by *Agilent© E3242A* before transmitted into CCU. Being the key unit of the system, CCU performed as both controller and interpreter, supported by an inhouse software developed on the *NI Labview©* platform using *Matlab©* package [29], and finally the diagnostic results were output to the user's interface.

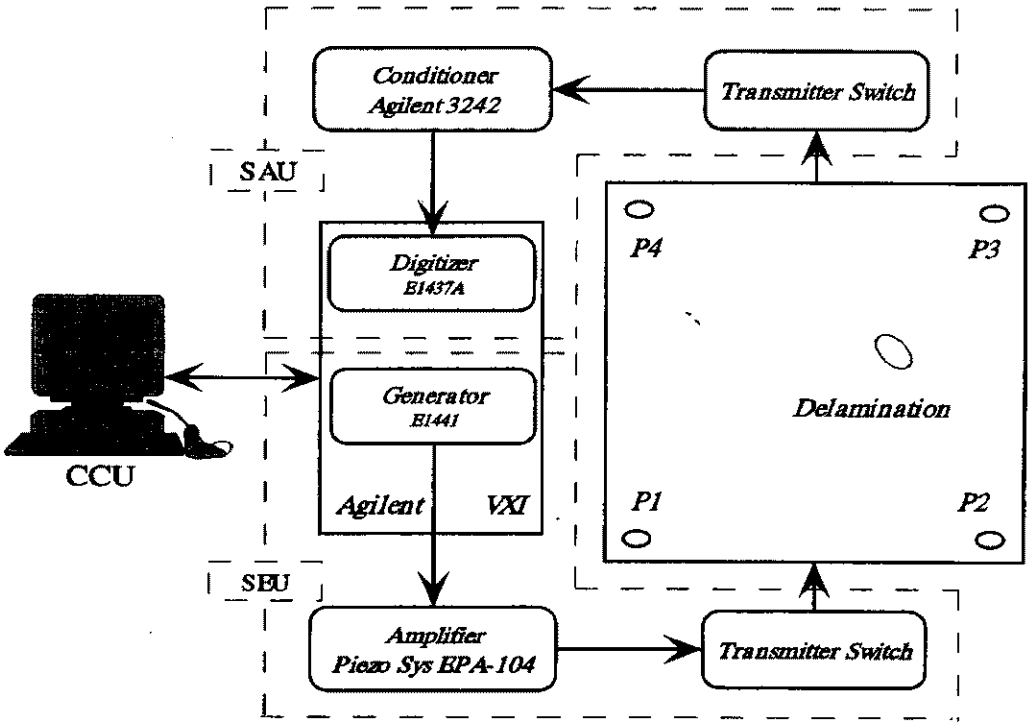

Figure 6 Configuration of diagnosis system using distributed piezoelectrics network.

3.3 Experimental Implementation

The proposed identification principle and developed diagnosis system were then validated by locating delaminations in CF/EP T650/F584 $[45/-45/0/90]_s$ quasi-isotropic laminates made from unidirectional (UD) prepreg, and CF/EP T650/F593 $[(0/90)/(-45/45)/(90/0)]_s$ orthotropic laminates made from plain woven fabric (WF) prepreg, respectively. The geometric identities for specimens are the same as those summarised in Table 1(c). A delamination with the same shape and size in the above numerical simulation was introduced using two pieces of *UPLEX©-R-25* film of 25 μm thickness during manufacturing. For comparison, the specimens without the delamination were also fabricated. The benchmark/defective laminates are represented by symbol $UD1^{\#}/UD2^{\#}$ for the unidirectional prepreg laminates and $WF1^{\#}/WF2^{\#}$ for the woven fabric prepreg laminates, respectively.

Amplified and modulated toneburst with various waveforms, at central excitation frequencies from 0.1 to 1.0 MHz, was applied on each PZT wafer in turn to generate the Lamb waves. When one wafer was activated, other three wafers were used to real-time monitor the structural response. By virtue of the two-way switches engaged in the SEU and SAU, totally 12 actuator–sensor paths were available with 4 transducers. Structural response signals were dynamically acquired for each actuator–sensor path in the experiment at the same sample rate used in simulation (20.48 MHz).

4 Damage Identification

4.1 Signal Interpretation

In the experiment, good repeatability for the signal acquisition was noticed. Arbitrarily chosen as typical examples, acquired signals for specimens $UD1^{\#}/UD2^{\#}$ via actuator–sensor path *P*1–*P*3 and those for specimens $WF1^{\#}/WF2^{\#}$ via path *P*2–*P*4 are displayed in Figures 7 and 8, respectively. Certain differences can be noticed between the structural responses for the benchmark and defective laminates in the time domain. Meanwhile, the frequency spectrum analyses by *Fast Fourier Transform* (FFT) were also performed, and the spectra for the chosen signals are correspondingly

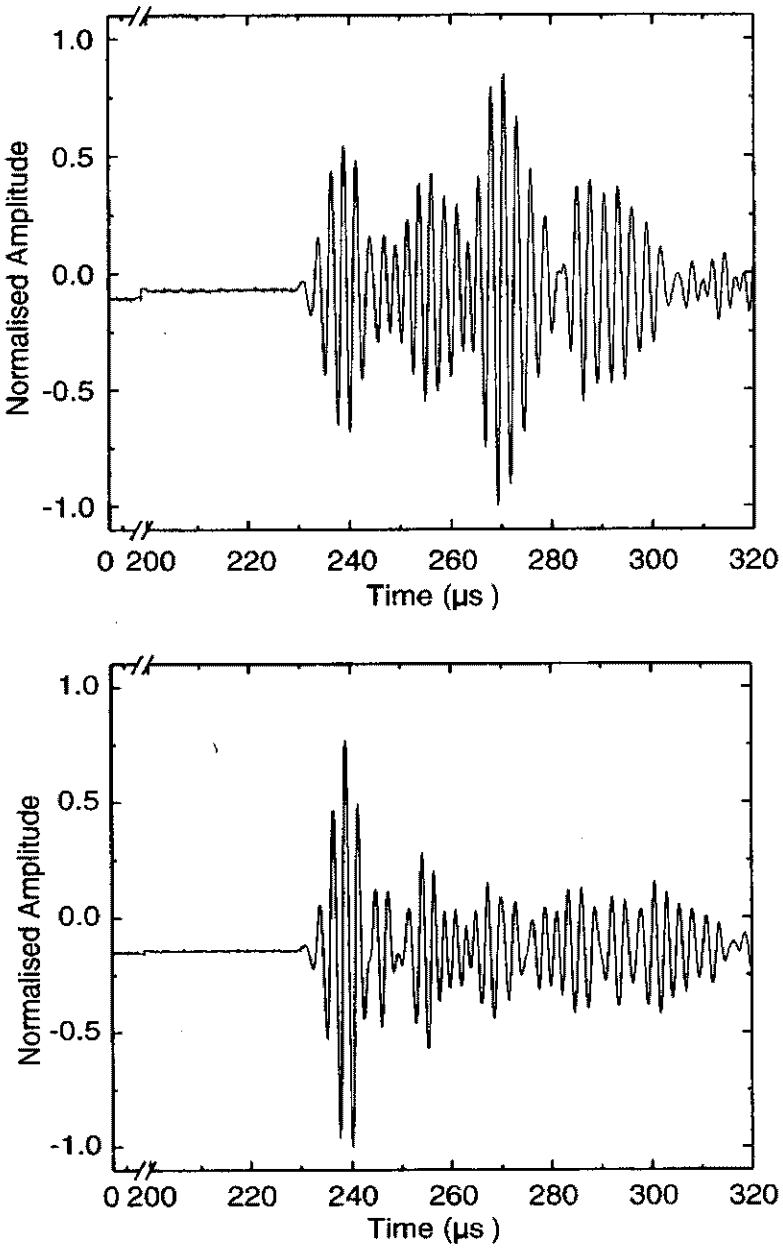

Figure 7 Sampled signals via *P*1–*P*3 for laminates made from unidirectional prepreg: (a) for benchmark laminate UD1# and (b) for defective laminate UD2#.

exhibited in Figure 9. The FFT analysis is able to provide an interrogation on the acquired signals in the diverse frequency ranges. In the spectra for UD2# and WF2#, extra frequency components, shaped as *spike*, could be noticed when compared with those for UD1# and WF1#. However, these characteristics or differences in either the time- or frequency-domain are not sufficient for quantitative identification of damage in the laminate.

The signal processing principles proposed in Section 3 were applied and the wave components pertaining to the incident excitation were correctly extracted from raw acquired signals via DWT analyses. The filtered signals are displayed in Figure 10, where fundamental symmetric Lamb mode, S_0, and basic shear mode, S_0', together with the reflected components from the boundaries, denoted by $S_{0\text{ref}}$, can be orderly observed

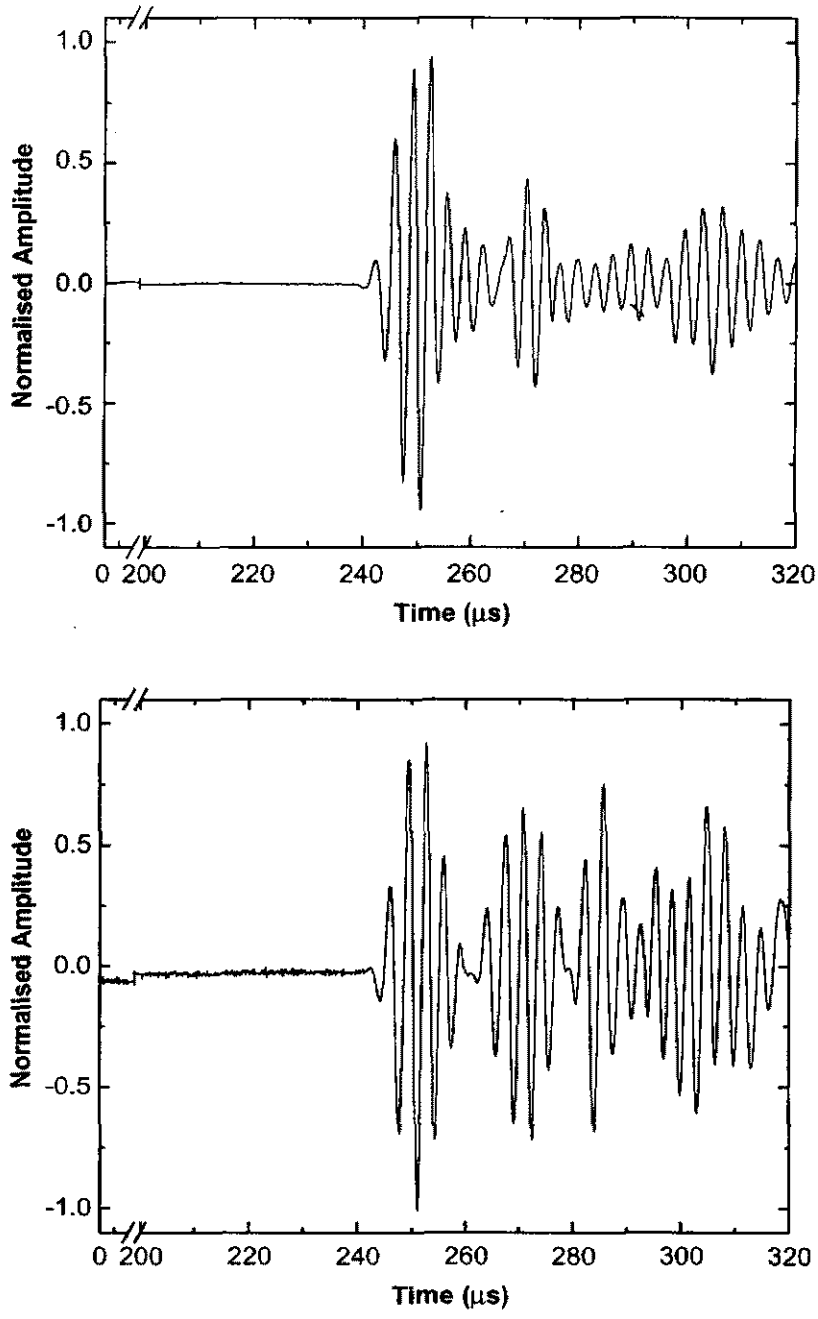

Figure 8 Sampled signals via *P2–P4* for laminates made from woven fabric prepreg: (a) for benchmark laminate WF1# and (b) for defective laminate WF2#.

within the selected frequency scope and time period. For identification purpose, only first several wave components in the acquired signals are useful while the rest may be corrupted by the boundary reflections. Compared with benchmark laminates, extra wave components between S_0 and S_{0ref} or following S_{0ref} were detected in Figure 10(b) and (d). In correlation with the study in Section 2, the extra components are recognised as the delamination-induced basic shear mode, S'_{0Delam}. The appearance order of the wave components in a signal is deterministically dependent on the relative locations among the delamination, boundaries and sensors. Herein, the *Sampling*

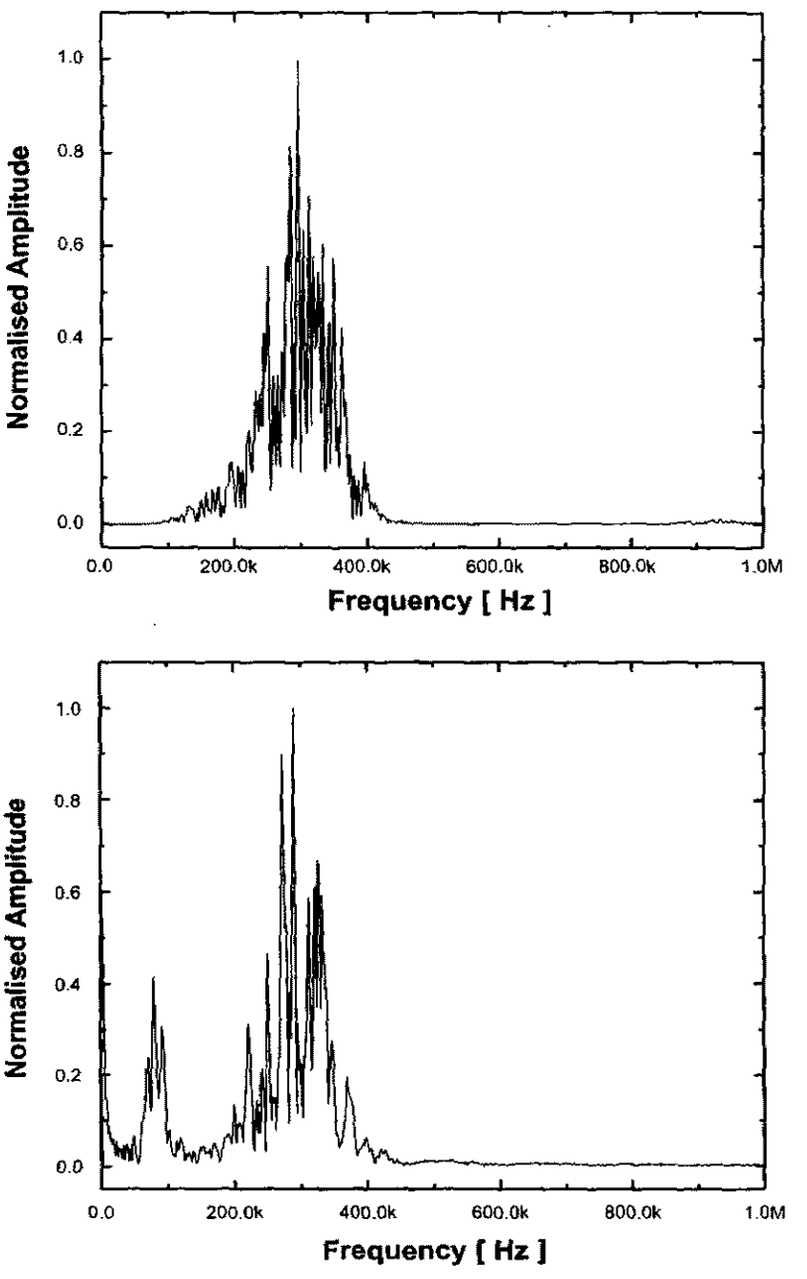

Figure 9 FFT analysis for paradigmatic signals shown in Figures 7 and 8: (a) for benchmark laminate UD1#; (b) for defective laminate UD2#; (c) for benchmark laminate WF1#; and (d) for defective laminate WF2#.

Point (SP) was introduced instead of the direct *Time Point* (TP) so as to expedite and facilitate the data processing in CCU.

Further, two- and three-dimensional spectrographic analyses based on the CWT technique were performed and relevant results for the paradigmatic signals are shown in Figures 11 and 12, respectively. In the two-dimensional spectra, the allocation of energy for various Lamb modes were calibrated by the CWT coefficients, represented by descending grayscale, where the darker the grayscale is, the higher the coefficients and the stronger the energy concentrates. In both two- and three-dimensional energy allocation plots, the defect-caused shear wave, $S'_{0\mathrm{Delam}}$, can visually be identified.

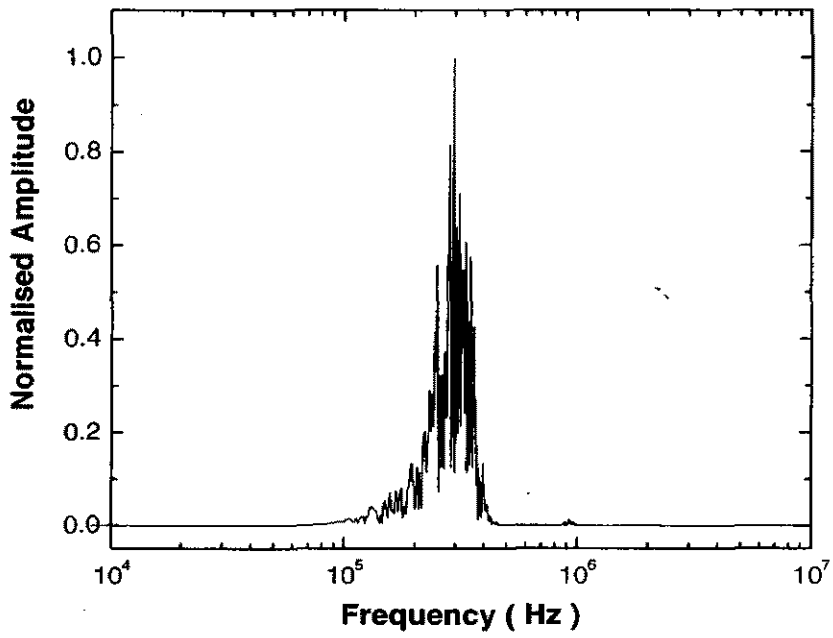

(c)

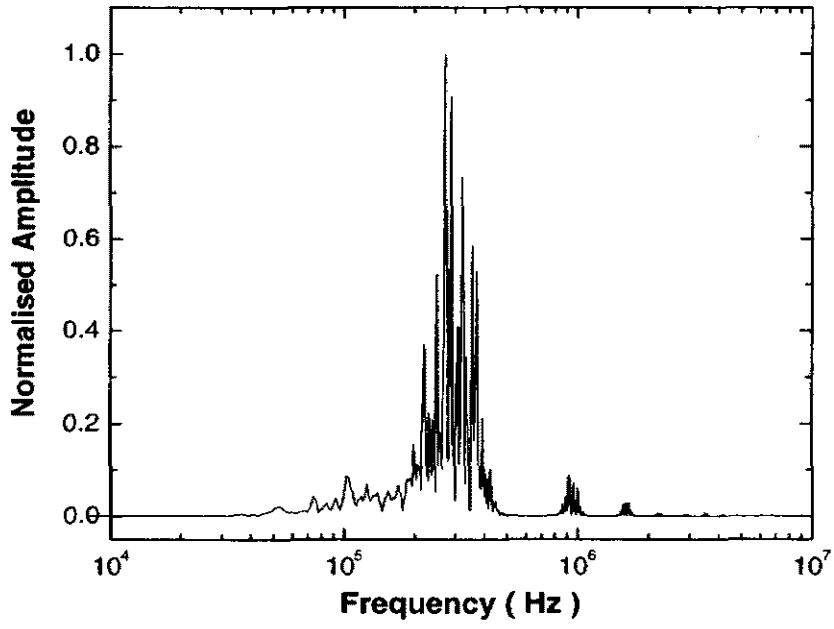

(d)

Figure 9 Continued.

The same geometric identity and delamination location were used in both numerical simulation and experimental analyses, which enables the comparison between the theoretical and experimental results. Representatively, the two- and three-dimensional CWT analyses for the signals from simulation, via the same actuator–sensor path *P*1–*P*3 for laminate UD2$^{\#}$ are displayed in Figure 13. Good correlation, in terms of the characteristic time and frequency for wave energy concentration, was found between the numerical simulation (Figure 13) and experimental measurements (Figures 11(b) and 12(b)), upon the application of signal processing.

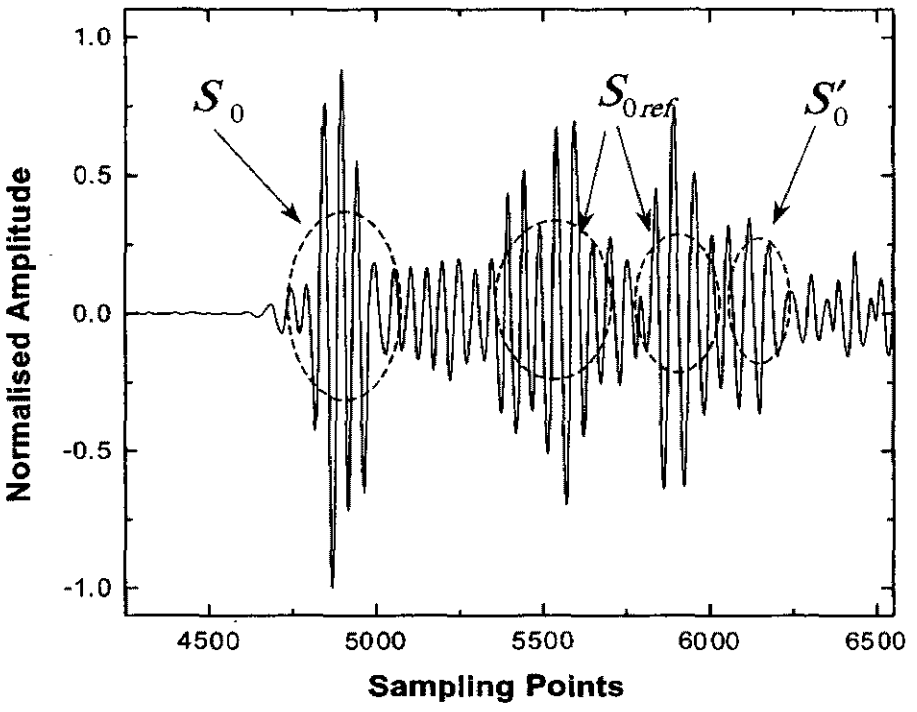

(a)

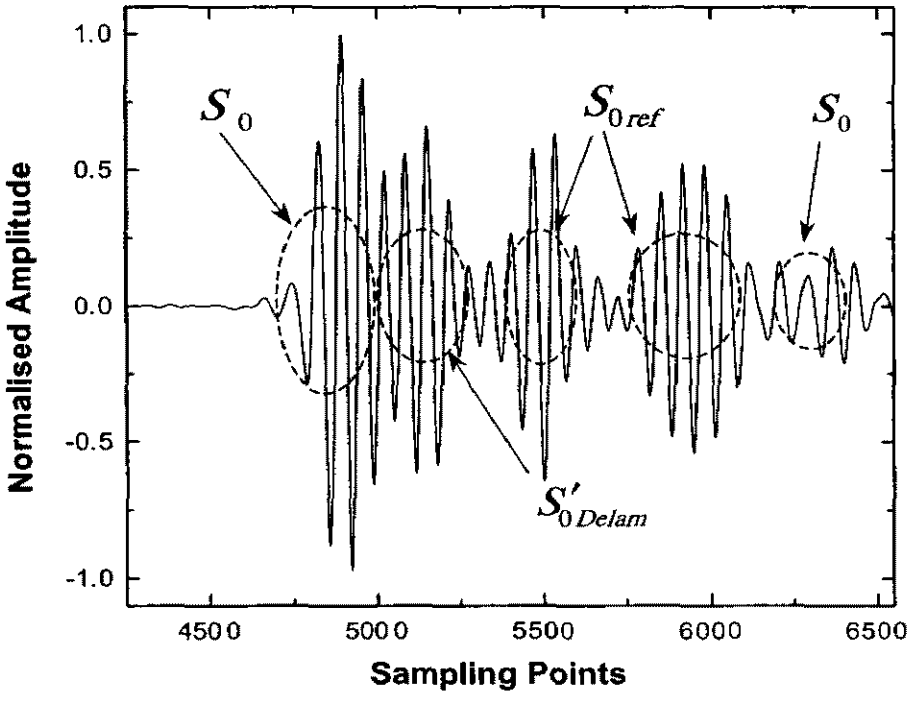

(b)

Figure 10 DWT analysis for paradigmatic signals shown in Figures 7 and 8: (a) for benchmark laminate UD1#; (b) for defective laminate UD2#; (c) for benchmark laminate WF1#; and (d) for defective laminate WF2#.

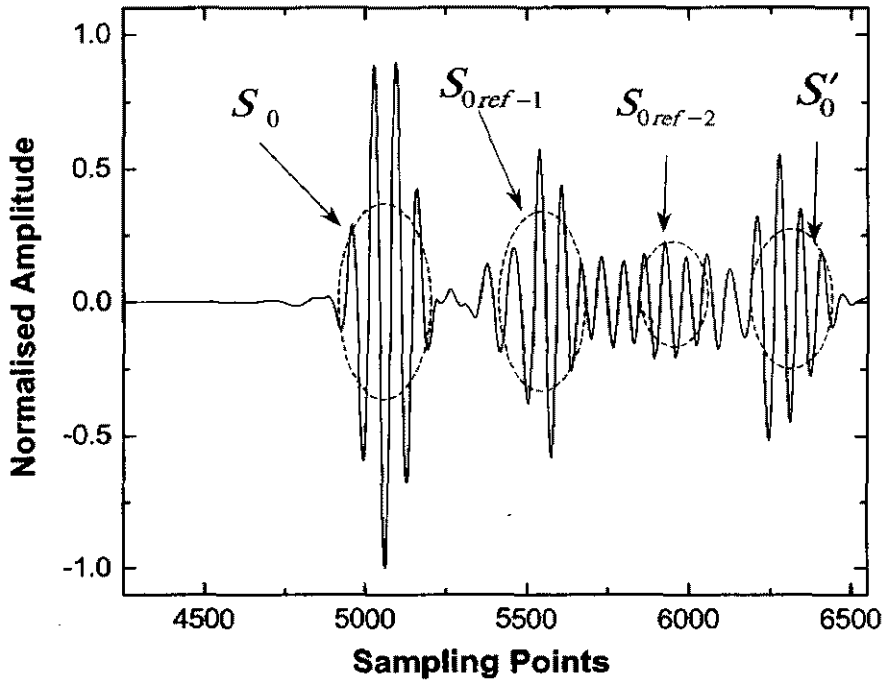

(c)

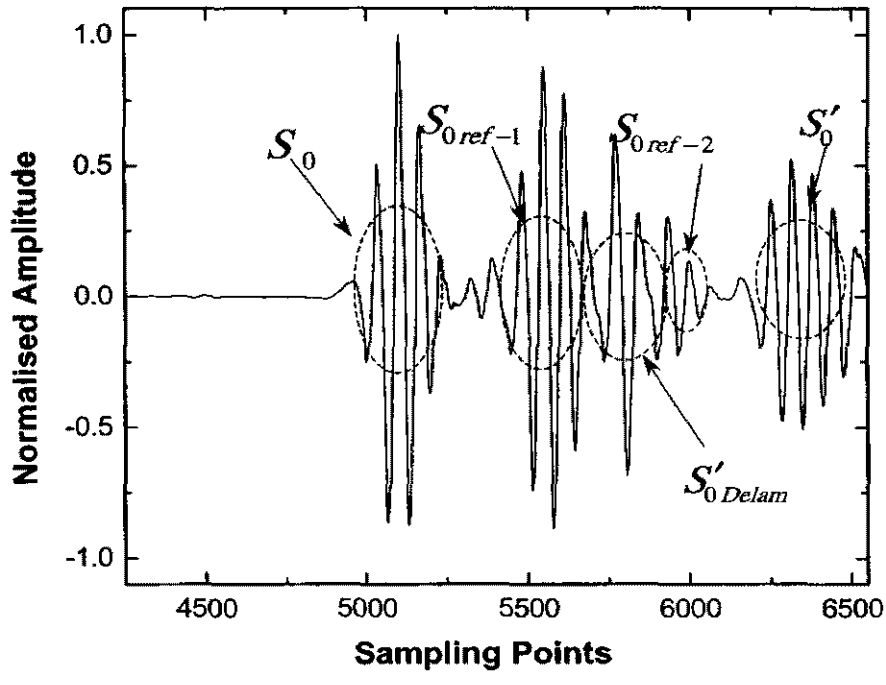

(d)

Figure 10 Continued.

4.2 Delamination Locating Algorithm

An internal structural damage locating algorithm based on the analyses conducted above was established. A preliminary searching for the possible and approximate delamination positions was executed to expedite the overall diagnosis, suggesting an initial point for the start of damage searching [27]. In this procedure, the whole

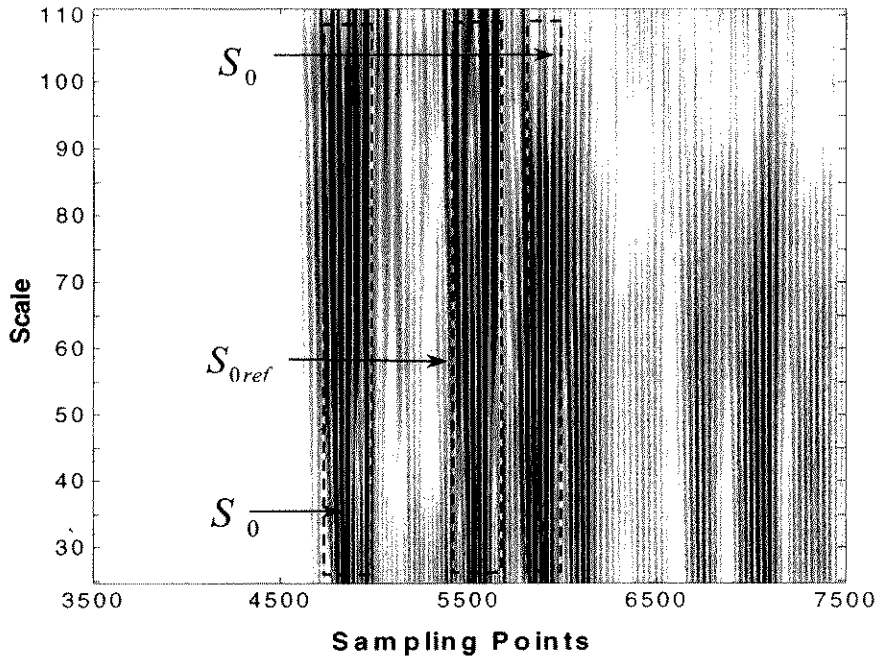

(a)

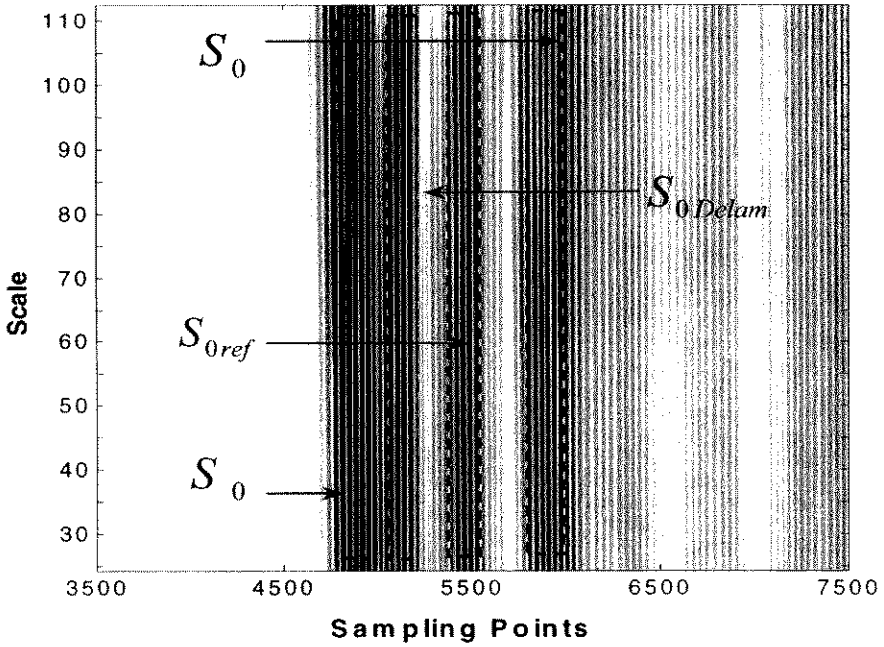

(b)

Figure 11 Two-dimensional CWT spectra for paradigmatic signals shown in Figures 7 and 8: (a) for benchmark laminate UD1#; (b) for defective laminate UD2#; (c) for benchmark laminate WF1#; and (d) for defective laminate WF2#.

laminate was supposed to be quartered evenly and the delamination was assumed to individually locate at the central position in each quadrant, respectively. The 3D dynamic FEM simulation was executed to calculate the relevant structural responses via concerned actuator–sensor paths under these presumed damage situations. The calculated signals were applied with DWT/CWT

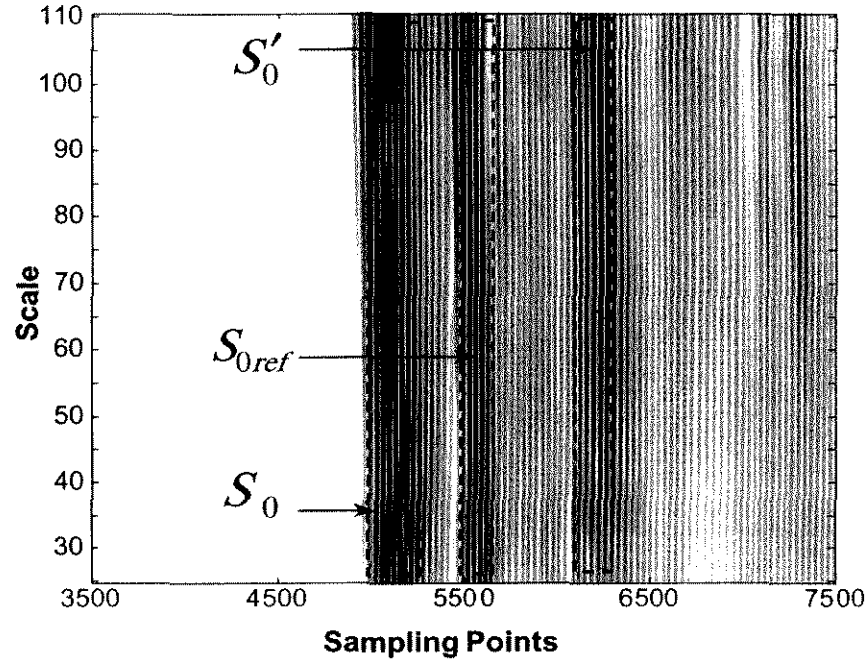

(c)

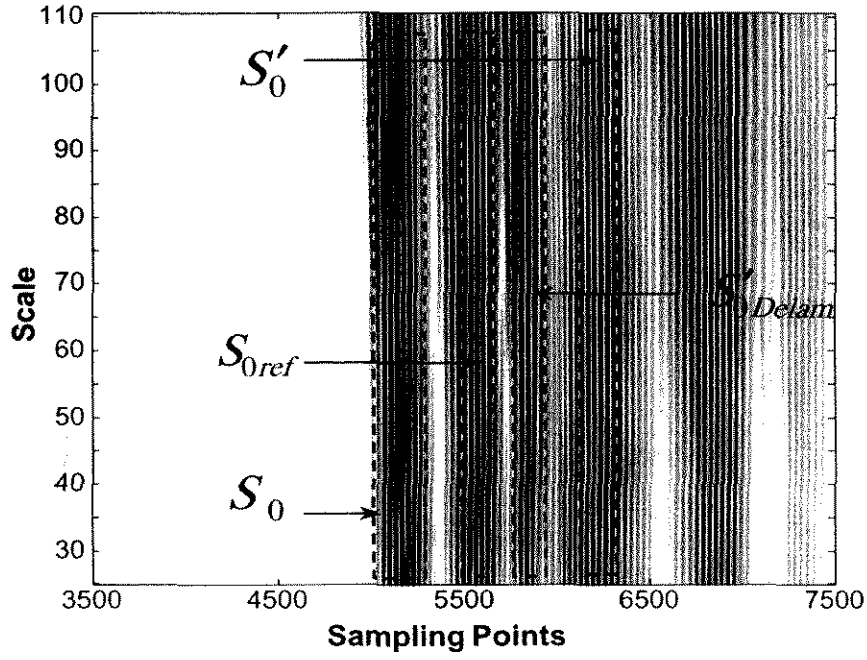

(d)

Figure 11 Continued.

analyses and then compared with the corresponding signals based on the experimental measurements. Least discrepancy indicated the most possible quadrant in which the damage might occur, where damage search should be concentrated. It was found that the damage searching and identification could be consequently simplified and expedited considerably through the preliminary estimation.

The time lags measured among concerned wave components from the DWT/CWT analyses were then used for the damage location

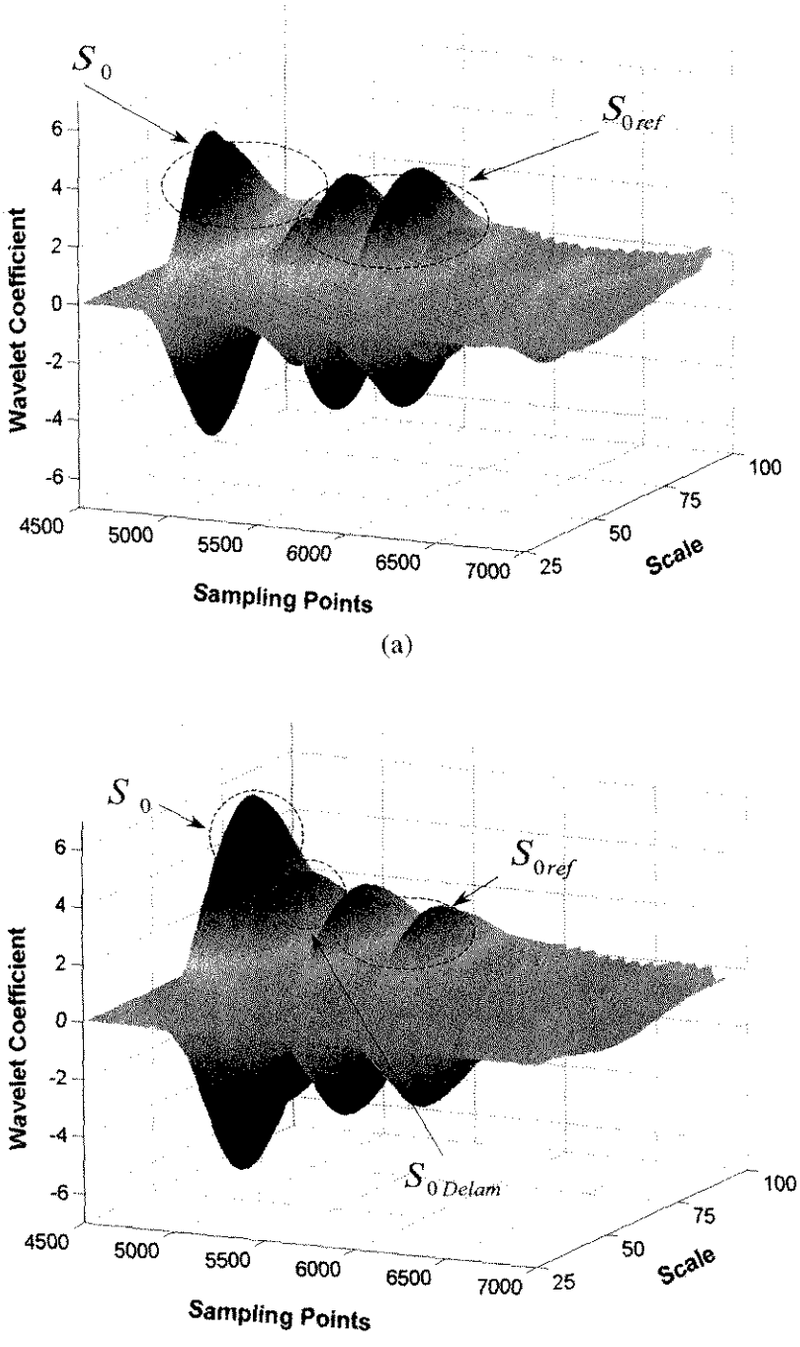

Figure 12 Three-dimensional CWT spectra for paradigmatic signals shown in Figures 7 and 8: (a) for benchmark laminate UD1#; (b) for defective laminate UD2#; (c) for benchmark laminate WF1#; and (d) for defective laminate WF2#.

identification. A searching algorithm based on a graphic optimisation [12,13,30,31] was devised. For example, in the case that the transducer $P1$ functioned as the actuator and the damage centre was supposed to locate at (x, y) (in the coordinate system that the actuator was the origin and the X-axis paralleled with the bottom edge of the laminate), a nonlinear set of equations can be

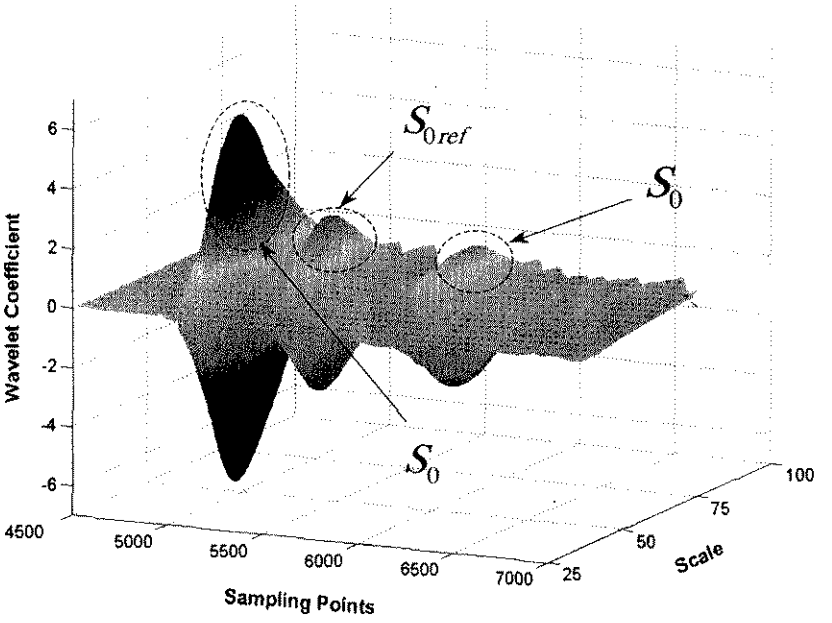

(c)

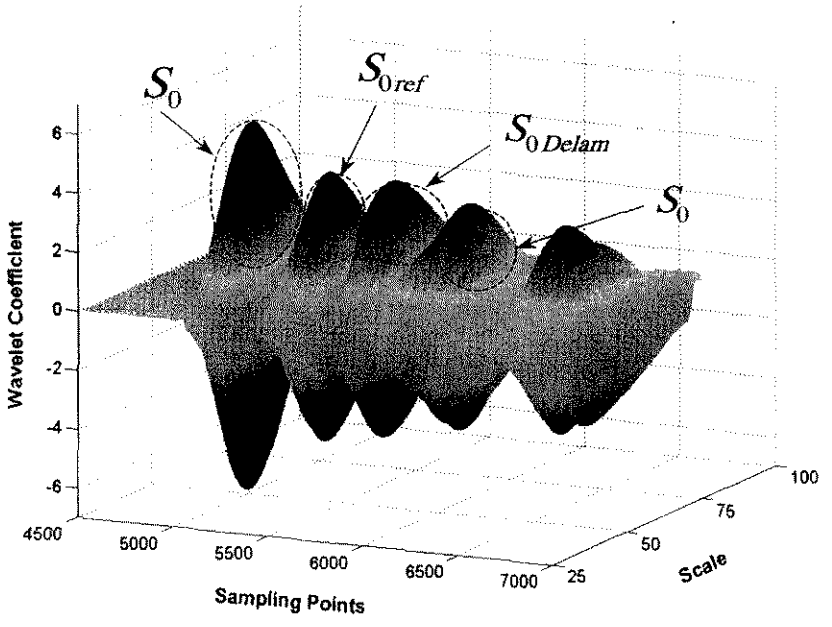

(d)

Figure 12 Continued.

established upon the relative distances among the transducers and the damage,

$$\frac{L_{A-D}}{V_{S_0}} + \frac{L_{D-S}}{V_{S'_{0\,\mathrm{Delam}}}} - \frac{L_{A-S}}{V_{S_0}} = T_{1-i} \quad (i = 2, 3, 4) \quad (6)$$

where L_{D-S}, L_{A-D} and L_{A-S} represent the distances between the damage centre (x, y) and the ith sensor, the selected actuator and the damage centre, the selected actuator and the ith sensor, respectively. $V_{S'_{0\mathrm{Delam}}}$ and V_{S_0} are the measured velocities of wave modes, $S'_{0\mathrm{Delam}}$ and S_0, respectively. T_{1-i} denotes the experimentally acquired time lag via actuator–sensor path P_1–P_i, by catching the characteristic times corresponding to the maximum/minimum energy concentration.

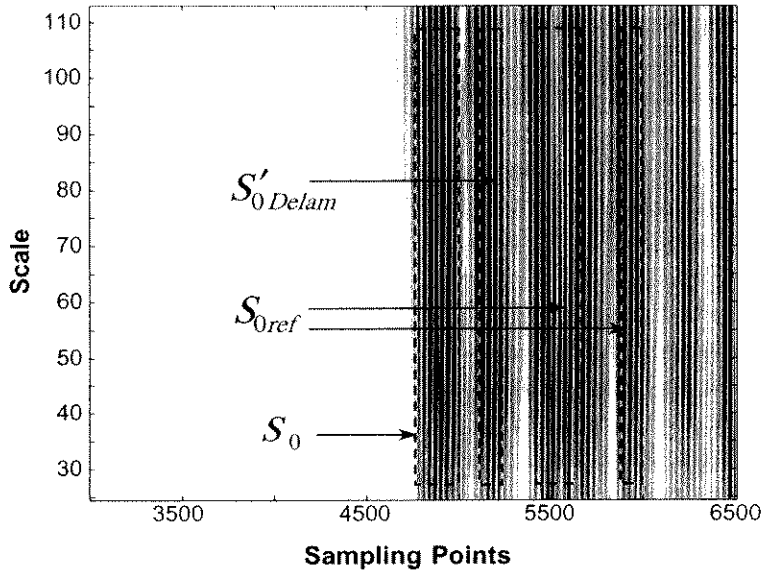

(a)

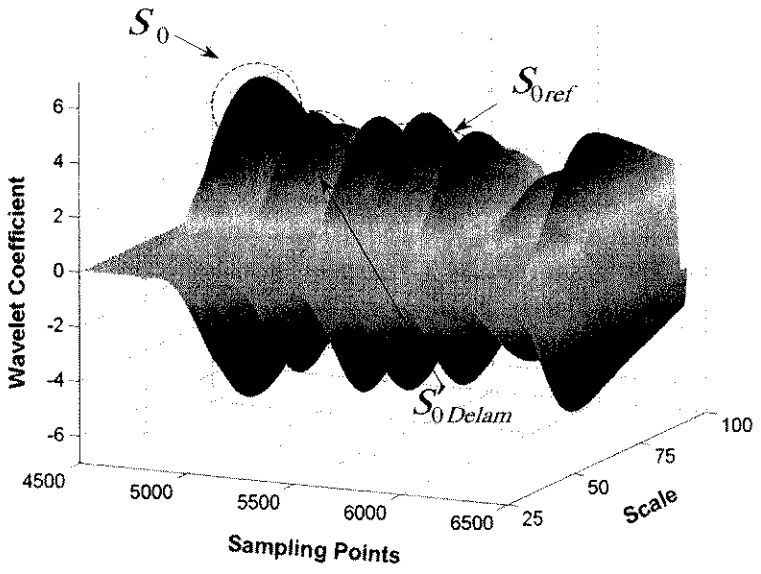

(b)

Figure 13 CWT spectra of simulated signal for UD2# via actuator–sensor path *P1–P3:* (a) two-dimensional and (b) three-dimensional.

In the referred Cartesian coordinate system, it has,

$$\begin{aligned} L_{D-S} &= \sqrt{(x-x_i)^2+(y-y_i)^2} \\ L_{A-D} &= \sqrt{x^2+y^2} \\ L_{A-S} &= \sqrt{x_i^2+y_i^2} \\ i &= 1,\ 2,\ 3,\ 4 \end{aligned} \tag{7}$$

where (x_i, y_i) represents the coordinates of the ith transducer in the current coordinate system. In practice, some paths in the theoretically 12 actuator–sensor paths were unexploitable because multi-reflection of waves from boundaries may spoil the damage-induced wave components in the sampled signal, incapable of providing essential diagnostic information.

Analogously, a non-linear system consisting of four equation sets were established after four

coordinate systems introduced, in which each PZT actuator took a turn to be nominated as the origin of its reference frames, respectively. A mathematic optimal method [30] was applied to solve the nonlinear system, with which the nonlinear system can be solved graphically using an inhouse program, facilitating an accurate locating for the damage centre. The searching procedure is schematically explained in Figure 14. In these diagrams, the signal acquired via each individual actuator–sensor path is contributing to the construction of one equation based on Equations (6) and (7). Involving the damage coordinates (x, y), each equation graphically indicates the locus for the possible damage locations, denoted by the dash-and-dot line in the figures. The intersection, taking into account the loci from all the available actuator–sensor paths, is recognised as the most possible position where damage occurs.

5 Discussion

The diagnosis results and estimation errors are summarised in Table 2. It is clear that the errors decrease with the increase of actuator–sensor paths involved for the damage identifying, while 4 paths are the minimum mathematic requirement to solve the nonlinear equation system. However, the more the paths were employed, the more time on experimental measurement was consumed. A compromise between expected accuracy and affordable efforts should be accordingly synchronised for actual applications. It is noted that a satisfactory accuracy can be ensured upon half of the total actuator–sensor paths involved.

In this study, it was found that a satisfactory accuracy for the location detection could be achieved when 4 PZT transducers were used, while the information that they can offer is yet not adequate for the identification of damage shape and size. The relationship between transducer numbers and detectable damage parameters is investigated in another study [21] by comparing a diversity of designed transducer networks.

During the experiment, the estimation errors were also noticed to be dependent on the interlaminar location of the delamination. The closer to the upper or bottom surfaces the delamination is located, the stronger the perturbance was detected in the signals, facilitating a precise detection. This deduction has also been theoretically demonstrated [2], in which the damage-induced shear stress, σ_{XZ} or σ_{YZ}, exists when the delamination situates between any two layers, except in the middlemost of the laminate, which has less influence on the propagation of Lamb waves. On the other hand, compared with the laminates made from unidirectional prepreg, relatively larger estimation errors were obtained for the laminates made from woven fabric prepreg, which may be attributed to the relatively complicated effect of woven fabric structures on the propagation of Lamb waves.

In this study, the benchmarks were introduced in both numerical simulation and experimental verification, to avoid any disturbance from boundary effects, etc. During the comparison between benchmark and defective laminates or the comparison between FEM simulation and experiment, certain distinction or incomplete agreement could also be noticed in addition to the delamination-induced extra wave components, which is attributed to the imperfect similarity of two individual laminates in manufacturing or discrepancy between theoretical emulation and laboratorial measurement. For detection based on a *forward* analysis, the information from benchmark is therefore essential, and more accurate identification is expected to be accomplished when the comparison of signals from the same laminate before and after the occurrence of damage can be conducted. While an *inverse* identification approach, independent of the benchmark, is developed [21,28] using artificial neural network algorithm to overcome this hindrance.

Undergoing the dispersion phenomenon, distortion of the incident diagnostic waveform could not be avoided in experiment, reducing the diagnosis precision to certain extent. Different diagnostic waveforms, 1-cycle, 3-cycle, 5-cycle, 7-cycle and 10-cycle windowed toneburst as well as pulse excitation, at different central frequencies, from 0.15 to 1.0 MHz, were conducted for comparison, respectively. The results show that the SNR (Signal-to-Noise Ratio) increases as the signal central frequency increases, consequently making the identification more accurate.

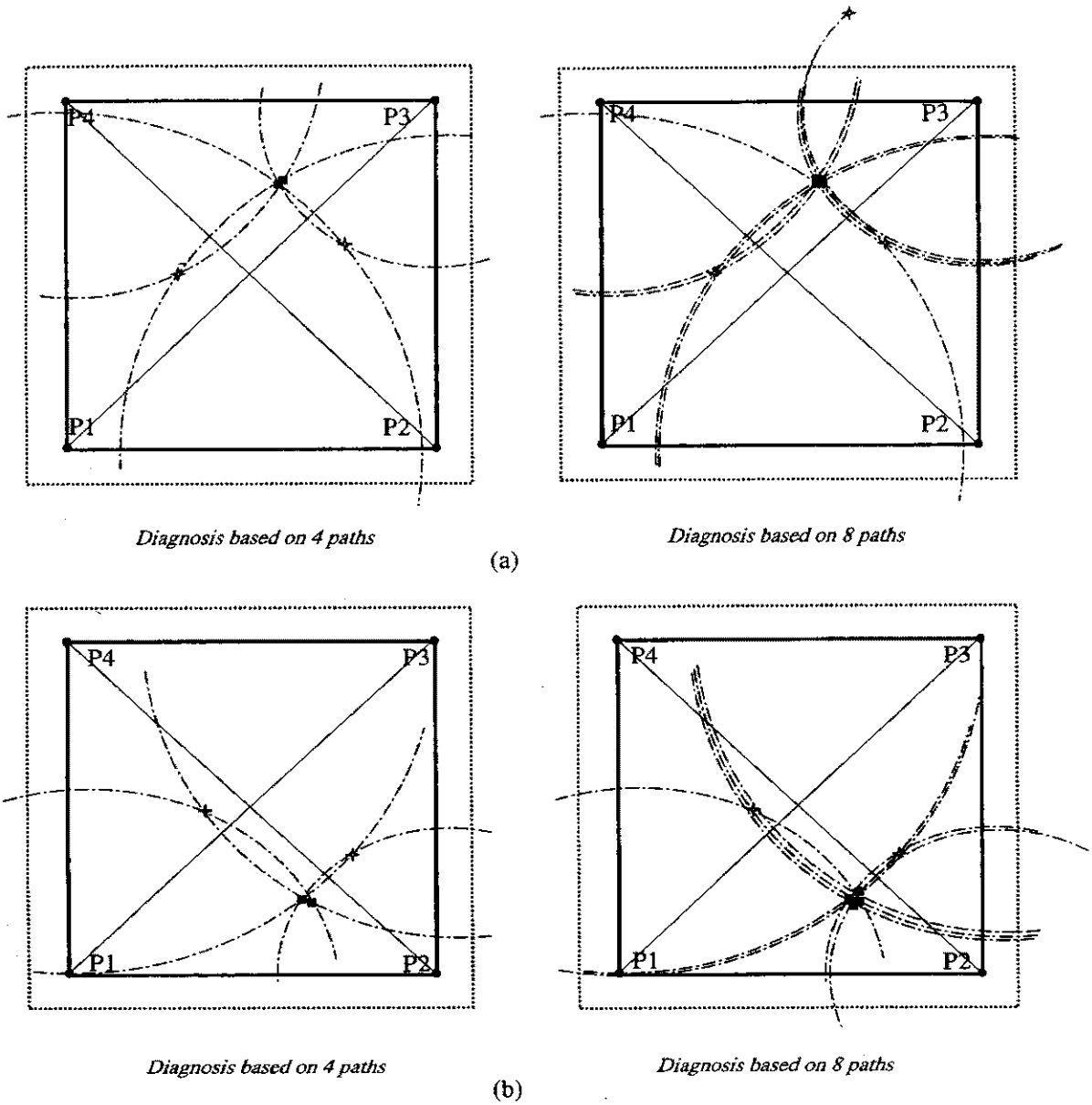

Figure 14 Delamination locating: (a) for specimen UD2# and (b) for specimen WF2#.

Table 2 Diagnosis results and estimation errors (Unit: mm).

	Based on 4 Paths		*Based on 6 Paths*		*Based on 8 Paths*	
Specimen	*Diagnostic Result**	*Relative Error (%)*	*Diagnostic Result**	*Relative Error (%)*	*Diagnostic Result**	*Relative Error (%)*
UD1#	(312, 266)	13.0	(293, 316)	6.8	(262, 313)	4.8
WF2#	(311, 218)	16.5	(249, 204)	7.7	(285, 201)	6.9

*The vertical distances away from the left and bottom edges of the laminates, respectively.

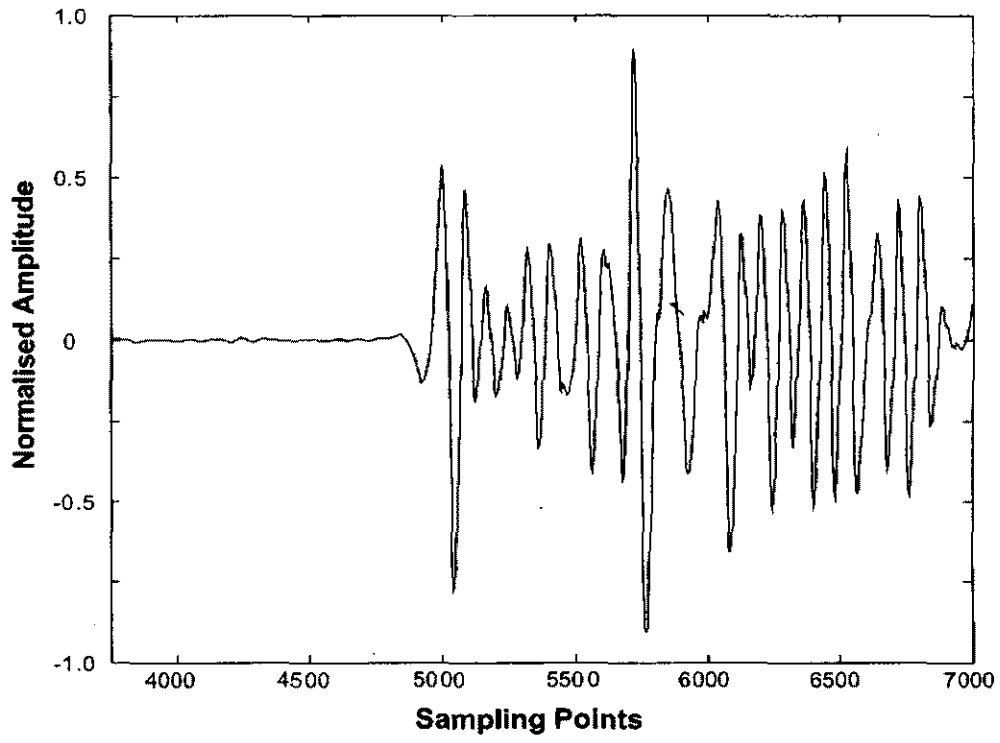

(a)

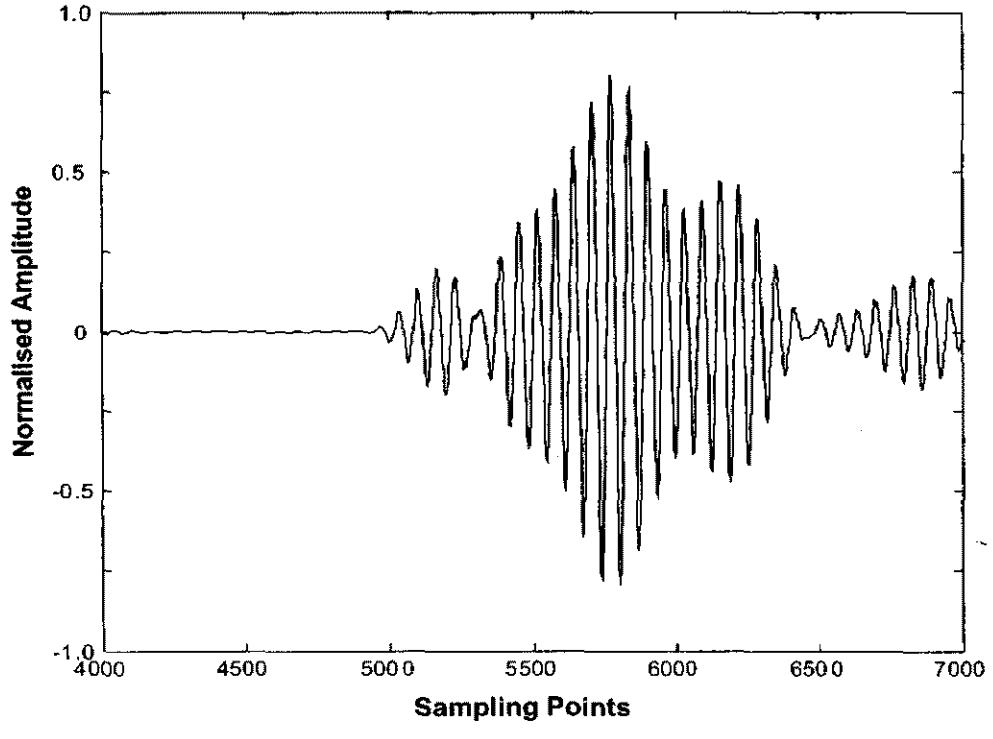

(b)

Figure 15 DWT analysis for structural responses under different excitations: (a) excited by pulse-excitation at 0.5 MHz and (b) excited by 10-cycle toneburst at 0.35 MHz.

However, synchronously, the high frequency weakens the capability of Lamb wave to propagate in the composites due to the attenuation mechanism. Meanwhile, it was also heeded that the high cycle number of toneburst may lower the risk of signal distortion. But an accompanying superposition of multiple wave modes occurs due to the large bandwidth, leading to the confusion in signal interpretation. As an example, the structural responses corresponding to the pulse-excitation at a central frequency of 0.5 MHz and 10-cycle *Hanning* windowed toneburst at a central frequency of 0.35 MHz were processed with DWT analyses and given in Figure 15, where evident distortion of the incident pulse excitation can be noticed in Figure 15(a), while immersion and superposition of multiplicate Lamb modes appear in Figure 15(b). Both the distortion and superposition make it more difficult to extract useful diagnostic components. In experiments, satisfactory resolution and accuracy could be met for the present system when 5-cycle toneburst in the central frequencies of 0.3–0.5 MHz was used.

6 Conclusion

A Lamb wave-based delamination locating approach was developed using the propagation characteristics of Lamb waves in laminated composites involving a delamination. An active diagnosis system using distributed piezoelectrics was consequently established, and it was then experimentally validated by identifying delaminations in CF/EP laminates made from unidirectional and woven fabric prepreg, respectively. It is shown that satisfactory diagnosis can be achieved by analysing the acquired scattering signal using the wavelet transform technique-based identification algorithm. Identification errors in damage location depend on the number of actuator–sensor paths to be used for diagnosis, and satisfactory precision can be obtained when half of the total actuator–sensor paths are taken into account. An algorithm based on a graphic approach was applied on solving the nonlinear equation system, to fulfill an accurate identification. Additionally, the strong reliance of the estimation accuracy on excitation waveforms and bandwidth was noticed. The present work is aimed at an active online damage assessment technique with hybrid numerical and experimental approaches, capable of continuously monitoring the structural integrity.

Acknowledgement

Part of the FEM simulation presented in the work was carried out through the APAC services provided by the *Australian National University*. Z.Su would like to gratefully acknowledge the support of the *International Postgraduate Research Scholarship* (IPRS) from the *Department of Education Science, and Training* (DEST), Australia, and the *International Postgraduate Award* (IPA) from the *University of Sydney*.

References

1. Badcock, R.A. and Birt, E.A. (2000). The use of 0–3 piezocomposite embedded Lamb wave sensors for detection of damage in advanced fibre composites. *Smart Materials and Structures*, *9*, 291–297.
2. Percival, W.J. and Birt, E.A. (1997). A study of Lamb wave propagation in carbon-fibre composites. *Insight*, *39*, 728–735.
3. Guo, N. and Cawley, P. (1992). Lamb waves for the NDE of composite laminates. In: Thompson, D.O. and Chimenti, D.E. (eds.), *Review of Progress in Quantitative Nondestructive Evaluation*, Vol. 11, (pp. 1443–1450). Plenum, New York.
4. Guo, N. and Cawley, P. (1993). The interaction of Lamb wave with delaminations in composite laminates. *Journal of the Acoustical Society of America*, *94*, 2240–2246.
5. Guo, N. and Cawley, P. (1993). Lamb wave propagation in composite laminates and its relationship with acousto-ultrasonics. *NDT & E International*, *26*, 75–84.
6. Guo, N. and Cawley, P. (1994). Lamb wave reflection for the quick nondestructive evaluation of large composite laminates. *Materials Evaluation*, *52*, 404–411.
7. Alleyne, D.N. and Cawley, P. (1992). The interaction of Lamb waves with defects. *IEEE Transactions on Ultrasonics, Ferroelectrics and Frequency Control*, *39*, 381–397.
8. Tan, K.S., Guo, N., Wong, B.S. and Tui, C.G. (1995). Experimental evaluation of delaminations in composite plates by the use of Lamb waves. *Composites Science and Technology*, *53*, 77–84.

9. Tang, B. and Henneke, E.G. (1989). Lamb-wave monitoring of axial stiffness reduction of laminated composite plates. *Materials Evaluation, 47*, 928–934.
10. Legendre, S., Massicotte, D., Goyette, J. and Bose, T.K. (2000). Wavelet-transform-based method of analysis for lamb-wave ultrasonic NDE signals. *Journal of IEEE, 49*, 524–530.
11. Wang, C.S. and Chang, F.-K. (1999). Built-in diagnostics for impact damage identification of composite structures. In: Chang, F.-K., (ed.), *Structural Health Monitoring* (pp. 612–621), 2nd ed. Lancaster: Technomic.
12. Lemistre, M., Gouyon, R., Kaczmarek, H. and Balageas, D. (1999). Damage localization in composite plates using wavelet transform processing on Lamb wave signals. In: Chang, F.-K. (ed.), *Structural Health Monitoring* (pp. 861–870), 2nd ed., Lancaster: Technomic.
13. Gaul, L. and Hurlebaus, S. (1999). Wavelet-transform to identify the location and force-time-history of transient load in a plate. In: Chang, F.-K. (ed.), *Structural Health Monitoring* (pp. 851–860), 2nd ed., Lancaster: Technomic.
14. Islam, A.S. and Craig, K.C. (1994). Damage detection in composite structures using piezoelectric materials. *Smart Materials and Structures, 3*, 318–328.
15. Inada, T., Shimamura, Y., Todoroki, A., Kobayashi, H. and Nakamura, H. (1999). Damage identification method for smart composite cantilever beams with piezoelectric materials. In: Chang, F.-K. (ed.), *Structural Health Monitoring* (pp. 986–994), 2nd ed. Lancaster: Technomic.
16. Wisnom, M.R. and Chang, F.-K. (2000). Modelling of splitting and delamination in notched cross-ply laminates. *Composites Science and Technology, 60*: 2849–2856.
17. Rose, J.L. (1999). *Ultrasonic waves in solid media*. Cambridge: Cambridge University Press.
18. Bull, J.W. (1996). *Numerical analysis and modelling of composite materials*. London: Blackie Academic & Professional.
19. *ABAQUS User's Manual*, Version: 6.2. (2001). Hibbitt, Karlsson and Sorensen, Inc.
20. Gommers, B., Verpoest, I. and Houtte, P.V. (1996). Modelling the elastic properties of knitted fabric-reinforced composites. *Composites Science and Technology, 56*, 685–694.
21. Su, Z. and Ye, L. (2003). Lamb wave propagation-based damage identification for quasi-isotropic composite laminates using artificial neural algorithm, Part I: methodology and database development. (submitted to *Journal of Intelligent Material Systems and Structures*).
22. Chan, Y.T. (1995). *Wavelet basic*. Boston: Kluwer Academic Publishers.
23. Newland, D.E. (1994). Wavelet analysis of vibration, Part I: theory. *Journal of Vibration and Acoustics, 116*, 409–425.
24. Boashash, B. (1992). *Time-frequency signal analysis*. Melbourne: Longman Cheshire.
25. Abbate, A., Koay, J., Frankel, J., Schroeder, S.C. and Das, P. (1997). Signal detection and noise suppression using a wavelet transform signal processor: application to ultrasonic flaw detection. *Journal of IEEE, 44*, 14–25.
26. Chui, C.K. (1997). *Wavelet: a mathematical tool for signal processing*. Philadelphia: SIAM.
27. Su, Z. and Ye, L. (2002). A damage identification technique for CF/EP composite laminates using distributed piezoelectric transducers. *Composite Structures, 57*: 465–471.
28. Su, Z. and Ye, L. (2002). Quantitative damage prediction for composite laminates based on wave propagation and artificial neural algorithm. Presented in *Australian Inaugural Workshop on Structural Health Monitoring*, 25–26, November, 2002, Melbourne, Australia.
29. The Mathworks, Inc. (2001). *Wavelet Toolbox User's Manual*. Ver.1.0.
30. The Mathworks, Inc. (2001). *Optimisation Toolbox User's Manual*. Ver. 2.0.
31. Su, Z., Ye, L. and Bu, X. (2002). Evaluation of delamination in laminated composites based on Lamb wave modes: FEM simulation and experimental verification. In: Balageas, Daniel (ed.), *Proceedings of the 1st European Workshop on Structural Health Monitoring* (pp. 328–335), 10–12 July, 2002, Paris, France.

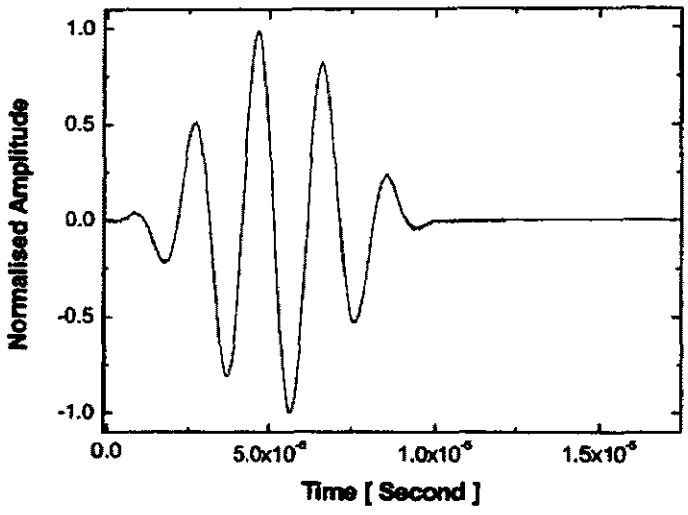

(a)

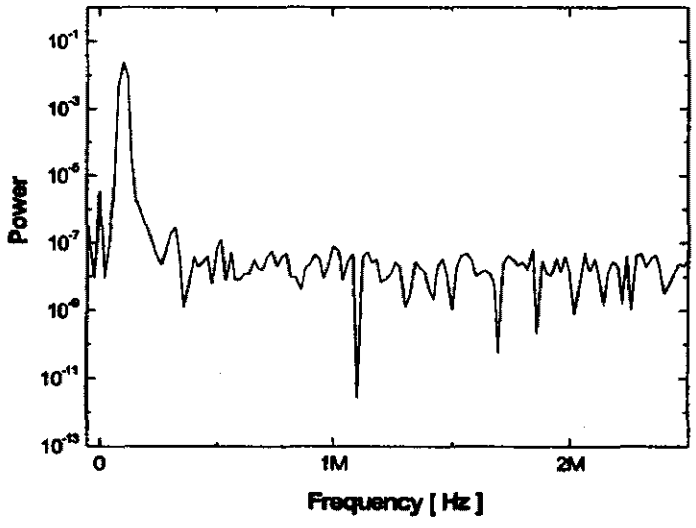

(b)

Fig. 3 Diagnostic wave generated by the control circuit: (a) in time domain; (b) in frequency domain

with a step of 100 Hz, were measured individually. The dispersion curves in the form of the averaged wave velocities versus excitation frequencies are plotted in Fig. 5. The dispersive curves simulated using the finite element method (FEM) [4] and those analytically calculated using the effective elastic constant method [4] are also compared with experimental measurements. Good correlation between them can be seen. Both experimental measurement and theoretical derivation reveal that symmetric and antisymmetric modes are synchronously available if without appropriate active control. Their phase velocities are dependent on the algebraic product of laminate thickness and central excitation frequency. A low-frequency region (<1.0 MHz mm) exists for the current structure, in which the fundamental antisymmetric Lamb mode, A_0, the symmetric Lamb mode, S_0 and the lowest-order shearing mode, S_0', exhibit reasonable non-dispersive behaviour.

4 NUMERICAL MODELLING

4.1 Actuator model

4.1.1 Single PZT activation

In parallel with the laboratory work, numerical simulations based on three-dimensional dynamic FEM modelling was conducted. A perfect bonding condition between piezoelectric discs and laminate was imposed to ensure strain continuity at the interfaces. The electromechanical constitutive mutuality, considering both direct and converse piezoelectric effects, for a piezoelectric disc is given as [41]

$$\begin{Bmatrix} Q_1 \\ Q_2 \\ Q_3 \\ \varepsilon_{11} \\ \varepsilon_{22} \\ \varepsilon_{33} \\ \varepsilon_{23} \\ \varepsilon_{13} \\ \varepsilon_{12} \end{Bmatrix} = \begin{bmatrix} p_1 & 0 & 0 & 0 & 0 & 0 & 0 & d_{15} & 0 \\ 0 & p_1 & 0 & 0 & 0 & 0 & d_{15} & 0 & 0 \\ 0 & 0 & p_3 & d_{31} & d_{31} & d_{33} & 0 & 0 & 0 \\ 0 & 0 & d_{31} & c_{11} & c_{12} & c_{13} & 0 & 0 & 0 \\ 0 & 0 & d_{31} & c_{12} & c_{11} & c_{13} & 0 & 0 & 0 \\ 0 & 0 & d_{33} & c_{13} & c_{13} & c_{33} & 0 & 0 & 0 \\ 0 & d_{15} & 0 & 0 & 0 & 0 & c_{55} & 0 & 0 \\ d_{15} & 0 & 0 & 0 & 0 & 0 & 0 & c_{55} & 0 \\ 0 & 0 & 0 & 0 & 0 & 0 & 0 & 0 & c_{66} \end{bmatrix} \times \begin{Bmatrix} E_1 \\ E_2 \\ E_3 \\ \sigma_{11} \\ \sigma_{22} \\ \sigma_{33} \\ \sigma_{23} \\ \sigma_{13} \\ \sigma_{12} \end{Bmatrix} \tag{7}$$

where the orthogonal components Q_i and E_i ($i = 1, 2, 3$) are the electric displacement (charge/area) and electric field (voltage/length) respectively, and σ_{ij} and ε_{ij} are the stresses and strains in the PZT actuator. Constants d_{ij}, p_i and c_{ij} represent piezoelectric strain constants, dielectric permittivity and compliance constants respectively. Considering that the poling direction is perpendicular to the surface of the PZT disc, equation (7), in the absence of in-plane external electric fields ($E_1 = E_2 = 0$), is simplified in the polar coordinate system in Fig. 6a as

$$Q_3 = p_3 E_3 + d_{31}(\sigma_r + \sigma_\theta) \tag{8a}$$

$$\sigma_r = \frac{E_{PZT}}{1 - \nu_{PZT}^2}[(\varepsilon_r + \nu_{PZT}\varepsilon_\theta) - (1 + \nu_{PZT})d_{31}E_3] \tag{8b}$$

$$\sigma_\theta = \frac{E_{PZT}}{1 - \nu_{PZT}^2}[(\varepsilon_\theta + \nu_{PZT}\varepsilon_r) - (1 + \nu_{PZT})d_{31}E_3] \tag{8c}$$

where σ_r/ε_r and $\sigma_\theta/\varepsilon_\theta$ are the radial and tangential stress/strain components in the polar coordinate system respectively,

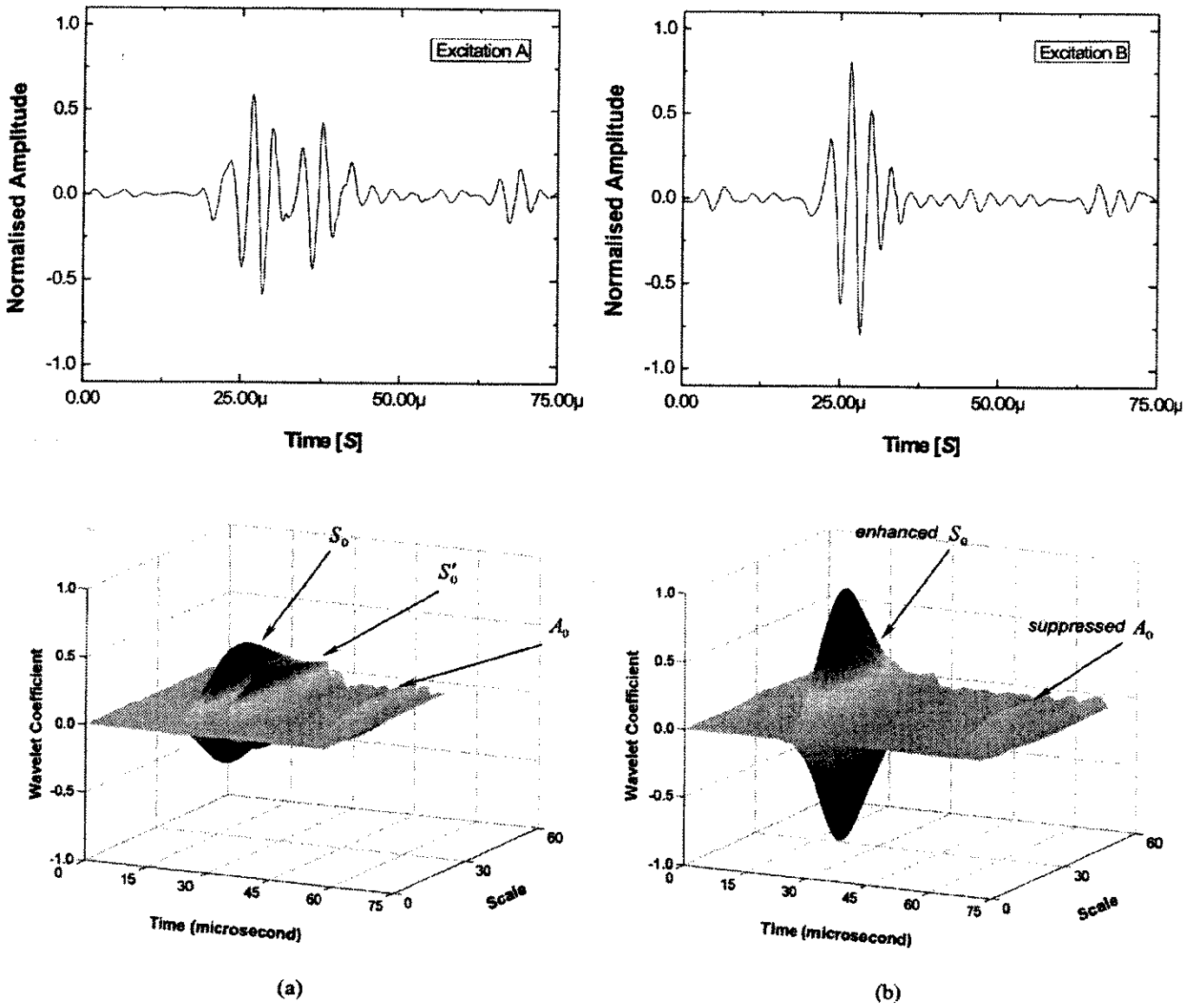

(a) (b)

Fig. 4 Raw signal and energy distribution spectrum for selectively generated Lamb modes (from experiment): (a) excitation case A; (b) excitation case B; (c) excitation case C

while E_{PZT} and ν_{PZT} denote Young's modulus and Poisson's ratio of the PZT disc respectively.

For a free thin piezoelectric disc of thickness h'_{PZT}, the in-plane strains, $\varepsilon_{r\text{-PZT}}$ and $\varepsilon_{\theta\text{-PZT}}$, will be generated when an external voltage, V, is applied

$$\varepsilon_{r\text{-PZT}} = \varepsilon_{\theta\text{-PZT}} = d_{31}E_3 = \frac{d_{31}}{h_{PZT}}V = \Pi \tag{9}$$

Introducing the strain continuity condition at the interface between the PZT actuator and laminate ($\varepsilon^i_{r\text{-PZT}} = \varepsilon^i_{r\text{-LMT}} = \varepsilon^i_r$ and $\varepsilon^i_{\theta\text{-PZT}} = \varepsilon^i_{\theta\text{-LMT}} = \varepsilon^i_\theta$, where superscript i denotes variables at the interface), equation (8b) can be rewritten as

$$\sigma^i_{r\text{-PZT}} = \frac{E_{PZT}}{1-\nu^2_{PZT}}[(\varepsilon^i_r + \nu_{PZT}\varepsilon^i_\theta) - (1+\nu_{PZT})d_{31}E_3] \tag{10}$$

Laterally depicted in Fig. 6b, the z axis of the referred polar coordinate system originates from the interface, while h_{neu} denotes the distance between the abscissa plane and the neutral plane of the coupled PZT–laminate. Considering that both the PZT and laminate are thin, lamination theory is applicable, and the through-thickness strain distribution within the laminate and PZT disc can therefore be assumed to be linear

$$\sigma_{r\text{-LMT}} = \frac{\sigma^i_{r\text{-LMT}}}{h_{neu}}(h_{neu}+z), \qquad -h_{LMT} \leqslant z \leqslant 0 \tag{11a}$$

$$\sigma_{r\text{-PZT}} = \frac{1-\nu_{LMT}}{1-\nu_{PZT}}\frac{E_{PZT}}{E_{LMT}}\frac{\sigma^i_{r\text{-LMT}}}{h_{neu}}(h_{neu}+z) - \frac{E_{PZT}}{1-\nu_{PZT}}\Pi, \qquad 0 \leqslant z \leqslant h_{PZT} \tag{11b}$$

as graphically shown in Fig. 6c, where the subscript LMT represents corresponding variables and constants for the laminate.

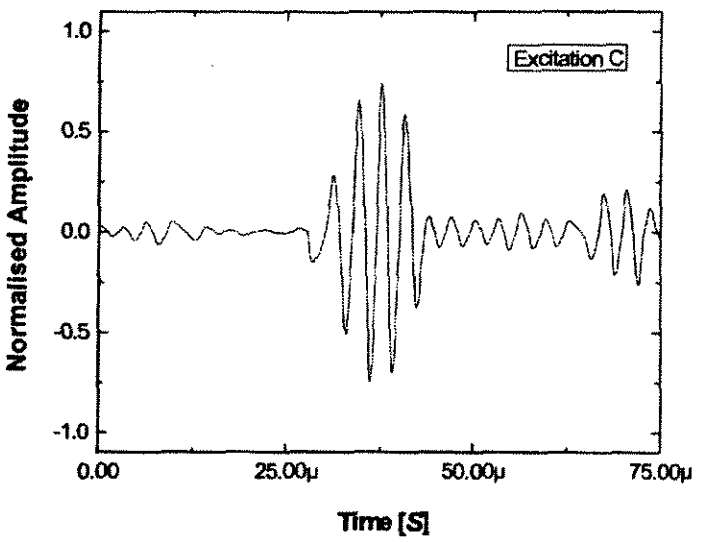

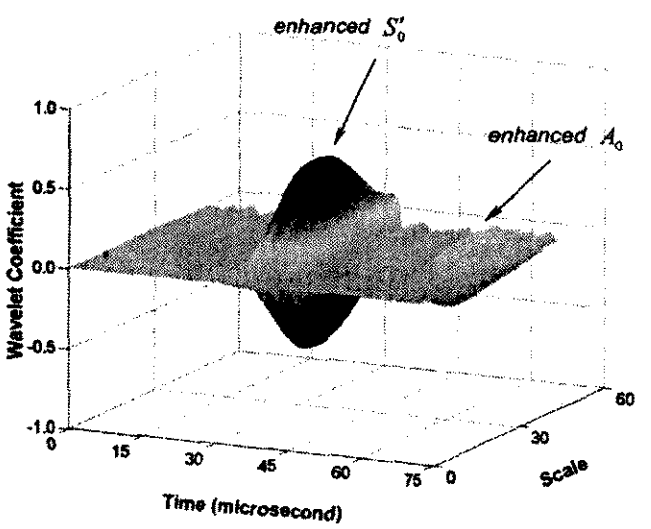

(c)

Fig. 4 (Continued)

Considering the moments and force equilibrium in relation to the neutral plane

$$\int_{-h_{\text{LMT}}}^{0} 2\pi r\sigma_{r\text{-LMT}} z\,\mathrm{d}z + \int_{0}^{h_{\text{PZT}}} 2\pi r\sigma_{r\text{-PZT}} z\,\mathrm{d}z = 0 \tag{12a}$$

$$\int_{-h_{\text{LMT}}}^{0} 2\pi r\sigma_{r\text{-LMT}}\,\mathrm{d}z + \int_{0}^{h_{\text{PZT}}} 2\pi r\sigma_{r\text{-PZT}}\,\mathrm{d}z = 0 \tag{12b}$$

leads to the stresses of the laminate and PZT actuator at the interface

$$\sigma_{r\text{-PZT}}^{i} = \tilde{A}\frac{E_{\text{PZT}}}{E_{\text{LMT}}}\tilde{D}\Pi - \frac{E_{\text{PZT}}}{1-\nu_{\text{PZT}}}\Pi = \tilde{E}\Pi \tag{13a}$$

$$\sigma_{r\text{-LMT}}^{i} = \tilde{D}\Pi \tag{13b}$$

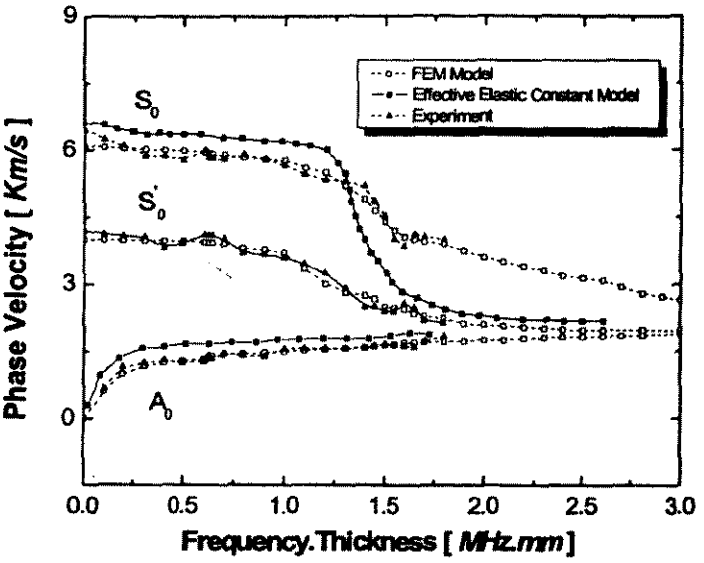

Fig. 5 Dispersive characteristics for generated Lamb waves in a T650/F584 CF/EP quasi-isotropic laminate

where

$$\tilde{A} = \frac{1-\nu_{\text{LMT}}}{1-\nu_{\text{PZT}}}$$

$$\tilde{B} = 2E_{\text{LMT}}E_{\text{PZT}}h_{\text{LMT}}h_{\text{PZT}}(1-\nu_{\text{LMT}}) \times (2h_{\text{LMT}}^2 + 3h_{\text{LMT}}h_{\text{PZT}} + 2h_{\text{PZT}}^2)$$

$$\tilde{C} = \frac{E_{\text{LMT}}^2 h_{\text{LMT}}^4(1-\nu_{\text{PZT}})^2 + E_{\text{PZT}}^2 h_{\text{PZT}}^4(1-\nu_{\text{LMT}})^2}{(1-\nu_{\text{PZT}})}$$

$$\tilde{D} = \frac{E_{\text{LMT}}E_{\text{PZT}}h_{\text{PZT}}(4E_{\text{LMT}}h_{\text{LMT}}^3 + 3E_{\text{LMT}} \times h_{\text{LMT}}^2 h_{\text{PZT}} + \tilde{A}E_{\text{PZT}}h_{\text{PZT}}^3)}{\tilde{B}+\tilde{C}}$$

$$\tilde{E} = \left(\tilde{A}\frac{E_{\text{PZT}}}{E_{\text{LMT}}}\tilde{D} - \frac{E_{\text{PZT}}}{1-\nu_{\text{PZT}}}\right)$$

Substituting equation (13) into equation (8) yields the strain of the PZT actuator at the interface. For a small PZT disc ($\varepsilon_r^i \approx \varepsilon_\theta^i = \varepsilon^i$), the equivalent radial elastic deformation, d_r, along the disc circumference is then achieved by integrating the interface strain

$$d_r = \int_0^R \varepsilon^i\,\mathrm{d}r = R\frac{d_{31}}{h_{\text{PZT}}}\left[\frac{\tilde{E}(1-\nu_{\text{PZT}})}{E_{\text{PZT}}} + 1\right]V \tag{14}$$

This implies that the resultant equivalent radial displacement along the circumference of the PZT actuator is proportional to the applied external voltage, whose scale factor can be determined by equation (14).

4.1.2 *Dual PZT activation*

A similar principle was applied for the case of dual PZT activation. Under these circumstances, the resulting neutral plane for the coupled dual PZT–laminate system was consistent with the neutral plane of the laminate, and the

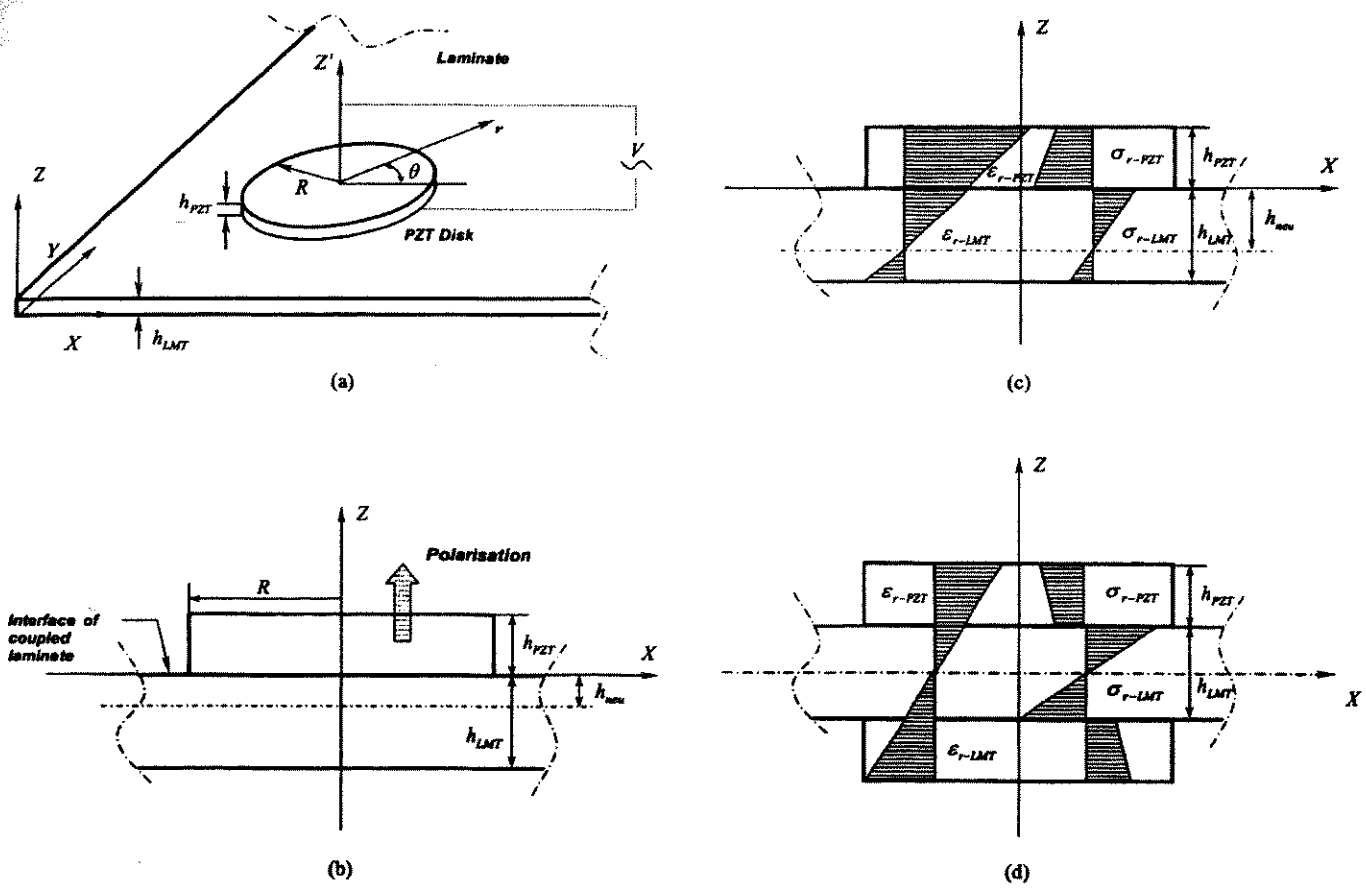

Fig. 6 PZT actuator and sensor model: (a) PZT disc in polar coordinate system; (b) single coupled PZT–laminate system; (c) stress/strain distribution for laminate coupled with single PZT; (d) stress/strain distribution for laminate coupled with double PZT

stress was symmetrically distributed in relation to the neutral plane

$$\sigma_{r\text{-LMT}} = \frac{2\sigma^{i}_{r\text{-LMT}}}{h_{\text{LMT}}} z, \qquad 0 \leqslant z \leqslant \frac{h_{\text{LMT}}}{2} \tag{15a}$$

$$\sigma_{r\text{-PZT}} = \tilde{A}\frac{E_{\text{PZT}}}{E_{\text{LMT}}}\frac{2\sigma^{i}_{r\text{-LMT}}}{h_{\text{LMT}}} z - \frac{E_{\text{PZT}}}{1-\nu_{\text{PZT}}}\Pi, \qquad 0 \leqslant z \leqslant h_{\text{PZT}} \tag{15b}$$

as graphically indicated in Fig. 6d. The equilibrium for moments in relation to the neutral plane is therefore simplified as

$$\int_{0}^{h_{\text{LMT}}/2} 2\pi r\sigma_{r\text{-LMT}} z\,\mathrm{d}z + \int_{h_{\text{LMT}}/2}^{h_{\text{LMT}}/2z+h_{\text{PZT}}} 2\pi r\sigma_{r\text{-PZT}} z\,\mathrm{d}z = 0 \tag{16}$$

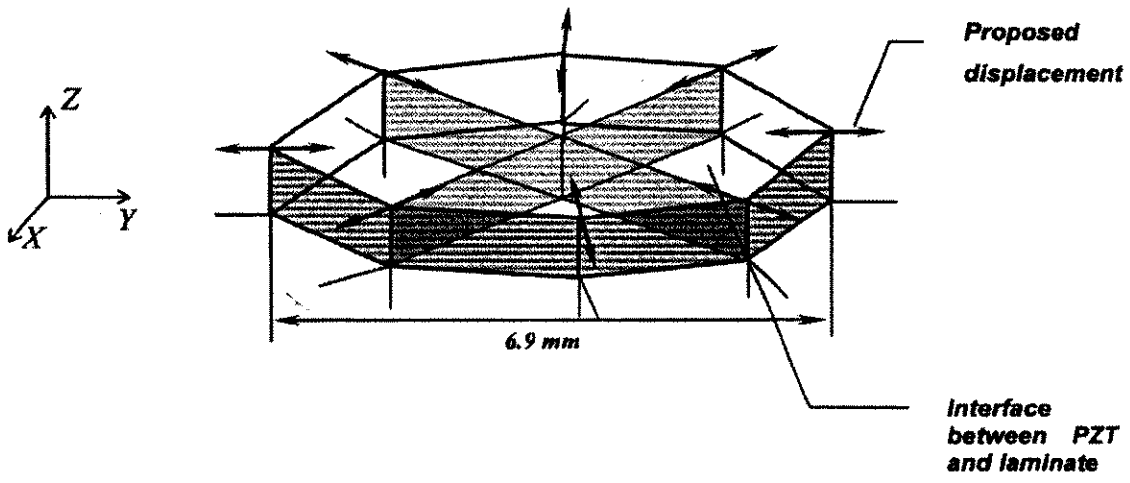

Fig. 7 Actuator model with applied displacement constraints

Table 3 Calculated effective elastic properties of T650/F584 CF/EP lamina

E_{11} (GPa)	E_{22} (GPa)	E_{33} (GPa)	G_{12} (GPa)	G_{13} (GPa)	G_{23} (GPa)	ν_{12}	ν_{13}	ν_{23}
153.67	9.49	9.49	4.26	4.26	3.44	0.295	0.295	0.381

which gives the stress of the laminate at the interface

$$\sigma^i_{r\text{-LMT}} = \tilde{F}V \tag{17}$$

where

$$\tilde{F} = \frac{6d_{31}h_{\text{LMT}}E_{\text{PZT}}(h_{\text{LMT}} + h_{\text{PZT}})}{(1-\nu_{\text{PZT}})[h^3_{\text{LMT}} + 2\tilde{A}(E_{\text{PZT}}/E_{\text{LMT}}) \times h_{\text{PZT}}(3h^2_{\text{LMT}} + 4h^2_{\text{PZT}} + 6h_{\text{LMT}}h_{\text{PZT}})]}$$

Substituting equation (17) into equation (15a) and integrating the strain at the interface results in

$$d_r = \int_0^R \varepsilon^i \, \mathrm{d}r = \tilde{F}\frac{R(1-\nu_{\text{LMT}})}{E_{\text{LMT}}}V \tag{18}$$

Serving a similar function to equation (14), equation (18) determines the scale proportional factor for activation using dual PZTs.

Based on equations (14) and (18), actuator models were consequently developed, shown in Fig. 7, with which Lamb

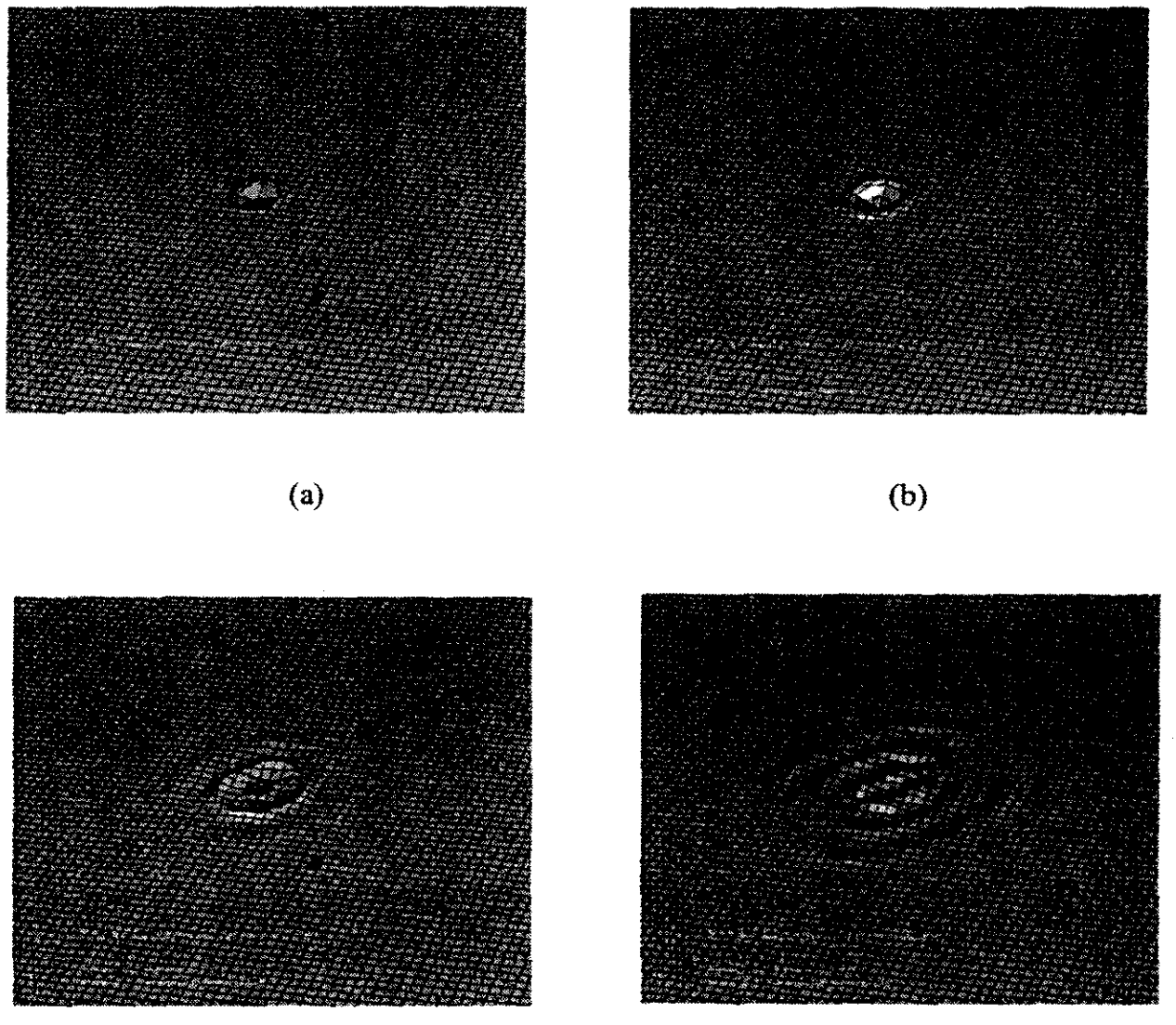

Fig. 8 Active Lamb wave in the CF/EP composite laminate generated by control circuit: (a) at 1.5 ms; (b) at 6 ms; (c) at 7.5 ms; (d) at 10 ms

were generated by applying uniform radial displacement straints in the x–y plane, in correlation with the excitation ual voltages, to simulate excitation case A, or by individu- ly applying in-phase or out-phase constraints in the dual PZT configuration to emulate excitation cases B or C.

4.2 Sensor model

The model for the PZT sensor was created in parallel. Considering the deformation in the x'–y' plane only, the constitutive relation, equation (7), for a PZT sensor of radius R and thickness h_{PZT} can be simplified in its local polar coordinate system r'–θ'–z', in the absence of external electric fields, as [41]

$$Q = d_{31}(\sigma_{r'} + \sigma_{\theta'}) = \frac{d_{31}E_{PZT}}{1 - \nu_{PZT}}(\varepsilon_{r'} + \varepsilon_{\theta'}) \tag{19}$$

where r' and θ' are the local polar coordinates. On the other hand, the electric charges, Θ, accumulated on both surfaces of the PZT sensor can be defined in terms of the externally applied voltage as

$$\Theta = \frac{1}{4\pi}\int\int\int \nabla Q \, dV \tag{20}$$

Substituting equation (19) into equation (20) and applying Gauss' theorem leads to [41]

$$\Theta = \frac{d_{31}E_{PZT}}{4\pi(1 - \nu_{PZT})}\int\int(\varepsilon_{r'} + \varepsilon_{\theta'})r' \, dr' \, d\theta' \tag{21}$$

Regarded as a capacitor of capacitance C, the PZT sensor induces the output voltage, V_{otp}, under the deformation

$$V_{otp} = \frac{\Theta}{C} = \frac{\Theta h_{PZT}}{\pi K_3 p_0 R^2} \tag{22}$$

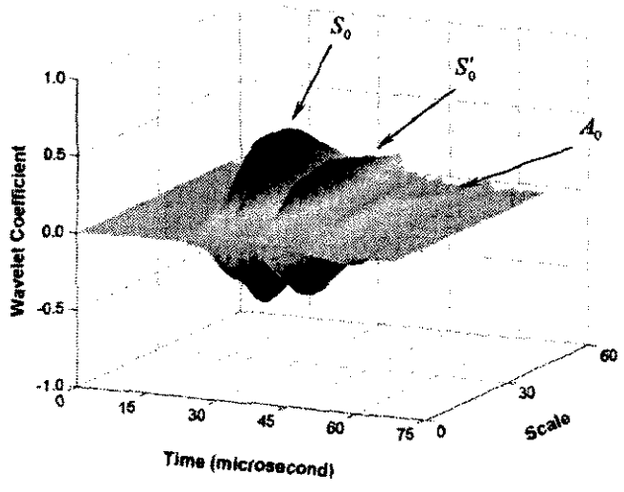

(a)

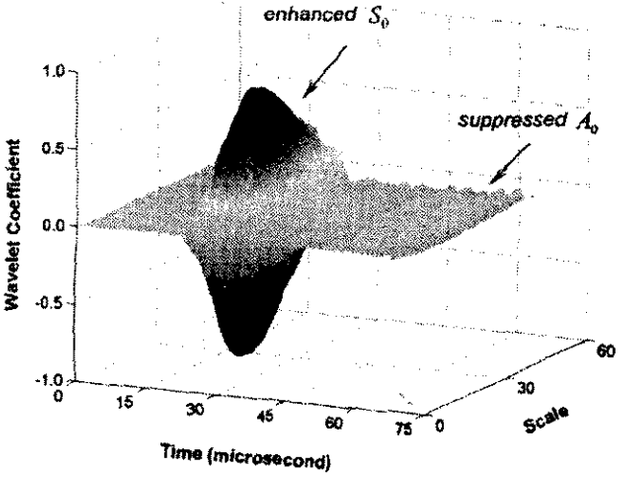

(b)

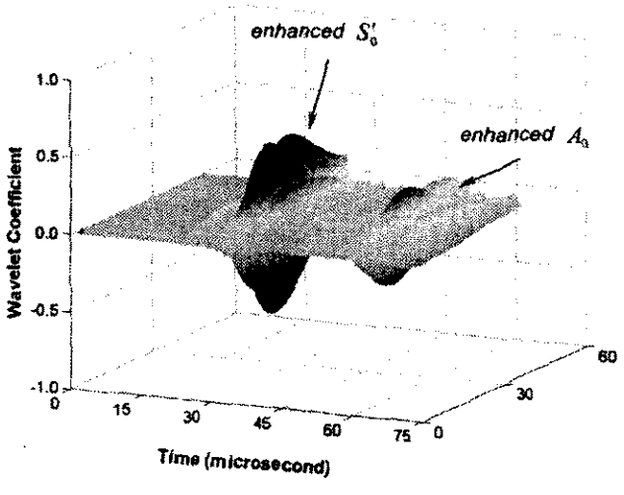

(c)

Fig. 9 Energy distribution spectrum for selectively generated Lamb modes (from FEM simulation): (a) excitation case A; (b) excitation case B; (c) excitation case C

where K_3 and p_0 represent the relative dielectric constant and the dielectric permittivity of a free PZT sensor respectively (Table 1). Combining equations (21) and (22) yields

$$V_{otp} = \frac{d_{31}E_{PZT}h_{PZT}}{4\pi K_3 p_0 R^2(1-\nu_{PZT})}\int\int(\varepsilon_{r'}+\varepsilon_{\theta'})r'\mathrm{d}r'\mathrm{d}\theta' \quad (23)$$

Compared with the laminate, the PZT sensor is geometrically small ($\varepsilon_{r'} \approx \varepsilon_{\theta'} \approx \varepsilon_{cen}$, where ε_{cen} is the strain at the centre of the PZT disc), and equation (23) can accordingly be simplified as [41]

$$V_{otp} = \tilde{G}\varepsilon_{cen} \quad (24)$$

where

$$\tilde{G} = \frac{d_{31}E_{PZT}h_{PZT}}{4\pi K_3\varepsilon_0(1-\nu_{PZT})}$$

This indicates that the output voltage for a PZT sensor, induced by geometrical deformation, is directly proportional to the central strain of the PZT sensor with a factor $\tilde{G}$. Based on equation (24), the PZT sensor output responses, in the form of induced output voltage, were achieved by the sensor model through calculating the strain at the PZT sensor centre.

4.3 Numerical simulation

Using the developed PZT actuator and sensor models, three-dimensional dynamic FEM simulation was accomplished employing ABAQUS/EXPLICIT® code. The relevant properties for the piezoelectric element can be found in Table 1. An eight-layer $[45/-45/0/90]_s$ CF/EP quasi-isotropic composite laminate (T650/F584) was modelled using eight-node solid brick elements with effective elastic properties,

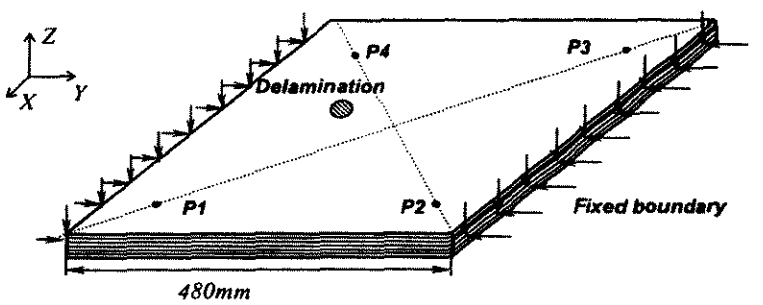

(a)

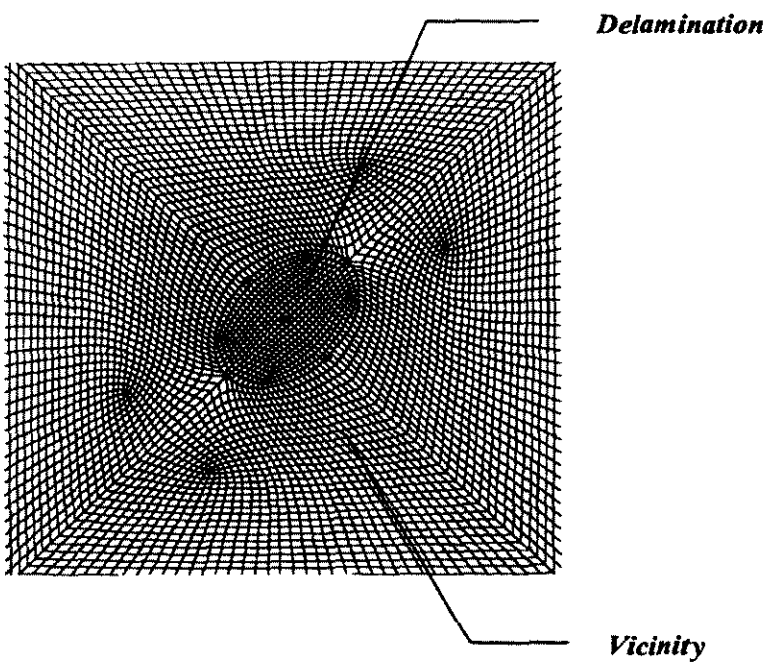

(b)

Fig. 10 Instrumented CF/EP laminate containing a delamination: (a) schematic description; (b) FEM model for vicinity of delamination

calculated using classical laminate theory from those of the unidirectional lamina [35], in Table 3, obtained from a micromechanics model [42].

Actively generated by the actuator model, visualized wave propagation from three-dimensional dynamic FEM simulations in the selected composite laminate at several representative times is plotted in Fig. 8. The energy allocations in the time-scale domain for signals numerically calculated for individual excitation cases (cases A, B and C) in accordance with experiments are compared in Fig. 9. Similar energy allocation (characteristic time and energy distribution) between the experimental measurements (Fig. 4) and numerical simulations (Fig. 9) can be observed upon application of the developed signal processing algorithm.

5 LAMB WAVE PROPAGATION IN DEFECTIVE LAMINATES

5.1 Specimen preparations and experimentation

Schematically depicted in Fig. 10a, two eight-layer [45/-45/0/90]$_s$ CF/EP quasi-isotropic laminates (T650/F584) with a pair of clamped edges, shaped at 480 mm × 480 mm × 1.275 mm, were manufactured using a unidirectional (UD) prepreg (Table 3) in an autoclave at 180 °C under 600 kPa pressure. In one laminate, an artificial delamination was introduced by inserting two elliptic UPLEX©-R-25 films (thickness 25 μm) between the first and the second layers (semi-major axis: 15 mm, semi-minor axis: 10 mm, angle

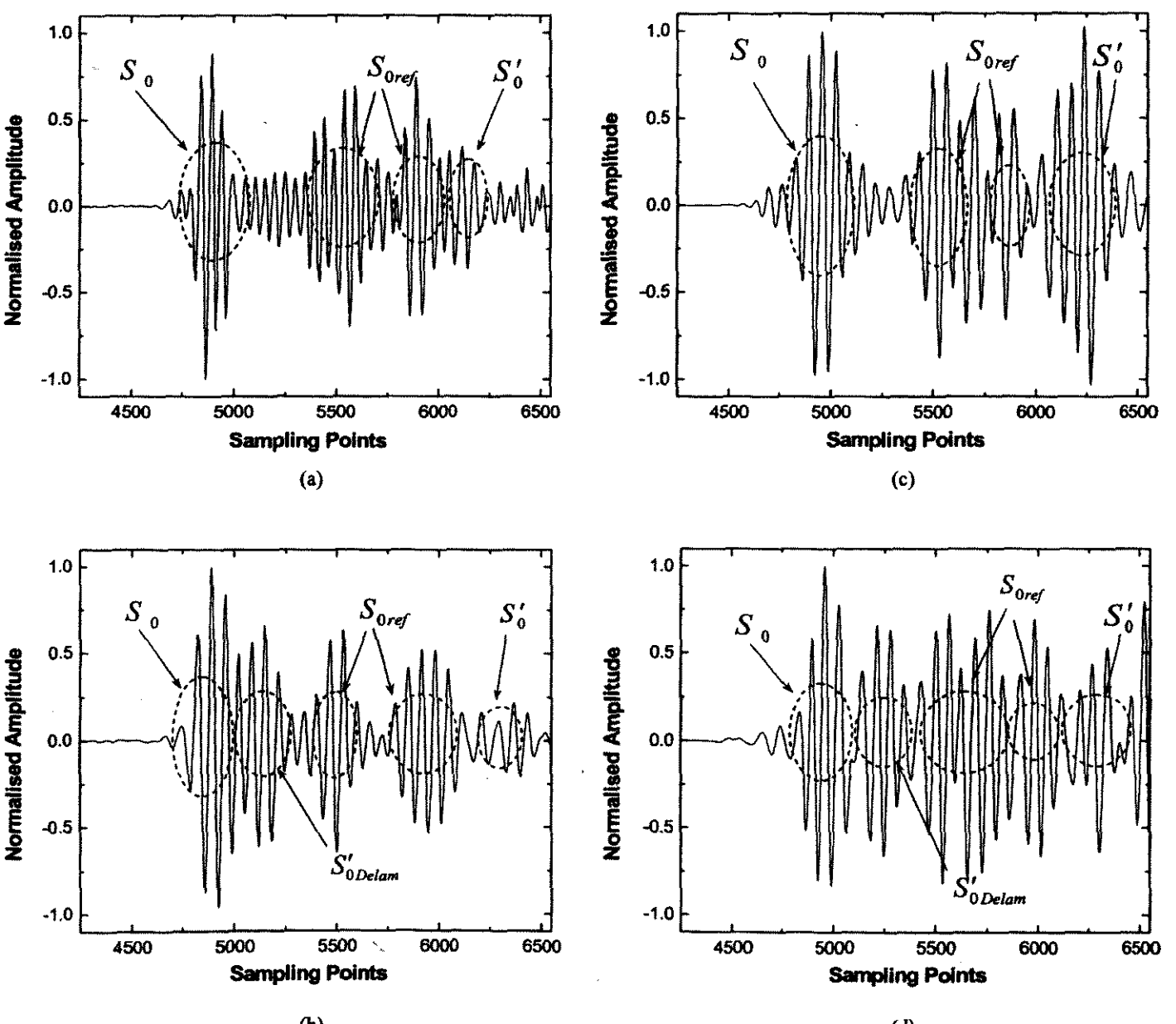

Fig. 11 DWT analysis processed signal acquired via actuator–sensor path P1–P3: (a) benchmark laminate from experiment; (b) delaminated laminate from experiment; (c) benchmark laminate from simulation; (d) delaminated laminate from simulation

between the major axis and 0° fibre direction: 135°, centre position: 276 and 299 mm away from the left and bottom edges of the laminate respectively). Another laminate was kept defect free as a benchmark for comparison. Four piezoelectric (PZT) discs, acting as both actuators and sensors, were bonded on the upper surface of each laminate, 65 mm away from the two neighbouring laminate edges and numbered counterclockwise P1, P2, P3 and P4 from the bottom left one. A diagnostic Lamb wave at the central excitation frequency of 0.5 MHz was activated by the designed control circuit. Signal acquisition was accomplished by an active online damage diagnosis system developed in a previous study [34].

5.2 Signal interpretation

The acquired signals were then identified using the signal processing algorithm described in section 3.2. The DWT-filtered wave signals for the benchmark and defective laminates, experimentally acquired through one actuator–sensor path P1–P3, corresponding to the incident excitation frequency, are displayed in Fig. 11a and b respectively. Their relevant energy allocation spectra in the time-scale domain are compared in Fig. 12. The fundamental symmetric Lamb mode, S_0, and basic shear mode, S_0', together with the reflected components from the boundaries, denoted by $S_{0\text{ref}}$, can be observed for both benchmark and delaminated

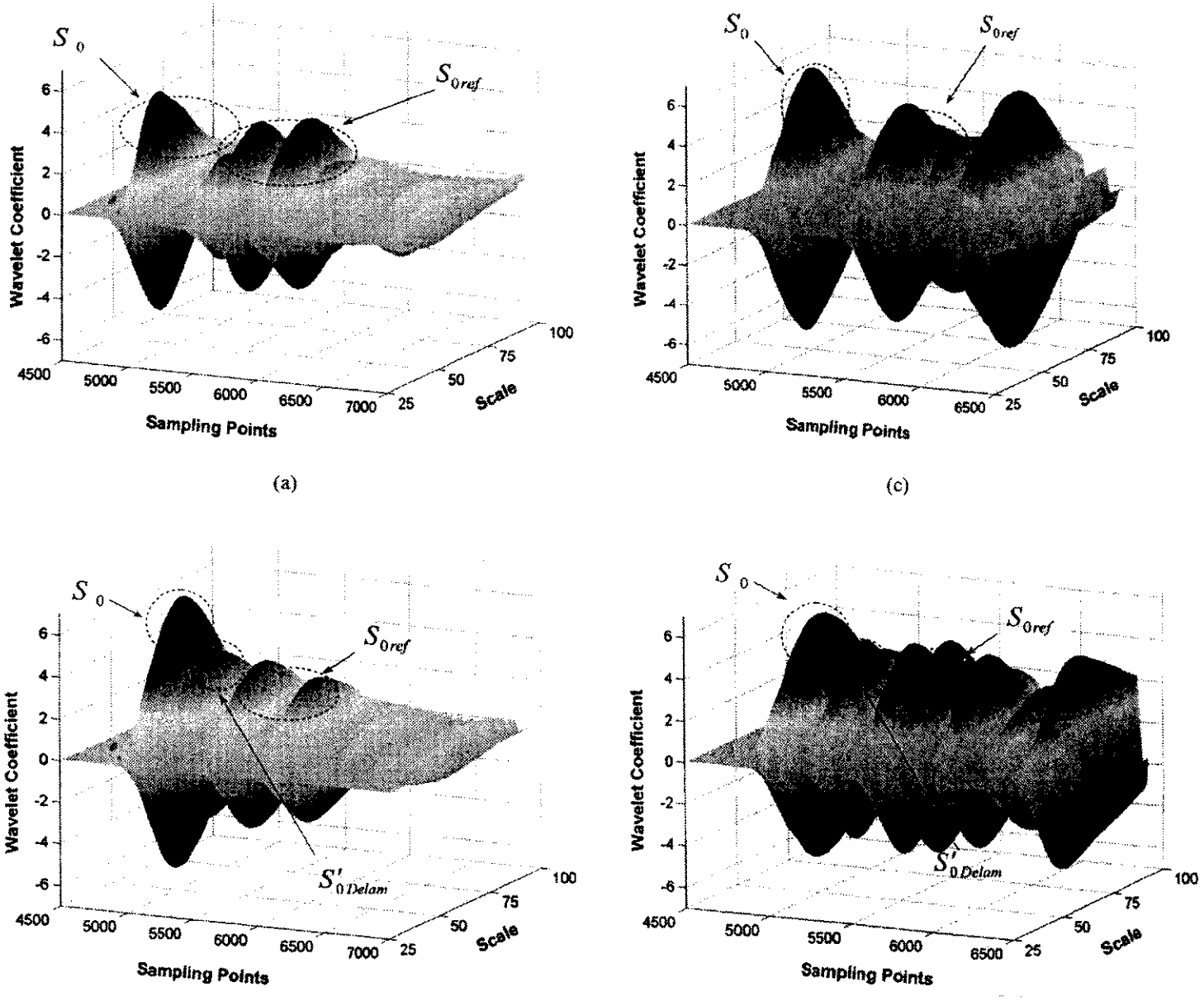

Fig. 12 Wave energy spectra for signal acquired via actuator–sensor path P1–P3: (a) benchmark laminate from experiment; (b) delaminated laminate from experiment; (c) benchmark laminate from simulation; (d) delaminated laminate from simulation

laminates. Compared with the benchmark laminate, extra wave components between S_0 and S_{0ref} are detected in Figs 11b and 12b, which are recognized as the delamination-induced basic shear mode, denoted by S'_{0Delam}. Based on the spectrographic analyses, the quantitative damage prediction can be fulfilled by capturing the variation in the energy spectra using a searching algorithm based on the artificial neural network technique, detailed in other work by the present authors [35].

For substantiation, FEM simulations were conducted in parallel. A previously developed modelling technique for the laminated CF/EP composite structures containing delamination [43] was employed. The FEM model for the vicinity of the delaminated area in the defective laminate is shown in Fig. 10b. The corresponding filtered signal and energy spectra are compared in Figs 11c and 12c for benchmark laminates and in Figs 11d and 12d for delaminated laminates. Good correlation, particularly the characteristic time and frequency for wave energy concentration in both time and time-scale spaces, was found between the numerical simulations and experimental measurements upon application of the proposed signal processing algorithm.

6 CONCLUSION

The practical utilization of Lamb waves for NDI purposes may be impeded by their complicated multimode and dispersive nature. An approach for active generation of selective Lamb wave modes in a CF/EP composite laminate was designed, by which the desirable single symmetric and antisymmetric modes can be individually stimulated. A signal processing and identification algorithm was devised using wavelet transform techniques in order to assist the filtration and interpretation of signal characteristics. Modelling techniques for PZT actuators and sensors were established and applied for the numerical simulation of Lamb wave generation and propagation in the chosen composite laminates. Good agreement between experimentation and FEM prediction has been achieved. The methodology was then implemented to investigate the propagation characteristics of Lamb waves in flawless and delaminated composite laminates. The results show that the utilization of Lamb waves and the interpretation of wave signals can be considerably facilitated by enhancing or suppressing certain Lamb modes via the proposed approach.

ACKNOWLEDGEMENTS

Z. Su would like to thank the Department of Education Science and Training (DEST), Australia for the financial support of an International Postgraduate Research Scholarship (IPRS), and the University of Sydney for an International Postgraduate Award (IPA).

REFERENCES

1 **Worlton, D. C.** Experimental confirmation of Lamb waves at megacycle frequencies. *J. Appl. Phys.*, 1961, **32**, 967–971.
2 **Lowe, M. J. S.** Matrix techniques for modeling ultrasonic waves in multilayered media. *IEEE Trans. Ultrasonics, Ferroelectrics and Freq. Control*, 1995, **42**, 525–541.
3 **Habeger, C. C., Mann, R. W.** and **Baum, G. A.** Ultrasonic plate waves in paper. *Ultrasonics*, 1979, **17**, 57–62.
4 **Percival, W. J.** and **Birt, E. A.** A study of Lamb wave propagation in carbon-fibre composites. *Insight*, 1997, **39**, 728–735.
5 **Alleyne, D. N.** and **Cawley, P.** The interaction of Lamb waves with defects. *IEEE Trans. Ultrasonics, Ferroelectrics and Freq. Control*, 1992, **39**, 381–397.
6 **Guo, N.** and **Cawley, P.** The interaction of Lamb waves with delamination in composite laminates. *J. Acoust. Soc. Am.*, 1993, **94**, 2240–2246.
7 **Guo, N.** and **Cawley, P.** Lamb wave propagation in composites and its relationship with acousto-ultrasonics. *NDT & E Int.*, 1993, **26**, 75–84.
8 **Guo, N.** and **Cawley, P.** Lamb wave reflection for the quick nondestructive evaluation of large composite laminates. *Mater. Evaluation*, 1994, **52**, 404–411.
9 **Birt, E. A.** Damage detection in carbon-fibre composites using ultrasonic Lamb waves. *Insight*, 1998, **40**, 335–339.
10 **Alleyne, D. N.** and **Cawley, P.** Optimisation of Lamb wave inspection techniques. *NDT & Int.*, 1992, **25**, 11–22.
11 **Wang, C. S.** and **Chang, F.-K.** Built-in diagnostics for impact damage identification of composite structures. In *Structural Health Monitoring* (Ed. F. -K. Chang), 2nd edition, 1999, pp. 612–621 (Technomic, Lancaster).
12 **Keilers Jr, C. H.** and **Chang, F.-K.** Identifying delamination in composite beams using built-in piezoelectrics. Part II: an identification method. *J. Intell. Mater. Syst. and Struct.*, 1995, **6**, 664–672.
13 **Dupont, M., Osmont, D., Gouyon, R.** and **Balageas, D. L.** Permanent monitoring of damaging impacts by a piezoelectric sensor based integrated system. In *Structural Health Monitoring* (Ed. F.-K. Chang), 2nd edition, 1999, pp. 561–570 (Technomic, Lancaster).
14 **Lemistre, M. B.** and **Balageas, D. L.** A new concept for structural health monitoring applied to composite materials. In Proceedings of the 1st European Workshop on *Structural Health Monitoring* (Ed. D. Balageas), France, Paris, 10–12 July 2002, pp. 493–507.
15 **Tan, K. S., Guo, N., Wong, B. S.** and **Tui, C. G.** Experimental evaluation of delaminations in composite plates by the use of Lamb waves. *Composites Sci. and Technol.*, 1995, **53**, 77–84.
16 **Tan, K. S., Guo, N., Wong, B. S.** and **Tui, C. G.** Comparison of Lamb waves and pulse echo in detection of near-surface defects in laminate plates. *NDT & E Int.*, 1995, **28**, 215–223.
17 **Bindal, V. N.** *Transducers for Ultrasonic Flaw Detection*, 1999 (Narosa Publishing House, New Delhi).
18 **Castaings, M.** and **Cawley, P.** The generation, propagation, and detection of Lamb waves in plates using air-coupled ultrasonic transducers. *J. Acoust. Soc. Am.*, 1996, **100**, 3070–3077.
19 **Hosten, B., Castaings, M., Tretout, H.** and **Vollaume, H.** Identification of composite materials elastic moduli from Lamb wave velocities measured with single sided, contactless ultrasonic method. In *Review of Progress in Quantitative Nondestructive Evaluation* (Eds D. O. Thompson and D. E. Chimenti), 2001, Vol. 20B, pp. 1023–1030 (Plenum, New York).

20 **Ghosh, T., Kundu, T.** and **Karpur, P.** Efficient use of Lamb modes for detecting defects in large plates. *Ultrasonics*, 1998, **36**, 791–801.

21 **Guo, Z., Achenbach, J. D.** and **Krishnaswamy, S.** EMAT generation and laser detection of single Lamb wave modes. *Ultrasonics*, 1997, **35**, 423–429.

22 **Legendre, S., Massicotte, D., Goyette, J.** and **Bose, T. K.** Wavelet-transform-based method of analysis for Lamb-wave ultrasonic NDE signals. *J. IEEE Trans. Instrum. and Measmt*, 2000, **49**, 524–530.

23 **Achenbach, J. D.** Quantitative nondestructive evaluation. *Int. J. Solids and Struct.*, 2000, **37**, 13–27.

24 **Yoshimura, S., Yagawa, G., Oishi, A.** and **Yamada, K.** Neural network based inverse analysis for defect identification with laser ultrasonics. *Key Engng Mater.*, 1998, **145–149**, 443–452.

25 **Niethammer, M., Jacobs, L. J., Qu, J.** and **Jarzynski, J.** Time–frequency representations of Lamb waves. *J. Acoust. Soc. Am.*, 2001, **109**, 1841–1847.

26 **Ishak, S. I., Liu, G. R., Shang, H. M.** and **Lim, S. P.** Locating and sizing of delamination in composite laminates using computational and experimental methods. *Composites: Part B*, 2001, **32**, 287–298.

27 **Valle, C.** and **Littles Jr, J. W.** Flaw localization using the reassigned spectrogram on laser-generated and detected Lamb modes. *Ultrasonics*, 2002, **39**, 535–542.

28 **Monkhouse, R. S. C., Wilcox, P. W.** and **Cawley, P.** Flexible interdigital PVDF transducers for the generation of Lamb waves in structures. *Ultrasonics*, 1997, **35**, 489–498.

29 **Blanas, P.** and **Das-Gupta, D. K.** Composite piezoelectric sensors for smart composite structures. In Proceedings of 10th International Symposium on *Electrets*, Athens, Greece, 22–24 September 1999, pp. 731–734.

30 **Monkhouse, R. S. C., Wilcox, P. W., Lowe, M. J. S., Dalton, R. P.** and **Cawley, P.** The rapid monitoring of structures using interdigital Lamb wave transducers. *Smart Mater. and Struct.*, 2000, **9**, 304–309.

31 **Gaul, L.** and **Hurlebaus, S.** Wavelet-transform to identify the location and forces-time-history of transient load in a plate. In *Structural Health Monitoring* (Ed. F.-K. Chang), 2nd edition, 1999, pp. 851–860 (Technomic, Lancaster).

32 **Lemistre, M.** and **Balageas, D.** Structural health monitoring system based on diffracted Lamb wave analysis by multiresolution processing. *Smart Mater. and Struct.*, 2001, **10**, 504–511.

33 **Su, Z., Ye, L.** and **Bu, X.** Quantitative assessment of structural damage by impact response. Accepted by *Structural Health Monitoring*.

34 **Su, Z.** and **Ye, L.** A damage identification technique for CF/EP composite laminates using distributed piezoelectric transducers. *Composite Struct.*, 2002, **57**, 465–471.

35 **Su, Z.** and **Ye, L.** Lamb wave propagation-based damage identification for quasi-isotropic composite laminates using artificial neural algorithm. Part II: implementation and validation. Submitted to *J. Intell. Mater. Syst. and Struct.*

36 **Schulz, M. J., Pai, P. F.** and **Inman, D. J.** Health monitoring and active control of composite structures using piezoceramic patches. *Composites: Part B*, 1999, **30**, 713–725.

37 **Kessler, S. S., Spearing, S. M.** and **Atalla, M. J.** In-situ damage detection of composites structures using Lamb wave. In Proceedings of 1st European Workshop on *Structural Health Monitoring* (Ed. D. Balageas), Paris, France, 10–12 July 2002, pp. 374–381.

38 **Boashash, B.** *Time-Frequency Signal Analysis*, 1992 (Longman Cheshire, Melbourne).

39 **Flandrin, P.** *Time-Frequency/Time-scale Analysis*, 1999 (Academic Press, San-Diego).

40 *Wavelet Toolbox: For Use with Matlab (User's Guide). Ver.1.0*, 2002 (The Mathworks, Inc.).

41 **Lin, X.** and **Yuan, F. G.** Diagnostic Lamb waves in an integrated piezoelectric sensor/actuator plate: analytical and experimental studies. *Smart Mater. and Struct.*, 2001, **10**, 907–913.

42 **Gommers, B., Verpoest, I.** and **Houtte, P. V.** Modelling the elastic properties of knitted-fabric-reinforced composites. *Composites Sci. and Technol.*, 1996, **56**, 685–694.

43 **Su, Z., Ye, L.** and **Bu, X.** Evaluation of delamination in laminated composites based on Lamb wave modes: FEM simulation and experimental verification. In Proceedings of 1st European Workshop on *Structural Health Monitoring* (Ed. D. Balageas), Paris, France, 10–12 July 2002, pp. 328–335.

ELSEVIER

Composite Structures 57 (2002) 465–471

COMPOSITE STRUCTURES

www.elsevier.com/locate/compstruct

A damage identification technique for CF/EP composite laminates using distributed piezoelectric transducers

Zhongqing Su [a], Lin Ye [a,*], Xiongzhu Bu [a,b]

[a] *Centre for Advanced Materials Technology (CAMT), School of Aerospace Mechanical and Mechatronic Engineering, The University of Sydney, Building J07, Sydney, NSW 2006, Australia*

[b] *School of Mechanical Engineering, Nanjing University of Science and Technology, 210094, China*

Abstract

In this study, a damage identification approach was developed for carbon fibre/epoxy composite laminates with localized internal delamination. Propagation of the Lamb wave in laminates and its interaction with the delamination were examined. The fundamental symmetric Lamb wave mode, S_0, and the lowest order shear wave mode, S_0', were chosen to predict damage location. A real-time active diagnosis system was therefore established. This technique uses distributed piezoelectric transducers to generate and monitor the ultrasonic Lamb wave with narrowband frequency. The two-way switches were employed to minimize the number of transducers. A signal-processing scheme based on the time–frequency spectrographic analysis was utilised to extract useful diagnostic information. Also, an optimal identification method was applied on damage searching procedure to reduce errors and obtain the diagnostic results promptly. Experiments were conducted on $[0/-45/45/90]_s$ CF/EP laminates to verify this diagnosis system. The results obtained show that satisfactory detection accuracy could be achieved.

Keywords: Structural health monitoring; Fibre-reinforced composite; Lamb wave; Signal processing; Smart structures

1. Introduction

Impact-induced damage is perhaps one of the most common defectives in carbon fibre reinforced composite laminates, which may result in a substantial impairment of structural integrity. Delamination, the most familiar impact damage in composite structures, plays a major role in inhibiting the further widespread application of laminated composites in practice. Particularly, its location and extent are of vital difficulty to predict in most cases. In the past two decades, both researchers and engineers have been pursuing effective techniques to detect the occurrence of delamination and to estimate its position at the early stage so as to reduce the risk of further catastrophic failure. Recently, vast of research indicates that non-destructive evaluation techniques based on the Lamb wave propagation offer one possible solution to this concern [1–11].

The Lamb wave in ultrasonic domain has the ability to propagate a relatively long distance in laminated composites, and a wide section can therefore be interrogated with a small number of transducers. In addition, the appearance of Lamb wave-caused interlaminar stresses makes the detection through the entire laminate thickness applicable, which affords a potential to detect the internal defects as well as the surface defects. For example, Tang and Henneke [1] proposed a monitoring technique for the stiffness reduction in laminated composite plates based on the Lamb wave; Guo and Cawley [2,3] examined the interaction between the ultrasonic Lamb wave and the delamination in terms of both numerical and experimental approaches; Tan et al. [4] developed a damage detection method for composites using ultrasonic probes. In most approaches, probes were usually used for the generation and collection of the Lamb wave due to good accessibility, with which the damage identification can be fulfilled conveniently and accurately. However, in most circumstances, a temporary out-of-service of the structure is required, ensuring the function of probes. As know, this confines the further application for on-line damage diagnosis. On the other hand, the advanced composite structures in aerospace industry are expected to be involved with built-in actuator/sensor networks to enhance the performance

* Corresponding author. Tel.: +61-2-9351-4798; fax: +61-2-9351-3760.

E-mail address: ye@aeromech.usyd.edu.au (L. Ye).

0263-8223/02/$ - see front matter
PII: S0263-8223(02)00115-0

and to reduce the operation and maintenance costs. For this target, innovations have been made in the past few years, in which piezoelectric elements instead of conventional probes are employed directly to facilitate a simple and reliable on-line damage detection with low expenditure. Wang and Chang [5] discussed the damage detection technique based on the Lamb wave generated by ultrasonic transmitter, and Lemistre et al. [6] reported a structural defect identification method using piezoelectrics.

The present work aims at developing a practical and effective real-time damage identification technique for CF/EP composite laminates, with which the structural health status can be in-service monitored. In this study, distributed piezoelectrics were involved into the structure during manufacturing to minimize the interference on the structural integrity. In correlation with the study on the propagation characteristics of Lamb wave in composites, a diagnosis system was developed. The feasibility of this system was then verified by applying it to quasi-isotropic laminates for the locating of delamination.

2. Characteristics of the Lamb wave in composites

Compared with the components produced by ultrasonic probes, the Lamb wave generated by the fixed piezoelectrics unavoidably contains multi-modes in plate-like laminated structure simultaneously due to the exclusive attenuation mechanism, which can be basically divided into two categories depending on the particulate motion, viz. symmetrical and asymmetrical modes. Additionally, the vibrational patterns and dispersive properties through the plate thickness are not identical for each mode, even for the same mode but in the different frequency domains, making the study for Lamb wave more intractable. Percival and Birt [7] verified that the dispersive characteristics of Lamb wave depend on both the plate thickness and frequency. In their study, an inhouse FEM software and a numerical simulation approach based on the effective elastic properties were developed to calculate the dispersive curves for typical composite laminates.

In this work, the propagation of Lamb wave in $[0/-45/45/90]_s$ quasi-isotropic CF/EP laminates within the frequency domain, ranging from 0.05 to 1.5 MHz, was investigated first. Four piezoelectric transducers were fixed on the laminates to establish 6 pairs of totally 12 actuator-sensor paths in order to characterise the wave velocity for different modes. The dispersive curve experimentally measured is plotted in Fig. 1, while the curve theoretically calculated by FEM [8] is also comparatively displayed, denoted by triangle and square symbols respectively. In Fig. 1, the fundamental asymmetric Lamb mode, A_0, symmetric Lamb mode, S_0, and

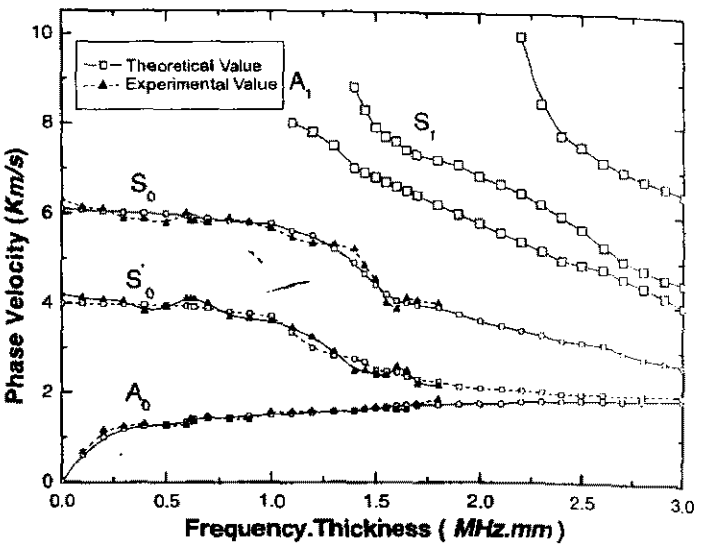

Fig. 1. The dispersive curve for quasi-isotropic CF/EP laminates.

the lowest order SH (shear mode) wave mode, S'_0, can be observed in low frequency region, while the higher order modes appear gradually with an increase of frequency. The dispersive curve implies that at least two Lamb modes are available synchronously and their phase/group velocity is dependent on the algebraic product of the laminate thickness and the mode central frequency. Nevertheless, a low-frequency domain (<1.0 MHz mm) can be noticed in the dispersive curve, where the fundamental Lamb wave modes and the lowest order shear wave mode exhibit reasonably non-dispersive behavior. In this research, the fundamental symmetric Lamb mode, S_0, and the internal defect-induced lowest order SH mode, S'_0, are utilised for the diagnosis.

3. Configuration of experiment

An active real-time diagnosis system was developed in this work, whose schematic description is given in Fig. 2. In this system, piezoelectric lead zirconate titanate (PZT) wafers (ϕ: 6.9 mm, thickness: 0.5 mm) acted as both actuators and sensors with the aid of two-way switches. *Agilent® E1441* arbitrary waveform generator was used to produce 5-cycle toneburst with *Hanning* window at a central frequency of 0.5 MHz. The simulated diagnostic signal was then applied on each PZT wafer after amplified with the PZT amplifier (*PiezoSys® EPA-104*) to generate ultrasonic Lamb wave. Response signals were conditioned by *Agilent® E3242A* and acquired via *E1437A* digitizer at a sampling rate of 20.48 MHz; Sampled signals were transmitted into the central control unit (CCU) for further analyses; All the diagnosis control and signal analyses were performed by CCU, supported on the *NI Labview©* and *Matlab©* platforms.

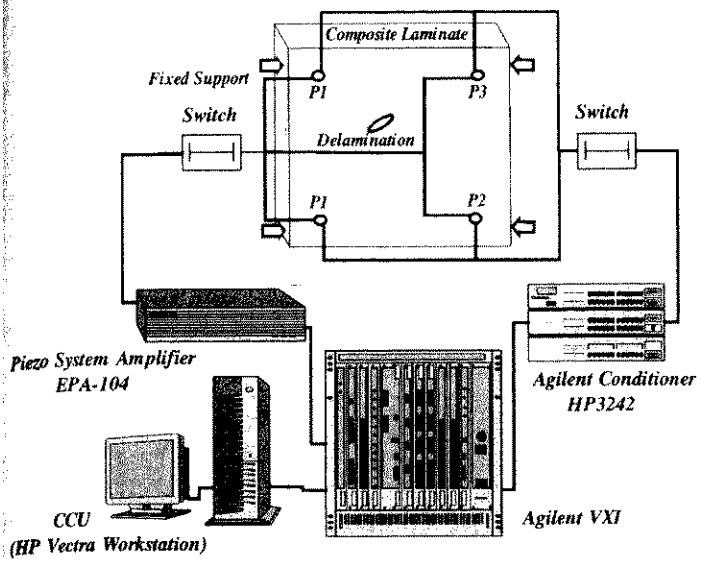

Fig. 2. Configuration of proposed diagnosis system.

The validity of this system was then verified by applying it to $[0/-45/45/90]_s$ CF/EP laminates (*HEXCEL© F854*). For comparison, two laminates ($480 \times 480 \times 1.275$ mm^3) without/with pre-treated internal defect were manufactured, which are hereafter recognised as the benchmark laminate and the defective laminate. An elliptic *UPLEX©-R*-25 film (thickness: 25 μm, semi-major axis: 15 mm, semi-minor axis: 10 mm, angle between semi-major axis and 0° fibre direction: 135°) was inserted at interfaces between the 1st and the 2nd layer, simulating the common impact-induced delamination. The centre of the artificial delamination lies 276 and 299 mm respectively away from the left edge and bottom edge of the laminates. Response signals were sampled for each actuator-sensor path in experiment.

In Fig. 2, four PZT wafers are denoted counterclockwise by *P1*, *P2*, *P3* and *P4* respectively from the bottom-left one. Each transducer locates 65 mm away from two neighboring edges. Thus, totally 12 pairs of actuator-sensor path are theoretically available. In experiment, each laminate was fixed-supported on one pair of its parallel edges while another pair was free.

4. Signal processing and damage diagnosis

Sampling signals for the benchmark laminate and the defective laminate via actuator-sensor paths *P1–P3* and *P2–P4*, as typical paradigms, are displayed in Figs. 3 and 4, respectively. Containing the structural vibration components and diverse bandwidth noises, the acquired raw signals can hardly be used directly for the diagnosis. Wavelet transform-based time–frequency spectrographic analyses were employed to extract the useful diagnostic information [12–18]. In this study, both the discrete wavelet transform (DWT) analysis and continuous wavelet transform (CWT) analysis were performed for the signal processing to effectively diminish the influence of broadband noises. *Daubechies* function $\Psi(a,b)$ at level 4 (*db4*) was chosen as the transform function and applied with the CWT transform [14],

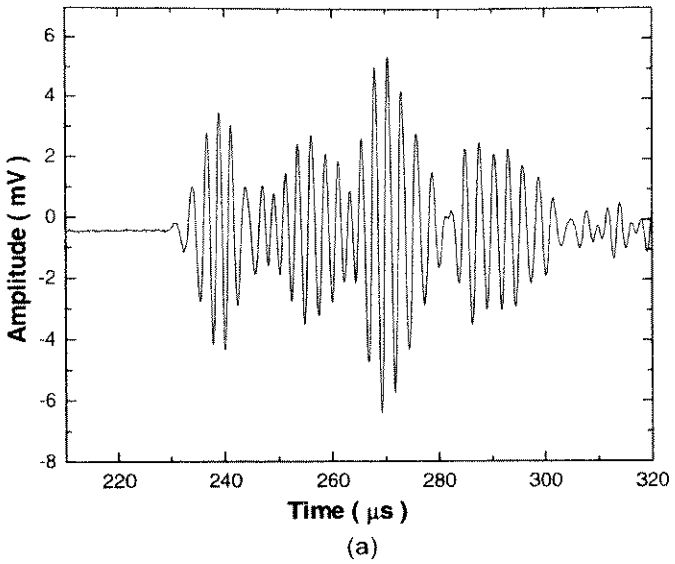

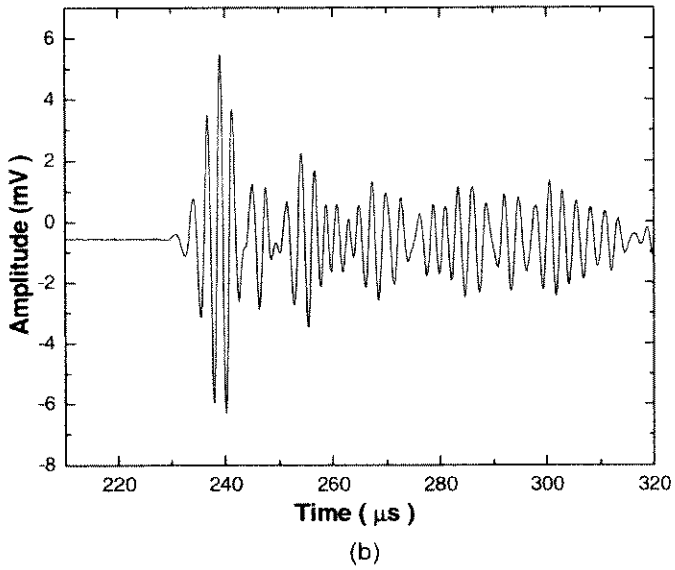

Fig. 3. Sampled signals via actuator-sensor path *P1–P3*: (a) the benchmark laminate, (b) the defective laminate.

$$W(a,b) = \frac{1}{\sqrt{a}} \int_{-\infty}^{+\infty} f(t)\,\Psi^*\left(\frac{t-b}{a}\right) \mathrm{d}t \qquad (1)$$

where $W(a,b)$ denotes the continuous wavelet coefficient. a and b are the scale parameter and the translation parameter, respectively. $f(t)$ represents arbitrary sampled signal, while $\Psi^*(t)$ denotes the complex conjugate of $\Psi(t)$. Furthermore, the CWT analysis can be simplified by calculating the wavelet coefficients at discretized scale, i.e., the DWT analysis, with which the sampled signal can be broken down into low-resolution compo-

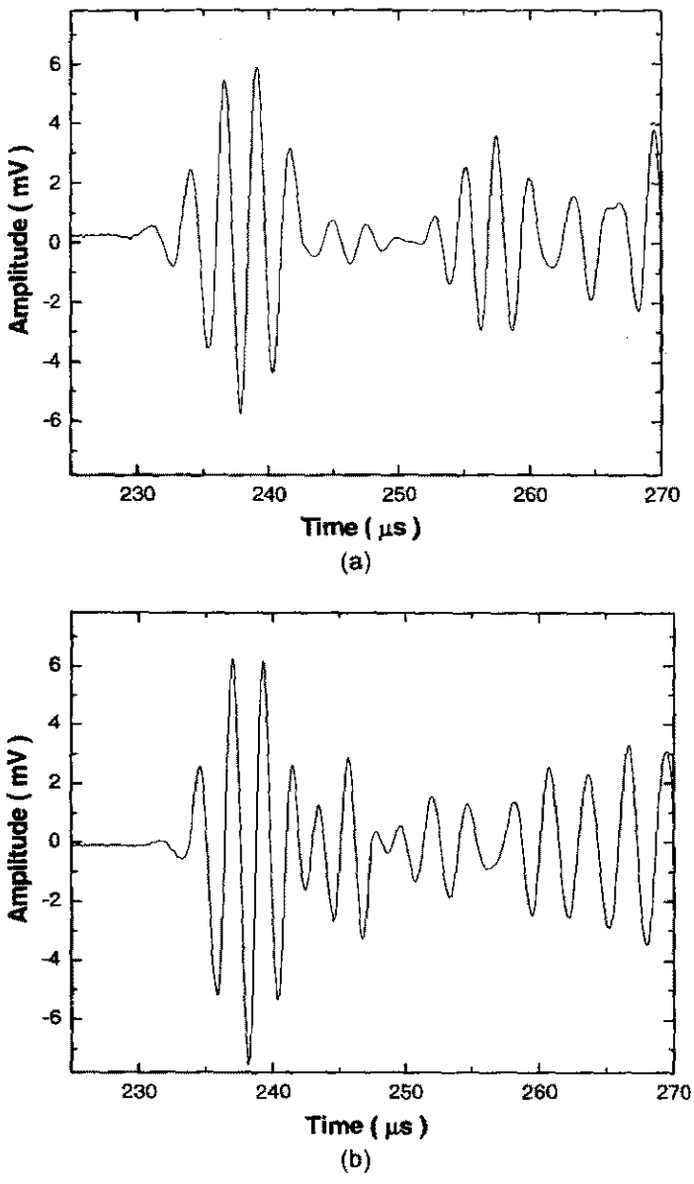

Fig. 4. Sampled signals via actuator-sensor path *P2–P4*: (a) the benchmark laminate, (b) the defective laminate.

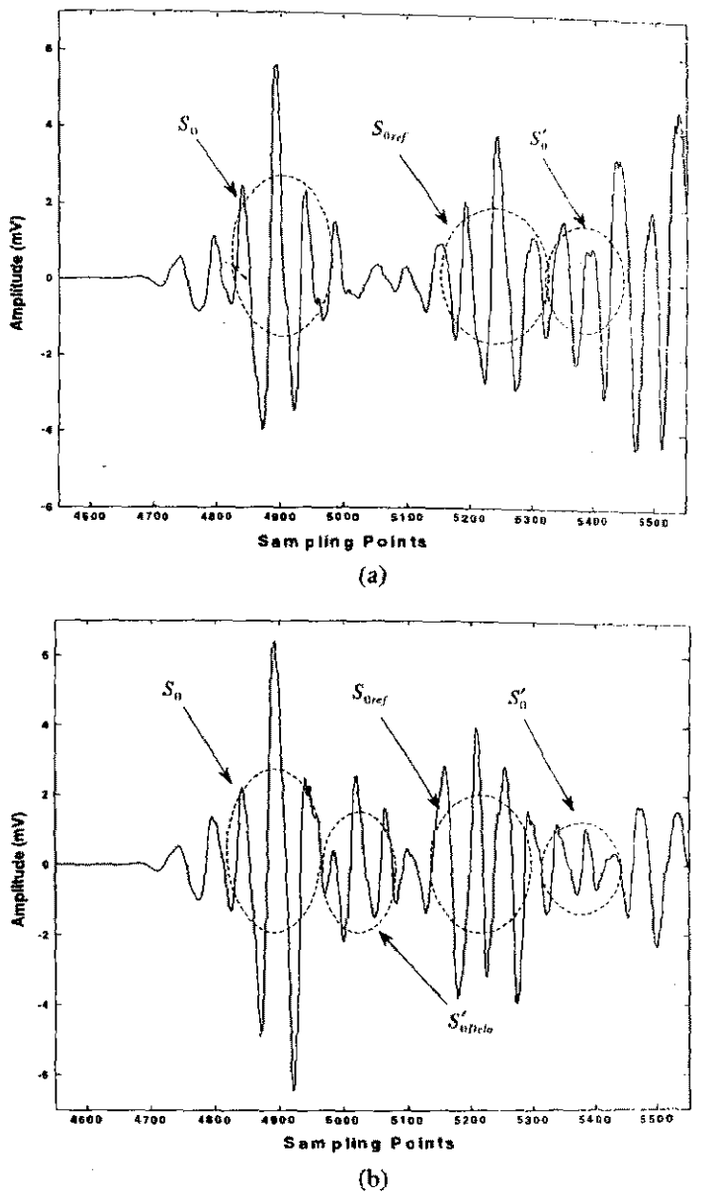

Fig. 5. DWT analytical results for signals via actuator-sensor path *P1–P3*: (a) the benchmark laminate, (b) the defective laminate.

nents. In addition, derived from Eq. 1, the total energy for sampling signal can be yielded as [14]:

$$E = C \int_{-\infty}^{+\infty} \int_{-\infty}^{+\infty} |W(a,b)|^2 \frac{\mathrm{d}a\,\mathrm{d}b}{a^2} \tag{2}$$

It indicates that the wavelet coefficient $W(a,b)$ can reflect the distribution of wave energy over the time and frequency domain.

The analytical results by DWT at the 5th level for signals shown in Figs. 3 and 4 are displayed and illustrated in Figs. 5 and 6, respectively. With the aid of DWT analysis, the fundamental symmetric Lamb modes, S_0, and the lowest order shear wave mode, S'_0, as well as their corresponding reflected waves from the boundaries which are herein denoted as $S_{0\mathrm{ref}}$ and $S'_{0\mathrm{ref}}$, can be observed in the analysed signals in Fig. 5(a) and Fig. 6(a), corresponding to the benchmark laminate.

Paralleled with the analysed signals for the benchmark laminate, extra wave components can be noticed in analysed signals corresponding to the defective laminate via the same actuator-sensor paths, which are contrastively shown in Figs. 5(b) and 6(b). The extra component in signal is recognised as the induced lowest order shear wave mode S'_0 due to the existence of delamination, denoted as $S'_{0\mathrm{Delam}}$. Other delamination-induced wave modes, $S_{0\mathrm{Delam}}$ and $A_{0\mathrm{Delam}}$, are unexploitable because their propagation velocities are either too high to be separated or too low to be sampled. For identification, only first several wave components in sampled signals are useful.

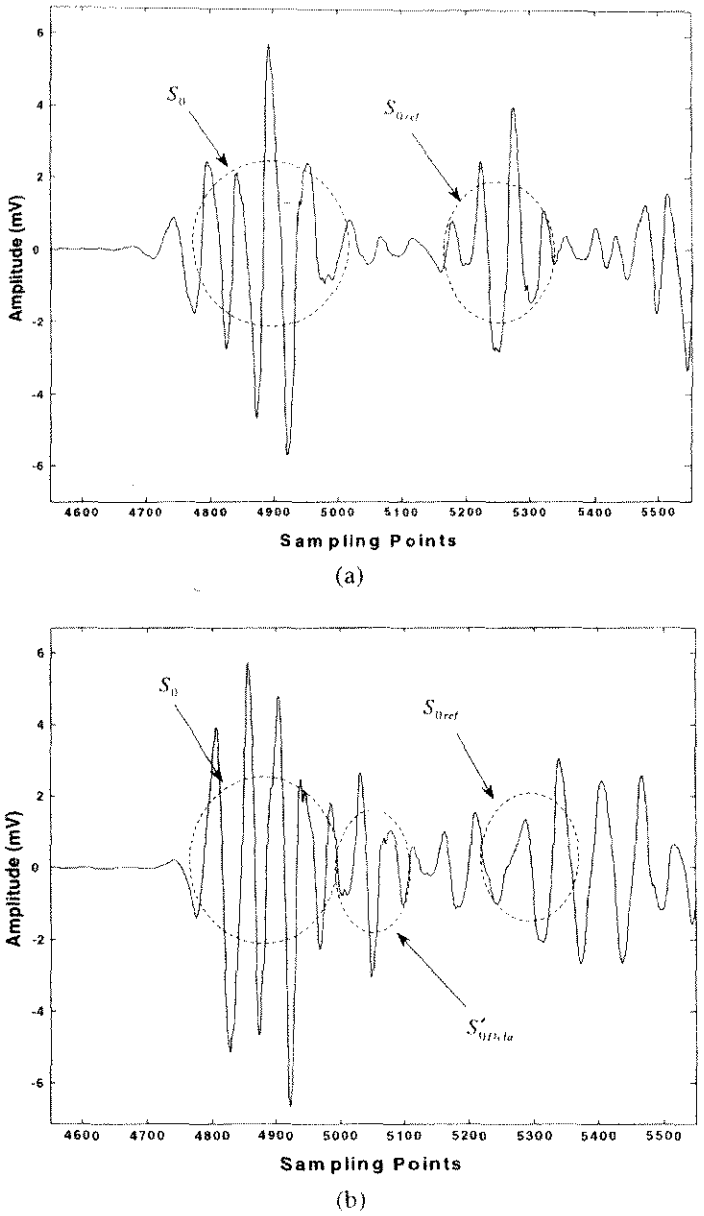

Fig. 6. DWT analytical results for signals via actuator-sensor path *P2–P4*: (a) the benchmark laminate, (b) the defective laminate.

Meanwhile, full-scale spectrographic analyses by CWT were also performed for the sampled signals. As example, 2D spectra of the raw signals for the benchmark laminate and the defective laminate via actuator-sensor path *P1–P3* are displayed in Fig. 7. In the spectra, the wavelet coefficients, represented by descending grayscale, reveal the distribution of wave energy density, deploying the local perturbations in the signals. More intuitively, 3D spectrum for the defective laminate is shown in Fig. 8. By virtue of DWT and CWT analyses, the damage can be located by calculating the related time lags upon consideration of multi-mode velocities [13].

A rough estimation for the possible delamination locations was preliminarily executed to expedite the

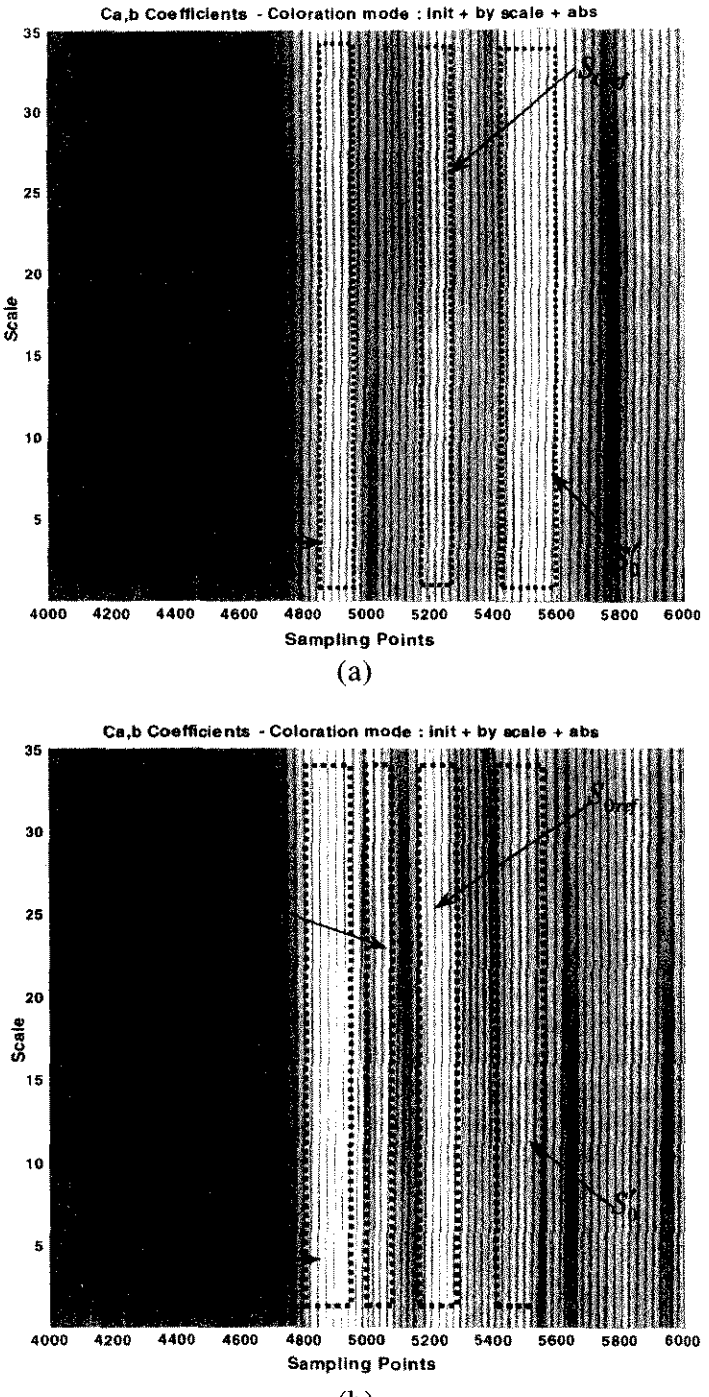

Fig. 7. 2D CWT spectra for signals via actuator-sensor path *P1–P3*: (a) the benchmark laminate, (b) the defective laminate.

diagnosis, approximately offering an initial position for the damage searching. It was found that the damage searching and identification could be consequently simplified by such initial estimation. During the searching procedure, the transducer *P1* is initially assumed as the origin of the coordinate system with the *X* axis paralleling with the bottom edge of the laminate, and a set of non-linear equations involving the position parameters for the delamination centre can be therefore

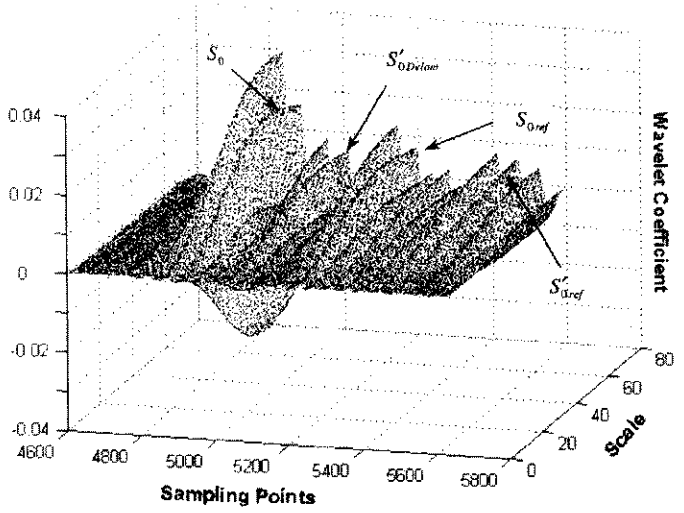

Fig. 8. 3D CWT spectrum for signals via actuator-sensor path *P1–P3* for the defective laminate.

setup in correlation with the geometric relationships among the locations of transducers and damage. The non-linear equations corresponding to the transducer *P1* can be given as [6,9],

$$\frac{\sqrt{(x-x_i)^2+(y-y_i)^2}}{V_{S'_{0\mathrm{Delam}}}}+\frac{\sqrt{x^2+y^2}}{V_{S_0}}-\frac{\sqrt{x_i^2+y_i^2}}{V_{S_0}}=T_{1-i}\quad(i=2,3,4) \tag{3}$$

where (x,y) denotes the coordinates of delamination centre in the current reference frame, and (x_i,y_i) represents the coordinates of the ith transducer. $V_{S'_{0\mathrm{Delam}}}$ and V_{S_0} are the velocities of wave modes $S'_{0\mathrm{Delam}}$ and S_0, respectively; while T_{1-i} is the measured time lag via actuator-sensor path *P1–Pi*.

Analogously, total four sets of the non-linear equations can be established upon four coordinate systems introduced, in which each PZT actuator takes turn to be nominated as the origin of the reference frames respectively. Further, an optimisation based on a graphic approach is then applied to solve the non-linear systems [13], fulfilling a prompt diagnosis with high accuracy. The whole searching procedure is schematically explained in Fig. 9. The dash-dot-lines represent the intercurrent lines generated by the searching algorithm, with which the proposed non-linear systems can be solved graphically, facilitating an accurate locating for the damage centre.

The results show that the diagnostic errors are dependent on the total number of the actuator-sensor paths involved for identification. The errors decrease with the increase of the path number for evaluation, while four paths are the minimum mathematic requirement to solve the nominated non-linear system sets for the location of delamination. However, the more the paths are taken into account, the more CCU computing time is consumed. In practice, a compromise between expected accuracy and affordable time/cost should be sychronised in accordance to the actual requirement.

5. Conclusion

An identification approach for delamination locating in laminated composites based on the Lamb wave propagation was proposed. The fundamental symmetric Lamb mode and the lowest order shear wave mode were identified. An active diagnosis system using built-in piezoelectrics was consequently developed and applied to quasi-isotropic CF/EP composite laminates to verify the feasibility and capability. Wavelet transform-based

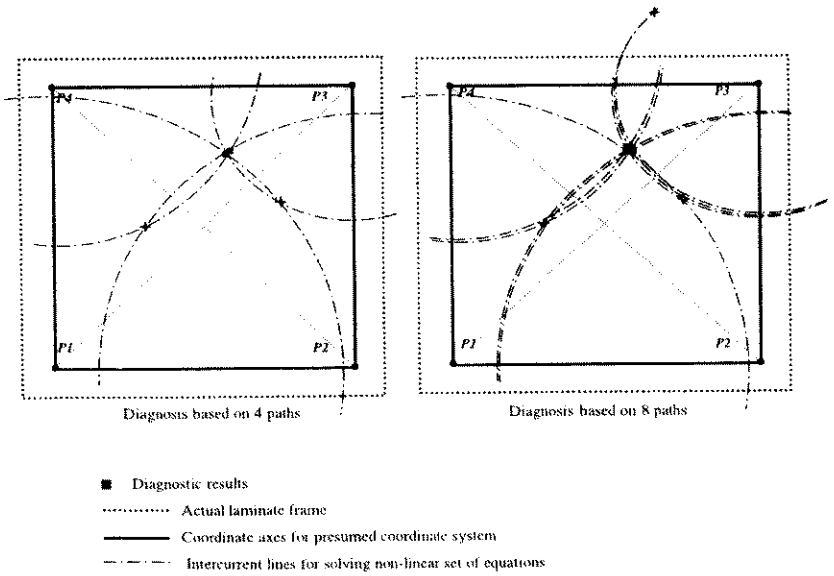

Fig. 9. Delamination locating procedure.

signal processing technique was employed in the identification scheme to suppress the diverse noises. It is shown that good diagnostic results can be achieved. Further studies will focus on the development of identification technique for the extent of delamination.

References

[1] Tang B, Henneke EG. Lamb-wave monitoring of axial stiffness reduction of laminated composite plates. Mater Eval 1991;47:928–34.

[2] Guo N, Cawley P. The interaction of Lamb wave with delaminations in composite laminates. J Acoust Soc Am 1993;94:2240–6.

[3] Guo N, Cawley P. Lamb wave reflection for the quick nondestructive evaluation of large composite laminates. Mater Eval 1994;52:404–11.

[4] Tan KS, Guo N, Wong BS, Tui CG. Experimental evaluation of delaminations in composite plates by the use of Lamb waves. Compos Sci Technol 1995;53:77–84.

[5] Wang CS, Chang F-K. Built-in diagnostics for impact damage identification of composite structures. In: Chang F-K, editor. Structural Health Monitoring. Lancaster: Technomic; 1999. p. 612–21.

[6] Lemistre M, Guoyon R, Kaczmarek H, Balageas D. Damage localization in composite plates using wavelet transform processing on Lamb wave signals. In: Chang F-K, editor. Structural Health Monitoring. Lancaster: Technomic; 1999. p. 861–70.

[7] Percival WJ, Birt EA. A study of Lamb wave propagation in carbon-fibre composites. Insight 1997;39:728–35.

[8] Badcock RA, Birt EA. The use of 0–3 piezocomposite embedded Lamb wave sensors for detection of damage in advanced fibre composites. J Smart Mater Struct 2000;9:291–7.

[9] Gaul L, Hurlebaus S. Wavelet-transform to identify the location and force–time-history of transient load in a plate. In: Chang F-K, editor. Structural Health Monitoring. Lancaster: Technomic; 1999. p. 851–60.

[10] Legendre S, Massicotte D, Bose TK. Wavelet-transform-based method of analysis for Lamb-wave ultrasonic NDE signals. J IEEE 2000;49:524–30.

[11] Hou Z, Noori M, Amand RS. Wavelet-based approach for structural damage detection. J Eng Mech 2000;126:677–83.

[12] Abbate A, Koay J, Frankel J, Schroeder SC, Das P. Signal detection and noise suppression using a wavelet transform signal processor: application to ultrasonic flaw detection. J IEEE 1997; 44:14–25.

[13] Su ZQ, Ye L, Xiong ZB. Lamb wave based delamination identification approach for fibre reinforced composite laminates, in preparation.

[14] Chan YT. Wavelet Basic. Boston: Kluwer Academic Publishers; 1995.

[15] Charles H, Keilers J. Identifying delamination in composite beams using built-in piezoelectrics: Part I—experiments and analysis. J Intel Mater Syst Struct 1995;6:649–63.

[16] Rose JL. Ultrasonic waves in solid media. Cambridge: Cambridge University Press; 1999.

[17] Chakraborty G, Mallil AK. Wave propagation in and vibration of a traveling beam with and without non-linear effects. J Sound Vib 2000;236:277–90.

[18] Doyle JF. Wave propagation in structures. second ed. New York: Springer-Verlag; 1997.

SHM
Structural Health Monitoring

Quantitative Assessment of Damage in a Structural Beam Based on Wave Propagation by Impact Excitation

Zhongqing Su,[1] Lin Ye,[1,*] Xiongzhu Bu[2], Xiaoming Wang[3] and Yiu-Wing Mai[1]

[1]*Centre for Advanced Materials Technology (CAMT), School of Aerospace, Mechanical and Mechatronic Engineering, The University of Sydney, NSW 2006, Australia*
[2]*School of Mechanical Engineering, Nanjing University of Science and Technology, 210094, P.R. China*
[3]*CSIRO Infrastructure Systems Engineering, Highett, VIC 3190, Australia*

A damage identification system involving a surface-attached piezoelectric transducer was developed in this study in correlation with an elastic wave propagation model. A signal processing and identification algorithm in the time–frequency domain based on the wavelet transform technique was proposed to suppress the diverse broadband interferences and effectively extract useful diagnostic information from the acquired raw impact responses, facilitating a prompt yet accurate structural health assessment. The developed system was then validated by applying it to a defective metal beam bearing a transverse crack with an increasing depth that simulates the crack growth. It is shown that the monitoring for the variable damage severity in the one-dimensional structure can be fulfilled quantitatively and exactly using this technique.

Keywords structural health monitoring (SHM) · wave propagation · impact response · signal processing · wavelet transform

Introduction

Great interest in the structural health monitoring with possibly less intrusion is increasing throughout the aerospace, mechanical and civil engineering communities. In the past decade, more demanding requirements for the identification accuracy and applicability as well as the operating/maintenance cost have considerably motivated the development of effective and economical structural health monitoring (SHM) techniques and damage diagnosis systems, leading to significant achievements in this area [1–19]. In particular, the detection approaches based on the elastic wave propagation have been attracting more and more attentions from both researchers and engineers, regarded as one of the most promising solutions to the quantitative assessment of the structural deterioration and the prevention for catastrophic failure.

On the other hand, signal processing is a key point to make an identification scheme applicable

*Author to whom correspondence should be addressed.
E-mail: ye@aeromech.usyd.edu.au

Vol 2(1): 0027–40
[1475-9217 (200303) 2:1;27–40; 10.1177/145792103029779]

and understandable. As known, neither traditional time-series nor frequency-spectrum analysis is capable of exhibiting the essence of signal at the full length, so that much useful diagnostic information may be lost. However, such an issue can be ameliorated with the aid of wavelet transform-based analysis in the time–frequency space, through which the time-dependent signal can be decomposed into the time and frequency domains simultaneously, and thus the characteristic details hidden in signal, such as trends, breakdown points or discontinuities, can be fully revealed. While probably Daubechies [1] and Newland [2] first systematically introduced the wavelet transform technique into the vibrational signal analyses in the early 1990s, it is in the past couple of years that the wavelet transform-based analyses have been widely applied into the structural damage detection. Actually, in its brief history, the wavelet transform technique has been proven to be a powerful analytical tool for signal processing, emerging as a substantial auxiliary implement for the system identification. Combined with the investigation on signals in the time–frequency space via the wavelet transform, elastic wave propagation-based detection approaches make the quantitative evaluation for structural health status more efficient and reliable. Kim et al. [3] reported their model and a signal-processing method for the identification of a fixed damage in a one-dimensional structure; Samuel et al. [4] accomplished a damage detection for a rotorcraft geartrain system; meanwhile Sung et al. [5] developed an impact monitoring technique for a composite structure using wavelet transform technique; and Kim et al. [6] thoroughly investigated the effectiveness of wavelet transform in the analysis for dispersive elastic waves; while other different analytical models and identification approaches have also been widely reported [7–19].

Damage growth, such as the extension of a crack in the metal alloy, is a common phenomenon for engineering structures in practice, which may result in the lethal malfunction of the whole system. It is therefore of vital importance to monitor the damage growth and consequently apply with appropriate remediation to minimise the risk of further structural destruction. The objective of the present research focuses on the development of a continuous monitoring scheme for the damage growth in one-dimensional structure. For this purpose, a damage diagnosis system incorporated with a piezoelectric transducer, in correlation with an elastic wave propagation model, was developed. The validity of this system was then investigated by applying it to a metal beam bearing a transverse crack with an increasing depth, simulating the damage growth. It is shown that the damage parameters, including the damage presence, location and its variable severity, can be identified promptly and accurately using this technique.

Model for Damage Identification

Consider a uniform Euler–Bernoulli beam owning a transverse crack-shaped damage perpendicular to the beam axis with an increscent depth, H_d, as depicted in Figure 1. With the assumption of the beam axis being the x-axis and neglecting the twisting effect, the motion equation for the Euler–Bernoulli beam can be expressed in terms of the lateral displacement $w(x,t)$ and the rotation angle $\theta(x,t)$ [20] upon the introduction of shear correction parameter κ,

$$\kappa^2 c_s^2\left[\frac{\partial^2 w}{\partial x^2}-\frac{\partial \theta}{\partial x}\right]-\frac{\partial^2 w}{\partial t^2}=0 \tag{1a}$$

$$c_0^2\frac{\partial^2 \theta}{\partial x^2}+\kappa^2\frac{c_s^2}{q^2}\left[\frac{\partial w}{\partial x}-\theta\right]-\frac{\partial^2 \theta}{\partial t^2}=0 \tag{1b}$$

$$c_0=\sqrt{E/\rho},\quad c_s=\sqrt{G/\rho},\quad q=\sqrt{I/A},\quad \left[\kappa=\pi/\sqrt{12}\right] \tag{1c}$$

where, E, I, A and ρ denote the elastic modulus, second moment of area, cross-section area and mass density of the beam, respectively.

Upon the consideration of the dispersion relations,

$$w=w_0\cdot e^{-i(kx-\varpi t)},\quad \theta=\theta_0\cdot e^{-i(kx-\varpi t)} \tag{2}$$

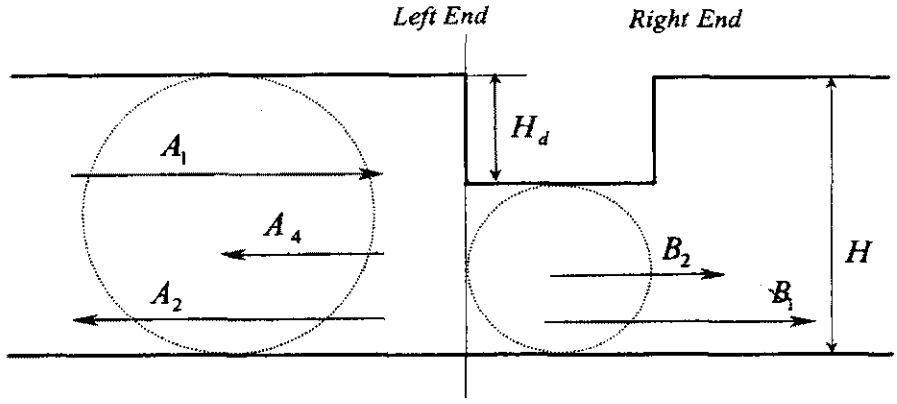

Figure 1 Damage model for diagnosis based on wave propagation.

the eigen roots (wavenumber) for Equation (1) can be yielded as,

$$k_n = \pm\left[\frac{1}{2}\left(1+\frac{c_0^2}{\kappa^2 c_s^2}\right) \pm \sqrt{\left(\frac{c_0}{q\varpi}\right)^2 + \frac{1}{4}\left(1-\frac{c_0^2}{\kappa^2 c_s^2}\right)^2}\right]^{1/2} \times \frac{\varpi}{c_0}, \quad (n=1,2,3,4) \tag{3}$$

Mathematically, the existence of four eigen roots determines that four propagating wave components are possibly available synchronously in the Euler–Bernoulli beam. The general solution to Equation (1) can be further expressed with a summation of four terms as below,

$$w(x,t) = \left[\sum A_1 e^{-ikx} + \sum A_2 e^{ikx} + \sum A_3 e^{-kx} + \sum A_4 e^{kx}\right] \cdot e^{i\varpi \cdot t} \tag{4}$$

where each term is respectively corresponding to one of the wave modes, which is hereafter recognised as the positively propagating wave, the negatively propagating wave, the positively growing evanescent wave or the negatively exponentially decaying wave, respectively, depending on their propagating direction and properties.

In Equation (4), the coefficient of exponential represents the amplitude of each wave component, which may be a complex. With the occurrence of a damage, Equation (4) yields two propagating equations before and after the left damage end (referring to Figure 1), respectively, denoted with w_- and w_+,

$$w_-(x,t) = \left[\sum A_1 e^{-ik_1 x} + \sum A_2 e^{ik_1 x} + \sum A_4 e^{k_1 x}\right] \cdot e^{i\varpi \cdot t} \tag{5a}$$

$$w_+(x,t) = \left[\sum B_1 e^{-ik_2 x} + \sum B_2 e^{-k_2 x}\right] \cdot e^{i\varpi \cdot t} \tag{5b}$$

where, the three terms in Equation (5a) correspond to the incident wave, reflected propagating wave and reflected exponentially decaying wave, respectively, which are induced by the interaction between the incident wave and the damage; while the two terms in Equation (5b) are recognised as the damage-induced positively propagating wave and growing attenuating wave, respectively. Note that the wave components A_4 and B_2 disappear very quickly due to exponentially decaying.

Applied with the continuity and compatibility conditions [3],

$$w_-(x,t) = w_+(x,t), \quad \frac{\partial w_-(x,t)}{\partial x} = \frac{\partial w_+(x,t)}{\partial x}$$

$$\begin{bmatrix} EI_1 \dfrac{\partial w_-^2(x,t)}{\partial^2 x} = EI_2 \dfrac{\partial w_+^2(x,t)}{\partial^2 x} \\ EI_1 \dfrac{\partial w_-^3(x,t)}{\partial^3 x} = EI_2 \dfrac{\partial w_+^3(x,t)}{\partial^3 x} \end{bmatrix} \tag{6}$$

the reflection ratio at the damage surface can be obtained as,

$$R=\frac{A_2}{A_1}$$
$$=\frac{-iI_1^2k_1^4+2I_1I_2k_1^3k_2+2iI_1I_2k_1^2k_2^2-2I_1I_2k_1k_2^3-iI_2^2k_2^4}{I_1^2k_1^4+2I_1I_2k_1^3k_2+2I_1I_2k_1^2k_2^2+2I_1I_2k_1k_2^3+I_2^2k_2^4} \quad (7a)$$

$$I_1=\frac{l\cdot H^3}{12}, \qquad I_2=\frac{l\cdot(H-H_d)^3}{12} \quad (7b)$$

where l and H denote the width and depth of the cross-section of the beam, respectively; while H_d represents the depth of the damage. Equation (7) implies that the depth of damage, H_d, can be therefore determined with a given reflection ratio. The relationship between the reflection ratio and the damage degree (H_d/H) for the present system was theoretically calibrated and shown in Figure 2.

Diagnosis Scheme

Daubechies function, $\Psi(a,b)$, at level 4 (db4) was chosen as the wavelet transform function, which was demonstrated most effective in this study to cater for the resolution requirement on the present problem compared with other

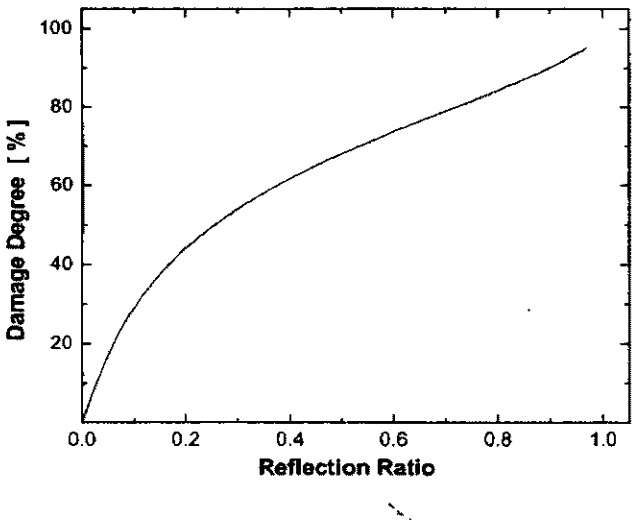

Figure 2 Theoretical relationship between reflection ratio and damage degree.

transform functions. $\Psi(a,b)$ was then applied with the Continuous Wavelet Transform (CWT) [21,22],

$$W(a,b)=\frac{1}{\sqrt{a}}\int_{-\infty}^{+\infty} f(t)\cdot\Psi^*\left(\frac{t-b}{a}\right)dt \quad (8)$$

where $W(a,b)$ denotes the continuous wavelet coefficient, which reflects the energy distribution of the signal over the time-scale domain. a and b are the scale and translation parameter, respectively. While $f(t)$ represents an arbitrary sampled signal; and $\Psi^*(t)$ denotes the complex conjugate of $\Psi(t)$. Contrarily, if the transform is invertible, the inverse wavelet transform exists,

$$f(t)=\frac{1}{C_\Psi}\int_{-\infty}^{+\infty}\int_{a>0}^{+\infty} W(a,b)\cdot\frac{1}{\sqrt{a}}\cdot\Psi\left(\frac{t-b}{a}\right)\cdot\frac{1}{a^2}da\cdot db \quad (9)$$

where $C\Psi$ is a constant that depends on $\Psi(t)$.

Practically, the CWT analysis can be simplified by calculating the wavelet coefficients only at discretised scale, namely, the Discretised Wavelet Transform (DWT) [21,22]. The sampled signal can be therefore decomposed into a series of Approximations and Details via DWT analysis, characterising the time-dependent signal in independently assorted frequency ranges.

The time–scale or time–frequency domain analysis offers a capability to quantitate the local perturbation or singularity in signal. In this study, the damage parameters (i.e., the location and severity), regarded as singularity involved in the signal, were determined using the CWT and DWT spectrographic analyses. In more detail, the damage location diagnosis was performed by calculating the time difference between the incident wave component and damage-induced wave component along the time axis within the discreted frequency scope pertaining to the impact excitation via the DWT analysis, or the time difference between incident wave energy concentration and damage induced-wave energy concentration in spectra through the CWT analysis. While the damage severity was calibrated upon the relation with the reflection ratio (see Figure 2), in which the reflection ratio was theoretically

proven to be equivalent to the root-mean-square (RMS) ratio of their related continuous wavelet coefficients along the scale axis at the time points corresponding to the maximum energy concentration over the time-scale domain [3] (see Appendix), while the RMS ratio could be achieved by experimental approach.

Configuration of Diagnosis System

The damage diagnosis system based on a VXI platform, described schematically in Figure 3, consists of the Signal Generation Unit (SGU), Signal Acquisition Unit (SAU) and Central Control Unit (CCU). With a low acoustic impedance and a broadband response range, a piezoelectric lead zirconate titanate (PZT) element (PI® 151), with the properties summarised in Table 1, was chosen as the signal sensor and surface-mounted on the beam with silver–epoxy adhesive (Farnell®). Signal acquisition was performed via the Agilent® E1437A digitizer at a sampling rate of 20.48 MHz after conditioned by the Agilent® E3242A conditioner. Being the kernel of the system, CCU performed as both the controller and the interpreter, supported by an inhouse software developed on the NI Labview© platform.

In order to evaluate the effectiveness of the proposed model and identification scheme, the diagnosis system was then applied to a defective aluminum alloy beam (cross-section of 10 mm × 10 mm, Young's modulus of 72.4 GPa and density of 2.69 g/cm^3) with dual-end fixed-supported, sketched in Figure 4. A transverse crack, extending across the entire width of the beam with a 0.15 mm span along the beam axis, was previously made using a diamond saw. The damage depth, H_d, varies from 1 mm to 8 mm with a step of 1 mm. In most previous studies, relatively complicated excitation sources, such as PZT actuators, were chosen for the generation of a diagnostic

Table 1 Geometry and mechanical properties of PZT sensor.

Product Name	*PI 151*
Geometry	20 mm × 10 mm × 1 mm
Density	7.80 g/cm^3
Charge constant d_{31}	-170×10^{-12} m/V
Charge constant d_{33}	450×10^{-12} m/V
Elastic constant E_{11}	66.67 GPa
Elastic constant E_{33}	86.21 GPa

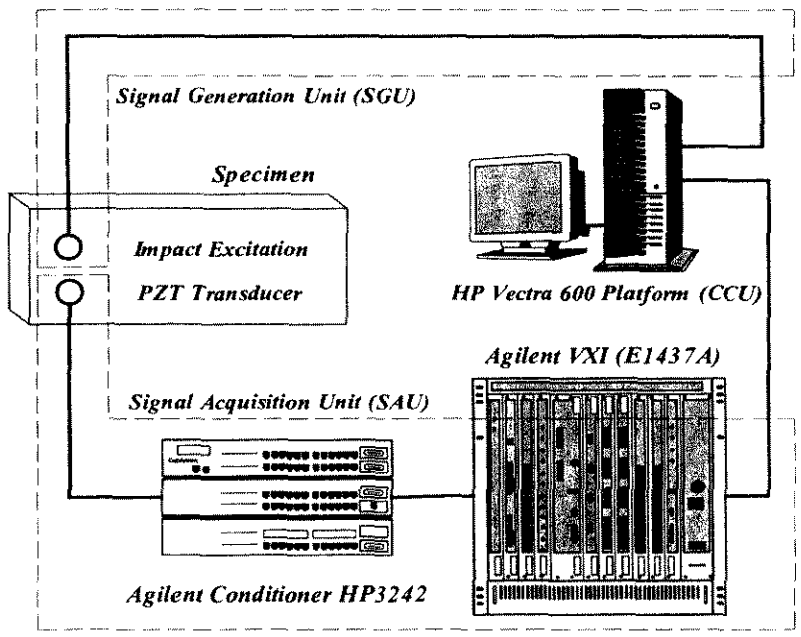

Figure 3 Configuration of identification system based on VXI platform.

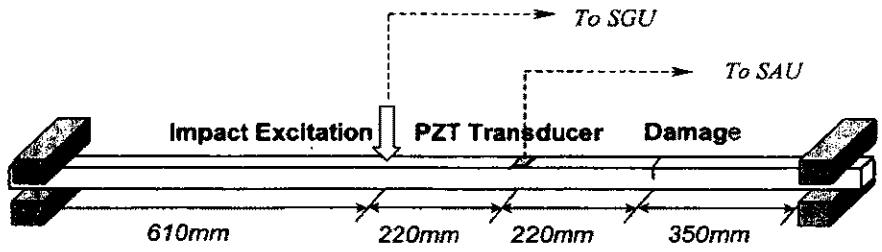

Figure 4 Configuration of experiment setup for a structural beam with damage.

signal. In the present study, a simple yet practical pendulum force hammer, controlled by the SGU to generate constant impact energy of 0.4 J, was used for the excitation of incident signal. It is of essence to keep a sufficient distance between the excitation spot and structural boundaries to ensure the reflected wave modes from the boundaries would not interfere the damage-induced wave component.

Table 2 Measured wave velocities in an aluminum alloy structural beam.

Wave Mode	*Measured* (m/s)	*Calculated** (m/s)
Longitudinal wave	6365	6314
Transverse wave	3205	3180

* $C_{Longitudinal} = \sqrt{E/\rho} \cdot \sqrt{(1-\mu)/(1+\mu)\cdot(1-2\mu)}$; $C_{Transverse} = \sqrt{E/\rho} \cdot \sqrt{1/2(1+\mu)}$; E: Elastic modulus, 72.4 GPa; ρ: Mass density, 2.69 g/cm^3; μ: Poisson's ratio, 0.33.

Signal Analysis

Inevitably, broadband responses will be induced by the impact excitation due to the wave dispersion, making the signal distinguish intractable. Meanwhile, muddled with the diverse noises and structural vibration patterns, the diagnostic information is usually ruined in the raw response signal. An improved signal processing and damage identification algorithm by virtue of CWT and DWT analysis based on the Matlab© mathematic platform [23] was hereby proposed to meliorate the identification.

In experiment, different wave components can simultaneously be observed. The propagating velocity for each possible wave is therefore required for the signal distinguish. The velocities measured experimentally and calculated theoretically are compared in Table 2. The response signals for different damage severities were sampled. As typical examples, the acquired structural response signals in the time domain for 4 mm and 6 mm-depth cracks, and their corresponding frequency spectra by the Fast Fourier Transform (FFT) analysis are shown in Figures 5 and 6, respectively. Interfered by the low-frequency structural vibration and various noises, only tiny differences can be noticed between the signals in the time or frequency domain, both of which can hardly be used directly for the accurate diagnosis. Spectrographic analyses based on the CWT and DWT techniques [24] were accordingly executed. A series of band filters with proposed threshold and different frequency scopes were designed and applied on the sampled signals to suppress the diverse interferences and effectively extract diagnostic components. Meanwhile, the Ansys© FEM software was employed to calculate the vibrational patterns of the structural beam, so that the components in the frequency scopes corresponding to the structural natural modals could be filtered. Thus the interrogation on the sampled signals can be concentrated in a specific frequency scope. On the other hand, in this study, the Sampling Point (SP) was hereafter introduced instead of the direct Time Point (TP) in CCU to expedite and facilitate the data processing procedure.

The DWT analytical results of the sampling signal for the 4 mm-depth crack, as a paradigm, from level 1 to level 10, and the distribution of its DWT coefficient are displayed in Figure 7, in which the DWT level refers to the different frequency ranges. The wave energy distribution is portrayed by the grayscale, and the darker the grayscale appears, the stronger the wave energy

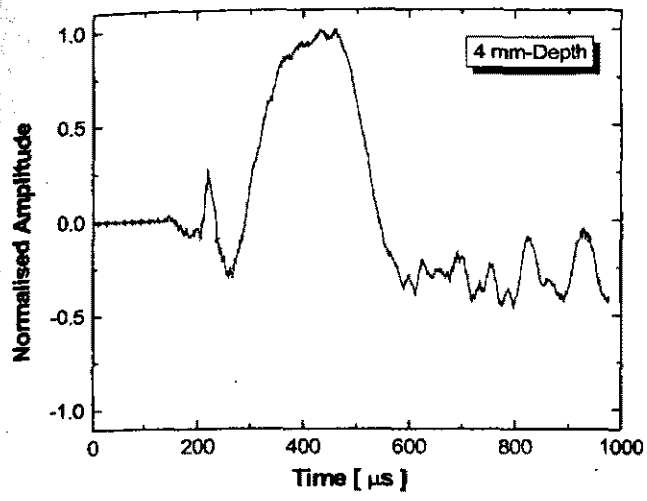

(a)

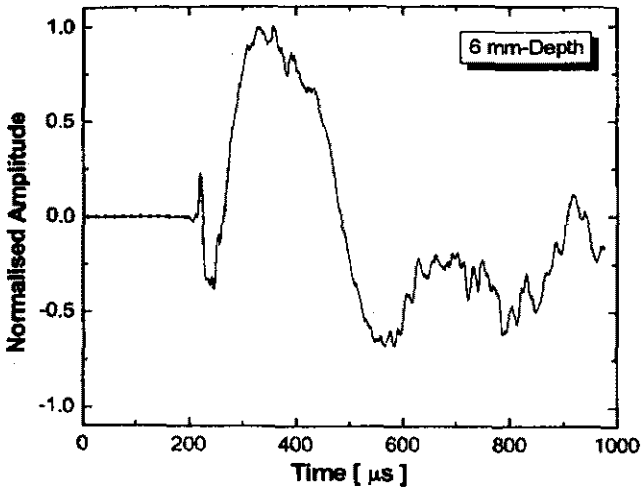

(b)

Figure 5 Sampled raw response signals in the time domain: (a) 4 mm-depth crack; (b) 6 mm-depth crack.

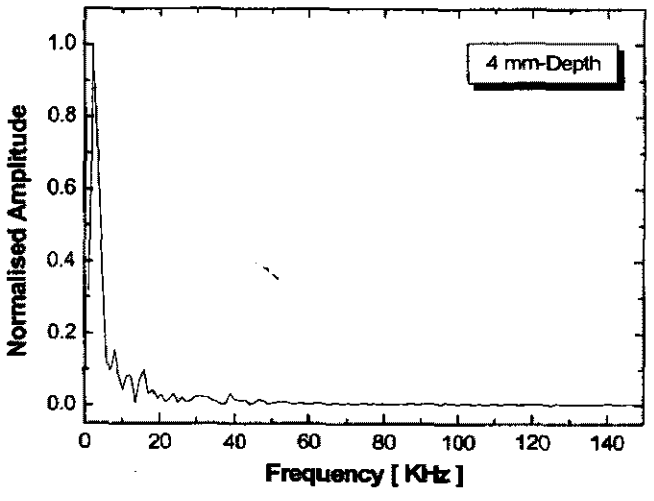

(a)

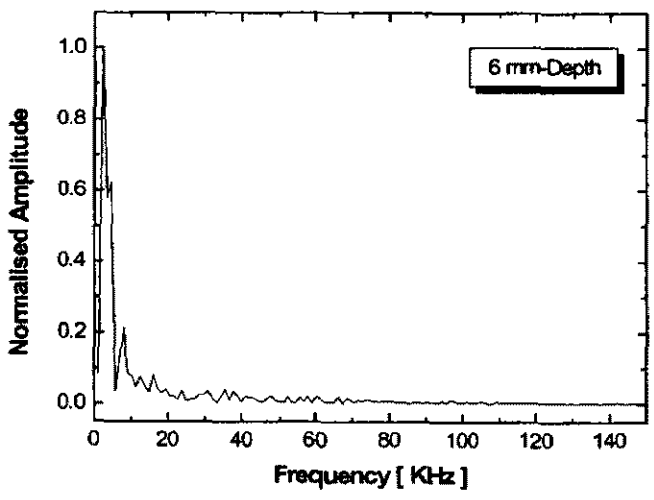

(b)

Figure 6 FFT analysis for signals in Figure 5: (a) 4 mm-depth crack; (b) 6 mm-depth crack.

is. The obvious energy concentration can be clearly noticed from level 5, while at level 8 the spectrogram well exhibits the response arisen from the impact excitation.

Particularly, the DWT analytical results at level 8 for 4 mm and 6 mm-depth cracks are displayed in Figure 8 for comparison. The first wave peak originates from the incident wave (transverse wave in this case), followed by the first reflected wave due to the crack as well as other reflected components from left/right boundaries or multi-reflected wave components from the damage. For the signal identification purpose, only the first several wave components in the sampling signal are useful while the others are not the concern. The time lags among the related wave components (peaks and wavefronts) were calculated to locate the crack.

Meanwhile, the 2D and 3D spectrographic analyses via CWT were performed. As instances, the 2D spectra for the paradigmatic sampling signals, shown in Figure 5, are displayed in Figure 9, where the grayscale reflects the density of wave energy over the time-scale domain, with the darker one indicating the higher energy. The damage-induced energy can be observed between

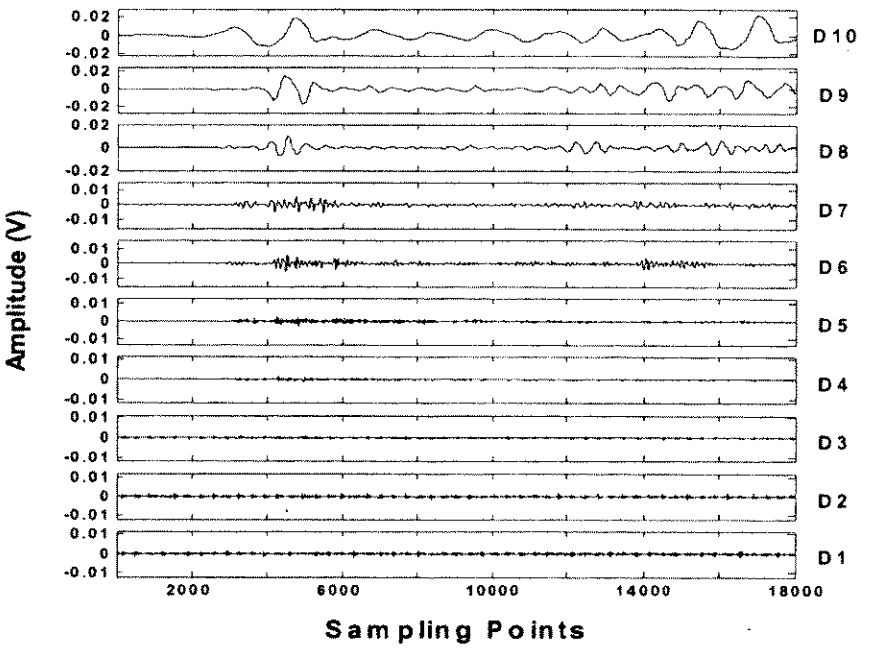

(a)

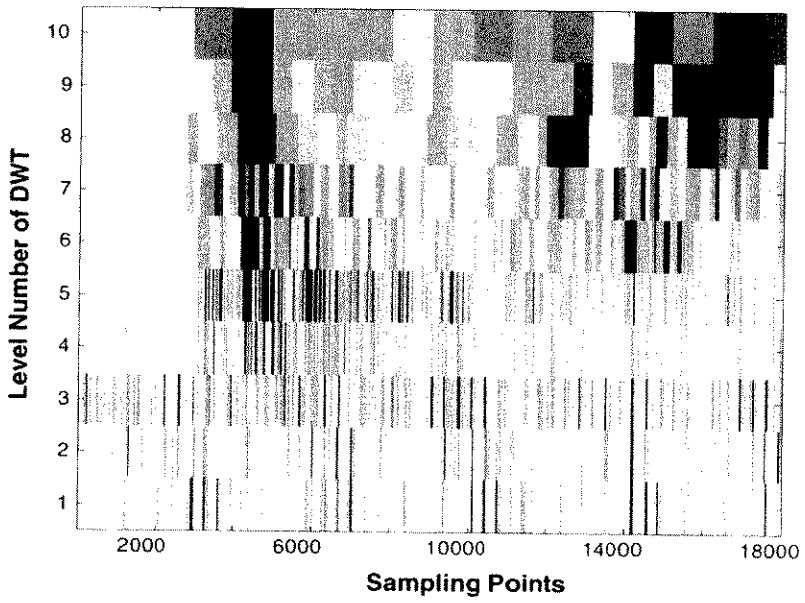

(b)

Figure 7 DWT analytical results of the sampled signal for 4 mm-depth crack: (a) details from level 1 to level 10; (b) distribution of DWT coefficients.

the incident energy and the first reflected energy from the boundary. More intuitively, the corresponding 3D spectrographic images for different damage severities and their partial magnification are displayed in Figure 10. In the 3D spectra, the intuitionistic ridges, relative to the CWT coefficients, also indicate the energy distribution. Similarly, the energy concentration induced by the damage can be visually observed in 3D spectra. From Figures 8–10, stronger energy

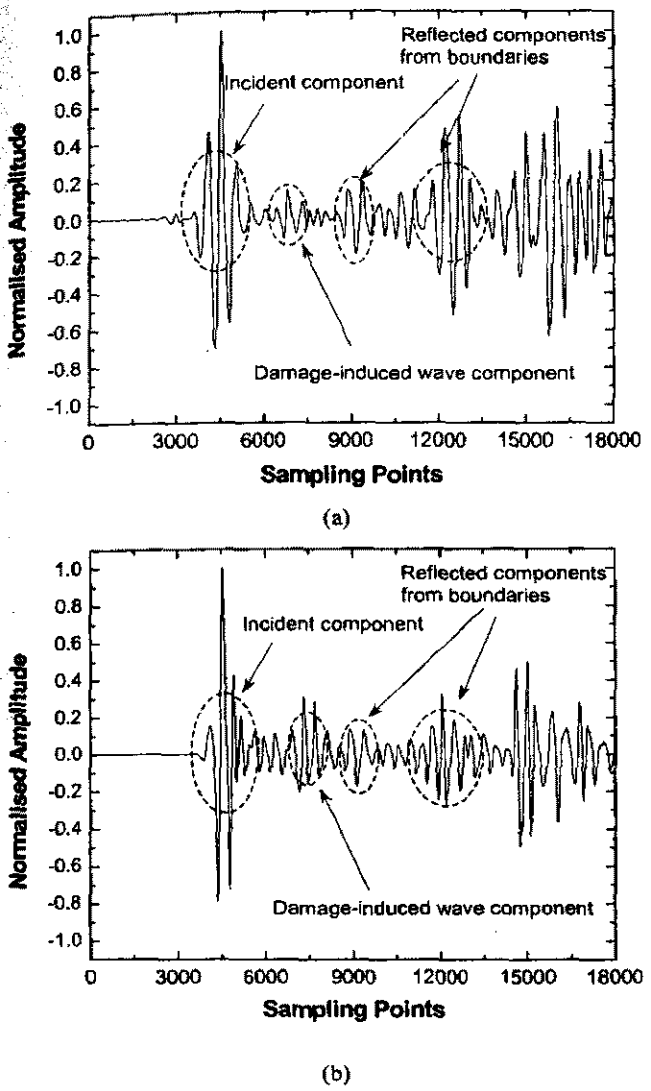

Figure 8 Detail at level 8 by DWT analysis for signals in Figure 5: (a) 4 mm-depth crack; (b) 6 mm-depth crack.

reflection from the crack can be noticed as the crack size increases because of the expansion of the valid reflection area. The resolution for sampling signal and identification accuracy for both the damage location and the severity are consequently improved. The full-scale CWT analyses are more wieldy of detecting local perturbations in signal.

Damage Diagnosis and Discussion

For diagnosis purpose, the energy ridges in the time-scale space at the time point, pertaining to the maximum energy concentration, are anatomised and investigated along the scale axis. The consequently anatomised profiles for the incident energy and induced-energy from 4 mm to 6 mm-depth crack are contrastively shown in Figure 11 as paradigms. In profile curves, a crestiform distribution of the wavelet coefficients along the scale axis within the assorted scale range can be observed. Two approaches were employed to calculate the magnitude of the distribution of wavelet coefficient in the profile curves, viz., RMS method [3] and integration method, so that the reflection ratio can be determined. Attention should be paid that the area encompassed by the profile curve and scale axis increases with the crack length from 1 mm to 8 mm. By virtue of the RMS value ratio of the wavelet coefficients for the incident energy to the damage-induced energy in the profile curves, the reflection ratio was calculated (Equation (A10)), leading to the determination of the damage severity (Figure 2). The damage diagnostic results achieved via the proposed identification scheme and the actual damage parameters are compared in Table 3.

Capability of the diagnoses for damage location and severity using the developed system was evaluated. The percentage diagnostic errors are listed in Table 3 and illustrated in Figure 12. The results imply that the identification accuracy for crack location, in spite of the actual damage severity, is acceptable with a high creditability. The precision of damage severity identification increases with the crack size and a satisfactory precision for the damage severity estimation is maintained until the crack size approaches 6 mm approximately when the transverse damage area occupies around 60–70% of the entire cross-section of the beam. Considerable errors occur when the crack size exceeds 70% of the height of the beam. This is attributed to the inapplicability of the basic hypotheses used in the Euler–Bernoulli beam theory, on which the model was developed. Under such a circumstance, the twisting effect cannot be neglected, leading to the inapplicability of the continuity and compatibility conditions.

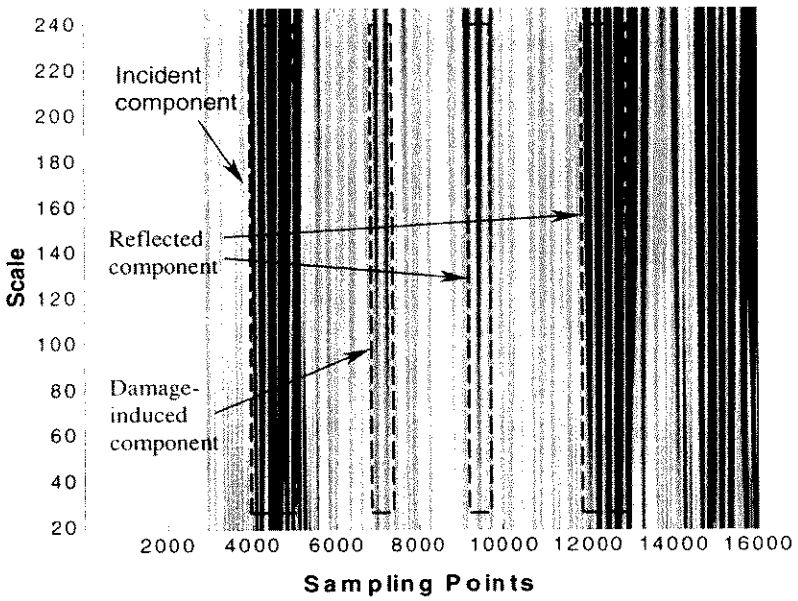

(a)

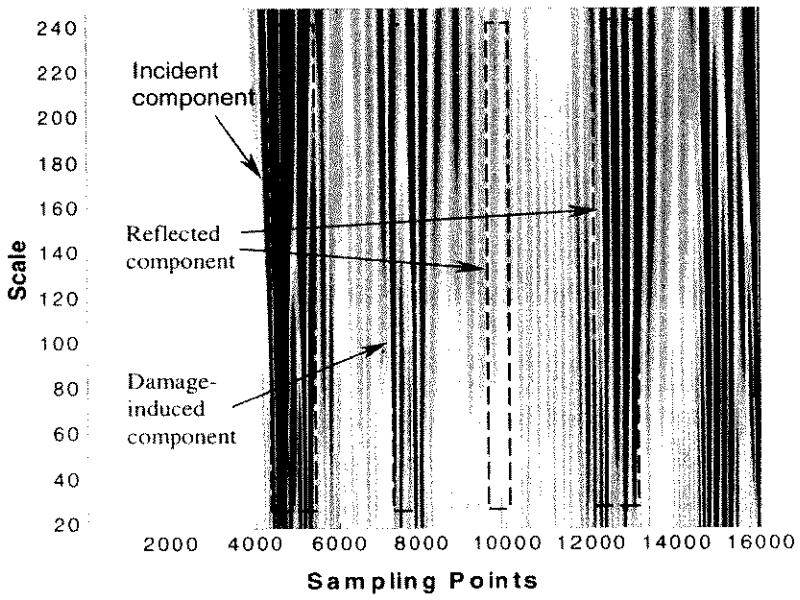

(b)

Figure 9 2D spectrographic analysis by CWT for signals in Figure 5: (a) 4 mm-depth crack; (b) 6 mm-depth crack.

Conclusion

An identification and monitoring scheme for structural damage in correlation with the impact response analysis has been developed, and its validity was examined experimentally through a quantitative diagnosis for the location and size of damage with an increasing depth in a one-dimensional structural beam. A simple and practical impact excitation source was used for the generation of diagnostic stress wave. The accompanying broadband interference of impact excitation was suppressed using an improved signal processing technique based on the wavelet

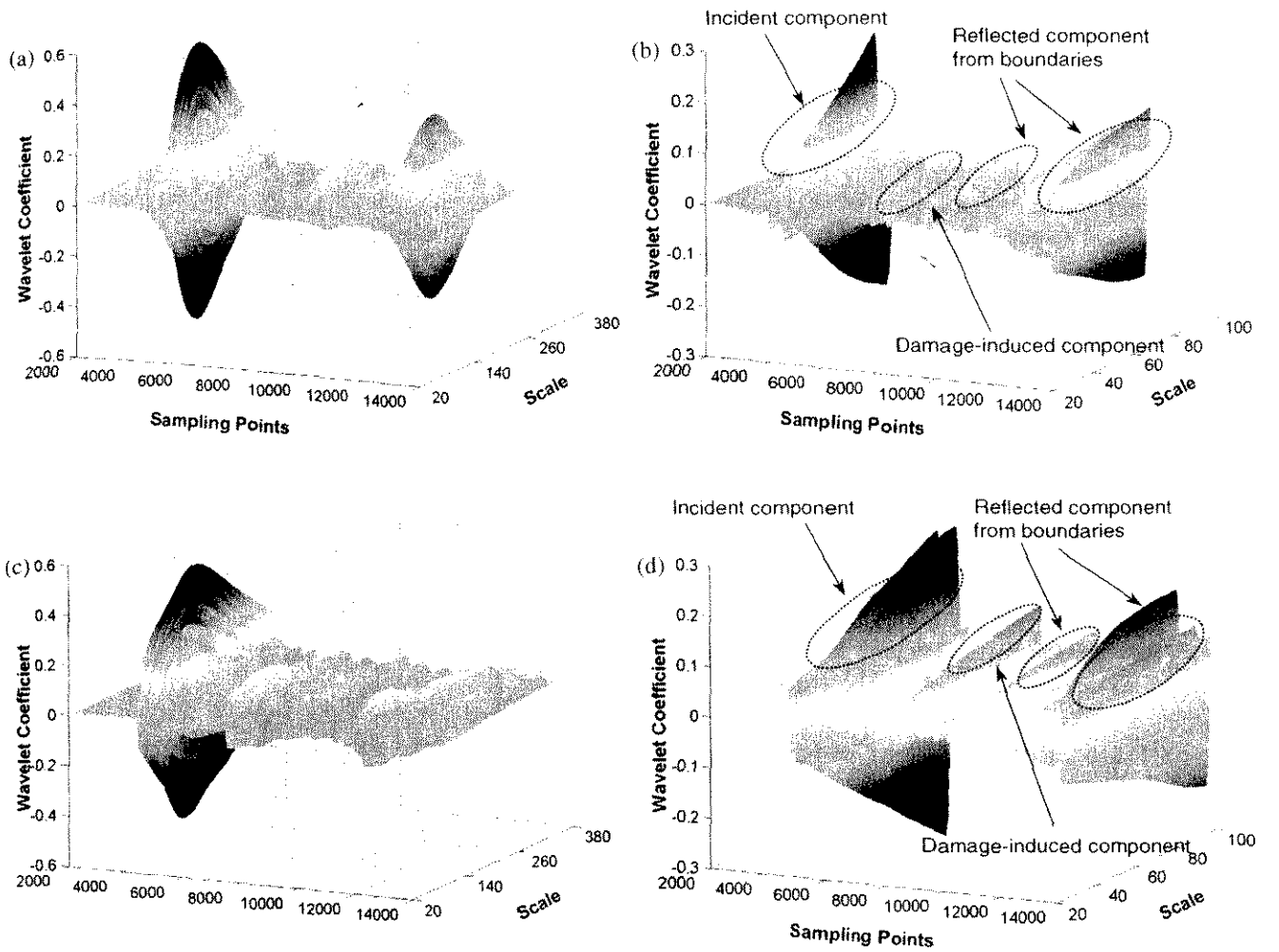

Figure 10 3D spectrographic analysis by CWT for signals in Figure 5: (a) 4 mm-depth crack; (b) partial magnification of (a); (c) 6 mm-depth crack; (d) partial magnification of (c).

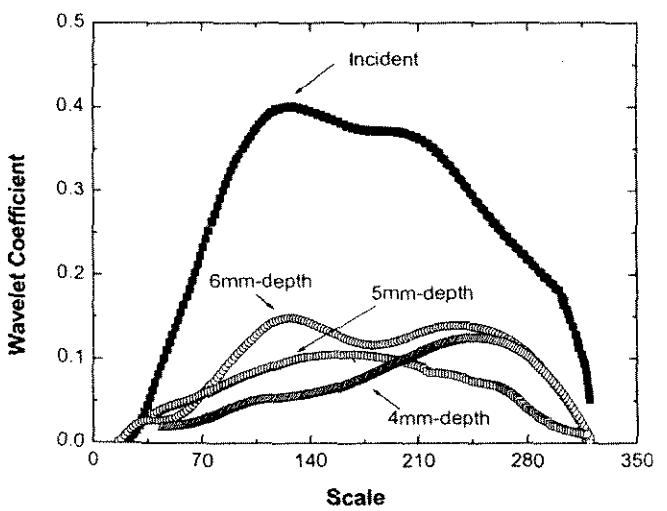

Figure 11 Profile curve of CWT coefficients for signals.

transform technique as well as a high-resolution data acquisition system, with which satisfactory diagnosis results have been achieved. The sensitivity of the identification algorithm was then evaluated. The experimental results indicate that the identification accuracy depends on the actual severity of the damage. Unacceptable error occurs only when the damage is very severe (the damage size is over 65% of the cross-sectional area of the beam). In practice, such a kind of large destruction is normally not the concern of the structural health monitoring.

Health monitoring techniques and identification systems for more complicated structures, such as laminated fibre composite plates, will be presented in forthcoming reports.

Table 3 Diagnosis results and relative percentage errors for a crack with variable depths in a beam.

Actual Damage Degree	*Location Diagnosis* (mm)		*Degree Diagnosis* (mm)			
	Calculated Value (To the Right End)*	*Minimum Error* (%)	*Calculated Value by RMS Method*	*Minimum Error* (%)	*Calculated Value by Integration Method*	*Minimum Error* (%)
1 mm	373	6.57	1.073	7.25	1.073	7.31
2 mm	336	4.00	2.100	4.90	2.104	5.19
3 mm	341	2.79	3.150	4.69	2.853	4.89
4 mm	359	2.65	3.832	4.17	4.161	4.02
5 mm	340	2.26	5.115	2.30	4.862	2.76
6 mm	357	2.05	6.123	2.05	6.141	2.35
7 mm	355	1.13	6.404	8.52	7.642	9.17
8 mm	346	1.02	6.200	22.5	6.152	23.1

*The actual damage position is 350 mm away from the right end of the beam.

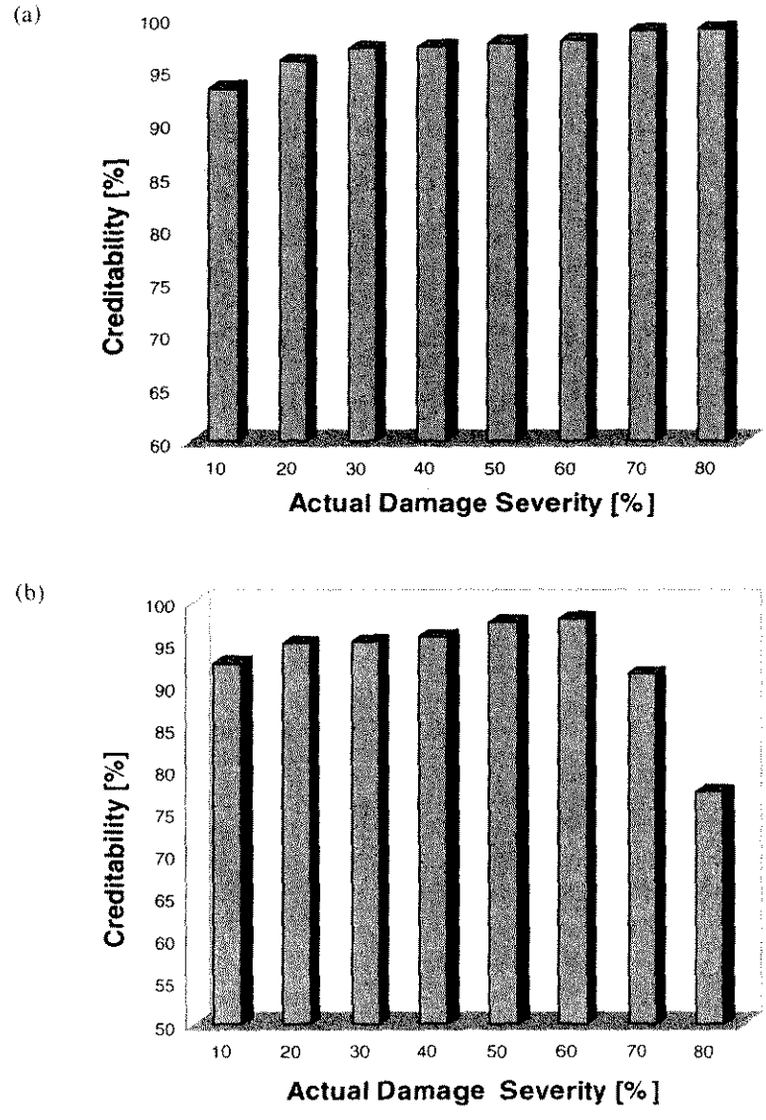

Figure 12 Credibility for proposed identification scheme: (a) for damage location diagnosis; (b) for damage degree diagnosis.

Acknowledgement

Z. SU would like to gratefully acknowledge the support of the International Postgraduate Research Scholarship (IPRS) from the Department of Education Science and Training (DEST), Australia, and the International Postgraduate Award (IPA) from the University of Sydney. While X. BU appreciates the support from the China Scholarship Council.

Appendix

Considering a 3D spectrum over the time-scale domain obtained via the CWT analysis, the magnitude of a wave energy ridge in this spectrum, denoted hereafter by A_{ridge}, along the scale axis at an arbitrary time point, can be calculated by RMS method [25],

$$A_{\text{ridge}} = \sqrt{\frac{W_1^2 + W_2^2 + \cdots + W_N^2}{N}} \tag{A1}$$

where $W_i (i = 1, N)$ is the ith wavelet coefficient on the profile curve along the scale axis, whilst N denotes the total number of discretised points, which is determined by the precision of the selected wavelet transform.

Similarly, as for two energy ridges in one spectrum, A_{ridge1} and A_{ridge2}, at different time points t_1 and t_2 respectively, their amplitude ratio can be defined as following if the same wavelet transform function and transforming precision are chosen,

$$\left(\frac{A_{\text{ridge1}}}{A_{\text{ridge2}}}\right) = \sqrt{\frac{W_1^2 + W_2^2 + \cdots + W_N^2|_{t=t_1}}{W_1^2 + W_2^2 + \cdots + W_N^2|_{t=t_2}}} \tag{A2}$$

When N is large enough, Equation (A2) is equivalent to,

$$\left(\frac{A_{\text{ridge1}}|_{t_1}}{A_{\text{ridge2}}|_{t_2}}\right)^2 = \frac{\int_{S_{\min}}^{S_{\max}} W^2|_{t=t_1} \cdot da}{\int_{S_{\min}}^{S_{\max}} W^2|_{t=t_2} \cdot da} \tag{A3}$$

where a represents the variable on the scale axis.

Meantime, derived from the definition of wavelet transform [21],

$$W(a,b) = \frac{1}{\sqrt{a}} \int_{-\infty}^{+\infty} f(t) \cdot \Psi^*\left(\frac{t-b}{a}\right) \cdot dt \tag{A4}$$

where $f(t)$ represents any time-dependent signal, its inverse wavelet transform exists,

$$f(t) = \frac{1}{C_\Psi} \int_{-\infty}^{+\infty} \int_{a>0}^{+\infty} W(a,b) \cdot \frac{1}{\sqrt{a}} \times \Psi\left(\frac{t-b}{a}\right) \cdot \frac{1}{a^2} da \cdot db \tag{A5}$$

where a is the scale parameter while b is the translation parameter, both of which are real number and a must be positive. C_Ψ is a constant and $\Psi^*(t)$ denotes the complex conjugate of $\Psi(t)$. Derived on Equations (A4) and (A5), the following proportional relation exists [21],

$$E \propto \int_{\text{Min}}^{\text{Max}} |W(a,b)_{b=t}|^2 da \tag{A6}$$

For two given energy components, E_1 and E_2, over time-scale domain, at different time points, t_1 and t_2, respectively, it exists,

$$\frac{E_1}{E_2} = \frac{\int_{\text{Min}}^{\text{Max}} |W(a,b)_{b=t_1}|^2 da}{\int_{\text{Min}}^{\text{Max}} |W(a,b)_{b=t_2}|^2 da} \tag{A7}$$

On the other hand, in the time domain, the energy ratio for two sampled signals is known to be equal to [21],

$$\frac{E_{t=t_1}}{E_{t=t_2}} = \frac{|f_1(t)|^2_{t_1}}{|f_2(t)|^2_{t_2}} \tag{A8}$$

Combining Equations (A7) and (A8), the energy ratio for two wave components, at specific time points, t_1 and t_2 respectively, can be

yielded as,

$$\frac{E_{t=t_1}}{E_{t=t_2}} = \frac{\int_{\text{Min}}^{\text{Max}} |W(a,b)_{b=t_1}|^2 da}{\int_{\text{Min}}^{\text{Max}} |W(a,b)_{b=t_2}|^2 da} = \frac{|f_1(t)|^2_{t_1}}{|f_2(t)|^2_{t_2}} \quad \text{(A9)}$$

Therefore, via Equations (A3) and (A9), the reflection ratio can be given:

$$\frac{|f(t_1)|}{|f(t_2)|} = \left| \left(\frac{A_{\text{ridge1}}|_{t_1}}{A_{\text{ridge2}}|_{t_2}} \right) \right| \quad \text{(A10)}$$

References

1. Daubechies, I. (1990). The wavelet transform, time-frequency localization and signal analysis. *Journal of IEEE Transactions on Information Theory, 36(5)*, 961–995.
2. Newland, D.E. (1994). Wavelet analysis of vibration, Part I: Theory. *Journal of Sound and Vibration, 116*, 409–416.
3. Kim, Y.Y. and Kim, E.H. (2000). A new damage detection method based on a wavelet transform. *Proceedings of 18th IMAC*. San Antonio, Texas, USA. pp. 1207–1212. 7–10 February.
4. Samuel, P. and Pines, D. (1997). Health monitoring/ damage detection of a rotorcraft planetary geartrain system using piezoelectric sensors. *SPIE, 3041*: 44–53.
5. Sung, D.U., Oh, J.H. and Kim, C.G. (2000). Impact monitoring techniques for smart composite laminates. *Proceedings of the Second Asian-Australasian Conference on Composite Materials*. Korea. pp. 1123–1128. 18–20 August.
6. Kim, Y.Y. and Kim, E.H. (2001). Effectiveness of the continuous wavelet transform in the analysis of some dispersive elastic waves. *J. Acoust. Soc. Am., 110(1)*, 1–9.
7. Chakraborty, G. and Mallik, A.K. (2000). Wave propagation and vibration of a traveling beam with and without non-linear effects, Part I: free vibration. *Journal of Sound and Vibration, 236*, 277–290.
8. Kawiecki, G. (1998). Feasibility of applying distributed piezo transducers to structural damage detection. *Journal of Intelligent Material Systems and Structures, 9(3)*, 189–197.
9. Zhou, Z., Noori, M. and Amand, R.S. (2000). Wavelet-based approach for structural damage detection. *Journal of Engineering Mechanics, 7*, 667–683.
10. Zou, Y., Tong, L. and Steven, G.P. (2000). Vibration-based model-dependent damage (delamination) identification and health monitoring for composite structures a review. *Journal of Sound and Vibration, 230*, 257–278.
11. Achenbach, J.D. (2000). Quantitative nondestructive evaluation. *International Journal of Solids and Structures, 37*, 13–27.
12. Wang, M.L., Heo, G. and Satpathi, D. (1998). Health monitoring system for large structural systems. *Smart Materials and Structures, 7*, 606–661.
13. Lakshmanan, K.A. and Pines, D.J. (1997). Modeling damage in rotorcraft flexbeams using wave mechanics. *Smart Materials and Structures, 6*, 383–392.
14. Vera, C.P.D. and Guemes, J.A. (1998). Embedded self-sensing piezoelectric for damage detection. *Journal of Intelligent Material Systems and Structures, 9(11)*, 876–887.
15. Wolfinger, C., Arendts, F.J. and Friedrich, K. (1996). Health-monitoring based on piezoelectric transducers. *Aerospace Science and Technology, 6*, 391–400.
16. Salawu, O.S. (1997). Detection of structural damage through changes in frequency: a review. *Engineering Structure, 19(9)*, 718–723.
17. Laura, P.A.A., Malfa, S.L. and Bambill, D.V. (1998). Monitoring structural health through changes in frequency. *Journal of Sound and Vibration, 212(5)*, 909–911.
18. Tracy, M. and Chang, F.-K. (1998). Identifying impacts in composite plates with piezoelectric strain sensors, Part I: Theory. *Journal of Intelligent Material Systems and Structures, 9(11)*, 920–927.
19. Boller, C. (2001). Ways and options for aircraft structural health monitoring. *Smart Materials and Structures, 10*, 432–440.
20. Doyle, J.F. (1997). *Wave propagation in structures*. Springer-Verlag, New York. 2nd Edn.
21. Chan, Y.T. (1995). *Wavelet basic*. Kluwer Academic Publishers, Boston. 1st Edn.
22. Chui, C.K. (1997). *Wavelets: a mathematical tool for signal processing*. SIAM, Philadelphia, 1st Edn.
23. The Mathworks Inc. (2000). Wavelet Toolbox: for Use with Matlab (User's Guide). Ver: 1.0.
24. Boashash, B. (1992). *Time-frequency signal analysis, Methods and applications*. 1st Edn. Longman Cheshire Press, Melbourne.
25. OriginLab Co. (2000). User's Guide, Ver: 6.1052.

SHM
Structural Health Monitoring

Fundamental Lamb Mode-based Delamination Detection for CF/EP Composite Laminates Using Distributed Piezoelectrics

Zhongqing Su and Lin Ye*

Laboratory of Smart Materials and Structures (LSMS),
Centre for Advanced Materials Technology (CAMT),
School of Aerospace, Mechanical and Mechatronic Engineering,
The University of Sydney, NSW 2006, Australia

A delamination detection scheme for the CF/EP composite laminates based on the Lamb wave propagation was proposed. The fundamental symmetric Lamb mode (S_0) and the delamination-induced basic shear mode (S_0') in an ultrasonic frequency range were utilised for locating the delamination. Both numerical simulation and experimental studies were performed to evaluate the propagation characteristics of Lamb waves in the composite laminates involving a delamination. An active online damage diagnosis system was established with a transducer network configured using distributed piezoelectrics. Bandpass filters were designed and spectrographic analyses in the time-scale space via wavelet transform technique were accomplished, to diminish diverse broadband interferences and consequently improve signal interpretation. Algorithm based on a graphic approach was introduced into the damage searching procedure to expedite the diagnosis and minimise the estimation errors. The proposed identification scheme and diagnosis system were then validated by detecting delaminations in CF/EP laminates made from unidirectional and woven fabric prepreg, respectively. Satisfactory prediction for the damage location has been achieved. Additionally, the influence of diagnostic waveforms and frequencies on the identification accuracy was also evaluated.

Keywords fibre-reinforced composite · structural health monitoring (SHM) · Lamb wave · finite element method (FEM) · wavelet transform

1 Introduction

Delamination, induced by the interlaminar stresses, is probably the most common internal defect in carbon fibre (CF)/epoxy (EP)-laminated composites, and it can originate and develop during manufacturing or as a result of accidental out-of-plane impact during service. The occurrence of delamination may considerably lower the strength, stiffness or damping properties of the composites and severely reduce the structural integrity and reliability. It is therefore momentous for engineers and researchers to pursue effective and reliable detection techniques, with which the delamination might be detected at its initial stage.

Conventional nondestructive evaluation (NDE) for structural criticality, such as C-scan

*Author to whom correspondence should be addressed.
E-mail: ye@aeromech.usyd.edu.au

Vol 3(1): 0043–68
[1475-9217 (200403) 3:1;43–68 10.1177/1475921704041874]

and radiographic inspection, or model-based methods, ranging from modal analyses to static parameters identification, are facing the challenge of compromise between satisfactory estimation accuracy and versatile applicability in practice. Motivated by this, innovations in NDE field have become an increasing concern over years, leading to intensive researches on the novel and improved techniques. Amongst them, Lamb wave-based detection approaches have been increasingly attracting noticeable preferences, encouraged for damage assessment with high precision requirement [1–13]. Generated and monitored by transducers expediently and efficiently, Lamb wave is able to propagate over a relatively long distance even in materials with high attenuation ratio, such as CF/EP laminated composites, and thus a broad area can be investigated with only a few transducers. Meanwhile, the entire thickness of the laminate may be interrogated in virtue of different vibration patterns of various Lamb modes, which affords possibility to detect the internal damages as well as the defects on the surface. In the majority of existing literatures [1–10], the ultrasonic probes were widely used for the generation and monitoring of Lamb waves for their excellent accessibility and accuracy. However, the further applications of ultrasonic probes for online detection may be hindered due to the poor affinity with practical engineering structures and the non-neglectable size and weight. Additionally, in most cases, a period of temporary out-of-service for the structures to be inspected is required to ensure the probes are operational. It is obvious that these deficiencies have considerably limited their applications, such as the health surveillance for in-service aircrafts, where the structural components are expected to combine the designed functions together with self-assessment and self-rehabilitation capabilities. Under such a circumstance, the integration of *in situ* transducers into the structures is regarded as a promising measure to feature the smart function for the real-time damage monitoring. Wang et al. [11] reported a practical damage identification approach using distributed piezoelectric devices; Lemistre et al. [12] successfully detected the structural damage using Lamb wave generated by piezoelectrics; while Gaul et al. [13] determined the history of an external transient force applied on a structure by analysing the responses measured by piezoelectric materials. In these studies, the piezoelectrics exhibit low acoustic impedance and wide frequency responses yet with minor intrusion into the structures, serving as a practical and reliable integrated signal transmitter.

On the other hand, the study upon characteristics of Lamb wave propagation in the laminated composites and the damage evaluation using numerical simulation have been rigorously explored for a couple of years, and related achievements are in a good supply [2,4–7,14–16]. Most of the related work, however, is limited in either one-dimensional or two-dimensional situations, in which the internal damage, a complicated three-dimensional pattern, usually has to be simplified with certain scenarios, leading to approximate simulations.

The efforts in this study are aimed at developing a delamination identification scheme for CF/EP composite structures based on the Lamb wave propagation. A detection algorithm using the wavelet transform technique was developed. The propagation properties of fundamental Lamb modes interacted with interlaminar delamination were examined through numerical and experimental analyses. For this, a full-scale three-dimensional finite element model was developed and structural dynamic analyses were performed. An active diagnosis system incorporated with piezoelectrics network was consequently established in accordance with the identification scheme, and it was then validated to locate delaminations in CF/EP laminates made from unidirectional and woven fabric prepreg, respectively.

2 Lamb Waves in the Composites

2.1 Propagation Characteristics of Lamb Wave in Laminated Composites

Lamb wave, a guided wave propagating in the plate-like structures, is known to be dispersive during propagation in the viscoelastic medium, whose properties rely on not only the material properties and structural geometry, but also the

excitation conditions. In most cases, more than two modes are synchronously available; and the vibration patterns and dispersive properties throughout the plate thickness are not identical for different modes, even for the same mode but in different frequency ranges. Practically, the angle-variable ultrasonic probes are normally employed to produce the pure and single Lamb mode in accordance with the Snell's law [17], shunning multiple modes. Compared with the components generated by ultrasonic probes, the Lamb waves induced by the piezoelectric elements directly, such as a PZT disk, unavoidably contain multi-modes simultaneously, which can be basically classified as *symmetrical* and *anti-symmetrical* modes, depending on the particulate motion patterns.

Dispersion characteristics of Lamb waves in the multilayered medium are some of the pivotal concerns for development of guided wave-based damage detection techniques. Lamb waves are known for owning a strong ability to propagate over a relatively long distance while without significant attenuation in the energy and wave amplitudes, even in the materials with a high attenuation ratio, such as CF/EP-laminated composites [17]. However, the dispersion phenomena with the variation in wave frequency were clearly observed, dependent on the structural thickness. The dispersive properties for fundamental Lamb wave modes in an 8-layers $[45/-45/0/90]_s$ CF/EP quasi-isotropic composite laminate were experimentally evaluated. In experiments, wave phase velocities for symmetric and anti-symmetric Lamb modes, excited by a PZT actuator in a sweep frequency ranging from 0.1 to 1.5 MHz with a step of 50 Hz, were measured individually by PZT sensors. The dispersion curves for fundamental Lamb waves in terms of wave phase velocities and excitation frequencies are plotted in Figure 1. Meanwhile the dispersion curves theoretically calculated using the method proposed by Percival et al. [2] are also included in Figure 1 for comparison. Good correlation between them can be noticed. The fundamental anti-symmetric Lamb mode, A_0, symmetric Lamb mode, S_0, and the lowest order shearing mode, S_0', are observed in the low frequency region, while higher order modes appear gradually with increase in frequency. The dispersion properties shown in Figure 1 indicate the presence of multiple Lamb modes in the laminated composite, whose phase/group velocities

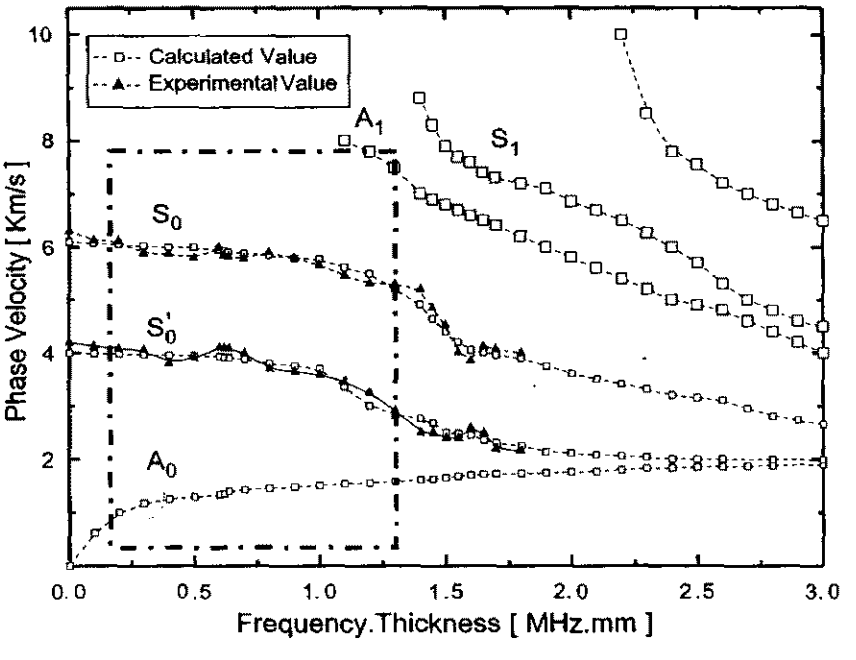

Figure 1 Dispersion properties for Lamb waves in an 8-ply quasi-isotropic CF/EP laminate.

are dependent on the algebraic product of the laminate thickness and the central excitation frequency. Whereas for the current structure, a low-frequency domain (< 1.2 MHz mm) exists, in which the fundamental modes exhibit reasonably non-dispersive behaviour. In the present work, the fundamental symmetric Lamb mode, S_0, and the defect-induced basic shear mode, S_0^v, were utilised for the damage detection.

2.2 Interaction between Lamb Modes and Internal Defect in the Composites

The interaction between fundamental Lamb modes and the interlaminar delamination in CF/EP $[45/-45/0/90]_s$ quasi-isotropic composite laminate was numerically investigated. A rectangular laminate ($480 \times 480 \times 1.275\,mm^3$) with an assumed elliptic delamination (semi-major axis: 15 mm, semi-minor axis: 10 mm, angle between the major axis and 0° fibre direction: 135°, centre position: 276 and 299 mm away from the left and bottom edges of the laminate, respectively, delaminated area: 0.25% of surficial area of laminate) between the 1st and the 2nd layers was considered. One pair of its edges were fixed-supported while the other pair were kept free. Four PZT disks, acting as both actuators and sensors, were located at the corners of a square route, 65 mm away from the two neighbouring laminate edges, counter-clockwise numbered with *P*1, *P*2, *P*3 and *P*4 from the bottom-left one, schematically delineated in Figure 2.

Full-scale three-dimensional FEM model with fine mesh description was created for the delaminated laminate on the PATRAN® platform [18], while the dynamic analyses were accomplished using ABAQUS/EXPLICIT® FEM code [19] using a super computer. Eight layers were divided along the laminate thickness to characterise each unidirectional lamina individually, leading to approximately 100,000 solid brick elements used for the simulation. The ichnographic FEM model for the vicinity of delaminated area is given in Figure 3(a), where more than 10 nodes exist within one wavelength. For comparison, modelling and numerical simulation for the laminate without artificial defect were also conducted. The time step adopted in dynamic calculation was controlled to be clearly less than the ratio of the minimum distance of any two adjoining FEM nodes to the maximum achievable wave velocity. A surface contact algorithm [19], permitting a small sliding relative displacement and arbitrary rotation of two delaminated surfaces, was introduced to process the contact problem arising from the delamination, sketched in Figure 3(b), which was proven in this study to be virtual in approximating the delamination. The technical information for the CF/EP composites considered in the simulation is listed in Table 1(a); while the mechanical properties for unidirectional laminae estimated using a micromechanics model [20] based on properties of constituents (carbon fibre and epoxy matrix), in accordance with the composite laminates used in the following experiments, were detailed in Table 1(b). In addition, PZT

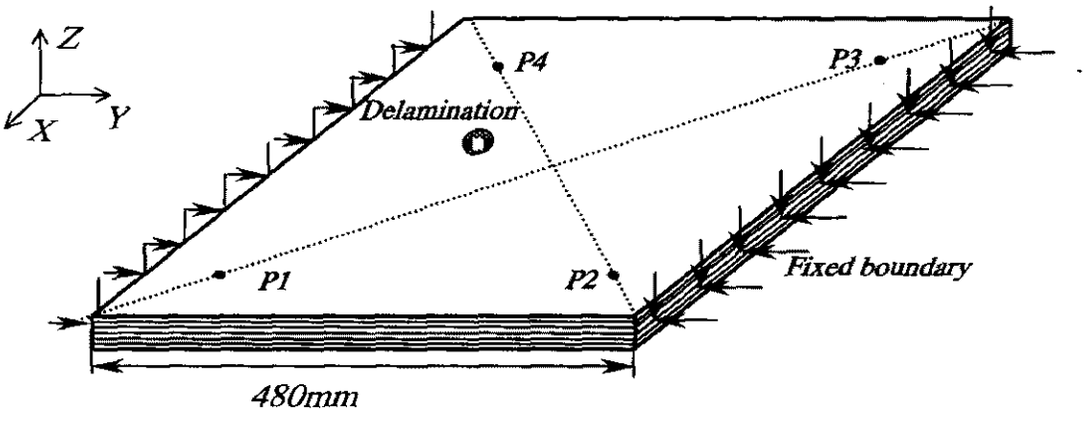

Figure 2 Composite laminate for numerical simulation.

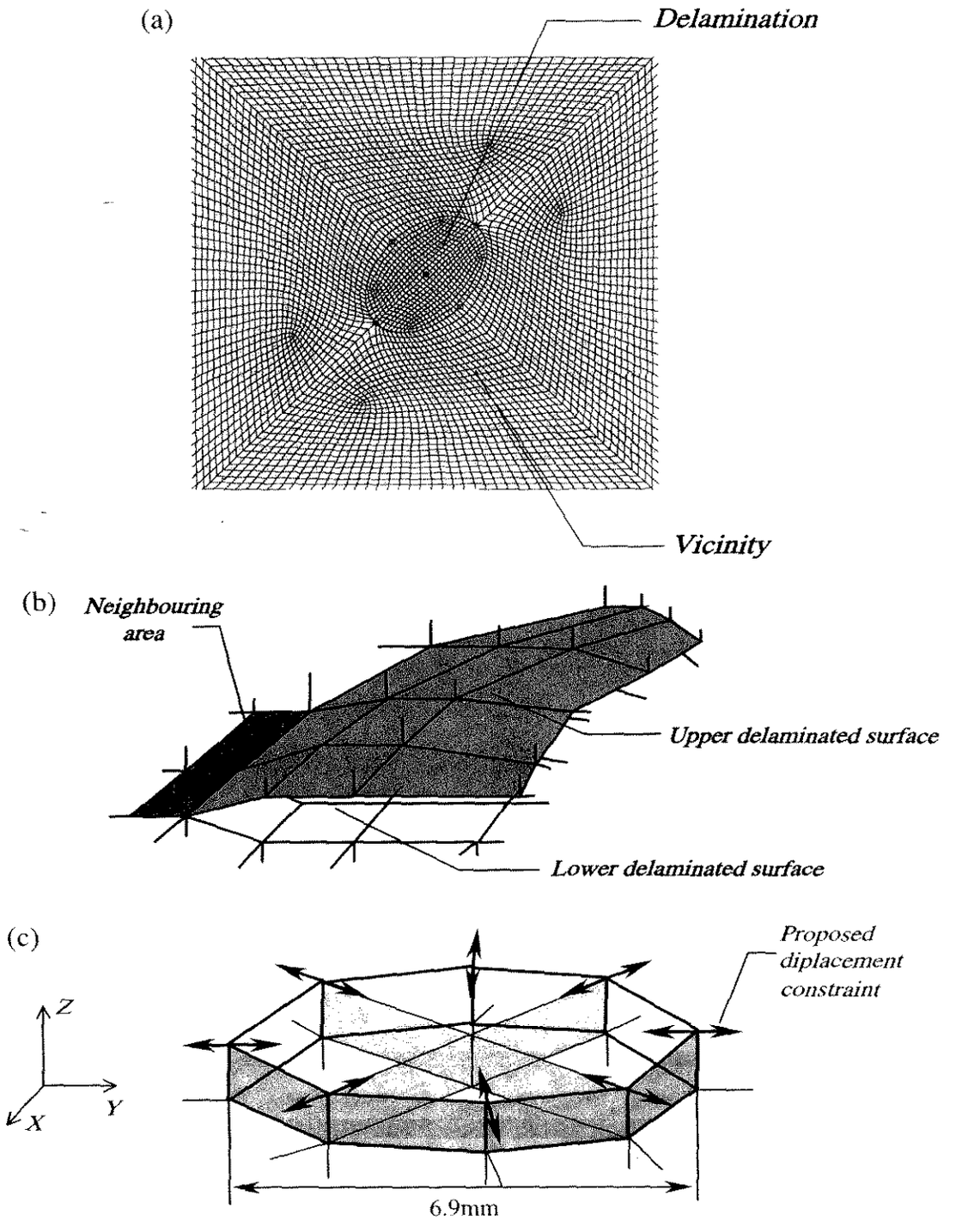

Figure 3 FEM modelling in numerical simulation: (a) mesh near delamination area; (b) contact surfaces for delamination; and (c) applied displacement constraints in the actuator area.

actuators/sensors were individually modelled [21]. A uniform radial displacement in the x–y plane, following a 5-cycle sinusoidal toneburst windowed with *Hanning* function at a central frequency of 0.5 MHz, was applied on the actuator model [21] to generate the Lamb modes, as described in Figure 3(c). The structural responses were dynamically monitored using the sensor model [21] at a

Table 1 Configurations of specimens

(a) Technical data for CF/EP composites used in simulation and experiment.

	Fibre Product Name	*Matrix Product Name*	*Fibre Fraction* (%)	*Matrix Fraction* (%)	*Laminate Density* (kg/m^3)	*Weave*	*Count Warp* × *Fill*
UD	T650/35-12K	F584	56	44	1528	N/A	N/A
WF	T300/3K	F593	48	52	1376	Plain	12.5 × 12.5

(b) Estimated elastic properties for unidirectional CF/EP lamina.

E_{11} (GPa)	E_{22} (GPa)	E_{33} (GPa)	G_{12} (GPa)	G_{13} (GPa)	G_{23} (GPa)	ν_{12}	ν_{13}	ν_{23}
153.67	9.49	9.49	4.26	4.26	3.44	0.295	0.295	0.381

(c) Geometric identities of laminates and delaminations (Unit: mm).

Specimen No.	*Geometric Dimension* (mm)	*Simulated Delamination*					
		α	β	ϕ	ξ	ζ	θ
UD1#	480 × 480 × 1.275	N/A	N/A	N/A	N/A	N/A	N/A
UD2#	480 × 480 × 1.275	15	10	135	276	299	0.25
WF1#	480 × 480 × 1.454	N/A	N/A	N/A	N/A	N/A	N/A
WF2#	480 × 480 × 1.454	17	12	45	268	190	0.18

α: semi-major axis; β: semi-minor axis; ϕ: angle between the major axis and 0° fibre direction; ξ: vertical distance to the left edge from centre of the delamination; ζ: vertical distance to the bottom edge from centre of the delamination; θ: percentage of delaminated area (%) in laminate.

sample rate of 20.48 MHz. Stereo-visualised plots from FEM for Lamb wave propagation in the delaminated composite plate with a time interval of 10 μs are shown in Figure 4, where the internal defect-imposed disturbance on the Lamb wave propagation can be clearly observed.

A series of bandpass filters with proposed thresholds were designed, introduced hereinafter, and applied on the simulated signals to screen the broadband noisy interferences and extract diagnostic components in the frequency scopes corresponding to the excitation. The filtered dynamic signals via actuator–sensor path *P*1–*P*3, as typical examples, for the composite laminates without/with delamination are displayed in Figure 5. Mode conversion induced by the existence of delamination is noticed in the signals for defective specimen. Compared with Figure 5(a), extra Lamb mode in the selected frequency scope is clearly observed in Figure 5(b), which is recognised as the damage-induced basic shear mode, hereafter denoted by $S'_{0\text{Delam}}$. Other damage-induced modes are unexploitable because their velocities are either too close to other actuator-generated wave modes in the limited sampling period, or too slow to be sampled in the specific time.

3 Signal Processing and Experimental Implementation

3.1 Wavelet Transform Principles

Muddled by the structural low-frequency vibration patterns and diverse broadband noise corruptions, the interpretation of both theoretically calculated structural responses and experimentally acquired signals are not straightforward for damage detection in either the time or frequency domain. An identification algorithm based on the spectrographic analysis in the time-scale space was developed using the *Discrete Wavelet Transform* (DWT) and *Continuous Wavelet Transform* (CWT) technique [22–26]. *Daubechies* function was chosen as the wavelet transform function, which was experimentally demonstrated in this study to be most effective for the present system compared with other transform functions.

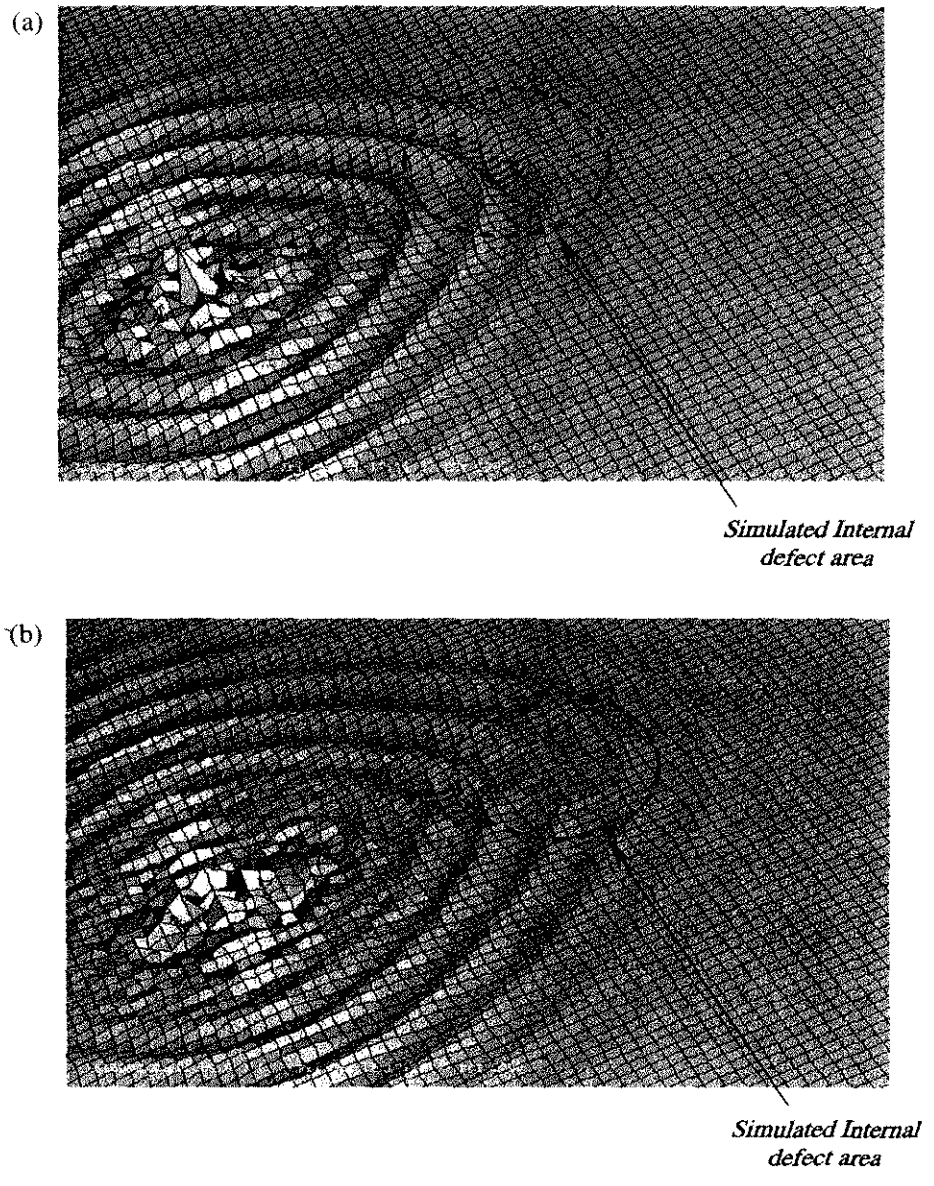

Figure 4 Defect-impacted disturbance on Lamb wave propagating in composite laminates: (a) at the 55th microsecond after excitation and (b) at the 65th microsecond after excitation.

Herein, for an arbitrary sampled signal $f(t)$, the discrete expression in the time-scale domain could be achieved by applying the selected basic wavelet function $\Psi(t)$ (*Daubechies* in this study) as [22],

$$a = a_0^m \text{ and } b = na_0^m b_0, \quad m, n \in Z \tag{1a}$$

$$DWT(m,n) = a_0^{-m/2} \int f(t) \cdot \Psi(a_0^{-m} t - nb_0) \cdot dt \tag{1b}$$

where a and b are the *scale* and *time* parameters, which were discreted by dyadic variables m and n, while a_0 and b_0 are constants determining the sampling intervals. Reversely, the signal could be reconstructed by [26],

$$f(t) = c \sum_m \sum_n C_{mn}(t) \cdot DWT(m,n) \tag{2a}$$

$$C_{mn}(t) = a_0^{-m/2} \Psi(a_0^{-m} t - nb_0) \tag{2b}$$

where c is a constant in correlation with $\Psi(t)$. Time-dependent function $C_{mn}(t)$, is defined as the

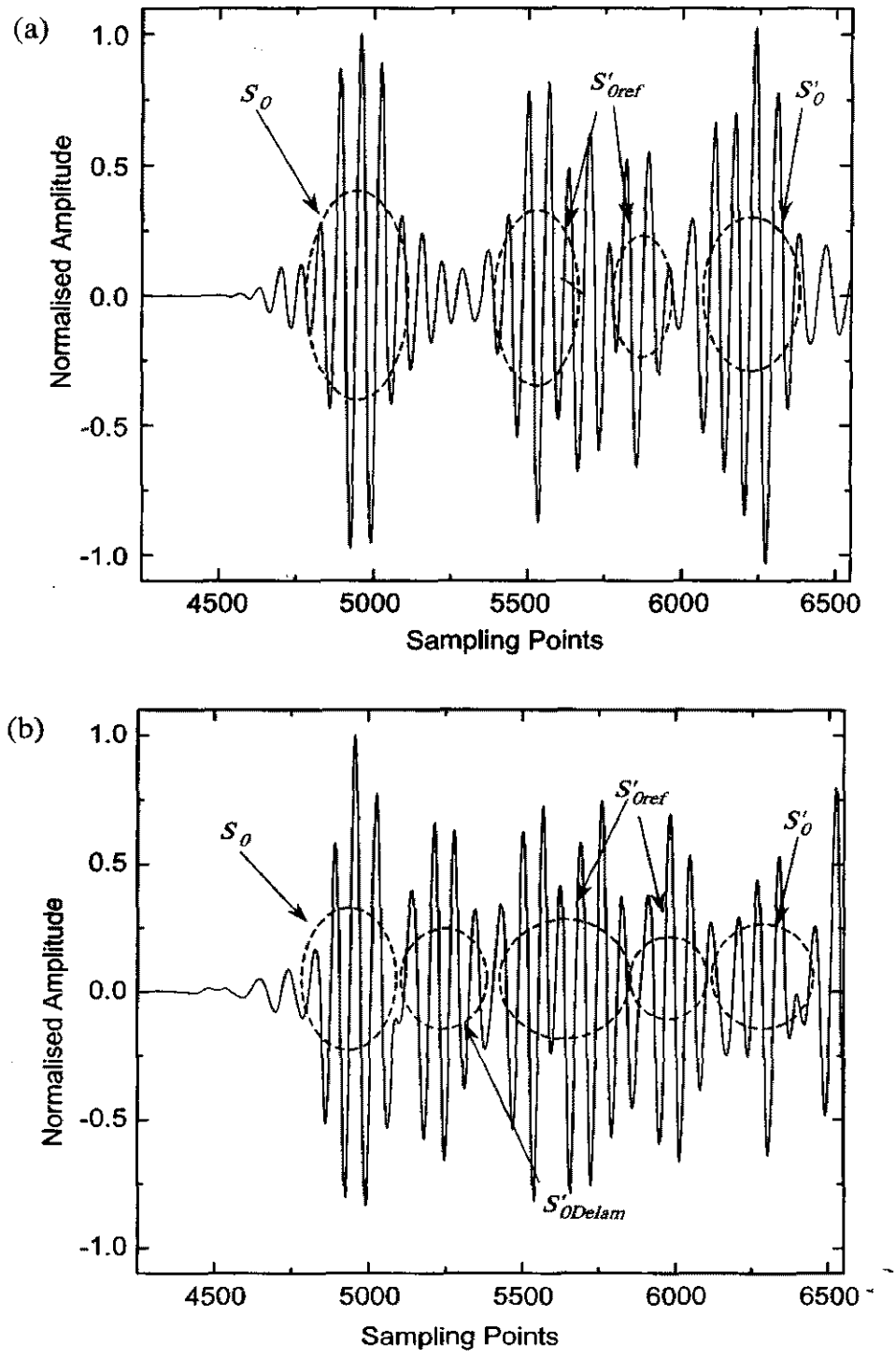

Figure 5 DWT analysis-processed structural responses via actuator–sensor path *P*1–*P*3 in simulation: (a) for laminate without delamination and (b) for laminate with delamination.

DWT coefficient, and the overline indicates the complex conjugate.

Based on Equations (1b) and (2), a series of bandpass filters with discreted initial thresholds and frequency scopes were established, with which the one-dimensional time-dependent wave signals were decomposed into associated band ranges according to frequency. Lamb wave components

pertaining to the excitation were therefore separated and characterised without diverse interferences.

Serialising Equation (1), signal $f(t)$ was converted into a quadratic description as [22],

$$CWT(a,b) = \frac{1}{\sqrt{a}} \int_{-\infty}^{+\infty} f(t) \cdot \overline{\Psi\left(\frac{t-b}{a}\right)} \cdot dt \qquad (3)$$

where $CWT(a,b)$ is defined as the *CWT wavelet coefficient*. Conversely, the signal was reconstructed via the inverse continuous wavelet transform,

$$f(t) = \frac{1}{C_\Psi} \int_{-\infty}^{+\infty} \int_{a>0}^{+\infty} CWT(a,b) \cdot \frac{1}{\sqrt{a}} \cdot \Psi\left(\frac{t-b}{a}\right) \cdot \frac{1}{a^2} da \cdot db \qquad (4)$$

where C_Ψ is a constant depending on $\Psi(t)$. Energy allocation for the wave signal was furthermore derived, in light of Equations (3) and (4) as,

$$E = \int_{-\infty}^{+\infty} \int_{a\geq 0}^{+\infty} |W(a,b)|^2 da \cdot db \qquad (5)$$

where $|CWT(a,b)|^2$, defined as the *scalogram*, indicates energy density in the time-scale domain. Based on Equations (3)–(5), the sampled signals were decomposed into two- and three-dimensional time-scale spaces with the intuitive illustration for the energy allocation, which offers a full display of the characteristics for acquired signals, more capable of detecting local perturbations in the signals. If the detected perturbation is not caused by the factors already known, such as a geometric boundary, it can be attributed to the existence of a damage. In the present study, the characteristic times for different Lamb modes in the time-scale space, at which the wave energy reached its maximum/minimum, were captured using a special program. The time differences among concerned Lamb modes, such as the one between incident and damage-reflected modes, were used to predict the damage location. In this study, identification of delamination location in the CF/EP composite laminates was conducted, while complete quantitative identification for damage severity using the energy allocation is reported elsewhere [27, 28].

In the above discussion, the spectrographic analyses were conducted in the time-scale domain, rather than the time–frequency space. The parameter *scale* (a) in Equations (1)–(5) is directly proportional to the *reciprocal of frequency* ($1/f$), depending on the selected wavelet transform function. It was found that the wave energy allocation could be more easily defined by representing the acquired signal into the time-scale domain [22, 29].

3.2 Configuration of Diagnosis System

An active online damage diagnosis system was established in accordance with the identification principle, sketched in Figure 6. It consists of Signal Excitation Unit (SEU), Signal Acquisition Unit (SAU) and Central Control Unit (CCU). A transducer network was designed using Piezoelectric Lead Zirconate Titanate (PZT) wafers, 6.9 mm in diameter and 0.5 mm in thickness, which was surface-bonded on each laminate and controlled by the SEU and SAU. Two-way switches were attached to SEU and SAU, making each PZT transducer function as both actuator and sensor, minimising the number of transducers and intrusion into the structure. While diagnostic signal, simulated by *Agilent© E1441* on *NI Labview©* platform, was applied on actuators through SEU after amplified to 60 V_{PP} (peak-to-peak) by a PZT amplifier (*PiezoSys© EPA-104*). Signal acquisition was performed via *Agilent© E1437A* digitizer at a sample rate of 20.48 MHz through *IEEE-488* bus; and the acquired signal was conditioned by *Agilent© E3242A* before transmitted into CCU. Being the key unit of the system, CCU performed as both controller and interpreter, supported by an inhouse software developed on the *NI Labview©* platform using *Matlab©* package [29], and finally the diagnostic results were output to the user's interface.

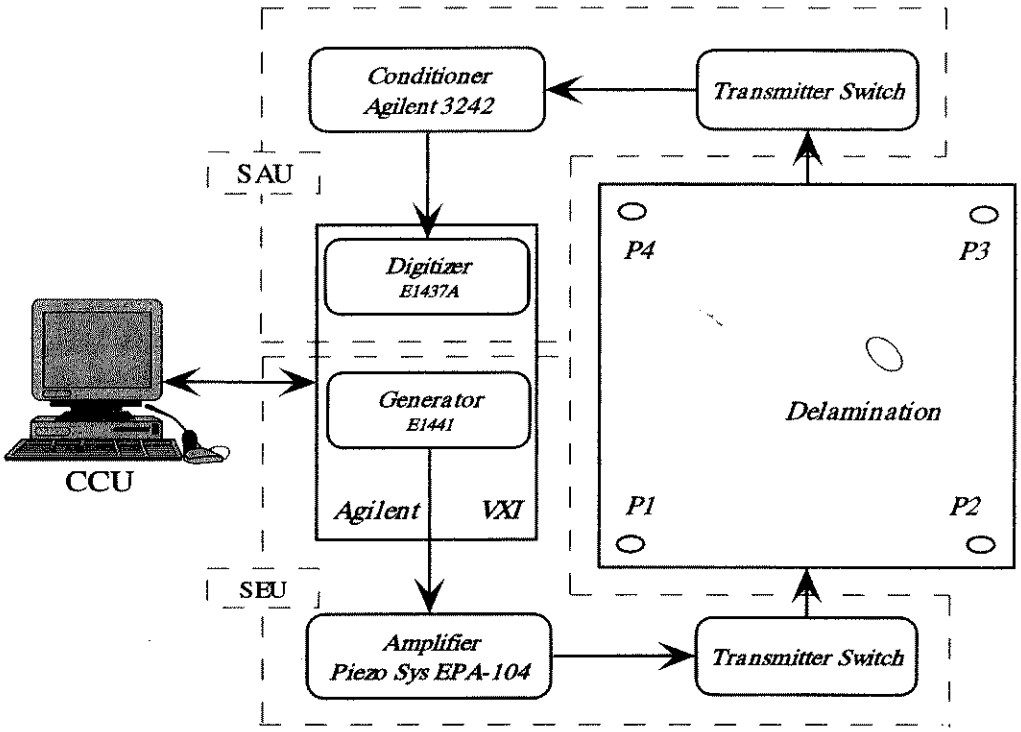

Figure 6 Configuration of diagnosis system using distributed piezoelectrics network.

3.3 Experimental Implementation

The proposed identification principle and developed diagnosis system were then validated by locating delaminations in CF/EP T650/F584 $[45/-45/0/90]_s$ quasi-isotropic laminates made from unidirectional (UD) prepreg, and CF/EP T650/F593 $[(0/90)/(-45/45)/(90/0)]_s$ orthotropic laminates made from plain woven fabric (WF) prepreg, respectively. The geometric identities for specimens are the same as those summarised in Table 1(c). A delamination with the same shape and size in the above numerical simulation was introduced using two pieces of *UPLEX©-R-25* film of 25 μm thickness during manufacturing. For comparison, the specimens without the delamination were also fabricated. The benchmark/defective laminates are represented by symbol $UD1^{\#}/UD2^{\#}$ for the unidirectional prepreg laminates and $WF1^{\#}/WF2^{\#}$ for the woven fabric prepreg laminates, respectively.

Amplified and modulated toneburst with various waveforms, at central excitation frequencies from 0.1 to 1.0 MHz, was applied on each PZT wafer in turn to generate the Lamb waves. When one wafer was activated, other three wafers were used to real-time monitor the structural response. By virtue of the two-way switches engaged in the SEU and SAU, totally 12 actuator–sensor paths were available with 4 transducers. Structural response signals were dynamically acquired for each actuator–sensor path in the experiment at the same sample rate used in simulation (20.48 MHz).

4 Damage Identification

4.1 Signal Interpretation

In the experiment, good repeatability for the signal acquisition was noticed. Arbitrarily chosen as typical examples, acquired signals for specimens $UD1^{\#}/UD2^{\#}$ via actuator–sensor path *P1–P3* and those for specimens $WF1^{\#}/WF2^{\#}$ via path *P2–P4* are displayed in Figures 7 and 8, respectively. Certain differences can be noticed between the structural responses for the benchmark and defective laminates in the time domain. Meanwhile, the frequency spectrum analyses by *Fast Fourier Transform* (FFT) were also performed, and the spectra for the chosen signals are correspondingly

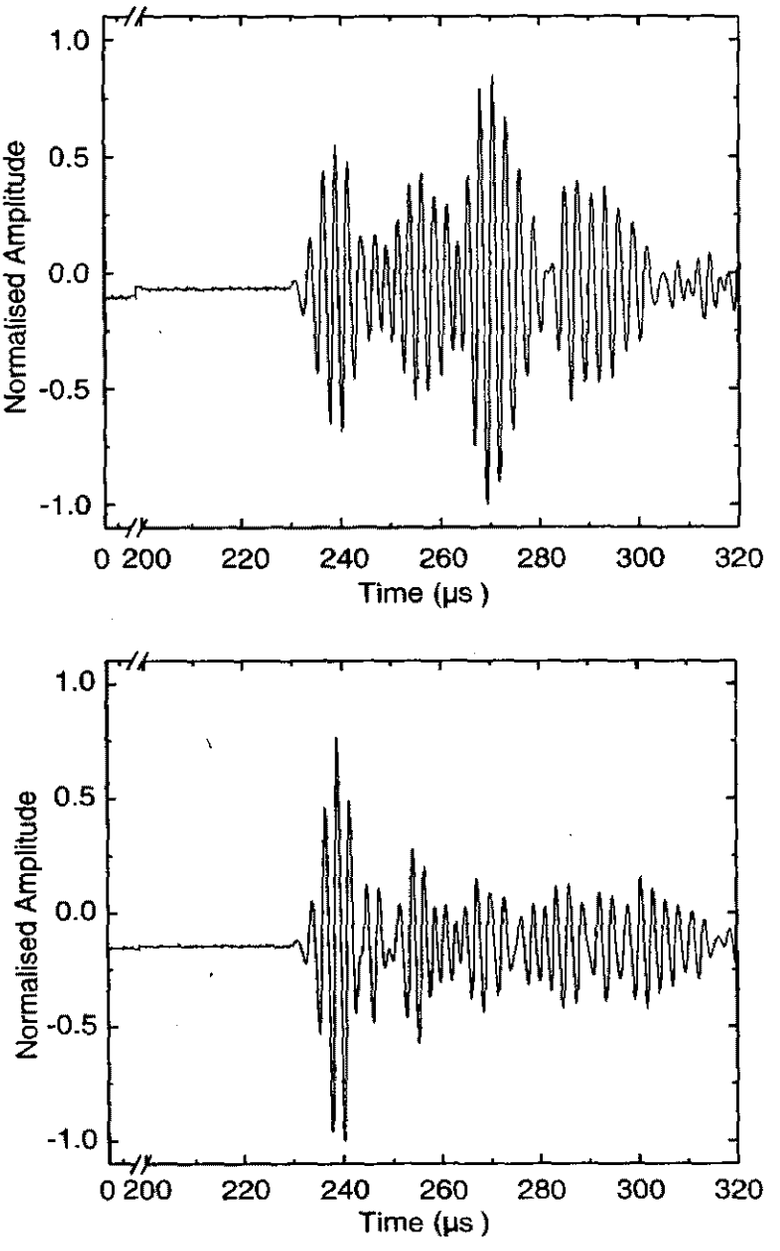

Figure 7 Sampled signals via *P*1–*P*3 for laminates made from unidirectional prepreg: (a) for benchmark laminate UD1# and (b) for defective laminate UD2#.

exhibited in Figure 9. The FFT analysis is able to provide an interrogation on the acquired signals in the diverse frequency ranges. In the spectra for UD2# and WF2#, extra frequency components, shaped as *spike*, could be noticed when compared with those for UD1# and WF1#. However, these characteristics or differences in either the time- or frequency-domain are not sufficient for quantitative identification of damage in the laminate. The signal processing principles proposed in Section 3 were applied and the wave components pertaining to the incident excitation were correctly extracted from raw acquired signals via DWT analyses. The filtered signals are displayed in Figure 10, where fundamental symmetric Lamb mode, S_0, and basic shear mode, S_0', together with the reflected components from the boundaries, denoted by $S_{0\text{ref}}$, can be orderly observed

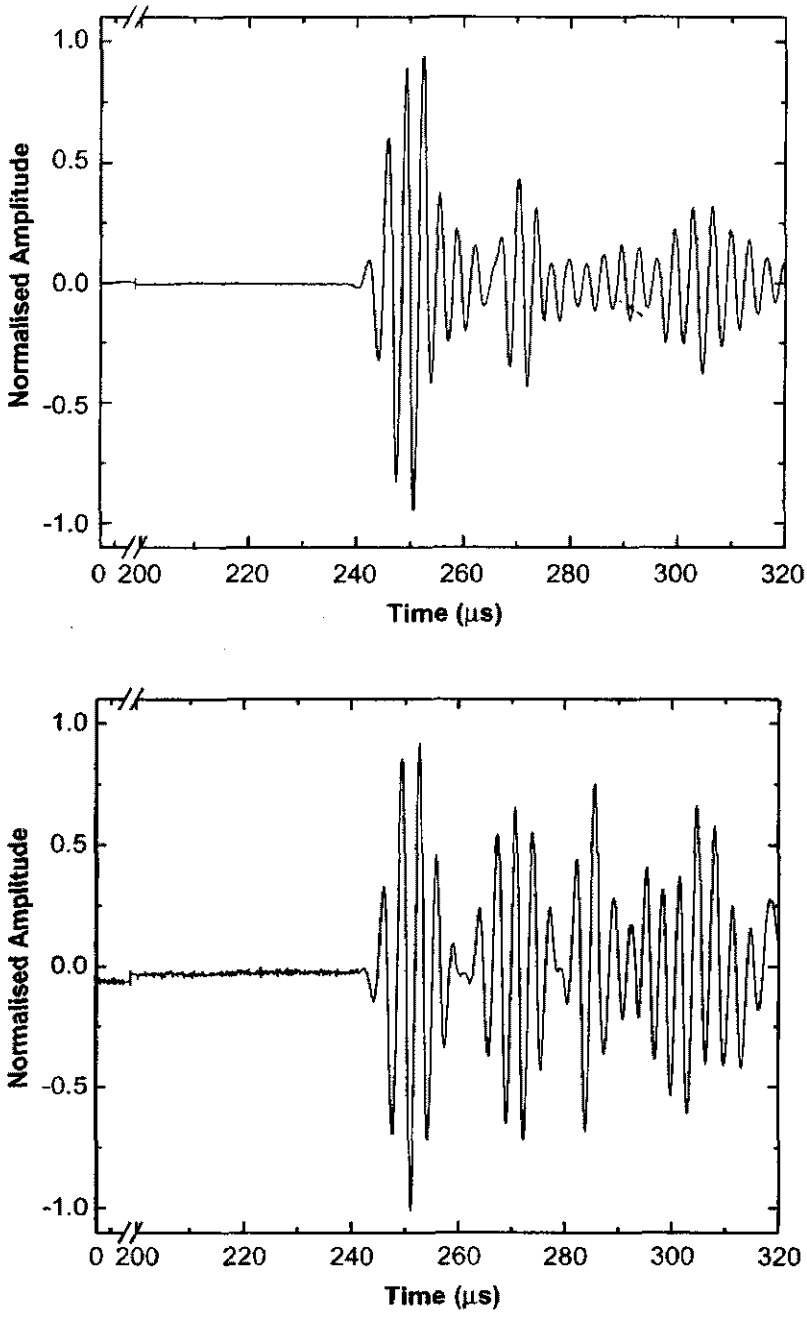

Figure 8 Sampled signals via *P2–P4* for laminates made from woven fabric prepreg: (a) for benchmark laminate WF1# and (b) for defective laminate WF2#.

within the selected frequency scope and time period. For identification purpose, only first several wave components in the acquired signals are useful while the rest may be corrupted by the boundary reflections. Compared with benchmark laminates, extra wave components between S_0 and S_{0ref} or following S_{0ref} were detected in Figure 10(b) and (d). In correlation with the study in Section 2, the extra components are recognised as the delamination-induced basic shear mode, S'_{0Delam}. The appearance order of the wave components in a signal is deterministically dependent on the relative locations among the delamination, boundaries and sensors. Herein, the *Sampling*

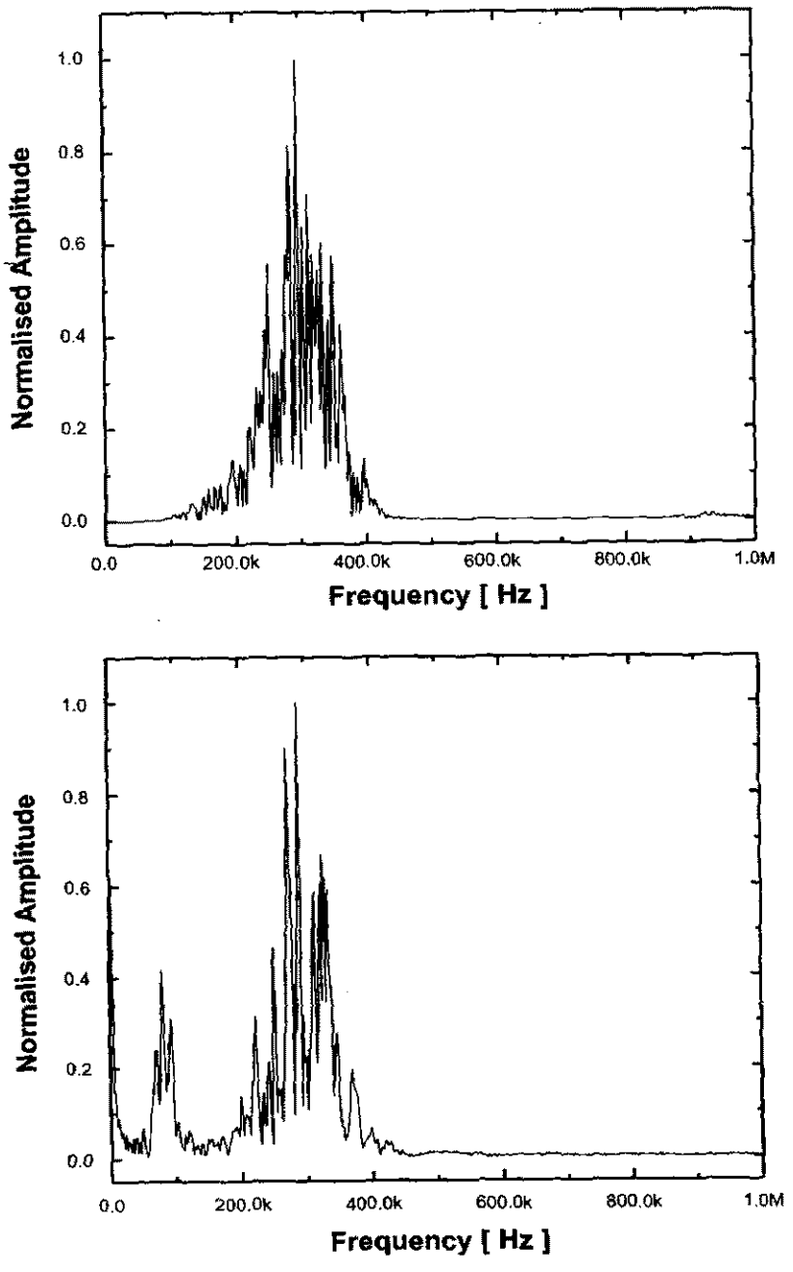

Figure 9 FFT analysis for paradigmatic signals shown in Figures 7 and 8: (a) for benchmark laminate UD1#; (b) for defective laminate UD2#; (c) for benchmark laminate WF1#; and (d) for defective laminate WF2#.

Point (SP) was introduced instead of the direct *Time Point* (TP) so as to expedite and facilitate the data processing in CCU.

Further, two- and three-dimensional spectrographic analyses based on the CWT technique were performed and relevant results for the paradigmatic signals are shown in Figures 11 and 12, respectively. In the two-dimensional spectra, the allocation of energy for various Lamb modes were calibrated by the CWT coefficients, represented by descending grayscale, where the darker the grayscale is, the higher the coefficients and the stronger the energy concentrates. In both two- and three-dimensional energy allocation plots, the defect-caused shear wave, $S'_{0\mathrm{Delam}}$, can visually be identified.

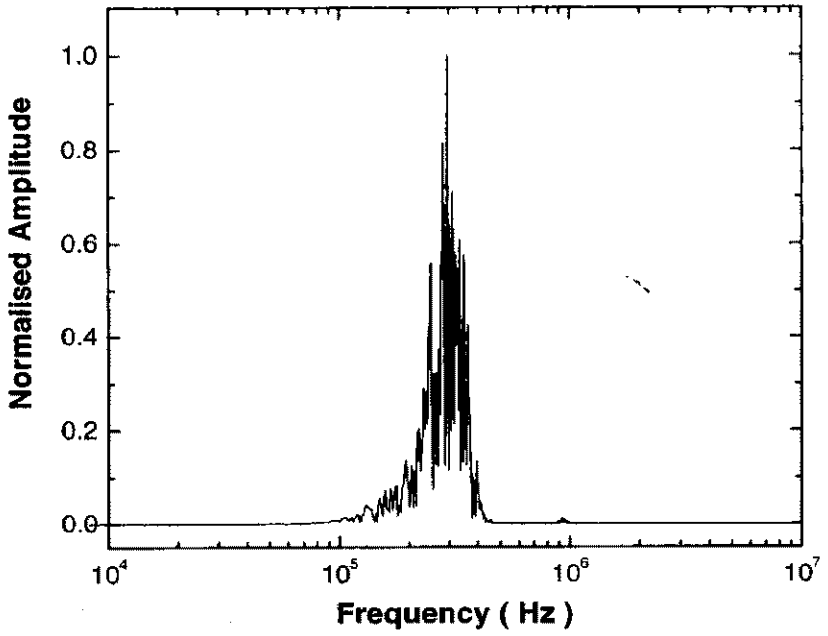

(c)

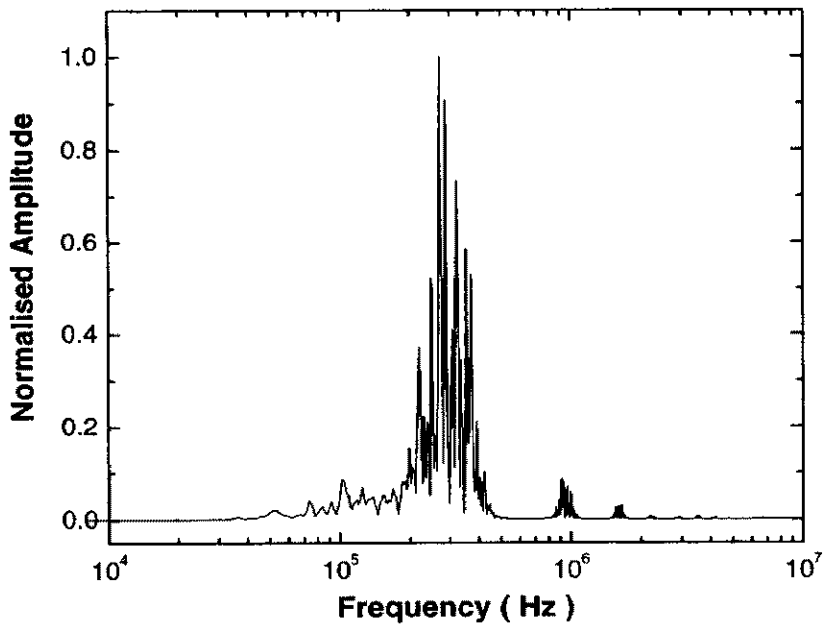

(d)

Figure 9 Continued.

The same geometric identity and delamination location were used in both numerical simulation and experimental analyses, which enables the comparison between the theoretical and experimental results. Representatively, the two- and three-dimensional CWT analyses for the signals from simulation, via the same actuator–sensor path $P1$–$P3$ for laminate UD2$^{\#}$ are displayed in Figure 13. Good correlation, in terms of the characteristic time and frequency for wave energy concentration, was found between the numerical simulation (Figure 13) and experimental measurements (Figures 11(b) and 12(b)), upon the application of signal processing.

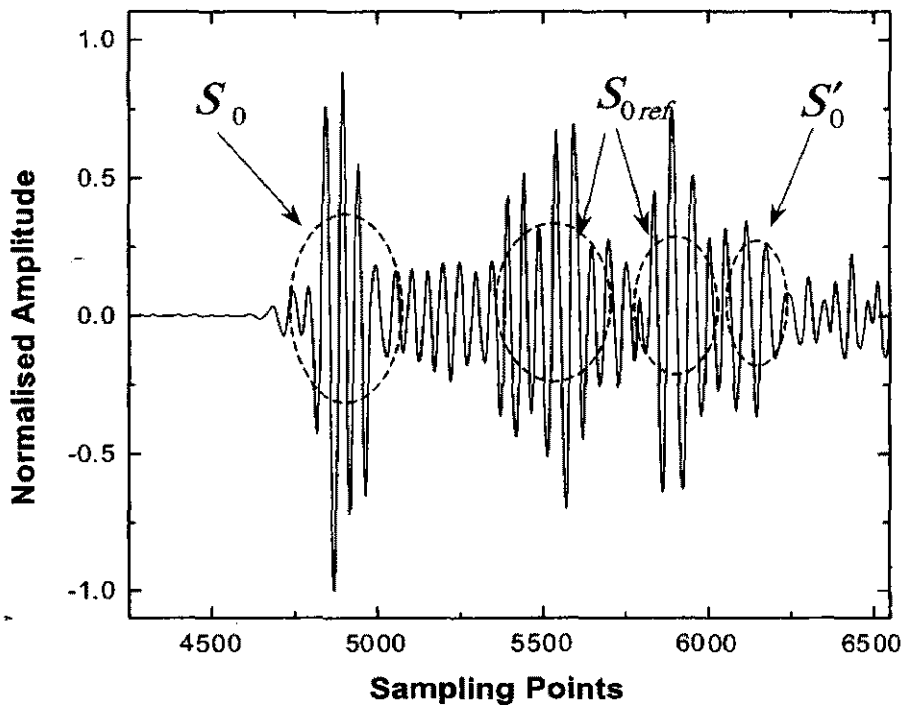

(a)

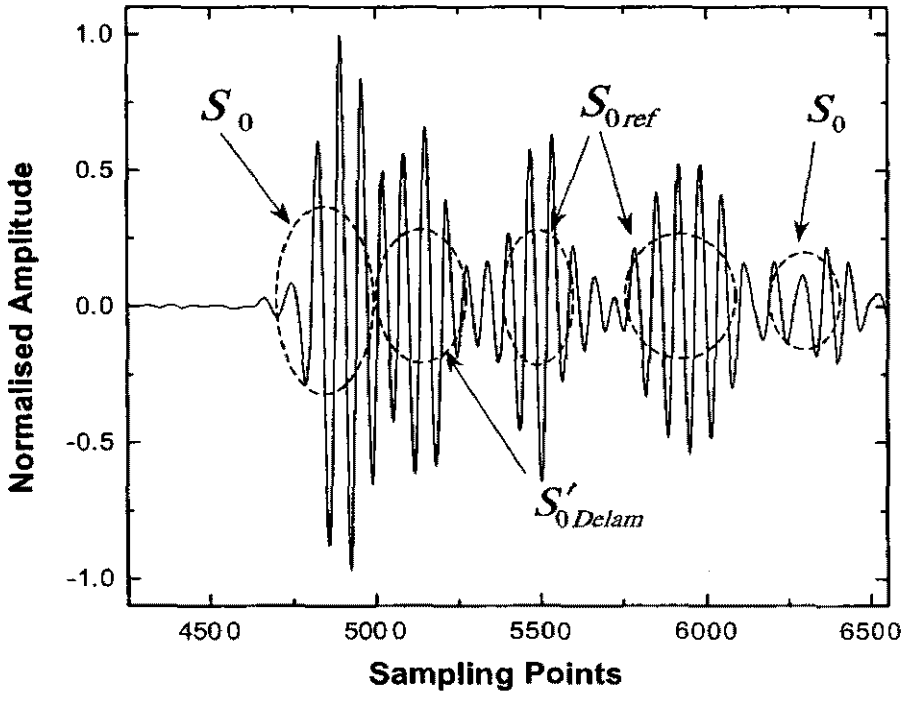

(b)

Figure 10 DWT analysis for paradigmatic signals shown in Figures 7 and 8: (a) for benchmark laminate UD1#; (b) for defective laminate UD2#; (c) for benchmark laminate WF1#; and (d) for defective laminate WF2#.

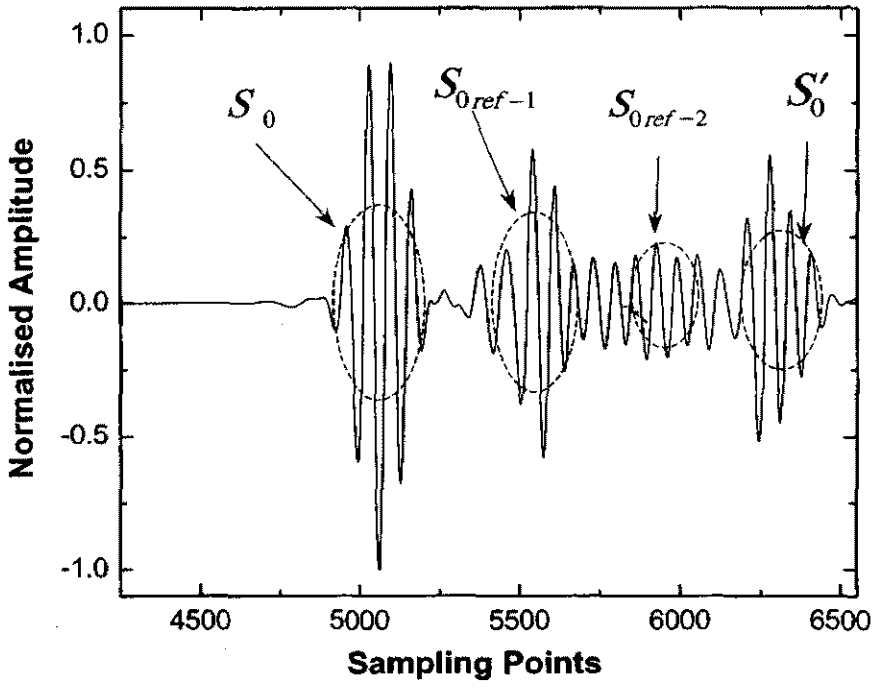

(c)

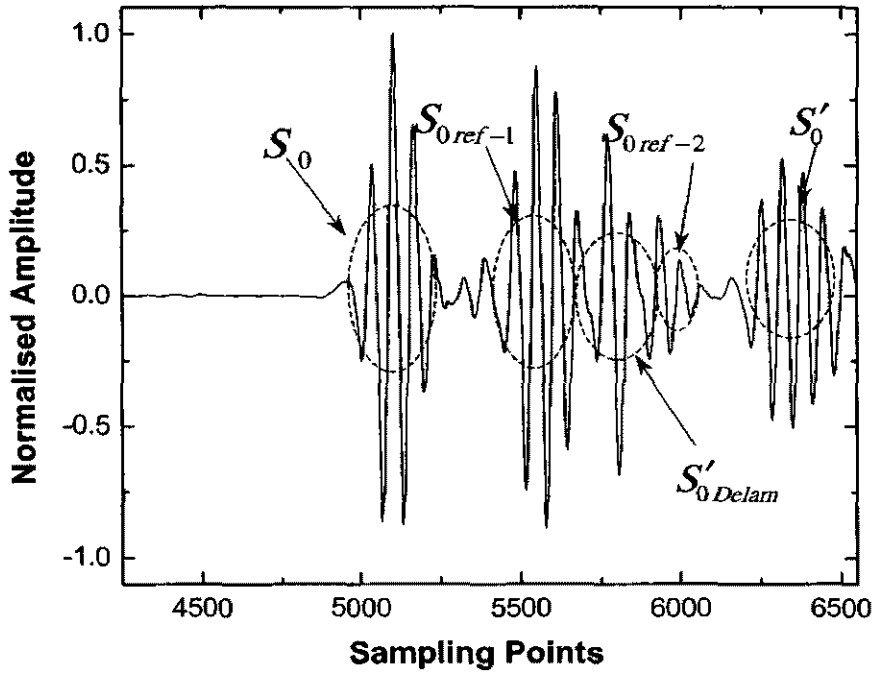

(d)

Figure 10 Continued.

4.2 Delamination Locating Algorithm

An internal structural damage locating algorithm based on the analyses conducted above was established. A preliminary searching for the possible and approximate delamination positions was executed to expedite the overall diagnosis, suggesting an initial point for the start of damage searching [27]. In this procedure, the whole

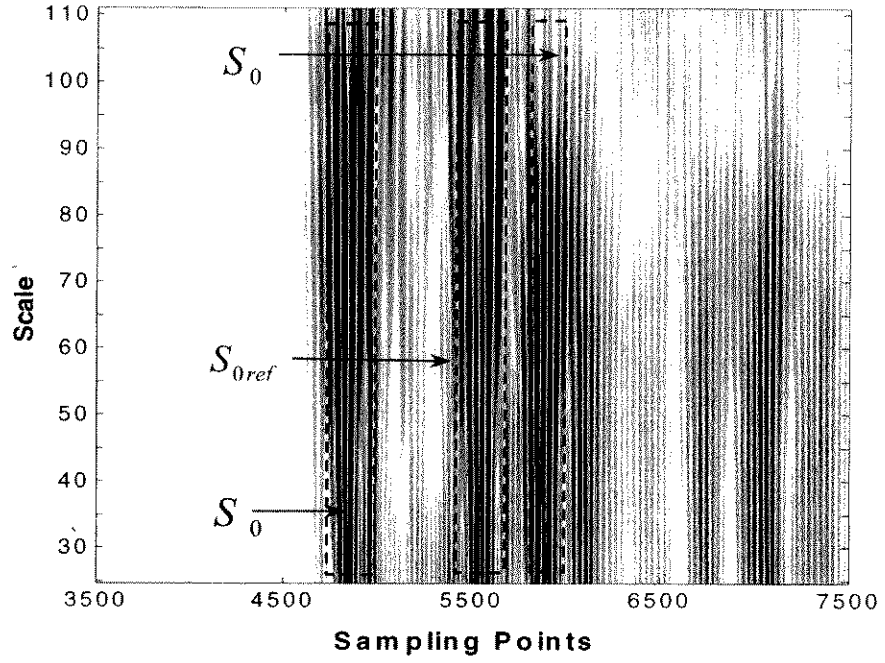

(a)

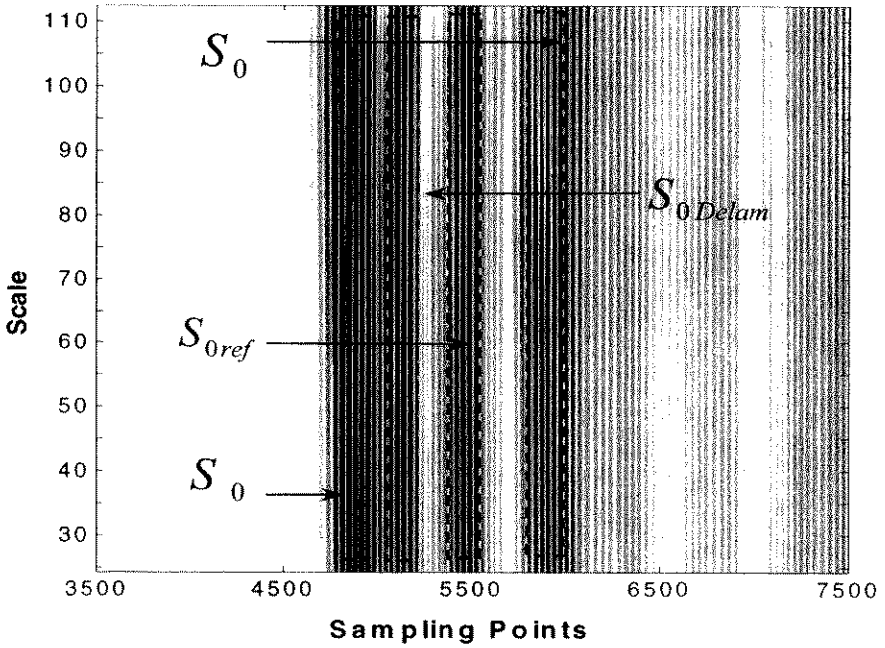

(b)

Figure 11 Two-dimensional CWT spectra for paradigmatic signals shown in Figures 7 and 8: (a) for benchmark laminate UD1#; (b) for defective laminate UD2#; (c) for benchmark laminate WF1#; and (d) for defective laminate WF2#.

laminate was supposed to be quartered evenly and the delamination was assumed to individually locate at the central position in each quadrant, respectively. The 3D dynamic FEM simulation was executed to calculate the relevant structural responses via concerned actuator–sensor paths under these presumed damage situations. The calculated signals were applied with DWT/CWT

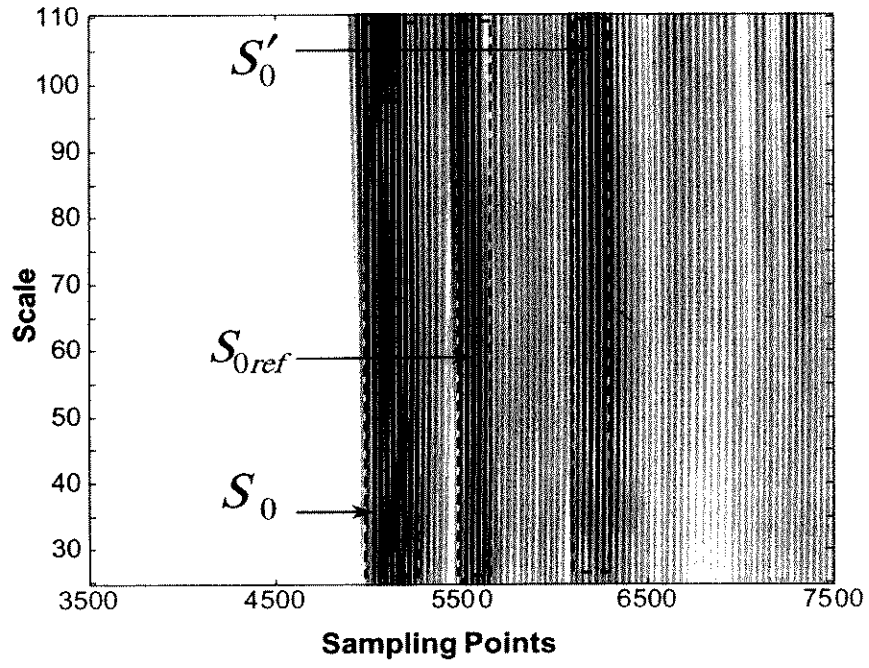

(c)

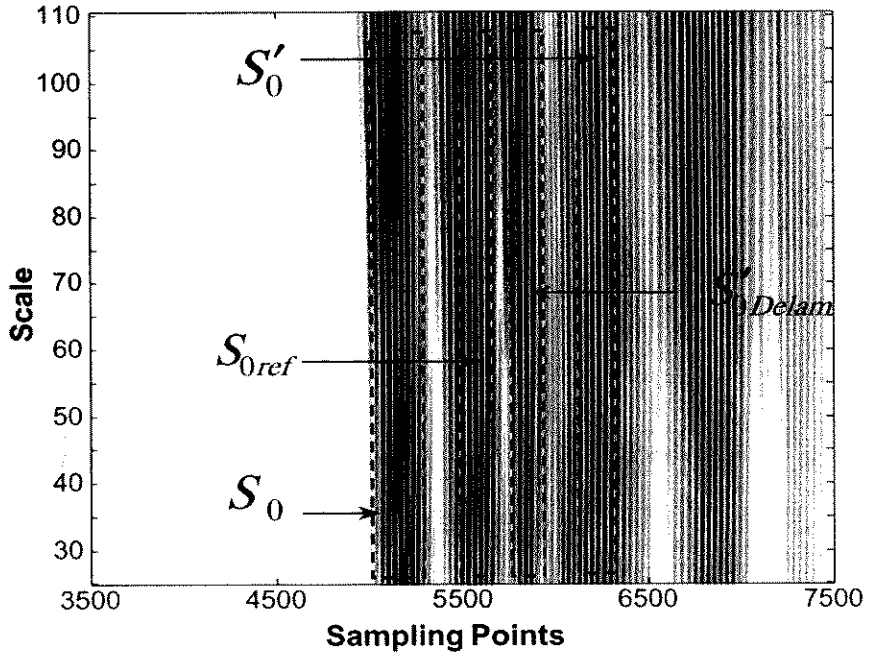

(d)

Figure 11 Continued.

analyses and then compared with the corresponding signals based on the experimental measurements. Least discrepancy indicated the most possible quadrant in which the damage might occur, where damage search should be concentrated. It was found that the damage searching and identification could be consequently simplified and expedited considerably through the preliminary estimation.

The time lags measured among concerned wave components from the DWT/CWT analyses were then used for the damage location

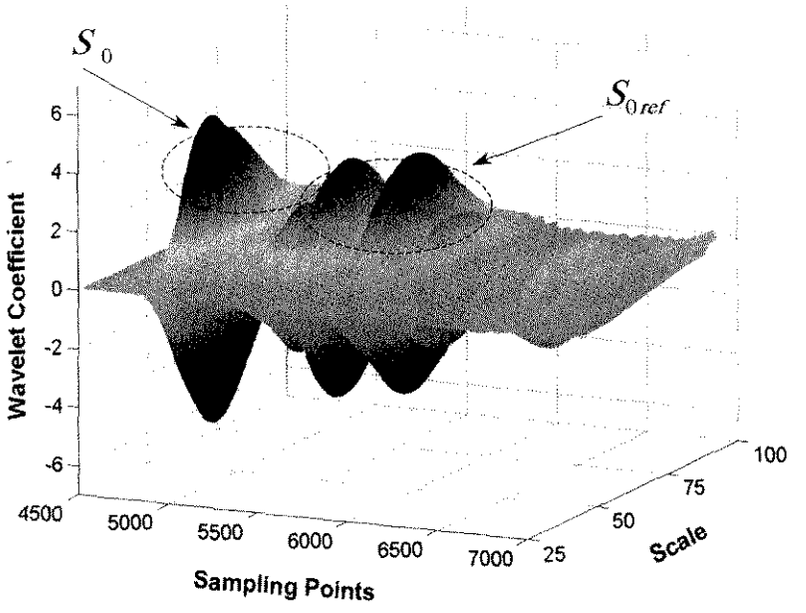

(a)

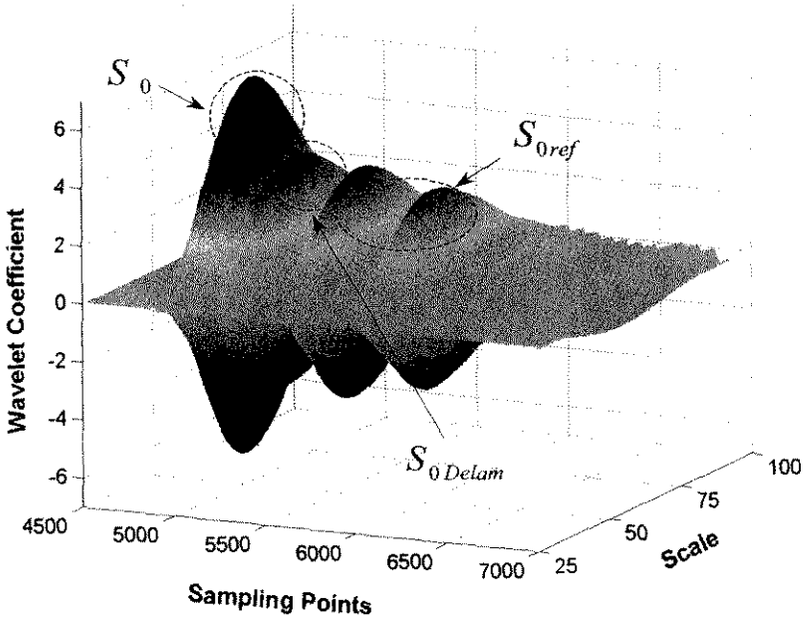

(b)

Figure 12 Three-dimensional CWT spectra for paradigmatic signals shown in Figures 7 and 8: (a) for benchmark laminate UD1#; (b) for defective laminate UD2#; (c) for benchmark laminate WF1#; and (d) for defective laminate WF2#.

identification. A searching algorithm based on a graphic optimisation [12,13,30,31] was devised. For example, in the case that the transducer $P1$ functioned as the actuator and the damage centre was supposed to locate at (x, y) (in the coordinate system that the actuator was the origin and the X-axis paralleled with the bottom edge of the laminate), a nonlinear set of equations can be

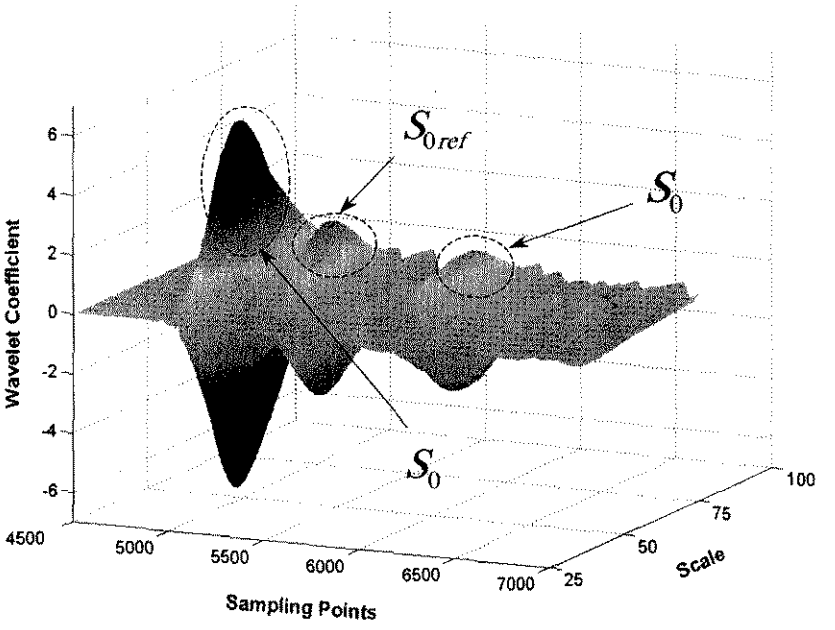

(c)

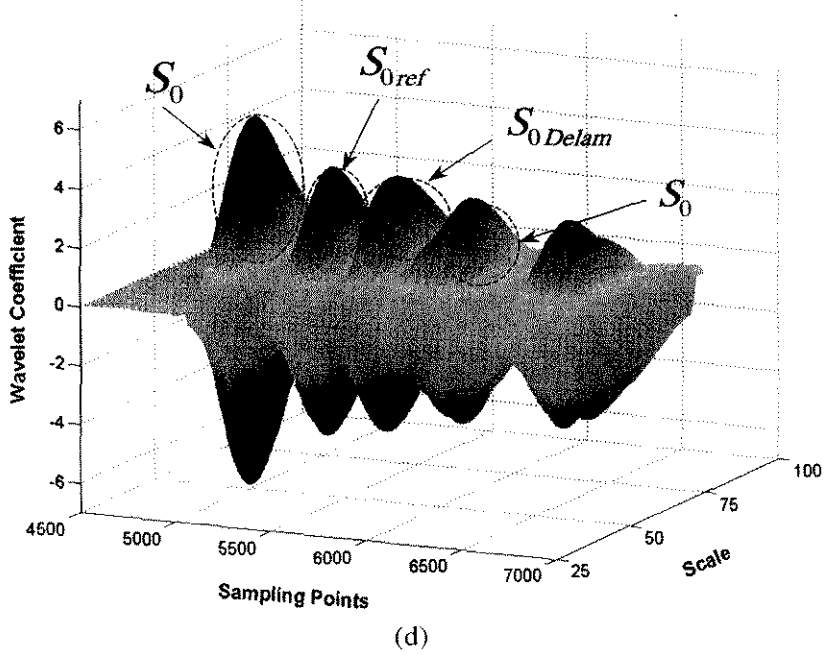

(d)

Figure 12 Continued.

established upon the relative distances among the transducers and the damage,

$$\frac{L_{A-D}}{V_{S_0}} + \frac{L_{D-S}}{V_{S'_{0\ \mathrm{Delam}}}} - \frac{L_{A-S}}{V_{S_0}} = T_{1-i} \quad (i = 2, 3, 4) \quad (6)$$

where L_{D-S}, L_{A-D} and L_{A-S} represent the distances between the damage centre (x, y) and the ith sensor, the selected actuator and the damage centre, the selected actuator and the ith sensor, respectively. $V_{S'_{0\mathrm{Delam}}}$ and V_{S_0} are the measured velocities of wave modes, $S'_{0\mathrm{Delam}}$ and S_0, respectively. T_{1-i} denotes the experimentally acquired time lag via actuator–sensor path P_1–P_i, by catching the characteristic times corresponding to the maximum/minimum energy concentration.

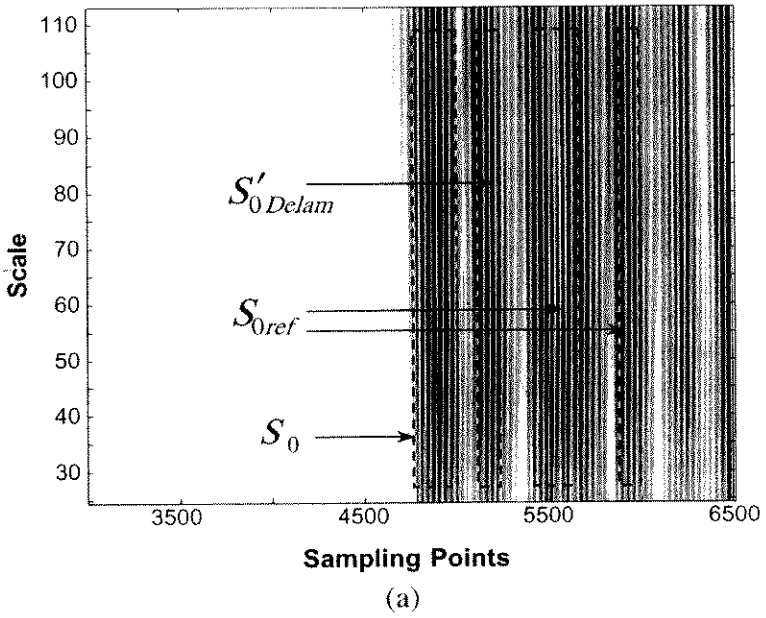

(a)

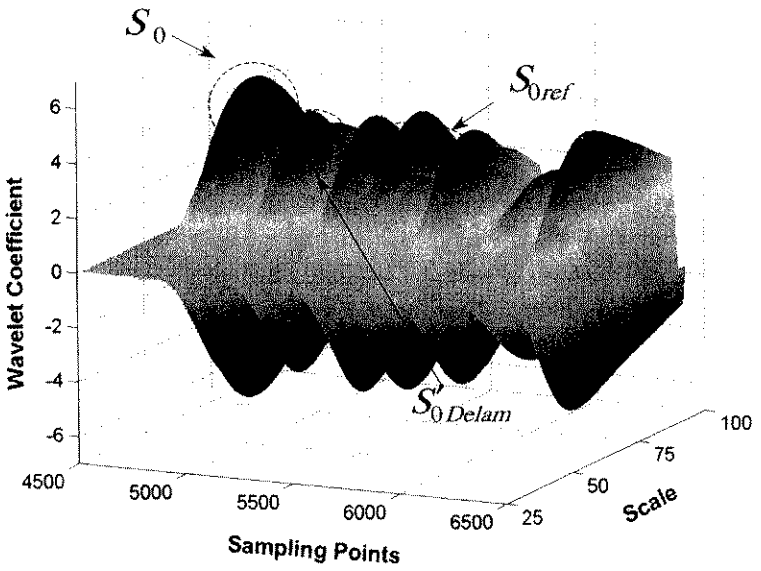

(b)

Figure 13 CWT spectra of simulated signal for UD2# via actuator–sensor path *P1–P3:* (a) two-dimensional and (b) three-dimensional.

In the referred Cartesian coordinate system, it has,

$$\begin{aligned} L_{D-S} &= \sqrt{(x - x_i)^2 + (y - y_i)^2} \\ L_{A-D} &= \sqrt{x^2 + y^2} \\ L_{A-S} &= \sqrt{x_i^2 + y_i^2} \\ i &= 1,\ 2,\ 3,\ 4 \end{aligned} \tag{7}$$

where (x_i, y_i) represents the coordinates of the ith transducer in the current coordinate system. In practice, some paths in the theoretically 12 actuator–sensor paths were unexploitable because multi-reflection of waves from boundaries may spoil the damage-induced wave components in the sampled signal, incapable of providing essential diagnostic information.

Analogously, a non-linear system consisting of four equation sets were established after four

coordinate systems introduced, in which each PZT actuator took a turn to be nominated as the origin of its reference frames, respectively. A mathematic optimal method [30] was applied to solve the nonlinear system, with which the nonlinear system can be solved graphically using an inhouse program, facilitating an accurate locating for the damage centre. The searching procedure is schematically explained in Figure 14. In these diagrams, the signal acquired via each individual actuator–sensor path is contributing to the construction of one equation based on Equations (6) and (7). Involving the damage coordinates (x, y), each equation graphically indicates the locus for the possible damage locations, denoted by the dash-and-dot line in the figures. The intersection, taking into account the loci from all the available actuator–sensor paths, is recognised as the most possible position where damage occurs.

5 Discussion

The diagnosis results and estimation errors are summarised in Table 2. It is clear that the errors decrease with the increase of actuator–sensor paths involved for the damage identifying, while 4 paths are the minimum mathematic requirement to solve the nonlinear equation system. However, the more the paths were employed, the more time on experimental measurement was consumed. A compromise between expected accuracy and affordable efforts should be accordingly synchronised for actual applications. It is noted that a satisfactory accuracy can be ensured upon half of the total actuator–sensor paths involved.

In this study, it was found that a satisfactory accuracy for the location detection could be achieved when 4 PZT transducers were used, while the information that they can offer is yet not adequate for the identification of damage shape and size. The relationship between transducer numbers and detectable damage parameters is investigated in another study [21] by comparing a diversity of designed transducer networks.

During the experiment, the estimation errors were also noticed to be dependent on the interlaminar location of the delamination. The closer to the upper or bottom surfaces the delamination is located, the stronger the perturbance was detected in the signals, facilitating a precise detection. This deduction has also been theoretically demonstrated [2], in which the damage-induced shear stress, σ_{XZ} or σ_{YZ}, exists when the delamination situates between any two layers, except in the middlemost of the laminate, which has less influence on the propagation of Lamb waves. On the other hand, compared with the laminates made from unidirectional prepreg, relatively larger estimation errors were obtained for the laminates made from woven fabric prepreg, which may be attributed to the relatively complicated effect of woven fabric structures on the propagation of Lamb waves.

In this study, the benchmarks were introduced in both numerical simulation and experimental verification, to avoid any disturbance from boundary effects, etc. During the comparison between benchmark and defective laminates or the comparison between FEM simulation and experiment, certain distinction or incomplete agreement could also be noticed in addition to the delamination-induced extra wave components, which is attributed to the imperfect similarity of two individual laminates in manufacturing or discrepancy between theoretical emulation and laboratorial measurement. For detection based on a *forward* analysis, the information from benchmark is therefore essential, and more accurate identification is expected to be accomplished when the comparison of signals from the same laminate before and after the occurrence of damage can be conducted. While an *inverse* identification approach, independent of the benchmark, is developed [21,28] using artificial neural network algorithm to overcome this hindrance.

Undergoing the dispersion phenomenon, distortion of the incident diagnostic waveform could not be avoided in experiment, reducing the diagnosis precision to certain extent. Different diagnostic waveforms, 1-cycle, 3-cycle, 5-cycle, 7-cycle and 10-cycle windowed toneburst as well as pulse excitation, at different central frequencies, from 0.15 to 1.0 MHz, were conducted for comparison, respectively. The results show that the SNR (Signal-to-Noise Ratio) increases as the signal central frequency increases, consequently making the identification more accurate.

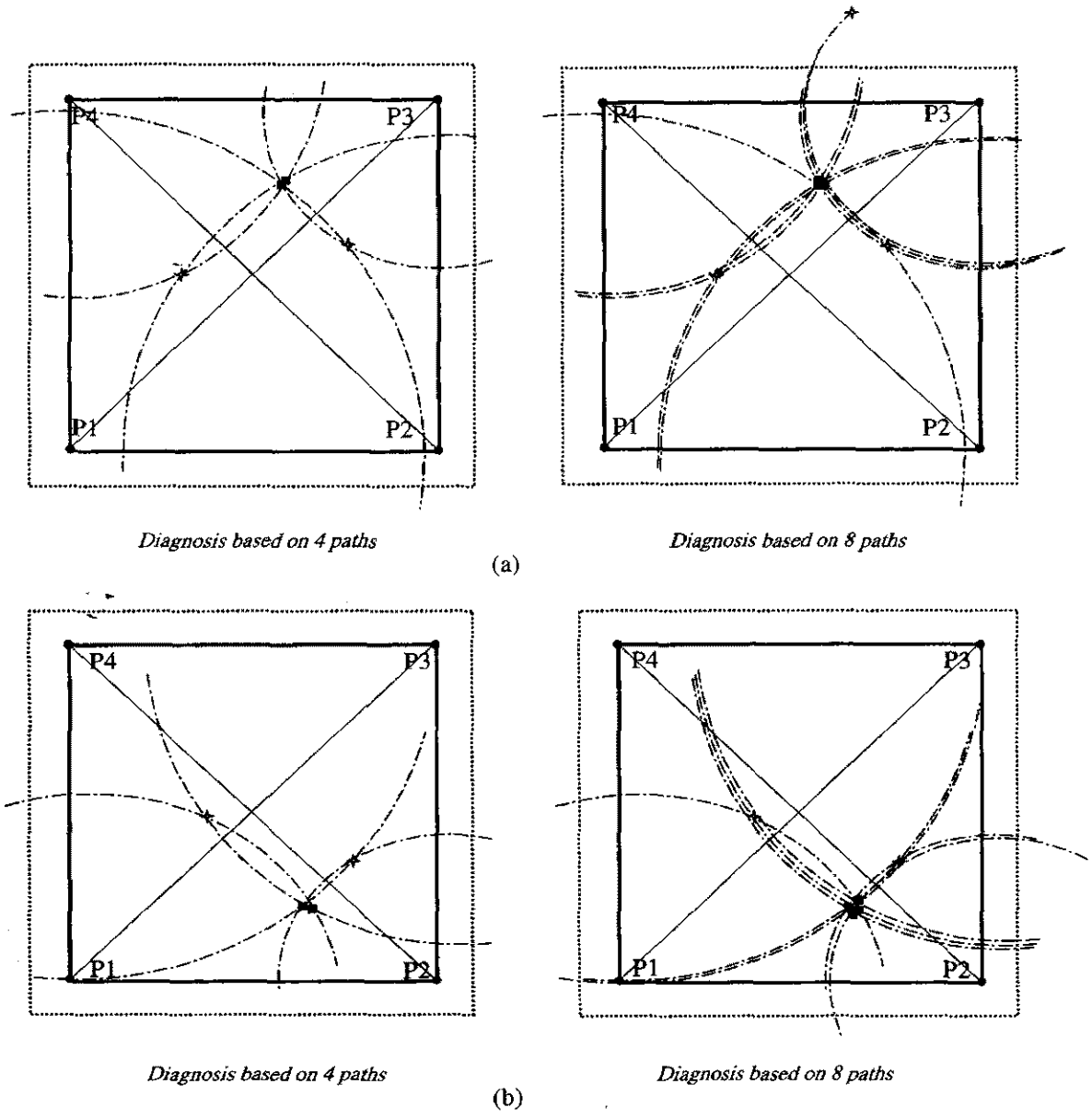

Figure 14 Delamination locating: (a) for specimen UD2# and (b) for specimen WF2#.

Table 2 Diagnosis results and estimation errors (Unit: mm).

	Based on 4 Paths		*Based on 6 Paths*		*Based on 8 Paths*	
Specimen	*Diagnostic Result**	*Relative Error (%)*	*Diagnostic Result**	*Relative Error (%)*	*Diagnostic Result**	*Relative Error (%)*
UD1#	(312, 266)	13.0	(293, 316)	6.8	(262, 313)	4.8
WF2#	(311, 218)	16.5	(249, 204)	7.7	(285, 201)	6.9

*The vertical distances away from the left and bottom edges of the laminates, respectively.

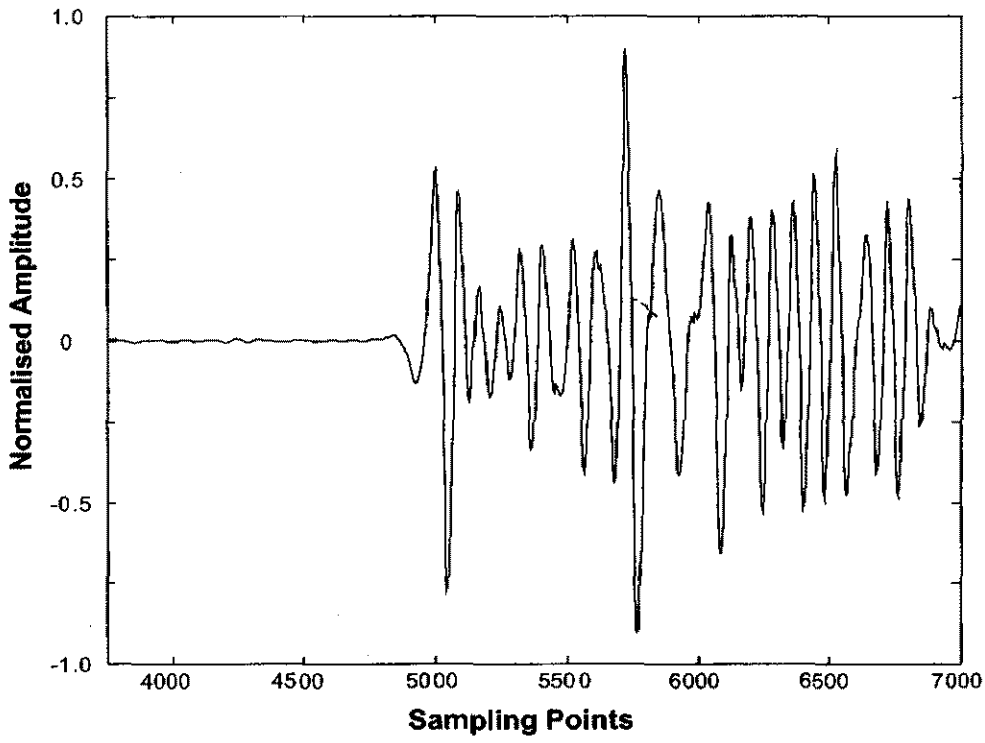

(a)

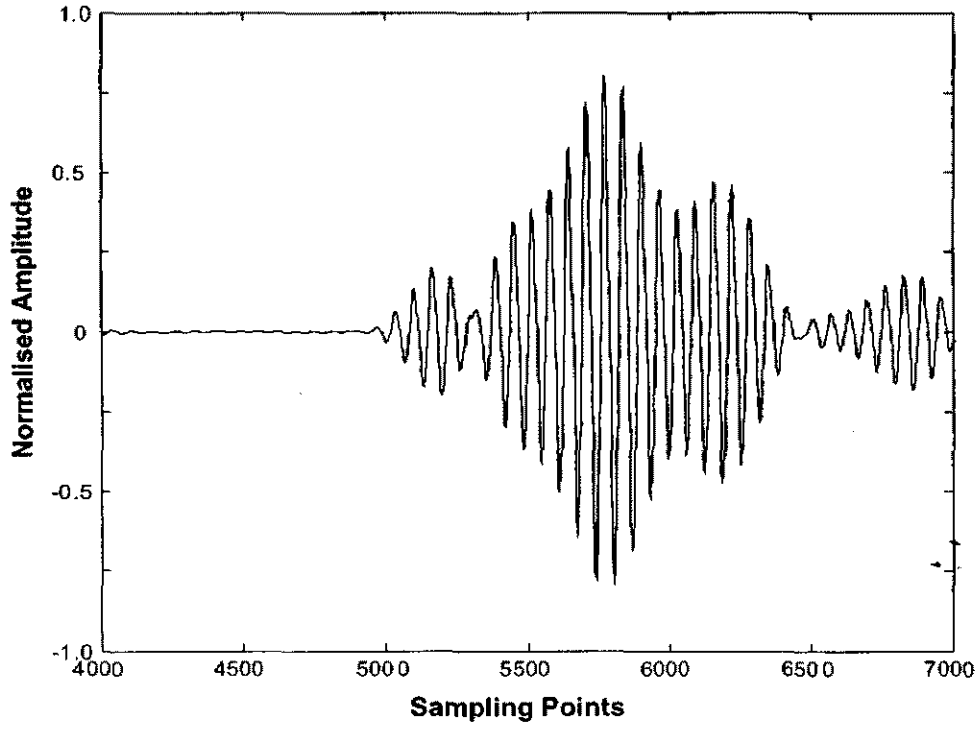

(b)

Figure 15 DWT analysis for structural responses under different excitations: (a) excited by pulse-excitation at 0.5 MHz and (b) excited by 10-cycle toneburst at 0.35 MHz.

However, synchronously, the high frequency weakens the capability of Lamb wave to propagate in the composites due to the attenuation mechanism. Meanwhile, it was also heeded that the high cycle number of toneburst may lower the risk of signal distortion. But an accompanying superposition of multiple wave modes occurs due to the large bandwidth, leading to the confusion in signal interpretation. As an example, the structural responses corresponding to the pulse-excitation at a central frequency of 0.5 MHz and 10-cycle *Hanning* windowed toneburst at a central frequency of 0.35 MHz were processed with DWT analyses and given in Figure 15, where evident distortion of the incident pulse excitation can be noticed in Figure 15(a), while immersion and superposition of multiplicate Lamb modes appear in Figure 15(b). Both the distortion and superposition make it more difficult to extract useful diagnostic components. In experiments, satisfactory resolution and accuracy could be met for the present system when 5-cycle toneburst in the central frequencies of 0.3–0.5 MHz was used.

6 Conclusion

A Lamb wave-based delamination locating approach was developed using the propagation characteristics of Lamb waves in laminated composites involving a delamination. An active diagnosis system using distributed piezoelectrics was consequently established, and it was then experimentally validated by identifying delaminations in CF/EP laminates made from unidirectional and woven fabric prepreg, respectively. It is shown that satisfactory diagnosis can be achieved by analysing the acquired scattering signal using the wavelet transform technique-based identification algorithm. Identification errors in damage location depend on the number of actuator–sensor paths to be used for diagnosis, and satisfactory precision can be obtained when half of the total actuator–sensor paths are taken into account. An algorithm based on a graphic approach was applied on solving the nonlinear equation system, to fulfill an accurate identification. Additionally, the strong reliance of the estimation accuracy on excitation waveforms and bandwidth was noticed. The present work is aimed at an active online damage assessment technique with hybrid numerical and experimental approaches, capable of continuously monitoring the structural integrity.

Acknowledgement

Part of the FEM simulation presented in the work was carried out through the APAC services provided by the *Australian National University*. Z.Su would like to gratefully acknowledge the support of the *International Postgraduate Research Scholarship* (IPRS) from the *Department of Education Science, and Training* (DEST), Australia, and the *International Postgraduate Award* (IPA) from the *University of Sydney*.

References

1. Badcock, R.A. and Birt, E.A. (2000). The use of 0–3 piezocomposite embedded Lamb wave sensors for detection of damage in advanced fibre composites. *Smart Materials and Structures, 9*, 291–297.
2. Percival, W.J. and Birt, E.A. (1997). A study of Lamb wave propagation in carbon-fibre composites. *Insight, 39*, 728–735.
3. Guo, N. and Cawley, P. (1992). Lamb waves for the NDE of composite laminates. In: Thompson, D.O. and Chimenti, D.E. (eds.), *Review of Progress in Quantitative Nondestructive Evaluation*, Vol. 11, (pp. 1443–1450). Plenum, New York.
4. Guo, N. and Cawley, P. (1993). The interaction of Lamb wave with delaminations in composite laminates. *Journal of the Acoustical Society of America, 94*, 2240–2246.
5. Guo, N. and Cawley, P. (1993). Lamb wave propagation in composite laminates and its relationship with acousto-ultrasonics. *NDT & E International, 26*, 75–84.
6. Guo, N. and Cawley, P. (1994). Lamb wave reflection for the quick nondestructive evaluation of large composite laminates. *Materials Evaluation, 52*, 404–411.
7. Alleyne, D.N. and Cawley, P. (1992). The interaction of Lamb waves with defects. *IEEE Transactions on Ultrasonics, Ferroelectrics and Frequency Control, 39*, 381–397.
8. Tan, K.S., Guo, N., Wong, B.S. and Tui, C.G. (1995). Experimental evaluation of delaminations in composite plates by the use of Lamb waves. *Composites Science and Technology, 53*, 77–84.

9. Tang, B. and Henneke, E.G. (1989). Lamb-wave monitoring of axial stiffness reduction of laminated composite plates. *Materials Evaluation, 47*, 928–934.
10. Legendre, S., Massicotte, D., Goyette, J. and Bose, T.K. (2000). Wavelet-transform-based method of analysis for lamb-wave ultrasonic NDE signals. *Journal of IEEE, 49*, 524–530.
11. Wang, C.S. and Chang, F.-K. (1999). Built-in diagnostics for impact damage identification of composite structures. In: Chang, F.-K., (ed.), *Structural Health Monitoring* (pp. 612–621), 2nd ed. Lancaster: Technomic.
12. Lemistre, M., Gouyon, R., Kaczmarek, H. and Balageas, D. (1999). Damage localization in composite plates using wavelet transform processing on Lamb wave signals. In: Chang, F.-K. (ed.), *Structural Health Monitoring* (pp. 861–870), 2nd ed., Lancaster: Technomic.
13. Gaul, L. and Hurlebaus, S. (1999). Wavelet-transform to identify the location and force-time-history of transient load in a plate. In: Chang, F.-K. (ed.), *Structural Health Monitoring* (pp. 851–860), 2nd ed., Lancaster: Technomic.
14. Islam, A.S. and Craig, K.C. (1994). Damage detection in composite structures using piezoelectric materials. *Smart Materials and Structures, 3*, 318–328.
15. Inada, T., Shimamura, Y., Todoroki, A., Kobayashi, H. and Nakamura, H. (1999). Damage identification method for smart composite cantilever beams with piezoelectric materials. In: Chang, F.-K. (ed.), *Structural Health Monitoring* (pp. 986–994), 2nd ed. Lancaster: Technomic.
16. Wisnom, M.R. and Chang, F.-K. (2000). Modelling of splitting and delamination in notched cross-ply laminates. *Composites Science and Technology, 60*: 2849–2856.
17. Rose, J.L. (1999). *Ultrasonic waves in solid media*. Cambridge: Cambridge University Press.
18. Bull, J.W. (1996). *Numerical analysis and modelling of composite materials*. London: Blackie Academic & Professional.
19. *ABAQUS User's Manual*, Version: 6.2. (2001). Hibbitt, Karlsson and Sorensen, Inc.
20. Gommers, B., Verpoest, I. and Houtte, P.V. (1996). Modelling the elastic properties of knitted fabric-reinforced composites. *Composites Science and Technology, 56*, 685–694.
21. Su, Z. and Ye, L. (2003). Lamb wave propagation-based damage identification for quasi-isotropic composite laminates using artificial neural algorithm, Part I: methodology and database development. (submitted to *Journal of Intelligent Material Systems and Structures*).
22. Chan, Y.T. (1995). *Wavelet basic*. Boston: Kluwer Academic Publishers.
23. Newland, D.E. (1994). Wavelet analysis of vibration, Part I: theory. *Journal of Vibration and Acoustics, 116*, 409–425.
24. Boashash, B. (1992). *Time-frequency signal analysis*. Melbourne: Longman Cheshire.
25. Abbate, A., Koay, J., Frankel, J., Schroeder, S.C. and Das, P. (1997). Signal detection and noise suppression using a wavelet transform signal processor: application to ultrasonic flaw detection. *Journal of IEEE, 44*, 14–25.
26. Chui, C.K. (1997). *Wavelet: a mathematical tool for signal processing*. Philadelphia: SIAM.
27. Su, Z. and Ye, L. (2002). A damage identification technique for CF/EP composite laminates using distributed piezoelectric transducers. *Composite Structures, 57*: 465–471.
28. Su, Z. and Ye, L. (2002). Quantitative damage prediction for composite laminates based on wave propagation and artificial neural algorithm. Presented in *Australian Inaugural Workshop on Structural Health Monitoring*, 25–26, November, 2002, Melbourne, Australia.
29. The Mathworks, Inc. (2001). *Wavelet Toolbox User's Manual*. Ver.1.0.
30. The Mathworks, Inc. (2001). *Optimisation Toolbox User's Manual*. Ver. 2.0.
31. Su, Z., Ye, L. and Bu, X. (2002). Evaluation of delamination in laminated composites based on Lamb wave modes: FEM simulation and experimental verification. In: Balageas, Daniel (ed.), *Proceedings of the 1st European Workshop on Structural Health Monitoring* (pp. 328–335), 10–12 July, 2002, Paris, France.